

1. Report No. <i>FHWA/TX-94+1234-3F</i>		2. Government Accession No.		3. Recipient's Catalog No.	
4. Title and Subtitle <i>MEASUREMENT BASED REVISIONS FOR SEGMENTAL BRIDGE DESIGN AND CONSTRUCTION CRITERIA</i>				5. Report Date <i>August 1993</i>	
				6. Performing Organization Code	
7. Author(s) <i>C. L. Roberts, J. E. Breen, and M. E. Kreger</i>				8. Performing Organization Report No. <i>Research Report 1234-3F</i>	
9. Performing Organization Name and Address <i>Center for Transportation Research The University of Texas at Austin 3208 Red River, Suite 200 Austin, Texas 78705-2650</i>				10. Work Unit No. (TRAIS)	
				11. Contract or Grant No. <i>Research Study 0-1234</i>	
12. Sponsoring Agency Name and Address <i>Texas Department of Transportation Research and Technology Transfer Office P. O. Box 5051 Austin, Texas 78763-5051</i>				13. Type of Report and Period Covered <i>Final</i>	
				14. Sponsoring Agency Code	
15. Supplementary Notes <i>Study conducted in cooperation with the U.S. Department of Transportation, Federal Highway Administration Research Study Title: "Instrumentation of Segmental Box Girder Bridges and Multipiece Winged Boxes"</i>					
16. Abstract <i>This report is the second and final in a series reporting the field study of several spans of the San Antonio "Y" project. The San Antonio "Y" project is a major urban viaduct comprising segmental concrete box girders post-tensioned with a mix of internal and external tendons and erected using span-by-span techniques. The instrumentation program targeted areas of segmental design and construction which are still uncertain due to lack of laboratory and field data or are still debated by designers and constructors. The targeted areas of uncertainty were:</i> <ol style="list-style-type: none"> <i>(1) Prestress losses in external tendons,</i> <i>(2) Distribution of stresses across flanges,</i> <i>(3) Thermal gradients and their effects,</i> <i>(4) Behavior of segmental joints,</i> <i>(5) Heavy end diaphragm behavior,</i> <i>(6) Deviator behavior,</i> <i>(7) Behavior under construction and live loads, and</i> <i>(8) Thermal gradients during match casting.</i> <i>Each topic is presented in an individual chapter which includes a literature review, a description of the instrumentation system, presentation of the results, analysis and comparison with current design methods, and recommendations for improvement of current design and construction criteria.</i>					
17. Key Words <i>post-tensioned, concrete, segmental, box-girder bridges, instrumentation, field measurements, external tendons, prestress losses, thermal gradients, end diaphragms, deviators</i>			18. Distribution Statement <i>No restrictions. This document is available to the public through the National Technical Information Service, Springfield, Virginia 22161.</i>		
19. Security Classif. (of this report) <i>Unclassified</i>		20. Security Classif. (of this page) <i>Unclassified</i>		21. No. of Pages <i>378</i>	22. Price

**MEASUREMENT BASED REVISIONS FOR SEGMENTAL
BRIDGE DESIGN AND CONSTRUCTION CRITERIA**

by

C.L. Roberts, J.E. Breen and M.E. Kreger

Research Report No. 1234-3F

**Research Project 3-5-90/3-1234
"Instrumentation of Segmental Box Girder Bridges
and Multipiece Winged Boxes"**

Conducted for the

**Texas
Department of Transportation**

**In Cooperation with the
U.S. Department of Transportation
Federal Highway Administration**

by the

**CENTER FOR TRANSPORTATION RESEARCH
BUREAU OF ENGINEERING RESEARCH
THE UNIVERSITY OF TEXAS AT AUSTIN**

August 1993

IMPLEMENTATION

This report provides detailed information on state-of-the-art instrumentation systems for use in the field study of segmental concrete bridges. The recommendations have already been used successfully in the instrumentation of four spans of the San Antonio "Y" Project. The recommendations are readily applicable to the study of similar segmental bridges erected using span-by-span techniques. The information can also be adapted to the field study of other types of segmental and conventional bridge structures. The results of the study should assist bridge engineers and research agencies to efficiently plan instrumentation programs for future bridge projects. Resulting savings from dependable observation programs should be possible through improvement of design and construction standards.

Prepared in cooperation with the Texas Department of Transportation and the U.S. Department of Transportation, Federal Highway Administration.

The contents of this report reflect the views of the authors who are responsible for the facts and accuracy of the data presented herein. The contents do not necessarily reflect the official views or policies of the Federal Highway Administration or the Texas Department of Transportation. This report does not constitute a standard, specification or regulation.

There was no invention or discovery conceived or first actually reduced to practice in the course of or under this contract, including any art, method, process, machine, manufacture, design or composition of matter, or any new and useful improvement thereof, or any variety of plant which is or may be patentable under the patent laws of the United States of America or any foreign country.

NOT INTENDED FOR CONSTRUCTION,
BIDDING OR PERMIT PURPOSES

John E. Breen, P.E. (Texas No. 18479)
Michael E. Kreger, P.E. (Texas No. 65541)
Research Supervisors

The United States Government and the State of Texas do not endorse products or manufacturers. Trade or manufacturers' names appear herein solely because they are considered essential to the object of this report.

APPROXIMATE CONVERSIONS TO METRIC MEASURES				
Symbol	When you know..	multiply by	To find...	Symbol
<u>LENGTH</u>				
in.	inches	2.5	centimeters	cm
ft.	feet	30	centimeters	cm
yd	yards	0.9	meters	m
mi	miles	1.6	kilometers	km
<u>AREA</u>				
in ²	square inches	6.5	square centimeters	cm ²
ft ²	square feet	0.09	square meters	m ²
yd ²	square yards	0.8	square meters	m ²
mi ²	square miles	2.6	square kilometers	km ²
	acres	0.4	hectares	ha
<u>MASS (weight)</u>				
oz.	ounces	28	grams	g
lb.	pounds	0.45	kilograms	kg
	short tons (2000 lbs.)	0.9	tonnes	t
<u>VOLUME</u>				
tsp	teaspoons	6	milliliters	ml
tbsp.	tablespoons	15	milliliters	ml
fl. oz.	fluid ounces	30	milliliters	ml
c	cups	0.24	liters	l
pt	pints	0.47	liters	l
qt	quarts	0.95	liters	l
gal.	gallons	3.8	liters	l
ft. ³	cubic feet	0.03	cubic meters	m ³
yd ³	cubic yards	0.76	cubic meters	m ³
<u>TEMPERATURE (exact)</u>				
°F	Fahrenheit temperature	5/9 (after subtracting 32)	Celsius temperature	°C

APPROXIMATE CONVERSIONS FROM METRIC MEASURES				
Symbol	When you know..	multiply by	To find...	Symbol
<u>LENGTH</u>				
mm	millimeters	0.04	inches	in.
cm	centimeters	0.4	inches	in.
m	meters	3.3	feet	ft.
m	meters	1.1	yards	yd.
km	kilometers	0.6	miles	mi.
<u>AREA</u>				
cm ²	square centimeters	0.16	square inches	in ²
m ²	square meters	1.2	square yards	yd ²
km ²	square kilometers	0.4	square miles	mi ²
ha	hectares (10,000 m ²)	2.5	acres	
<u>MASS (weight)</u>				
g	grams	0.035	ounces	oz.
kg	kilograms	2.2	pounds	lb.
t	tonnes (1000 kg)	1.1	short tons	
<u>VOLUME</u>				
ml	milliliters	0.03	fluid ounces	fl. oz.
l	liters	2.1	pints	pt.
l	liters	1.06	quarts	qt.
l	liters	0.26	gallons	gal.
m ³	cubic meters	35	cubic feet	ft ³
m ³	cubic meters	1.3	cubic yards	yd ³
<u>TEMPERATURE (exact)</u>				
°C	Celsius temperature	9/5 (then add 32)	Fahrenheit temperature	°F

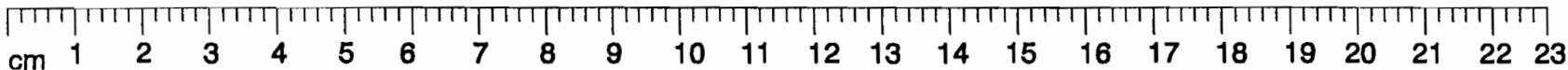


TABLE OF CONTENTS

		Page
CHAPTER 1	INTRODUCTION	1
1.1	Introduction	1
1.2	Development of Segmental Concrete Bridges	1
	1.2.1 Segmental Construction.	2
	1.2.2 Box Shaped Cross-sections.	2
	1.2.3 Prestressing.	2
	1.2.4 Post-tensioned Segmental Box Girder Bridges.	3
1.3	Past Problems in Segmental Bridges	3
	1.3.1 Corrosion Problems.	3
	1.3.1.1 Afon River Bridge.	3
	1.3.1.2 Early Externally Post-Tensioned Bridges.	3
	1.3.2 Creep Problems.	4
	1.3.2.1 Early Segmental Bridges.	4
	1.3.2.2 Florida Key Bridges.	4
	1.3.2.3 Wando River.	4
	1.3.3 Anchor Zone and Deviator Problems.	5
	1.3.3.1 Washington D.C. Metro Bridges.	5
	1.3.4 Construction Loading Problems.	5
	1.3.4.1 San Antonio "Y" Phase IA.	5
	1.3.4.2 San Antonio "Y" Phases IIB and IIIA&B.	5
	1.3.4.3 Zilwaukee Bridge.	5
	1.3.5 Thermal Distress.	5
	1.3.6 Construction and Contractual Problems.	5
	1.3.7 Summary of Problems.	6
1.4	Previous Laboratory and Field Studies	6
	1.4.1 Field Studies.	7
	1.4.2 Laboratory Studies.	7
1.5	Current Guidelines	7
1.6	Problem Areas in the <i>AASHTO Guide Specification</i>	7
	1.6.1 Prestress Losses in External Tendons.	7
	1.6.2 Shear Lag and Effective Flange Width.	11
	1.6.3 Diffusion of Post-tensioning Forces.	11
	1.6.4 Thermal Gradients.	11
	1.6.5 Joint Behavior.	12
	1.6.6 Anchor Zone Behavior.	12
	1.6.7 Deviator Behavior.	13

1.7	Problems of Special Interest to Texas DOT	14
1.7.1	Creep Model for Long Term Moment Redistribution.	14
1.7.2	Behavior of a Semi-Continuous Unit.	14
1.7.3	Behavior of Dual Boxes.	15
1.7.4	Thermal Gradients Caused by Match Casting.	15
1.8	Project Objectives	16
1.9	Scope	16
1.10	Organization	17
1.11	Summary	17
CHAPTER 2	SAN ANTONIO "Y" PROJECT OVERVIEW	19
2.1	Introduction	19
2.2	Project Description	19
2.2.1	Layout.	19
2.2.2	Project Phasing.	19
2.3	Structural System	21
2.3.1	Box Shapes.	21
2.3.2	Tendon Layouts.	23
2.4	Construction Procedures	23
2.4.1	Precasting Operations.	24
2.4.1.1	Short Line Match Casting.	24
2.4.1.2	Scheduling.	26
2.4.2	Erection Operations.	26
2.5	Summary	29
CHAPTER 3	INSTRUMENTATION LAYOUT AND INSTALLATION	31
3.1	Introduction	31
3.1.1	Instrumentation Systems.	31
3.1.2	Instrumented Spans.	31
3.1.2.1	Contractor's Schedule.	32
3.1.2.2	Box Shape.	32
3.1.2.3	Location in Span.	32
3.1.2.4	Transverse Post-tensioning to Adjacent Boxes.	32
3.1.2.5	Length of Span.	32
3.1.2.6	Accessibility.	32
3.2	Tendon Forces	35
3.2.1	Epoxy Sleeve System.	36
3.2.2	Electrical Resistance Strain Gages.	37
3.2.3	Tendon Force Instrumentation Layouts.	37
3.3	Reinforcing Steel Strains	40
3.3.1	System.	40

	3.3.2	Layouts	40
3.4		Concrete Strains	43
	3.4.1	System.	43
	3.4.2	Layouts.	44
3.5		Span Deflections	46
	3.5.1	System.	46
	3.5.2	Layouts.	46
3.6		Concrete Temperatures	48
	3.6.1	System.	48
	3.6.2	Layouts.	48
3.7		Joint Openings	51
	3.7.1	System.	51
	3.7.2	Layouts.	51
3.8		Summary	54
CHAPTER 4		LOSSES IN EXTERNAL POST-TENSIONING TENDONS	55
4.1		Introduction	55
4.2		Background Information	55
	4.2.1	Losses Through Stressing Hardware.	56
	4.2.2	Friction Losses.	57
	4.2.3	Seating Losses.	60
	4.2.4	Elastic Shortening Losses.	62
	4.2.5	Creep and Shrinkage Losses.	62
	4.2.6	Relaxation.	62
	4.2.7	Effect of Moment Redistribution on Prestress Losses.	62
4.3		Literature Review	64
	4.3.1	AASHTO Guide Specification.	64
	4.3.2	ACI 318-89.	64
	4.3.3	PTI Manual.	65
	4.3.4	Zia, Preston, Scott and Workman.	65
	4.3.5	Tadros, Ghali and Dilger.	66
	4.3.6	PCI Committee on Prestress Losses.	67
	4.3.7	ACI Committee 435.	68
	4.3.8	Ketchum.	69
4.4		Measurement Program	69
	4.4.1	Losses During Stressing Operations.	69
		4.4.1.1 Losses Through Stressing Hardware.	76
		4.4.1.2 Friction Losses.	77
		4.4.1.3 Seating Losses.	83
		4.4.1.4 Elastic Shortening Losses.	86
	4.4.2	Changes with Time.	91

4.5	Recommendations	109
4.5.1	Losses Through Stressing Hardware.	109
4.5.2	Friction Losses.	110
4.5.3	Elastic Shortening Losses.	111
4.5.4	Time Dependent Losses.	111
4.6	Summary	112
CHAPTER 5	LONGITUDINAL STRESS DISTRIBUTIONS ACROSS FLANGES	113
5.1	Introduction	113
5.1.1	Background Information.	113
5.1.1.1	Shear Lag.	113
5.1.1.2	Transverse Diffusion of Post-Tensioning Forces.	113
5.1.2	Current AASHTO Approach.	114
5.2	Literature Review	118
5.2.1	Ontario Bridge Code.	118
5.2.2	Song and Scordelis.	119
5.2.3	The PTI Precast Segmental Box Girder Bridge Manual.	119
5.2.4	DIN 1075.	120
5.3	Surveillance Program	120
5.3.1	Concrete Strain Readings.	120
5.3.2	Additional Measurements.	120
5.3.3	Material Tests.	123
5.4	Presentation of Results	123
5.4.1	Methods of Analysis.	123
5.4.1.1	Simple Beam Theory.	123
5.4.1.2	SHLAG Computer Program.	125
5.4.1.3	AASHTO Guide Specification.	125
5.4.2	Stresses from Measured Final Surface Strains Compared to Theory.	128
5.4.2.1	Top Slab Stress Distributions.	128
5.4.2.2	Bottom Slab Stress Distributions.	136
5.4.2.3	Summary.	144
5.4.2.4	Possible Errors in Measurement System.	144
5.4.3	Ontario Highway Bridge Design Code.	147
5.4.4	Isolated Dead Load Bending Stresses.	147
5.4.4.1	Measured Strains Due to Partial Dead Load.	148
5.4.5	Long Term Strain Changes.	150
5.4.6	Deflections.	150
5.4.7	Modified Approach.	153

5.5	Discussion	155
5.6	Recommendations	158
5.7	Conclusions	161
CHAPTER 6	THERMAL GRADIENTS AND THEIR EFFECTS	163
6.1	Introduction	163
6.1.1	Background Information.	164
6.1.1.1	Factors Affecting Gradient.	164
6.1.1.2	Factors Affecting Structural Response.	165
6.1.2	AASHTO Guide Specification Approach.	169
6.2	Literature Review	170
6.2.1	Hoffman, McClure and West.	170
6.2.2	Hawkins and Clark.	171
6.2.3	Shiu and Rasoulian.	171
6.2.4	Hirst and Dilger.	172
6.2.5	Baber and Hilton.	172
6.2.6	Shiu.	172
6.2.7	Priestley.	173
6.2.8	Potgieter and Gamble.	174
6.2.9	NCHRP 276.	175
6.3	Surveillance Program	179
6.3.1	Thermocouples.	179
6.3.2	Bridge Response.	180
6.3.3	Weather Conditions.	180
6.3.4	Coefficient of Thermal Expansion.	180
6.4	Presentation of Results	180
6.4.1	Measured Thermal Gradients.	180
6.4.1.1	Positive Temperature Gradients.	180
6.4.1.2	Negative Temperature Gradients.	183
6.4.1.3	Solar Radiation.	185
6.4.2	Bridge Response.	186
6.4.2.1	Spans A43 and A44.	186
6.4.2.2	Span C11.	186
6.4.2.3	Observations.	191
6.5	Discussion	192
6.5.1	Thermal Gradients.	192
6.5.1.1	Positive Gradients.	192
6.5.1.2	Negative Gradients.	194
6.5.1.3	Behavior.	195
6.6	Recommendations	199
6.6.1	Design Thermal Gradients.	199
6.6.2	Allowable Stresses.	200
6.6.3	Ultimate Strength.	202

6.7	Conclusions	202
	6.7.1 Observations.	202
	6.7.2 Recommendations.	203
	6.7.3 Further Study.	203
	6.7.4 Summary.	203
CHAPTER 7	BEHAVIOR OF SEGMENTAL JOINTS	205
7.1	Introduction	205
	7.1.1 Background Information.	205
	7.1.1.1 Shear Failure Modes.	205
	7.1.1.2 Other Differences between Dry and Epoxy Joints.	206
	7.1.2 Current AASHTO Guide Specification Approach.	207
7.2	Literature Review	209
	7.2.1 Koseki and Breen.	209
	7.2.2 Ramirez.	210
	7.2.3 MacGregor.	210
	7.2.4 Kordina and Weber.	211
	7.2.5 Bakhoun, Buyukozturk and Beattie.	211
7.3	Surveillance Program	212
	7.3.1 Grid Crack Monitors.	212
	7.3.2 Surface Strain Gages.	213
7.4	Presentation of Results	215
	7.4.1 Temporary Prestress.	215
	7.4.2 Joint Behavior Under Permanent Post-Tensioning.	217
	7.4.2.1 During Stressing.	217
	7.4.2.2 Long Term Behavior.	218
	7.4.2.3 Summary.	219
7.5	Discussion of Joint Capacity	219
	7.5.1 Bakhoun, Buyukozturk and Beattie Approach.	220
	7.5.2 Proposed Method.	220
	7.5.3 Comparison of Equation and Tests.	225
	7.5.4 Summary.	225
7.6	Recommendations	225
	7.6.1 Epoxied Joint Behavior.	225
	7.6.2 Dry Joint Capacity.	227
7.7	Conclusion	228
CHAPTER 8	HEAVY END DIAPHRAGM BEHAVIOR	229
8.1	Introduction	229
8.2	Literature Review	229
	8.2.1 Powell et. al.	229
	8.2.2 Woodward.	230

	8.2.3 Kreger.	230
	8.2.4 Wollmann.	230
	8.2.5 Schlaich et. al.	231
	8.2.6 AASHTO Guide Specification.	231
	8.2.7 NCHRP Report.	233
8.3	Description of Field Study	233
	8.3.1 Diaphragm Design.	233
	8.3.2 Vertical Post-Tensioning.	237
	8.3.3 Longitudinal Post-Tensioning.	239
	8.3.3.1 Strain Readings.	239
	8.3.3.2 Crack Patterns.	239
	8.3.3.3 Top Slab Spalling.	239
8.4	Discussion of Results	247
	8.4.1 Previous Strut-and-Tie Model Applications.	247
	8.4.2 Strut-and-Tie Models for Current Diaphragms.	249
	8.4.3 Assessing Design Based on Strut-and-Tie Modelling.	250
	8.4.3.1 Total Factored Vertical Tension on Diaphragm Face.	250
	8.4.3.2 Compression Strut Check.	251
	8.4.3.3 Shear Friction Check.	251
	8.4.3.4 Conclusions.	251
	8.4.4 Top Slab Spalling.	252
	8.4.4.1 Description of Problem.	252
	8.4.4.2 Possible Causes of Spalling.	252
	8.4.4.3 Conclusions.	253
8.5	Recommendations	256
8.6	Conclusions	257
CHAPTER 9	DEVIATOR BEHAVIOR	259
9.1	Introduction	259
	9.1.1 Background Information.	259
	9.1.2 AASHTO Guide Specification Approach.	260
9.2	Literature Review	261
	9.2.1 Beaupre, Powell, Breen and Kreger.	261
	9.2.2 Kreger.	262
9.3	Surveillance Program	262
	9.3.1 Description of Deviators and Instrumentation.	262
	9.3.2 Presentation of Results.	265
9.4	Discussion of Strut-and-Tie Modelling	268
	9.4.1 Models for Laboratory Specimens.	268
	9.4.2 Model for Span C11.	268
	9.4.3 Model for Spans A43 and A44.	268
9.5	Recommendations	273

9.6	Conclusions	274
CHAPTER 10	CONSTRUCTION AND LIVE LOADS	275
10.1	Introduction	275
10.2	Background Information	275
	10.2.1 Spans A43 and A44 - Typical Spans.	275
	10.2.2 Span C9 - "Poor-Boy" Continuity.	275
	10.2.3 Span C11 - Transverse Post-Tensioning.	278
10.3	Test Procedures	279
	10.3.1 Test Load Vehicles.	279
	10.3.1.1 Crane Loading.	279
	10.3.1.2 HS20-44 Trucks.	279
	10.3.2 Personnel.	280
	10.3.3 Three Span Continuous Unit.	280
	10.3.3.1 Crane Loading.	280
	10.3.3.2 Truck Loads.	282
	10.3.4 "Poor-Boy Unit".	283
	10.3.5 Transversely Post-Tensioned Span - C11.	283
10.4	Presentation of Results	284
	10.4.1 Three Span Continuous Unit - Spans A44 and A43.	284
	10.4.1.1 Crane Loads.	284
	10.4.1.2 HS20-44 Truck Loading.	285
	10.4.2 "Poor-Boy" Continuous Unit - Span C9.	290
	10.4.3 Transverse Post-Tensioning - Span C11.	296
10.5	Recommendations	301
	10.5.1 Live Load Deflections.	301
	10.5.2 External Tendon Stress Increases.	301
	10.5.3 "Poor-boy" Continuity.	301
	10.5.4 Transversely Post-tensioned Dual Boxes.	301
10.6	Conclusions	301
CHAPTER 11	TEMPERATURE INDUCED DEFORMATIONS IN	
	MATCH CAST SEGMENTS	303
11.1	Introduction	303
11.2	Literature Review	304
11.3	Description of Measurement Program	305
11.4	Results	308
11.5	Analysis	311
	11.5.1 Method of Calculating Deformation.	311
	11.5.2 Calculated Deformations.	312
11.6	Erection Observations	313
11.7	Recommendations	318

	11.7.1 Recommended Design Gradient.	318
	11.7.2 Recommended Design and Construction Approach.	319
	11.7.3 Measures to Reduce Thermal Gradients.	320
11.8	Conclusions	320
CHAPTER 12	RECOMMENDATIONS	321
12.1	Introduction	321
12.2	Losses in External Tendons	321
	12.2.1 Addition of Design Specifications Section 10.5.	321
	12.2.2 Changes to Design Specifications Section 10.2.	321
	12.2.3 Changes to Design Commentary Section 10.2.	322
	12.2.4 Changes to Design Commentary Section 10.1.	322
12.3	Stress Distributions Across Flanges	322
	12.3.1 Changes to Design Specifications Section 4.3.1.	322
	12.3.2 Changes to Design Specifications Section 4.3.2.	323
	12.3.3 Changes to Design Commentary Section 4.3.2.	323
12.4	Thermal Gradients	326
	12.4.1 Changes to Design Specification Section 7.4.4.	326
	12.4.2 Changes to Design Commentary Section 7.4.4.	326
	12.4.3 Changes to Design Specification Section 9.2.	326
	12.4.4 Changes to Design Commentary Section 9.2.1.3.	327
	12.4.5 Changes to the Design Specification Section 8.2.2.	327
12.5	Joint Behavior	328
	12.5.1 Changes to Design Specifications Section 12.2.	328
	12.5.2 Changes to Design Commentary Section 12.2.21.	328
	12.5.3 Change to Design Specifications Section 8.3.6.	329
12.6	Heavy End Diaphragm Behavior	330
	12.6.1 Changes to Design Specifications Section 14.4.	330
	12.6.2 Changes to Design Commentary Section 14.4.	330
	12.6.3 General Recommendations for Diaphragm Design.	330
12.7	Deviator Behavior	331
	12.7.1 Changes to Design Specifications Section 14.6.	331
	12.7.2 Changes to Design Specifications Section 14.6.3.	331
	12.7.3 Changes to Design Commentary 14.6.	331
12.8	Construction and Live Loads	331
	12.8.1 Changes to the Guide Specification.	331
	12.8.2 General Recommendations.	331
	12.8.2.1 Live Load Deflections.	331
	12.8.2.2 External Tendon Stress Increases.	331
	12.8.2.3 "Poor-boy" Continuity.	332
	12.8.2.4 Transversely Post-tensioned Dual Boxes.	332
12.9	Thermal Effects of Match Casting	333

	12.9.1	Change to Construction Specifications Section	
		14.1.	333
	12.9.2	Changes to Construction Commentary Section	
		14.1.	333
CHAPTER 13		CONCLUSIONS	335
	13.1	Overview of Project	335
	13.2	Conclusions	336
	13.2.1	Prestress Losses in External Tendons.	336
	13.2.2	Stress Distributions Across Flanges.	336
	13.2.3	Thermal Gradients and Their Effects.	337
	13.2.4	Behavior of Segmental Joints.	338
	13.2.5	Heavy End Diaphragm Behavior.	338
	13.2.6	Deviator Behavior.	338
	13.2.7	Construction and Live Loads.	339
	13.2.8	Temperature Induced Deformations in Match Cast Segments.	339
	13.3	Future Research Needs	339
	13.3.1	Prestress Losses in External Tendons.	340
	13.3.2	Thermal Gradients.	340
	13.3.3	Joint Behavior.	340
	13.3.4	Diaphragm and Deviator Behavior.	340
Appendix A		341
References		343

LIST OF FIGURES

	Page
Figure 1.1	Heavy end diaphragm in segmental box girder with external tendons. 13
Figure 1.2	External Tendon Deviator. 13
Figure 1.3	Types of Deviators in Study. 14
Figure 1.4	"Poor-boy" continuity. 15
Figure 2.1	San Antonio "Y" Project. 19
Figure 2.2	Cross-sections of the San Antonio "Y" Project. 20
Figure 2.3	Phasing of the San Antonio "Y" Project. 20
Figure 2.4	TYLI design for San Antonio "Y" Project. 21
Figure 2.5	Sample box shapes from previous and current phases of the San Antonio "Y" Project. 22
Figure 2.6	Schematic of tendon layout for three span continuous unit for Phase IIC. 23
Figure 2.7	Geometry control hairpins and leveling bolts. 24
Figure 2.8	Temporary post-tensioning pockets. 27
Figure 3.1	Project IIC layout. 33
Figure 3.2	Instrumented segment shapes. 34
Figure 3.3	Span C11 Details. 35
Figure 3.4	Schematic of epoxy sleeve system. 36
Figure 3.5	Demec extensometer. 36
Figure 3.6	Schematic of grout by-pass system. 37
Figure 3.7a	Tendon force instrumentation layouts. 38
Figure 3.7b	Tendon force instrumentation layouts. 39
Figure 3.8a	Reinforcing steel strain gage layouts. 40
Figure 3.8b	Reinforcing steel strain gage layouts. 41
Figure 3.8c	Reinforcing steel strain gage layouts. 42
Figure 3.9	Demec extensometer. 43
Figure 3.10	Modified Demec attachment system. 43
Figure 3.11a	Demec point layouts. 44
Figure 3.11b	Demec point layouts. 45
Figure 3.12	Taut wire baseline system. 46
Figure 3.13	Deflection measurement system layouts. 47
Figure 3.14a	Thermocouple layouts. 48
Figure 3.14b	Thermocouple layouts. 49
Figure 3.14c	Typical horizontal thermocouple layout. 50
Figure 3.15	Grid crack monitor and demec points. 51
Figure 3.16a	Joint movement instrumentation layouts. 52
Figure 3.16b	Joint movement instrumentation layouts. 53
Figure 4.1	Angle changes in strands passing from duct through anchorage

	device and ram.	56
Figure 4.2	Austin Bridge and Road bench test frame.	57
Figure 4.3	Friction loss along length dx.	58
Figure 4.4	Reduction in tendon force due to duct misalignment (wobble).	59
Figure 4.5	Wobble in external tendons.	59
Figure 4.6	Movement of strand during seating of wedges.	60
Figure 4.7	Change in tendon stress due to movement of strand during seating.	61
Figure 4.8	Instrumentation layouts and tendon designations.	70
Figure 4.9	Manipulation of raw data to determine tendon forces.	71
Figure 4.10	Tendon stresses after stressing, before seating.	74
Figure 4.11	Notation for Table 4.3.	75
Figure 4.12	Elevation views of tendon layouts.	78
Figure 4.13	Vertical curves of Spans A43 and A44.	79
Figure 4.14	Effect of deviator duct misalignment.	81
Figure 4.15	Field measurements of friction coefficients.	82
Figure 4.16	Losses in tendon stress due to seating.	85
Figure 4.17	Elastic shortening losses.	88
Figure 4.18	Comparison of concrete compression and elastic shortening losses.	89
Figure 4.19	Moments between deviators.	90
Figure 4.20	Creep functions for Spans A43, A44 and C11.	92
Figure 4.21a	Erection schedule and operations of long term analysis for Spans A43 and A44.	93
Figure 4.21b	Erection schedule and operations for long term analysis for Span C11.	94
Figure 4.22	Comparison of measured and calculated deflection.	96
Figure 4.23	Raw tendon stress readings and ambient daily temperatures.	97
Figure 4.24	Tendon stress readings after temperature adjustment.	98
Figure 4.25	Comparison of raw and adjusted average tendon stresses for Tendon T1N and Span A43.	99
Figure 4.26	Adjusted average tendon stresses for Tendon T1S and Span A43	100
Figure 4.27	Adjusted average tendon stresses for Tendons T2N and T2S in Span A43.	101
Figure 4.28	Adjusted average tendon stresses for Tendons T3N and T3S in Span A43.	102
Figure 4.29	Adjusted average tendon stresses for Tendons T1N and T1S in Span A44.	103
Figure 4.30	Adjusted average tendon stresses for Tendons T2N and T2S in Span A44.	104

Figure 4.31	Adjusted average tendon stresses for Tendons T3N and T3S in Span A44.	105
Figure 4.32	Adjusted average tendon stresses for Tendons T1N and T1S in Span C11.	107
Figure 4.33	Adjusted average tendon stresses for Tendons T2N and T2S in Span C11.	108
Figure 5.1	Shear lag and resulting deformations.	114
Figure 5.2	Distribution of normal stresses caused by diffusion of concentrated post-tensioning anchor forces.	115
Figure 5.3	Definition of effective flange width.	115
Figure 5.4	Flange widths as defined by the <i>AASHTO Guide Specification</i>	116
Figure 5.5	AASHTO effective flange width graph.	116
Figure 5.6	Effective flange widths over piers and at mid-span, and the transition area.	117
Figure 5.7	AASHTO effective flange widths for normal forces.	117
Figure 5.8	Effective span lengths for <i>Ontario Bridge Code</i> effective flange width calculations.	118
Figure 5.9	Type I Demec point layout.	121
Figure 5.10	Type III Demec point layout.	122
Figure 5.11	Segment properties.	123
Figure 5.12	Loading diagrams.	124
Figure 5.13	Segment properties for SHLAG program.	125
Figure 5.14	Loading diagrams for use with SHLAG.	126
Figure 5.15	Effective segment properties per AASHTO.	127
Figure 5.16a	Top slab stress distributions, five feet (1524 mm) from anchors.	129
Figure 5.16b	Top slab stress distributions, five feet (1524 mm) from anchors.	130
Figure 5.16c	Top slab stress distributions, one segment from anchors.	131
Figure 5.17a	Top slab stress distributions, eleven feet (3353 mm) from anchors.	132
Figure 5.17b	Top slab stress distributions, eleven feet (3353) from anchors.	133
Figure 5.17c	Top slab stress distributions, two segments from anchors.	134
Figure 5.18a	Top slab stress distributions, at mid-span.	135
Figure 5.18b	Top slab stress distribution, at mid-span.	136
Figure 5.19a	Bottom slab stress distributions, five feet (1524 mm) from anchors.	137
Figure 5.19b	Bottom slab stress distributions, five feet (1524 mm) from anchors.	138
Figure 5.19c	Bottom slab stress distributions, one segment from anchors.	139

Figure 5.20a	Bottom slab stress distributions, eleven feet (3353 mm) from anchors. . .	140
Figure 5.20b	Bottom slab stress distributions, eleven (3353) feet from anchors.	141
Figure 5.20c	Bottom slab stress distributions, two segments from anchors.	142
Figure 5.21	Bottom slab stress distributions, at mid-span.	143
Figure 5.22a	Accuracy of peak stress calculation methods for top slab stresses.	145
Figure 5.22b	Accuracy of peak stress calculation methods for bottom slab stresses.	145
Figure 5.23	Separation of load effects.	149
Figure 5.24	Top slab stress distribution, at mid-span, due to 54% dead load addition upon lowering erection truss.	150
Figure 5.25	Changes in top slab strains with time.	151
Figure 5.26	Comparison of actual and calculated span deflections (dead load and simple span tendons only).	152
Figure 5.27	Effective segment properties using modified AASHTO method.	154
Figure 5.28	Comparison of actual deflections and span deflections calculated with modified AASHTO properties (dead load and simple span tendons only).	156
Figure 5.29	Pattern of force diffusion, showing lack of compression on sections of first joint.	157
Figure 5.30	Modifications to the AASHTO effective flange width figures 4-1 and 4-2.	159
Figure 5.31	Modifications to AASHTO effective flange width figure 4-3.	160
Figure 6.1	Factors affecting thermal gradient.	164
Figure 6.2	Determinant beam subjected to linear gradient.	165
Figure 6.3	Beams subjected to non-linear gradient.	167
Figure 6.4	Indeterminate beam subjected to non-linear gradient.	168
Figure 6.5	Hoffman, McClure and West study.	170
Figure 6.6	Denny Creek Bridge Carlson gage layout.	171
Figure 6.7	Red River Bridge thermocouple layout.	171
Figure 6.8	James River Bridge thermocouple layout.	172
Figure 6.9	Kishwaukee Bridge and Linn Cove Viaduct temperature measurements.	172
Figure 6.10	New Zealand design thermal gradient.	173
Figure 6.11	Comparison of thermal effects at service and ultimate loads.	174
Figure 6.12	SOLMET stations and projected peak positive temperature differences.	175
Figure 6.13	Division of U.S. into zones for thermal gradient (Hawaii - Zone 3 and Alaska - Zone 4).	176

Figure 6.14a	Design positive thermal gradients.	177
Figure 6.14b	Design negative thermal gradients.	177
Figure 6.15	Summary of measured gradient.	178
Figure 6.16	Thermocouple layouts.	179
Figure 6.17a	Maximum positive temperature gradient recorded between July 16, 1992 and March 25, 1993 (no topping). Gradient occurred August 11, 1992.	181
Figure 6.17b	Maximum positive temperature gradient recorded between March 26, 1993 and May 25, 1993 (2 in. asphalt topping). Gradient occurred May 14, 1993.	181
Figure 6.18	Comparison of wing, web and slab temperatures on July 16, 1992.	182
Figure 6.19	Maximum positive gradients from July 25, 1992 to July 14, 1993.	182
Figure 6.20a	Maximum negative temperature gradient recorded between July 16, 1992 and March 25, 1993 (no topping). Gradient occurred November 5, 1992.	184
Figure 6.20b	Maximum negative temperature gradient recorded between March 26, 1993 and May 25, 1993 (2 in. (51 mm) asphalt topping). Gradient occurred May 23, 1993.	184
Figure 6.21	Maximum negative gradients from July 25, 1992 to July 14, 1993.	185
Figure 6.22	Solar radiation on July 16, 1992.	185
Figure 6.23	Thermal forces on fully restrained Type III unit, caused by temperature changes on July 16, 1992. (See Appendix B ⁶¹ for integration).	187
Figure 6.24	Determination of restraint moments for July 16, 1992.	188
Figure 6.25	Measured and calculated deflections caused by thermal gradients.	188
Figure 6.26	Web strains profiles from spans A43 and A44, caused by thermal gradients.	189
Figure 6.27	Thermal forces on fully restrained Type I unit, caused by temperature changes on March 19, 1992. (See Appendix B ⁶¹ for integration).	190
Figure 6.28	Measured and calculated deflections caused by thermal gradients in span C11.	191
Figure 6.29	Web strain profiles for span C11 caused by thermal gradients on March 9, 1992.	191
Figure 6.30	Comparison of measured and calculated temperature differences.	193
Figure 6.31	Self-equilibrating stresses for negative gradient on Type I cross-section, ignoring restraint moments.	194
Figure 6.32	Calculated Moment diagrams for Type III unit.	195

Figure 6.33a	Comparison of bottom fiber stresses without prestressing, with and without self-equilibrating stresses.	197
Figure 6.33b	Comparison of top fiber stresses without prestressing, with and without self-equilibrating stresses.	198
Figure 7.1	Definition of a/d ratio.	206
Figure 7.2	Shear failure modes for prestressed concrete beams.	206
Figure 7.3	Joint shear failure.	206
Figure 7.4	Figure 25-1 from <i>AASHTO Guide Specification</i> . Example of fine indentation joint faces.	208
Figure 7.5	Specimens of Koseki and Breen.	209
Figure 7.6	Specimens by Ramirez.	210
Figure 7.7	Strength comparison of Ramirez's specimens.	210
Figure 7.8	Specimens by Kordina and Weber.	211
Figure 7.9	Push-off specimens by Bakhoun, Buyukozturk and Beattie.	212
Figure 7.10	Instrumentation layouts.	213
Figure 7.11	Segment Demec point layouts.	214
Figure 7.12	Temporary post-tensioning details.	215
Figure 7.13	Typical uniform strain distribution across joint during temporary post-tensioning.	216
Figure 7.14	Typical non-uniform strain distributions across joints during temporary post-tensioning.	216
Figure 7.15	Comparison of strains across joints to strains in adjacent concrete.	217
Figure 7.16	Changes in strains with time across a typical joint.	218
Figure 7.17	Comparison of average change in strain with time, joint vs. adjacent concrete.	219
Figure 7.18	Joints in situations with high shear.	220
Figure 7.19	Joint shear failure plane.	220
Figure 7.20	State of stress on an element near a joint.	221
Figure 7.21	Mohr's circle description of state of stress on element near joint.	221
Figure 7.22	Mohr's circle description of state of stress on element near joint with normal stress.	222
Figure 7.23	Shear stress at failure for element with no normal stress.	222
Figure 7.24	Shear stress at failure for element with normal stress across the joint.	224
Figure 7.25	Calculation of constant for increase in shear capacity due to confining pressure.	224
Figure 7.26	Calculated vs. actual joint capacities.	226
Figure 7.27	Joint shear failure plane.	228
Figure 8.1	Diaphragms in segmental box girders with external tendons.	229
Figure 8.2	Cracking in Washington Metro pier segments.	230
Figure 8.3	Diaphragm as deep beam supported by flanges and web.	231

Figure 8.4	Failure of Wollmann's diaphragm specimens.	231
Figure 8.5	Diaphragm strut-and-tie models by Schlaich et al.	232
Figure 8.6	Geometry of instrumented pier segments.	233
Figure 8.7	Reinforcing steel details of pier segments.	234
Figure 8.8	Two dimensional strut-and-tie models.	235
Figure 8.9	Strain gage layout.	235
Figure 8.10	Design and as-built Dywidag bar locations.	236
Figure 8.11	Vertical strains after vertical prestressing.	238
Figure 8.12	Stresses in vertical reinforcing bars.	240
Figure 8.13	Stresses in horizontal reinforcing bars.	241
Figure 8.14	Stresses in U-shaped reinforcing bars.	242
Figure 8.15	Stresses in top and bottom slab bars.	243
Figure 8.16a	Segment 44A-1 north side crack patterns.	244
Figure 8.16b	Segment 43A-1 north side crack patterns.	245
Figure 8.17	Typical spalls in expansion joint segment.	246
Figure 8.18	Strut-and-tie model developed by Wollmann for laboratory specimens.	246
Figure 8.19	Strut-and-tie model for Washington Metro pier segments.	247
Figure 8.20	Strut-and-tie models for diaphragm.	248
Figure 8.21	Top slab stress distribution strut-and-tie prediction vs. measured.	251
Figure 8.22	Shear friction check.	252
Figure 8.23	Dimensions of local zone test block.	253
Figure 8.24	Comparison of reinforcing steel in local zone test specimen and expansion joint segment.	254
Figure 8.25	Comparison of compression struts in local zone test specimen and in expansion joint segment.	255
Figure 8.26	Comparison of well anchored and inadequately anchored vertical post-tensioning bar.	255
Figure 9.1	Deviator types.	259
Figure 9.2	Beaupre et al. strut-and-tie model for deviator.	260
Figure 9.3	Simplified model for deviator design by Beaupre et al.	261
Figure 9.4	Retrofit to strengthen deviators.	262
Figure 9.5	Span C11 deviator.	263
Figure 9.6	Span A43 and A44 deviator.	264
Figure 9.7	Stresses in vertical bars.	265
Figure 9.8	Stresses in horizontal bars.	266
Figure 9.9	Stresses in top and bottom bars.	267
Figure 9.10a	Modified strut-and-tie model for specimen 4A by Beaupre et al.	269
Figure 9.10b	Modified strut-and-tie model for specimen 4B by Beaupre et al.	270
Figure 9.11	Strut-and-tie model for Span C11 deviator.	271

Figure 9.12	Calculated vs. measured stresses in C11 deviator.	271
Figure 9.13	Strut-and-tie model for spans A43 and A44 deviators.	272
Figure 9.14	Section of strut-and-tie model for spans A43 and A44 deviators.	272
Figure 10.1	Full continuity between precast I-beams.	276
Figure 10.2	"Poor-boy" continuity between precast I-beams.	276
Figure 10.3	Details of "poor-boy" closure slab.	277
Figure 10.4	Ramp box merging with mainline box.	278
Figure 10.5	Span C11 detail.	278
Figure 10.6	HC-238B truck crane.	279
Figure 10.7a	AASHTO HS20-44 standard truck.	279
Figure 10.7b	Dump trucks used in tests.	280
Figure 10.8	Comparison of HS20-44 loading and dump truck loading.	281
Figure 10.9	Truck positions in spans A42, A43 and A44.	282
Figure 10.10	Truck positions in spans C9 and C10, "poor-boy" unit.	283
Figure 10.11	Truck positions in spans C11 and A45.	284
Figure 10.12	Deflections of spans A43 and A44 with crane on span A44.	285
Figure 10.13	Mesh for use with FRAME2D ²⁴ program.	286
Figure 10.14a	Deflections of spans A43 and A44 with live load on span A44.	287
Figure 10.14b	Deflections of spans A43 and A44 with live load on span A43.	287
Figure 10.14c	Deflections of spans A43 and A44 with live load on span A42.	288
Figure 10.15	Tendon stress changes with live loads.	288
Figure 10.16	Method for calculating tendon stress increase.	289
Figure 10.17	Web strains in span A43 and A44 with live loads.	291
Figure 10.18	Calculated vs. actual deflections of span C9 with live load on span C9.	292
Figure 10.19	Mesh for use with FRAME2D ²⁴ program.	293
Figure 10.20	Calculated vs. actual deflections of span C9 with live load on span C10.	294
Figure 10.21	Stresses in "poor-boy" continuity slab.	294
Figure 10.22	Web stresses in span C9 with live load on C9.	295
Figure 10.23	Continuity between spans C9 and C10.	295
Figure 10.24	Calculated vs. actual deflections of span C11 with live loads.	297
Figure 10.25	Model of spans A45 and C11.	298
Figure 10.26	Change in tendon stress in span C11 under live loads.	298
Figure 10.27	Method for calculating tendon stress increase.	299
Figure 10.28	Web stress profiles in span C11.	300
Figure 11.1	Bowing of match cast segments.	303
Figure 11.2	Temporary post-tensioning operations.	304

Figure 11.3	Segment types.	305
Figure 11.4	Typical thermocouple layout.	306
Figure 11.5	Deformation measurement system.	307
Figure 11.6	Typical temperature readings during match casting.	309
Figure 11.7	Typical temperature differences.	310
Figure 11.8	Deformed shapes.	310
Figure 11.9	Cracks indicate joint opening.	311
Figure 11.10	Thermal gradient in match cast segment.	312
Figure 11.11	Comparison of measured and calculated deformations.	317
Figure 11.12	Calculated vs. measured segment deformations at time of wingtip crack opening.	317
Figure 11.13	Thermal gradient in match cast segment at time of initial set of new cast segment.	318
Figure 11.14	Design thermal gradient.	319
Figure 12.1	Modifications to the AASHTO effective flange width figures 4-1 and 4-2.	324
Figure 12.2	Modifications to AASHTO effective flange width figure 4- 3.	325
Figure 12.3	Joint shear failure plane.	329
Figure 12.4	Model for "poor-boy" closure slab area.	332
Figure 12.5	Model of transversely post-tensioned box girders.	332
Figure 13.1	Project timeline.	335

LIST OF TABLES

		Page
Table 1.1	Previously Instrumented Bridges	8
Table 1.2	Previous Laboratory Studies	9
Table 4.1	Value of Modulus of Elasticity	72
Table 4.2	Measured Tendon Stresses, ksi.	73
Table 4.3	Measured Elongations Compared to Calculated.	75
Table 4.4	Losses through Stressing Hardware.	76
Table 4.5	Tendon Angle Changes.	80
Table 4.6	Measured Friction Coefficients.	80
Table 4.7	Measured vs. Calculated Seating Losses.	84
Table 4.8	Difference in Live End Friction Values Before and After Seating.	86
Table 4.9	Elastic Shortening Losses.	87
Table 4.10	Elastic Shortening Losses at Mid-Span in Spans A43 and A44.	91
Table 4.11	Comparison of Measured and Calculated Prestress Losses.	109
Table 5.1	Measured Concrete Moduli.	123
Table 5.2	Calculated vs Measured Stresses	146
Table 5.3	Comparison of Ontario Bridge Code and AASHTO Guide Specification.	147
Table 5.4	Accuracy of Modified Effective Flange Width Method.	155
Table 7.1	Comparison of Actual and Calculated Capacities of Dry Jointed Beams.	226
Table 11.1	Calculated and Measured Deformations Current Project Segments	314
Table 11.2	Calculated and Measured Deformations Prescon Project Segments	315
Table 11.3	Calculated and Measured Deformations Prescon Project Segments	316

SUMMARY

This report is the first in a series reporting the field study of several spans of the San Antonio "Y" Project. The San Antonio "Y" Project is a major urban viaduct comprising segmental concrete box girders post-tensioned with a mix of internal and external tendons and erected using span-by-span techniques.

This report describes the development of the instrumentation systems which were installed in the field project. The major systems were:

1. External post-tensioning tendon forces,
2. Span deflections and segment deformations,
3. Concrete temperatures
4. Concrete strains,
5. Reinforcing steel strains,
6. Joint openings,
7. Bearing movements,
8. Solar radiation.

A comprehensive literature review of each system was performed and the most promising systems were tested in the laboratory and in the field. Recommendations on the best system for each type of measurement were made, and the systems were installed in four spans of the San Antonio "Y" Project. Also in this report the performance of each system in the field is evaluated and recommendations for future field studies are presented.

CHAPTER 1 INTRODUCTION

1.1 Introduction

The use of segmental post-tensioned concrete box girder bridges is steadily increasing in the USA. The many advantages of these types of bridges have made them the preferred solution for many long span river and valley crossings as well as multiple span water crossings and metropolitan viaducts. As more designers and more contractors became involved with segmental bridges, AASHTO saw a need to provide guidelines to ensure safe and durable segmental structures. The result was the 1989 *AASHTO Guide Specification for the Design and Construction of Segmental Concrete Bridges*¹ (referred to in this document as the *AASHTO Guide Specification*). The original specification document was prepared under the NCHRP Project 20-7/32.⁹⁹

The authors of the document were faced with the situation that segmental bridges are a relatively new development, with the first precast segmental bridge in the US completed in 1973. Because of its relative youth, this bridge type has not been as extensively researched as some more traditional systems. In some instances the authors used "good engineering judgement" to write specifications in areas where actual data was scarce or completely lacking.

The research program described in this report was initiated to determine those areas in the *AASHTO Guide Specification* which were debatable due to lack of data, or which involve as yet unresolved differences between members of the design and construction communities. After the determination of these areas of uncertainty, a plan was developed to instrument related portions of four spans of the final phase of the San Antonio Downtown "Y" Project. The instrumentation was installed during both the casting and erection phases. Segments were monitored during casting and storage. The bridge was monitored during erection operations, under construction loadings, under live loadings and under long term dead loads. The data collected was analyzed and recommendations for revision of the *AASHTO Guide Specification* are proposed herein. This report is based on the dissertation of the senior author.⁶¹

The remainder of this chapter presents a brief outline of the development of segmental box girder bridges, describes problems which have occurred in the past, and outlines previous laboratory and field research. The primary interest areas in the *AASHTO Guide Specification* are then defined and the current research program is described.

1.2 Development of Segmental Concrete Bridges

Segmental post-tensioned concrete box girder bridges have many advantages. They are economical, versatile and aesthetically pleasing. They can be adapted to any reasonable horizontal or vertical curvature. They can be erected in ways which create minimal disruptions

at ground level. This can be especially important in urban and environmentally sensitive areas. Segmental bridges can be constructed quickly, especially when precast segments are used.

External post-tensioning further enhances the advantages of segmental construction by allowing thinner webs and hence reduced dead loads, by allowing easier installation of longitudinal tendons, and by creating more efficient tendons by eliminating the wobble losses inherent in internal tendons. External post-tensioning also allows easier inspection of tendons and easier replacement of damaged tendons.

Segmental bridges, although a relatively recent development, represent a meshing of technologies and construction techniques which can be traced back to the seventh century. Some important developments are outlined below.

1.2.1 Segmental Construction. Segmental construction was used first in China for the construction of arch bridges in the seventh century. The technique was first used in Europe much later, in the twelfth century.²³

1.2.2 Box Shaped Cross-sections. In 1899 Boussiron in France and in 1901 Maillart in Switzerland utilized box shapes for concrete arch bridges. Thus, by the early 1900's segmental construction and box girder construction had been used in bridge engineering. The next step, modern prestressing of concrete structures, was developed a short time later.

1.2.3 Prestressing. The earliest "prestressed concrete" technique applied to bridges was used in the three arch Le Veudre Bridge over the Allier River in France, built by Eugene Freyssinet and completed in 1912. Freyssinet left an opening at the crown of the arch where he installed jacks. These jacks were used, after considerable creep had occurred, to push the two halves of the arch back into their original positions. Freyssinet continued his studies of creep in concrete and in 1928 he patented prestressing technology.

The first modern prestressed bridge was the Saale-brucke, built by Franz Dischinger in Germany in 1928. It was a 200 foot (61 m) span concrete bridge, post-tensioned with large diameter rods. These first post-tensioning bars were of relatively low strength and as a result creep, shrinkage and relaxation introduced prestress losses equal to 75% of the original prestress level.⁴⁶

Prestressed concrete made considerable advances with the introduction of higher strength steel and improved anchoring techniques. In 1939 Freyssinet developed conical wedges for end anchorage. At the same time similar systems were developed in Belgium and the British Isles. A number of the early prestressed bridges utilized external tendons. However, because of problems with corrosion protection, this system was generally discontinued.

In 1946 Freyssinet used precast segments to construct the girder of the Pont de Luzancy in France. This was the first major example of the process of prefabricated segments in prestressed concrete bridge construction.

1.2.4 Post-tensioned Segmental Box Girder Bridges. The first cast-in-place segmental prestressed concrete box girder bridge built by the cantilever method was completed in 1950 in Germany. The first major commercial application of precast segmental box girder construction was the Choisy-le-Roi Bridge over the Seine River, designed and built by Enterprises Campenon Bernard and completed in August 1965. The Choisy-le-Roi project was particularly important because it marked the introduction of match casting of segments. This was the key idea in enabling geometry control of segmental bridges as well as epoxy joints.

From these beginnings, post-tensioned segmental box girder bridges have been refined and modified in many different ways. Segments can be precast or cast-in-place. Precasting can be done with short line or long line casting beds. Erection can proceed using cantilever construction techniques, progressive placement, incremental launching, or span-by-span methods. Tendons can be internal, external or a mixture.

A post-tensioned segmental box girder bridge is a very flexible construction system which can be molded to meet almost any particular situation. Bridges of this type are an excellent choice for many bridge applications, but they have not been without problems.

1.3 Past Problems in Segmental Bridges

1.3.1 Corrosion Problems.

1.3.1.1 Afon River Bridge. The only recorded failure of a post-tensioned segmental bridge was the 1985 collapse of a bridge over the Afon River in South Wales. The bridge was built in 1953 and was an eight celled box girder structure (actually constructed of nine I-girders) with a single 60 foot (18.3 m) span. The beams were made of eight segments, each 7 feet-11 inches (2.4 m) long, joined with 1 inch (25 mm) thick cast-in-situ mortar joints and post-tensioned together with Freyssinet tendons consisting of 12-0.2 inch (5 mm) diameter wires. Each beam contained five tendons.

The collapse was attributed to tendon corrosion which occurred at the porous cast-in-situ joints between segments. Chlorides, the primary cause of corrosion, were found in the surface concrete, the mortar in the transverse joints, the asbestos packing around the tendons, and the grout around the tendons. The mortar which was used in the joints had a much higher permeability than concrete which made it easier for the chlorides, water and oxygen to penetrate to the tendons. An asbestos packing was used to "protect" the tendons at the transverse joints, but in reality it acted as a sponge to soak up moisture. These factors caused the corrosion of the tendons at the joints, which in turn caused the collapse of the bridge.⁷⁵

1.3.1.2 Early Externally Post-Tensioned Bridges. Four bridges were built in France in the early 1950's utilizing external post-tensioning. The Vaux-Sur-Seine and Port a Binson bridges built by Coignet provided tendon corrosion protection with bitumen paint. On the Port

a Binson bridge the protection proved to be effective. The Vaux-Sur-Seine tendons, however, suffered severe corrosion, which was attributed to bird droppings. The bridge required strengthening with additional external tendons.⁷³

The 1953 Villeneuve-Saint-George Bridge, designed by Lossier, utilized large monostrands which were protected by a single coat of bitumen paint. Only one tendon showed signs of corrosion and it was consequently replaced. The bridge, due to excellent maintenance, has suffered no other problems.⁷³

The 1953 Can Bia Bridge, on the other hand, had many problems. There were cracks in the diaphragms over the piers and there was severe corrosion of the prestressing wires. The bridge was closed to traffic some years ago.⁷³

1.3.2 Creep Problems.

1.3.2.1 Early Segmental Bridges. Some early prestressed segmental bridges built using the cantilever method of construction had hinges at mid-span. Due to creep, however, these bridges eventually developed depressed cusps at the joints. As a result, this type of construction is no longer used.¹⁰ Later continuous bridges neglected the redistribution of moments due to creep and experienced joint openings and cracking in the positive moment area. Many had to be strengthened by the addition of external tendons⁷³

1.3.2.2 Florida Key Bridges. Four precast segmental post-tensioned box girder bridges in the Florida Keys required extensive repair after only six years of service. Although the bridges initially saved the state of Florida \$12 million, in 1988 alone \$5 million worth of repair contracts were approved.⁴⁷ Problems included cracking in the deck slabs, failed expansion joints, damage to the bearing pads, and corrosion of the epoxy coated reinforcing steel.

Much of the trouble has been linked to the higher than expected creep in the concrete. The local aggregate used in the concrete is softer and exhibits more creep than most aggregates. Allegedly, the poor material properties were not taken into account sufficiently in the original design.⁴⁷

Csagoly and Bollman, then of the Florida Department of Transportation, who studied the Key Bridges, reported orally to the PTI-NCHRP Specification group of NCHRP Project 20-7/32 that their measurements indicated substantial opening of some of the dry joints under daily thermal fluctuations. They also reported a substantial deficiency in post-tensioning in some spans due to combinations of underestimation of time dependent losses and apparent high friction losses at the deviators.

1.3.2.3 Wando River. The Interstate 526 Bridge over the Wando River has experienced cracking in the deck slabs. A \$717,000 modification calls for adding post-tensioning within the structure and sealing cracks in the deck. Although the cracks have been deemed only a serviceability problem, a consultant has been hired to look more deeply into the problem.⁷¹

1.3.3 Anchor Zone and Deviator Problems.

1.3.3.1 Washington D.C. Metro Bridges. Three aerial structures for the Washington D.C. Metro system were built using simple span, single cell, externally post-tensioned box girders. Before they were opened to traffic, spalling and cracking were discovered in the pier segments and the deviators. After review by Kreger³⁸ the deviators and diaphragms were substantially strengthened. Subsequent live load and dynamic tests indicated that the bridge was adequately repaired and is currently performing well under train traffic.

1.3.4 Construction Loading Problems.

1.3.4.1 San Antonio "Y" Phase IA. During the construction of the first span with a 21 foot (6.4 m) wide box, a retro-fit of the box was deemed necessary. It was determined that the top deck which spanned over 25 feet (7.6 m) between web walls, could not withstand the erection load imposed by the crane positioned on the deck and lifting a segment. The diaphragms in the boxes required modification to strengthen the top slabs.

1.3.4.2 San Antonio "Y" Phases IIB and IIIA&B. The contractors of these two projects discovered prior to casting any of their segments that the wings required strengthening in order to support themselves on the erection truss. The original designs, in both cases, called for partially hollow wings, to reduce dead load. Calculations showed, however, that the shims supporting the segments on the erection truss (two points under one wing and one point under the opposite wing) would punch through the 4 inch (102 mm) bottom slab of the wing. The contractors solved the problem by designing a thickened section in the region of the support shims.

1.3.4.3 Zilwaukee Bridge. In August of 1982 an accident occurred during the construction of the Zilwaukee Bridge on I-75 between Saginaw and Bay City, Michigan. The bridge is a variable depth, precast box girder built using the cantilever construction method. While one of the segments was being positioned by the launching girder, temporary shims in the expansion joint began to crush. The bridge tilted significantly and the bearings were ruined. The primary cause was heavier than expected construction loads.⁷²

1.3.5 Thermal Distress. Temperature gradients have caused problems in segmental bridge structures. The Newmark Viaduct in New Zealand, the Fourth Danube Bridge in Vienna, and the Jagst Bridge in Untergreisheim have all experienced cracking attributed to thermal gradients.³²

1.3.6 Construction and Contractual Problems. Other problems experienced in segmental bridge construction have been caused by inexperience on the part of the contractor, designer, owner, or all three. Construction problems have led to large claims filed by contractors against owners and designers. A group of 10 bridges whose total original bid price was \$242 million, had claims of around \$101 million.⁷⁰

There is still a difference of opinion about the appropriateness of alternative bid packages and value engineered alternatives in bridge design. The Federal Highway Administration requires that any bridge costing over \$10 million have at least two design alternatives. This is often done by having different design firms each prepare an alternate design. For the designers this presents a tempting incentive to "over" optimize the bridge design to reduce cubic yards of concrete and pounds of steel to their lowest possible values. There is a similar tendency to underestimate the time and difficulty involved in the construction process in order to make their alternative more attractive. All of this can lead to "marginal" designs, and possibly unconservative or unconstructable structures.

With respect to the contractors, the problem is often inexperience. An experienced segmental bridge contractor is aware of reasonable construction schedules and of the time and effort required to transform design documents (often schematics) into detailed constructable shop drawings. An inexperienced contractor often bids a job too low out of ignorance of the real cost and time involved. Hence, there is a continuing cycle of inexperienced people losing money on projects and filing claims afterward. When the owner, the designer, and the contractor are experienced in segmental technology (as in the current study of the San Antonio "Y" Phase IIC), the projects proceed well and are on time and within budget.

The *AASHTO Guide Specification*, recognizing these existing problems, has made the effort to provide guidance in areas such as completeness of specifications and contract drawings, inclusion of construction methods, contractor alternates, value engineering, and the handling of shop drawings. In this way the *AASHTO Guide Specification* helps the design and construction operations proceed with less trouble.

1.3.7 Summary of Problems. These problems, with the exception of the complete collapse of the South Wales Bridge, have not been severe. It is, however, unfortunate that the costs of maintenance, repair, retro-fit, testing and claims on some projects have nullified the initial savings realized by the use of segmental technology. However, for segmental construction as a whole, experience to date has shown it to be a competitive, cost saving technology.²⁶

Recent introduction of a comprehensive code, such as the *AASHTO Guide Specification*, should help to alleviate these types of problems in the future. However, these problems do indicate the need for further research into corrosion protection for post-tensioning tendons, post-tensioning losses (especially for external tendons), bridge response to thermal gradients, end diaphragm and deviator behavior, construction load effects and long term bridge behavior.

1.4 Previous Laboratory and Field Studies

A valuable source of data for the authors of the *AASHTO Guide Specification* was information gathered from previous instrumentation studies of actual segmental bridges and scale models in laboratory tests. The following is a brief description of earlier studies.

1.4.1 Field Studies. Arréllaga⁷ provides a thorough review of previously instrumented segmental bridges whose results have been published in English language sources. Table 1.1 presents the names of these structures and the types of instrumentation which were installed. Field studies have provided valuable information on the performance of these structures, but the data has often been incomplete or even in error. Some of the projects are discussed in more detail in other chapters.

1.4.2 Laboratory Studies. Laboratory studies also provide a great deal of information on the design and construction of segmental concrete bridges. Table 1.2 lists some of the important model bridges which have been built and tested in laboratories around the world.

The number of field and laboratory studies is impressive considering the relative youth of segmental bridge construction. Unfortunately, even with the substantial amount of data which has been collected, there are still many areas in segmental design which are hotly debated. The basic behavior of these bridges is understood, but many of the details are still uncertain. The goal of this project is to clear up some of the uncertainties.

1.5 Current Guidelines

A US designer embarking on a segmental bridge project would probably consult the *AASHTO Standard Specification for Highway Bridges*² and the *AASHTO Guide Specification for the Design and Construction of Segmental Concrete Bridges*.¹ Other references are available to segmental bridge designers. The *CEB Model Code*¹⁷ and *ACI-209*⁴ are often cited as a source of information on creep and shrinkage. The *Ontario Bridge Code*⁵⁰ gives information on the use of effective flange widths to compensate for shear lag effects in wide boxes. References such as the *PTI Concrete Box Girder Manual*⁶⁹ and *Segmental Box Girder Bridges*⁵² are available to give guidance on basic design principles. Even with these documents available, problems still persist and questions still remain.

1.6 Problem Areas in the *AASHTO Guide Specification*

The following section briefly outlines the areas in the *AASHTO Guide Specification* which have been targeted for study in this research program. They are specifically those areas which could benefit from the data collected in a full scale field instrumentation project of span-by-span erected box girder bridges such as those of the San Antonio "Y".

1.6.1 Prestress Losses in External Tendons. Prestress losses fall into two categories: immediate and long term.

Table 1.1 Previously Instrumented Bridges

Name	Location	Description	Finished	Types of Instrumentation			
				Temperature	Deflection	PT Force	Concrete Strain
Pelotas River	Brazil	Progressive Cantilever	1966	X	X		
Japan Bridges		Cast-in-Place Balanced Cantilevers	1972		X		
Caltrans Study- 6 Bridges	San. Francisco, Fresno, Sacramento	Cast-in-Place Box Girders	1972			X	
Turkey Run	Indiana	Precast Balanced Cantilever	1978	X	X		
Kishwaukee	Illinois	Precast Balanced Cantilever	1982	X			X
Denney Creek Viaduct	Near Seattle Wash.	Cast-in-Place Box Girders	1982	X	X		
Red River	Boyce, Louisiana	Cast-in-Place Balanced Cantilever	1984	X	X		X
Sunshine Skyway	Tampa, Florida	Precast Cable Stayed	1987	X			X
River Torrigge	England	Precast Balanced Cantilever	1987	X	X		
Nevada Bridges	Reno, Henderson	Cast-in-Place Box Girders	1988			X	X
James River	Virginia	Precast Cable Stayed		X			X

Table 1.2 Previous Laboratory Studies

Study	Year of Report	Type of Structure	Type of Tendons	Joint Type
Kashima & Breen	1975	Parallel Single Boxes - 3 span continuous unit- built in balanced cantilever	internal-bonded	single keys w/ epoxy
McClure, West and Abdel-Halim	1982	Simple-Span - single cell boxes - erected span-by-span	internal-bonded	no keys- epoxy
Kupfer, Guckenberger & Daschner	1982	2 I-girders, simple spans with cantilever	bonded internal	Single key w/ epoxy and multi-key w/mortar
Hoang & Pasquinon	1985	5 simple span box girders	varied	dry multi-keyed
Specht & Veilhaber	1986	6 simple span I-girders	internal unbonded	multi-keys w/epoxy, and with bars through joints
Sowlat & Rabbat	1987	3 simple span I-girders	varied	dry multi-keyed
MacGregor	1989	3 span continuous - single cell box, built span-by-span	external grouted	multi-keys, 2 spans w/epoxy, 1 span w/o
Hindi, Kreger & Breen	1991	Same model as MacGregor	internal and external w/discrete bond	multi-keys, 2 spans w/ epoxy, 1 span w/o
Arockiasamy, Sinha & Reddy	-	Simple span single cell box girder	external	dry multi-keyed

Immediate losses are:

1. **Elastic Shortening.** Since external tendons are not physically located within the concrete cross-sections of the box-girder, traditional methods of calculating elastic shortening losses may not apply. Such losses occur in post-tensioning when multiple tendons are used. The losses vary in magnitude depending on the order of stressing.

2. **Friction and Wobble.** The *AASHTO Guide Specification* suggests a value of the friction coefficient of 0.25 for tendons through deviation pipes. It is noted that lubrication may be required to achieve such a low value. A wobble coefficient of 0.0 for external tendons is suggested. One of the contractors on the San Antonio "Y" Project stated that they had to use a wobble coefficient greater than 0 on their external tendons in order to match the calculated and actual elongations.
3. **Seating Losses.** These losses are dependent on the type of stressing hardware used. The *AASHTO Guide Specification* recommends using 1/4 inch (6.4 mm) for the wedge seat movement. However, with new power seating rams, the actual movement may be reduced to as low as 1/16 inch (1.6 mm).
4. **Losses Through Stressing Hardware.** This is a type of loss which many post-tensioners are aware of, but it has no code mention. The force which is calculated by multiplying the hydraulic pressure times the ram area is not the same as the force in the tendon immediately below the live end anchor head. Losses can occur due to the slight angle changes in the tendons as they pass through the hardware. Losses can also occur due to internal friction in the piston of the ram. These losses can be quite substantial, 4-6%, but they are not mentioned in the *AASHTO Guide Specification*.

Long term losses are:

1. **Creep and Shrinkage.** This value is difficult to precisely calculate. Many methods of calculating the creep coefficient exist and none has proven to be correct in all cases. The method of calculating long term losses in external tendons is also in question since the tendons are not within the cross-section of the concrete and are not subject to strain compatibility.
2. **Relaxation.** This is the tendency of steel to experience less stress with constant strain over time. It is a characteristic which is most often tested by the prestressing strand manufacturers. Their results will be used in this study and no additional tests for relaxation will be done.

In order to learn more about these losses the external tendons of three spans were instrumented on each straight length of tendon. Measurements were taken during stressing and for many months. The results are presented in Chapter 4.

1.6.2 Shear Lag and Effective Flange Width. No distress in any existing segmental bridge has been attributed to shear lag. This is most probably because most box girder shapes are proportioned so that shear lag will not be a significant problem.

The *AASHTO Guide Specification* presents a lengthy and complex method for calculating effective flange widths for those boxes which are proportioned in such a way that significant shear lag effects are expected. This method is tedious, and at the same time leaves the designer with many unanswered questions. This is a significant problem for designers. The method and the problem itself require further study.

The San Antonio "Y" Project has cross-sectional shapes with long cantilever wings and webs spaced far apart, and hence are susceptible to significant shear lag effects. Several segments in three spans were equipped with surface strain gages. The arrays of gages provided information on the strain profile across the width of the bridge. The information provided by these strain profiles indicated how shear lag affected the span. The results of this study are presented in Chapter 5.

1.6.3 Diffusion of Post-tensioning Forces. This question is analytically similar to the shear lag problem. A great deal of force is introduced into the bridge cross-section at the anchorage devices. At some distance from the anchorages, that force has diffused into the entire cross-section. Designers need to know the basic flow of these forces so they may design the box girder to resist the high local compression forces, and the tensile forces which result as the forces spread. It is known that simple beam theory will not suffice in the design of the segments close to the pier, but the spreading angle of the forces is still debatable.

In the instrumented spans, surface strain gages were used to track the diffusion of the post-tensioning forces into the structure. The results of this study are also presented in Chapter 5.

1.6.4 Thermal Gradients. A thermal gradient, from the top slab to the bottom soffit, is often present in a box girder bridge. The gradient is caused by the sun shining on and warming the top slab, while the wings of the box keep the lower portion of the box in the shade. The portion in the shade remains much cooler than the top of the box. The effects of this thermal gradient must be accounted for in the design of a box girder bridge.

The *AASHTO Guide Specification* presents design gradients, both positive and negative, based on an NCHRP Report.³³ Many questions exist concerning this gradient:

1. **Is it accurate?** It is based primarily on computer analysis and there is limited real data confirmation.
2. **Is it too harsh?** There are questions about whether the actual environmental conditions assumed in the report ever really coincide so as to cause the design gradient.

3. **How does the bridge respond?** There are theoretical answers, but little data to confirm.
4. **Should all bridges be designed with the gradient?** Currently only segmental concrete girders are required to be designed for this thermal gradient. For steel bridges, cast-in-place monolithic box girders, and other non-segmental reinforced and prestressed concrete bridges the gradient is suggested but not required. This makes segmental bridges less economical by comparison.

As part of this research the thermal gradients, climatic conditions, and bridge response were measured and analyzed. The results are presented in Chapter 6.

1.6.5 Joint Behavior. Currently, the *AASHTO Guide Specification* makes many distinctions between dry and epoxied joints. Dry joints may only be used in bridges with external tendons in regions where freeze-thaw conditions do not exist. In cases where dry joints are allowed, the design must incorporate a lower ϕ (strength reduction) factor for ultimate strength design, and they are required to have higher levels of pre-compression under service loads. This may result in bridges with thicker webs, more mild shear reinforcing and greater amounts of prestressing. The dry jointed structures can still be very appealing because of the cost and time savings achieved by the elimination of epoxy and the temporary post-tensioning equipment and operations needed to properly close the joints. During construction, dry jointed bridges are also less sensitive to weather conditions such as rain or cold where epoxy could not be applied.

Laboratory tests have shown that the joint types behave very similarly under most ultimate loading conditions; the exception is direct shear loading, where dry joints have significantly less capacity. At service load levels, epoxy gives a substantial reserve against cracking above the decompression load.

The design and construction community is divided on the relative merits of dry and epoxied joints. Some believe that epoxy joints are clearly superior to dry joints and hence believe the differences in the specification are desirable. Others cite old cases where epoxy has been applied improperly, or did not set; they claim the epoxy is not reliable and should not be taken into account in design. In other words, dry and epoxy joints should be treated equally.

In this research many joints were instrumented to observe their behavior. All the joints in the San Antonio "Y" Project are epoxy joints. In addition to the field study, previous laboratory studies were reviewed. The results of this study are presented in Chapter 7.

1.6.6 Anchor Zone Behavior. Post-tensioned anchor zone behavior has been studied thoroughly in the laboratory,¹³ but few field studies have been performed. The anchor zone type studied in this project was heavy end diaphragms, (see Figure 1.1).

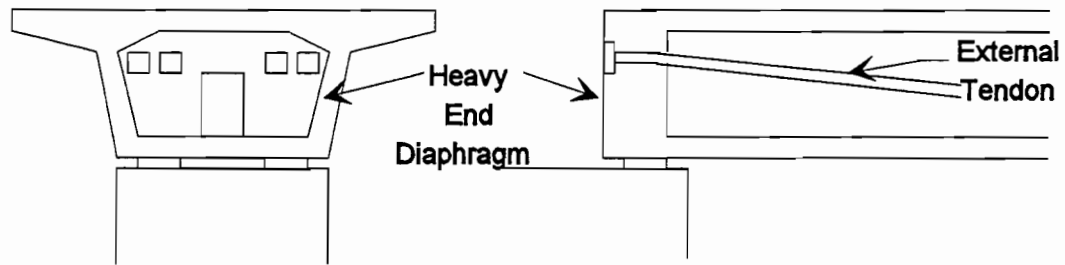


Figure 1.1 Heavy end diaphragm in segmental box girder with external tendons.

These diaphragms not only transfer the dead and live loads to the bearings, they also contain the anchorages for the majority of the longitudinal post-tensioning tendons. Large concentrated forces are acting on these massive concrete segments, and problems of cracking have occurred in the past.³⁸

In this project two end diaphragms were instrumented with reinforcing steel strain gages to observe the flow of forces through the segment, to assess the adequacy of the design, and to compare the behavior with current methods of analysis. The results are presented in Chapter 8.

1.6.7 Deviator Behavior. Deviators are the locations where the longitudinal tendons are forced through an angle change, normally to create a draped tendon path (see Figure 1.2). The behavior of deviators has been studied in the laboratory, and design methods have been proposed.¹² The *AASHTO Guide Specification* gives general guidance on what forces and force effects must be considered in the design, but does not provide information on how to design this region.

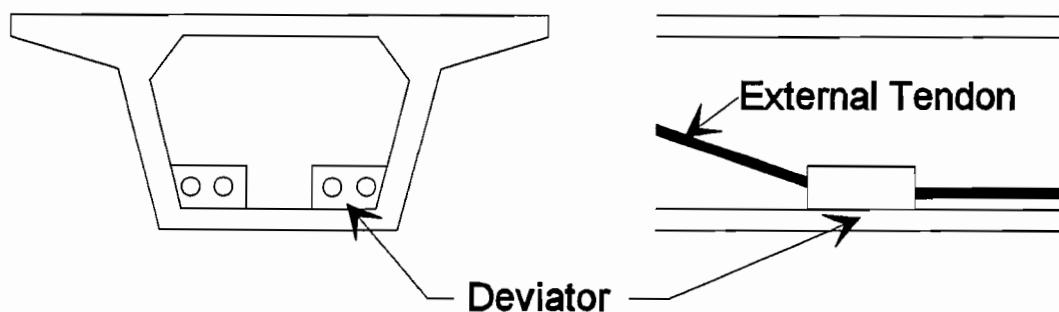


Figure 1.2 External Tendon Deviator.

Two different styles of deviation saddle were instrumented as part of this research. The two types were: a continuous (web to web) beam, and deviators with diaphragm walls (see Figure 1.3). The deviators were instrumented with strain gages on the reinforcing steel. The stresses in the bars in the deviators were studied to determine the adequacy of the deviator itself. Reinforcing bars in other locations in the segment were also instrumented to track the flow of forces from the deviator into the rest of the structure, and to study the effects of the forces on the section. The results are presented in Chapter 9.

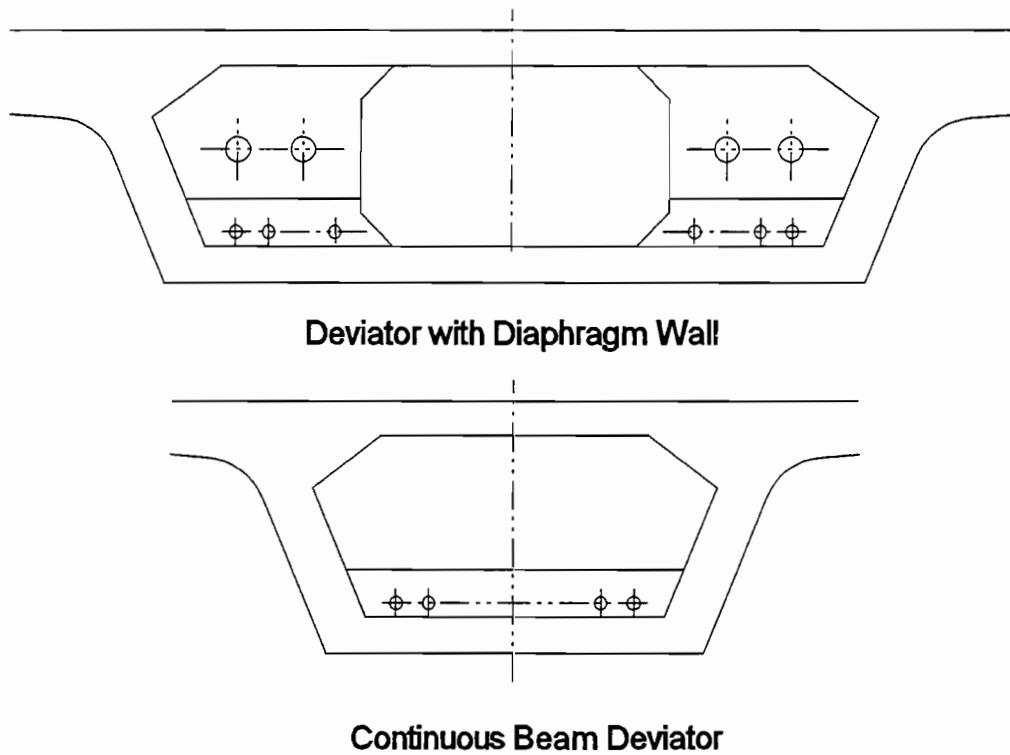


Figure 1.3 Types of Deviators in Study.

1.7 Problems of Special Interest to Texas DOT

The following section describes areas of study which were specifically requested by the Bridge Design Division of the Texas Department of Transportation.

1.7.1 Creep Model for Long Term Moment Redistribution. The designers of the San Antonio "Y" Project used a time-dependent, highly specialized frame solver to calculate the long term behavior of the bridge. The design team was interested in comparing their results to the actual long term behavior of the bridge.

Four spans were monitored over the course of this project. The actual changes in camber and changes in concrete stresses were recorded for many months. These actual changes have been compared to the behavior predicted by the original computer analysis and by an analysis based on the actual material properties and construction schedules. The changes in camber with time, along with the changes in post-tensioning force, are presented in Chapter 4.

1.7.2 Behavior of a Semi-Continuous Unit. The final phase of the San Antonio "Y" Project contains one two-span continuous unit which incorporates an unusual form of continuity. The two spans are actually simple spans made continuous only by the top slab ("poor-boy" continuity), which is continuous over the intermediate pier (see Figure 1.4). This concept simplifies both the design and construction operations. Its primary drawbacks are that in terms

of material costs, continuous structures are more economical than simple spans when carrying live loads, and a simple span structure has less redundancy and less ultimate strength than a multi-span continuous unit. However, the additional material costs for the simple spans can be offset by the savings realized by the simpler construction processes.

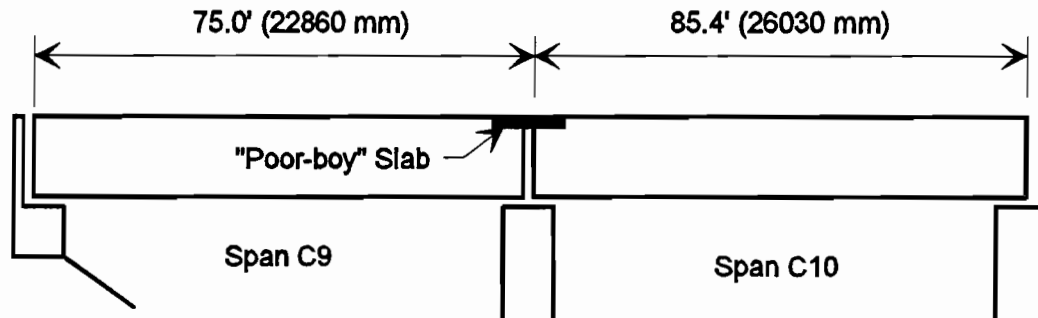


Figure 1.4 "Poor-boy" continuity.

The designers were interested to see how this design behaved. One of the two spans and the top slab closure were instrumented and the span's behavior under live loads was observed. The results of this study are presented in Chapter 10.

1.7.3 Behavior of Dual Boxes. In many locations in the San Antonio "Y" Project, two adjacent spans are transversely post-tensioned together. The designers were interested in how the two spans interact. One span, which was eventually post-tensioned to the adjacent span, was equipped with full instrumentation. The systems were monitored during live load tests to investigate the interaction of the adjacent spans. The results of this study are reported in Chapter 10.

1.7.4 Thermal Gradients Caused by Match Casting. When a new segment is cast next to a recently cast, cooling segment, the heat of hydration of the new segment causes a thermal gradient to occur in the older segment. This gradient causes the old segment to bow away from the new segment. While the concrete is still fluid, it will conform to the bowed shape. The resulting new segment will have one flat face (cast against the bulkhead) and one curved face (cast against the old, bowed segment.) When the old segment returns to its original shape, the new and old segments will not fit together properly. There will be a gap.

This problem occurred during the casting of the second phase of the San Antonio "Y" Project. The problem was discovered during erection operations when the gap was very noticeable and difficult to close with temporary post-tensioning. Texas DOT designers requested that the problem be studied so it might be avoided in the future.

Several segments were instrumented to monitor the thermal gradients and the resulting bowed shape during casting. These joints were also monitored during temporary post-tensioning operations to determine what difficulties resulted. The results of this study are presented in Chapter 11.

1.8 Project Objectives

These problem areas in segmental bridges led to the initiation of this project. With the goal of shedding new light on these areas of uncertainty the project objectives were determined.

The objectives of this project were:

1. To identify those areas in the *AASHTO Guide Specification* which would benefit from additional data collected from a full scale instrumentation project of a span-by-span segmental box girder bridge,
2. To determine through literature review, laboratory trials and field trials, which instrumentation systems were best suited for the field study,
3. To devise an instrumentation plan for four spans of the final phase of the San Antonio "Y" Project,
4. To prepare special provisions, to be included with the project specifications, which prepare prospective contractors for all work stoppages, work slow-downs and other special requirements of the research team (see Appendix A),
5. To perform the field study,
6. To analyze the data,
7. To recommend changes to the *AASHTO Guide Specification* where required.

1.9 Scope

The type of segmental bridge instrumented in this project is a precast segmental box girder bridge with a mixture of external and internal tendons. The bridge was erected using span-by-span techniques. The concrete is normal weight and actual strength at time of erection averaged 9000 psi (62 MPa). The studies in this program are focused on this type of structure. However, some of the recommendations are applicable to all segmental bridge types.

1.10 Organization

The first report of this series presents in detail the instrumentation systems and their performance in the field study. This report presents the findings of the field study and is organized as follows:

- Chapter 1 - Introduction and Background Information.
- Chapter 2 - San Antonio "Y" Project Overview.
- Chapter 3 - Instrumentation Layout and Installation.
- Chapter 4 - Prestress Losses in External Tendons.
- Chapter 5 - Longitudinal Stress Distributions Across Flanges.
- Chapter 6 - Thermal Gradients and Their Effects.
- Chapter 7 - Joint Behavior.
- Chapter 8 - Anchor Zone Behavior.
- Chapter 9 - Deviator Behavior.
- Chapter 10 - Construction and Live Loads.
- Chapter 11 - Thermal Gradients Caused By Match Casting.
- Chapter 12 - Recommendations.
- Chapter 13 - Summary and Conclusions.

Chapters 4 through 11 each contain an introduction to the problem, a literature review, a brief description of the instrumentation systems utilized for the particular study, a presentation of results, recommendations on code revisions if applicable, and conclusions. Each of these chapters is essentially self-contained except for precise details on instrumentation, which are presented in detail in the first report of this series and briefly introduced in Chapter 3 of this report.

1.11 Summary

Segmental bridges are versatile and economical structures, but they can benefit from further study. A comprehensive field study of the behavior of a segmental bridge during erection operations and during its early life will provide new and valuable information on segmental structures. As more is learned from previous experience and from new research, the state of the art of segmental bridges can continue to improve.

A document such as the *AASHTO Guide Specification for the Design and Construction of Segmental Concrete Bridges* is required to ensure the design and construction of safe and durable structures. Only through a continuous process in which new data is collected and assimilated into the document, can the *AASHTO Guide Specification* continue to perform well. This research was initiated with the goal of assisting in the ongoing improvement and refinement of the *AASHTO Guide Specification*.

CHAPTER 2 SAN ANTONIO "Y" PROJECT OVERVIEW

2.1 Introduction

This chapter presents a brief introduction to the San Antonio "Y" Project. The layout, phasing, box shapes and tendon layouts are introduced. Also a description of casting yard and erection site operations is given. This information about the project and the construction procedures was vital in the determination of the instrumentation program, since it was desirable to fit the instrumentation systems into the construction process with the minimum disruption possible.

2.2 Project Description

2.2.1 Layout. The San Antonio "Y" Project derives its name from the shape of the intersection of Interstate Highways 35 and 10 near downtown (see Figure 2.1). The finished project provides three or more lanes of new highway for both inbound and outbound traffic. Along some of the north-south leg of the "Y" the new roadway comprises entirely elevated lanes, while on the other two legs the lanes are split between elevated structure and pavement on grade (see Figure 2.2). The majority of the elevated structures are precast segmental box girder bridges which use a mix of internal and external tendons and which were erected using the "span-by-span" technique.

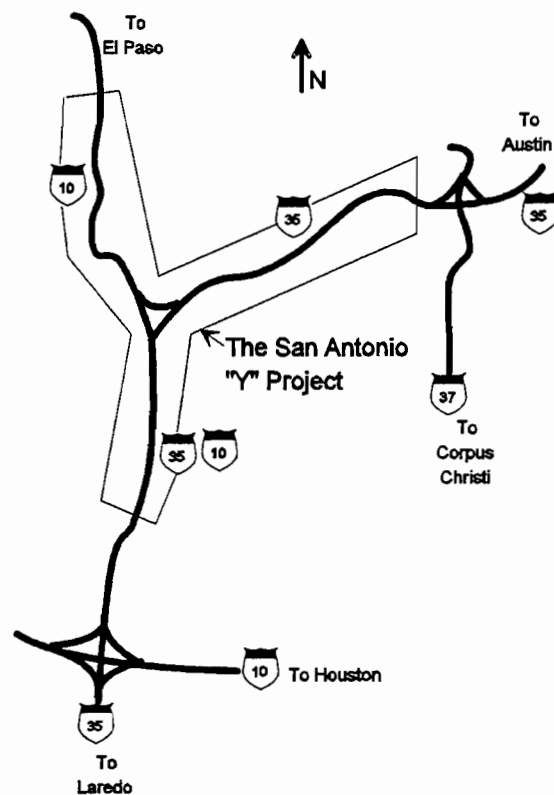


Figure 2.1 San Antonio "Y" Project.

2.2.2 Project Phasing. The project was divided into many phases, six of which involved segmental bridge construction (see Figure 2.3). The contracts for the various projects were let at intervals beginning with Project IA awarded in November of 1984 and ending with Project IIC awarded in October of 1990.

One objective of the phasing was to first complete all of the new outbound lanes. Outbound traffic is more of a problem than inbound traffic because people filter into the city

slowly in the morning but when the 5 o'clock whistle blows, everyone seems to be on the highway at once. After completion of the outbound lanes, the inbound roadway was begun. The order of the award of contracts was:

1. IA
2. IIIA&B
3. IIB
4. IC
5. IIIC&D
6. IIC

The subject of this research is Project IIC.

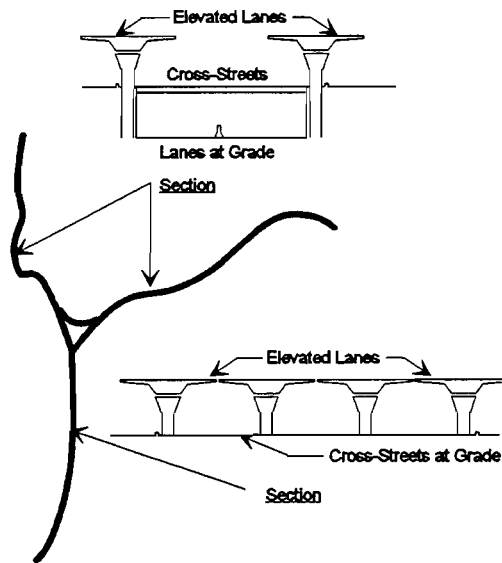


Figure 2.2 Cross-sections of the San Antonio "Y" Project.

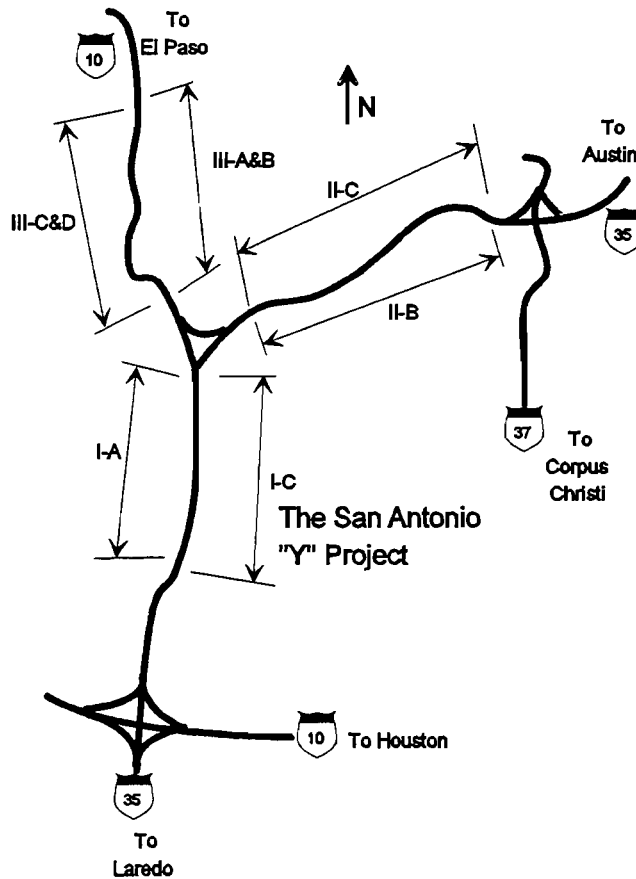


Figure 2.3 Phasing of the San Antonio "Y" Project.

2.3 Structural System

The six phases of the San Antonio "Y" Project have had a wide variety of box shapes and tendon layouts. The following sections provide a summary.

2.3.1 Box Shapes. The shape of the box on the first phase of the "Y" Project was dictated by an original design by T. Y. Lin International (TYLI). TYLI formulated the original design of Phase IA, in which the elevated structures were to be of a composite wing girder design featuring a partial cast-in-place spine beam and precast wings (see Figure 2.4). An alternate design of the project was required under the Federal Highway Administration policies since the cost of the project exceeded \$10 million. One requirement of the alternate design was that the shape of the structure adhere closely to the TYLI general cross-sectional shape. This requirement set the basic parameters, such as the depth of the section, the narrowness of the spine, the angle of the web wall and taper of the cantilever wings, which were used throughout all phases of the project.

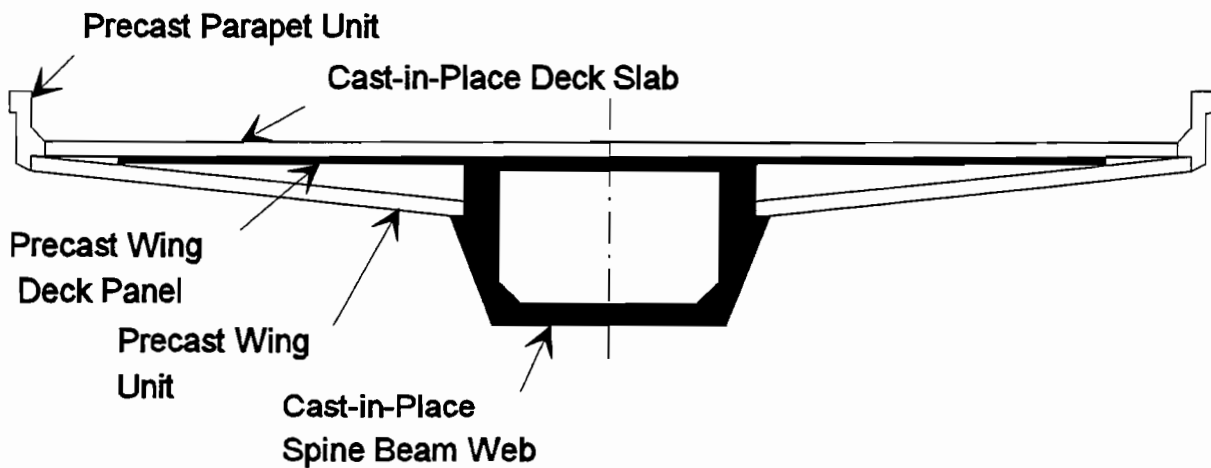


Figure 2.4 TYLI design for San Antonio "Y" Project.

Figure 2.5 shows some of the variety of box shapes used in the "Y" Project. The two most common variables were the width of the bottom of the box, from 6 (1.83 m) feet to 21 feet (6.4 m), and the width of the wingspan, from 26 feet (7.92 m) to 60 feet (18.28 m). Another variation on the box shape was the use of hollow wings on Phases IIB and IIIA&B. The use of intermediate diaphragms and top slab stiffening ribs also varied from project to project.

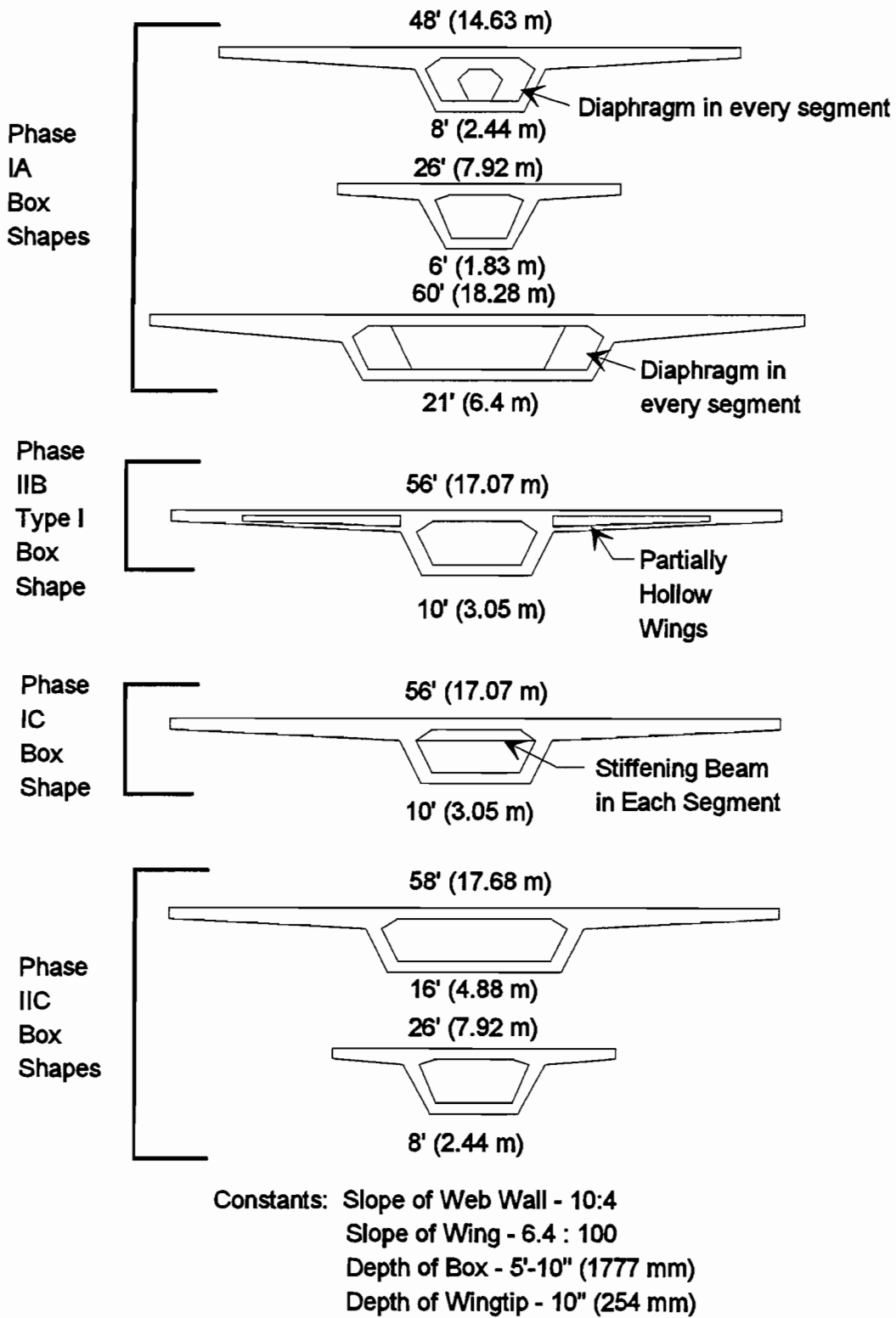


Figure 2.5 Sample box shapes from previous and current phases of the San Antonio "Y" Project.

2.3.2 Tendon Layouts. The tendon layouts have varied considerably through the course of the project. Both the ratio of internal to external tendons and the method of creating continuity between spans has varied. Methods of creating continuity have included criss-crossing tendons at pier segments, coupling tendons and adding continuity tendons, and criss-crossing some tendons and adding continuity tendons. Figure 2.6 illustrates the general tendon layouts in the current project, which involves some cross-over tendons and some continuity tendons.

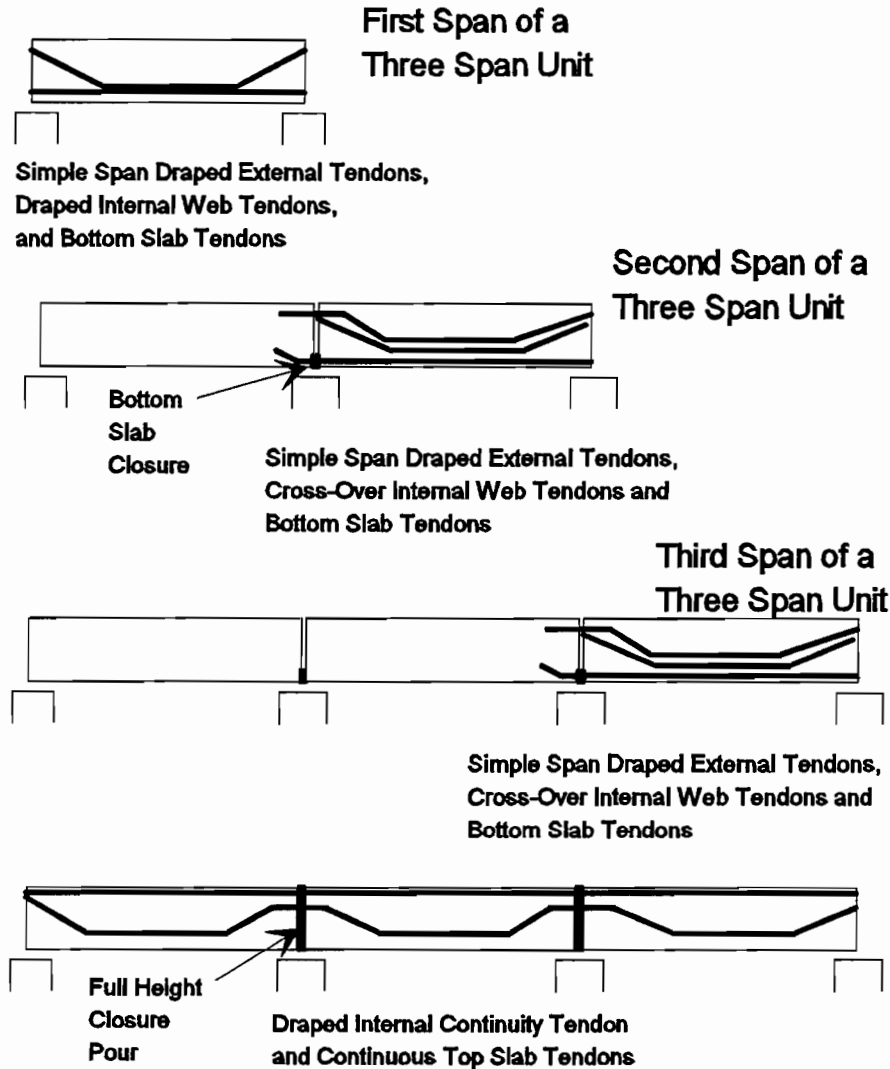


Figure 2.6 Schematic of tendon layout for three span continuous unit for Phase IIC.

2.4 Construction Procedures

The construction procedures did not vary drastically from phase to phase. The primary differences were in the number and locations of closure pours. The following section outlines the construction operations for the final phase, IIC.

2.4.1 Precasting Operations.

2.4.1.1 Short Line Match Casting. A major advantage of short line match casting is that it requires less space and less formwork than long line match casting. Short line casting is also more adaptable to a wide variety of horizontal and vertical curvatures than long line casting. Since the curvatures on this project, an urban viaduct, are extreme, short line casting was the best approach.

The following is a chronological listing of operations involved in the short line casting operations. The operations begin early in the morning after the most recently cast segment has cured approximately 16 to 18 hours.

1. Surveyors check the relative positions of the segments to each other. This is accomplished by using four vertical leveling bolts and two horizontal centerline hairpins per segment (see Figure 2.7). At the same time concrete control cylinders from the new segment are tested. When the compression strength has reached the required level (4000 psi (28 MPa)) the transverse prestressing in the deck may be released.

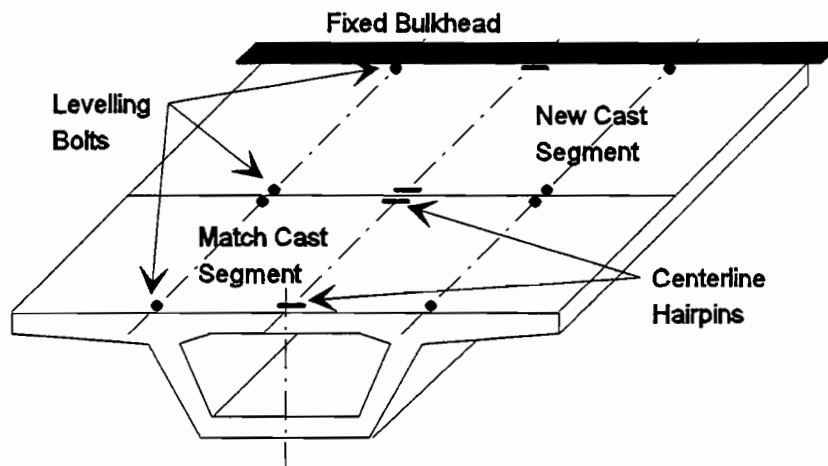


Figure 2.7 Geometry control hairpins and leveling bolts.

2. The wing forms are dropped, the core form collapsed, and the previously cast match cast segment is pulled away from the new cast segment. The transverse deck prestressing is cut.
3. The old match cast segment is moved to storage and the newly cast segment is moved into the match cast position. The empty soffit form (just vacated by the old match cast segment) is moved into the new cast position.

4. The forms are cleaned and oiled. The "donuts" which are used to position the post-tensioning ducts against the fixed bulkhead are moved as required.
5. The reinforcing steel cage, which was tied in a jig behind the forms the previous day, is set into the forms.
6. Post-tensioning ducts are positioned and tied to the reinforcing steel. Transverse deck prestressing is put into place. Final reinforcing steel adjustments are made.
7. The new match cast segment is moved into approximate position, and the core form is slipped in and expanded.
8. The surveyors and crew position the match cast segment in proper orientation with respect to the fixed bulkhead. The wing forms and core form are brought up snug against the match cast segment. Care is taken to ensure that snugging does not change the match cast segment's position.
9. The transverse deck prestressing strands are stressed.
10. Final adjustments to the reinforcing steel and wing end forms are made. The forms are cleaned out with compressed air to remove all loose objects.
11. A TxDOT inspector checks the segment and gives approval for the concrete placement.
12. The concrete is placed, beginning with the webs. Vibration is done very carefully to insure no honeycombing. The concrete in the bottom and top slabs and cantilever wings is then placed. Cylinders are made by quality control personnel.
13. After the top surface of the segment has been finished, surveying bolts and hairpins are inserted.
14. Curing mats are laid on the top slab and thoroughly wetted.

This entire operation requires a crew of two steel workers and four form setters and concrete workers, with the assistance of two surveyors, approximately six hours per segment to complete.

2.4.1.2 Scheduling. The contractor for Phase IIC, Austin Bridge and Road, operated a casting yard which had nine casting beds of varying segment shapes. They were able to cast up to eight segments per day. Two things which occasionally hindered their production were availability of approved shop drawings and adequate storage space for segments. During most of the yard's operation the shop drawing production group, a department of Austin Bridge and Road, was able to provide shop drawings in a timely fashion. The erection operations began much later than originally expected, and this caused a severe storage problem. Some segments were stored at the erection site, and additional land was leased adjacent to the casting yard for segment storage.

The only requirements of segment storage were that the segments cure at least 28 days before erection, and that they be supported at three points, two under one web and one under the other, to avoid warping problems.

In general, all casting operations proceeded very smoothly. The casting yard crews were very experienced. Some of the personnel had been working in the yard since the first project began in early 1985. The yard ran much like a manufacturing operation as opposed to a construction operation. The quality control team worked hard to ensure a very high quality product, since superior segment production results in fewer erection problems.

2.4.2 Erection Operations. Construction operations also varied little from phase to phase. The following is an outline of erection operations. The operations are idealized, assuming no problems occur, and organized into crew days. An erection crew normally comprised a foreman and six highly skilled laborers. The trusses were advanced and segments set by another highly skilled crew of riggers.

Crew Day 1 - Riggers

Preparation: supports for truss at next pier already in place and mid-span rollers also positioned.

1. The erection trusses are lowered to free them from the previously erected span. The truss then rests on rollers at each pier bracket and at the mid-span temporary supports.
2. A crane lifts the front end of one truss and pulls it forward. As the truss advances it is supported at various stages by different combinations of rollers. Finally the truss leading end is set on the new pier bracket.
3. The second truss is likewise advanced.
4. The trusses are raised to the correct elevation with jacks at each support location.

5. The positions of the trusses are checked to ensure that they are parallel.
6. Safety nets are pulled into position.
7. Segments are hauled to the site on flat bed trucks. A high capacity crane lifts the segments from the truck and places them on the trusses. The segments are rolled along the trusses and placed close to their final positions.

Crew Day 2 - Erection Crew

1. The pier segment closest to the previously erected span is accurately positioned by the crew and the surveyors.
2. The first typical segment is adjusted to fit properly against the pier segment (this is known as dry matching.)
3. The two segments are pulled slightly apart and the faces are smeared with a high strength epoxy. They are then pulled together with a required pressure of ~40 psi (275 kPa) on the faces. This is accomplished using a temporary post-tensioning system which uses Dywidag threaded rods anchored in intermediate slab blisters (see Figure 2.8.)

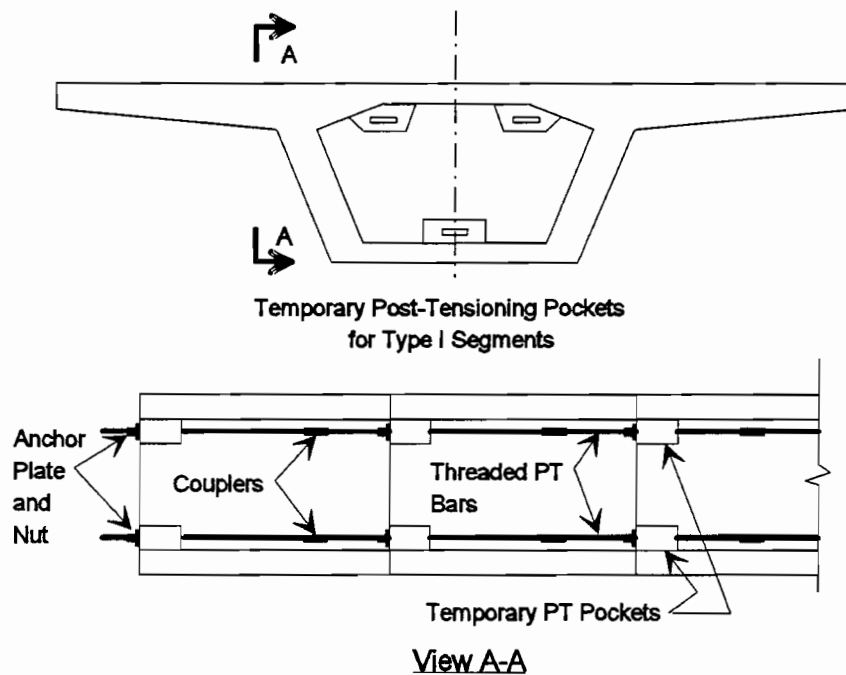


Figure 2.8 Temporary post-tensioning pockets.

4. The position of the second segment is checked by the surveyors. Any required adjustments are made.
5. All remaining segments (from 9 to 19 segments per span) are dry matched.

Crew Day 3

1. The segments are pulled back so an approximately one foot gap is opened between the second and third segments of the span.
2. One at a time the segments are epoxied and temporarily post-tensioned together.
3. After the last segment is epoxied the position of the span is checked again by the surveyors.
4. The span position is corrected as required.
5. Mortar is dry packed between the pier segments and their bearing plates.
6. Any required closure pours are made.

Crew Day 4

1. The high density polyethylene ducts for the external post-tensioning tendons are cut and positioned.
2. All post-tensioning strands are cut and bundled into proper size tendons. The ends are welded together and an eye for the pulling cable is attached.
3. For each tendon a lead wire is first pushed through the duct. Next, the tugging line is pulled through and attached to the tendon. Finally a winch is used to pull the tendon into its duct.
4. The ends of the tendons are trimmed and the wedge plates and wedges are installed.
5. After the bearing dry packed mortar and closure pour concrete have reached the proper strength, the tendons are stressed.
6. The temporary post-tensioning is removed.

This is a description of an ideal, problem free erection procedure. Almost every span had its own special dilemma which slowed down the erection process. The average erection rate was one span for every 5 1/2 crew days.

2.5 Summary

An understanding of the general layout of the project as well as the precasting and erection operations was required to prepare the instrumentation program. In developing and selecting instrumentation systems, a great deal of attention was paid to how the installation of the systems would fit into the construction operations. One objective was to disrupt contractor activities as little as possible. This chapter describes the basic background information on the project from which the instrumentation program was developed.

CHAPTER 3 INSTRUMENTATION LAYOUT AND INSTALLATION

3.1 Introduction

This chapter briefly describes the instrumentation systems which were installed in the San Antonio "Y" Project. A detailed description of the instrumentation systems, their installation and their field performance is provided in the first report of this series.. Instrumentation layouts are provided in this chapter for easy reference.

This chapter also introduces the four spans which were selected for instrumentation and some details about those spans.

3.1.1 Instrumentation Systems. Chapter 1 outlined the primary areas of uncertainty in the *AASHTO Guide Specification*¹ which were chosen for study in this project. A preliminary study of these areas was made to determine the types of measurements of the structure which were needed to provide information on the specific areas.

The following is a list of measurements which were deemed necessary:

1. Tendon Forces,
2. Reinforcing Steel Strains,
3. Concrete Strains,
4. Span Deflections,
5. Concrete Temperatures,
6. Joint Openings.

A comprehensive study was undertaken by Arréllaga⁷ to determine those instrumentation systems which were best suited for the field project. The chosen systems are briefly described in sections 3.2 to 3.7.

3.1.2 Instrumented Spans. It was determined that, based on the resources of the project, three spans would be extensively instrumented and one semi-continuous unit would also be partially instrumented. After the number of spans was determined, the particular spans were selected

Many factors were taken into account in the selection of the spans to be instrumented. The primary considerations were:

1. Location of the spans in the contractor's erection schedule,
2. The type of box shape in the span,
3. The location of each span in its unit,
4. The transverse post-tensioning to adjacent boxes,

5. The length of the span,
6. Accessibility.

The following sections describe each of these factors in more detail.

3.1.2.1 Contractor's Schedule. Figure 3.1 shows the entire project layout and the positions of the four instrumented spans. One of the primary reasons for these spans' selection was their position early in the erection schedule. Based on the contractor's original schedule, erection was to begin at abutment C9 and progress up the ramp (Spine C-2) until the gore area spans (C15 and A49) were erected. At this time the erection would proceed both up-station and down-station on the mainline (Spine A). Based on this erection schedule, the instrumented spans were to be the 1st, 3rd, 13th and 14th spans erected.

3.1.2.2 Box Shape. Another factor taken into consideration was the box shape. The ramp spans (C9 and C11) are constructed of Type I boxes (see Figure 3.2a) which are 8 feet (2.44 m) wide at the bottom of the box and have a 26 foot (7.92 m) wingspan. The mainline spans (A43 and A44) comprise Type III boxes (Figure 3.2b) which are 16 feet (4.88 m) wide at the bottom of the box and have a considerably wider wingspan, 58 feet (17.68 m). Studying both types of boxes provides more complete information on shear lag effects, which are in part a function of the wingspan and the distance between web walls.

3.1.2.3 Location in Span. It was desirable to study spans which occupied different positions in a unit. Span C9 is the first span of a semi-continuous unit. Span C11 is the first span of a two span fully continuous unit. Span A44 is the first and Span A43 the second span of a three span continuous unit.

3.1.2.4 Transverse Post-tensioning to Adjacent Boxes. One question raised by TxDOT designers concerned the behavior of adjacent boxes which were post-tensioned together transversely (see Figure 3.3). This transverse post-tensioning complicates the behavior significantly, so only one span of this type (Span C11) was chosen. The other three spans are symmetric and independent.

3.1.2.5 Length of Span. The spans were also selected based on their length. The spans with the greatest length, and hence greatest number of external tendons, would be the most critical. Areas such as anchor zones and deviators would be subjected to the worst case loads in the longest spans. Span C11, at 110 feet (33.53 m) long, is the longest Type I box span on the project. Spans A43 and A44, at 110 feet (33.53 m) long, are exceeded in length by only one span, A42 at 115 feet (35.05 m).

3.1.2.6 Accessibility. Finally, access to the spans during all construction processes and after the bridge had been opened to traffic was considered. Access to the inside of the bridge is gained through openings in the first down-station (closest to the east end) typical segment of each span. Spans C9 and C11 can be accessed through the opening in span C9, which requires a 10 foot (3 m) ladder. Spans A43 and A44 pass directly over an exit ramp

foot (3 m) ladder. Spans A43 and A44 pass directly over an exit ramp and must be accessed through the access opening in span A46, which requires a longer 20 foot (6 m) ladder.

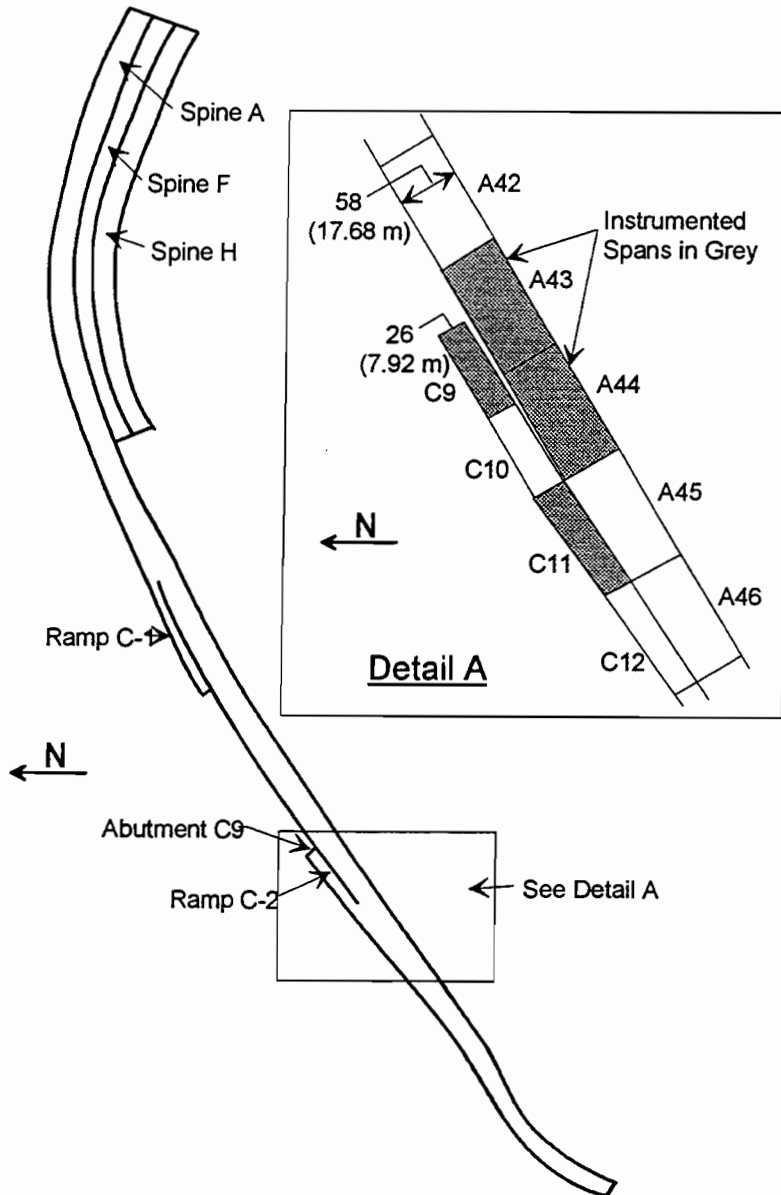
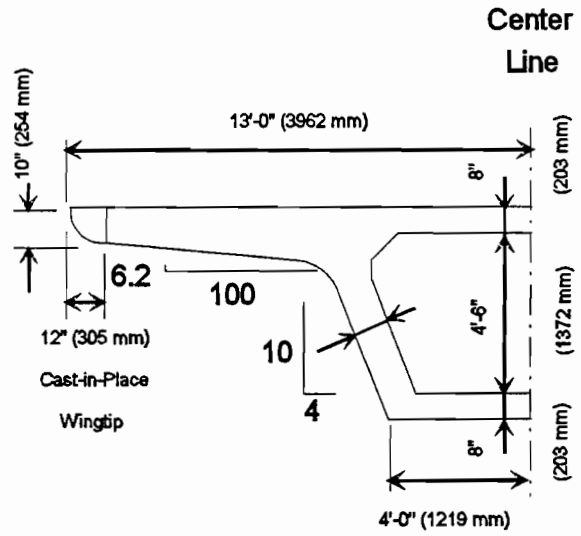
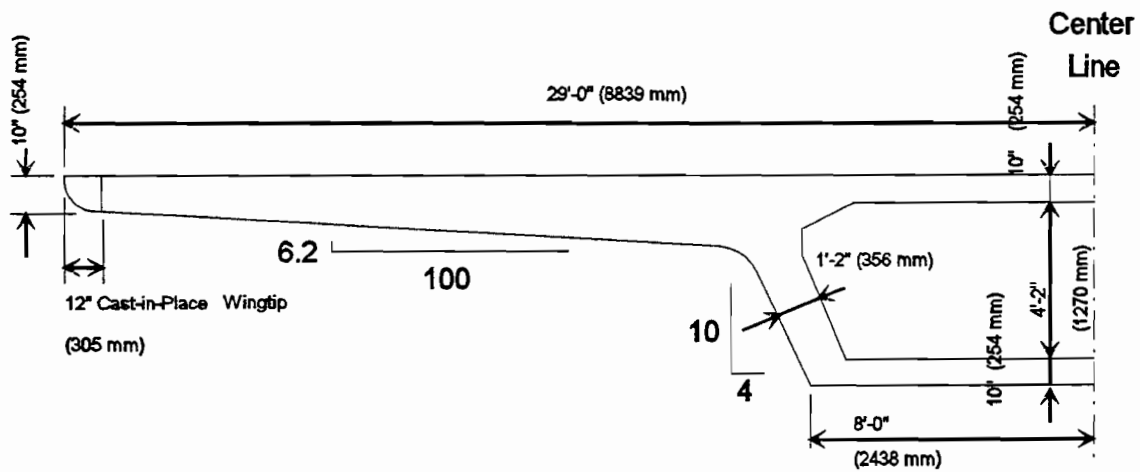


Figure 3.1 Project IIC layout.



a) Typical Type I Segment
Spans C9 and C11



b) Typical Type III Segment
Spans A43 and A44

Figure 3.2 Instrumented segment shapes.

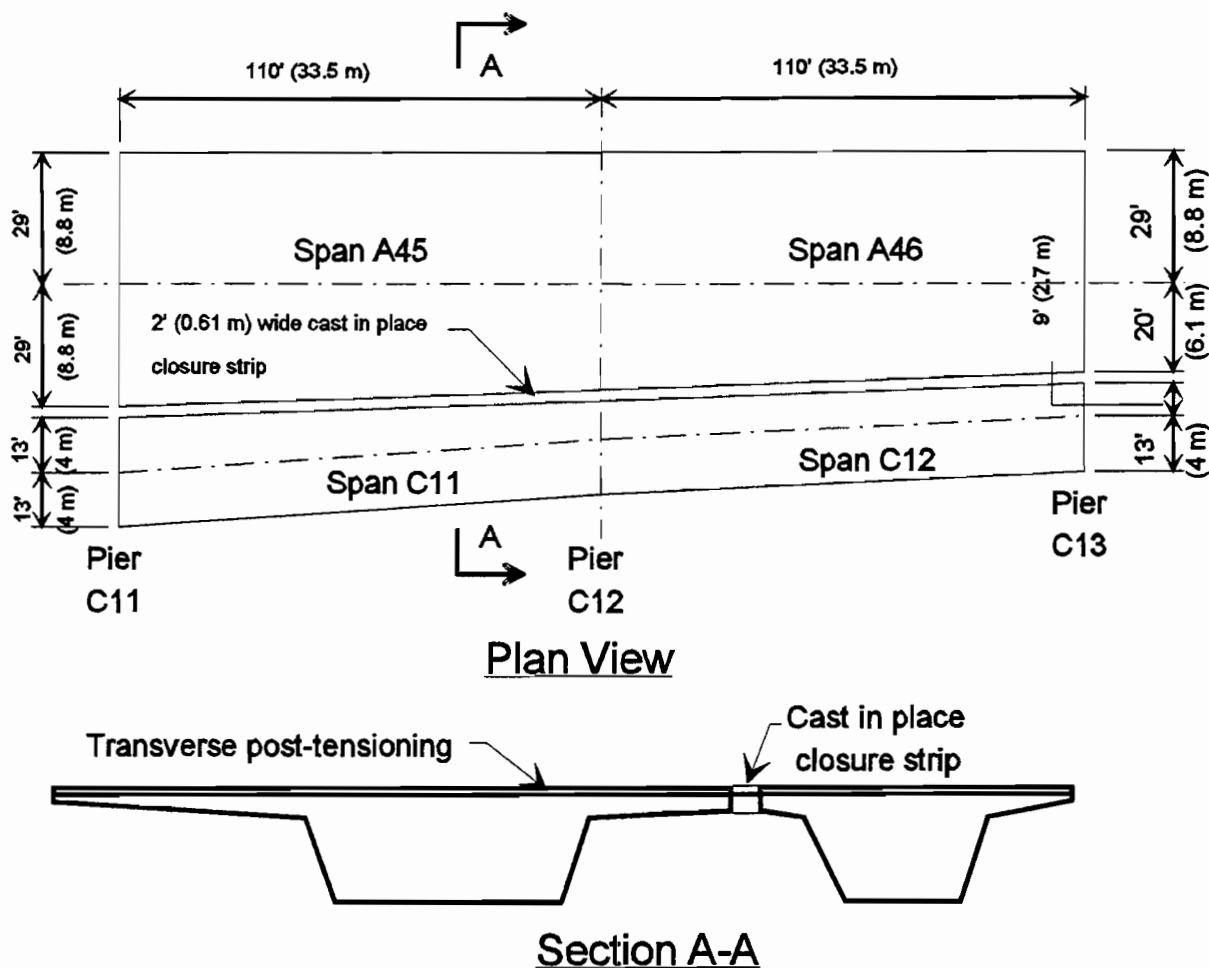


Figure 3.3 Span C11 Details.

The four spans, after selection was finalized, were then studied more thoroughly to determine the optimum placement of instrumentation systems. The following sections describe the systems and their locations in the spans. Details on system selection and installation are presented in the first report of this series.

3.2 Tendon Forces

Tendon force measurement is obviously crucial in understanding losses in post-tensioning tendons. It is also a necessary piece of information when studying other aspects of the bridge such as anchor zone and deviator behavior and overall span deflections. Since this is such a critical measurement, two systems used in conjunction were selected. The systems are briefly described in the following sections.

3.2.1 Epoxy Sleeve System. Many problems are inherent in measuring total tendon forces. Each strand which makes up a multi-strand tendon carries a different force due to variations in seating at the anchor head and interaction between strands at deviation points. Also each wire of a seven wire strand has a slightly different stress. Hence a strain gage placed on a single wire of a single strand might not accurately represent the tendon force. A system was required which would measure the average strain in the entire tendon.

Figure 3.4 illustrates the system which was developed in the laboratory by Arréllaga.⁷ Two large epoxy sleeves are cast around the multi-strand tendon. The epoxy is Sikadur-32, Hi-Mod which is manufactured by SIKA Corporation. It is packaged in two equal sized containers, one containing the resin and one the hardener. The two parts are mixed together for a minimum of three minutes and the mixture has a pot life of 30 minutes. The sleeves have a center to center distance of approximately sixteen inches (406 mm). Two sets of Demec locating discs are epoxied to the sleeves. Demec locating discs are small stainless steel discs with a small hole drilled in the center. The Demec extensometer (see Figure 3.5) has two points which seat firmly into the holes in the locating discs. The dial gage reading on the Demec extensometer registers changes in the distance between the two points. The resolution is 4 microstrain, and the reader error is approximately plus or minus 8 microstrain.

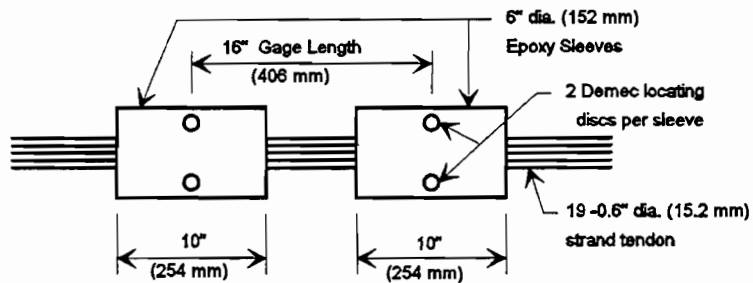


Figure 3.4 Schematic of epoxy sleeve system.

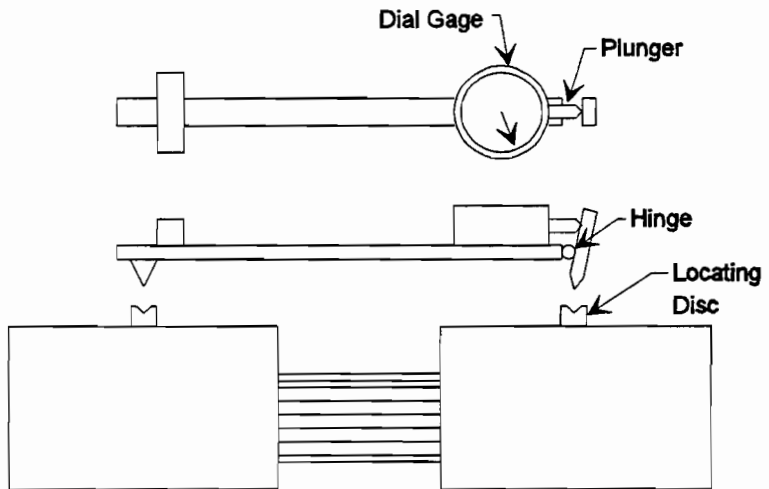


Figure 3.5 Demec extensometer.

3.2.2 Electrical Resistance Strain Gages. Tests performed on the epoxy sleeve system indicated that many of the problems of electrical resistance gages used on post-tensioning strands could be eliminated if the gages were used in conjunction with the epoxy sleeve system. The epoxy grips the strands and forces them to work more as a unit between the two sleeves. Electrical resistance gages placed between the sleeves would therefore give a better indication of the average strain in the tendon.

Other problems of the electrical resistance gages were solved by carefully selecting the gage system. 350 ohm gages were chosen, as opposed to standard 120 ohm gages, to reduce the signal to noise ratio. A Campbell Scientific 21X Data Acquisition system was chosen and designed to be placed permanently in each span. The systems are powered by large 12 volt batteries. This eliminates errors involved in connecting and disconnecting data acquisition systems, because connection resistances vary. The possibility of losing data due to a power failure is also eliminated.

The gages were attached to the strands with a high strength, long-life 2 part epoxy (M-Bond AE-10/15). This eliminates, to some degree, the problem of gages debonding during stressing or with time.

To eliminate the problem of gages shorting out during pressure grouting operations, grout was by-passed around the area between the sleeves (see Figure 3.6). The strand between the sleeves was protected with a rust inhibiting grease (PT-1001 by Viscosity Oil.)

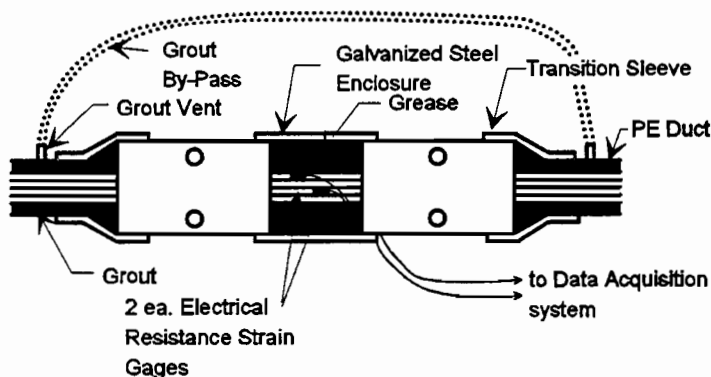


Figure 3.6 Schematic of grout by-pass system.

3.2.3 Tendon Force Instrumentation Layouts.

Figure 3.7a and b show the basic layout of the tendon strain measurements. Each external tendon comprises three straight lengths of tendon. It was assumed that the strain would be constant along each straight length of tendon, so only one reading location was required. In this way each tendon provided a live end, middle, and dead end reading. The figure also shows the locations of the Campbell data acquisition systems, which were placed in specially fabricated lock boxes. The lock boxes were designed to position the data acquisition system just above the external tendons which run at 4 inches (102 mm) above the top of the bottom slab of the box. This placed the data acquisition system approximately 10 inches (254 mm) above the top of the bottom slab. A severe rain storm caused flooding inside two of the spans and in one span the data acquisition system was damaged by the water. In future instrumentation projects, the system should be placed in a safer location.

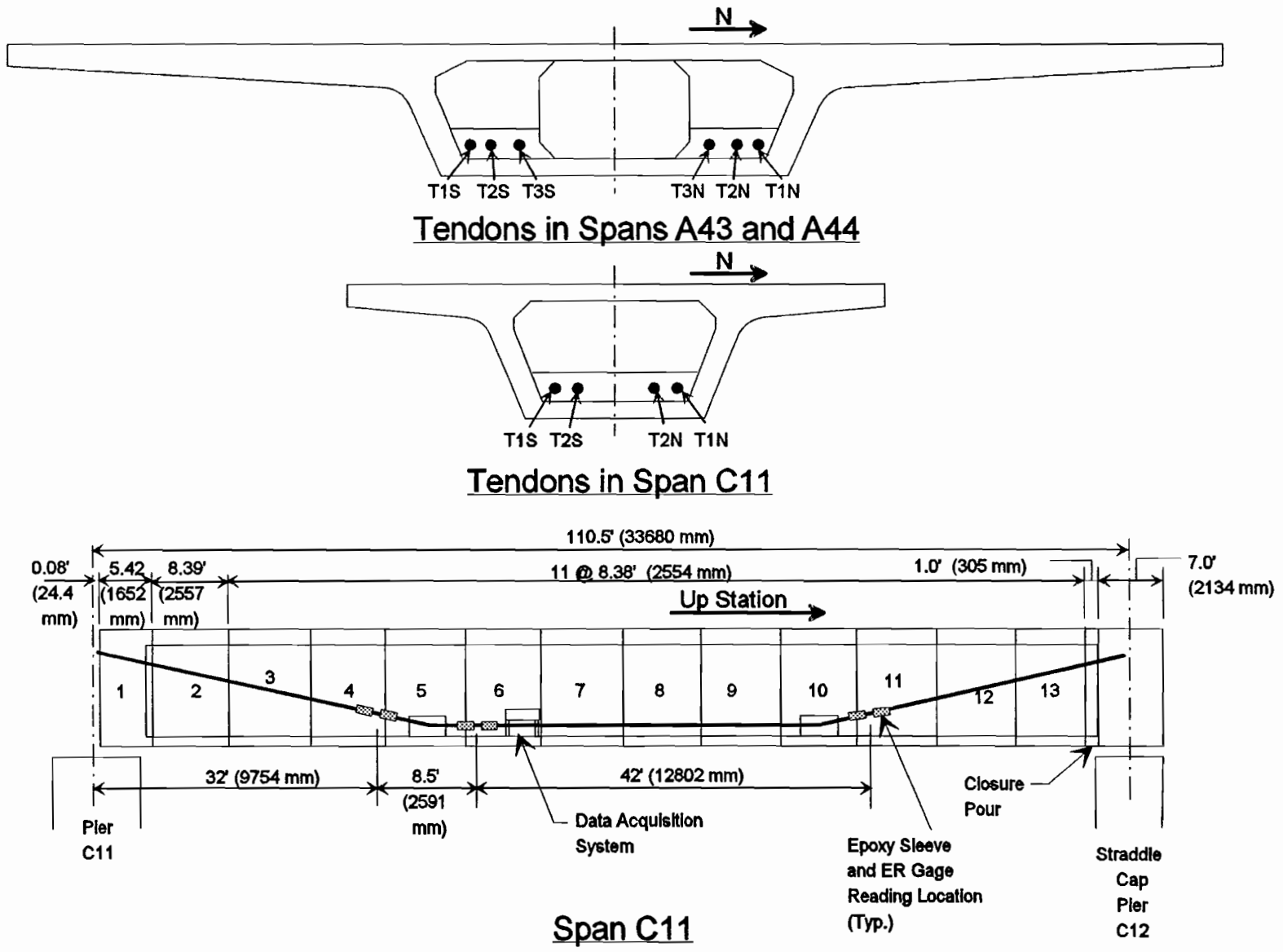
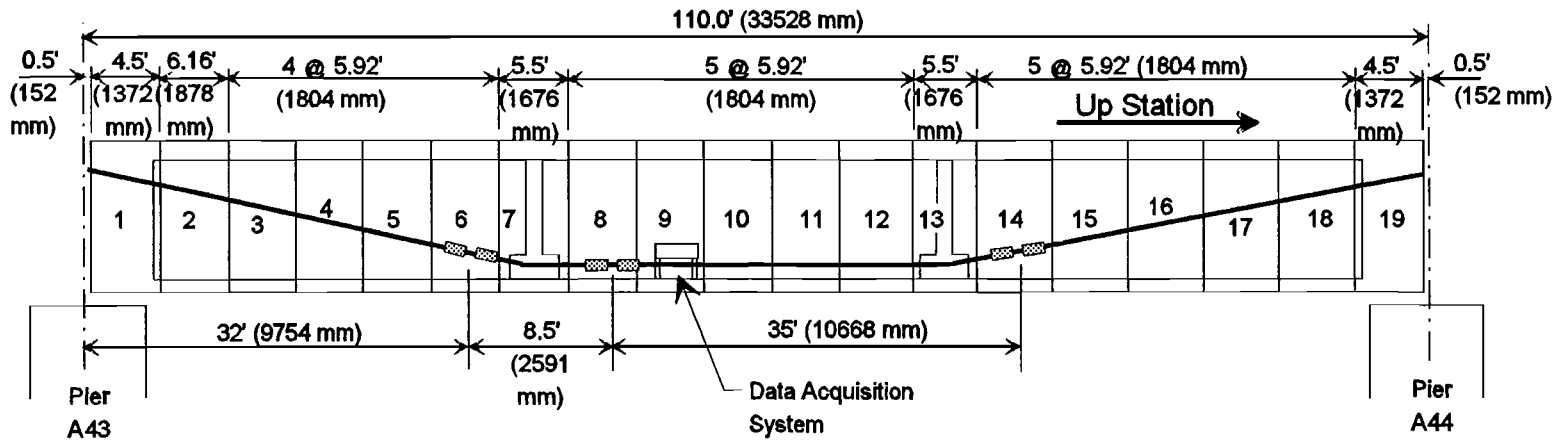
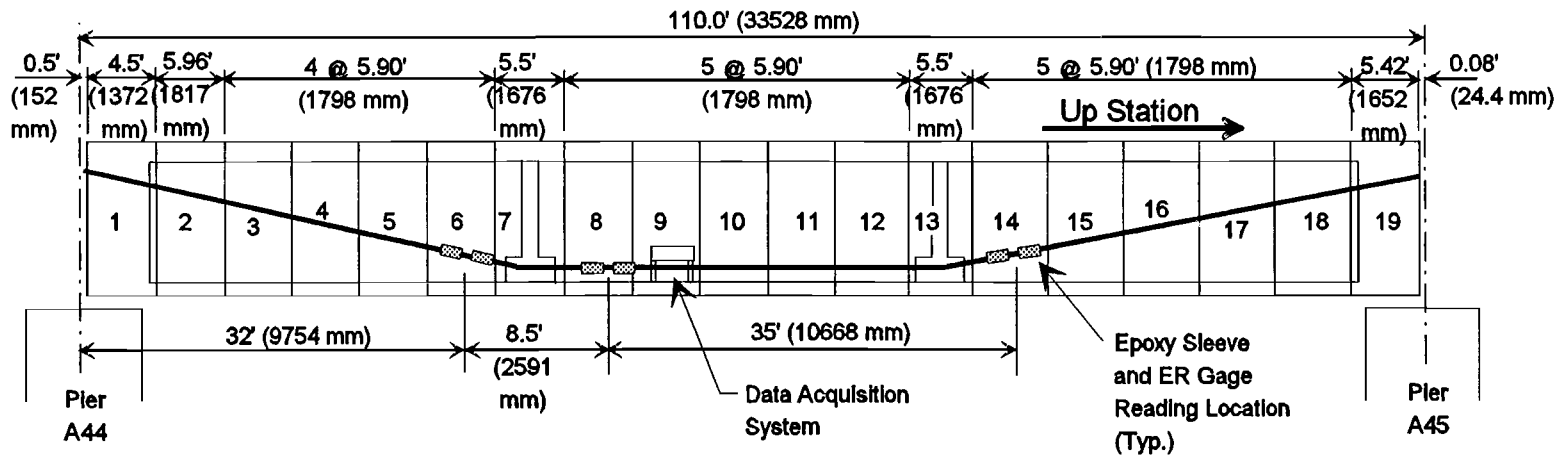


Figure 3.7a Tendon Force instrumentation layouts.

Figure 3.7b Tendon force instrumentation layouts.



Span A43



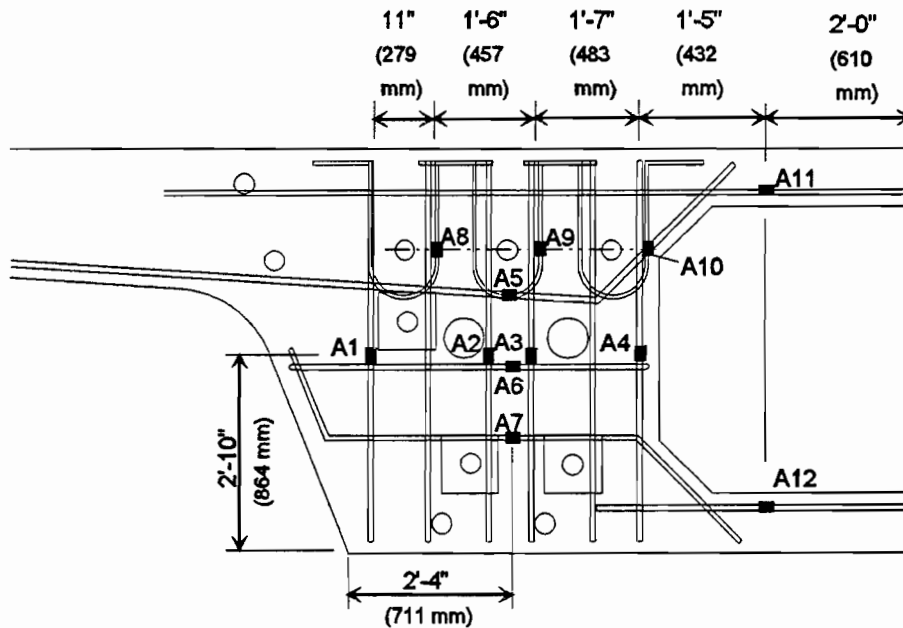
Span A44

3.3 Reinforcing Steel Strains

3.3.1 System. Reinforcing steel strains were needed to study anchorage zone and deviator behavior. The same ER gages which were used on the post-tensioning strands were also used on the reinforcing steel, and the gages were similarly connected to the data acquisition system.

The primary difference between the reinforcing steel gages and the post-tensioning strand gages was the waterproofing. Since the gages on the reinforcing steel were to be cast in concrete, it was necessary to protect them well from moisture. After the leads were soldered, the gages were painted with M-Coat B (by Measurements Group Inc.), a waterproofing sealant. Then the gages were covered with a moldable rubber sealant and a piece of vinyl covering, held in place with cable ties. Finally the edges were given another coat of M-Coat B to ensure no moisture penetration.

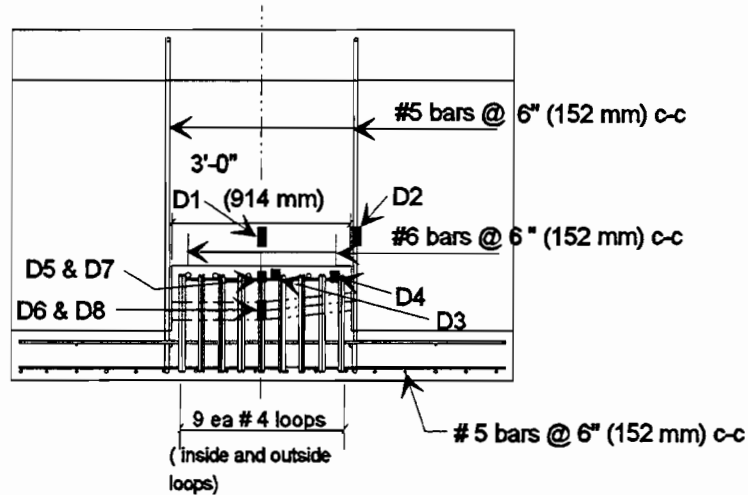
3.3.2 Layouts. Figures 3.8a, 3.8b, and 3.8c show the locations and designations of the reinforcing steel strain gages. Gages in deviators were given a "D" designation and those in the anchorage zones an "A".



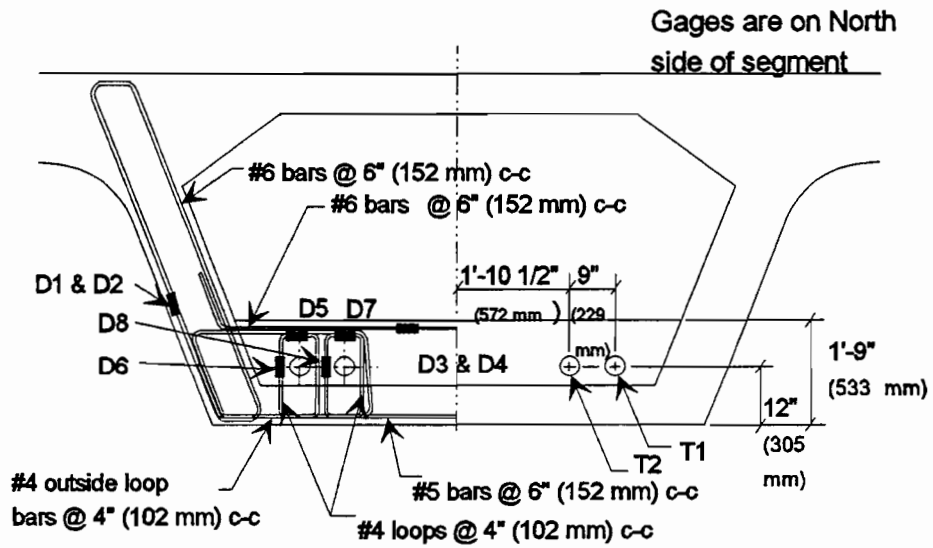
**Reinforcing Steel Strain Gage Layout
Pier Segments 43A-1 and 44A-1**

Gages are on the layer of reinforcing steel farthest from the anchor heads (most up station)

Figure 3.8a Reinforcing steel strain gage layouts.



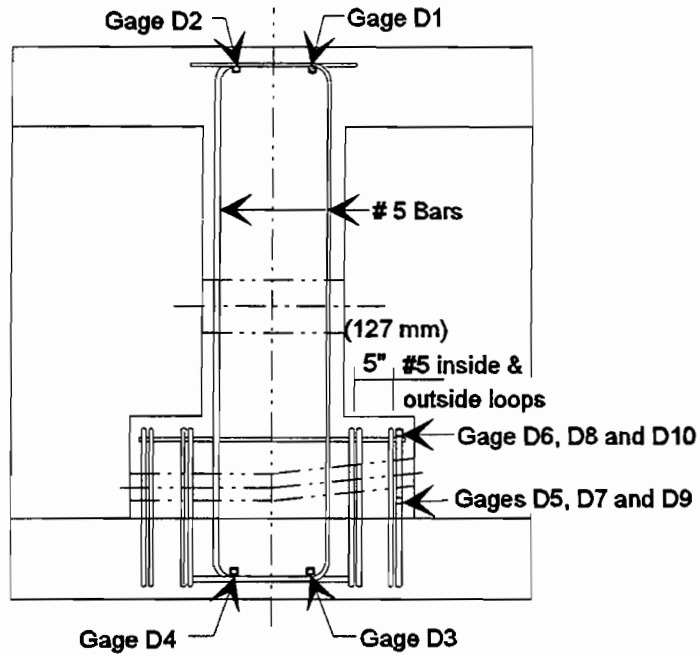
Segment 11C-5 Section View



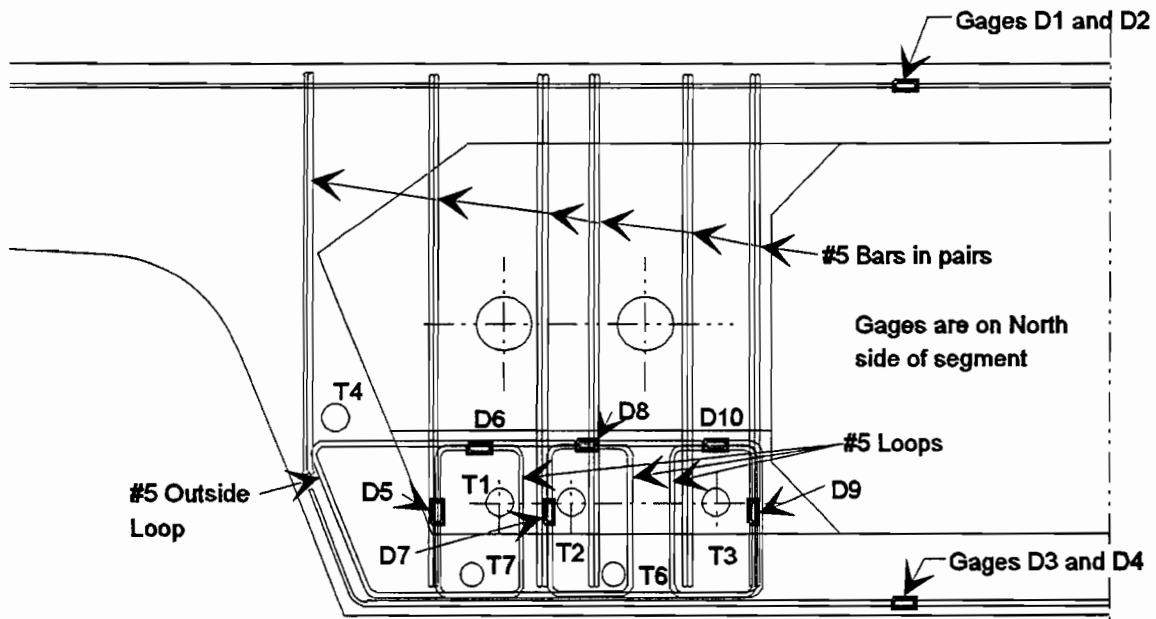
Segment 11C-5 Deviator Segment Elevation View

Typical segment bars not shown for clarity

Figure 3.8b Reinforcing steel strain gage layouts.



Segment 44A-7 and 43A-7
Section View



Segments 43A-7 & 44A-7
Deviator Segment Elevation View

Typical segment bars not shown for clarity

Figure 3.8c Reinforcing steel strain gage layouts.

3.4 Concrete Strains

3.4.1 System. The system chosen for measuring concrete strains is a Demec system with a modified locating disc attachment system. The Demec system normally consists of two small stainless steel discs which are epoxied to the surface of the concrete at a set gage length (200 mm for this project). The discs have a small drilled hole in the center. A removable mechanical extensometer seats into the holes in the discs and measures very precisely changes in the distance between the discs (see Figure 3.9).

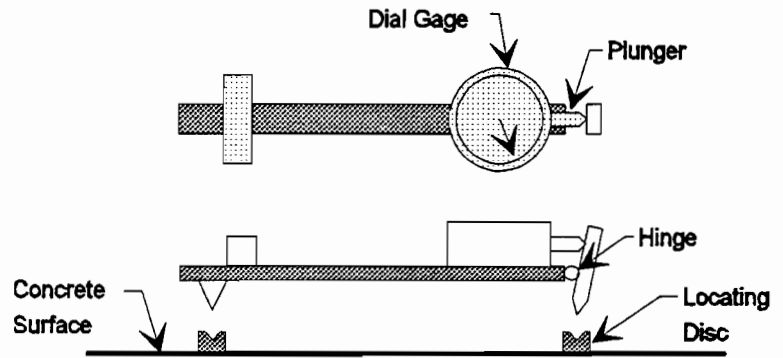


Figure 3.9 Demec extensometer.

One problem with this system which had been reported in previous field projects³⁴ was the debonding of the discs, particularly in cold or wet weather. To overcome this problem, a modified attachment system was developed (see Figure 3.10). Commercially available stainless steel nail wedges were purchased and a hole, precisely matching the diameter of the hole in the Demec locating discs, was drilled in each. The holes were drilled slightly off center to allow for misplaced drill holes in the concrete. The concrete was marked at the proper gage length and two holes were drilled with a hammer drill. The nail inserts were then placed in the holes and the gage length between the holes on the nails checked. The distance between the Demec points can be adjusted by rotating the off center holes. Then, noting the orientation of the insert, the insert was removed from the hole and a small amount of epoxy was placed in the hole. The insert was then replaced and struck with a hammer to drive the nail into its sleeve and engage the expansion wedges. In this way the locating discs had both a mechanical and an epoxy attachment to the concrete.

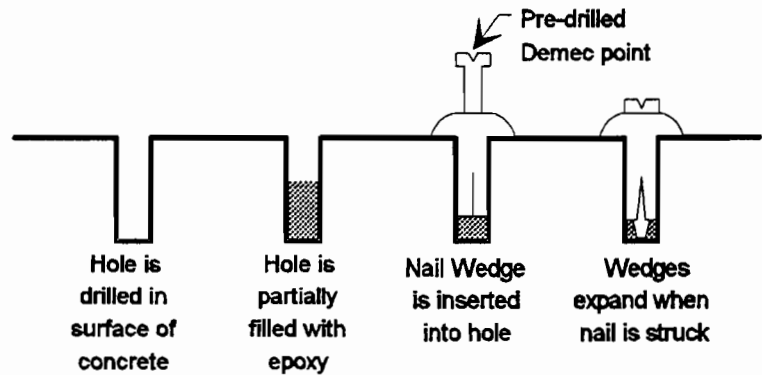
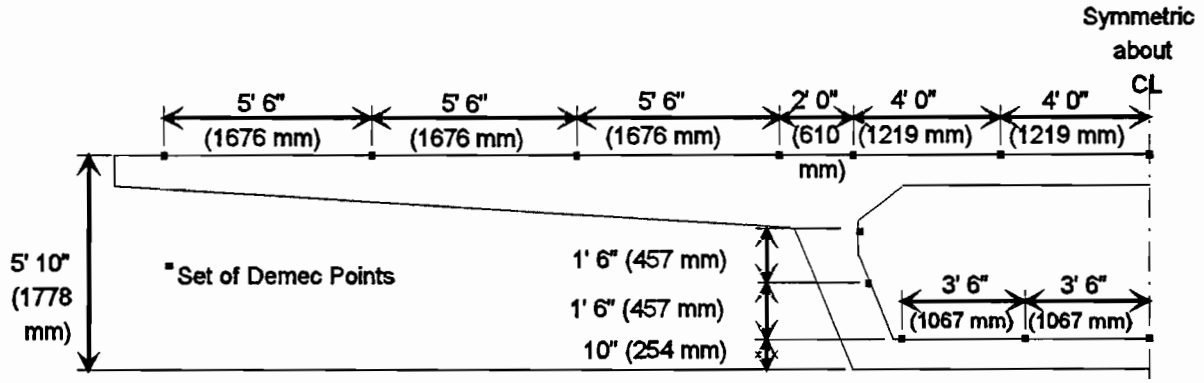
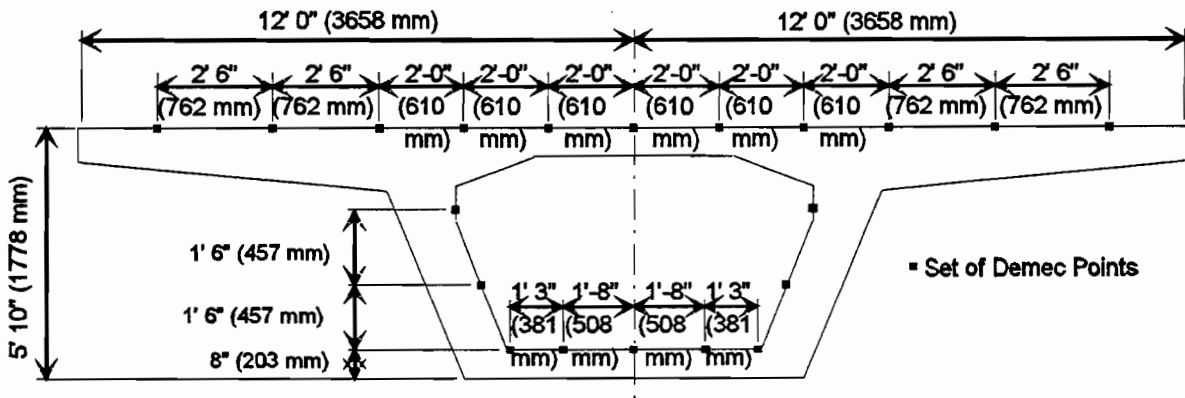


Figure 3.10 Modified Demec attachment system.

3.4.2 Layouts. Figures 3.11a and 3.11b show the layouts of the surface strain gages. During stressing operations one reader and one recorder measured the top slab points and another pair measured the points inside of the box.

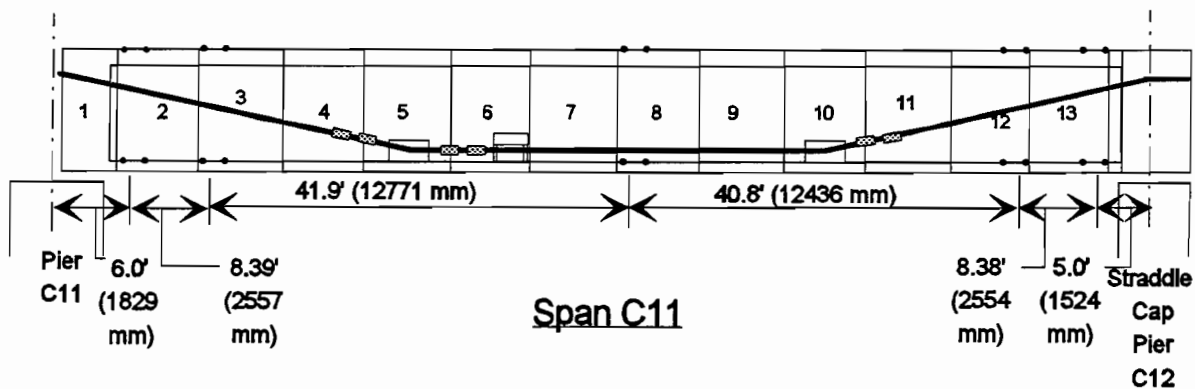
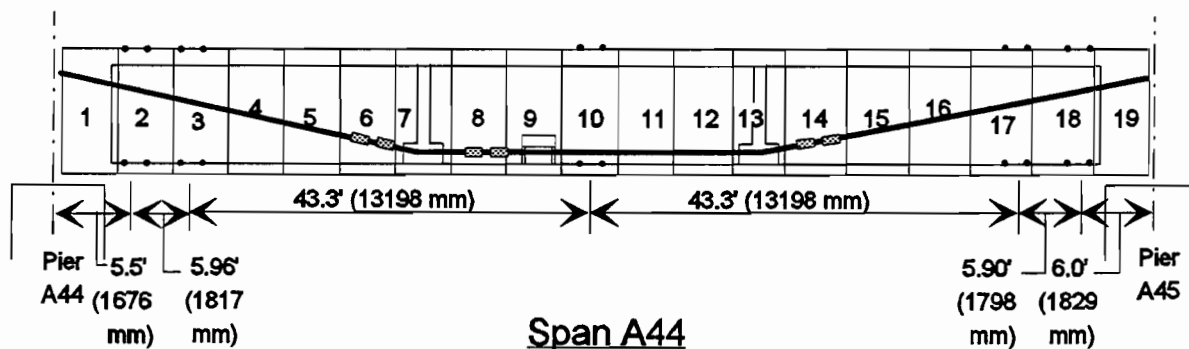
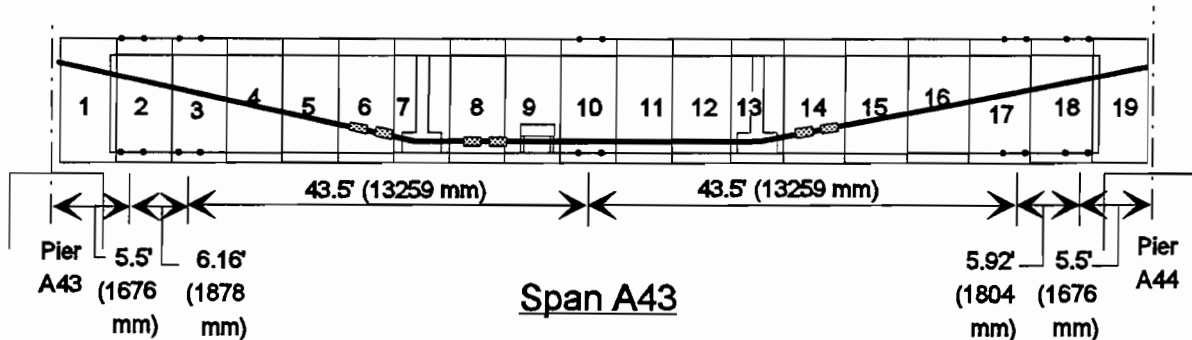


Spans A43 and A44 Demec Point Layout



Span C11 Demec Point Layout

Figure 3.11a Demec point layouts.



Dimensions are to the center of pair of Demec Points
 Demec Point gage length is 8" (203 mm)

Figure 3.11b Demec point layouts.

3.5 Span Deflections

3.5.1 System. The system chosen to measure span deflections is known as the taut wire baseline system (see Figure 3.12). The system consists of a bracket placed on the underside of the top slab immediately above the bearings, to which a high strength piano wire is attached. A second bracket, with a low friction roller, is placed above the bearings at the opposite pier. The piano wire is placed in a groove on the roller and a weight is hung on the wire. In this way the wire is tensioned with a constant weight and should maintain a constant profile. Non-corroding, but magnetic, steel plates are attached to the underside of the top slab at the quarter points, mid-point of the span and directly adjacent to the dead end bracket. A digital sliding ruler on a magnet base can then be placed on each plate, in a precise location delineated by guide bars, and can measure the distance from the plate to the wire. As the profile of the bridge changes, the difference in the distance to the wire can be measured very accurately ($\pm 0.005''$ (± 0.0013 mm)).

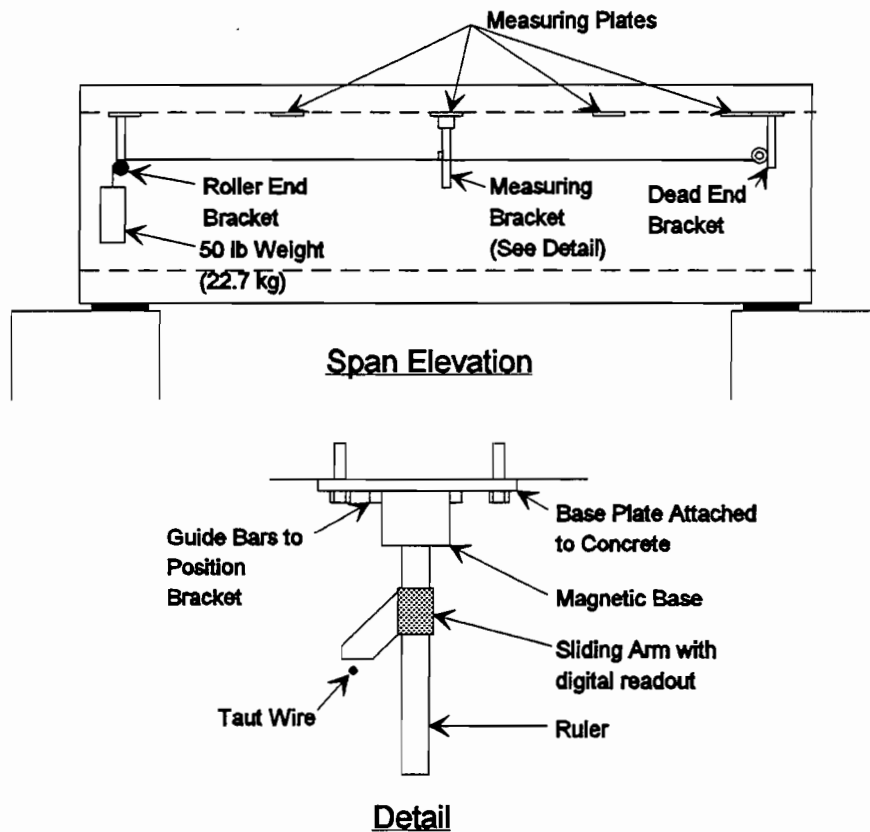


Figure 3.12 Taut wire baseline system.

3.5.2 Layouts. Figure 3.13 shows the layouts of the deflection measurement system. In three of the spans the deflections could not be read directly on the centerline of the box because a drainage pipe was to be installed directly on the centerline. The measurement brackets were therefore slightly offset.

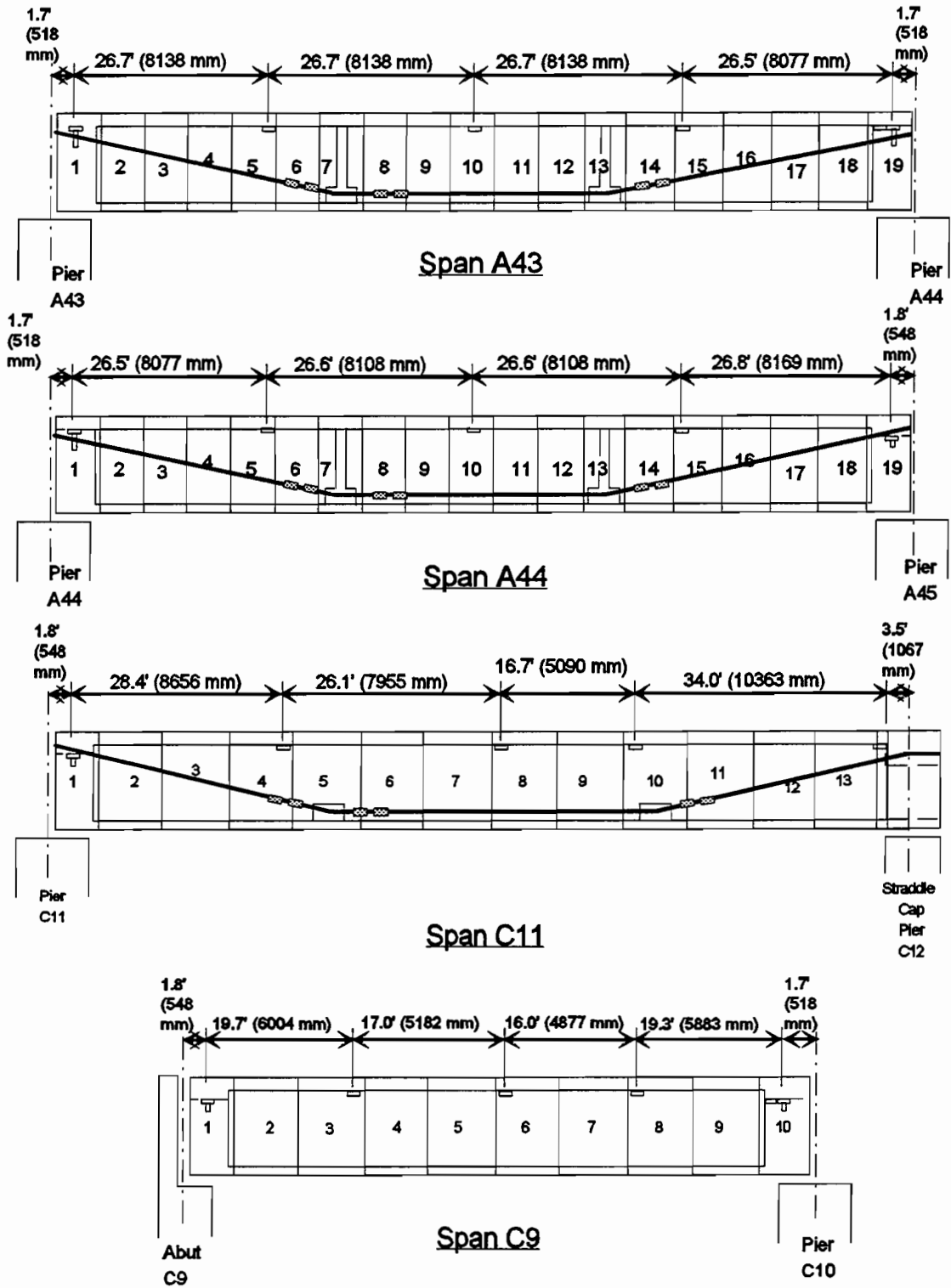


Figure 3.13 Deflection measurement system layouts.

3.6 Concrete Temperatures

3.6.1 System. Type T, copper-constantan, thermocouples were chosen to measure concrete temperatures. They are simple to install and very stable for long periods of time. Two systems for reading the thermocouples were used. One was a manually operated switch box to which a hand-held digital thermometer was attached. All gages to be read were connected to the panel of the switch box, as was the thermometer. Then the dial could be switched from thermocouple to thermocouple and the temperatures read from the thermometer. The other system was a Campbell 21X data logger. Eight thermocouples could be hooked to the data logger and the logger programmed to read temperatures at set time intervals. The data could then be extracted with the notebook PC.

3.6.2 Layouts. Figure 3.14 shows the thermocouple layouts. Thermocouples were installed for two purposes: to read horizontal gradients during match casting and to read vertical gradients due to climatic conditions.

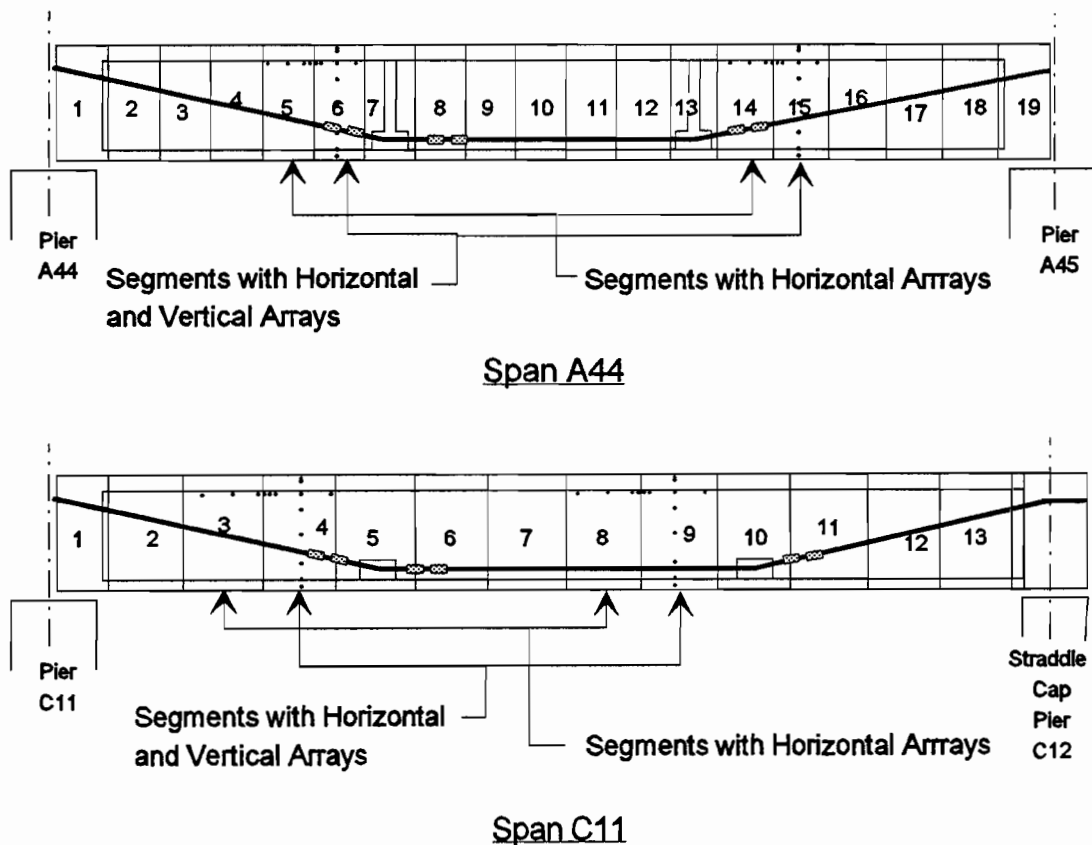
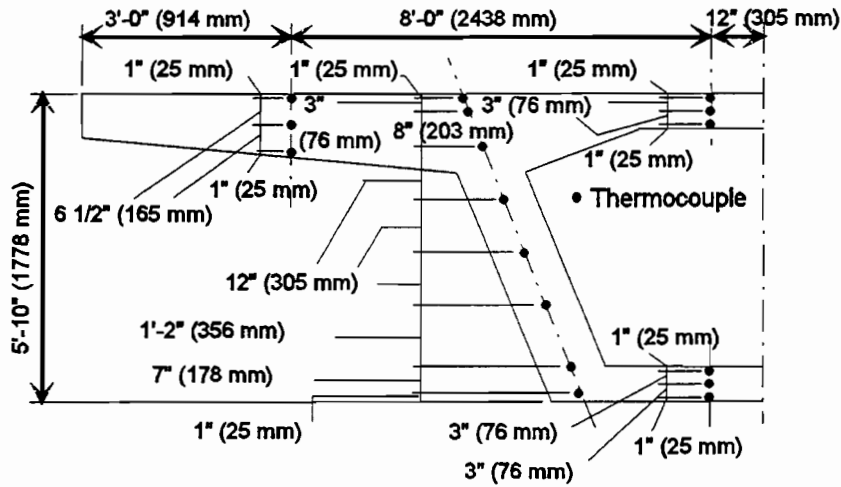
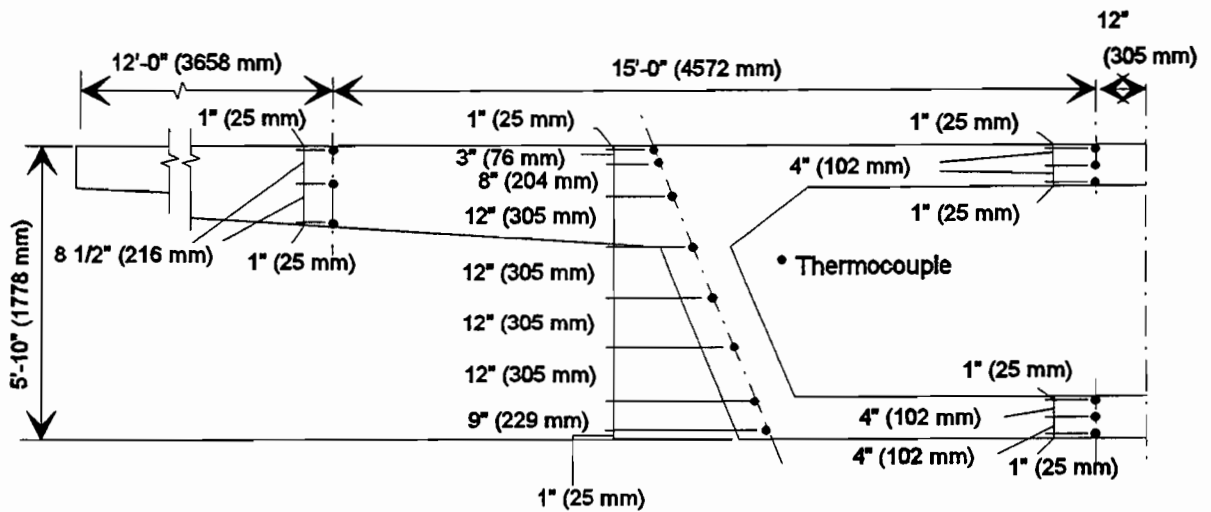


Figure 3.14a Thermocouple layouts.



Segments 11C-4 and 11C-9
Vertical Thermocouple Layout



Segments 44A-6 and 44A-15
Vertical Thermocouple Layout

Vertical arrays were placed at the longitudinal mid-point of the segment

Figure 3.14b Thermocouple layouts.

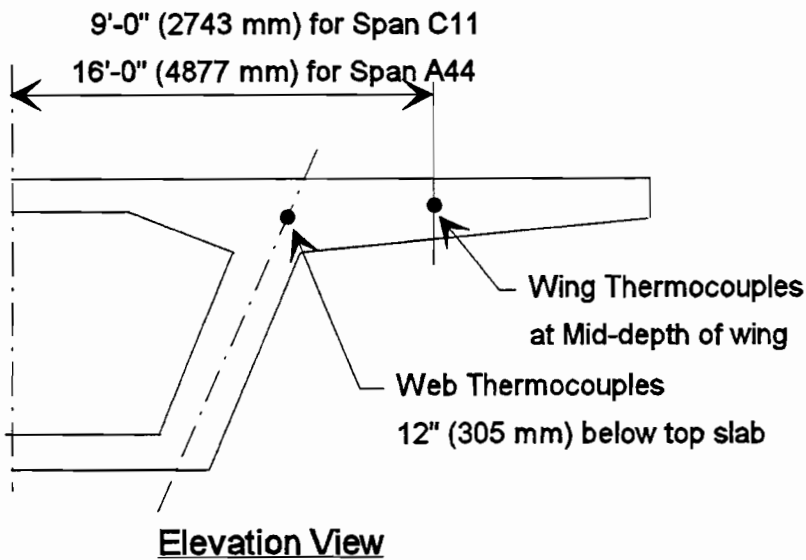
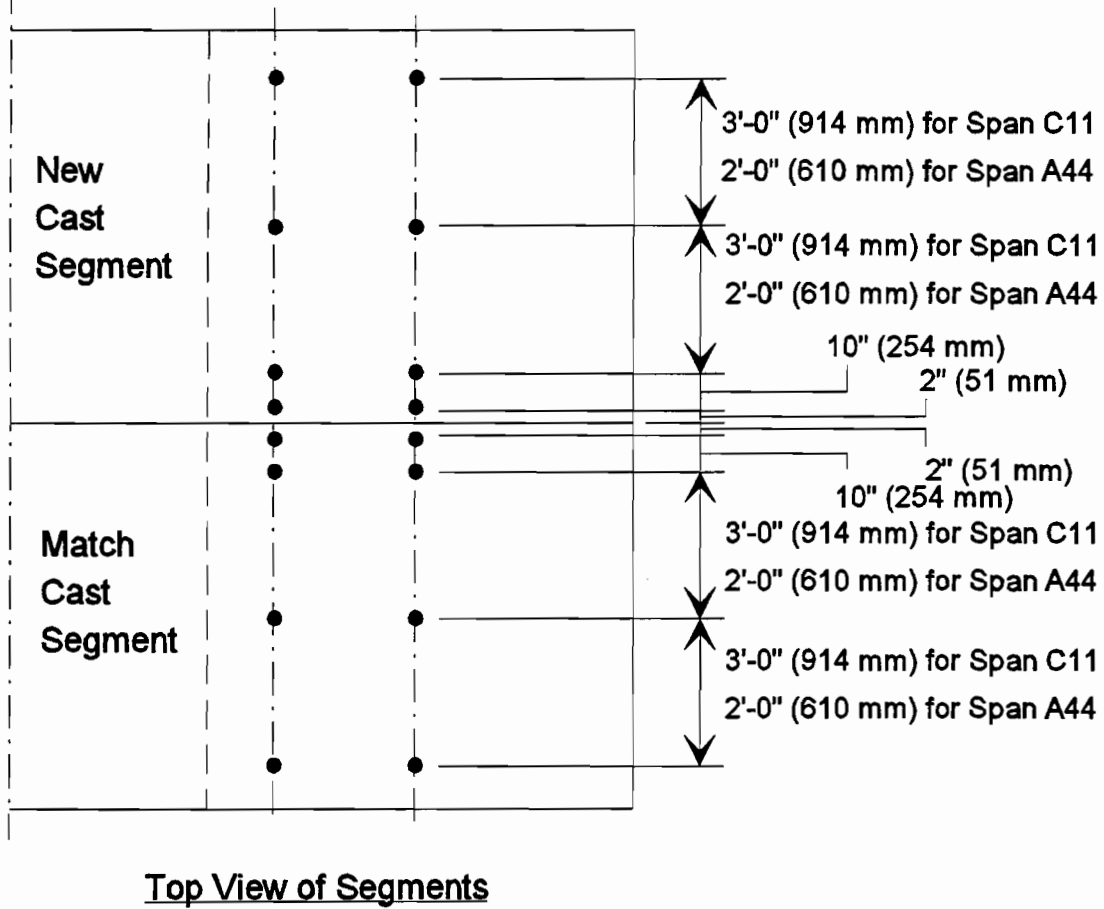


Figure 3.14c Typical horizontal thermocouple layout.

3.7 Joint Openings

3.7.1 System. A dual measurement system was chosen to measure joint openings. Both grid crack monitors and Demec gages were used (see Figure 3.15). In this way, a strain might be associated with the point at which a joint opens. A grid crack monitor is made up of one opaque and one transparent plastic plate. The opaque plate is mounted on one side of the joint, and the transparent plate is mounted on the opposite side and overlays the first plate. The opaque plate has a grid imprinted on it and the transparent plate has a cross-hair. If the plates move relative to one another, the amount of movement can be read off of the grid.

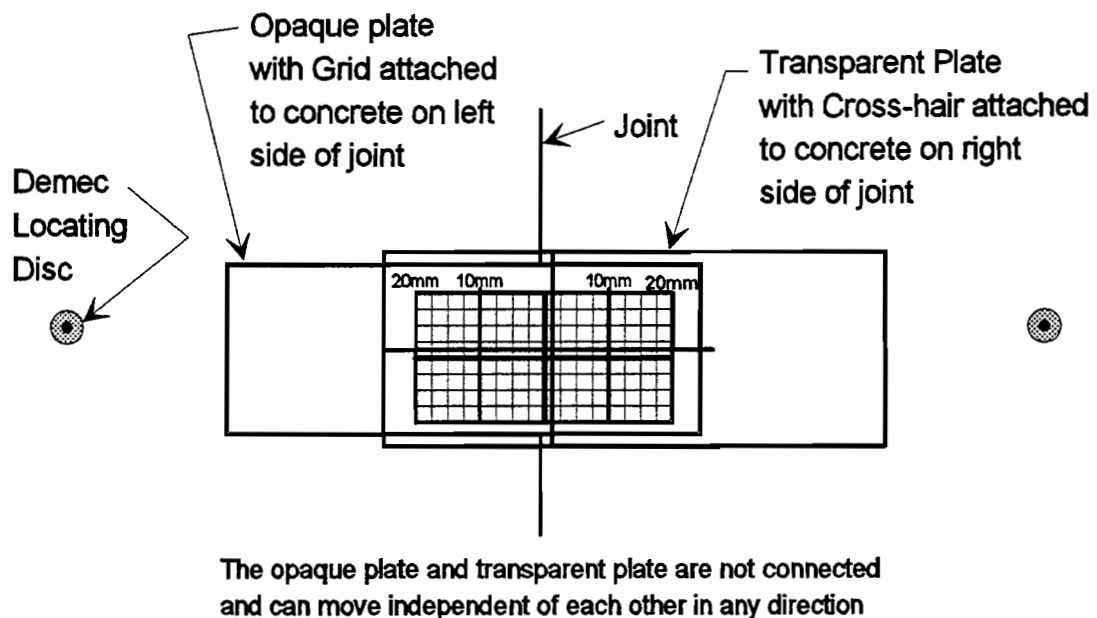


Figure 3.15 Grid crack monitor and demec points.

3.7.2 Layouts. Figure 3.16 shows the layouts of the joint opening measurement system. Due to the high cost of the grid crack monitors, only one web wall in each span was instrumented. Since all but one span were symmetric, one web wall was considered adequate.

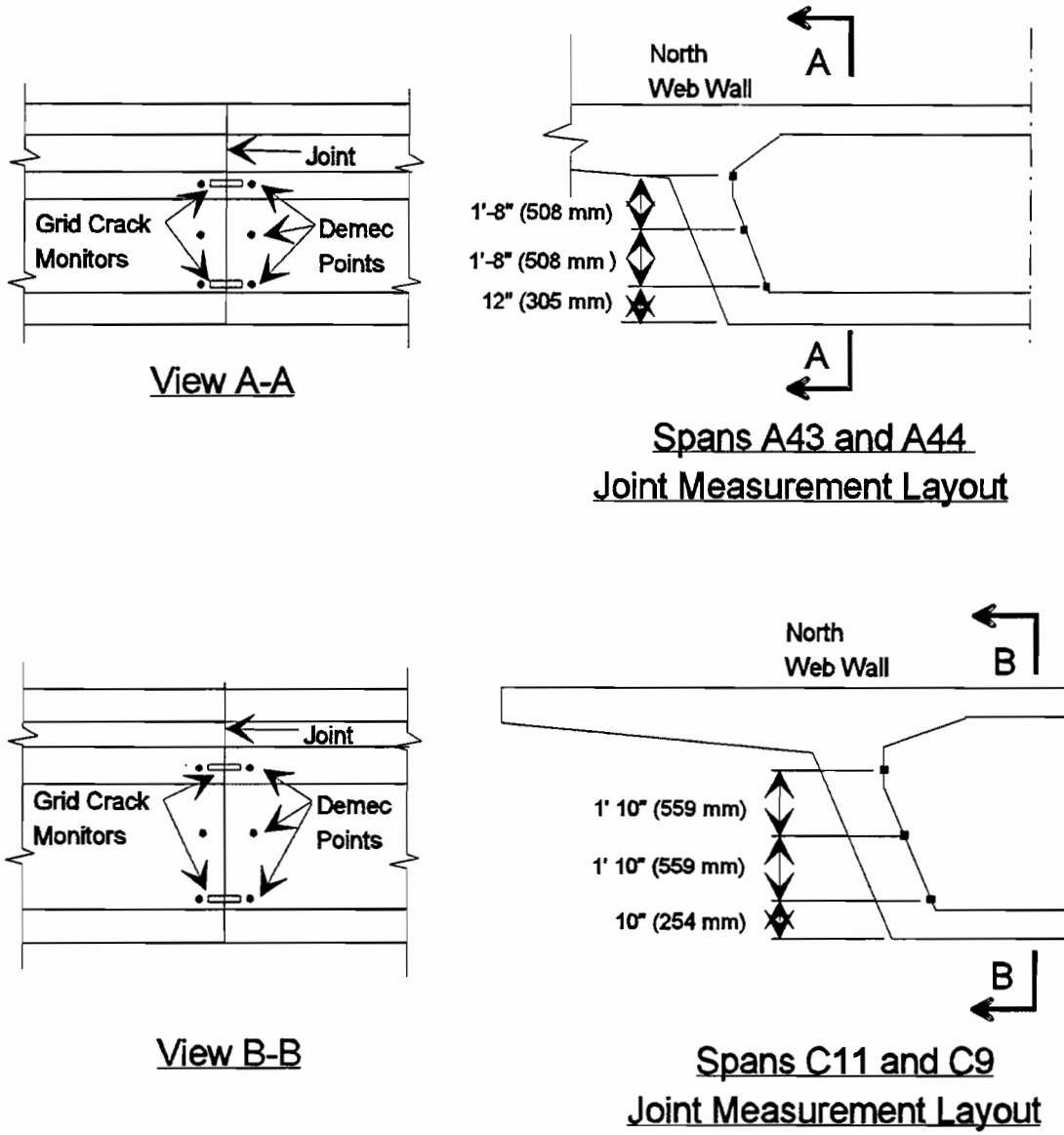


Figure 3.16a Joint movement instrumentation layouts.

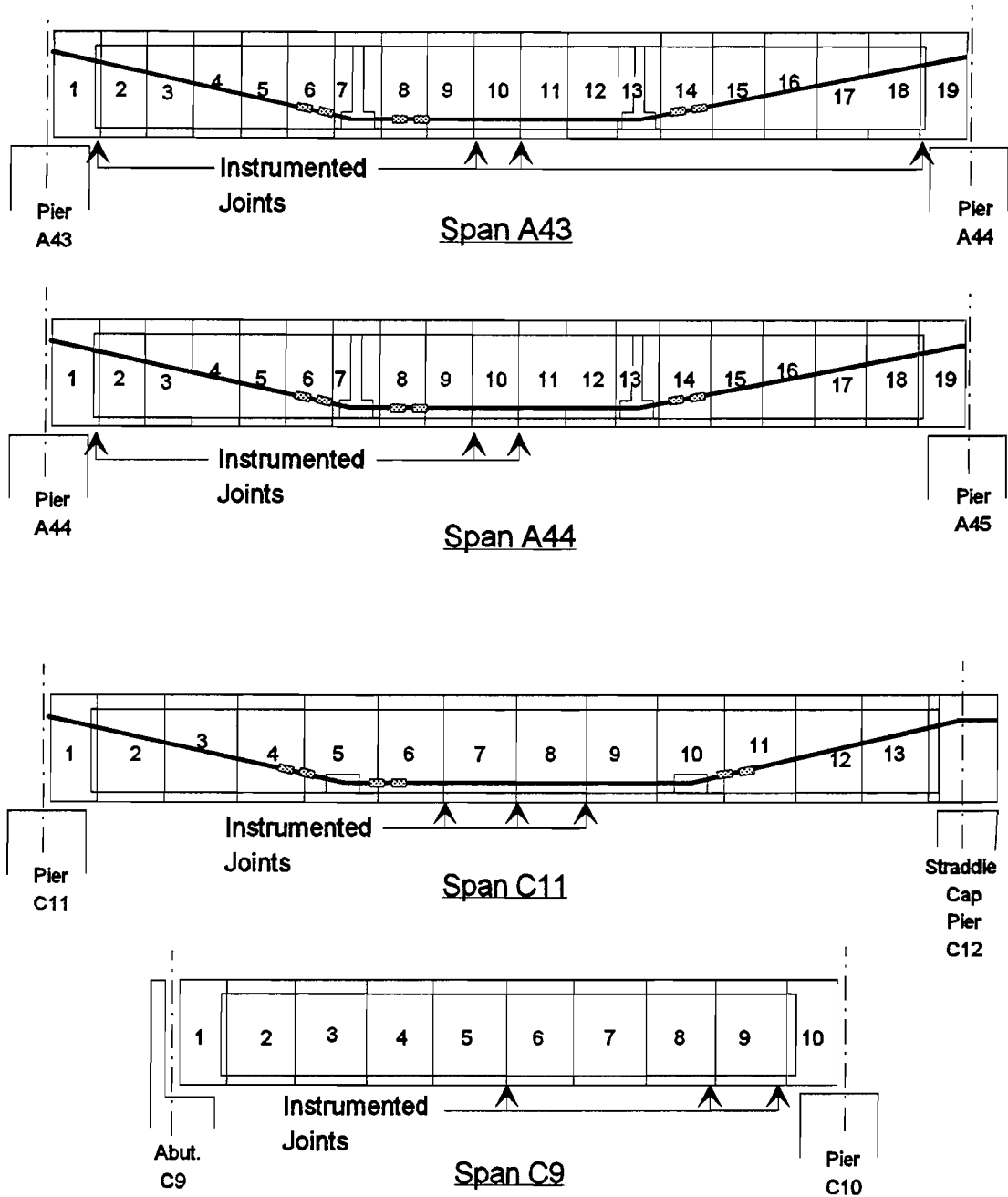


Figure 3.16b Joint movement instrumentation layouts.

3.8 Summary

This chapter has introduced the instrumented spans and detailed the instrumentation systems. Overall, all systems performed very well for short term readings and somewhat less reliably for long term readings. The installation processes were for some systems very labor intensive, and work inside of the box girder was often quite uncomfortable. In all cases the work was accomplished within the time parameters set down in the special provisions (see Appendix A). In two cases the contractor vacated the span after work on Thursday and the systems were installed on Friday, Saturday and Sunday. In this way only one working day was lost for the contractor.

The systems worked well, but based on this experience, changes could be made which would improve performance on future field instrumentation projects. Recommendations for modifications to the instrumentation systems are presented in the first report of this series.

CHAPTER 4

LOSSES IN EXTERNAL POST-TENSIONING TENDONS

4.1 Introduction

The efficiency of post-tensioning tendons may be defined as the lowest post-tensioning force in the tendons which may be counted on as being effective in providing prestressing over the service life of the tendon divided by the highest post-tensioning force which is allowed to be applied to the tendon. The tendon efficiency is reduced by the occurrence of losses in the prestressing force during stressing operations, during seating of the wedges and with time. Current AASHTO Specifications allow a tendon to be stressed to 80% of its ultimate breaking strength, but after initial and time dependent losses the actual effective stress in the tendon may be as low as 50 to 60% of the breaking strength. Thus the efficiency may be of the order of 0.50/0.80, or 62%. This is relatively inefficient.

In order for a bridge to perform satisfactorily at service loads the effective long term prestress must be adequate. To ensure this, the magnitude of the losses must be well known. The deflection of prestressed concrete members is quite sensitive to the actual prestress force. Underestimating the losses can lead to service load cracking, joint openings or droop; overestimating can lead to excessive camber and increased creep. Stress ranges in the tendons under traffic load are also quite sensitive to prestress forces. Underestimating the actual losses can lead to excessive stress ranges and possible fatigue problems.

This chapter describes the observations of external tendon forces in three instrumented spans. A total of sixteen tendons were monitored to evaluate losses through stressing hardware, friction losses, seating losses, elastic shortening losses, and losses with time.

4.2 Background Information

Tendons lose force due to many causes. Some losses are immediate, occurring during stressing operations. These losses are:

- a) Losses through stressing hardware,
- b) Friction losses,
- c) Seating losses,
- d) Elastic shortening losses.

Other losses occur with time. These are:

- a) Creep and shrinkage losses,
- b) Relaxation.

4.2.1 Losses Through Stressing Hardware. Losses through stressing hardware are acknowledged by the design and construction communities but have traditionally been considered to be too insignificant for code and specification mention.⁴³

Figure 4.1 shows a schematic of tendons passing from a duct, through an anchorage device and into a typical multi-strand ram. It is obvious that each strand makes a slight deviation as it passes from duct to ram. Every deviation point is a location where friction losses can occur.

A typical angle change for the most deviated strands is 0.18 radians. Using the same friction coefficient as a tendon in a galvanized duct ($\mu = 0.25$), a loss of 4.5% would result in the most deviated strands ($\approx 3\%$ average for tendon bundle).

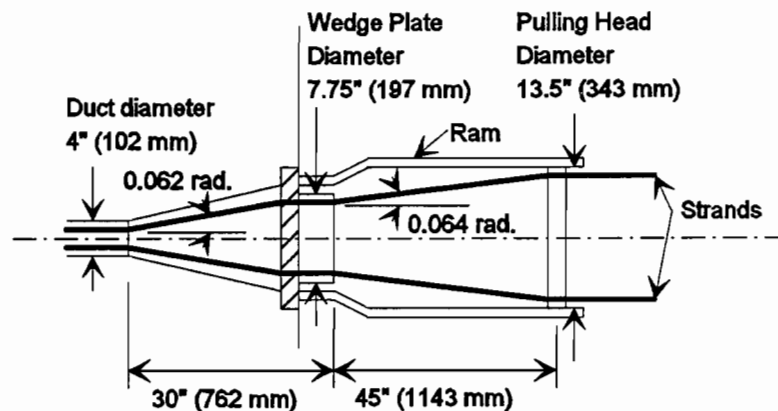


Figure 4.1 Angle Changes in strands passing from duct through anchorage device and ram.

Another source of loss is internal friction in the ram. Often calibrations of rams are conducted in laboratories in large displacement-controlled testing machines. The piston of the ram is extended until it is in contact with the loading head of the test machine. Then the pressure in the ram is increased and the corresponding load in the test machine is recorded. A calibration chart showing pressure vs. load is created from this data.

In the field, on the other hand, the piston will travel through a distance of 9 or more inches during the course of stressing a tendon. The friction of the piston against its housing, which is not present in the static calibration, could also be a source of loss.

Austin Bridge and Road measured losses of this type while conducting strand modulus of elasticity tests on previous segmental projects. Their test was conducted in a frame which comprised two large concrete end blocks with two I-beams between the blocks (see Figure 4.2). A 40 foot (12.2 m) tendon was anchored in each block and ran freely between the anchors. Any losses recorded from the stressing end to the dead end must have occurred in the ram or the anchor hardware. The difference between the live end force, measured by the pressure in the calibrated ram, and the dead end force, measured with a load cell, was normally 8 to 12% of the live end force.

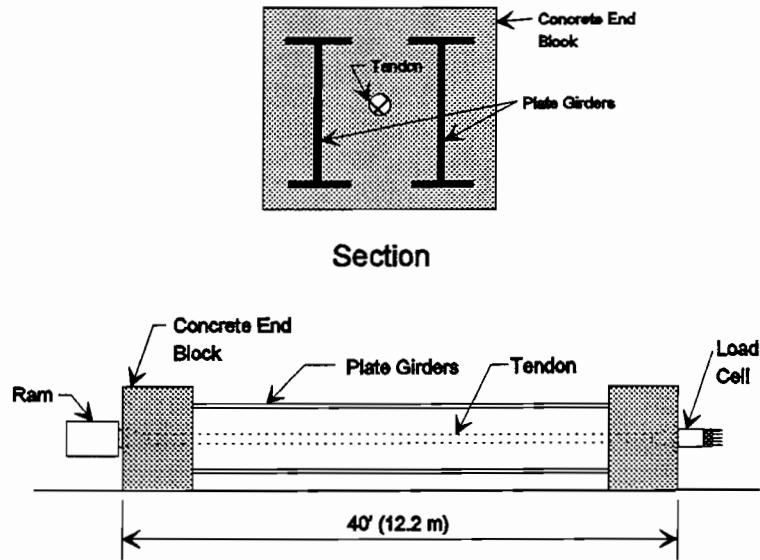


Figure 4.2 Austin Bridge and Road bench test frame.

The losses through stressing hardware are examined briefly in this chapter by comparing measured ram forces, based on the gage pressure times the theoretical ram area from the supplier's calibration charts, with the measured forces in the tendons after they pass out of the end diaphragm anchorage zone.

4.2.2 Friction Losses. Friction losses along the length of the tendon excluding any losses in the stressing hardware, are traditionally divided into two types:

- a) **Curvature Effect** (friction losses): reduction in tendon force due to curvature in the tendon path,
- b) **Length Effect** (wobble losses): reduction in tendon force due to inadvertent duct misalignment.

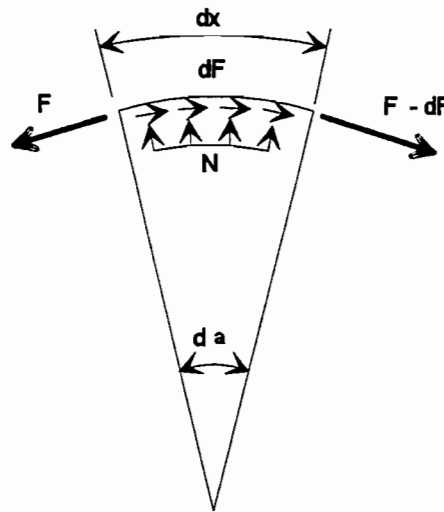
Figure 4.3 illustrates the effect of curvature friction on tendon forces pictorially. Based on the free body diagram of the tendon passing through the deviator, a simplified expression for the relationship of the force in the tendon before the curve, F_0 , and the force after the curve, F_1 , is as follows:

$$F_1 = F_0 e^{-\mu\alpha}$$

where:

- F_0 = Initial force,
- F_1 = Force after friction loss,
- μ = Friction coefficient,
- α = angle of deviation.

The value of μ is generally based on experimental results⁴³ and varies depending on the type of steel used (wires, strands or bars), and the surface of the duct (smooth or corrugated, galvanized steel or plastic). The *AASHTO Guide Specification for the Design and Construction of Segmental Concrete Bridges*¹ (referred to for the remainder of the chapter as the *AASHTO Guide Specification*) recommends $\mu=0.15$ to 0.25 for strand in galvanized sheathing, 0.23 for strand in polyethylene duct and 0.25 for strand in rigid pipe deviators.



$$\begin{aligned}
 N &= Fd a \\
 dF &= -mN \\
 F + mN &= F - dF \\
 dF &= -mFd a \\
 \frac{dF}{F} &= -md a \\
 \int_{F_0}^{F_x} \frac{dF}{F} &= -\int_0^{Sa} md a \\
 \ln F_x - \ln F_0 &= -mSa \\
 \ln \frac{F_x}{F_0} &= -mSa \\
 \frac{F_x}{F_0} &= e^{-mSa} \\
 F_x &= F_0 e^{-mSa}
 \end{aligned}$$

Figure 4.3 Friction loss along length dx.

Small deviations in the duct path result in the tendon rubbing against the duct (see Figure 4.4). At every contact point a small amount of force is lost in the tendon and transferred to the concrete. As shown in Figure 4.4, the wobble effect in a tendon is calculated by the expression:

$$F_x = F_0 e^{-kx}$$

where:

- F_0 = Initial force,
- F_x = force at a distance x along the tendon,
- k = wobble coefficient,
- x = length along tendon, ft. (m)

The coefficients to describe the length effect or wobble losses have also been determined experimentally by tests on supposedly straight tendons. The *AASHTO Guide Specification* recommends a wobble factor of 0.0002/ft. (0.00066/m) for most internal tendons and 0.0 for external tendons. The Texas Department of Transportation, based on their previous segmental experience, recommends a wobble coefficient of 0.0015/ft. (0.00492/m) for internal tendons in segmental structures.

As indicated by the wobble coefficient of 0.0, an external tendon in a polyethylene (PE) duct should not experience significant wobble losses. In an internal tendon the friction forces are due to the resistance of the stiff concrete at contact points and are transferred directly into the concrete at these points. In an external tendon, the normal force between the PE pipe and the tendon is the relatively small weight of the quite flexible duct so that the resulting friction is quite small. Furthermore, the friction force can only be transferred into the duct, as shown in Figure 4.5, and then transferred into the concrete through the relatively flexible connections of the PE

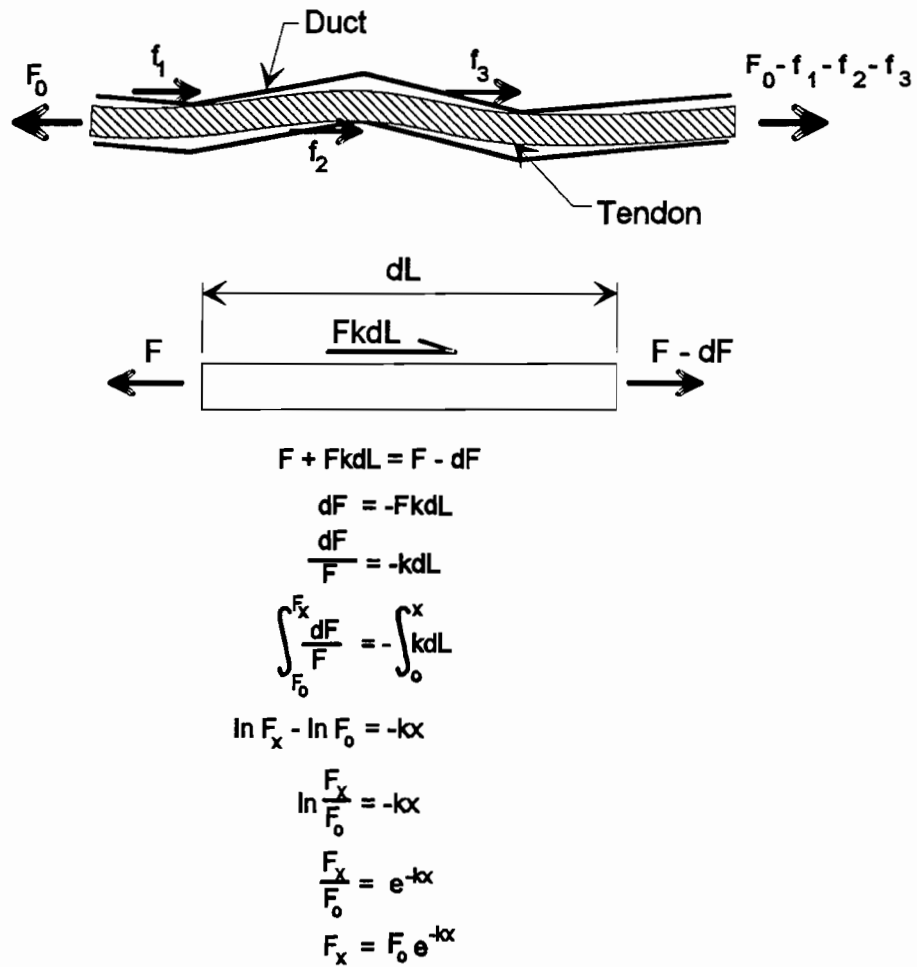


Figure 4.4 Reduction in tendon force due to duct misalignment (wobble).

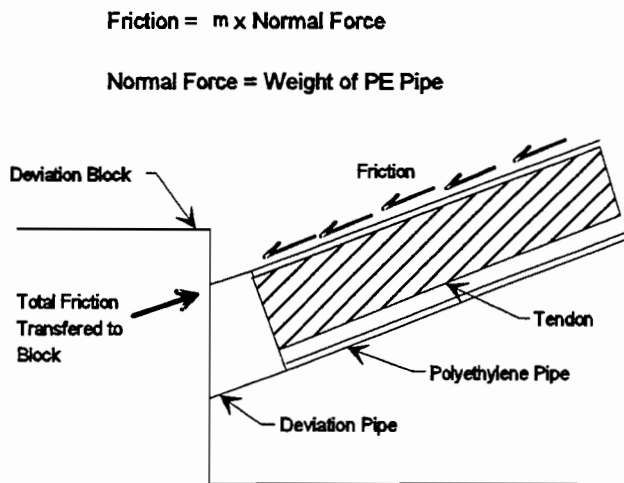


Figure 4.5 Wobble in external tendons.

pipe to the internal ducts at the deviators and diaphragms. Thus, the wobble effect in an external tendon can be considered essentially zero.

The friction and wobble losses in external tendons were studied in three instrumented spans by measuring the forces in the tendons on each side of every deviation point.

4.2.3 Seating Losses. Seating is the construction process of transferring the load from the temporary grips used during stressing to the permanent anchorage devices. A loss in tendon force is caused by the movement of the tendon which is required to seat the wedges in the wedge plate (see Figure 4.6). This movement of the tendon results in a slight reduction in tendon force.

The seating movement is usually assumed to be between 1/8" (3.2 mm) and 3/8" (9.5 mm), with a value of 1/4" (6.4 mm) common for preliminary calculations. Newer rams which are equipped with power seating devices, which physically force the chucks into the wedge plate, reduce the seating losses considerably.

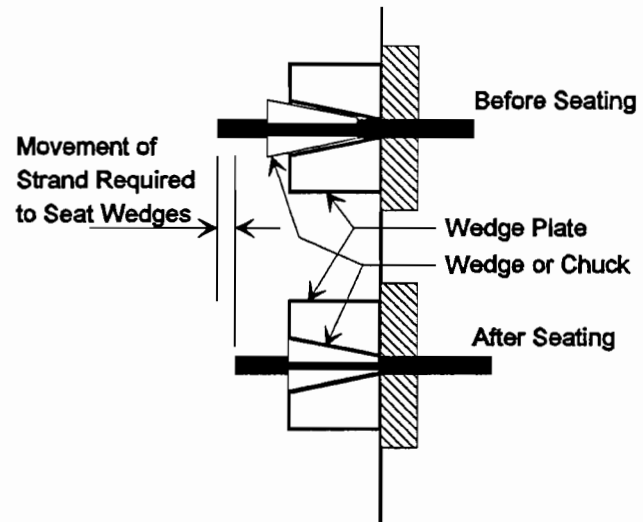


Figure 4.6 Movement of strand during seating of wedges.

The length of tendon which experiences a loss in stress due to the wedge seating movement depends upon the friction acting on the tendon along its length. If a tendon had no friction along its length, the entire length would experience a uniform loss in stress which can be calculated as:

$$\Delta \sigma = \frac{\Delta s}{L} \cdot E_s$$

where:

$\Delta \sigma$ = change in stress in tendon,

Δs = seating loss, inches, (mm)

L = length of tendon,

E_s = modulus of tendon steel.

For tendons with friction acting along the length, it is generally assumed that the loss in tendon force per unit length during stressing will be equal and opposite as the tendon moves the other direction during the wedge seating operation. For external tendons, therefore, the change in stress across a deviator during seating operations is commonly assumed to be equal but opposite to the change during stressing (see Figure 4.7).

The determination of the loss in tendon stress due to seating of the wedges is an iterative process for external tendons. First the total loss in stress is assumed to occur in the length of tendon from the stressing end to the first deviator:

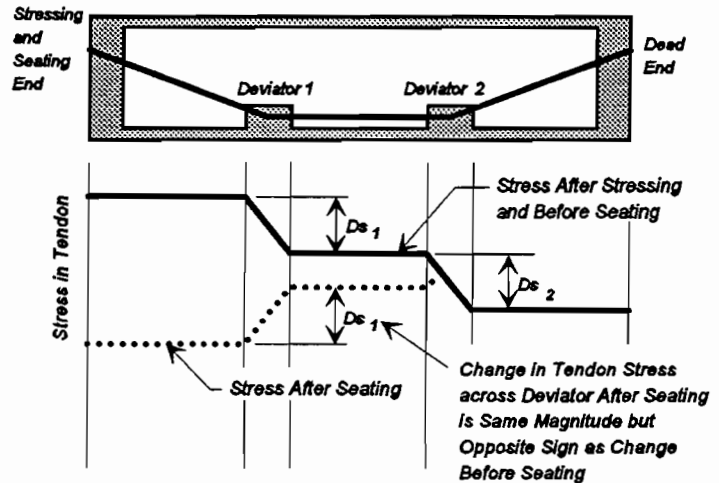


Figure 4.7 Change in tendon stress due to movement of strand during seating.

where:

L_1 = length of tendon from anchor to first deviator.

If $\Delta \sigma$ is greater than two times the change in stress across the first deviator, $\Delta \sigma_1$, then a second iteration must be done, which assumes the first two lengths of tendon experience a loss in tendon stress due to seating. The loss in the second length of the tendon, $\Delta \sigma_2$, is calculated as:

$$\Delta \sigma_2 = \frac{\Delta \sigma E_s - 2 \Delta \sigma_1 L_1}{L_1 L_2}$$

where:

L_2 = length of tendon from first to second deviator,

$\Delta \sigma_1$ = change in tendon stress across first deviator during stressing

If $\Delta \sigma_2$ is less than two times the change in tendon stress across the second deviator, then the solution is complete. If it is still greater, then a third iteration must be done.

Seating movements and resulting changes in tendon stresses were measured in the three instrumented spans.

4.2.4 Elastic Shortening Losses. Elastic shortening losses occur in previously stressed and seated tendons when a subsequently stressed tendon causes elastic shortening of the concrete girder. In a post-tensioned girder, the first tendon stressed will have the greatest elastic shortening loss and the final tendon stressed will have none.

In pretensioned concrete beams, in which the strands are bonded to the concrete when the prestressing force is transferred to the member, the elastic shortening loss is computed by determining the compressive strain in the concrete at the level of the strand and equating that strain change to a force change in the pretensioned strand.

In post-tensioned beams, whether internally or externally post-tensioned, the tendons are unbonded during the stressing operations so strain compatibility between the concrete and the tendon cannot be assumed. Still the average shortening of the concrete is normally used to calculate the average loss due to the concrete compressing. The problem is slightly more complicated with draped external tendons. The elastic shortening loss can be determined by precisely calculating the change in the distance between points where the tendon is in contact with the structure (deviators and diaphragms) if it is assumed that there is no slip at these points. This could be a tedious calculation for a relatively small loss. A simpler method is to calculate the average strain at the center of gravity of the tendon along its length between points of discrete bonding.

Elastic shortening losses were studied by comparing individual tendon strains immediately after seating to strains after the completion of all stressing operations.

4.2.5 Creep and Shrinkage Losses. Losses in the prestress forces occur with time due to creep and shrinkage of the concrete. As the concrete shortens with time, the tendons also shorten which results in a prestress loss. The magnitude of the loss depends on the creep and shrinkage characteristics of the concrete. A step-wise approach is usually recommended to calculate the constantly changing forces in the tendons and the concrete.

The instrumented tendons were monitored continuously for many months after installation. Also companion creep tests were performed to determine the creep characteristics of the concrete.

4.2.6 Relaxation. Relaxation is the tendency of prestressing steel to lose stress under constant strain. This characteristic has been studied by steel manufacturers and was not investigated directly as part of this program.

4.2.7 Effect of Moment Redistribution on Prestress Losses. In segmental construction there are often changes in the statical system during the course of construction. Systems built using balanced cantilever methods are often made fully continuous by casting closures at mid-span

and then adding continuity tendons across the closure. Similarly in span-by-span segmental structures, the spans are erected as simple spans, then made into continuous multi-span units by casting closures over piers and adding continuity tendons. In this type of system, initial dead loads and initial post-tensioning loads are carried by the simple spans immediately after erection. After the continuity is established, all additional loads such as topping and live loads are carried by the continuous system. With time and creep, the moments can redistribute.

If the structure is not made continuous, over time the simple spans would increase in deflections and curvatures. The increase would be proportional to the initial elastic deformations which are magnified by the creep, shrinkage and relaxation effects. However when made continuous, the closures and continuity tendons effectively restrain the creep induced rotations at the piers and cause moment changes over the piers. This is known as moment redistribution, and it effects the long term post-tensioning losses in the structure.

The *PTI Precast Box Girder Bridge Manual*⁹ presents a method for calculating moment redistribution if the creep factor (ϕ) is known. ϕ is defined as:

$$\phi = \frac{\epsilon_{cr} + \epsilon_{cr} E_{c28}}{\epsilon_e \sigma}$$

where:

- ϵ_{cr} - creep strain, additional strain which develops with time,
- ϵ_e - Initial elastic strain,
- σ - Applied stress,
- E_{c28} - 28 day modulus of concrete.

A derivation is presented therein which results in the following formula:

$$M_{cr} = (1 - e^{-\phi})(M_B - M_A)$$

where:

- M_{cr} - Actual moment caused by creep restraint effects resulting from change in statical system,
- M_A - Actual moment due to loads before change in statical system,
- M_B - Moment due to load applied to changed statical system.

This simply means that the system, with time, creeps slowly from its original system towards its final system. For instance, if a ϕ value of 2 for a time interval is determined, $(1 - e^{-\phi}) = 0.86$, so after that time interval 86% of the moments of the continuous structure have developed.

The effects of moment redistribution must be considered in the calculation of long term prestress losses, and in turn the effect of the loss of prestress must be considered in the long term moment redistribution.

4.3 Literature Review

The following section presents some methods currently available for determining losses.

4.3.1 AASHTO Guide Specification. Section 10.0 covers prestress losses. Lump sum losses are allowed only for preliminary designs. A detailed analysis which takes into account construction schedules is required for the final design. The commentary suggests many references on time dependent analysis which include the ACI 209 creep model,⁴ the CEB-FIP creep model¹⁶ and recommendations by PCI.⁵¹ Beyond this, and a worked example in its Appendix A, there is little guidance on the specifics of the time dependent analysis.

Short term losses are more directly addressed. Friction and wobble coefficients are given for a wide variety of duct types. For external tendons passing through rigid steel pipe deviators:

$$\mu = 0.25 \text{ and } k = 0.0$$

It is noted that lubrication will probably be required to achieve a value of $\mu = 0.25$. A value for anchor seat of $\frac{1}{4}$ " (6.4 mm) is recommended. Equations are presented for calculating steel relaxation losses.

4.3.2 ACI 318-89. Chapter 18 covers prestressed concrete. ACI suggests several references for determining prestress losses. The references include ACI-ASCE Committee 423,³ ACI Committee 435,⁶ PCI Committee on Prestress Losses⁵¹ and a paper by Zia, Preston, Scott and Workman.⁷⁷

Friction losses can be calculated with the equation:

$$F_x = F_o \cdot e^{-(kx + \mu\alpha)}$$

where:

F_o = Initial force in the tendon.

F_x = Force in the tendon at a distance x from the stressing end,

k = wobble coefficient,

x = distance along tendon,

μ = friction coefficient,

α = cumulative angle change from stressing point to distance x.

or if $(kx + \mu\alpha) < 0.3$ a simpler equation may be used:

$$F_p = F_x(1 + kx + \mu \alpha)$$

Values of wobble coefficients, k , for multi-strand tendons vary from 0.0005/ft. (0.00164/m) to 0.0020/ft. (0.00656/m) and friction coefficients, μ , vary from 0.15 to 0.25. No other losses are addressed specifically.

4.3.3 PTI Manual.⁵⁸ The *PTI Manual* provides design aids for determining friction losses and anchor seat losses. The same two equations for friction losses as those in ACI 318-89 are presented, but it is recommended that the approximate equation only be used if $\mu \alpha + kx < 0.15$. Friction coefficients, μ , for rigid thin wall tubing of 0.20-0.30 for non-galvanized and 0.16-0.24 for galvanized are recommended. No recommendations for polyethylene duct are made.

A procedure for determining the effect of anchor seating is presented, but no approximate design values are given.

The *PTI Manual* also gives references to be used in determining long term losses. Recommended sources are PCI Committee on Prestress Losses,⁵¹ ACI-ASCE Committee 423,³ and the AASHTO Standard Specification.² The *PTI Manual* also provides lump sum losses, but states that these values are to be used only for preliminary estimates of quantities of prestressing materials, and not for final designs.

4.3.4 Zia, Preston, Scott and Workman.⁷⁷ This paper, authored by members of ACI-ASCE Committee 423, is a comprehensive examination of loss in prestress. The following is a summary of their recommendations.

Elastic shortening, ES, for post-tensioned members with unbonded tendons can be calculated as follows:

$$ES = 0.5 E_s \frac{f_{cpa}}{E_{ci}}$$

where:

E_s = Modulus of elasticity of prestressing steel,

E_{ci} = Modulus of elasticity of concrete,

f_{cpa} = Average compressive stress in the concrete along the member length at the center of gravity of the tendons immediately after the prestress has been applied to the concrete.

Creep losses, CR, for post-tensioned members with unbonded tendons can be calculated as:

$$CR = 1.6 \cdot \frac{E_s}{E_c} f_{cpa}$$

Shrinkage, SH, for post-tensioned members can be computed as:

$$SH = 8.2 \cdot 10^{-6} K_{sh} E_s (1 - 0.006 \frac{V}{S}) (100 - RH)$$

where K_{sh} varies depending on the time elapsed between the end of moist curing and the application of prestress. Other variables are as follows:

V/S= Volume to surface ratio - Gross cross-sectional area divided by perimeter.

RH= Average relative humidity surrounding the concrete member. Numbers are provided on a map.

Relaxation, RE, can be calculated as:

$$RE = [K_{re} - J(SH + CR + ES)]C$$

where K_{re} and J vary depending on the type of strand and C varies with the strand type and the level of stress in the tendon divided by the ultimate breaking stress (f_{pi} / f_{pu}).

The friction and wobble coefficients and procedures are the same as those presented in ACI 318-77, which are essentially the same as ACI 318-89.

In the commentary of the specification presented in this paper, it is claimed that this method gives a good approximation of prestress losses for "normal designs", but notes that "unusual designs" will require a more detailed procedure.

The commentary also provides maximum values for total losses. for stress relieved strand the maximum loss is 50,000 psi (345 MPa) and for low-relaxation strand it is 40,000 psi (276 MPa).

4.3.5 Tadros, Ghali and Dilger.⁶⁹ These authors present a method for predicting prestress losses which takes into account the reduction of stress in the tendon due to creep, shrinkage and relaxation. The loss of prestressing force, due to shrinkage and creep of concrete and relaxation of steel, reduces the concrete stress and induces elastic strain and creep recoveries. A recovery parameter μ is presented to account for reduced losses due to this recovery. Also a factor ψ is presented to account for steel relaxation creep recoveries.

Experimental verification showed the method was quite accurate.

4.3.6 PCI Committee on Prestress Losses.⁵¹ The report presented by this committee is a comprehensive guide to calculating prestress losses. The following is a brief summary;

Total losses, TL, for post-tensioned members:

$$TL = FR + ANC + ES + \sum_i(CR + SH + RET)$$

where:

FR -	Friction loss,
ANC -	Anchor seat loss,
ES -	Elastic shortening loss,
$\sum_i(CR + SH + RET)$ -	Summation of time dependent losses, CR - creep, SH - shrinkage and RET - relaxation, over a series of time intervals.

Four intervals are recommended for the loss calculation:

Step 1:	End of curing to application of prestress,
Step 2:	Application of prestress to age 30 days or a time when the member is subjected to an additional dead load,
Step 3:	30 days to one year,
Step 4:	One year to end of service life.

The recommendations for calculating losses due to friction, anchor seat and elastic shortening are similar to previously outlined references.

The losses due to creep over each time interval is to be calculated as:

$$CR = UCR * SCF * MCF * PCR * f_c$$

where :

f_c =	net compressive stress at the center of gravity of the prestressing force at time t_1 ,
---------	---

UCR=	$95 - 20E_c/10^6 \geq 11$ (for a moist cure of not more than 7 days and normal weight concrete),
SCF=	Effect of size and shape, depending on volume to surface ratio,
MCF=	Effect of age of concrete at transfer and length of moist cure,
PCR=	Portion of ultimate creep which occurs over the time interval, values provided in a table.

The shrinkage loss over each time interval is given as:

$$SH = USH * SSF * PSH,$$

where:

USH=	Ultimate shrinkage loss = $27000 - 3000E_c/10^6 \geq 12000$ psi (83 Mpa) for normal weight concrete,
SSF=	Effect of size and shape, depending on volume to surface ratio,
PSH=	Portion of ultimate shrinkage which occurs over the time interval, values provided in a table.

Formulas for calculating relaxation losses for stress-relieved strand and low relaxation strand are also provided.

A simplified method is also provided for calculating total prestress losses, TL:

$$TL = 12.5 + 7.0 f_{cr} - 4.1 f_{cds},$$

where:

f_{cr} -	net stress due to prestressing and weight of prestressed member at the time of prestress transfer at the center of gravity of the tendons at the critical location in the span where the maximum tension (or minimum compression) occurs under full live load.
f_{cds} -	Stress due to dead loads applied after prestress transfer.

This equation is based on many assumed basic parameters such as volume to surface ratio, tendon tension, concrete strength and age at prestressing.

4.3.7 ACI Committee 435.⁶ This report recommends a step-wise summation of time-dependent losses. It also presents an approximate single step loss calculation. Ranges of the value

for the ultimate creep coefficient, C_w , are presented in a table. Values vary according to concrete strength and relative humidity.

4.3.8 Ketchum.³⁵ Ketchum presents computer aided solutions, using a program SFRAME, of time dependent moment redistributions in segmentally constructed bridges. He compares solutions using creep coefficients determined with the CEB-FIP model and the ACI 209 method.

He concludes that the simplified method for determining the amount of moment redistribution:

$$M_a = (1 - e^{-\Phi})(M_B - M_A)$$

(see Section 4.2.7) is based on several simplifying assumptions which are not necessarily met by many of the segmentally erected bridges being built today. Under the influence of prestressing, which is undergoing a change in force due to creep and shrinkage at the same time that internal moments are redistributing due to creep, moments in the girder redistribute quite differently than indicated by the simplified equation. He recommends the simplified solution for preliminary designs, but a complete time dependent analysis considering the actual construction sequence and schedule for the final analysis.

He also concludes that the CEB-FIP creep model predicts significantly greater moment redistribution and prestress losses than the ACI-209 model.

4.4 Measurement Program

A total of 16 tendons in three different spans were instrumented with epoxy sleeves and electrical resistance (ER) strain gages to determine the actual prestress losses in external tendons. This section presents the results of the measurements.

4.4.1 Losses During Stressing Operations. As described in Chapter 3, each external tendon in Spans A43, A44 and C11 was instrumented in three locations (see Figure 4.8). During stressing operations the Campbell data acquisition system recorded strains every 20 seconds. Manual Demec readings on the epoxy sleeves were taken before stressing, at stressing stages corresponding to 20%, 40%, 60%, and 77% of the ultimate strength of the tendon (GUTS). Demec readings were also made after seating of each tendon, on all tendons immediately after all stressing was completed, and after the erection truss was lowered.

As described by Arréllaga,⁷ some manipulation of the raw data is required to determine the exact force in the tendon. Figure 4.9 shows the procedure in which the four measurements at each location (2 ER gages and 2 Demec readings) at each stage of stressing are plotted against the force in the ram. The force in the ram is determined by the theoretical ram area from calibration procedures, multiplied by the pressure recorded by a calibrated pressure transducer

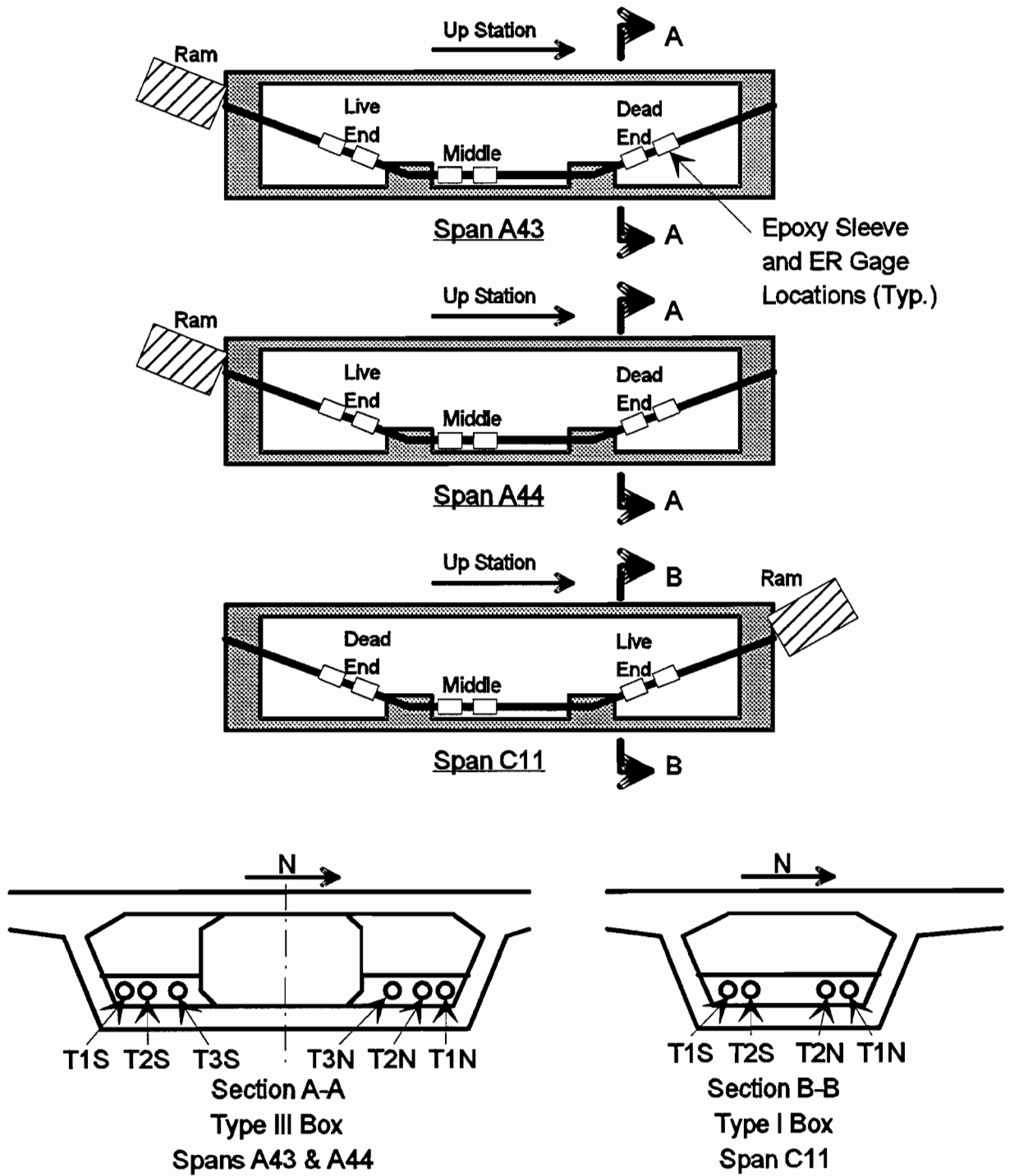
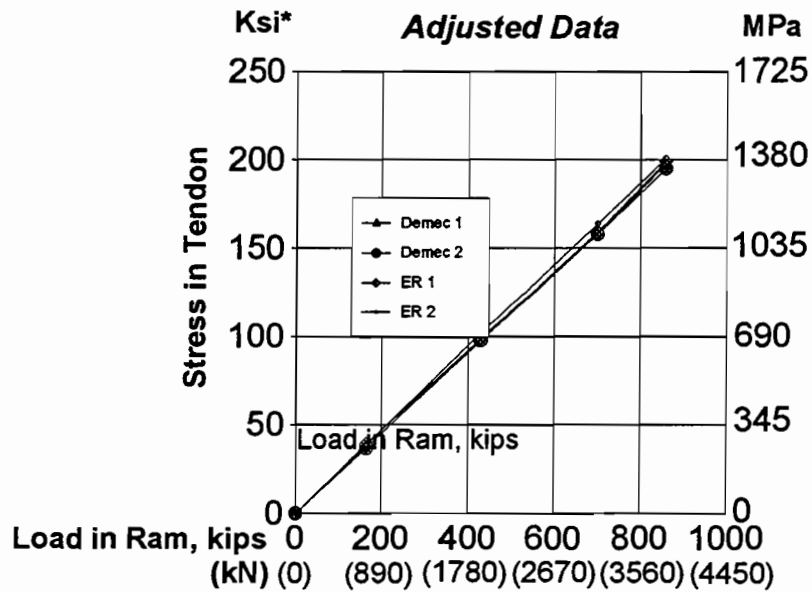
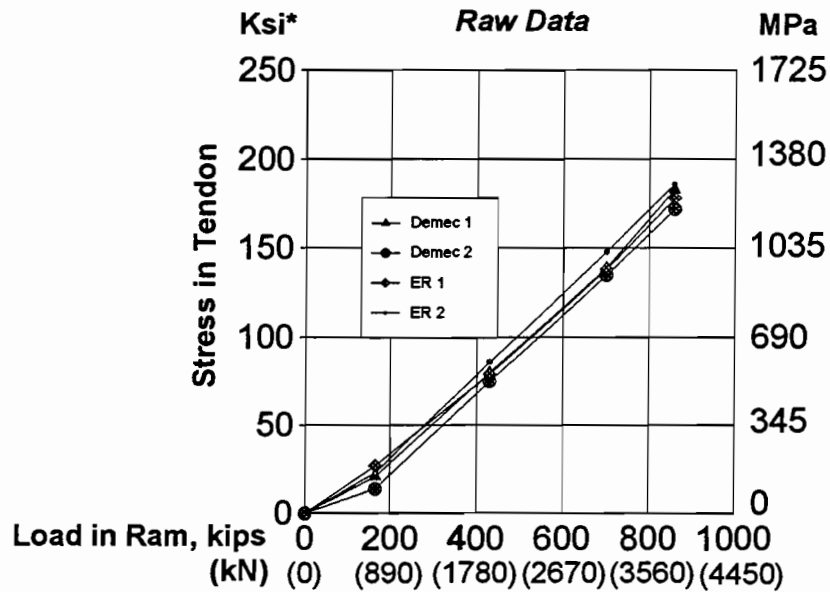


Figure 4.8 Instrumentation layouts and tendon designs.

Tendon T1S - Live End - Span A43



*Tendon stresses are measured tendon strains times appropriate modulus of elasticity.

Figure 4.9 Manipulation of raw data to determine tendon forces.

read by the Campbell system. The best fit slopes of the raw data lines are determined using a linear regression analysis. The lines are then adjusted so they pass through the origin, and the final adjusted data gives the stress as indicated by each device. Laboratory tests showed the method of data reduction to give measurement of tendon stress to $\pm 2\%$ of the stress measured with other methods (testing machines and load cells.)

The gage factors of the electrical resistance gages were slightly altered to reflect the parasitic resistances in the data acquisition system (determined through testing) and in the lead wires (determined theoretically). The lead wires were 30 gage stranded tinned copper wire with a resistance of 0.01032Ω per linear foot. The gage factor is altered by the following equation:

$$G_D = G_0 \frac{R_G}{R_G + R_W}$$

where:

- G_D = Desensitized Gage Factor,
- G_0 = Manufacturer's Gage Factor,
- R_G = Gage Factor Resistance, ohms,
- R_W = Lead Wire Resistance, ohm

Using the desensitized gage factors the strains at each location as read by the ER gages were calculated.

The strains are equated to stresses using moduli of elasticity determined in the laboratory. Two six foot samples were cut from each reel of strand used in the instrumented spans. These samples were tested, as recommended by Arréllaga,⁷ to determine the modulus to be used for the electrical resistance gages and the epoxy sleeve Demec points. The moduli of the two measurement systems are different because the Demec readings are taken directly along the tendon axis, while the electrical resistance gage measures strain in a helical wire. The strain along the axis is greater than that on the helical wire, so the modulus is smaller. The Demec modulus is in better agreement with the manufacturer's modulus which is normally measured with an extensometer which measures strains along the axis of the tendon. The value of each modulus of elasticity for each span is shown in Table 4.1.

Table 4.1 Value of Modulus of Elasticity

Span	Demec Modulus		ER Gage Modulus		Manufacturer's Modulus	
	ksi	(GPa)	ksi	(GPa)	ksi	(GPa)
C11	28,000	(193)	29,600	(204)	28,000	(193)
A44	29,000	(200)	30,600	(211)	28,000	(193)
A43	29,000	(200)	30,600	(211)	28,000	(193)

The stresses in each tendon at the end of stressing, before seating, are presented in Table 4.2 and graphically in Figure 4.10. The four readings at each measuring point were quite similar, with the high and low readings on average $\pm 2\%$ of the average of the four readings.

Table 4.2 Measured Tendon Stresses

Tendon	Live End		Middle		Dead End		Ram	
	ksi	(MPa)	ksi	(MPa)	ksi	(MPa)	ksi	(MPa)
C11-T1N	210	(1448)	204	(1407)	199	(1372)	210	(1448)
T1S	215	(1482)	207	(1427)	201	(1386)	215	(1482)
T2N	208	(1434)	201	(1386)	193	(1331)	209	(1441)
T2S	208	(1434)	196	(1351)	193	(1331)	209	(1441)
A43-T1N	202	(1393)	195	(1345)	186	(1282)	208	(1434)
T1S	198	(1365)	189	(1303)	186	(1282)	210	(1448)
T2N	205	(1413)	194	(1338)	190	(1310)	213	(1469)
T2S	202	(1393)	193	(1331)	189	(1303)	214	(1476)
T3N	205	(1413)	202	(1393)	191	(1317)	213	(1469)
T3S	198	(1365)	190	(1310)	184	(1269)	215	(1482)
A44-T1N	203	(1400)	191	(1317)	187	(1289)	210	(1448)
T1S	198	(1365)	191	(1317)	183	(1262)	208	(1434)
T2N	201	(1386)	195	(1345)	187	(1289)	209	(1441)
T2S	199	(1372)	192	(1324)	187	(1289)	211	(1455)
T3N	194	(1338)	188	(1296)	180	(1241)	208	(1434)
T3S	202	(1393)	191	(1317)	180	(1241)	210	(1448)

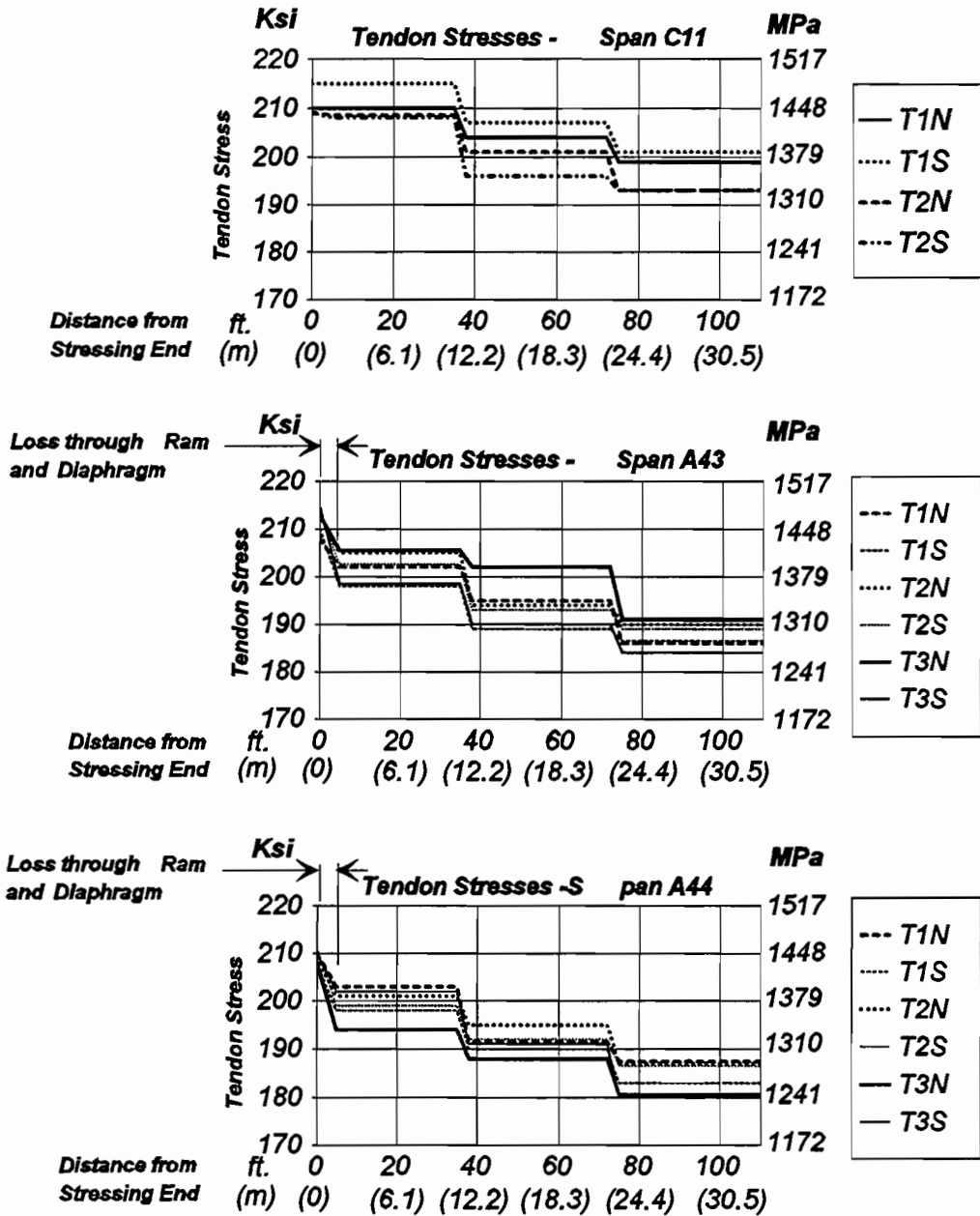


Figure 4.10 Tendon stresses after stressing, before seating.

The accuracy of the readings was studied by comparing measured tendon elongations to the elongations which would be calculated with the measured tendon stresses. Table 4.3 shows each tendon, the measured stress and the tendon segment length for each of the three tendon segments, the measured elongation and the calculated elongation (see Figure 4.11 for notation). Finally, the ratio of the calculated to the measured elongation is shown.

Table 4.3 Measured Elongations Compared to Calculated.

Span	Tendon	F1		F2		F3		Calc. Elong. inches (mm)	Meas. Elong. inches (mm)	Calc/ Meas %
		ksi (MPa)	ft (m)	ksi (MPa)	ft (m)	ksi (Mpa)	ksi (Mpa)			
C11	T1N	210 (1448)	37.4 (11.40)	204 (1406)	41.9 (12.77)	199 (1372)	33.5 (231)	9.87 (251)	10.07 (256)	98.0
	T1S	215 (1482)	37.4 (11.40)	207 (1427)	41.9 (12.77)	201 (1386)	33.5 (231)	10.04 (255)	10.07 (256)	99.7
	T2N	208 (1434)	37.5 (11.43)	201 (1386)	41.9 (12.77)	193 (1331)	33.5 (231)	9.71 (247)	9.42 (239)	103.1
	T2S	208 (1434)	37.5 (11.43)	196 (1351)	41.9 (12.77)	193 (1331)	33.5 (231)	9.61 (244)	9.49 (241)	101.3
A43	T1N	202 (1393)	37.2 (11.34)	195 (1345)	35.1 (10.70)	186 (1282)	37.0 (255)	9.10 (231)	9.32 (237)	97.6
	T1S	198 (1365)	37.2 (11.34)	189 (1303)	35.1 (10.70)	186 (1282)	37.0 (255)	8.95 (227)	9.28 (236)	96.4
	T2N	205 (1413)	37.2 (11.34)	194 (1338)	35.1 (10.70)	189 (1303)	37.0 (255)	9.19 (233)	9.44 (240)	97.4
	T2S	202 (1393)	37.2 (11.34)	193 (1331)	35.1 (10.70)	189 (1303)	37.0 (255)	9.12 (232)	9.32 (237)	97.9
	T3N	205 (1413)	37.2 (11.34)	202 (1393)	35.1 (10.70)	191 (1317)	37.0 (255)	9.32 (237)	9.62 (244)	96.9
	T3S	198 (1365)	37.2 (11.34)	190 (1310)	35.1 (10.70)	184 (1269)	37.0 (255)	8.94 (227)	9.23 (234)	96.9
A44	T1N	203 (1400)	37.0 (11.28)	198 (1365)	35.0 (10.67)	189 (1303)	36.4 (251)	9.22 (234)	9.37 (238)	98.4
	T1S	198 (1365)	37.0 (11.28)	191 (1317)	35.0 (10.67)	183 (1262)	36.4 (251)	8.86 (225)	8.96 (228)	98.9
	T2N	201 (1386)	37.0 (11.28)	195 (1345)	35.0 (10.67)	187 (1289)	36.4 (251)	9.02 (229)	9.08 (231)	99.3
	T2S	199 (1372)	37.0 (11.28)	192 (1324)	35.0 (10.67)	187 (1289)	36.4 (251)	8.94 (227)	9.00 (229)	99.3
	T3N	194 (1338)	37.0 (11.28)	188 (1296)	35.0 (10.67)	180 (1241)	36.4 (251)	8.70 (221)	8.73 (222)	99.7
	T3S	202 (1398)	37.0 (11.28)	191 (1317)	35.0 (10.67)	180 (1241)	36.4 (251)	8.88 (226)	8.96 (228)	99.1
Average									98.7	
Stand. Deviation									1.7	

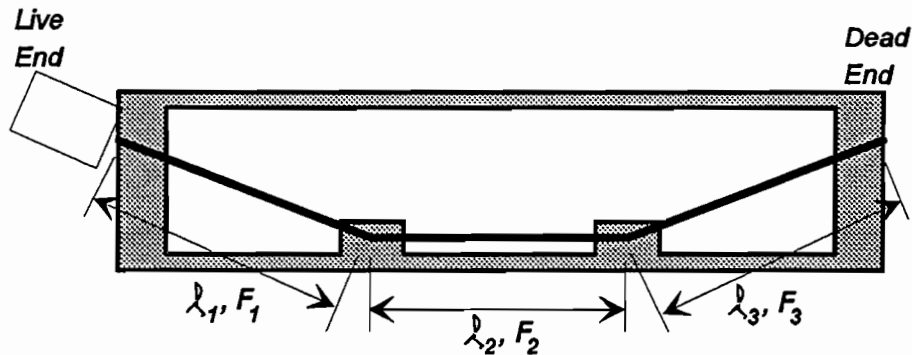


Figure 4.11 Notation for Table 4.3.

Some assumptions are required in determining the measured elongation. Field elongation measurements were made when the tendon was stressed to 20% of GUTS and again at the final stress of 77% GUTS. The total elongation is calculated for the full range of 0-77% GUTS by assuming a linear relation between ram pressure and elongation. From the extrapolated total elongation the following values are subtracted:

- Dead End Seating Loss - 0.13 inches (3.3 mm) at expansion joints,
0.19 inches (4.8 mm) at interior piers (less access for placing wedges).
- Ram Wedge Seat - 0.15 inches (3.8 mm)
- Elongation Inside of Ram - Varies according to ram length and stress in tendon.

The overall average of the elongation calculated with measured stress to the adjusted measured elongations is 98.7% , with a standard deviation of 1.7%. This is a difference of approximately 0.12 inches (3 mm).

The total assumed losses (wedge seats and internal ram elongations) are between 0.45 and 0.56 inches (11.4 and 14.2 mm). Slight variations in these numbers could have considerable effects on the elongation calculations.

Based on the scatter in the measurements and the variance between calculated and measured elongations, an assumption of $\pm 2\%$ error in the readings is appropriate.

4.4.1.1 Losses Through Stressing Hardware. Significant losses were measured from the stressing force in the ram, based on the measured pressure times the theoretical ram area, to the first measuring station on the tendon. These losses occurred through the ram, the anchor hardware and the short length of corrugated metal duct in the diaphragm. Table 4.4 shows the ram force, which is based on the measured hydraulic pressures and the theoretical ram area from calibration charts, and the

Table 4.4 Losses through Stressing Hardware.

Span	Tendon	Ram Force		Force at 1 st Measurement Station		1 st /Ram %
		kips	kN	kips	kN	
A43	T1N	858	(3816)	833	(3705)	97.0
	T1S	866	(3852)	818	(3638)	94.9
	T2N	878	(3905)	845	(3759)	96.2
	T2S	882	(3923)	831	(3696)	94.2
	T3N	878	(3905)	844	(3754)	96.2
	T3S	886	(3941)	816	(3630)	92.1
A44	T1N	866	(3852)	835	(3714)	96.4
	T1S	858	(3816)	818	(3638)	95.3
	T2N	862	(3834)	829	(3687)	96.1
	T2S	870	(3870)	820	(3647)	94.2
	T3N	858	(3816)	801	(3563)	93.4
	T3S	866	(3852)	833	(3705)	96.2
Average						95.2
Standard Deviation						1.4

force in the tendon at the first measuring location. Span C11 is not included in this table because at the time of stressing the rams were severely out of calibration.

A slight loss would be predicted in the diaphragm region due to curvature and wobble of the tendon in the corrugated duct. The loss would be calculated as:

$$F_1 = F_0 e^{-(\mu\alpha + k\ell)}$$

For $\alpha=0.097$ (average for all external tendons in Spans A43 and A44) and $\mu=0.20$, and $k = 0.0002/\text{ft.}$ (0.00066/m) (k and μ values recommended by the *AASHTO Guide Specification*) and $\ell = 4$ feet (1.22 m), the calculated loss would be 2% of the initial force. The average of the actual measured losses is 4.8%, with 2.8% attributable to losses in the stressing hardware (standard deviation 1.4%).

Losses through stressing hardware should be considered in design and in field elongation measurements. Losses through two anchorage devices and one ram have previously been recorded at 8 to 12 %. In this study a loss of approximately 3% was measured through the ram and one anchorage device. A design value of 2 to 3% for the loss through the stressing hardware is recommended.

4.4.1.2 Friction Losses. Figure 4.12 shows the tendon layouts for the three instrumented spans. Only tendon T1 has horizontal deviation, which is not shown but which was taken into account in the angle calculation. Based on these tendon layouts, theoretical angle changes can be calculated. The horizontal and vertical alignments of the spans must also be taken into account in the calculation of the angle changes. The three spans have no horizontal curvature, and Span C11 is on a constant uphill grade. Spans A43 and A44 are situated in vertical sag curves. The sags increase the angle changes slightly (see Figure 4.13). Table 4.5 presents each tendon and its live and dead end angle changes.

The equation:

$$\mu = \frac{F_1}{F_0} \left(-\frac{1}{\alpha} \right)$$

was used to calculate the apparent friction coefficients for each tendon deviation. At every deviation, the force on each side (F_0 and F_1) and the theoretical angle change (α) are known, so the friction coefficient (μ) can be determined. Table 4.6 presents each friction value and the average for the entire tendon.

The average friction value, 0.38 (standard deviation of 0.07), is considerably higher than the 0.25 value recommended by the *AASHTO Guide Specification*.¹ It is also higher than the range of 0.25-0.30 suggested by the CEB-FIP Model Code.¹⁷

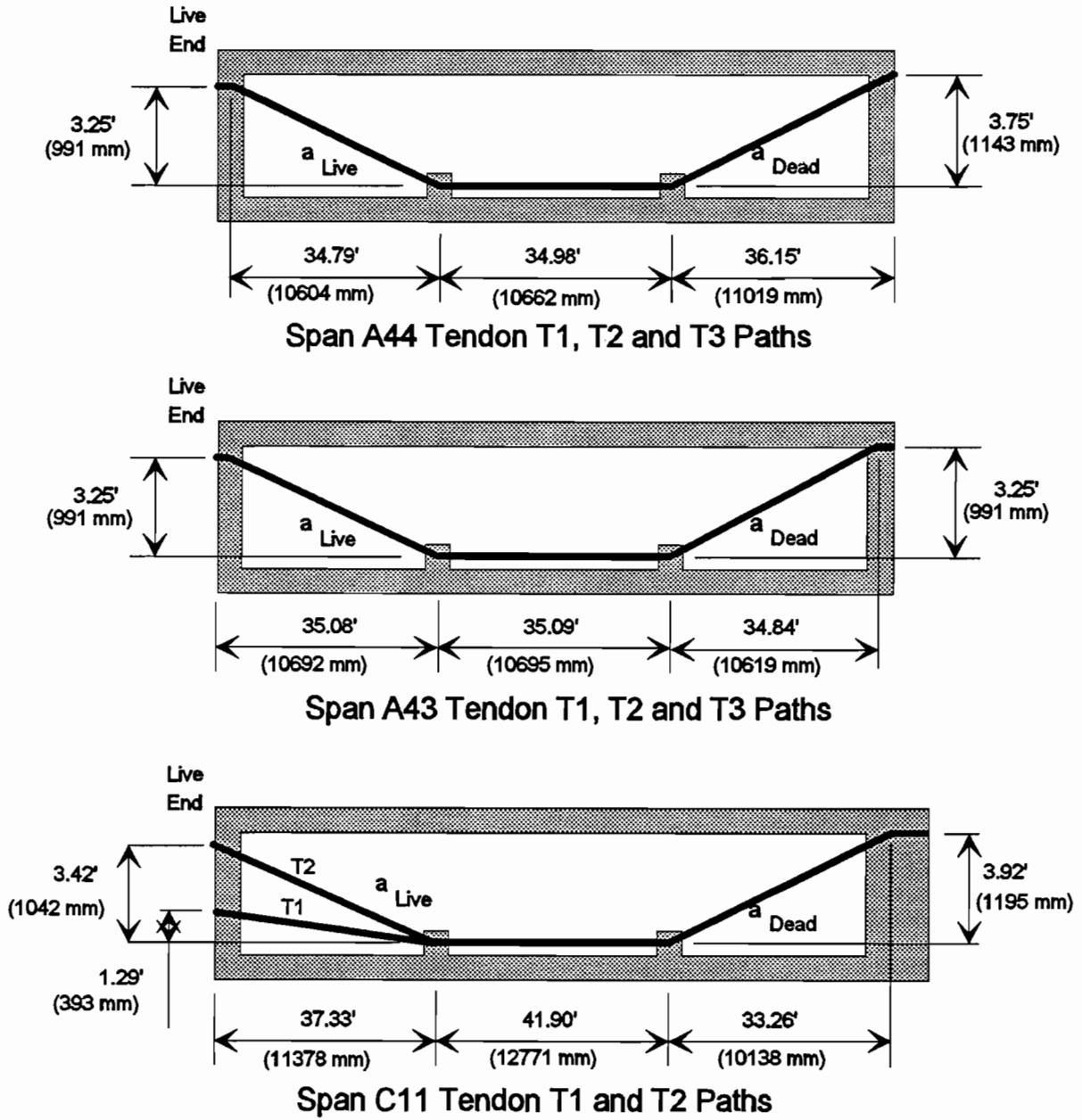
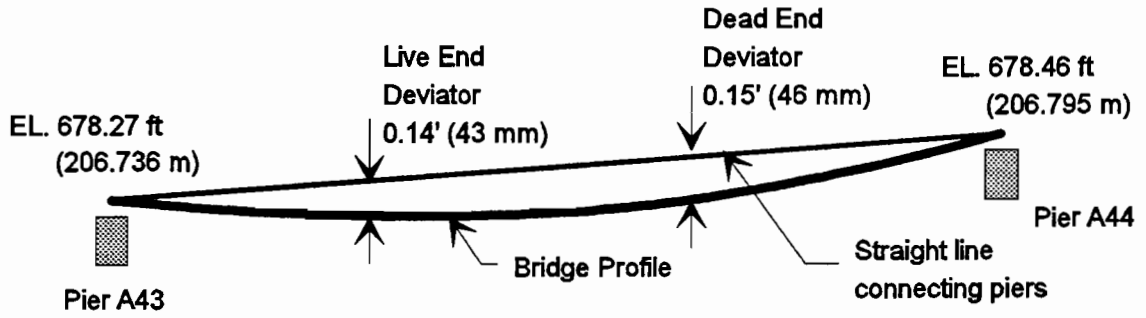
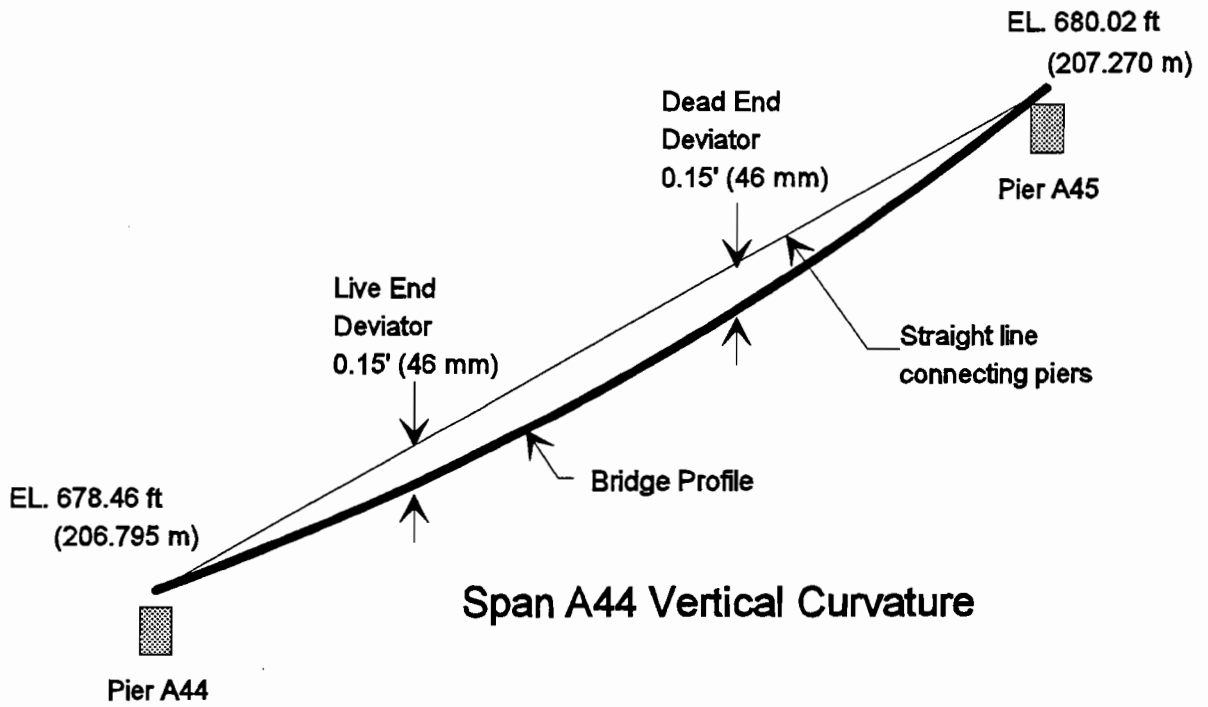


Figure 4.12 Elevation views of tendon layouts.



Span A43 Vertical Curvature



Span A44 Vertical Curvature

Figure 4.13 Vertical curves of Spans A43 and A44.

Table 4.5 Tendon Angle Changes.

Span	Tendon	Live End Angle, Radians	Dead End Angle, Radians
C11	T1	0.0346	0.1179
	T2	0.0960	0.1179
A43	T1	0.0984	0.1054
	T2	0.0960	0.0988
	T3	0.0960	0.0988
A44	T1	0.0994	0.1092
	T2	0.0970	0.1078
	T3	0.0970	0.1078

Table 4.6 Measured Friction Coefficients.

Span	Tendon	Live End Friction Coeff.	Dead End Friction Coeff.	Average Friction Coeff.
C11	T1N	0.84	0.21	0.35
	T1S	1.10	0.25	0.44
	T2N	0.36	0.34	0.35
	T2S	0.62	0.13	0.35
A43	T1N	0.36	0.45	0.41
	T1S	0.47	0.15	0.31
	T2N	0.57	0.21	0.39
	T2S	0.47	0.21	0.34
	T3N	0.15	0.57	0.36
	T3S	0.43	0.32	0.38
A44	T1N	0.61	0.19	0.40
	T1S	0.36	0.39	0.38
	T2N	0.31	0.39	0.35
	T2S	0.37	0.24	0.31
	T3N	0.32	0.40	0.36
	T3S	0.58	0.55	0.57

It can be observed that the friction value for the live end deviators was somewhat higher than that for the dead end deviators. Previous researchers¹⁹ have noted differing friction coefficients for deviation points with identical ducts and angle changes but with differing distances of travel of the tendon along the duct. The researchers noted that for corrugated duct the friction value decreased with greater travel of the tendon. The current test results indicate that the friction values increase with greater tendon travel. The other difference from the live end to the dead end deviator is that the angle changes at the live end are generally smaller than those at the dead end.

Field measurements in the past have shown that the recommended friction coefficient, $\mu = 0.25$, is difficult to achieve and to compensate contractors have often included wobble coefficients for external tendons. To illustrate this, consider a tendon with a total length of 110 feet (33.53 m) and a total angle change of 0.2 radians. If a friction value of 0.38 is used with a wobble value of 0.0 then:

$$kl + \mu\alpha = 0.2 * 0.38 = 0.076$$

If a friction value of 0.25 is used in conjunction with wobble value of 0.0002/ft. (0.00066/m), then:

$$kl + \mu\alpha = 0.2 * 0.25 + .0002 * 110 = 0.072.$$

The elongation calculations result in similar values, but the wobble assumed in the second calculation does not occur.

It is possible that the higher losses across the deviators are due in part to a misplacement of the deviator pipes. Figure 4.14 illustrates a possible duct misalignment, within the 3/8" (9.5 mm) tolerance allowed in the San Antonio "Y" Project. It is apparent that due to duct misalignments, actual angle changes of the tendons can be substantially different than the design value. The duct misalignment explains the higher than expected losses across the deviators.

Conti¹⁸ reported field measured values of friction coefficients based on the live and dead end force measurements and the total angle change for tendons from three different projects. Figure 4.15 shows the measured friction values plotted

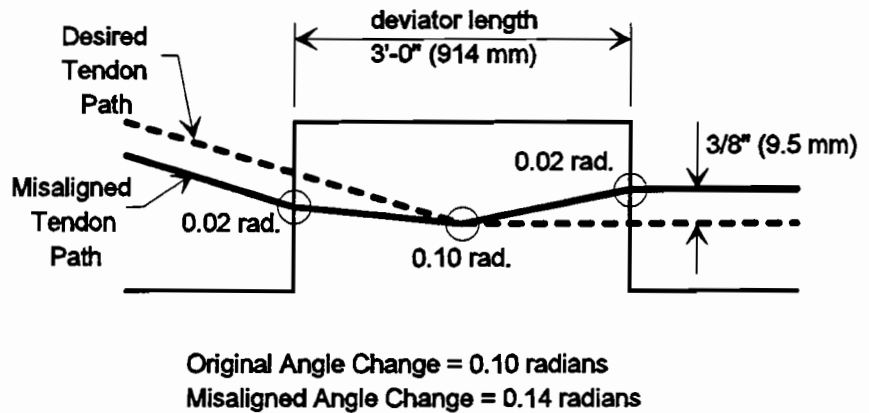
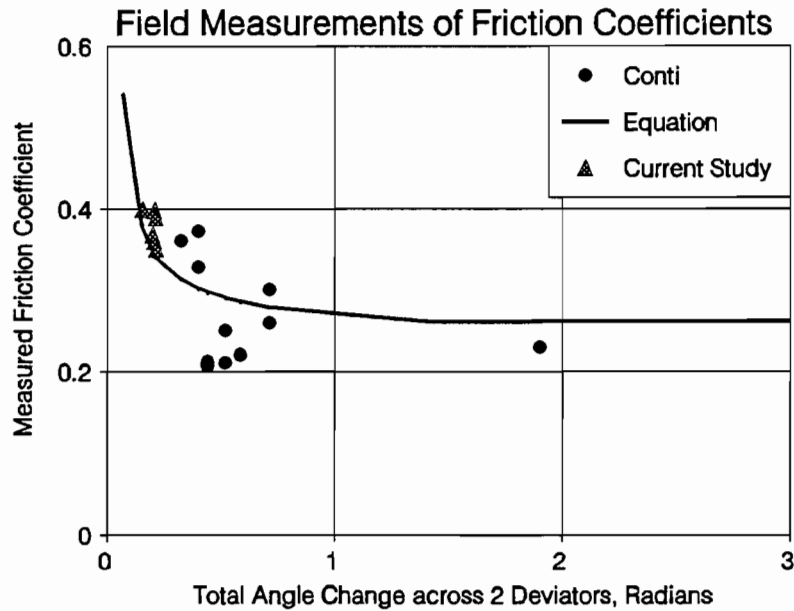


Figure 4.14 Effect of deviator duct misalignment.

against the total angle change across two deviators per tendon. Also shown are data points from tendons in the current project. It is apparent that the smaller angle changes have much larger friction coefficients than the larger angle changes. This is consistent with the misalignment problem. For the same placement tolerance, a small angle would be far more affected by misalignment than a large angle. For instance, the misalignment shown in Figure 4.14 increases the small angle of 0.1 radians by 40% to 1.4 radians. A larger angle of 1 radian would be increased only 4% to 1.04 radians.



Equation -
$$\mu = 0.25 * \left(\frac{\alpha_{tot} + 2 * 0.04}{\alpha_{tot}} \right)$$

The equation alters the friction coefficient by adding an inadvertent angle change of 0.04 radians per deviator.

Data from Current Study

Tendon	Angle, radians	Friction Coeff.
C11-T1	.153	.40
C11-T2	.214	.35
A44-T1	.204	.36
A44-T2&T3	.195	.37
A43-T1	.209	.39
A43-T2&T3	.205	.40

Figure 4.15 Field measurements of friction coefficients.

Another factor contributing to the higher friction is the very tight radius of curvature which the tendons have as they pass through the deviators. The deviator pipe lengths are three feet and the average angle change is 0.1 radians. This equates to a radius of curvature of 30' (9.2 m). This is not extremely tight compared to a proposed limit for radius of curvature for a 19-0.6" (15.2 mm) ϕ strand tendon which is 12 ft. (3.66 m) in the developing Eurocode. The radius is small compared to the internal tendons in which the same angle changes are spread out over six to eight feet (1.8 to 2.4 m) so the radius of curvature is much larger.

Cordes, Trost and Schütt¹⁹ showed in laboratory tests that the apparent friction exhibited by a tendon in a duct is a factor of a basic friction value plus a constant times the normal force per unit length plus another constant times the travel of the tendon along the duct. It is possible that the tight radii of curvature are also tending to increase the apparent friction across the deviators.

The higher friction values can be accounted for by the use of an inadvertent duct misalignment angle change of 0.04 radians added to the theoretical angle change at each deviator. The equation for the change in tendon force for an external tendon across a single deviator would be:

$$F_x = F_o e^{-\mu(\alpha + 0.04)}$$

The additional angle change of 0.04 radians accounts for inadvertent angle changes caused by duct misalignment, and as stated earlier, reflects that large angle changes are less affected than smaller changes. If angle changes are relatively consistent within a project, the equation can be used to compute an increased friction value which could be used for all external tendons.

4.4.1.3 Seating Losses. The strains in the tendons immediately after seating were recorded for every tendon. Table 4.7 presents the stress loss for each length of tendon, the calculated wedge seating travel based on the measured stress changes, and the measured seating travel. The average span losses are presented graphically in Figure 4.16. The average calculated seating travel value of 0.26 (6.6 mm) inches is only slightly less than the measured value of 0.29 inches (7.4 mm), and is in good agreement with design assumptions.

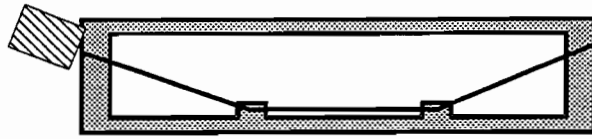
Current design practice assumes that the change in tendon stress across the live end deviators during stressing is equal to but opposite the change in tendon stress after seating. Table 4.8 compares the calculated friction across the deviator during stressing and after seating for each live end deviator. The average during stressing is 0.47. The average after seating is 0.26. This difference could be related to the differences in friction for a tendon which moves a significant distance toward the stressing end (6 inches (152 mm) during stressing) and a tendon which moves only slightly in the opposite direction (0.23 inches (5.8 mm) during seating).

An interesting phenomenon which occurred for all tendons is the increase in stress on the dead end length of each tendon. This stress rise is not large, normally 1-2 ksi (7-14 MPa), but is very consistent.

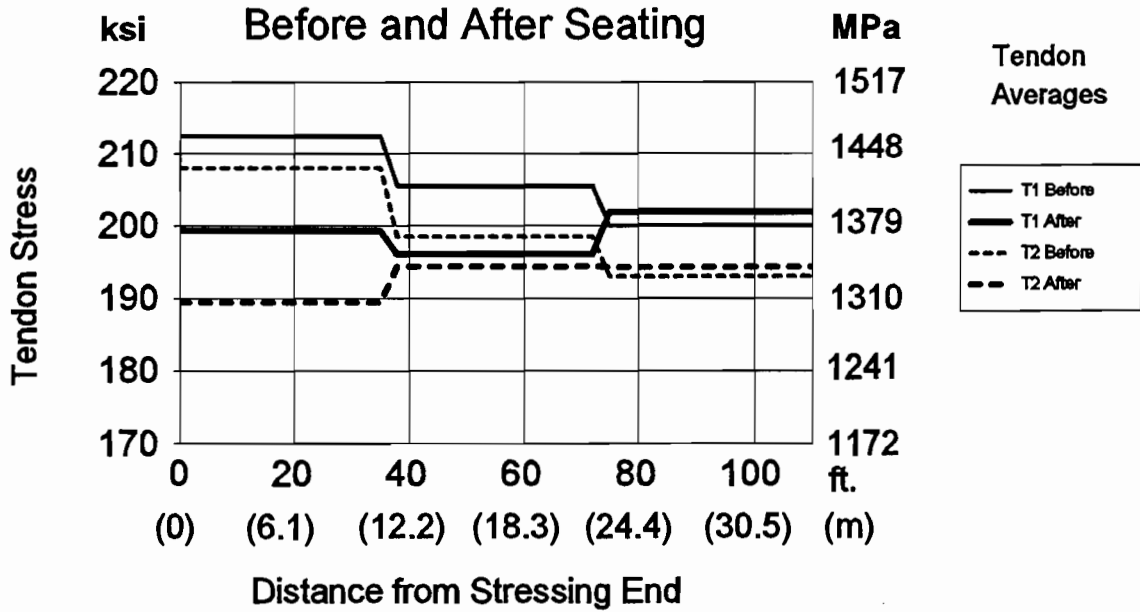
Table 4.7 Measured vs. Calculated Seating Losses.

Span	Tendon	Loss in Length 1,		Loss in Length 2,		Loss in Length 3,		Calculated Seating Loss,		Measured Seating Loss,	
		ksi	MPa	ksi	MPa	ksi	MPa	inches	mm	inches	mm
C11	T1N	-11.8	-81	-8.8	-61	+1.7	11.7	0.32	8.1	0.36	9.1
	T1S	-14.6	-101	-10.1	-70	+2.0	13.8	0.39	9.9	0.38	9.7
	T2N	-17.8	-123	-3.2	-22	+0.8	5.5	0.33	8.4	0.32	8.1
	T2S	-19.5	-134	-5.1	-35	+1.7	11.7	0.38	9.7	0.28	7.1
A43	T1N	-13.5	-93	-1.3	-9	+1.1	7.6	0.22	5.6	0.27	6.9
	T1S	-13.3	-92	-2.3	-16	+0.9	6.2	0.24	6.1	0.25	6.4
	T2N	-13.9	-96	-2.3	-16	+1.3	9.0	0.24	6.1	0.22	5.6
	T2S	-14.4	-99	-2.2	-15	+1.8	12.4	0.24	6.1	0.28	7.1
	T3N	-13.7	-94	-3.2	-22	+1.4	9.7	0.25	6.4	0.30	7.6
	T3S	-12.7	-88	-1.2	-8	+1.4	9.7	0.20	5.1	0.25	6.4
A44	T1N	-15.5	-107	-1.2	-8	+1.5	10.3	0.24	6.1	0.32	8.1
	T1S	-14.7	-101	-1.1	-8	+0.5	3.4	0.24	6.1	0.26	6.6
	T2N	-14.9	-103	-2.2	-15	+1.2	8.3	0.25	6.4	0.27	6.9
	T2S	-14.7	-101	-2.9	-20	+3.5	24.1	0.22	5.6	0.3	7.6
	T3N	-13.7	-94	-2.3	-16	+1.1	7.6	0.23	5.8	0.29	7.4
	T3S	-13.1	-90	-3.9	-27	+2.1	14.5	0.24	6.1	0.31	7.9
Averages								0.26	6.6	0.29	7.4
Standard Deviation								0.06	1.5	0.04	1.0

Length 1 is closest to live end
Length 2 is middle section
Length 3 is closest to dead end



Tendon Stresses - Span C11



Tendon Stresses - Span A43 & A44

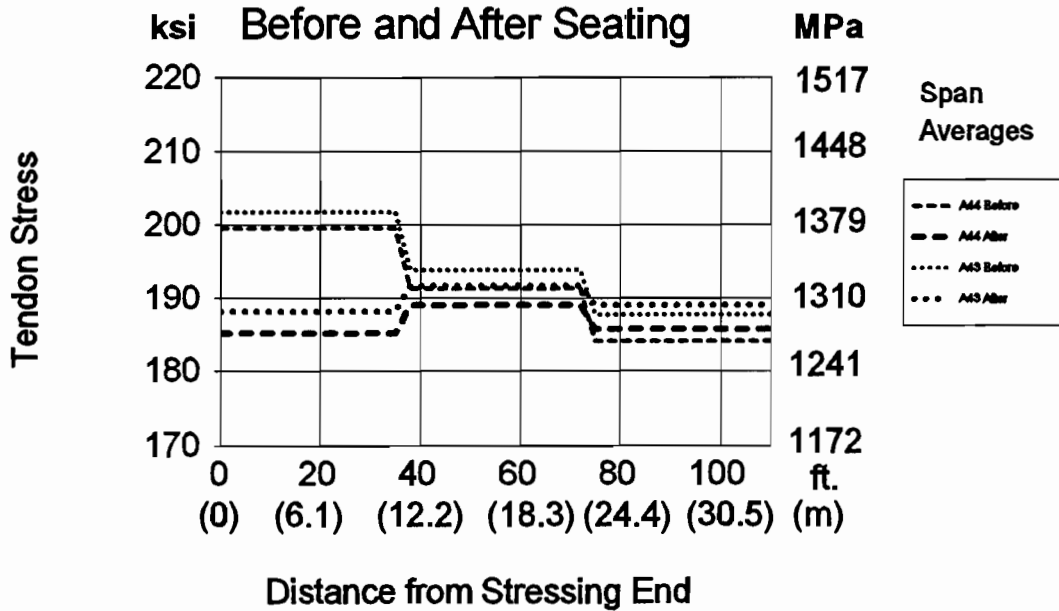


Figure 4.16 Losses in tendon stress due to seating.

Table 4.8 Difference in Live End Friction Values Before and After Seating.

Span	Tendon	Before Seat Stress Difference		Before Seat Friction Coefficient	After Seat Stress Difference		After Seat Friction Coefficient
		ksi	MPa		ksi	MPa	
C11	T1N	6	41	0.84	+3.0	20.7	0.44
	T1S	8	55	1.1	+3.5	24.1	0.51
	T2N	7	48	0.36	-7.6	-52.4	0.41
	T2S	12	83	0.62	-2.4	-16.5	0.13
A43	T1N	7	48	0.36	-5.1	-35.2	0.27
	T1S	9	62	0.47	-2	-13.8	0.11
	T2N	11	76	0.57	-0.6	-4.1	0.03
	T2S	9	62	0.47	-3.2	-22.1	0.18
	T3N	3	21	0.15	-7.5	-51.7	0.4
	T3S	8	55	0.43	-3.5	-24.1	0.19
A44	T1N	12	83	0.61	-2.3	-15.9	0.12
	T1S	7	48	0.36	-6.6	-45.5	0.36
	T2N	6	41	0.31	-6.7	-46.2	0.36
	T2S	7	48	0.37	-4.8	-33.1	0.27
	T3N	6	41	0.32	-5.4	-37.2	0.3
	T3S	11	76	0.58	-1.8	-12.4	0.1
Average		8.1	56	0.47	-4.1	-28.3	0.26
Standard Deviation		2.5	17	0.14	2.9	20.0	0.12

4.4.1.4 Elastic Shortening Losses. Table 4.9 lists each tendon, in the order in which it was stressed, and the losses which occurred in the tendon from the time it was seated until after the final tendon was seated. Figure 4.17 displays these losses graphically.

As expected, the first tendon stressed in each span experienced the greatest loss. Also as expected, the middle portion of the tendon, which runs in the lower portion of the cross-section, experienced greater losses than the live end and dead end regions where the tendons were draped and hence closer to the centroid.

The strains in the concrete were also measured before and after stressing of the external tendons. The changes in the compressive strains in the concrete at the level of the tendons should be comparable to the changes in the tendon strains. Figure 4.18 shows the concrete strain changes as measured with Demec gages, and the tendon strain changes. The values compare reasonably well with the Demec readings predicting 1.16 times the measured elastic shortening loss with a standard deviation of 0.19.

The values do not correspond as well with results from traditional analysis because of the effect of the erection truss. The truss does not shed all of the dead load during stressing. At the completion of stressing the truss is still carrying 35-50% of the dead load. This means that the compression at the level of the tendon is greater than would normally be calculated.

Table 4.9 Elastic Shortening Losses.

Span	Tendon	Order	Loss in Stress, ksi (MPa)			Average loss, ksi (MPa), and % of Initial		
			Live	Mid	Dead	Live	Mid	Dead
C11	T1N	1	-2.7 -18.6	-3.2 -22.1	-1.1 -7.6	-1.8 ksi, (-12.4) 1.0%	-2.2 ksi, (-15.2) 1.1%	-1.0 ksi, (-6.9) 0.5%
	T1S	2	-2.2 -15.2	-2.7 -18.6	-1.6 -11.0			
	T2N	3	-2.5 -17.2	-2.5 -17.2	-1.0 -6.9			
	T2S	4	0.0 0.0	0.0 0.0	0.0 0.0			
A43	T1N	1	-3.3 -22.8	-4.0 -27.6	-2.1 -14.5	-1.5 ksi, (-10.3) 0.7%	-2.3 ksi, (-15.9) 1.2%	-1.5 ksi, (-10.3) 0.7%
	T1S	2	-2.9 -20.0	-3.7 -25.5	-2.5 -17.2			
	T2S	3	-1.2 -8.3	-2.7 -18.6	-2.1 -14.5			
	T2N	4	-1.6 -11.0	-2.1 -14.5	-1.9 -13.1			
	T3N	5	-0.1 -0.7	-1.4 -9.7	-0.5 -3.4			
	T3S	6	0.0 0.0	0.0 0.0	0.0 0.0			
A44	T1N	1	-2.8 -19.3	-4.2 -29.0	-3.0 -20.7	-1.6 ksi, (-11.0) 0.8%	-2.5 ksi, (-17.2) 1.3%	-1.9 ksi, (-13.1) 1.0%
	T1S	2	-2.9 -20.0	-3.6 -24.8	-3.0 -20.7			
	T2S	3	-2.3 -15.9	-3.4 -23.4	-2.3 -15.9			
	T2N	4	-0.8 -5.5	-2.5 -17.2	-1.7 -11.7			
	T3N	5	-0.4 -2.8	-1.1 -7.6	-1.0 -6.9			
	T3S	6	0.0 0.0	0.0 0.0	0.0 0.0			

By the same token, an elastic lengthening of the tendons occurred when the trusses were finally lowered. The tendons tensile stresses then increased to resist the dead load bending moments. The net effect is more or less equal to the recommended procedure⁷⁷ of calculating the compression in the concrete, at the level of the tendon, which is caused by the combination of prestress and dead load.

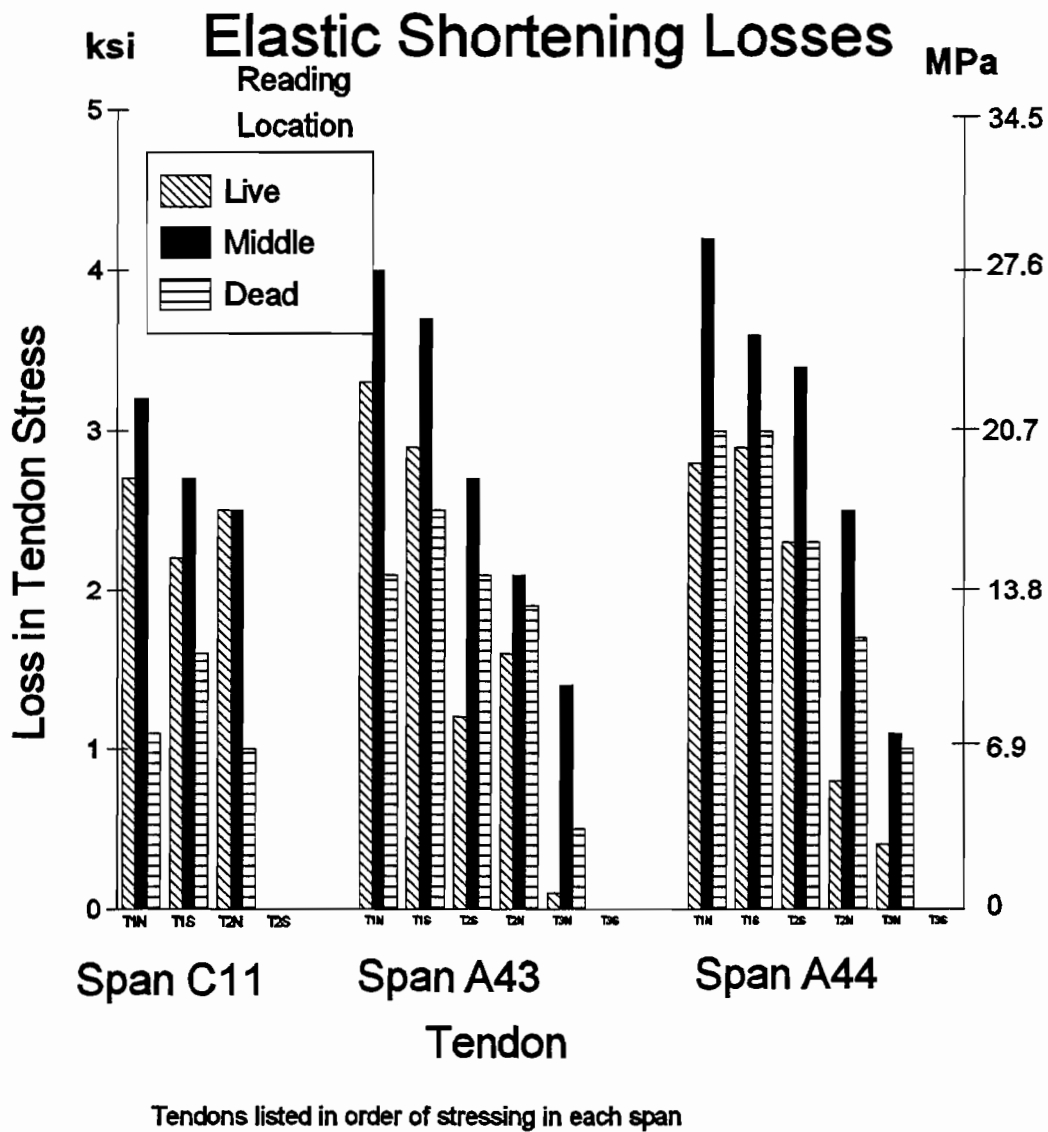
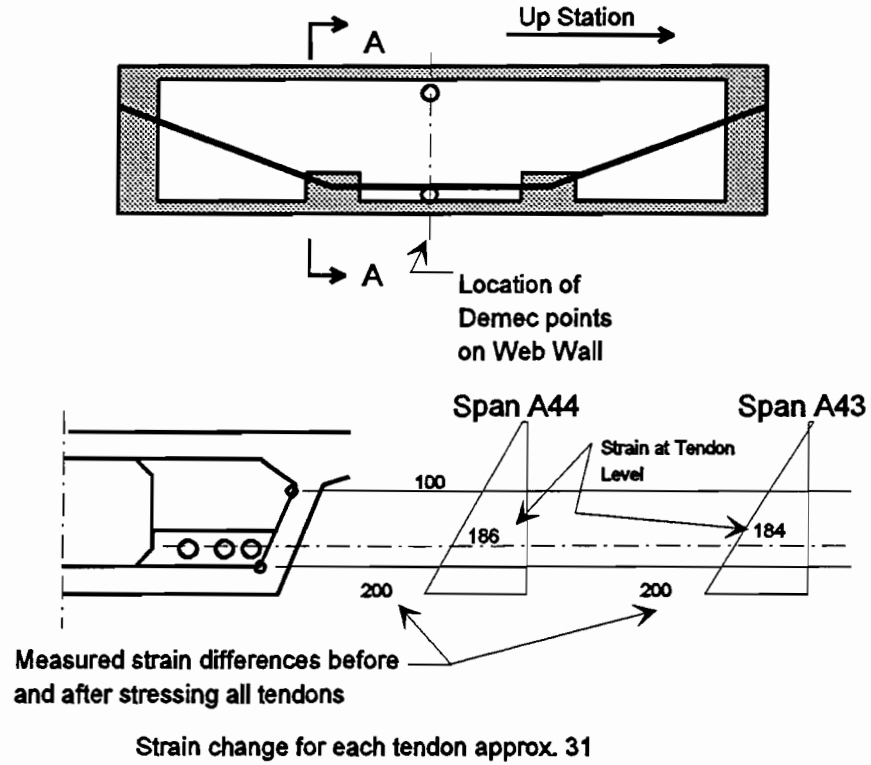


Figure 4.17 Elastic shortening losses.



Tendon	Interpolated Strain Change $\mu\epsilon$	B		Span 44			Span 43			
		Measured Strain x Steel Modulus		A Measured Loss		A/B	A Measured Loss		A/B	
		ksi	MPa	ksi	MPa		ksi	MPa		
T1N	155	4.3	29.6	4.2	29.0	0.98	4.0	27.6	0.93	
T1S	124	3.4	23.4	3.6	24.8	1.06	3.7	25.5	1.09	
T2S	93	2.6	17.9	3.4	23.4	1.31	2.7	18.6	1.04	
T2N	62	1.7	11.7	2.5	17.2	1.47	2.1	14.5	1.23	
T3N	31	0.9	6.2	1.1	7.6	1.22	1.4	9.7	1.55	
T3S	0	0.0	0	0.0	0	-	0.0	0	-	
Measured loss at middle measuring location on each tendon.						Average	1.17	1.14		1.16
						Standard Deviation	0.18	0.21		0.19

Figure 4.18 Comparison of concrete compression and elastic shortening losses.

Figure 4.19 shows, for Spans A43 and A44 the moments at the deviators and at mid-span for the post-tensioning loads plus full dead load. The average stress along the tendon axis between the deviators is calculated as 1300 psi (8964 kPa) for Span A43 and 1060 psi (7309 kPa) for Span A44. With a concrete modulus of 5440 psi (37509 kPa) and a steel modulus of 28000 psi (193060 kPa) (manufacturers) this translates to a steel stress change of 6.7 ksi (46.2 MPa) for Span A43 and 5.5 ksi (37.9 MPa) for Span A44. To compute the average elastic shortening loss for all tendons in a beam, Zia et al.⁷⁷ recommend, for unbonded tendons, the formula:

$$ES = 0.5 f_{cpa} \frac{E_s}{E_c}$$

where:

f_{cpa} = Average stress in the concrete along the member length at the center of gravity of the tendons immediately after the prestress has been applied to the member.

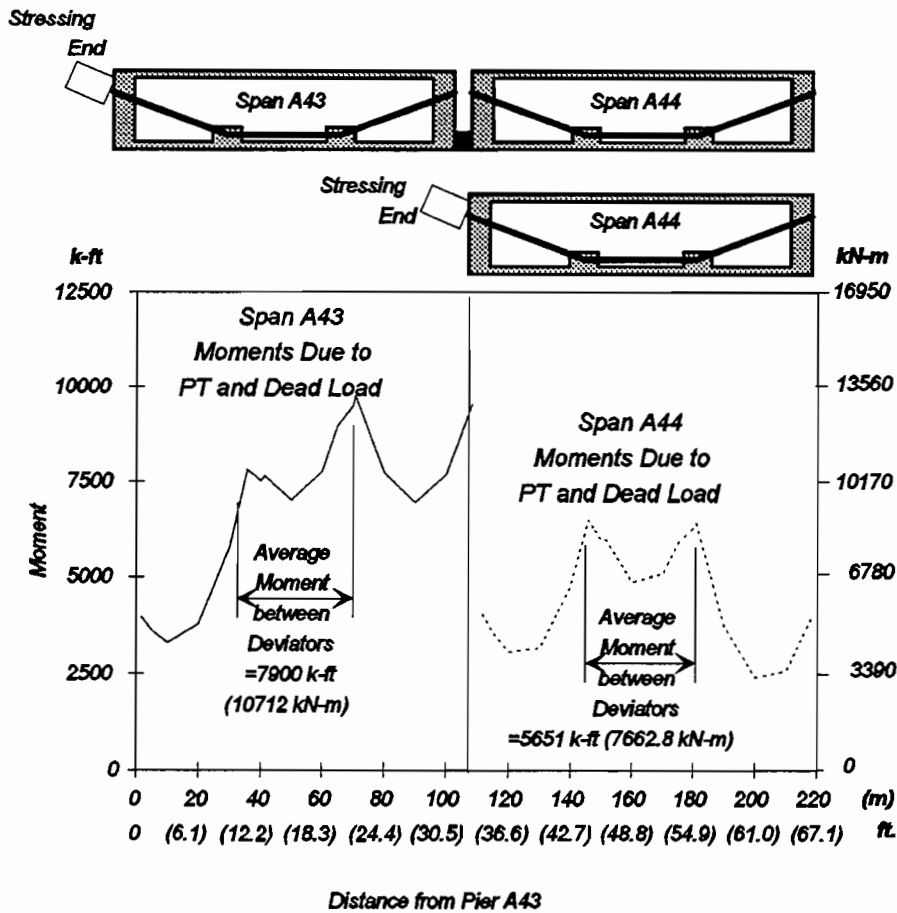


Figure 4.19 Moments between deviators.

Since the six external tendons were stressed after the six internal tendons, the average elastic shortening of the external tendons should be approximately half that of the average for all tendons. Therefore, the average elastic shortening for the six external tendons should be:

$$ES = 0.25 f_{cpa} \frac{E_s}{E_d}$$

$$\text{Span A43 } ES = (0.25)(1300) \left(\frac{5440}{28000} \right) = 1.67 \text{ ksi } (11.51 \text{ MPa})$$

$$\text{Span A44 } ES = (0.25)(1060) \left(\frac{5440}{28000} \right) = 1.37 \text{ ksi } (9.45 \text{ MPa})$$

These values compare well with the average difference in tendon stress from the stress at the end of stressing of each tendon to the stress after the truss was lowered. Table 4.10 compares these values for Spans A43 and A44.

The calculated values are within 10% of the measured values. For elastic shortening losses, which are very small (approximately 1.5 ksi (10.3 MPa) for the instrumented spans), greater rigor in analysis is unwarranted.

Table 4.10 Elastic Shortening Losses at Mid-Span in Spans A43 and A44.

Span	Initial Elastic Shortening Loss,		Elastic Lengthen @ Truss Down,		Total Change Since Stressing,		Calculated Elastic Shortening Loss		Measured/ Calculated Loss,	
	ksi	MPa	ksi	MPa	ksi	MPa	ksi	MPa	ksi	MPa
A43	-2.3	-15.9	0.8	5.5	-1.5	-10.3	-1.67	-11.5	0.90	6.2
A44	-2.5	-17.2	1.0	6.9	-1.5	-10.3	-1.37	-9.4	1.09	7.5

4.4.2 Changes with Time. Three factors, creep, shrinkage and relaxation, affect the changes in force in the tendons with time. The strains in the external tendons were monitored with the Demec gages and electrical resistance (ER) gages connected to the Campbell data acquisition system on a regular basis over the course of many months. In conjunction with these measurements, creep specimens (cylinders from the instrumented spans) were loaded within one week of the stressing operations to determine the actual creep coefficient of the concrete in the spans. Companion shrinkage specimens were also monitored.

Figure 4.20 shows the strain changes in the creep test cylinders for spans A43 and A44 and for spans C9 and C11. The creep function is compared with several models used for prediction of creep. The A43 and A44 measurements fall slightly above the ACI 209, CEB-FIP Model Code 90 Revised Summation and Product Models, except for the higher than predicted values between 350 days and 550 days. The measurements fall generally below the CEB-FIP Model Code 78 Model. The C9 and C11 measurements fall above all prediction methods. The

creep coefficient, ϕ , which was used in the time dependent analysis was taken from the measured creep curves. The measured shrinkage, which was quite small, was also included.

Figure 4.21a and b show the construction schedule of the erection operations for spans A43 and A44, and for span C11. It also shows the time intervals used to calculate long term tendon losses, and moment redistribution. The cross-sectional properties of the box-section which were used in the analysis are those recommended in the *AASHTO Guide Specification*, with the slight modification of a step-wise rather than gradual transition from pier to mid-span properties.

The analysis was performed using a two dimensional frame solver (FRAME2D²⁴) and a computer spread sheet. The spans were discretized into segments along their length so the cross-sectional properties could be varied along the length, and so the dead and post-tensioning loads could be applied at the nodes. At each time step the deflections were increased in accordance with the measured creep and shrinkage functions, and a corresponding tendon stress loss was calculated. A loss of prestress due to relaxation for the time step was calculated and added to the creep and shrinkage loss. The total prestress loss was then applied to the model to determine the creep recovery due to the loss of prestress. At each time step the analysis was run and the results of each step were summed in the spread sheet. Appendix B presents the meshes and input files for the analysis.

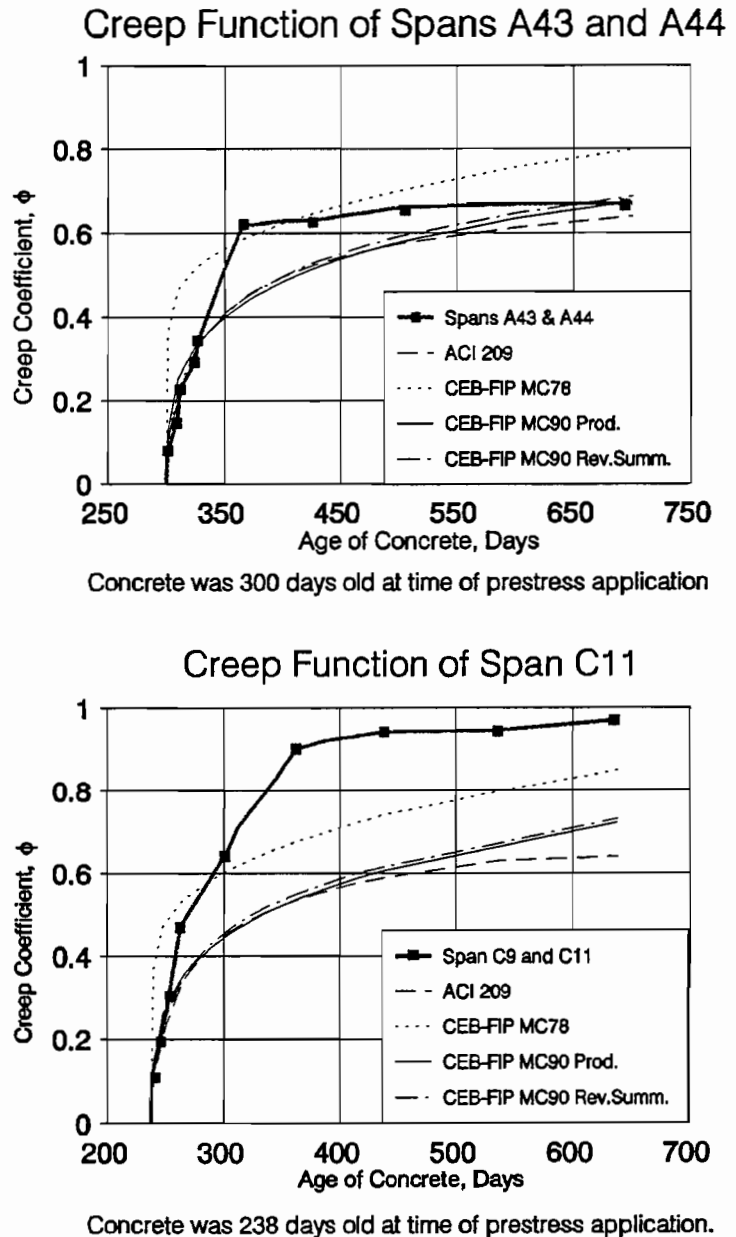


Figure 4.20 Creep functions for Spans A43, A44 and C11.

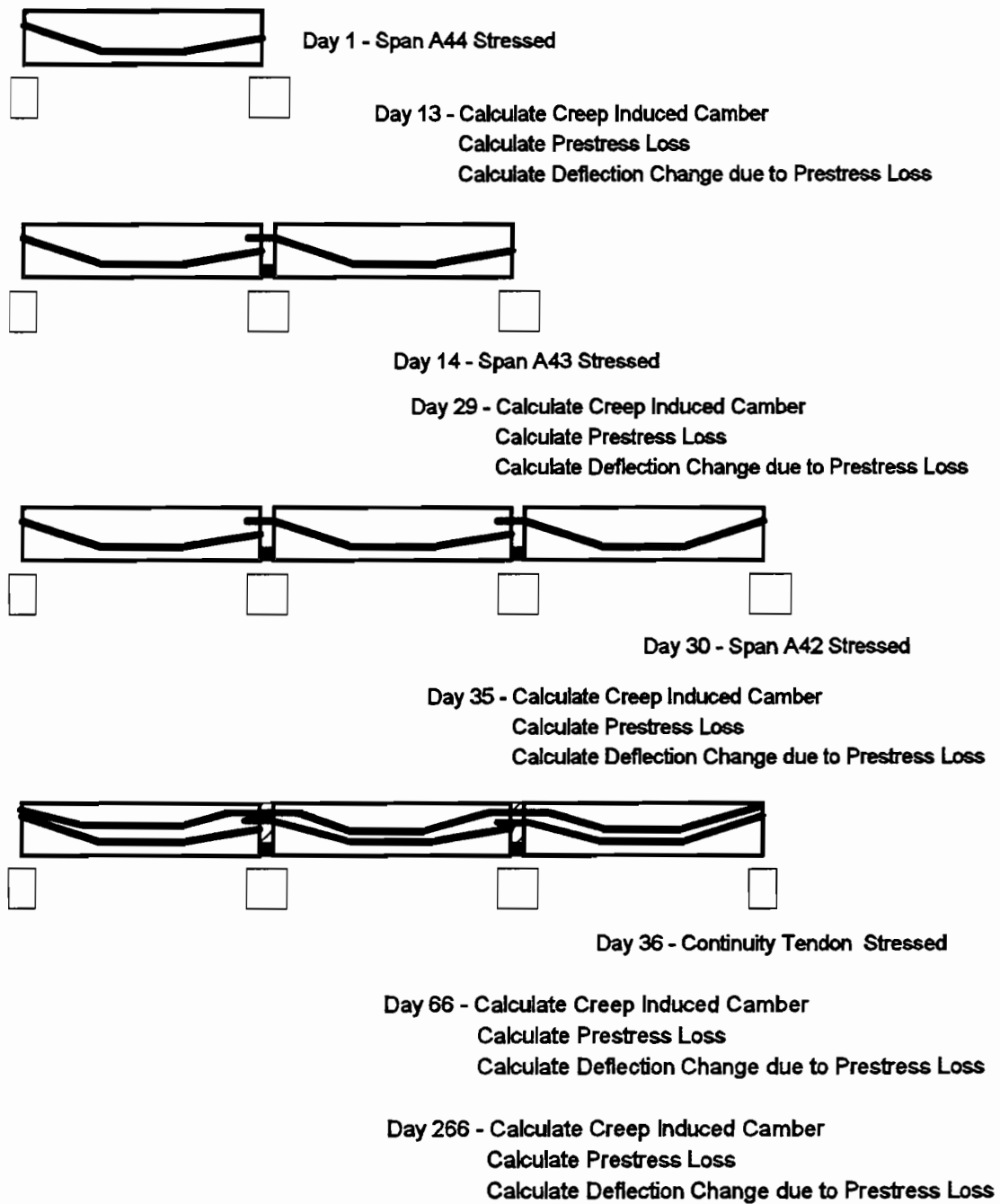


Figure 4.21a Erection schedule and operations of long term analysis for Spans A43 and A44.

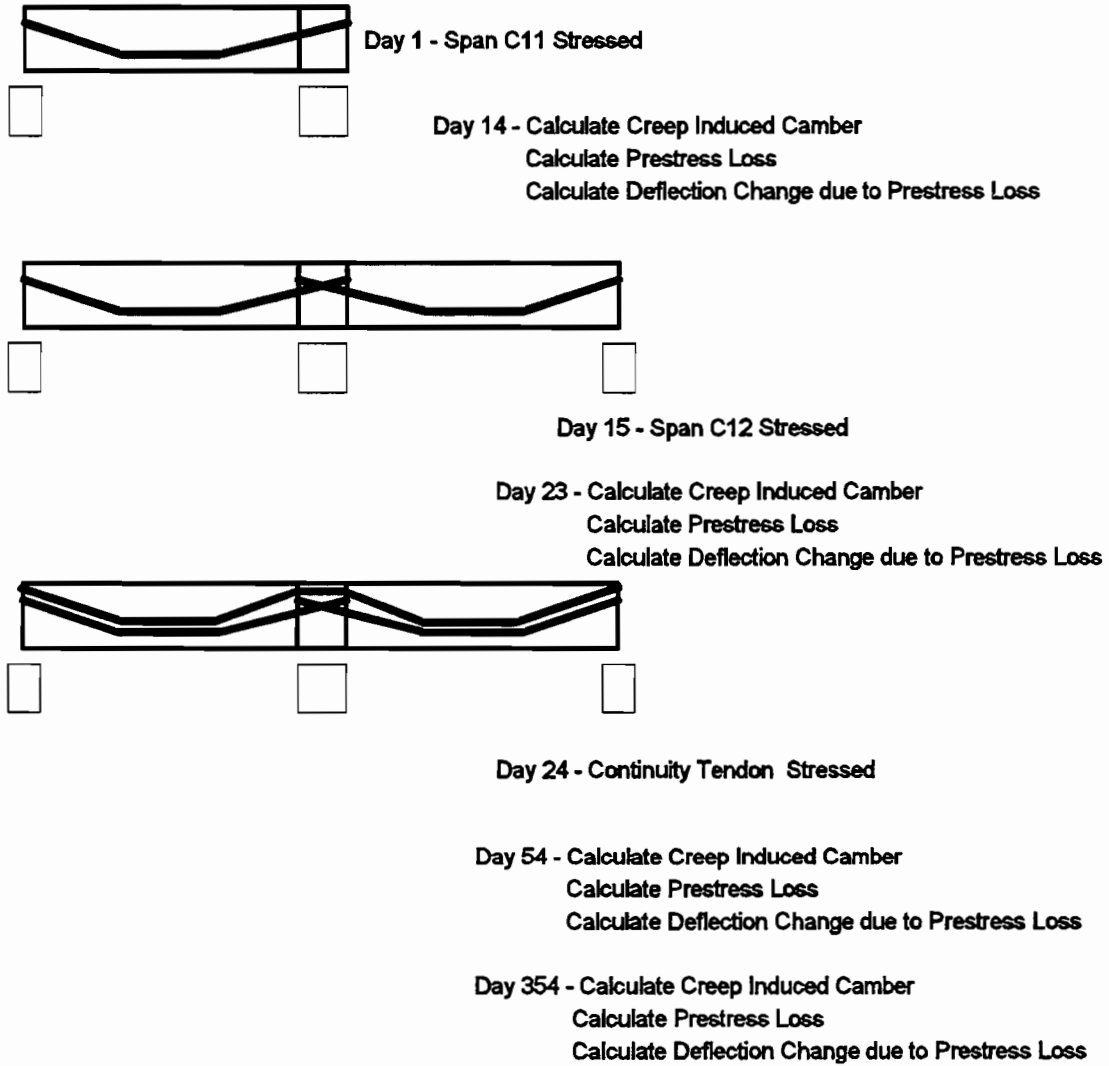


Figure 4.21b Erection schedule and operations for long term analysis for Span C11.

The time dependent analysis gave reasonably accurate results in terms of measured vs. calculated deflections. Figure 4.22 compares the measured mid-span deflections of the three spans with the time dependent analysis calculated deflections and with the deflections calculated by the TxDOT program "Bridge Designer". The "Bridge Designer" analysis was performed prior to the beginning of construction and as a result included many design assumptions. The design included higher than actual tendon forces, lower than actual concrete modulus, full cross-sectional properties and a very optimistic construction schedule.

Figure 4.23 shows the four individual tendon stress readings, two Demec gages and two ER gages, from a typical tendon. Also shown in the figure is the calculated change in tendon stress with time. The calculated loss value includes only changes in measurable strain. Since relaxation losses are not associated with a strain change they are not considered.

From the figure it is apparent that the Demec gage readings fluctuated much more than the ER gages. The figure also shows the tendon forces dropping from day 1 to approximately day 130, then increasing. This effect is caused by the seasonal changes in temperature and the difference in the coefficient of thermal expansion of concrete and steel.

The measured coefficient of thermal expansion of the concrete for this structure is $5 \times 10^{-6}/^{\circ}\text{F}$ ($9 \times 10^{-6}/^{\circ}\text{C}$). The value of the coefficient of thermal expansion for high strength steel is $8 \times 10^{-6}/^{\circ}\text{F}$ ($14.4 \times 10^{-6}/^{\circ}\text{C}$).⁷ This would indicate that as temperatures cool, the steel tries to shorten more than the concrete, so steel tension increases due to the restraint of the concrete. As temperatures rise, the steel tries to elongate more than the concrete, which results in a decrease in tension in the steel. Figure 4.23 also shows the average daily temperature on the days readings were made. The tendon force decreases with high temperatures and increases with low temperatures, as indicated in the above discussion.

It has also been suggested that there is a seasonal difference between the average temperature of the concrete and the external post-tensioning tendons. If the steel, on average, is warmer than the concrete in summer and cooler than the concrete in winter, this would add to the stress fluctuation. Unfortunately, no measurements were made to confirm this hypothesis.

Figure 4.24 shows the same four readings after an adjustment for differing coefficients has been made. This adjustment causes the ER gage readings to follow the shape of the predicted curve more closely. The Demec gage readings still fluctuate greatly. This could be due to other thermal effects caused by the interaction of the epoxy sleeve. It is recommended that this phenomenon be studied further before future use of the sleeve system.

Figure 4.25 shows the averages of the four readings for the live, middle and dead end locations of Tendon T1N in span A43, before and after the temperature adjustment. It is apparent that the adjustment reduces the seasonal effects and causes readings to appear closer to predicted.

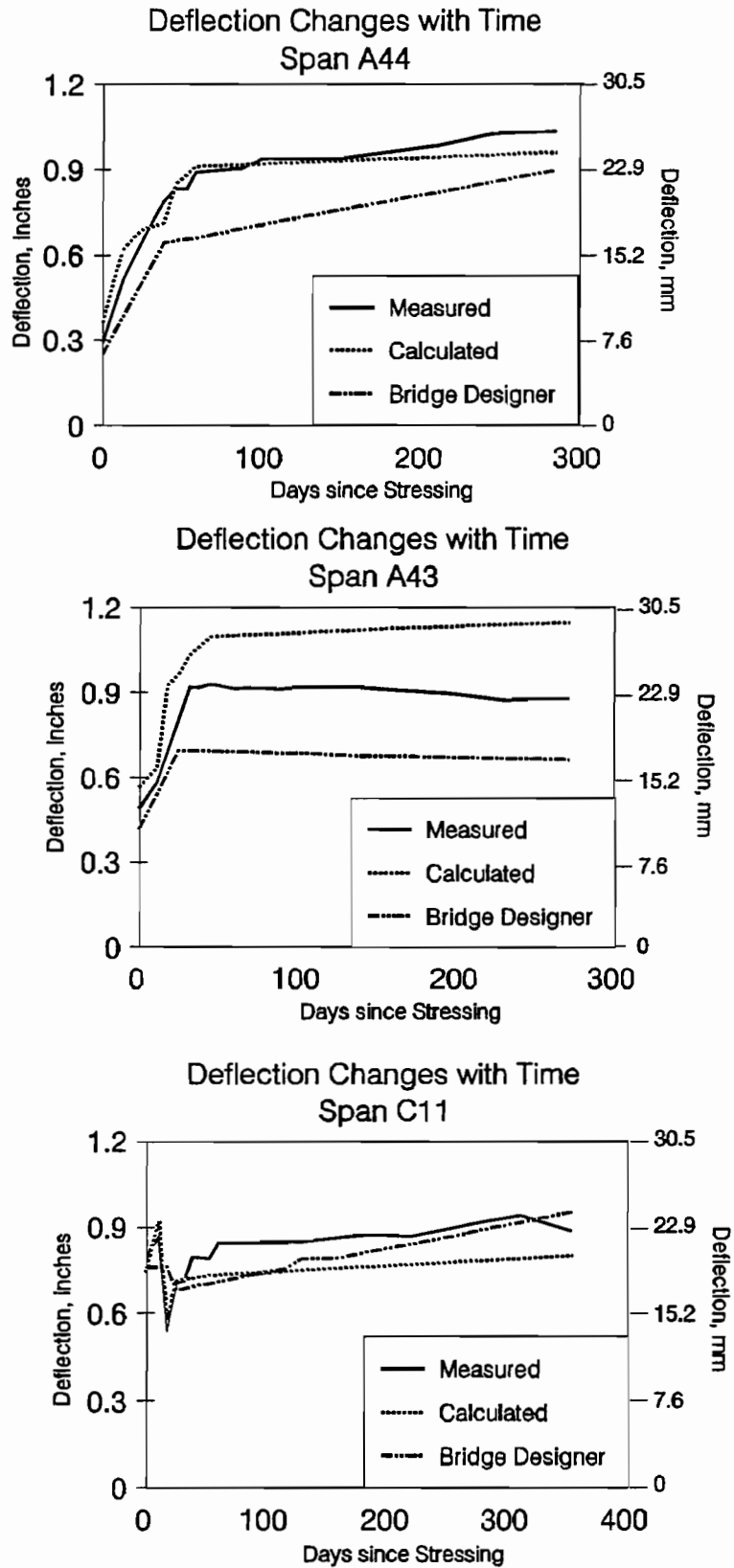
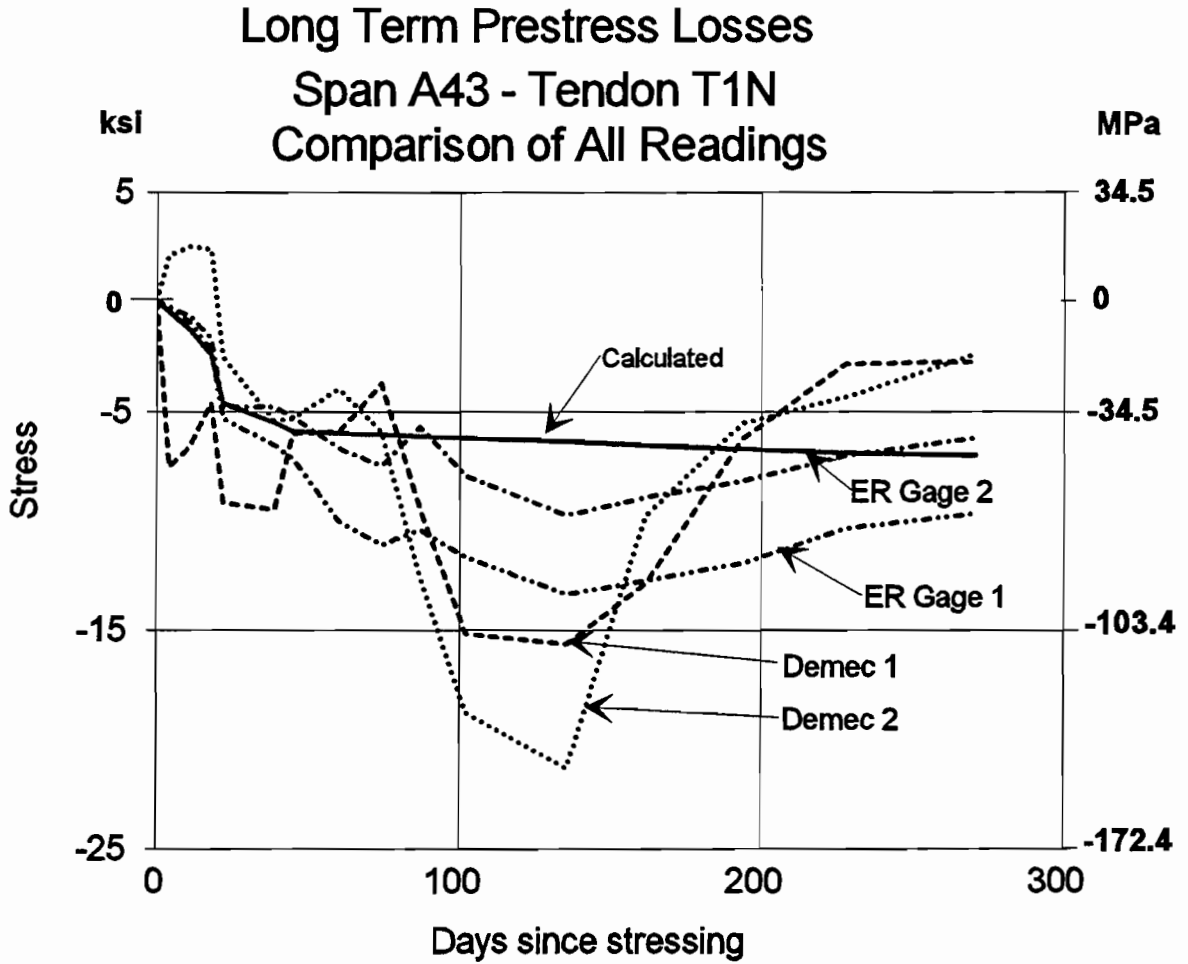


Figure 4.22 Comparison of measured and calculated deflection.



Values not adjusted for difference in coefficient thermal expansion of concrete and steel.

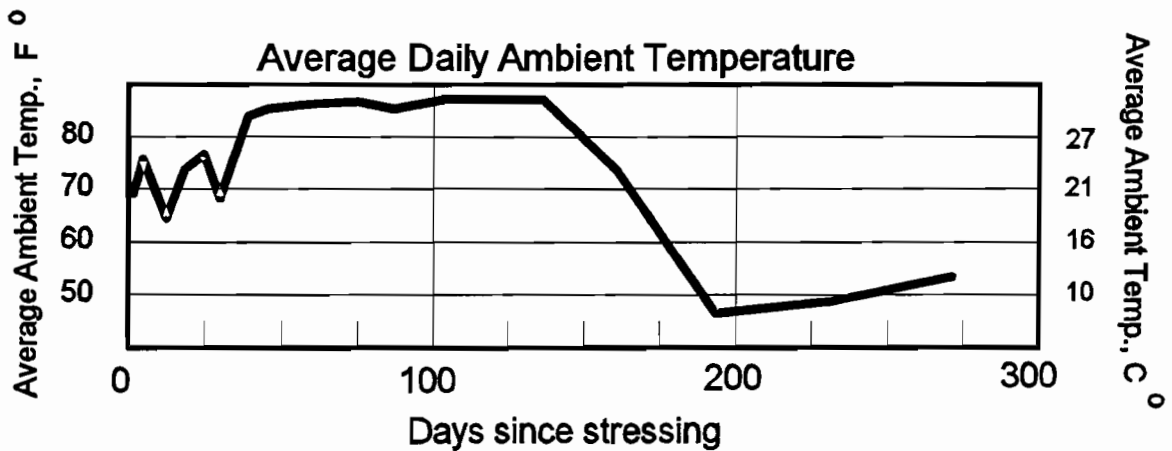
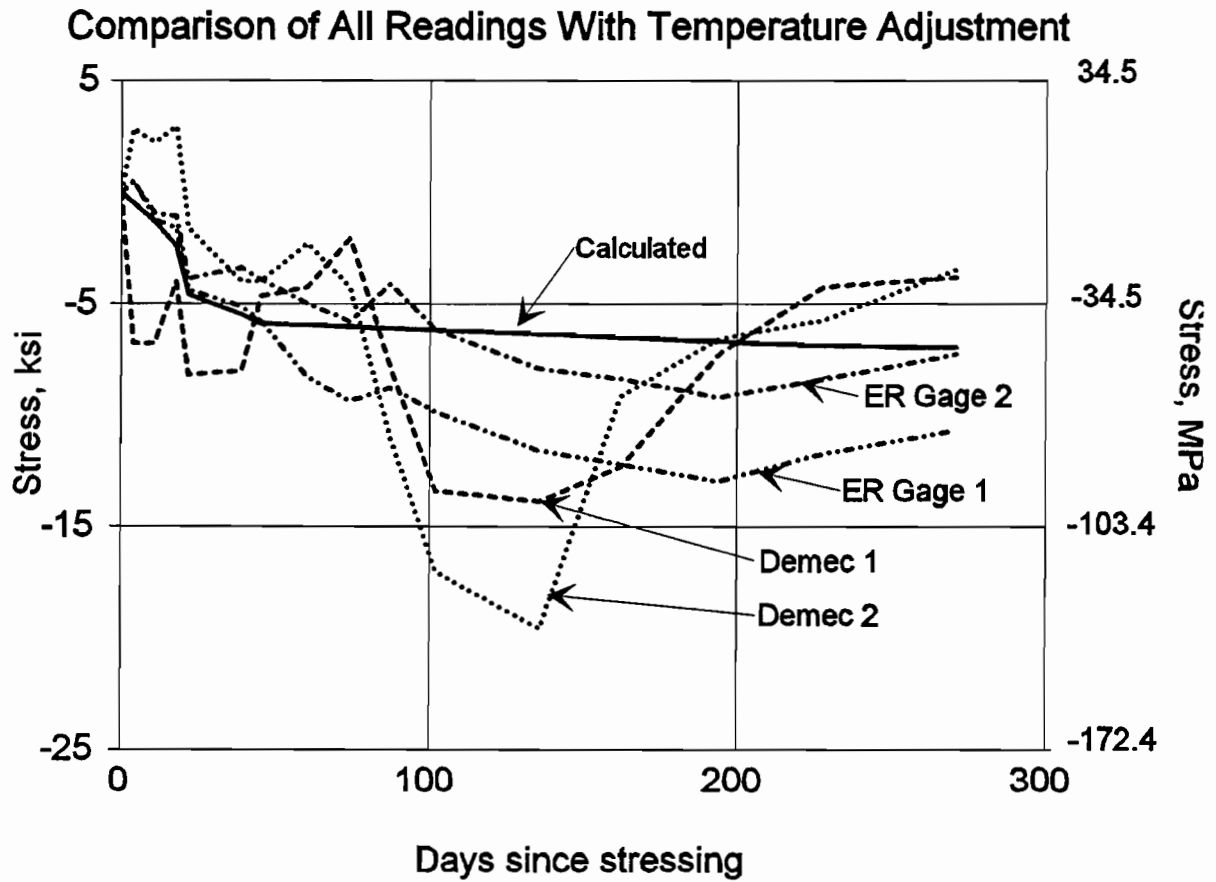


Figure 4.23 Raw tendon stress readings and ambient daily temperatures.

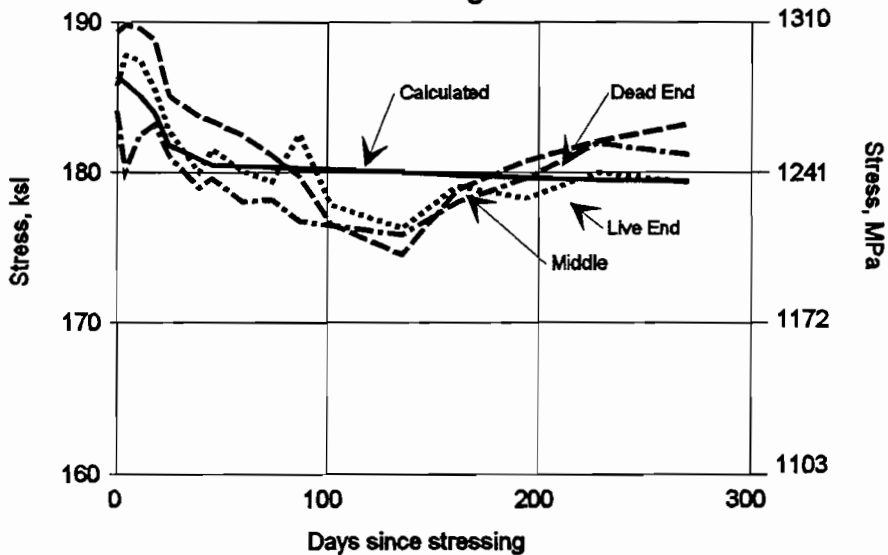
Long Term Prestress Losses Span A43 - Tendon T1N



Values adjusted for difference in coefficient thermal expansion of concrete and steel.

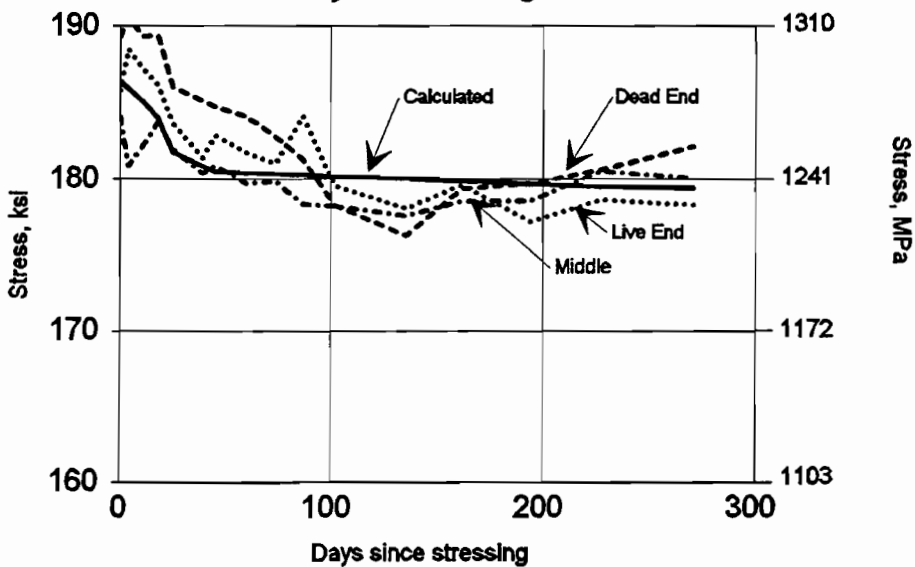
Figure 4.24 Tendon Stress readings after temperature adjustment.

Long Term Prestress Losses
Span A43 - Tendon T1N
Raw Averages



Values not adjusted for difference in coefficient thermal expansion of concrete and steel.

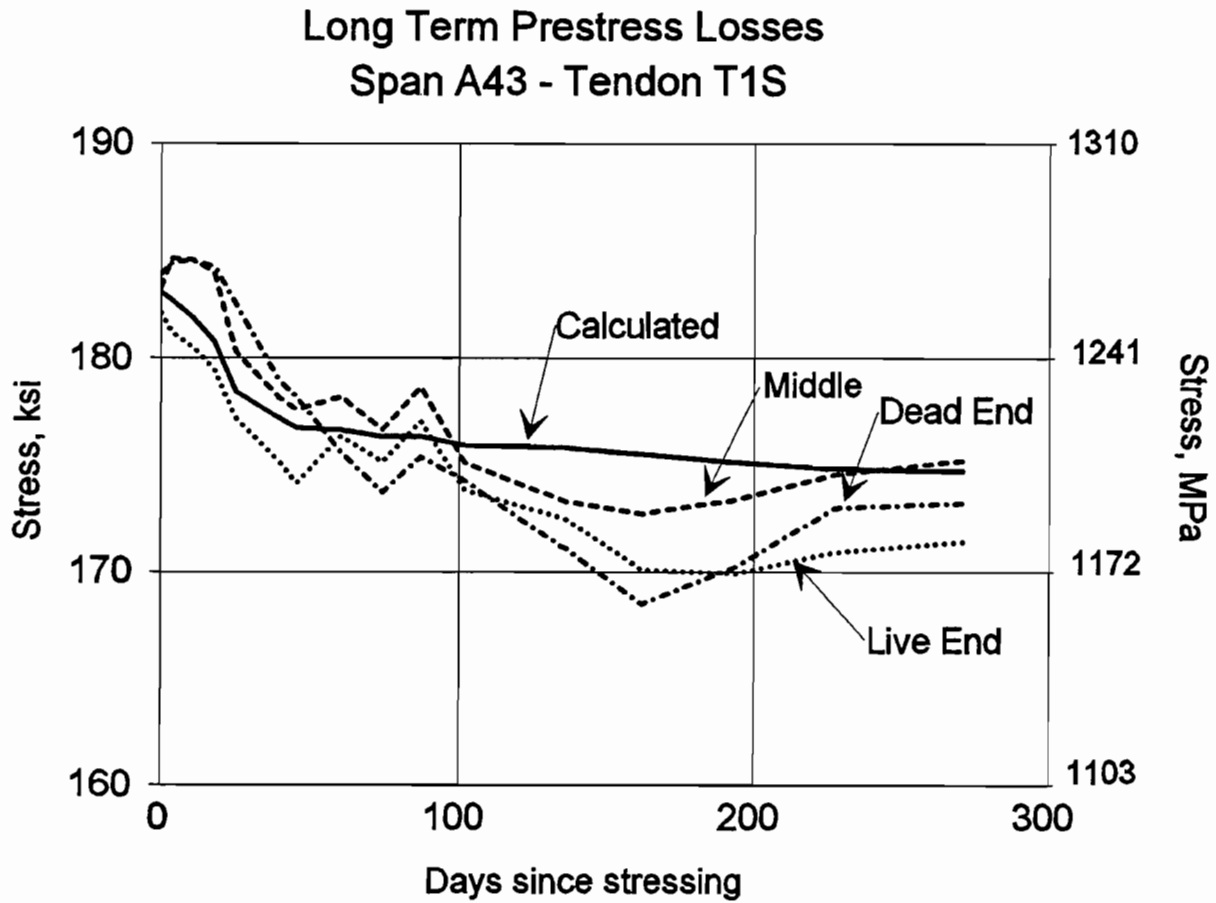
Long Term Prestress Losses
Span A43 - Tendon T1N
Adjusted Averages



Values adjusted for difference in coefficient of thermal expansion of concrete and steel.

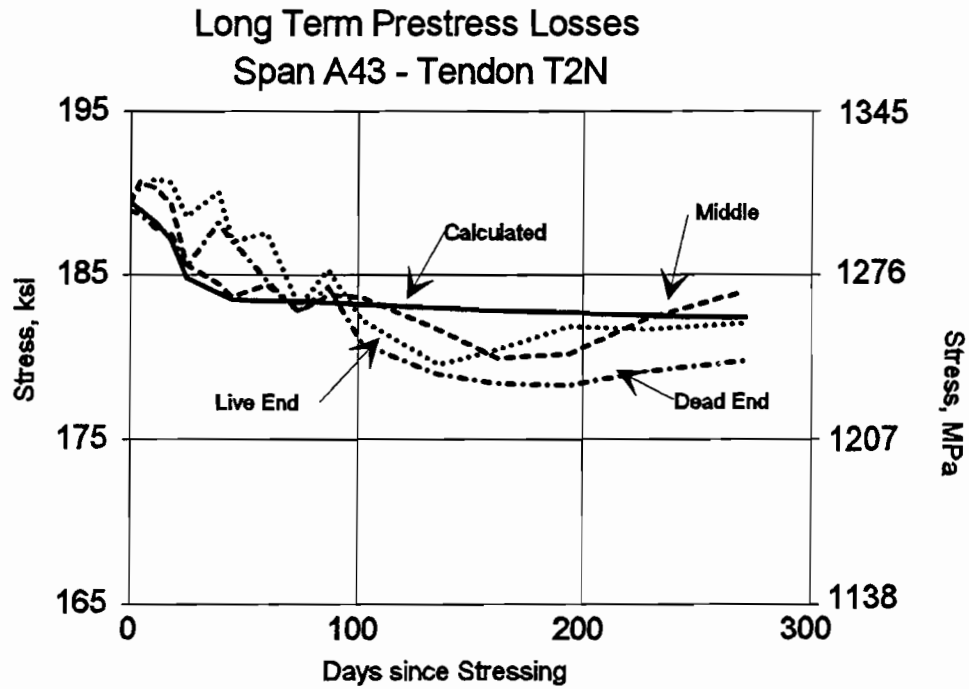
Figure 4.25 Comparison of raw and adjusted average tendon stresses for Tendon T1N and Span A43.

Figures 4.26 through 4.31 show the adjusted average stresses over time for all the tendons in Spans A43 and A44. Generally the shapes of the curves are close to predicted, except for the still evident seasonal variation. For Span A43 the day 271 stress loss average is 7.7 ksi (53.1 MPa) compared to the predicted value of 6.9 ksi (47.6 MPa). For Span A44, the measured day 285 loss is 11.8 ksi (81.4 MPa) compared to a predicted value of 6.6 ksi (45.5 MPa). Span A44 experienced difficulties with the data acquisition system due to flooding inside the box girder. As a result the measurements depend more on the less reliable Demec readings.

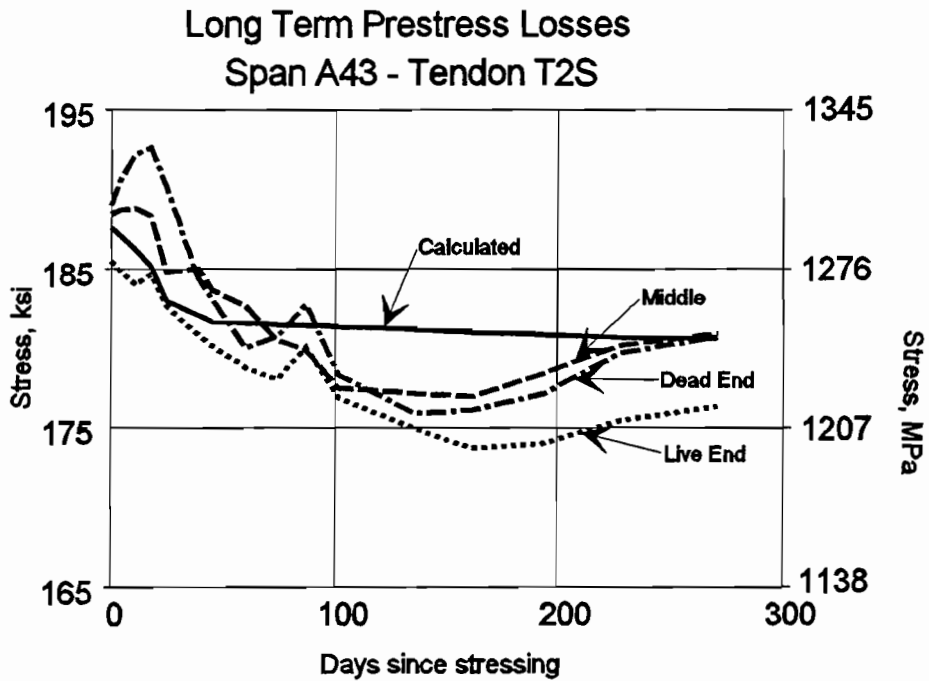


Values adjusted for difference in coefficient of thermal expansion of concrete and steel.

Figure 4.26 Adjusted average tendon stresses for Tendon T1S and Span A43.

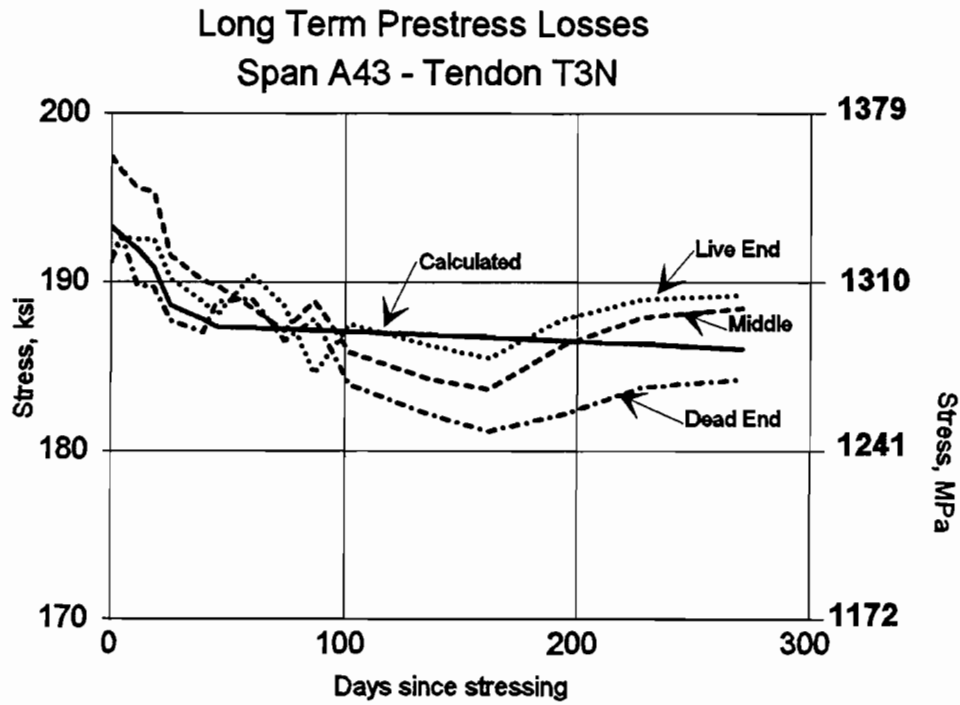


Values adjusted for difference in coefficient of thermal expansion of concrete and steel.

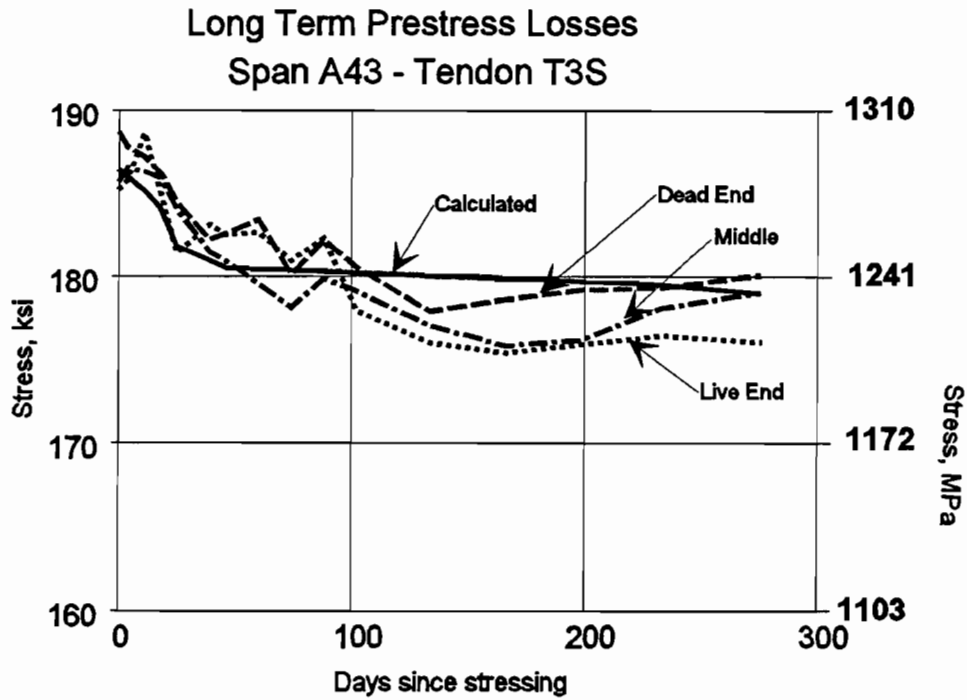


Values adjusted for difference in coefficient of thermal expansion of concrete and steel

Figure 4.27 Adjusted average tendon stresses for Tendons T2N and T2S in Span A43.

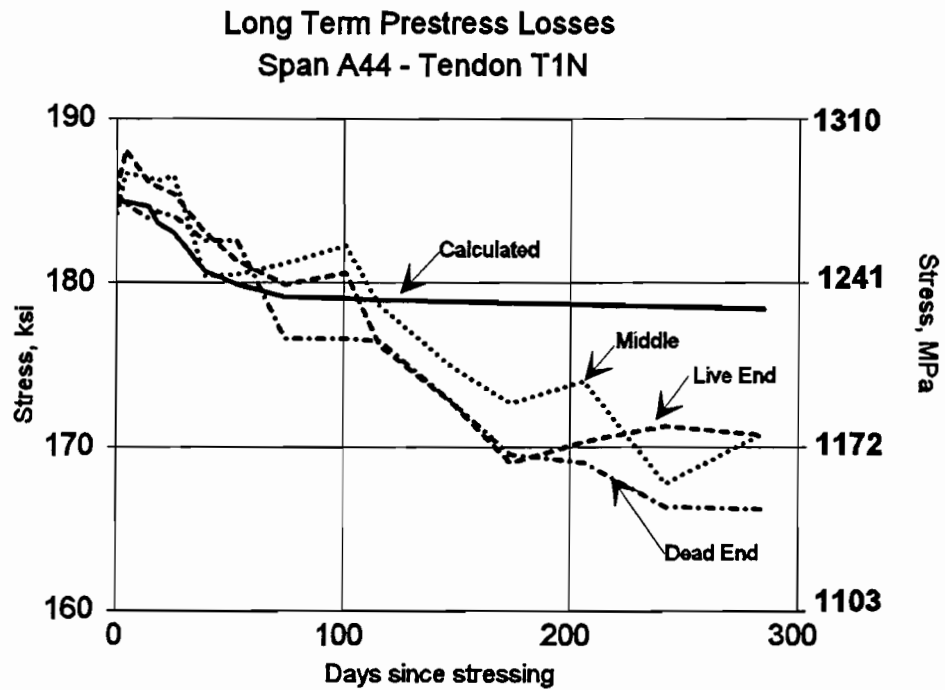


Values adjusted for difference in coefficient of thermal expansion of steel and concrete.

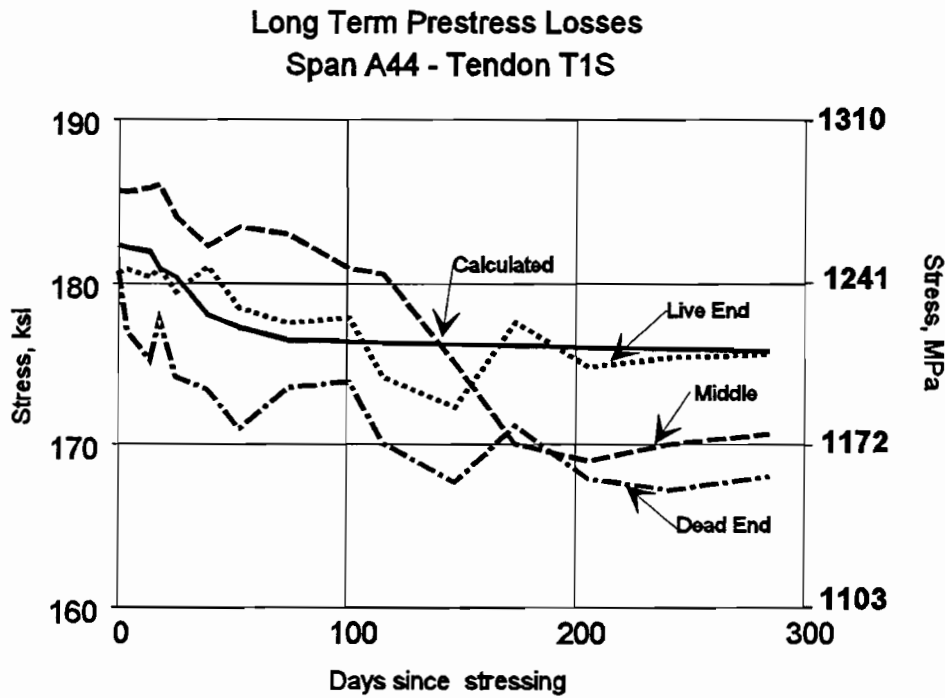


Values adjusted for the difference in coefficient of thermal expansion of concrete and steel.

Figure 4.28 Adjusted average tendon stresses for Tendons T3N and T3S in Span A43.

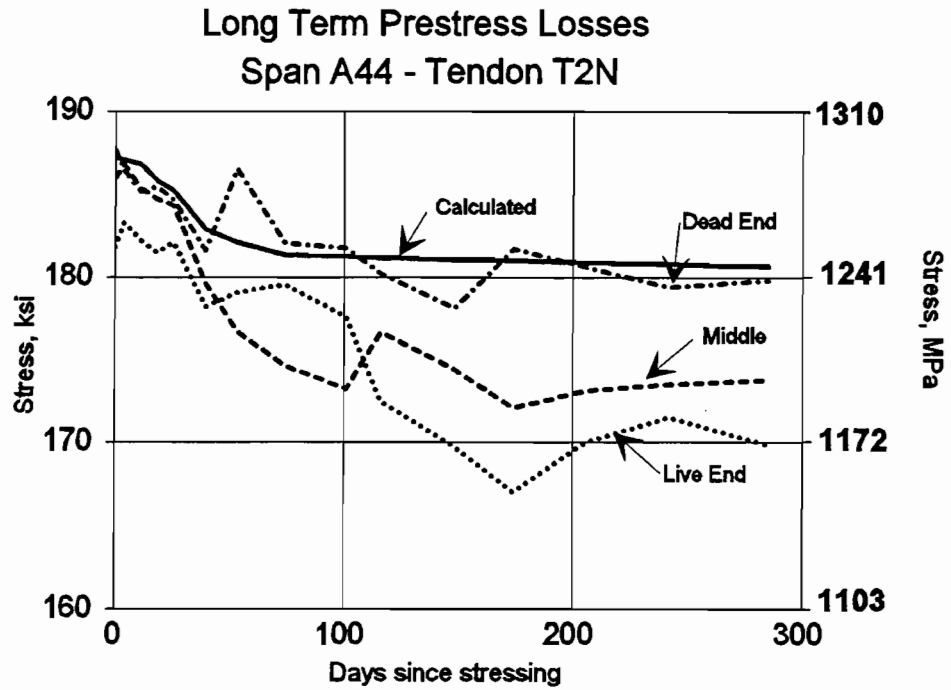


Values adjusted for difference in coefficient of thermal expansion of concrete and steel

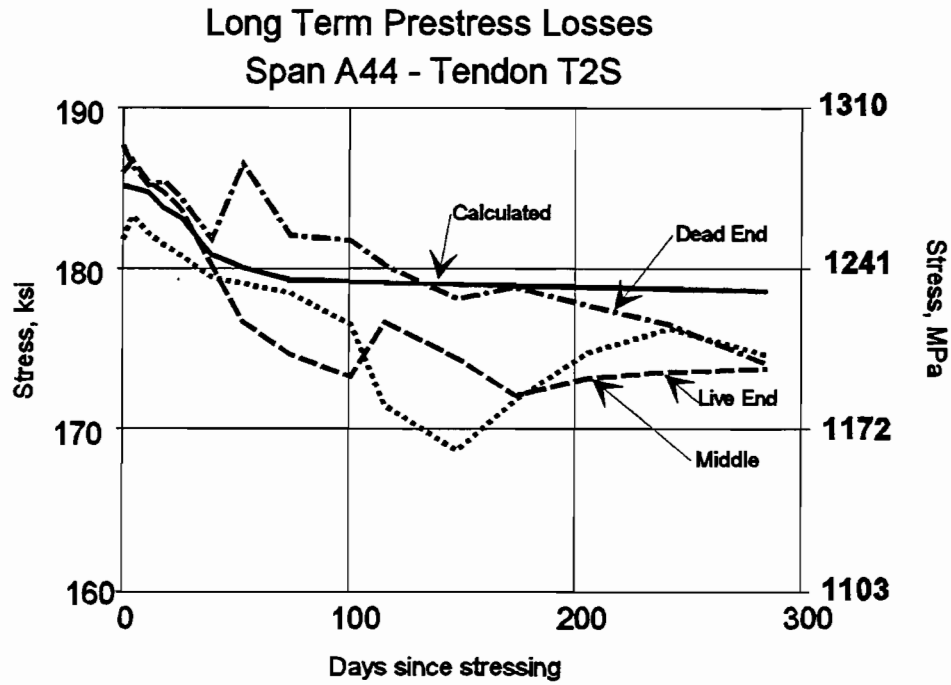


Values adjusted for difference in coefficient of thermal expansion of concrete and steel.

Figure 4.29 Adjusted average tendon stresses for Tendons T1N and T1S in Span A44.

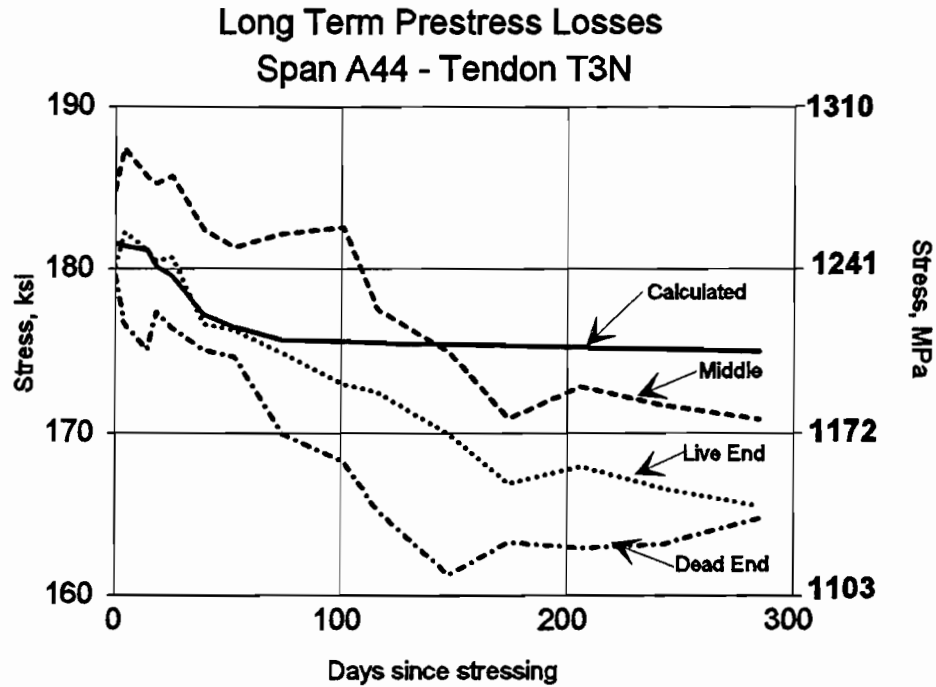


Values adjusted for difference in coefficient of thermal expansion of concrete and steel.

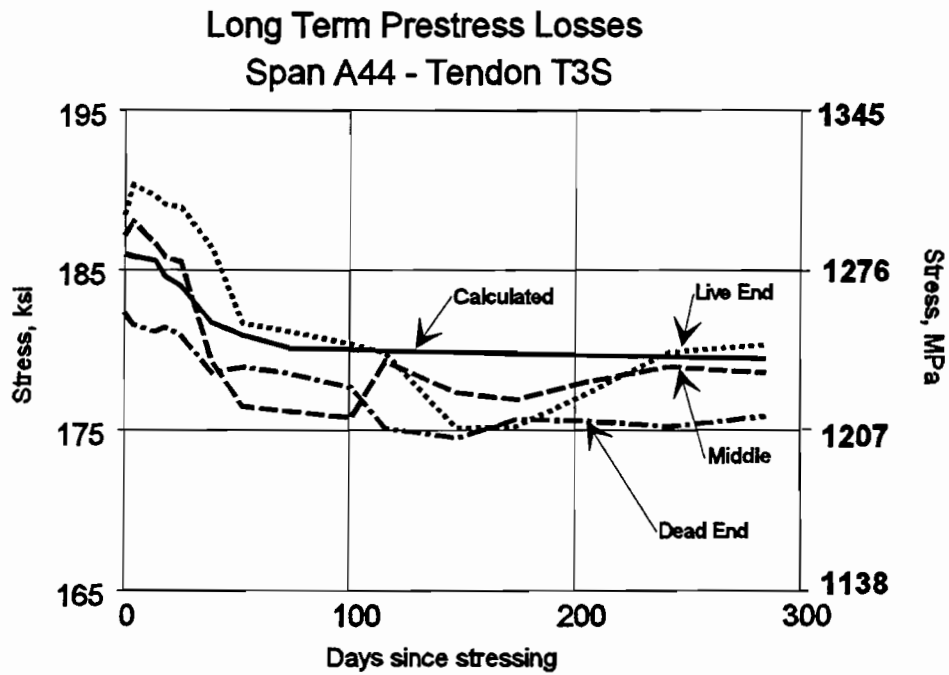


Values adjusted for difference in coefficient of thermal expansion of concrete and steel.

Figure 4.30 Adjusted tendon stresses for Tendons T2N and T2S in span A44.



Values adjusted for difference in coefficient of thermal expansion of concrete and steel.



Values adjusted for difference in coefficient of thermal expansion of concrete and steel.

Figure 4.31 Adjusted average tendon stresses for Tendons T3N and T3S in Span A44.

Figures 4.32 and 4.33 show the calculated and adjusted measured values of the Span C11 tendon stresses. Span C11 had more instrumentation difficulties than Spans A43 and A44. As described in Chapter 3, Span C11 was erected in February when the temperatures were quite low. This hindered efforts to use the two part epoxy glue on the tendon ER gages, because the epoxy requires a temperature of at least 70°F (21°C) for 6 hours to cure properly. As a result of low temperatures, the first attempt to adhere gages with the two part epoxy was futile on a majority of the tendons. Because of time constraints, a fast setting super glue was used in place of the two part epoxy to replace the gages which had not held.

The super glue is not as durable as the two part epoxy. As a result, many of the gages experienced a gradual loss of bond over time. At the end of one year only 6 of the original 24 gages in Span C11 are still providing reasonable readings.

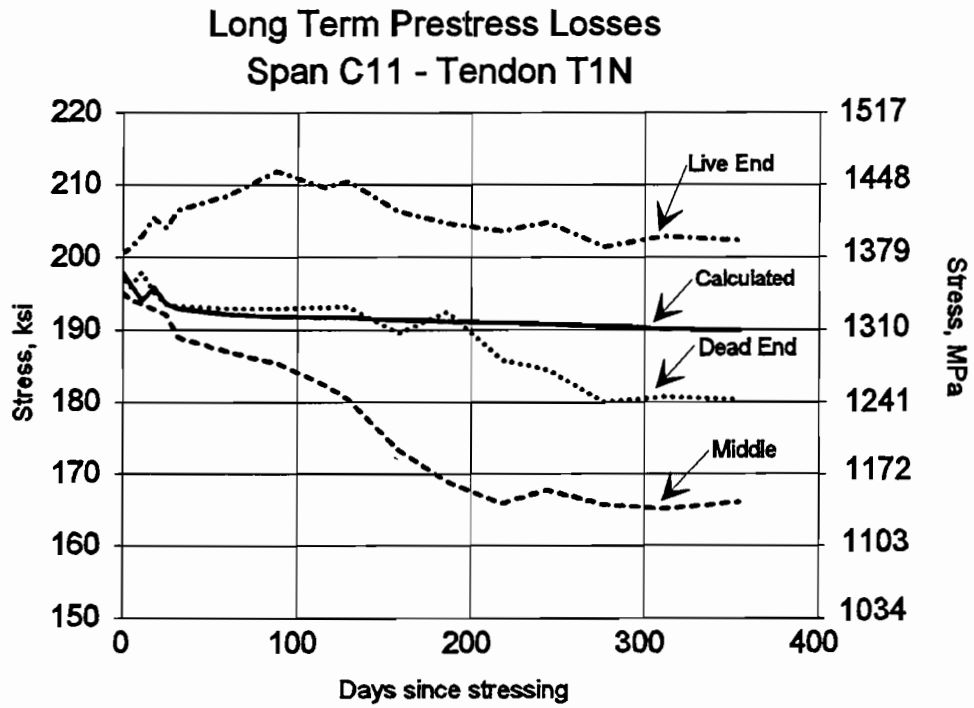
The measured tendon losses, therefore, are based almost exclusively on the Demec readings which, as mentioned previously, have some temperature fluctuations which cannot be compensated for precisely.

The average measured loss in Span C11 is 25.6 ksi (176.5 MPa) compared to a calculated value of 8.0 ksi (55.2 MPa). The measured value is assumed to be in error.

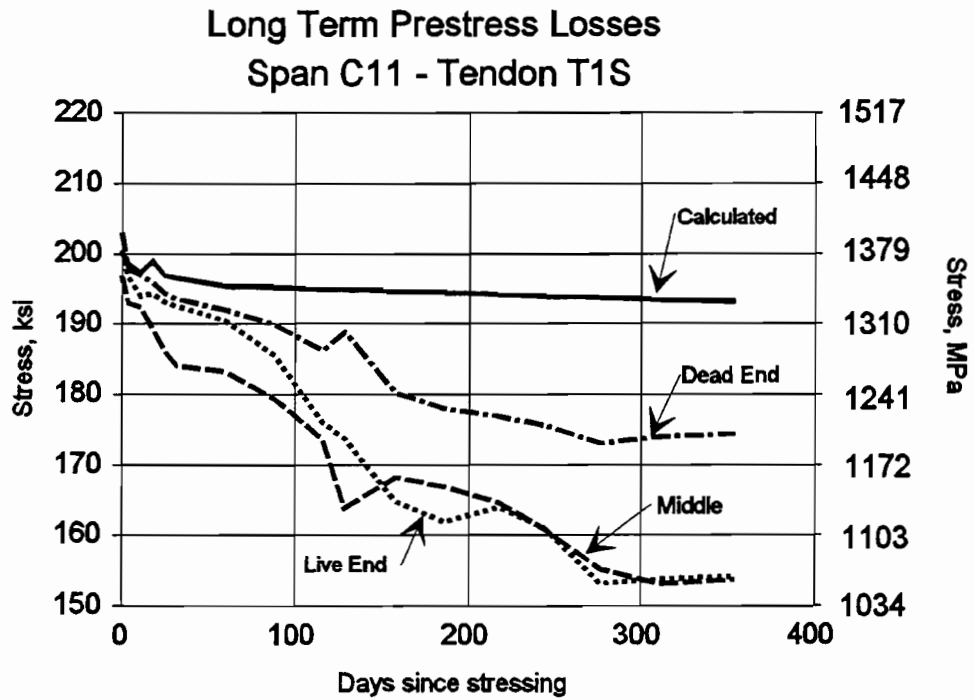
The time dependent step-wise, long term analysis recommended by the *AASHTO Guide Specification* and demonstrated by Ketchum predicts long term losses in external tendons quite well. The measured losses in this structure were small, less than 10% over the first year (except in Span C11 where the readings are not considered to be reliable), due to the age of the concrete at the time the prestressing was applied. All segments in the instrumented spans were over 270 days old at the time of erection. Shrinkage had virtually stopped and creep of old concrete is considerably less than that of younger concrete.

Possible causes of measured losses which were higher than predicted are:

1. A greater than expected effect of shear lag, particularly with respect to high stresses near post-tensioning anchors could have caused higher losses. If initial strains in the concrete were greater than expected, creep strains and hence losses would also be greater.
2. The shrinkage of epoxy, both in the sleeves and in the epoxy which adheres the ER gages to the strand could cause the readings to show greater than actual losses. This could be an additional source of error in the system.
3. Loss of bond between the ER gages and the post-tensioning tendons.



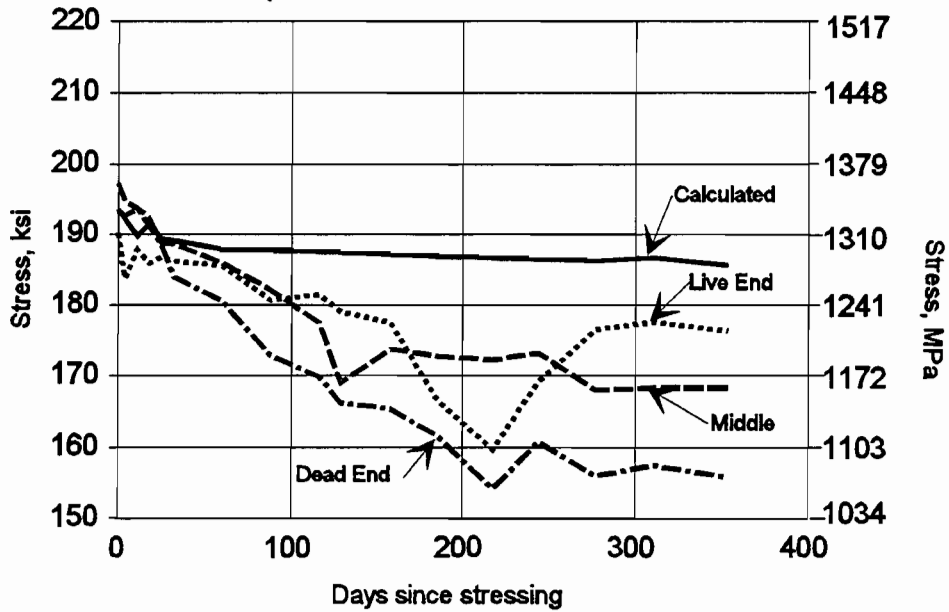
Values adjusted for difference in coefficient of thermal expansion of concrete and steel.



Values adjusted for difference in coefficient of thermal expansion of concrete and steel.

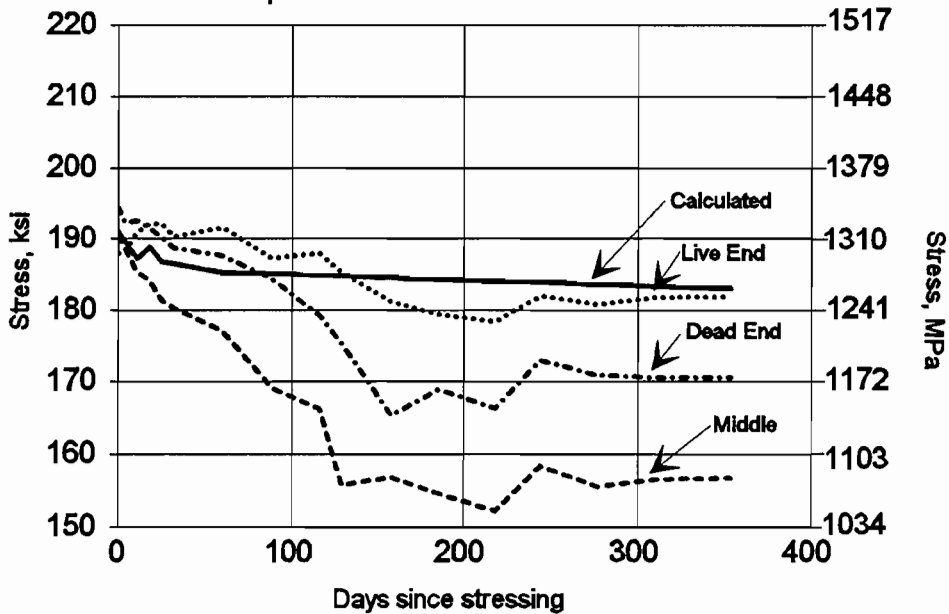
Figure 4.32 Adjusted average tendon stresses for Tendons T1N and T1S in Span C11.

Long Term Prestress Losses Span C11 - Tendon T2N



Values adjusted for difference in coefficient of thermal expansion of concrete and steel.

Long Term Prestress Losses Span C11 - Tendon T2S



Values adjusted for difference in coefficient of thermal expansion of concrete and steel.

Figure 4.33 Adjusted average tendon stresses for Tendons T2N and T2S in Span C11.

A comparison of measured long term losses with other prediction methods are shown in Table 4.11.

Table 4.11 Comparison of Measured and Calculated Prestress Losses.

Span	Meas. Loss,		Step-wise Calc. Loss,		Zia et. al., Calc Loss,		PCI Step-wise,		PCI Simplified,		AASHTO Standard,	
	ksi	MPa	ksi	MPa	ksi	MPa	ksi	MPa	ksi	MPa	ksi	MPa
C11	25.6	176.5	8.0	55.2	12.7	87.6	4.9	33.8	23.3	160.7	23.6	162.7
A43	7.7	53.1	6.9	47.6	16.4	113.1	6.5	44.8	24.4	168.2	28.5	196.5
A44	11.8	81.4	6.6	45.5	13.7	94.5	5.2	35.9	24.3	167.5	24.6	169.6

The PCI step-wise method predicts losses less than measured. This method is very much geared toward pretensioned concrete members. Some of the tables in the publication do not cover extreme age of concrete at time of loading and correspondingly high moduli of elasticity. The Zia et.al. method predicts higher than measured losses, but both this method and the PCI step-wise approach would be accurate enough for initial estimates of losses. The PCI simplified method and the *AASHTO Standard Specification* method are geared toward pretensioned beams in which the application of the prestress force is done at a very early age, and the beams experience high prestress losses. These methods are inadequate for segmental structures which are usually quite mature at time of stressing.

One other lesson learned from this study is that tendons experience seasonal fluctuations in tendon stress. The tendons lose stress in the summer and gain stress in the winter. The magnitude of this variation depends on the difference in seasonal temperatures, the differences between the tendon temperature and the concrete temperature, and the differences in coefficients of thermal expansion, but can be assumed to be approximately 5-7 ksi (34.5 - 48.3 MPa).

4.5 Recommendations

The following are recommendations for changes in the current *AASHTO Guide Specification*. Changes are indicated by italicized print.

4.5.1 Losses through stressing hardware. Mention should be made in the code that some loss will occur through stressing hardware and it will depend on the anchorage device, the ram, and the method of calibration. The commentary would state that a loss of 3% should be assumed unless evidence is available to warrant a different value. The specification and commentary revisions should be as follows:

Design Specification Section 10.5 - Stressing Hardware - *A loss in tendon force occurs through the stressing hardware and anchorage device during stressing, prior to seating. This loss shall be considered in design and is additive to seating losses.*

Design Commentary Section 10.5 - Stressing Hardware - *The loss across stressing hardware and anchorage devices has been measured from 2 to 6%^[61] of the force indicated by the ram pressure times the calibrated ram area. The loss varies depending on the ram and the anchor. An initial design value of 3% is recommended.*

4.5.2 Friction losses. It must be recognized that friction across deviators is higher than through more gradually curved internal ducts and that friction values are affected by inadvertent duct misalignment. Designs should be performed assuming that the theoretical angle change at each deviator will be inadvertently increased by 0.04 radians due to duct placement tolerances. A zero wobble coefficient should be assumed for external tendons. To account for the smaller friction values across the deviators during the seating operations, the misalignment factor need not be used when calculating seating losses.

The following changes are recommended for the *AASHTO Guide Specification*:

Changes to Design Specifications Section 10.2

The following change is suggested for Section 10.2:

10.2 Duct Friction and Wobble

The loss of prestress force due to friction and wobble within an internal tendon duct shall be calculated using the equation:

$$T_o = T_x e^{(\mu\alpha + k\ell)}$$

For tendons in webs of curved bridges, or in inclined webs of straight bridges, α shall be calculated as the total vector accumulation of the horizontal and vertical angle changes, and ℓ shall be the total tendon length. Friction and wobble coefficients may be estimated using the values in Table 10-2. However, these values do not consider misalignment of *internal* ducts at joints. Where large discrepancies occur between measured and calculated tendon elongations, in place friction tests are required.

The loss of prestress force in an external tendon due to friction across a single deviator pipe shall be calculated using the equation:

$$T_o = T_x e^{\mu(\alpha + 0.04)}$$

The inadvertent angle change of 0.04 radians per deviator may vary depending on job specific tolerances on deviator pipe placement. The inadvertent angle change need not be considered for calculation of losses due to wedge seating movement.

Changes to Design Commentary Section 10.2

The following wording should be added to Section 10.2 of the Design Commentary:

Field tests conducted on the external tendons of a segmental viaduct in San Antonio, Texas, indicate that the loss of prestress at deviators is higher than the usual friction coefficient ($\mu = 0.25$) would estimate. This additional loss is due in part to the tolerances allowed in the placement of the deviator pipes. Small misalignments of the pipes can result in significantly increased angle changes of the tendons at the deviation points. The inadvertent angle change of 0.04 radians added to the theoretical angle change accounts for this effect. The 0.04 value is to be added to the theoretical value at each deviator. The value may vary with tolerances on pipe placement.

The tests also indicated that the friction across the deviators was higher during the stressing operations than during the seating operations.

4.5.3 Elastic Shortening Losses. No changes to the elastic shortening recommendations in the specification, however, the following is recommended for the commentary:

Changes to Design Commentary Section 10.1

The following should be added to the Design Commentary Section 10.1:

Elastic shortening losses may be calculated in accordance with methods presented in previously published guidelines.^[51,77] Elastic shortening losses for external tendons may be calculated in the same manner as for internal tendons.

4.5.4 Time Dependent Losses. Current methods, requiring a step-wise time dependent analysis which takes into account all construction procedures, are acceptable. Creep and shrinkage models proposed by ACI-209 and CEB-FIP Model Code 1990 Revised Summation and Product are all acceptable. The CEB-FIP Model Code 1978 may overestimate creep losses.

Approximate methods by Zia et. al. and by the PCI Committee on Prestress Losses are both acceptable for initial designs although not specifically geared toward post-tensioned concrete which is mature when prestress is applied.

The only change recommended for the *AASHTO Guide Specification* is that reference 18 in Section 10.1, which is the *CEB Model Code 78*¹⁶ should be updated to the *CEB Model Code 90*.¹⁷

4.6 Summary

Except for friction losses and losses through stressing hardware, current design criteria for prestress losses predicts losses close to measured values. The loss of tendon stress due to friction through deviators should be increased by adding an inadvertent angle change to the theoretical angle change at each deviator, and the existence of losses through stressing hardware should be recognized and allowed for in design. With these two changes, the prediction of prestress losses in external tendons should more accurately reflect reality.

CHAPTER 5

LONGITUDINAL STRESS DISTRIBUTIONS ACROSS FLANGES

5.1 Introduction

Unlike modern reinforced concrete design which has moved away from allowable stress design to focus principally on ultimate strength design with relatively modest serviceability checks, prestressed concrete design involves large amounts of both allowable stress and ultimate strength design. In order to avoid cracking at service load levels, tension stresses must be checked, and in order to prevent compression failures with creep over time, compression stresses must be checked. Such allowable stress checks frequently govern the quantity of prestress required. The *AASHTO Guide Specification for the Design and Construction of Segmental Concrete Bridges*¹ (to be referred to for the remainder of the chapter as the *AASHTO Guide Specification*) presents allowable compression and tension stresses for segmental bridges, depending on the type of joint and the presence or absence of bonded reinforcing across the joints. To satisfy these requirements, designers perform service load calculations to determine the maximum tensile and compressive stresses. Normal procedure is to use simple beam theory, which assumes that plane sections remain plane, along with the full cross-sectional properties of the box girder. These assumptions may not be valid near supports, near concentrated loads, and for box girders with slender wing spans, widely spaced webs, and small span length to deck width ratios.

This chapter addresses the problems of shear lag and transverse diffusion of post-tensioning forces on the distribution of longitudinal stresses across the flange of box girders. Three spans were instrumented to measure concrete strains. The measured strains are presented and compared with current design and analysis tools.

5.1.1 Background Information.

5.1.1.1 Shear Lag. In a box girder subjected to bending moments, a large shear is transmitted from the vertical webs into the horizontal flanges. This causes in-plane shear deformations in the flanges. The resulting longitudinal deformations of the flanges near the wingtips and near the longitudinal center line of the top and bottom slabs lag behind the deformation of the flanges next to the webs, (see Figure 5.1). This results in a non-linear distribution of stresses across the flanges, where simple beam theory predicts uniform stress.³⁹ This phenomenon is known as shear lag, and it can have significant effects on the maximum stresses in a segmental box-girder bridge.

5.1.1.2 Transverse Diffusion of Post-Tensioning Forces. The transverse diffusion of post-tensioning forces concerns the transmission of the highly concentrated normal forces applied by the post-tensioning anchors, into the cross-section. Simple beam theory would assume a uniform distribution of the post-tensioning force immediately ahead of the anchors. In reality, it

takes a distance along the length of the bridge for the post-tensioning force to completely diffuse across the section (see Figure 5.2).

5.1.2 Current AASHTO Approach. The approach currently recommended in the *AASHTO Guide Specification* is considered by many to be excessively complex and as a result is often ignored. The *AASHTO Guide Specification* (Section 4.3) advocates the use of an effective flange width which may be determined by elastic analysis, by provisions of the *1983 Ontario Bridge Code*,⁵⁰ or by provisions in the *AASHTO Guide Specification*, which were adopted from Germany's *Bridge Specification* (DIN 1075).²⁰

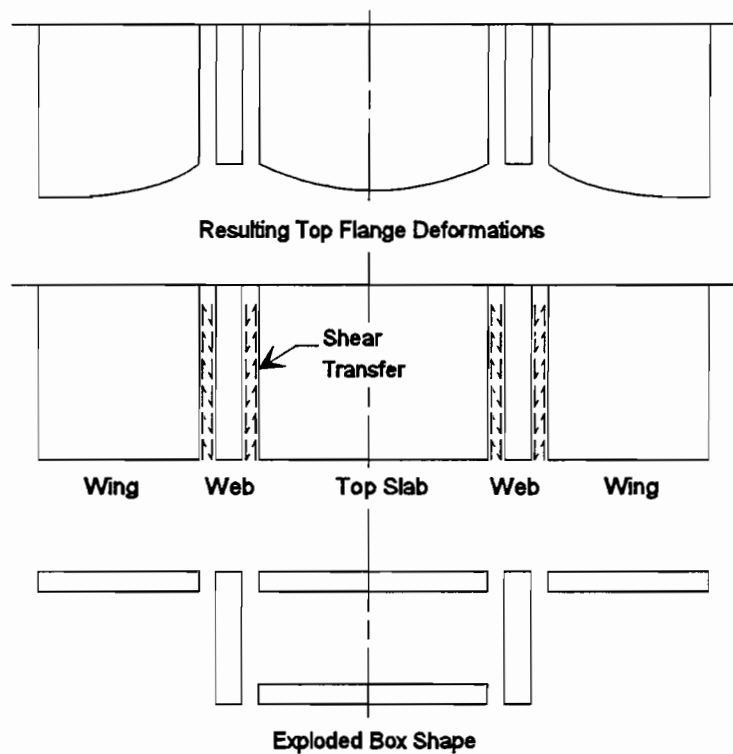


Figure 5.1 Shear lag and resulting deformations.

The effective flange width is defined as that width which would resist a longitudinal force equal to the actual force in the flange, if the longitudinal stresses across the flange were constant and equal to the actual maximum stress,⁶⁶ (see Figure 5.3).

The procedure in the *AASHTO Guide Specification* requires that first an effective span length be determined. For a simple span, the effective span length (l_e) is taken equal to the actual span length (l). For end spans in continuous girders it is taken as $0.8l$ and for interior spans it is taken as $0.6l$. Once the effective span length is known, each actual flange width (b_i) may be determined as shown in Figure 5.4. Then, for each flange, the ratio of b_i/l_e is calculated and a graph (see Figure 5.5) is used to determine the effective flange widths to be used near supports (b_s) and near mid-span (b_f). Finally, the flange widths for other locations along the span may be determined using a linear variation from b_s to b_f along a length equal to b at exterior supports, or $0.1l$ at interior supports (see Figure 5.6).

For the analysis of a segmental bridge, where stresses at every joint should be checked, the determination of cross-sectional properties can be quite involved.

The *AASHTO Guide Specification* also provides information on determining cross-sectional properties to be used in calculating normal stresses. Figure 5.7 illustrates the recommended 30° angle of diffusion of post-tensioning forces.

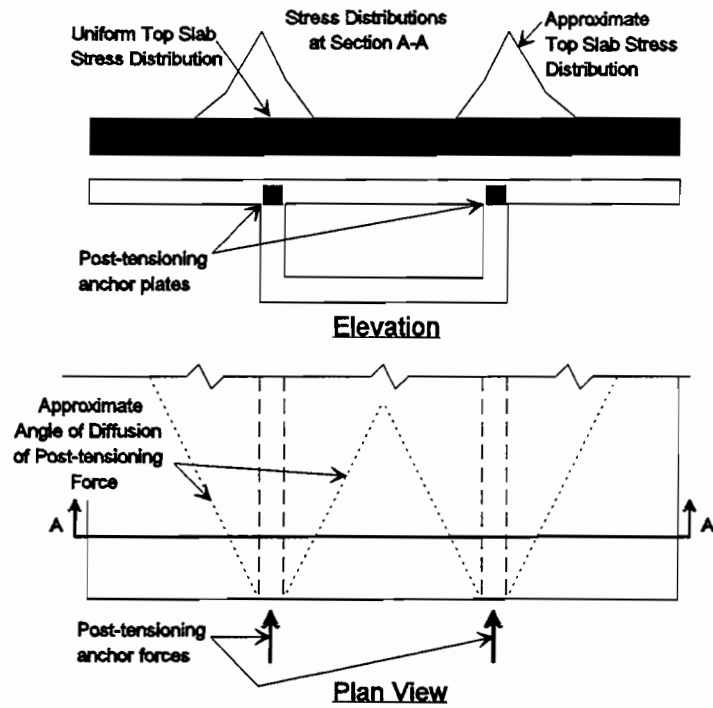


Figure 5.2 Distribution of normal stresses caused by diffusion of concentrated post-tensioning anchor forces.

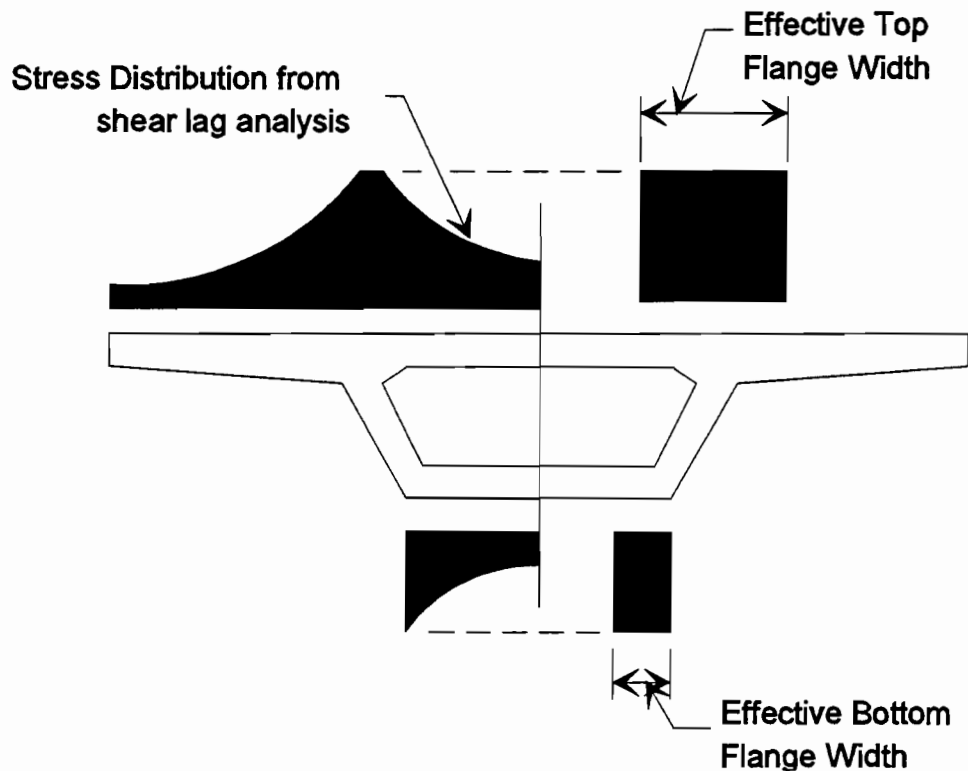


Figure 5.3 Definition of effective flange width.

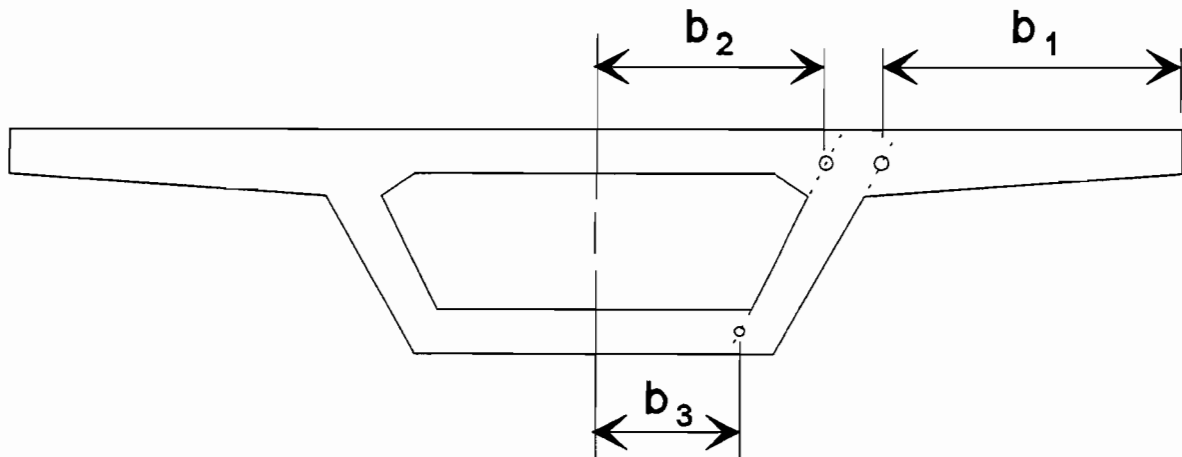
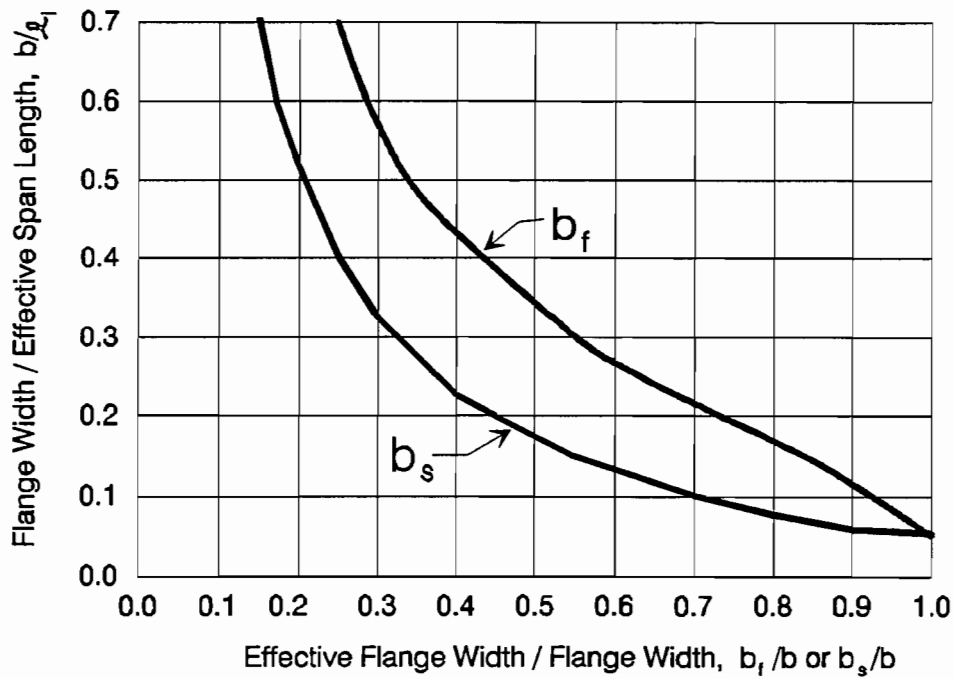


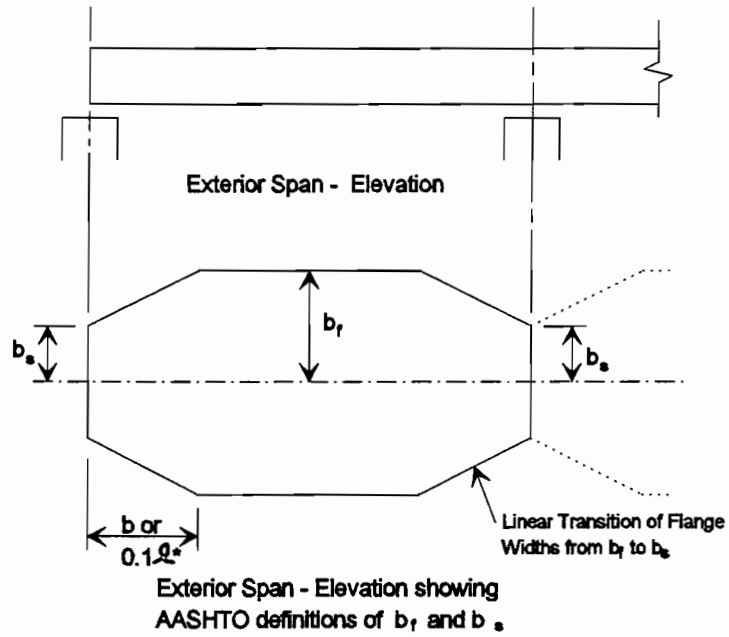
Figure 5.4 Flange widths as defined by the *AASSTO Guide Specifications*.



For $b/l_1 \geq 0.7$:
 $b_f = 0.173l_1$
 $b_s = 0.104l_1$

Where b_f = effective flange width near mid-span
 b_s = effective flange width near support

Figure 5.5 AASHTO effective flange width graph.



* b for exterior supports (b not to exceed 0.25ℓ)
 0.1ℓ for interior supports

Figure 5.6 Effective flange widths over piers and at mid-span, and the transition area.

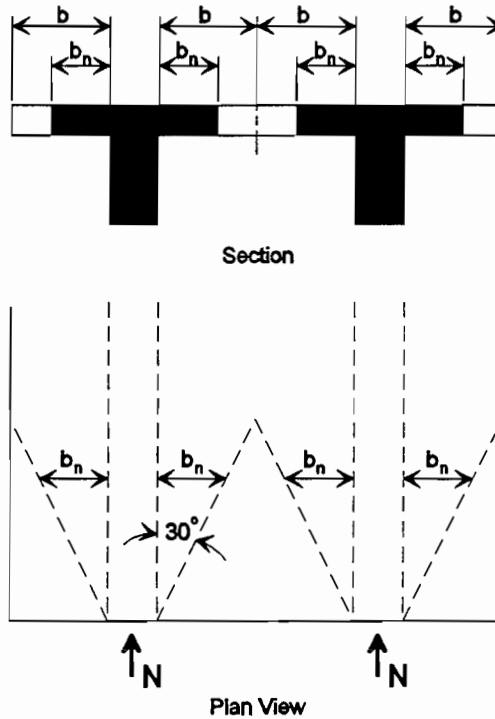


Figure 5.7 AASHTO effective flange widths for normal forces.

In order for a designer to check allowable stresses, one set of cross-sectional properties must be determined for bending stresses and another set for normal stresses. These properties are constantly changing along much of the length of the span. Designers refer to this as excessively complicated.

The *AASHTO Guide Specification* also addresses the shear lag and transverse diffusion problems indirectly, with guidelines for box shapes. In *AASHTO Guide Specification* Section 21.1 it is recommended that the ratio of the depth of the box to the width of the flanges exceed 1/6. If the ratio is less than 1/6 a more rigorous analysis is recommended.

5.2 Literature Review

5.2.1 Ontario Bridge Code. An alternate approach acceptable under the *AASHTO Guide Specification* for the determination of effective flange widths is in the *1983 Ontario Bridge Code*.⁵⁰ Section 3-10.2 presents a simple equation for the ratio of the effective to the actual flange width:

$$\frac{B_e}{B} - 1 - \left(1 - \frac{L_e}{15B}\right)^3 < 1.0$$

where:

B_e = Effective Flange Width,
 B = Actual Flange Width,
 L_e = Effective Span Length.

The effective width is dependent on the ratio of effective span length to actual flange width. The effective width varies depending on whether the portion of the bridge in question is in the positive or negative moment region of a continuous girder, or in a simple span, since the effective span length varies for each case (see Figure 5.8). A step-wise change of effective flange width from one region to the next is assumed.

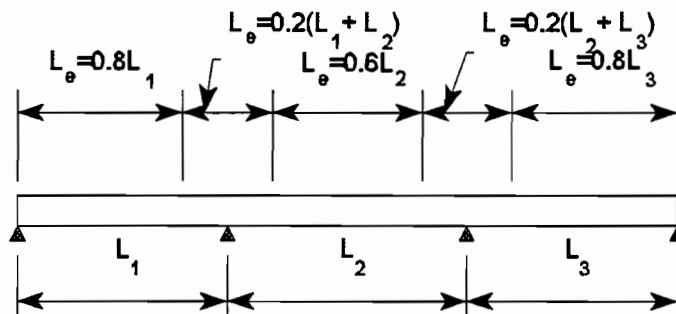


Figure 5.8 Effective span lengths for *Ontario Bridge Code* effective flange width calculations.

This approach is somewhat less involved than the *AASHTO Guide Specification* method, but still involves a great deal of additional work. Normal force diffusion is not addressed by the *Ontario Code*.

5.2.2 Song and Scordelis.⁶⁷ Song and Scordelis provide a simplified solution for the shear lag analysis of simple and continuous beams. Formulas for determining effective flange widths which are suitable for hand calculations are presented along with a computer program (SHLAG).

The computer program is easy to use, requiring a simple input file which includes cross-sectional geometry information, span lengths, and loading patterns. It is somewhat limited in that it assumes vertical web walls, uniform slab thicknesses, and has no provisions for the presence of end diaphragms.

The formulas which are presented were empirically derived to match the output of the SHLAG program. Song and Scordelis also provide some sample parametric studies.

5.2.3 The PTI Precast Segmental Box Girder Bridge Manual. The *PTI Manual*⁶⁸ includes a brief discussion of shear lag effects in segmental box girders. A study of four single cell box girder bridges with varying depths and span lengths was performed using a computer program, MUPDI. MUPDI⁶³ is based on the folded plate method using elastic theory. The four trial bridges were each loaded in four different ways (dead load, post-tensioning load, live load plus impact for maximum negative moment, and live load plus impact for maximum positive moment). The following conclusions were made based on this study:

- 1) An increase in span, for a given flange width, decreases the stress ratio (stress ratio is the stress calculated using shear lag theory over the stress calculated with simple beam theory). It is generally recognized that shear lag is directly proportional to the span length to plate width ratio.
- 2) Stress ratios are essentially independent of variation in depth for a given span (l/d ratios between 20 and 30).
- 3) The stress ratios are highest at interior supports and drop off rapidly a few feet away. Stress ratios are a function of the magnitude of shear change, which is greatest at interior supports.

The *PTI Manual* states that the shear lag effect from the prestressing counter-acts the shear lag due to dead load and live load. Also they emphasize that the length of the bridge in which significant shear lag effects were found to occur is quite small. These two factors, in conjunction with the specification requirement of zero tensile stress across joints, provide justification for disregarding shear lag in most practical design projects. If, however, the span is short (less than 150 feet (45.7 m)) and the wing span of a single cell box girder is wide (greater

than 40 feet (12.2 m)), a more rigorous analysis should be performed, or some additional residual compressive stress across joints should be required.

5.2.4 DIN 1075.²⁰ The approach for determining effective flange widths for bending which is presented in *DIN 1075* is precisely the same as that in the *AASHTO Guide Specification*.¹ The approach to the transverse diffusion of post-tensioning forces is almost identical, except the diffusion angle is 26.5° , instead of 30° .

5.3 Surveillance Program

5.3.1 Concrete Strain Readings. Three spans of the San Antonio "Y" Project were instrumented with concrete surface mechanical strain gage stations to study the problems of shear lag and transverse diffusion of post-tensioning forces. Figure 5.9 illustrates the Demec point layouts for Type I segments and Figure 5.10 shows the Type III layout. The five locations in each span where the points were installed is also shown.

The gages in each span were read at the conclusion of temporary post-tensioning and again immediately prior to stressing the permanent post-tensioning. The readings taken immediately prior to stressing are used as the zero point for subsequent readings, and the readings after temporary post-tensioning are used as a check of the zero readings. Approximately three days elapsed between the conclusion of temporary post-tensioning and the beginning of permanent post-tensioning. The gages were read after the bottom slab and web tendons were stressed, after all external tendons were stressed, and finally after the erection trusses were lowered. Readings were then taken on a regular basis over the following months.

No temperature adjustments of the concrete strain readings were needed or made. Span C11 was stressed over the course of 2 hours on a rainy day in February, when there was no significant change in temperature. Similarly, Spans A43 and A44 were stressed over short periods of time (around 2 hours) with no significant temperature changes.

5.3.2 Additional Measurements. Tendon forces were measured as described in Chapters 3 and 4. The actual measured tendon forces are used in the analyses in this chapter. Deflections were also read, using the taut wire method described in Chapter 3.

Figure 5.9 Type I Demec point layout.

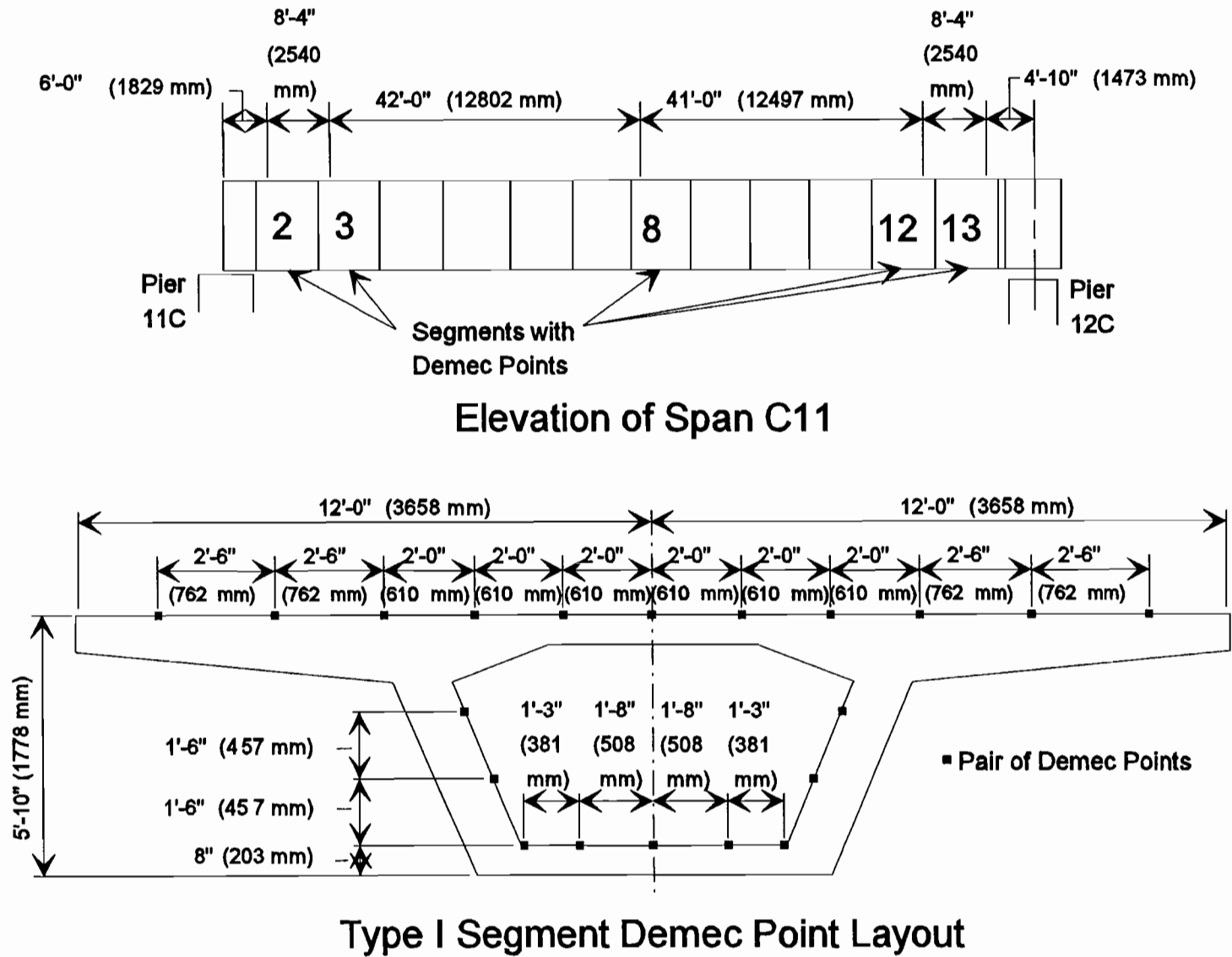
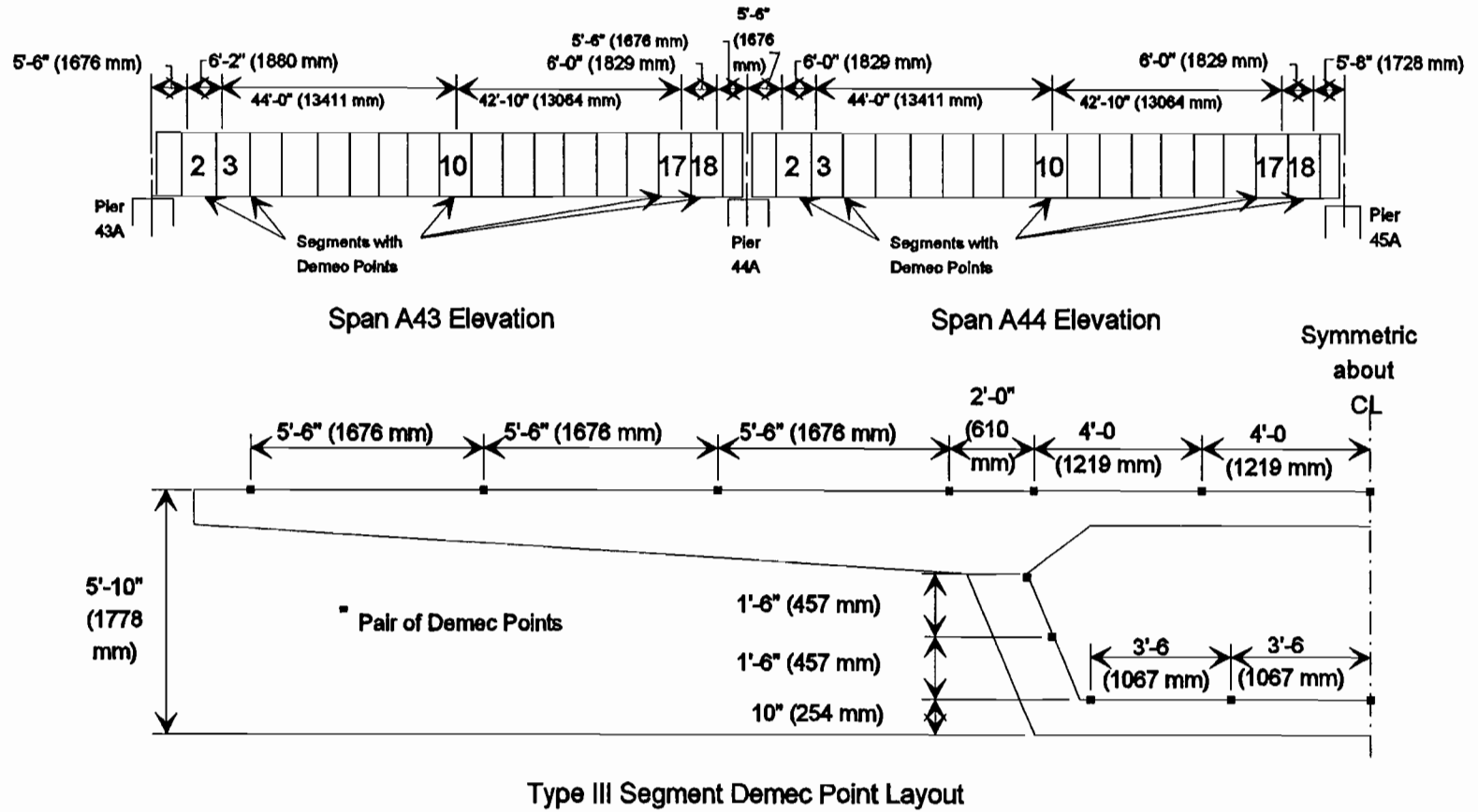


Figure 5.10 Type III Segment Demec point layout.



5.3.3 Material Tests. A series of modulus of elasticity tests were performed for each instrumented span. Pairs of cylinders from several segments in each span were tested. The results are listed in Table 5.1. These moduli were used in translating concrete strains to stresses for comparison with analytical methods. In the following discussion reference will be made to "measured stresses" meaning more precisely "stresses determined from measured strains".

Table 5.1 Measured Concrete Moduli

Span	Modulus of Elasticity
C11	5240 ksi (36130 MPa)
A43 and A44	5440 ksi (37509 MPa)

5.4 Presentation of Results

5.4.1 Methods of Analysis. In this section the stresses computed from the actual measured strains (termed "measured stresses") are compared with results from three analysis methods:

- 1) Simple beam theory using full cross-sectional properties,
- 2) SHLAG computer program,⁶⁷
- 3) *AASHTO Guide Specification Recommendations.*

5.4.1.1 Simple Beam Theory. The box shapes and full cross-sectional properties are shown in Figure 5.11, and the loads applied to each span are shown in Figure 5.12. These properties and loads were used in conjunction with a simple two dimensional elastic frame solver (FRAME2D²⁴) to calculate stresses and deformations in the bridge. The post-tensioning loads from the external tendons are based on actual measured tendon forces. The post-tensioning loads from the internal tendons are the plan values.

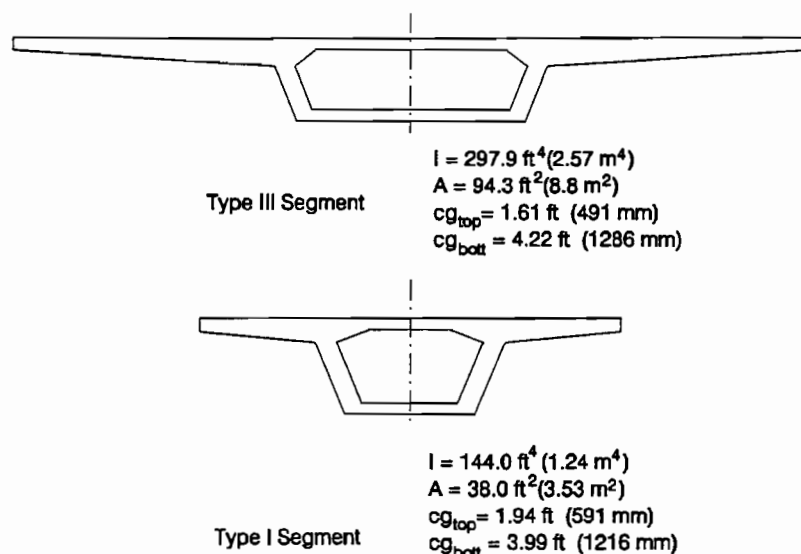
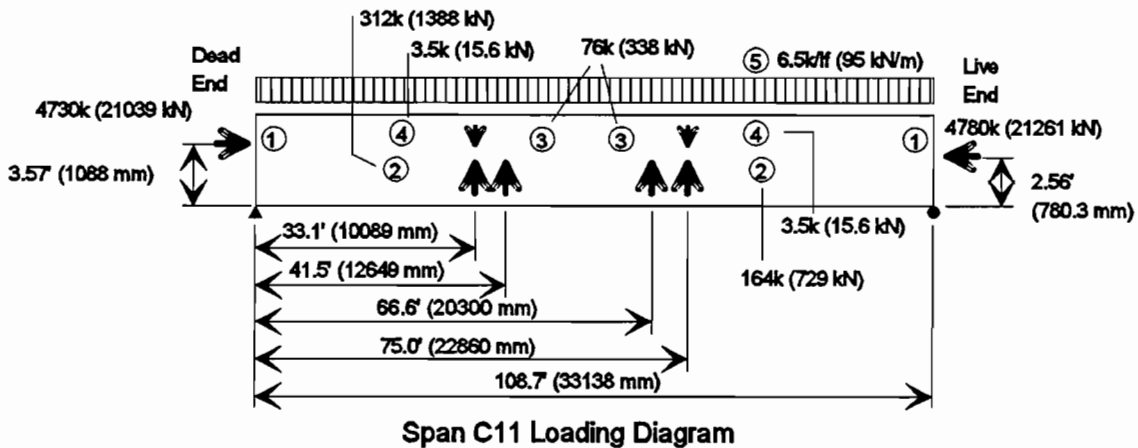
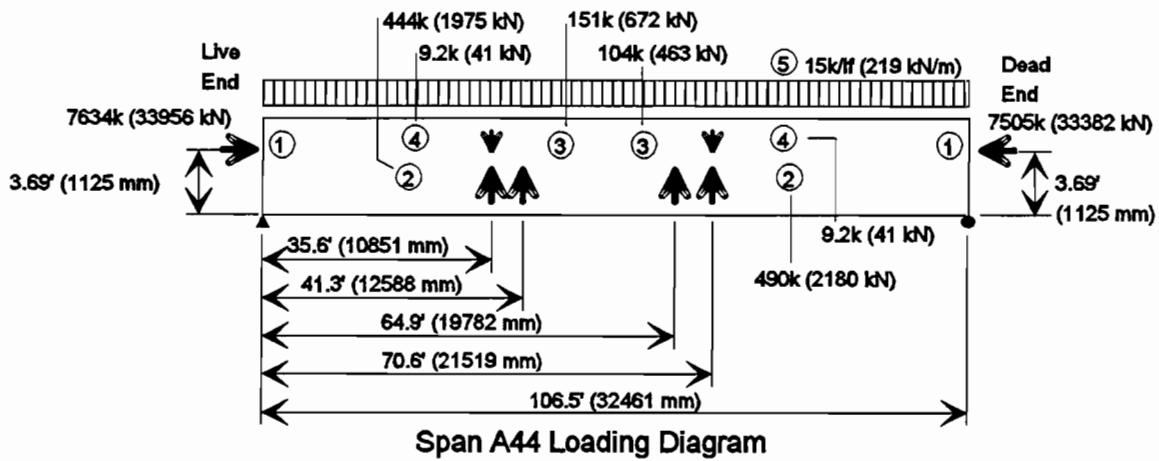
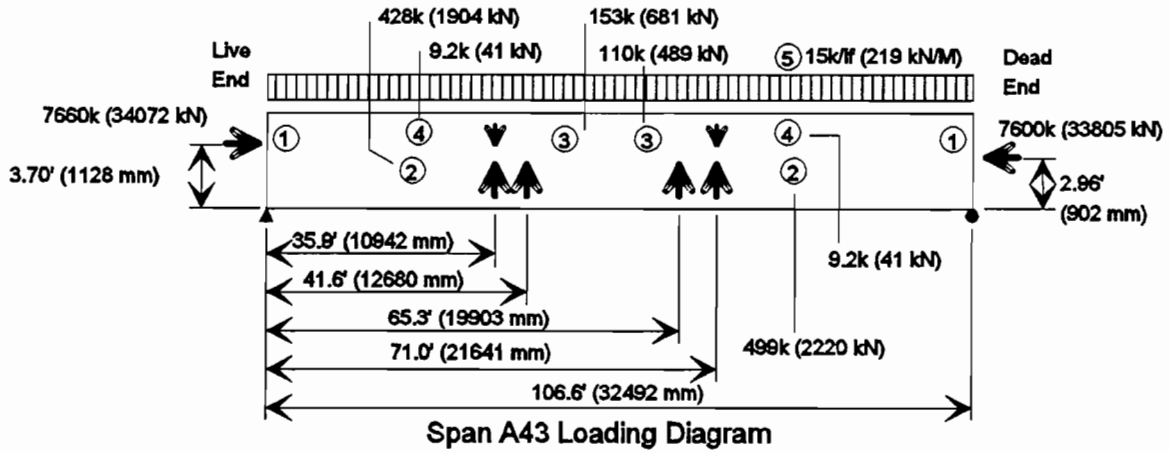


Figure 5.11 Segment properties.



- ① Post-Tensioning Anchor Forces
- ② External Tendon Deviation
- ③ Internal Tendon Deviation
- ④ Weight of Deviator
- ⑤ Uniform Dead Load

Figure 5.12 Loading diagrams.

5.4.1.2 SHLAG Computer Program. This program, as described in Section 5.2.2, requires simple input, and calculates the stress distributions across the flanges of box girders. Figure 5.13 shows the idealized box girders with vertical webs and prismatic members used with this program. Compared to actual cross-sectional properties, the moments of inertia are similar but the cross-sectional areas and location of the centers of gravity are somewhat different.

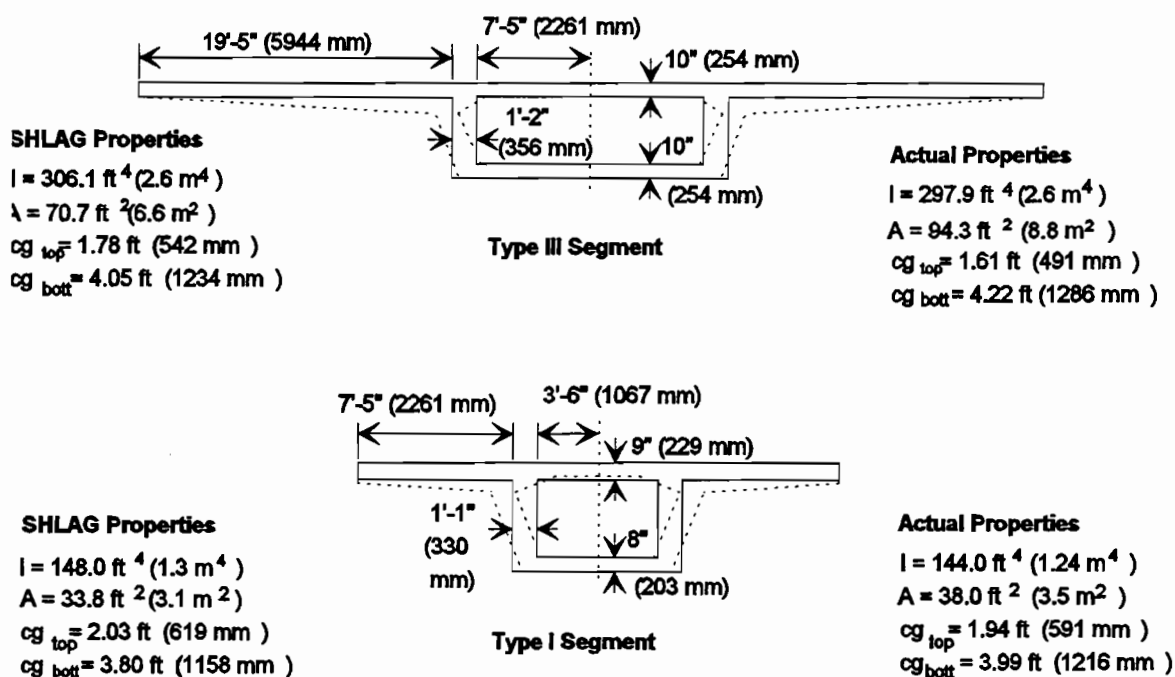
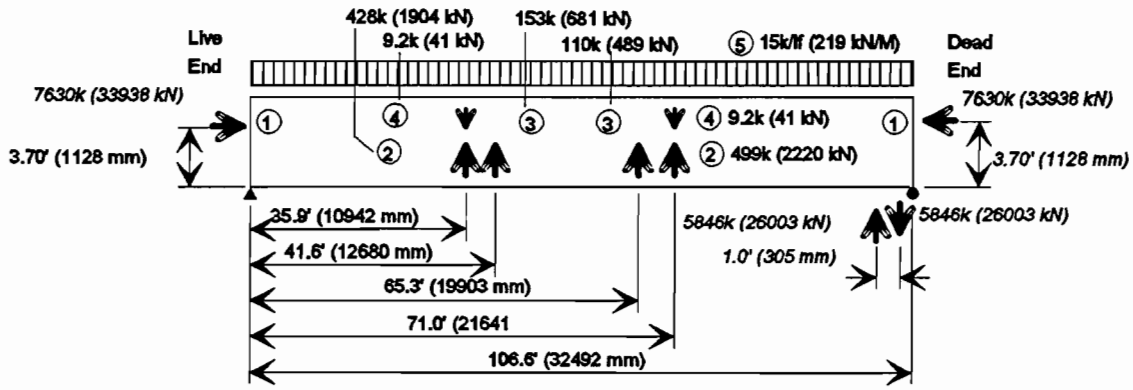


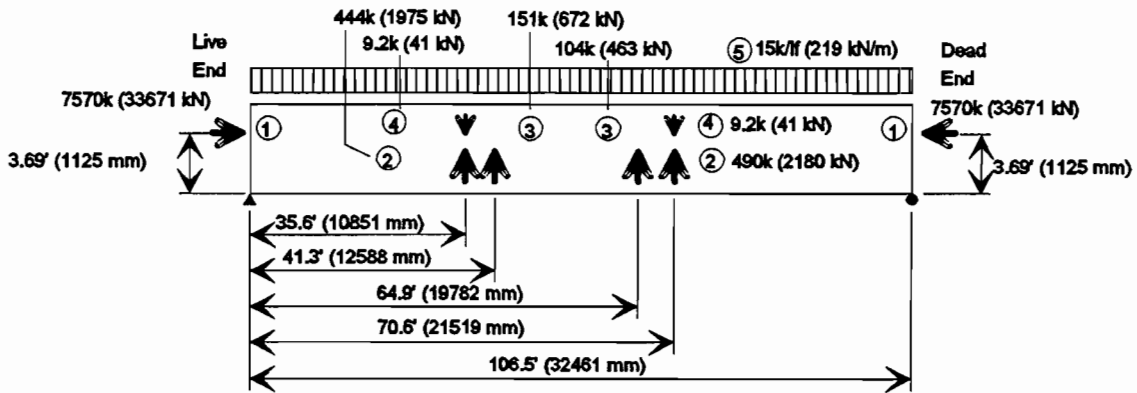
Figure 5.13 Segment properties for SHLAG program.

A slight manipulation of the loading pattern is required in order to be compatible with the limitations of the program's input parameters (see Figure 5.14). For the SHLAG input file the two normal forces must be the same distance from the center of gravity of the section. An additional couple is added to compensate for the actual location of the application of the post-tensioning forces.

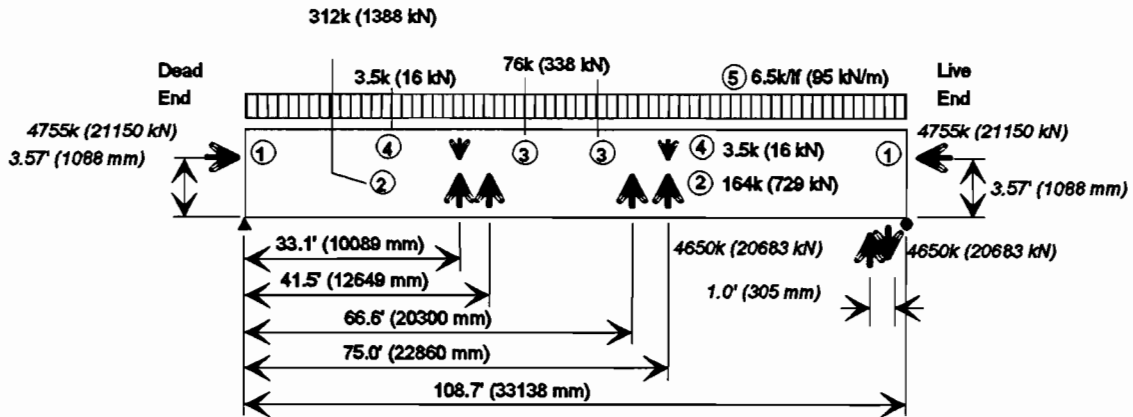
5.4.1.3 AASHTO Guide Specification. A Fortran computer program was written to assist in the calculation of effective flange widths and cross-sectional properties along the length of the span. The program was specially written for the Type I and Type III box shapes. The wing-tip width, span length, and span type (simple, end or exterior) are input, along with locations along the length of the bridge where cross-sectional properties are required. The output includes the full cross-sectional properties, the effective properties over supports, at mid-span, and at the requested locations. Properties provided are area, moment of inertia, center of gravity and effective flange widths.



Span A43 Loading Diagram for SHLAG



Span A44 Loading Diagram for SHLAG



Span C11 Loading Diagram for SHLAG

- ① Post-Tensioning Anchor Forces
- ② External Tendon Deviation
- ③ Internal Tendon Deviation
- ④ Weight of Deviator
- ⑤ Uniform Dead Load

Figure 5.14 Loading diagrams for use with SHLAG.

The cross-sectional properties for normal stress calculations were also calculated in accordance with the guidelines in the *AASHTO Guide Specification*. Figure 5.15 presents the cross-sectional properties used for bending at each investigated location.

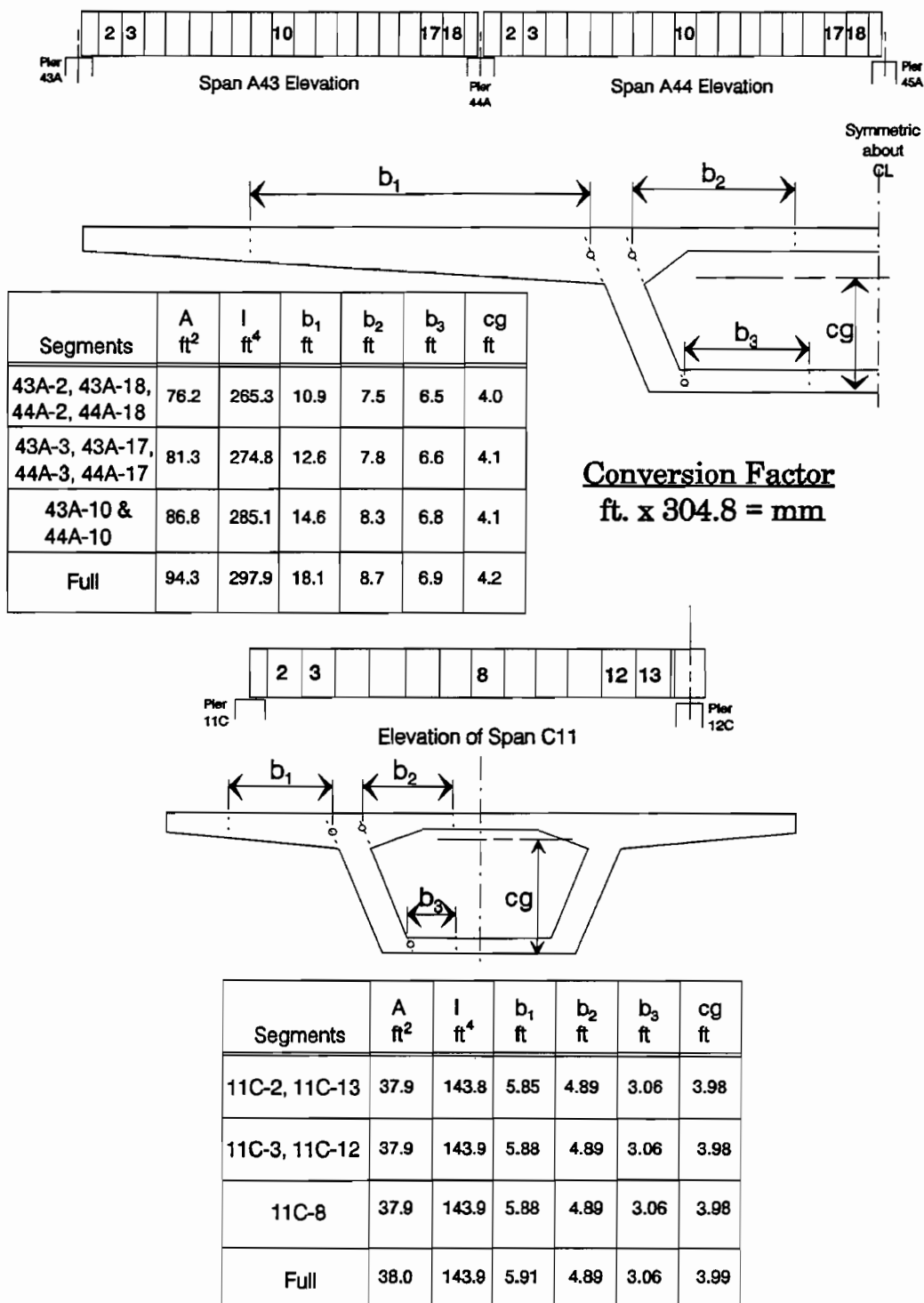


Figure 5.15 Effective segment properties per AASHTO.

5.4.2 Stresses from Measured Final Surface Strains Compared to Theory.

5.4.2.1 Top Slab Stress Distributions. Figures 5.16a, b, and c show the measured and calculated top slab stress distribution of segments 43A-2, 43A-18, 44A-2, 44A-18, 11C-2 and 11C-13. These six segments were immediately adjacent to the pier segments, and hence approximately five feet (1.5 m) from the post-tensioning anchorage devices.

The SHLAG stresses are somewhat lower than the measured peak stresses in four of these six cases, averaging 89% of the measured peak stress for the six segments. Also, the peaks are closer to the centerline of the segment in four of the six cases. This is probably due to the presence of the heavy end diaphragms, which stiffen the top slab between the web walls. The pattern of the measured stresses from the web walls outward to the wingtips is much more similar to the SHLAG results than to the other procedures.

The *AASHTO Guide Specification* method somewhat approximates the pattern of stress distribution, but the magnitude of the maximum predicted stress is quite low compared to the measured peak stresses, averaging 74% of the measured peak stress for these six segments. The stresses predicted by simple beam theory are considerably lower than the measured peak stresses, averaging only 29% of the measured peak for these six segments.

Figures 5.17a, b and c show measured and calculated stresses for segments 43A-3, 43A-17, 44A-3, 44A-17, 11C-3 and 11C-12. These measurement locations are six to eight feet (1.8 to 2.4 m) further removed from the pier segments than the previous locations and should be less influenced by local discontinuities from points of tendon anchorage.

Again the beam theory based on actual cross-sectional properties greatly underestimates peak stresses (averaging only 31% of the measured peak stresses), although the measured peaks are generally smaller than those in the previously described outer segments. Only Segment 11C-3 has a higher peak than its adjacent segment which is closer to the anchorage locations. The SHLAG result again is reasonably accurate in most wing areas, but often significantly underestimates the stresses in the top slab between the web walls. The AASHTO approach crudely represents the general distribution but severely underestimates the magnitude, averaging only 45% of the measured peak stress for these six segments.

Figures 5.18a and b show the distribution for segments 43A-10, 44A-10 and 11C-8, all of which are situated essentially at the center of their respective span. Once again the peak measured stresses are higher than all calculated peak values. In segments 43A-10 and 44A-10 the measurements show that the actual stresses are more uniform across the section, although marked peaks exist for the stubby section 11C-8. The peak values are best approximated by the SHLAG program although peak values are still substantially underestimated, particularly in segment 11C-8.

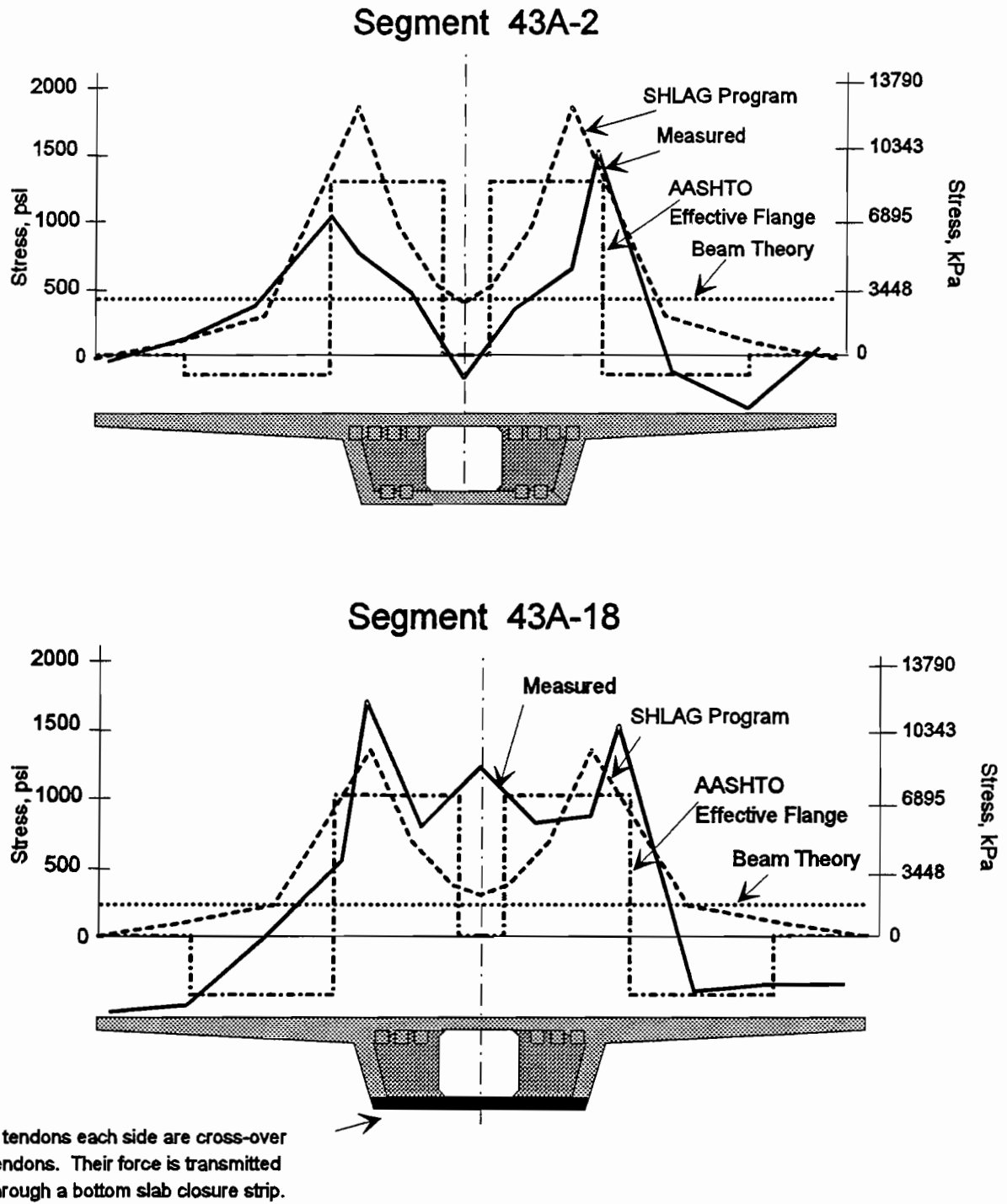


Figure 5.16a Top slab stress distributions, five feet (1524 mm) from anchors.

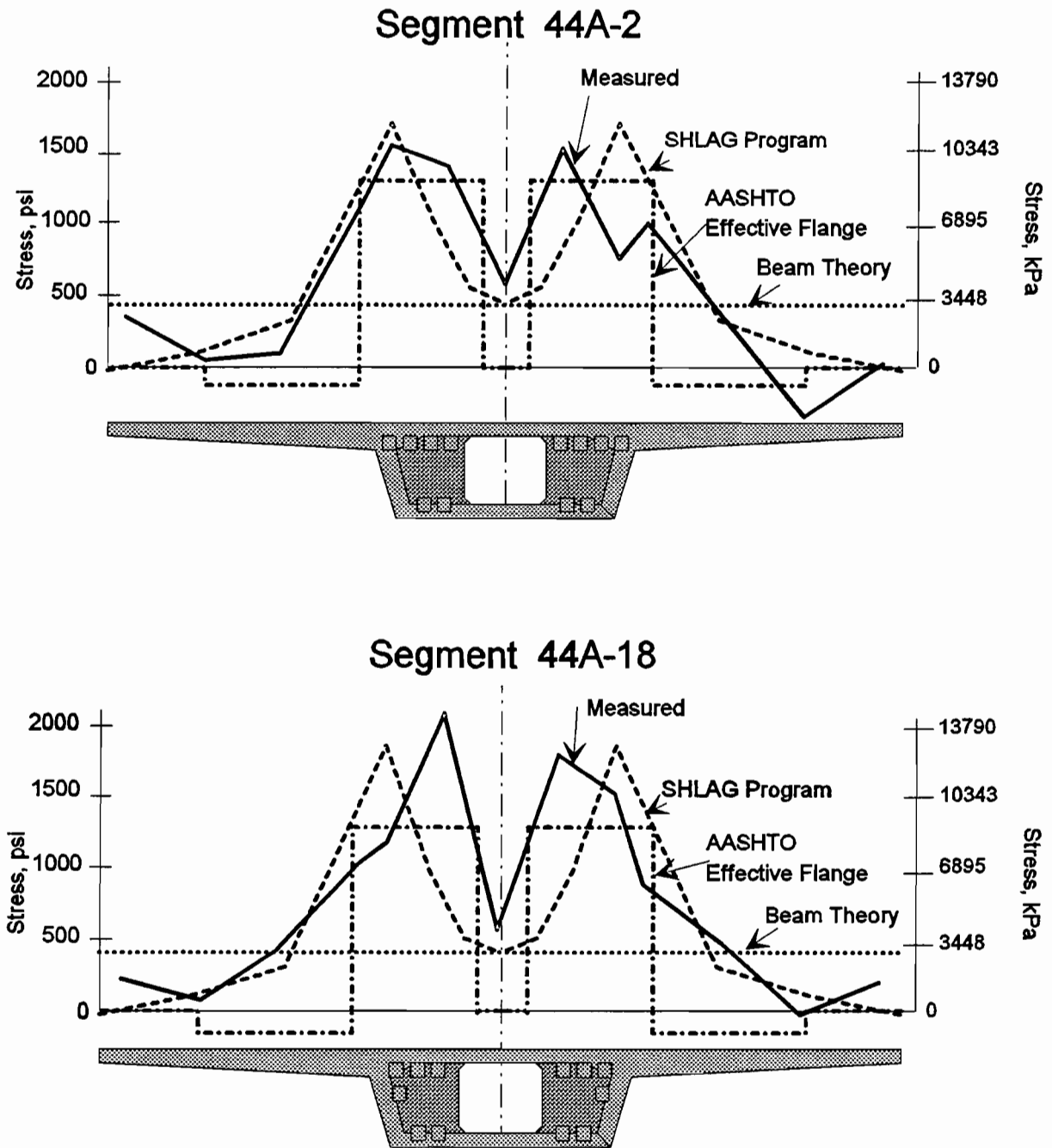


Figure 5.16b Top slab distributions, five feet (1524 mm) from anchors.

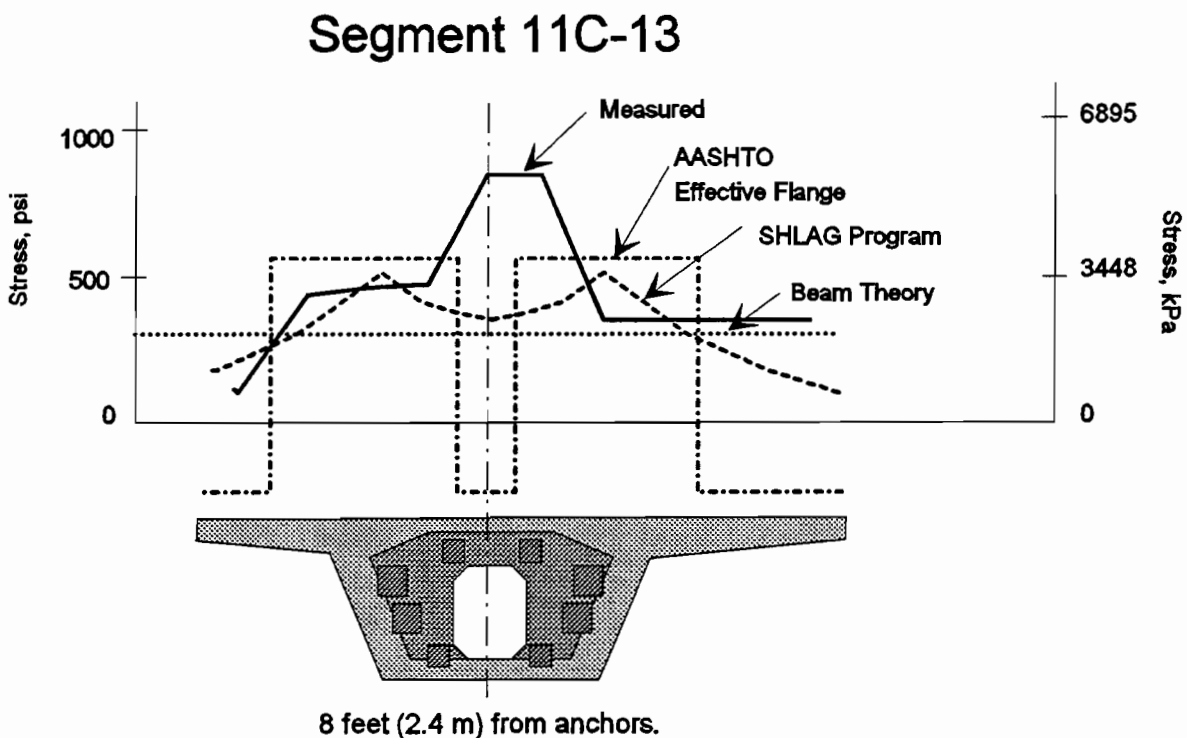
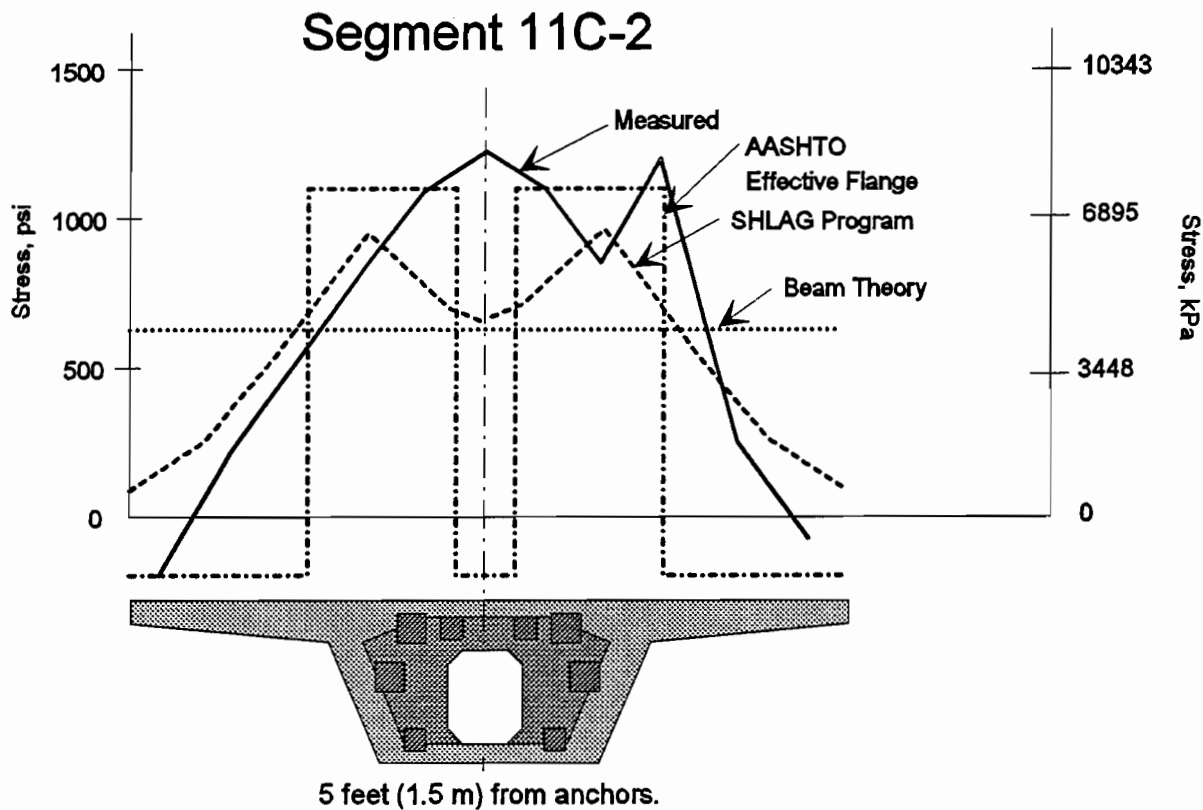


Figure 5.16c Top slab stress distributions, one segment from anchors.

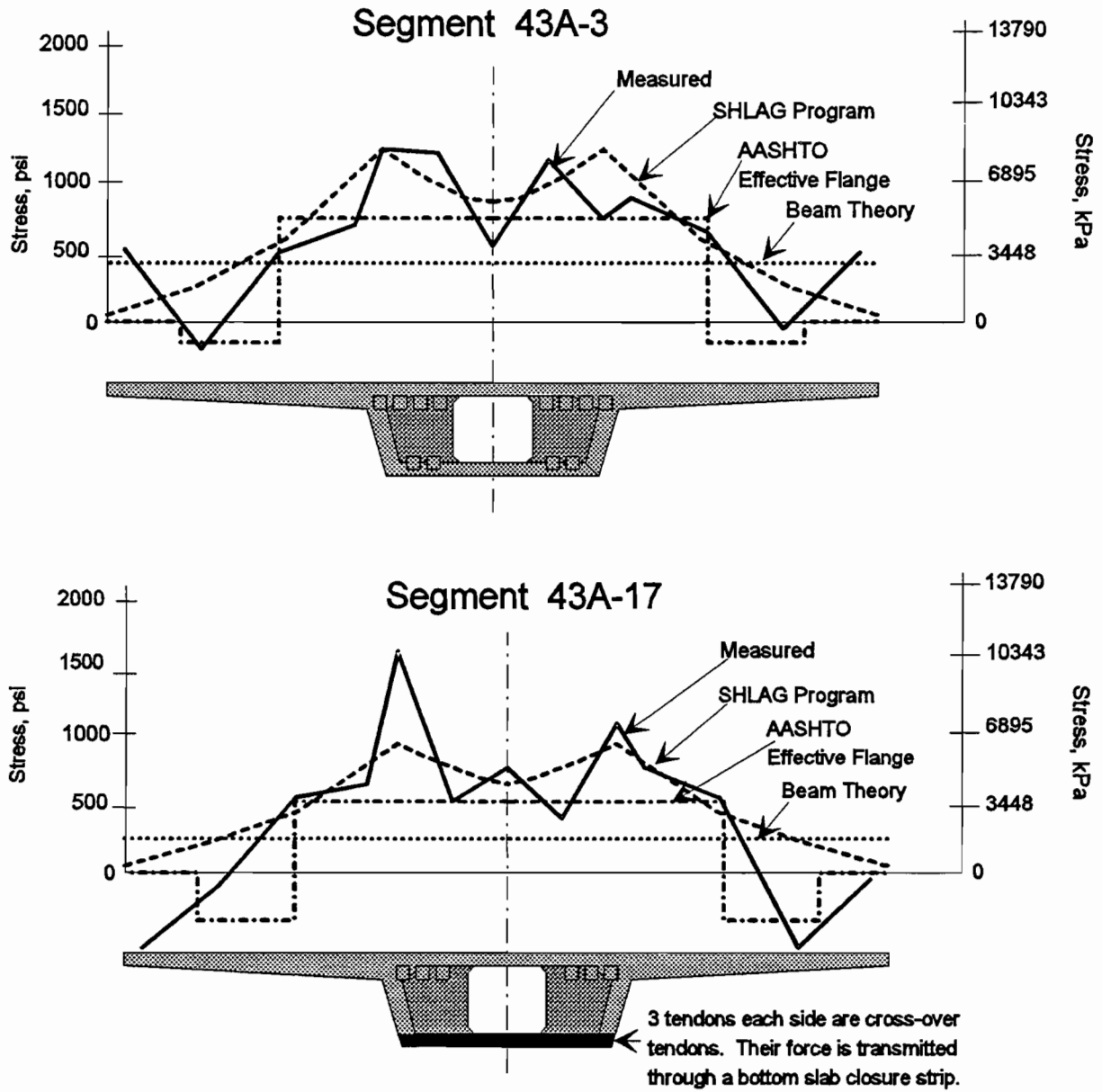


Figure 5.17a Top slab stress distributions, eleven feet (3353 mm) from anchors.

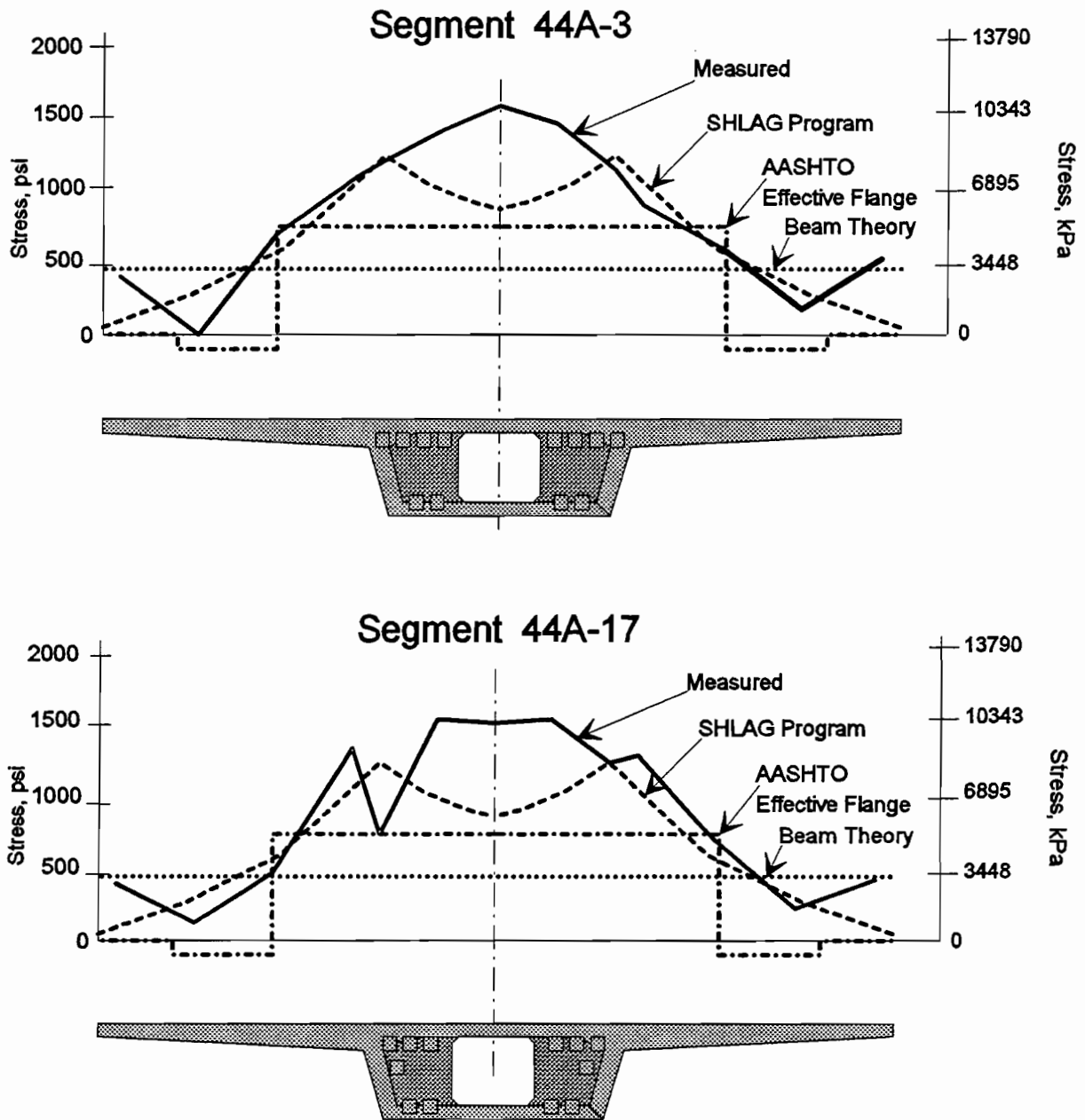


Figure 5.17b Top slab stress distributions, eleven feet (3353 mm) from anchors.

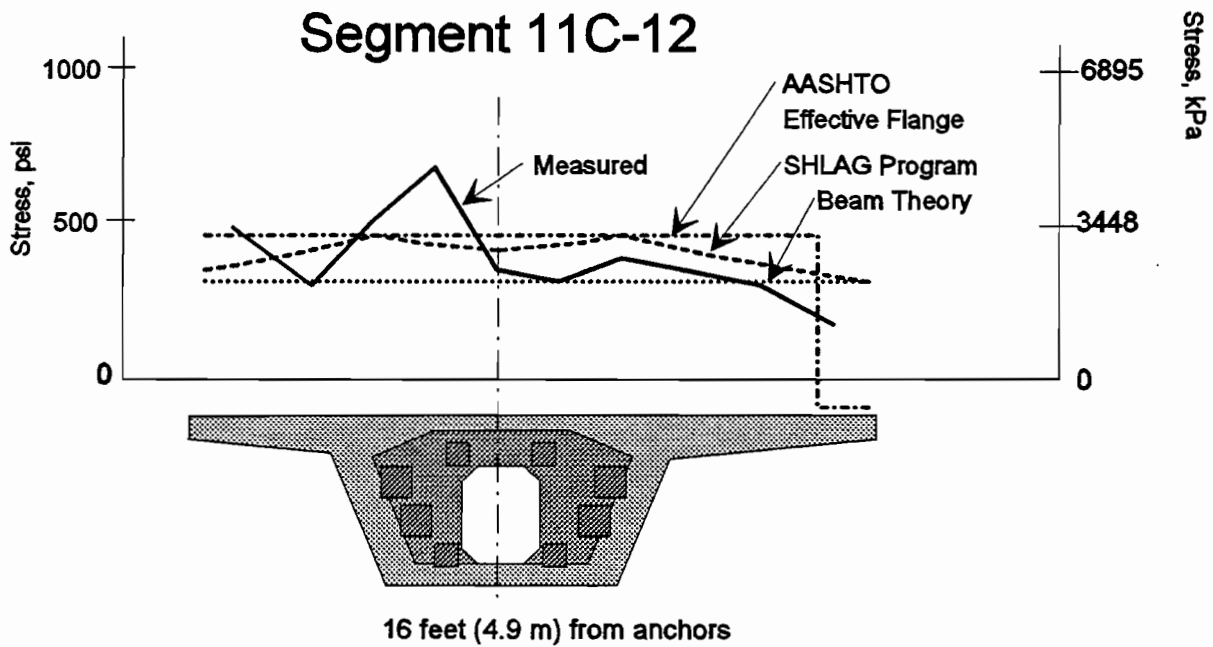
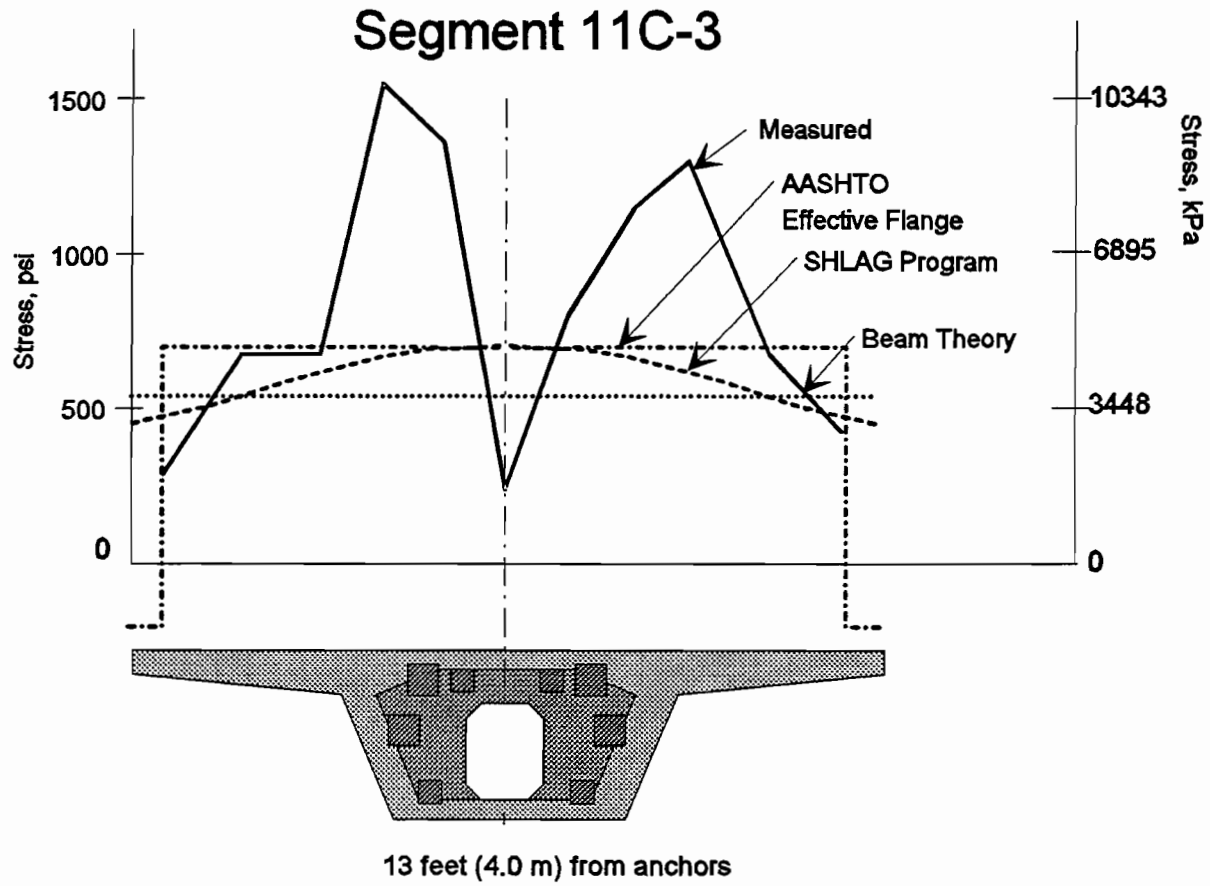


Figure 5.17c Top slab stress distributions, two segments from anchors.

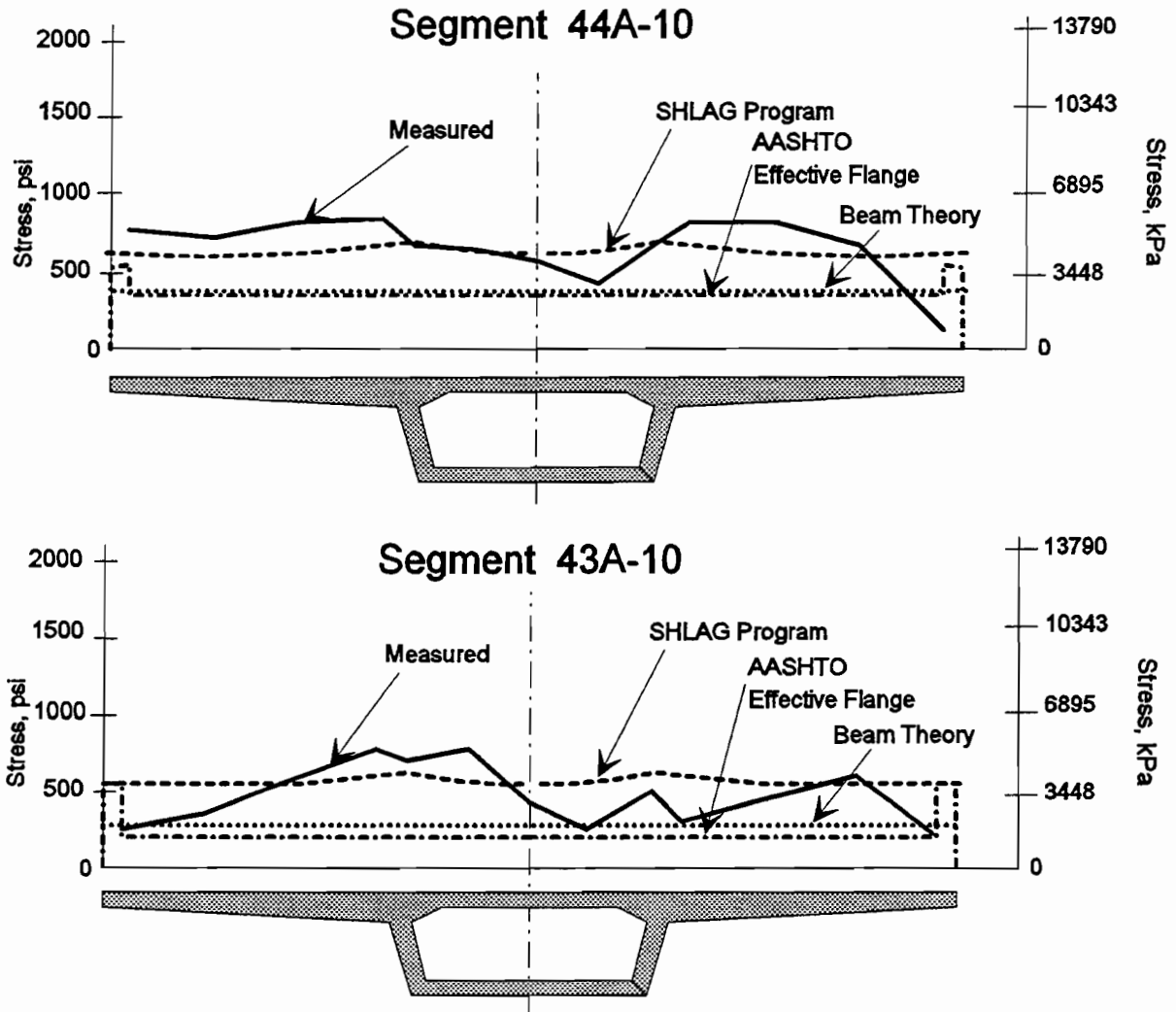


Figure 5.18a Top slab stress distributions, at mid-span.

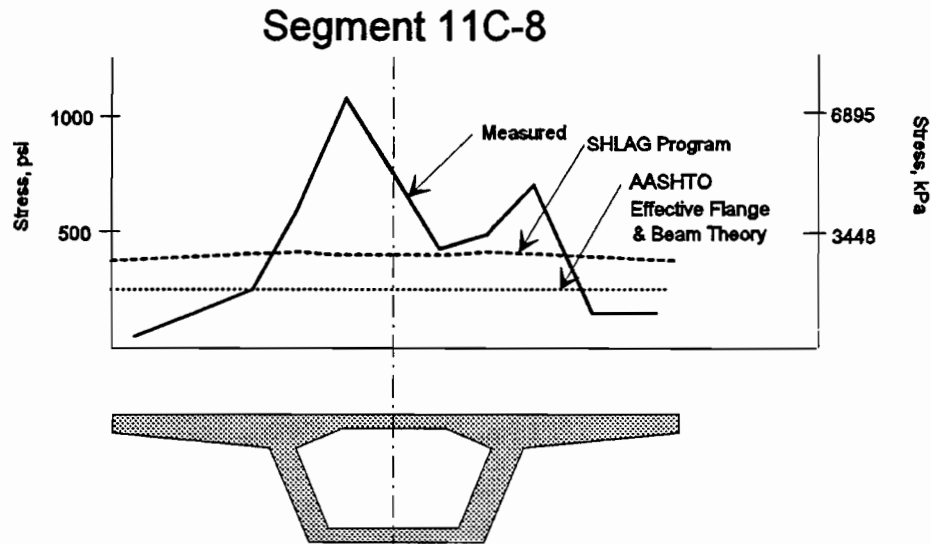


Figure 5.18b Top slab stress distribution, at mid-span.

5.4.2.2 Bottom Slab Stress Distributions. Figures 5.19a, b and c show the measured and calculated bottom slab stress distributions for segments 43A-2, 43A-18, 44A-2, 44A-18, 11C-2 and 11C-18. In these segments the influence of the end diaphragms is very evident. The measurement locations directly in front of the solid sections of the diaphragm show high stresses, while the location directly in front of the diaphragm opening shows substantially smaller compression. This would indicate that the majority of the post-tensioning force has not diffused toward the center of the bottom slab at this point. The measured strains are most similar in pattern and magnitude to the AASHTO predictions. Since SHLAG cannot be programmed to recognize the presence of the diaphragm, the SHLAG calculated stresses are more highly concentrated near the web walls. Once again the beam theory solution significantly underestimates the peak stresses in the bottom slab, calculating only 56% of the measured peak stresses for these six segments.

Measured and calculated bottom slab stresses of segments 43A-3, 43A-17, 44A-3, 44A-17, 11C-3 and 11C-12 are shown in Figure 5.20(a), (b) and (c). In the Span A43 and A44 segment plots, the measured strains appear to be fairly uniform across the bottom slab at this point. All three calculation methods approximate the actual distribution, but the magnitudes are still somewhat low with SHLAG predicting 72%, AASHTO predicting 84% and beam theory predicting 61% of the measured peak stress on average for the six cases. The measurements from Span C11 show less uniform distributions across the sections.

Figure 5.21 presents the bottom slab transverse stress distributions for segments 43A-10 and 44A-10, which are located at mid-span of their respective spans. Several measurement points were damaged in the mid-span segment of Span C11, so the results are not presented. The measured stress distribution is almost uniform in Segment 43A-10 and matches very well the calculated values. The measured stress distribution in Segment 44A-10 is considerably more erratic and peak values are in poor agreement with the three analysis methods.

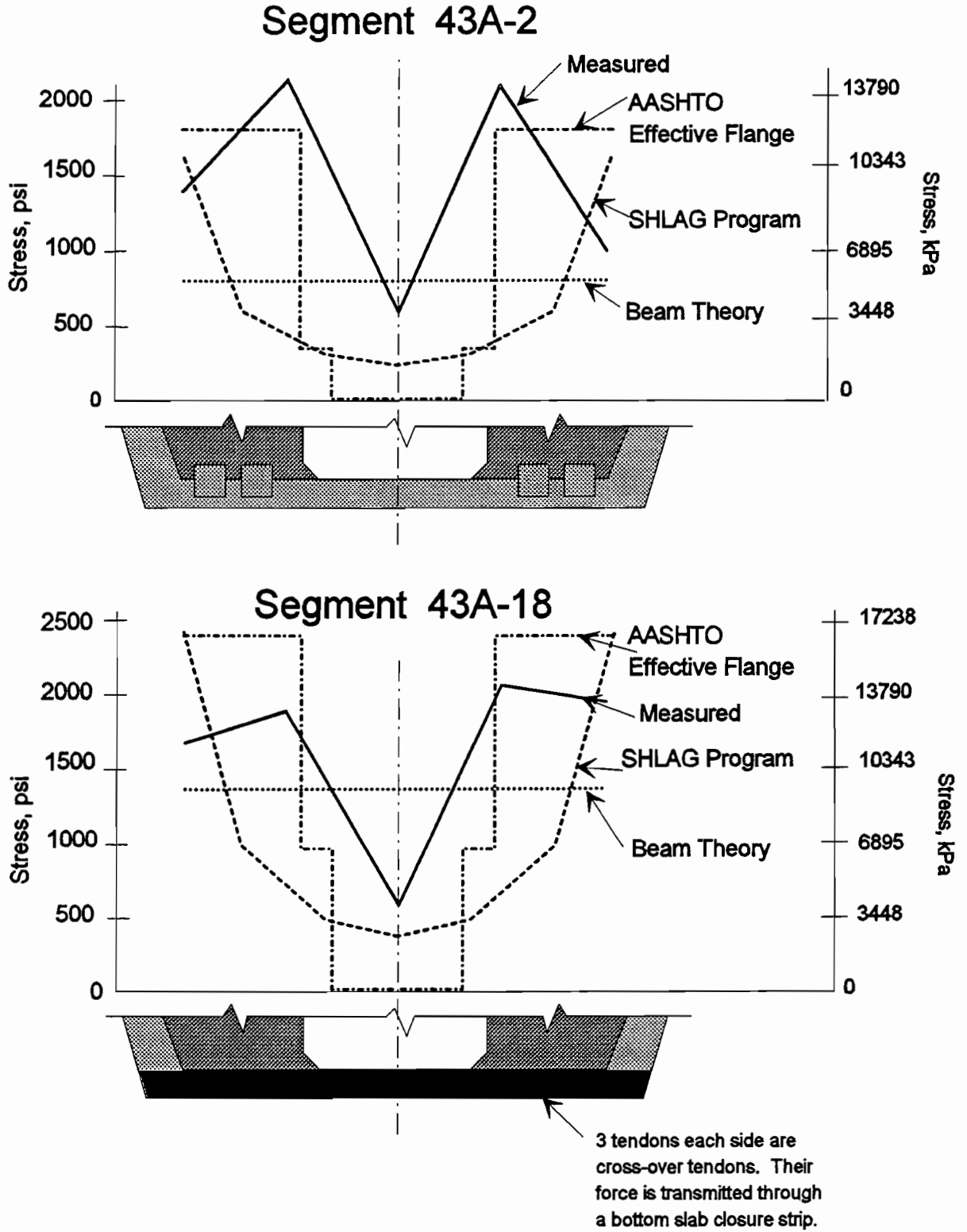


Figure 5.19a Bottom Slab Stress distributions, five feet (1524 mm) from anchors.

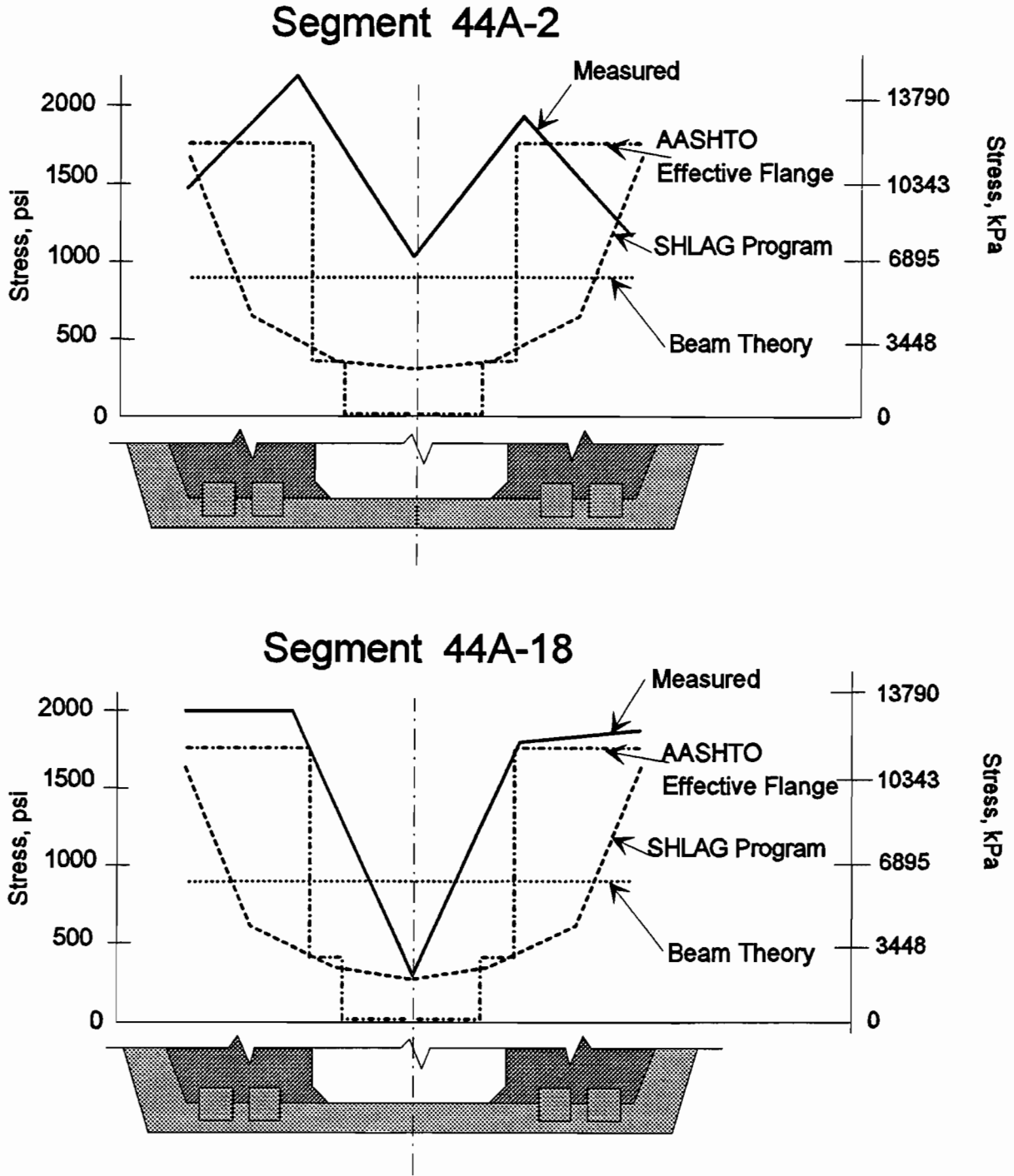


Figure 5.19b Bottom slab stress distributions, five feet (1524 mm) from anchors.

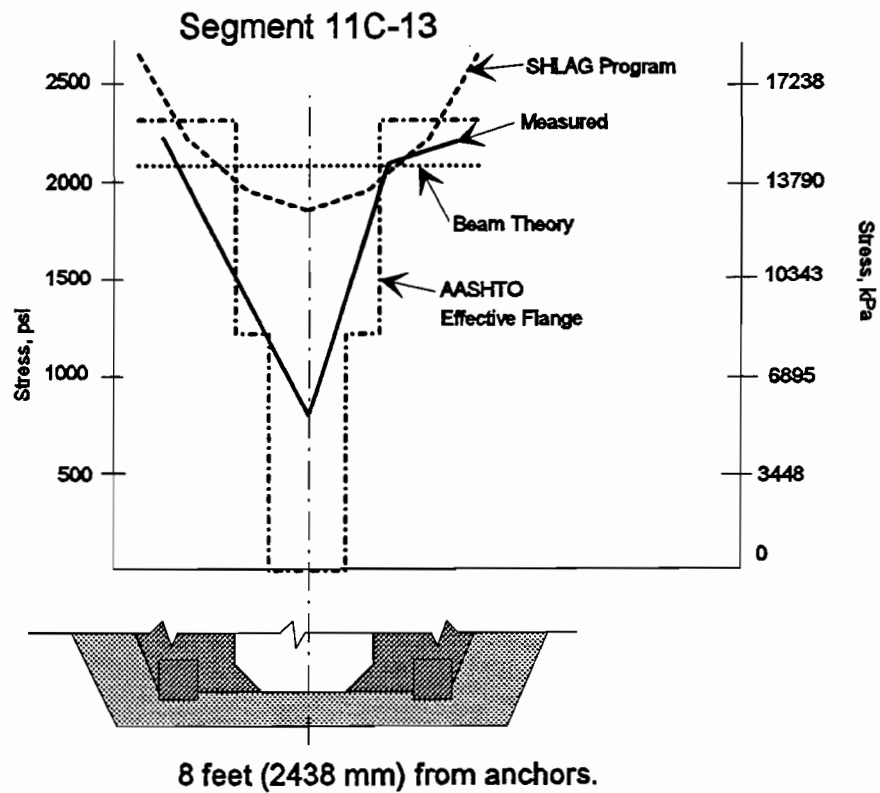
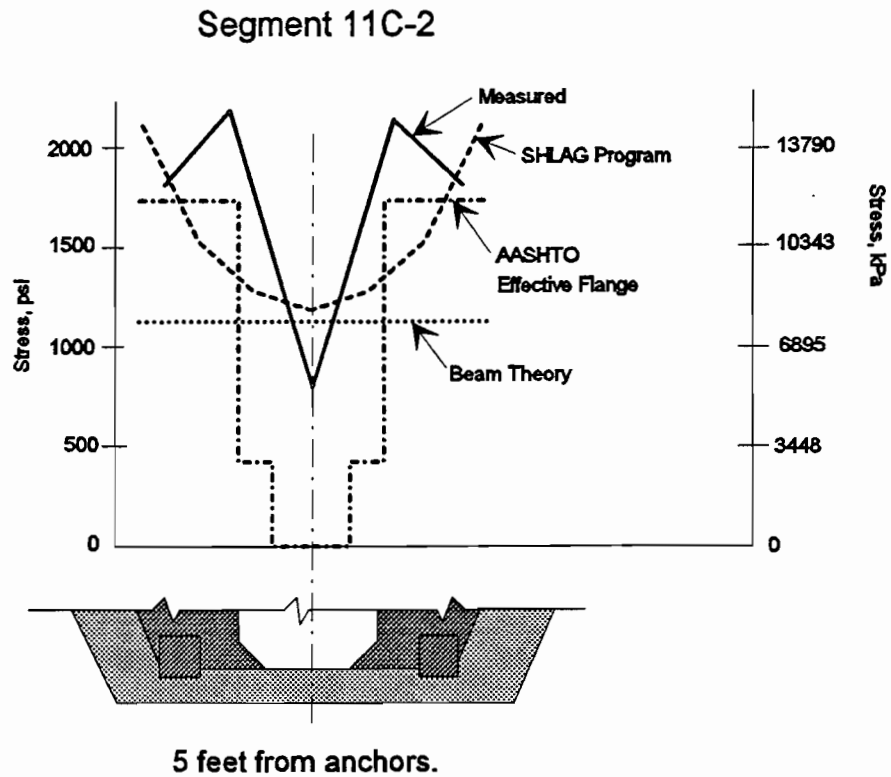


Figure 5.19c Bottom slab stress distributions, one segment from anchors.

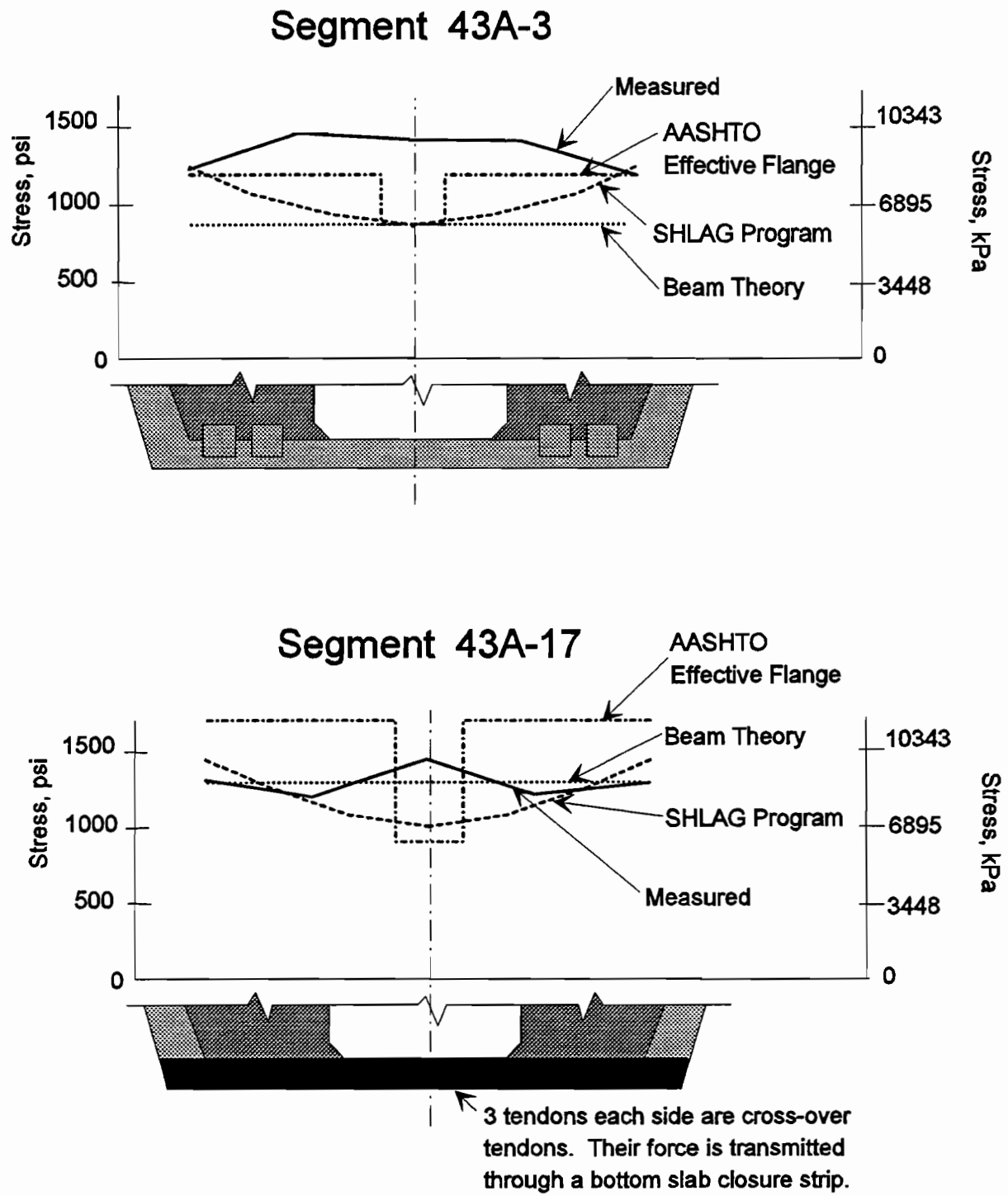


Figure 5.20a Bottom slab stress distributions, eleven feet (3353 mm) from anchors.

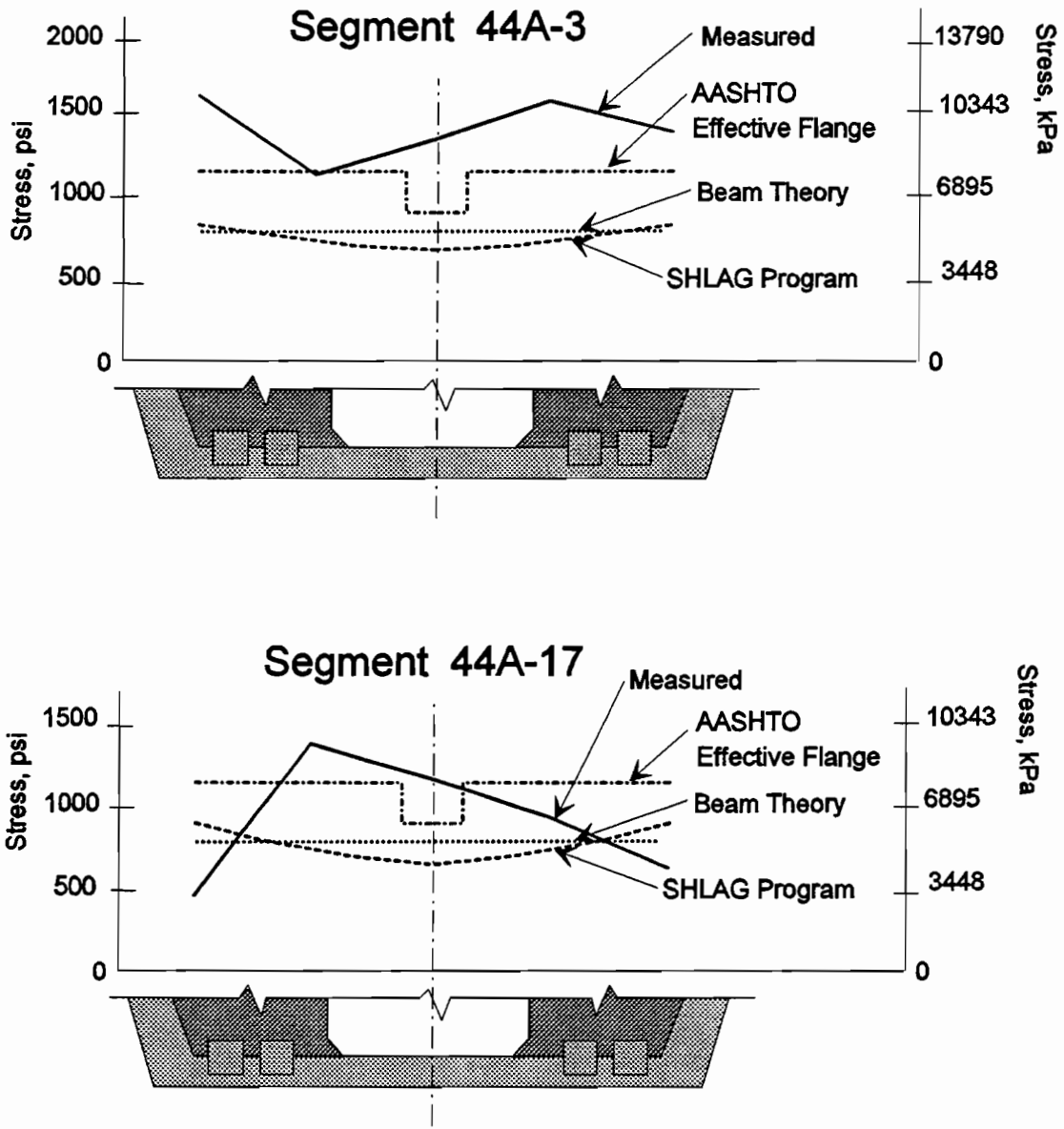


Figure 5.20b Bottom slab stress distributions, eleven feet (3353 mm) from anchors.

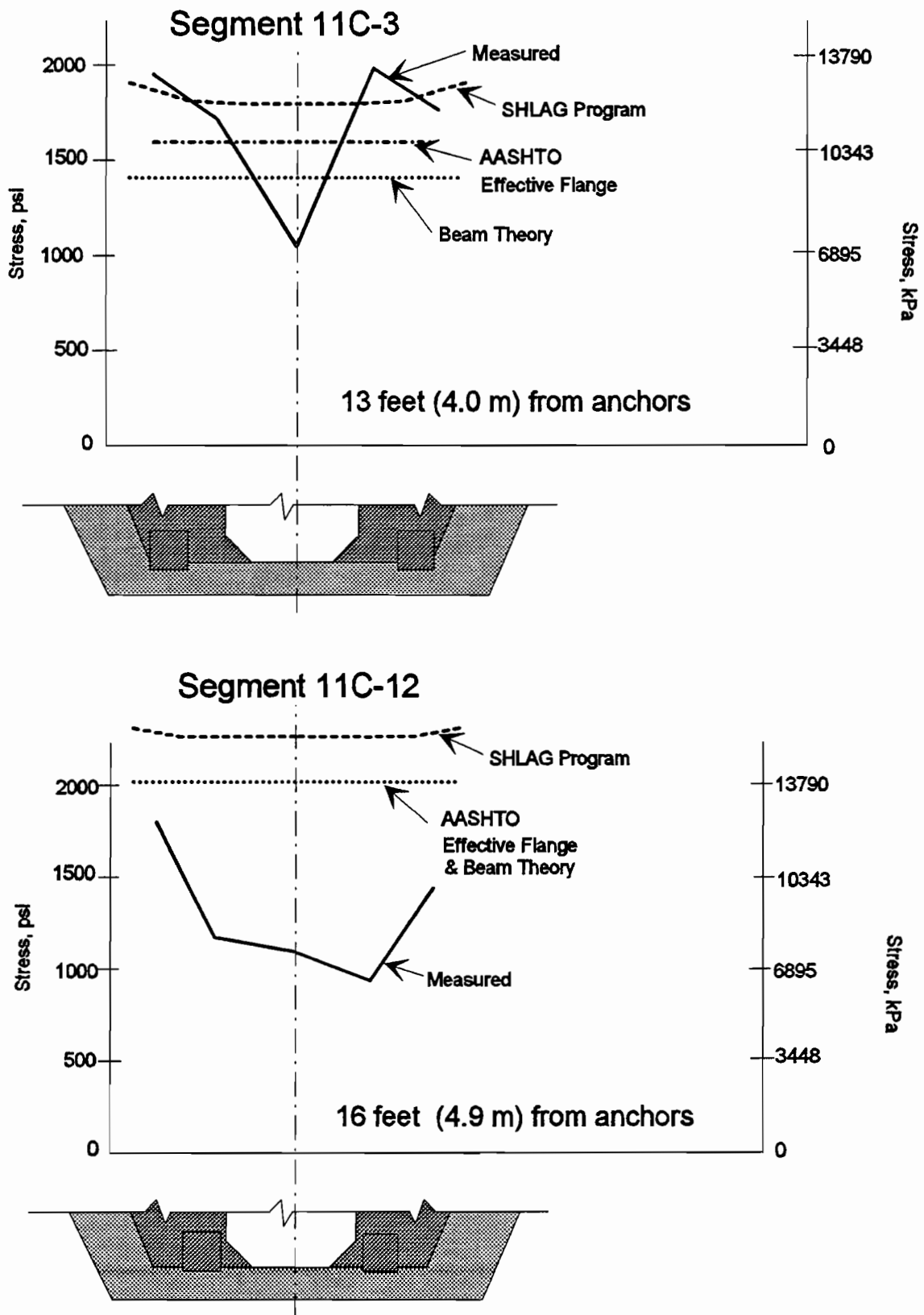


Figure 5.20c Bottom slab stress distributions, two segments from anchors.

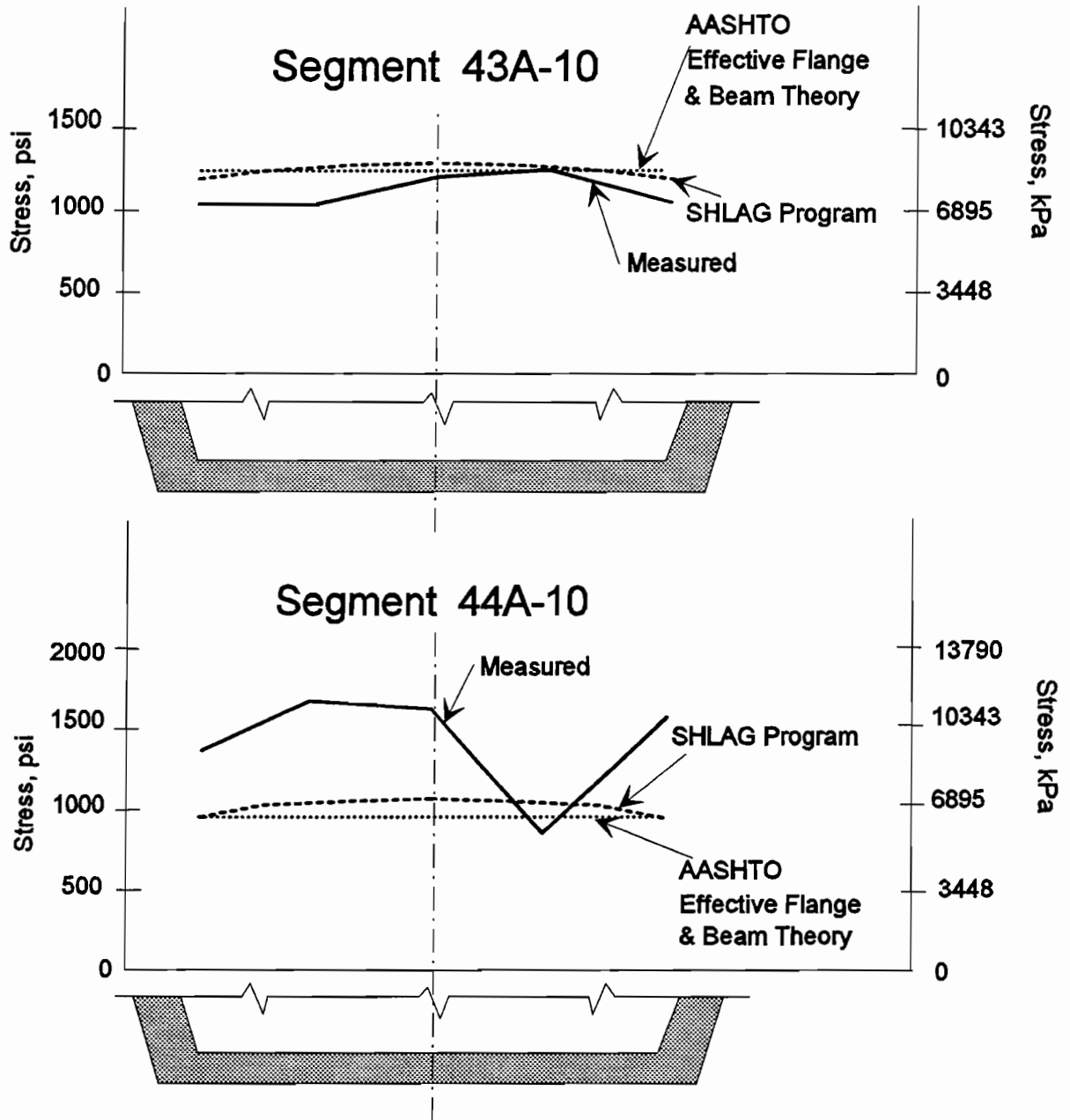


Figure 5.21 Bottom slab stress distributions, at mid-span.

5.4.2.3 Summary. Figure 5.22 shows the overall accuracy of each calculation method compared to measured stresses. The accuracy ratio of each method in predicting top and bottom slab stresses is presented in Table 5.2. From Figures 5.22a and b it is apparent that the SHLAG program is the most consistently accurate method of calculating peak stresses even though it tends to underestimate peak stresses in many cases. The *AASHTO Guide Specification* method tends to be more accurate in its predictions close to the piers, less accurate near mid-span and tends to substantially underestimate top slab stresses. Simple beam theory is clearly woefully inadequate in predicting the peak stresses in these cross-sectional shapes.

On average for all segments, top and bottom slab measurements, the SHLAG program predicts 84% of the measured peak stresses, beam theory 49% and the *AASHTO Guide Specification* Method 72%. Clearly beam theory is inadequate for the determination of maximum compressive stresses, and might also never predict areas near the wingtip which are in tension. The preferred method would be a program such as SHLAG or MUPDI (presented in the PTI Manual) to predict the maximum stresses and the stress distributions. The *AASHTO Guide Specification* is generally acceptable if the designer recognizes that peak stresses may be underestimated. The allowable compressive stresses, $0.4f_c$ at service, are conservative enough that a 20 to 30% underestimation of peak stresses, which occur over only a small portion of the cross-section, should not be very detrimental to the design.

5.4.2.4 Possible Errors in Measurement System. The readings must be assessed in terms of their reliability. A reading with a Demec gage is highly dependent on the skill and experience of the reader and the condition of the points. A perfectly positioned pair of points, read by a skilled reader will be easily dependable to ± 2 units on the dial gage which equals $16\mu\epsilon$. If the points are in some way not perfectly aligned or perfectly cleaned, or if the reader applies a variable pressure or holds the gage at a variable angle, the readings will not be reliable. For most of the readings taken in this field project, the reliability can be estimated at ± 4 units, or $32\mu\epsilon$, which equals 170 psi (1172 kPa). This range can account for many of the irregularities in the readings.

The measured peak stresses of Spans A43 and A44 are affected by a slight amount of creep. When Span C11 was completed, the trusses were lowered immediately so essentially no creep occurred from the beginning of stressing to the final reading taken after the trusses were lowered. For both spans A43 and A44, however, the erection schedule was such that the trusses were left in place for several days before they were lowered. The final measured peak stresses, therefore, also include the effects of approximately 4 days of creep. The additional compressive strain due to creep causes the final readings to be slightly higher than if the truss had been immediately lowered. This, in turn, indicates that the computational methods are slightly more accurate than the averages in Table 5.2 show.

In general, however, the Demec readings should do an excellent job of predicting the patterns and trends of the stresses in the concrete.

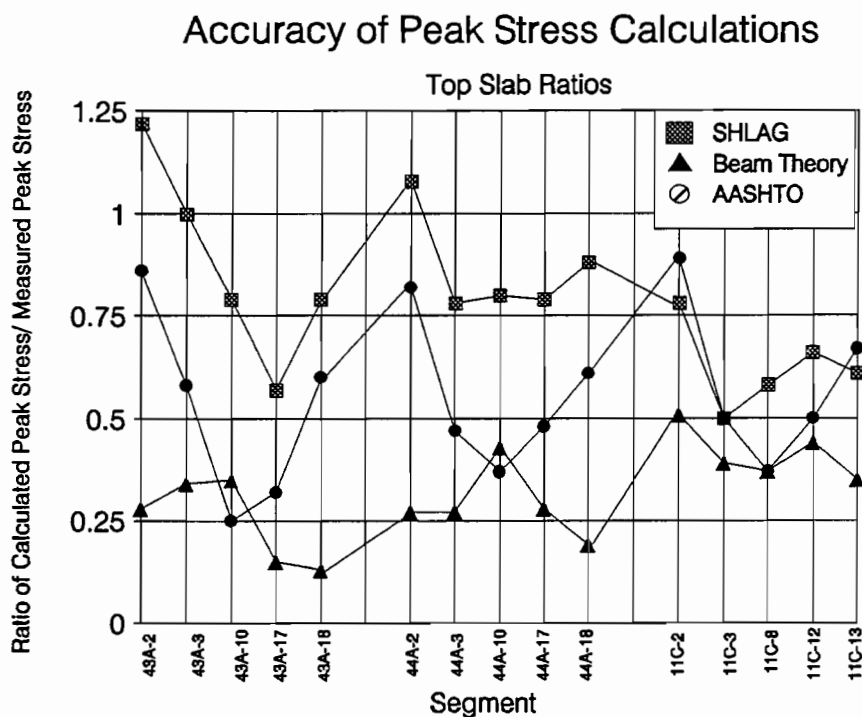


Figure 5.22a Accuracy of peak stress calculation methods for top slab stresses.

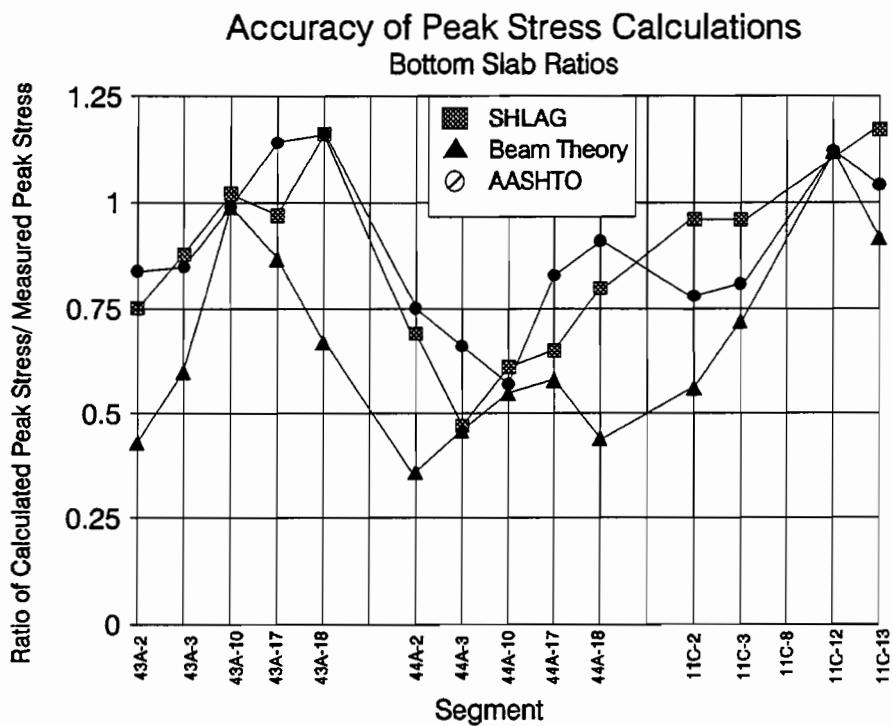


Figure 5.22b Accuracy of peak stress calculation methods for bottom slab stresses.

Table 5.2 Calculated vs Measured Stresses

Segment	Bottom Slab Ratio (Calc./Actual Peak Stress)			Top Slab Ratio (Calc. /Actual Peak Stress)		
	SHLAG	Beam Theory	AASHTO	SHLAG	Beam Theory	AASHTO
43A-2	0.75	0.43	0.84	1.22	0.28	0.86
43A-3	0.88	0.60	0.85	1.00	0.34	0.58
43A-10	1.02	0.99	0.99	0.79	0.35	0.25
43A-17	0.97	0.87	1.14	0.57	0.15	0.32
43A-18	1.16	0.62	1.16	0.79	0.13	0.60
44A-2	0.69	0.36	0.75	1.08	0.27	0.82
44A-3	0.47	0.46	0.66	0.78	0.27	0.47
44A-10	0.61	0.55	0.57	0.80	0.43	0.37
44A-17	0.65	0.58	0.83	0.79	0.28	0.48
44A-18	0.80	0.44	0.91	0.88	0.19	0.61
11C-2	0.96	0.56	0.78	0.78	0.51	0.89
11C-3	0.96	0.72	0.81	0.50	0.37	0.37
11C-8				0.58	0.37	0.37
11C-12	1.29	1.12	1.12	0.66	0.44	0.50
11C-13	1.17	0.92	1.04	0.61	0.35	0.67
average	0.89	0.66	0.89	0.79	0.32	0.55

5.4.3 Ontario Highway Bridge Design Code. The *Ontario Highway Bridge Design Code*⁵⁰ method for calculating effective flange widths produces results which are very similar to the *AASHTO Guide Specification*. Table 5.3 presents, for Span A44, the peak bottom and top slab stresses calculated with the AASHTO and Ontario methods. The two methods give very similar results, although the Ontario method (see Section 5.2.1) is considerably simpler.

Table 5.3 Comparison of Ontario Bridge Code and AASHTO Guide Specification.

Segment	Peak Stresses						Ratios	
	Ontario Bridge Code		AASHTO Guide Spec		Measured		Ontario/ Measured	AASHTO/ Measured
Top Slab	psi	kPa	psi	kPa	psi	kPa		
44A-2	1307	9012	1286	8867	1565	10791	0.84	0.82
44A-3	761	5247	752	5185	1609	11094	0.47	0.47
44A-10	344	2372	324	2234	869	5992	0.4	0.37
44A-17	755	5206	745	5137	1565	10791	0.48	0.48
44A-18	1288	8881	1264	8715	2087	14390	0.62	0.61
Bott Slab	Average						0.56	0.55
44A-2	1752	12080	1769	12197	2358	16258	0.74	0.75
44A-3	1133	7812	1143	7881	1719	11853	0.66	0.66
44A-10	925	6378	961	6626	1676	11556	0.58	0.57
44A-17	1149	7922	1159	7991	1392	9598	0.83	0.83
44A-18	1797	12390	1817	12528	1996	13762	0.9	0.91
							0.74	0.74

5.4.4 Isolated Dead Load Bending Stresses. The stress distributions across the width of the flanges are the sum of three load effects superimposed on one another:

1. The stress distribution caused by shear lag related to uniformly distributed dead loads.
2. The stress distribution caused by shear lag related to point application of post-tensioning deviator loads, and loads imposed by draped internal tendons.

3. The stress distribution caused by transverse diffusion of post-tensioning anchorage loads.

When load-balancing design solutions are employed, the dead load moments and post-tensioning moments almost balance one another. If the moments are generally balanced, the calculated peak stresses caused by shear lag should be small because the effects tend to cancel (see Figure 5.23). With these peaks effectively cancelled, the stress distributions are dominated by the diffusion of post-tensioning forces from the anchorages.

5.4.4.1 Measured Strains Due to Partial Dead Load. The data collected can be examined to study only dead load shear lag effects. In each span a reading was taken immediately following the post-tensioning operations. At this time a substantial portion of the dead load of the span was still being carried by the erection trusses. The trusses were then lowered and another reading was taken. The differences in concrete strain readings from the measurement before lowering and after lowering should be attributable to only the additional dead load, and some minor creep effects as described in section 5.4.2.4.

The amount of load still carried by the truss was determined by comparing the fully loaded deflection of the trusses to the deflection after all tendons were stressed but before the truss was lowered. The percentage of dead load still being carried by the truss was equated to the ratio of the remaining deflection to the deflection under full dead load. This was verified by comparing the change in span deflection after the truss was lowered to the calculated span deflection under full dead load. The two methods were quite close. They indicate that the truss was still carrying 54% of the dead load of span A44 and 38% of the dead load of span A43.

Figure 5.24 shows the stress increases in Segment 44A-10 due to the lowering of the erection trusses. Also shown are calculated stress distributions for a load of 54% of full dead load. The measured stresses are best approximated by the AASHTO effective flange width method. It must be noted, however, that with a possible error of ± 170 psi (1172 kPa), all of the calculated solutions are somewhat feasible.

The other segments showed similar patterns. Unfortunately, near the piers the expected stress increases were quite small, less than 200 psi (1379 kPa), so reading error and 4 days of creep made evaluation almost impossible. In general, the variation of stresses across the sections was less than 500 psi (3448 kPa), much smaller than the 1500 to 2000 psi (10343 to 13790 kPa) differences measured with full dead and post-tensioning loads.

The readings confirm that stress variations across the width of the section are relatively small for bending stresses, and are dominated by the effects of the transverse diffusion of post-tensioning force.

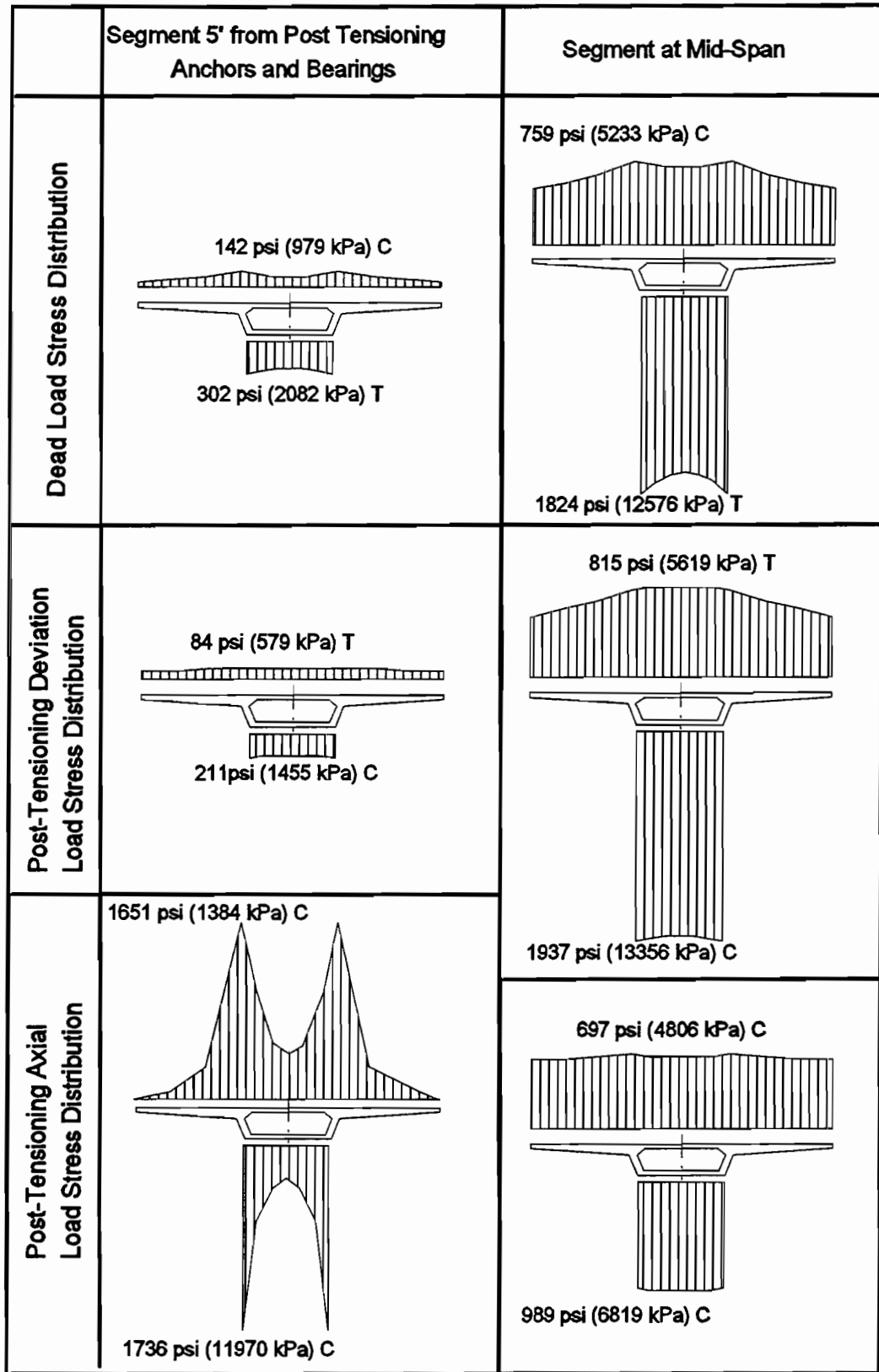


Figure 5.23 Separation of load effects.

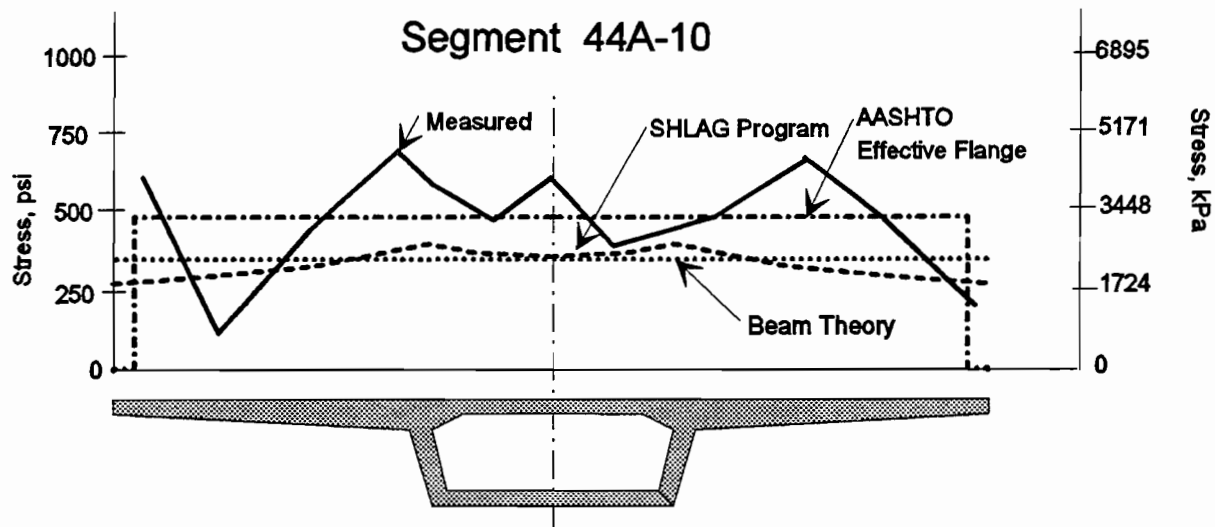


Figure 5.24 Top slab stress distribution, at mid-span, due to 54% dead load addition upon lowering erection truss.

5.4.5 Long Term Strain Changes. The question of how creep affects the strain distributions across the flanges was investigated by examining readings taken over the course of several months. It was considered possible that the more highly stressed regions of the slabs above and below the webs would experience more rapid strain changes than the wings. This could cause some load to be shed outward, reducing the peak stresses.

Figure 5.25 shows top slab strain changes with time for two typical segments (43A-2 and 43A-18). Considering the $\pm 32\mu\epsilon$ possible reading error, the strain changes are essentially uniform across the section at 7 days. At 74 days the compression strain has increased significantly, however, some of the additional compression is due to the addition of continuity tendons in the webs and the wings. Some of the new peaks are due to the proximity of newly stressed continuity tendons. Generally, the readings show the entire width of the top slab creeping more or less equally in compression.

5.4.6 Deflections. Figure 5.26 compares calculated cambers, using in one case actual cross-sectional properties and in the other case AASHTO effective cross-sectional properties, to measured deflections. The difference between the two calculated deflections is quite small, with an average increase in camber of 5% due to the change from actual properties to AASHTO effective properties. In all cases the measured camber is smaller than the calculated value, indicating a stiffer than expected cross-section, internal tendon forces smaller than theoretical, dead load greater than assumed, or a combination of these factors. However, both methods give reasonably accurate results, with the differences between measured and calculated falling between $1/33000$ and $1/9400$ of the span length for the two methods. Either method is therefore quite acceptable for determining cambers.

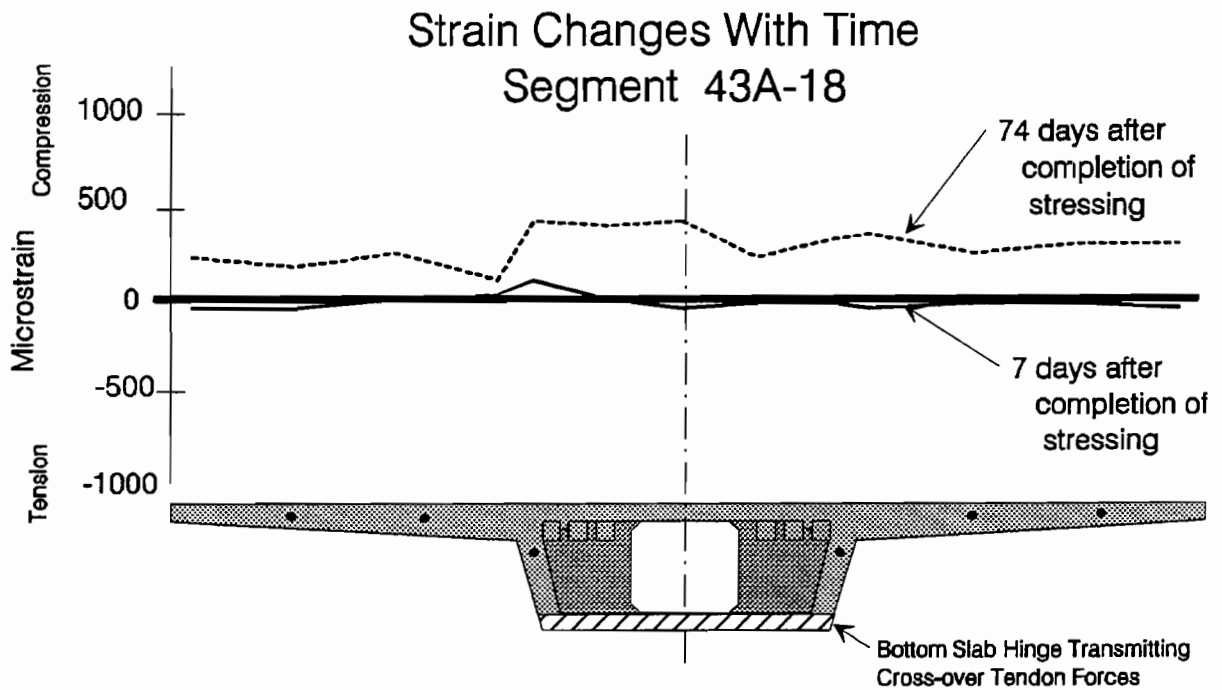
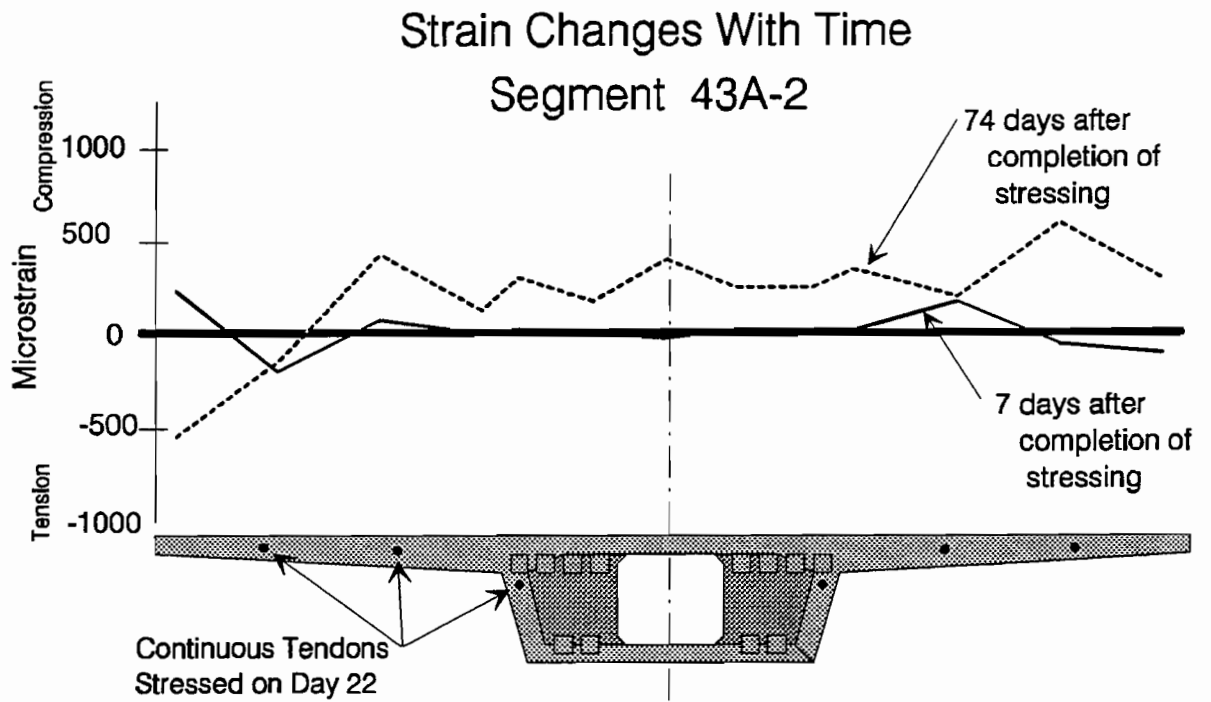


Figure 5.25 Changes in top slab strains with time.

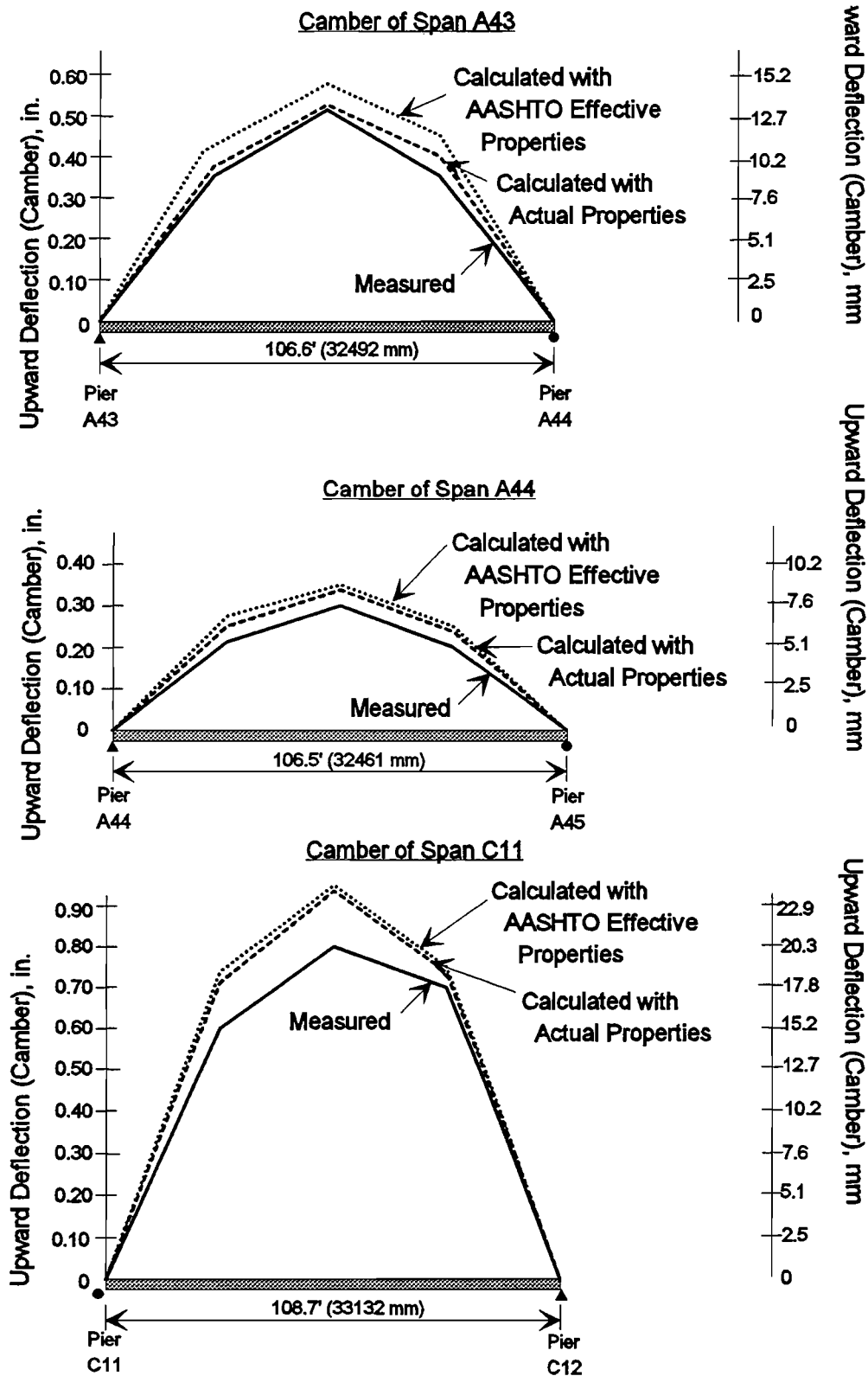


Figure 5.26 Comparison of actual and calculated span deflections (dead load and simple span tendons only).

5.4.7 Modified Approach. This section presents the calculation of maximum stresses using a modified version of the *AASHTO Guide Specification* method for determining effective flange widths. The primary modifications are:

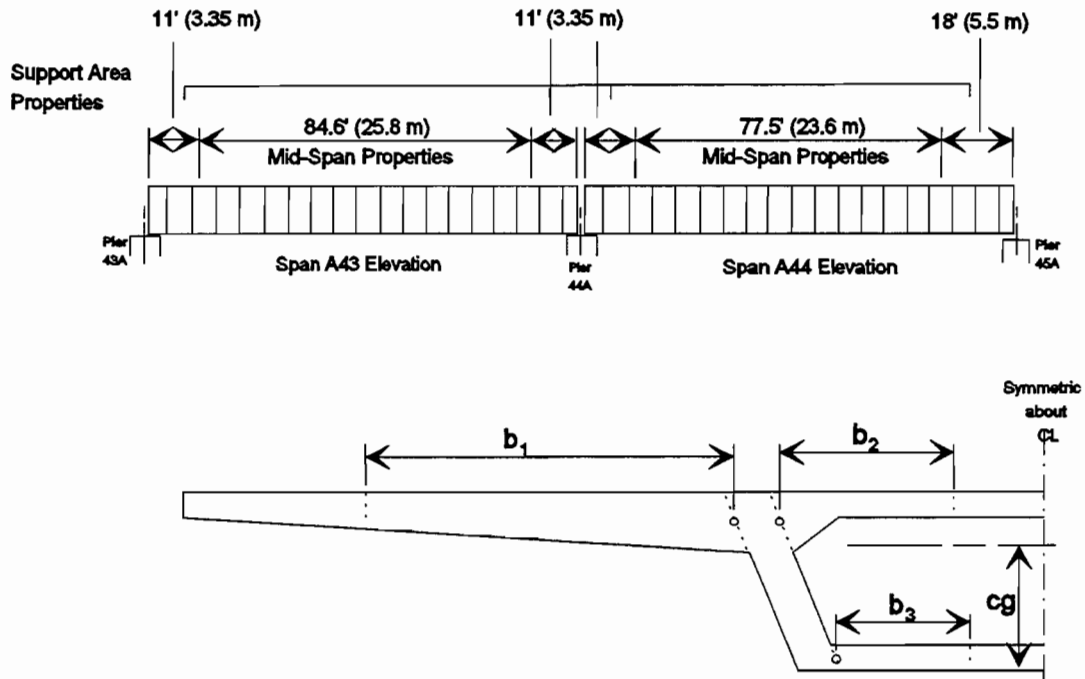
1. **Simplified Transitions.** A step transition is made from the pier area properties to the mid-span properties, instead of the currently advocated linear transition.
2. **Flange Width Limits.** If the flange width (measured from the edge of the web to the edge of the flange) is less than 0.1 times the effective span length, no adjustments are required for that flange.
3. **Cross-sectional Properties Are Considered in Analysis.** The moment which is applied to the end of the girder is equal to the applied post-tensioning force times its distance to the neutral axis of the section. The neutral axis of the section computed using the effective flange widths is used in this analysis. At the location of transition from pier area properties to mid-span properties, an additional moment is applied to reflect the change in the center of gravity of the section.

Figure 5.27 shows the effective cross-sectional properties spans A43 and A44. The loading diagrams are the same as those shown in Figure 5.12. Table 5.4 shows the calculated and measured top and bottom stresses.

This method, on average, predicts 70% of the measured stresses, which is very similar to the current AASHTO method. This method is, however, much less involved and the predictions do not show as much variability between the top and bottom slab ratios. The current method predicts 89% of the peak bottom slab stresses and only 55% of the peak top slab stresses. The proposed method predicts 75% of the peak bottom slab stresses and 64% of the peak top slab stresses, which is more consistent. This is primarily due to using the center of gravity of the effective cross-section for the determination of the end moment.

Figure 5.28 compares the actual and calculated deflections using the modified method. This method predicts the deflections to within .03" (7.6 mm) (1/44000 of the span length) for these two spans.

Overall this modified method is less tedious, more consistent and only slightly less accurate than the current method.



Location	A		I		b_1		b_2		b_3		cg	
	ft ²	m ²	ft ⁴	m ⁴	ft	m	ft	m	ft	m	ft	m
Span A43 Support Area	61.4	5.7	246.0	2.1	6.5	2.0	5.2	1.6	6.9	2.1	3.7	1.1
Span A43 Mid-Span	79.9	7.4	260.2	2.3	10.9	3.3	7.7	2.3	6.9	2.1	3.9	1.2
Span A44 Support Area	72.5	6.7	231.2	2.0	8.2	2.5	8.7	2.7	6.9	2.1	3.9	1.2
Span A44 Mid-Span	86.5	8.0	291.0	2.5	13.4	4.1	8.7	2.7	6.9	2.1	4.1	1.2
Full	94.3	8.8	297.9	2.6	18.1	5.5	8.7	2.7	6.9	2.1	4.2	1.3

Figure 5.27 Effective segment properties using modified AASHTO method.

Table 5.4 Accuracy of Modified Effective Flange Width Method.

Segment	Calculated Peak Stress				Measured Peak Stress				Calc./Meas. Peak Stress	
	Top Slab		Bottom Slab		Top Slab		Bottom Slab		Top Slab	Bottom Slab
	psi	kPa	psi	kPa	psi	kPa	psi	kPa		
43A-2	1559	10749	1718	11846	1522	10494	2131	14693	1.02	0.81
43A-3	811	5592	997	6874	1261	8695	1435	9894	0.64	0.70
43A-10	271	1869	1149	7922	782	5392	1478	10191	0.35	0.78
43A-17	644	4440	1280	8826	1652	11391	1304	8991	0.39	0.98
43A-18	1323	9122	2116	14590	1696	11694	2261	15590	0.78	0.94
44A-2	1561	10763	1672	11528	1565	10791	2358	16258	1.00	0.71
44A-3	857	5909	894	6164	1609	11094	1719	11853	0.53	0.52
44A-10	402	2772	911	6281	869	5992	1676	11556	0.46	0.54
44A-17	849	5854	911	6281	1565	10791	1392	9598	0.54	0.65
44A-18	1531	10556	1733	11949	2088	14397	1996	13762	0.73	0.87
Averages									0.64	0.75

5.5 Discussion

The data collected in this study indicates that simple beam theory is very inadequate to calculate peak compressive stresses, predicting on average only 49% of the measured peak stresses. Beam theory also does not predict that tensile stresses can develop at the wingtips of segments near supports. An analysis which better approximates the actual stress distributions is needed.

The current AASHTO effective flange width procedure for bending stresses does a fair job of approximating the peak stresses, predicting on average 72% of the measured peak stresses, and the stress distribution. The procedure, unfortunately, is excessively complex, especially given that the dominant factor is the transverse diffusion of post-tensioning forces. The rigor required in the method should be more in line with the accuracy of method and the consequences of error.

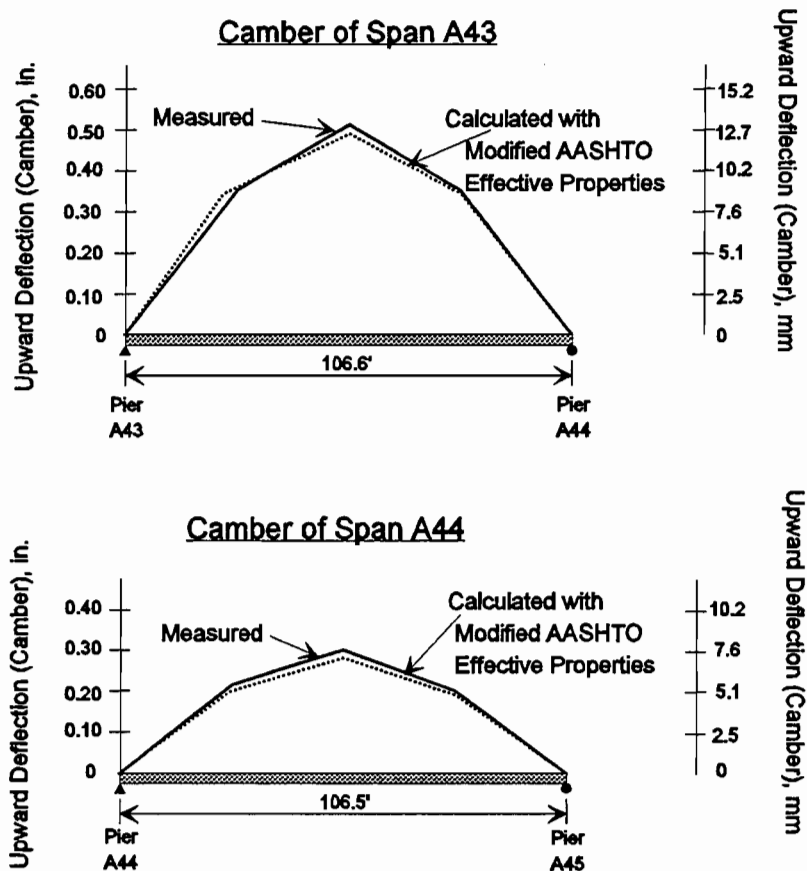


Figure 5.28 Comparison of actual deflections and span deflections calculated with modified AASHTO properties (dead load and simple span tendons only).

The SHLAG program is a good alternative for the calculation of peak stresses. The input is simple and the results were closer to the measured peak stresses than beam theory or the AASHTO effective flange width method. SHLAG predicted on average 84% of the measured peak stresses.

The complexity of the computational problem using effective flange widths can be overwhelming in a segmental project where a span is erected as a simple span and then made continuous at a later stage. One set of cross-sectional properties would be needed for the simple span carrying dead and post-tensioning loads, and another set of properties would be needed for the same span in a continuous unit carrying additional post-tensioning loads, super-imposed dead loads and live loads.

Based on the observed accuracy of the method, less rigor is appropriate. The *Ontario Highway Bridge Design Code* method is an equally accurate, but less involved method. Simplifications to the *AASHTO Guide Specification* can reduce the rigor without compromising the accuracy. The first simplification is to allow a stepwise transition, instead of the current linear transition, from pier area properties to mid-span properties. A second simplification would

be to state that, in span-by-span construction, the cross-sectional properties based on the conditions of the final span configuration can be used for the complete analysis, regardless of intermediate configurations. In this way designers would not have to calculate multiple cross-sectional properties for spans which change from simple span to continuous configurations. This would be conservative.

The analysis can be further simplified by indicating a ratio of widest flange width to span length for which the effective flange width evaluation is not needed. A flange width to effective span length ratio of less than 0.1 would ensure that at least 70% of all flange widths are effective in resisting bending stresses. A flange width, as defined in Figure 5.4, is the distance from the edge of the web to the end of the flange for a free flange, or the centerline of the segment for a top or bottom slab of a box section.

The transverse diffusion of post-tensioning force is a critical issue. The angle for diffusion of 30° seems to be acceptable. A gradual transition of cross-sectional properties is the most accurate approach, but it does make the analysis more complicated.

This problem is critical from two standpoints. The first is the over-compression of the areas near the piers. Since tests have shown that concrete loaded to $0.8f'_c$ will eventually creep to failure, high compression stresses could be a problem. The second area of concern is the adequate compression across the full width of every joint. Figure 5.29 shows how, if anchors are widely spaced and the first joint is very close to the anchors, part of the joint will not be precompressed. This could cause problems, especially for dry-jointed structures.

The transverse diffusion of post-tensioning force must be considered, if not in a rigorous analysis, then at least in the development of good post-tensioning details to ensure adequate compression of the full length of the joints.

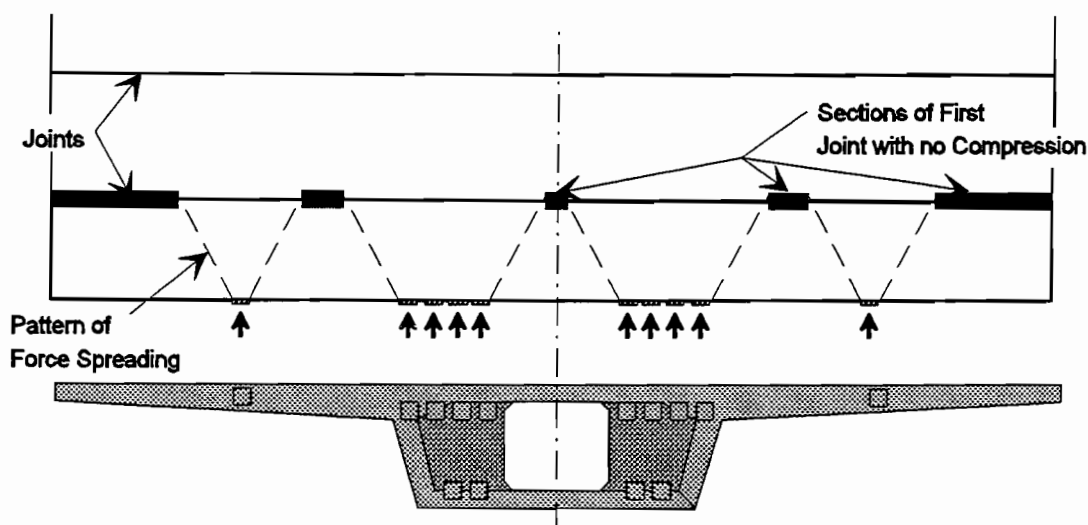


Figure 5.29 Pattern of force diffusion, showing lack of compression on sections of first joint.

5.6 Recommendations

The following is a possible modification to the *AASHTO Guide Specification* to simplify and clarify the calculation of effective cross-sectional properties. Changes are presented in italicized print.

4.3 Effective Flange Width

4.3.1 General

Effective flange width may be determined by elastic analysis procedures, (SHLAG Program to be included in suggested references), by the provisions of Section 3-10.2 of the 1983 Ontario Highway Bridge Design Code, or by the provisions of Sections 4.3.2.

4.3.2 Effective Flange Width for Analysis and for Calculation of Section Capacity and Stresses

Section properties for analysis and for calculation of the effects of bending moments and shear forces may be based on the flange widths specified in this section, or may be based on flange widths determined by other procedures listed in Section 4.3.1. The effects of unsymmetrical loadings on effective flange width may be disregarded.

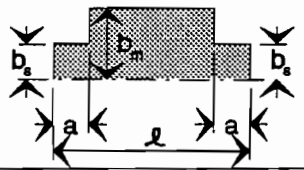
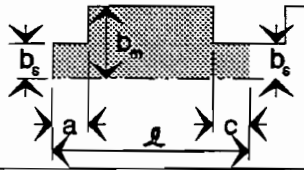
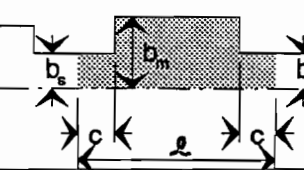
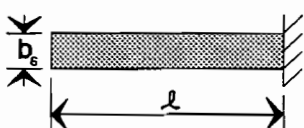
The effective flange width, b_e (see Figure 4-3 (Figure 5.31)) may be assumed equal to the full flange width, b , if:

- 1) $b \leq 0.1 \ell_1$ ($\ell_1 =$ effective span length)
- 2) $b \leq 0.3d_o$ ($d_o =$ web height).

For flange widths, b , greater than $0.3d_o$ or $0.1\ell_1$, the effective width may be determined in accordance with Figures 4-1 and 4-2 (see Figure 5.30). The value of b_{es} , *the effective flange width in the support area*, shall be determined using the greater of the effective span lengths adjacent to the support. If b_{em} , *the effective flange width in the mid-span area*, is less than b_{es} , in a span, the pattern of the effective width within the span may be determined by the connecting line of the effective support widths, b_{es} , at adjoining support points. However, the effective width, b_e , shall not be taken greater than b . *A step-wise transition from support area properties to mid-span properties is allowed.*

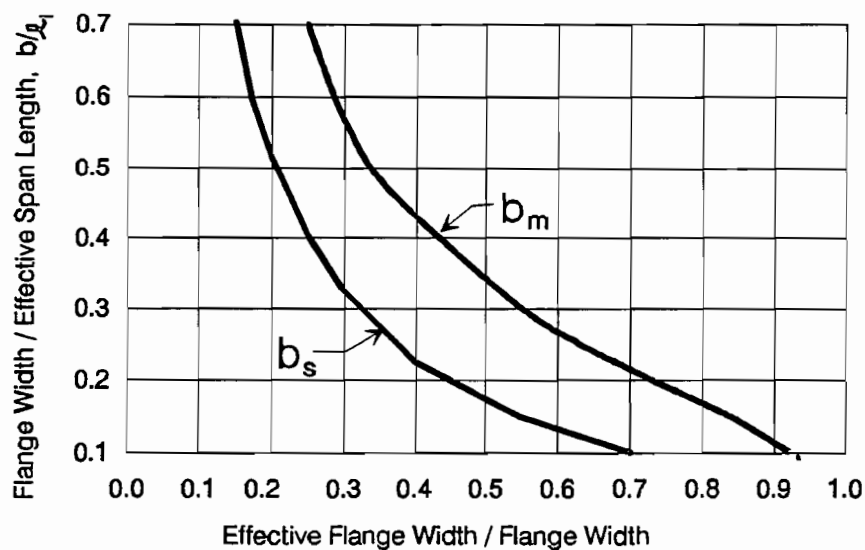
If the construction procedure is such that the configuration of a span within a unit changes, the final configuration may be used in the determination of the effective flange widths.

No other changes are required for the text. The figures shall be clarified as shown in Figures 5.30 and 5.31.

System	Pattern of Effective Flange Widths	Effective Span Length for use with Figure 4-2
Single-Span Girder		$l_i = l$
End Span of Continuous Girder		$l_i = 0.8 l$
Inner Span of Continuous Girder		$l_i = 0.6 l$
Cantilever Arm		$l_i = 1.5 l$

$a = \text{largest } b, \text{ but not exceeding } 0.25 l$
 $c = 0.1 l$

Figure 4-1



For $b/l_i \geq 0.7$:
 $b_m = 0.173 l_i$
 $b_s = 0.104 l_i$

Where $b_m = \text{effective flange width near mid-span}$
 $b_s = \text{effective flange width near support}$

Figure 4-2

Figure 5.30 Modifications to the AASHTO effective flange width figures 4-1 and 4.2.

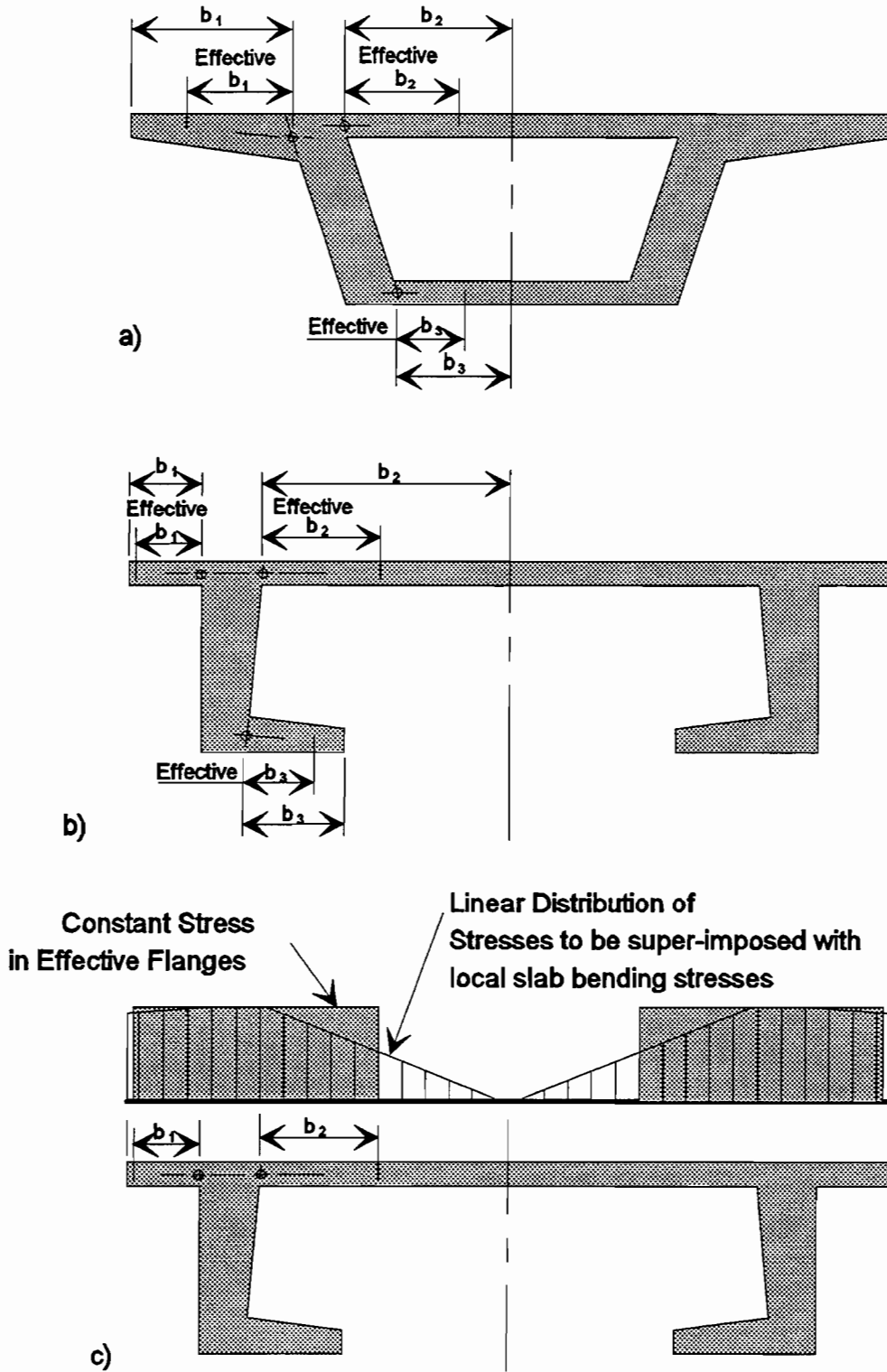


Figure 4-3 Cross Sections and Corresponding Effective Flange Widths for Bending and Shear
 Figure 5.31 Modifications to AASHTO effective flange width figure 4-3.

The following should be added to the Design Commentary Section 4.3.2:

It is important that effective flange width properties are used in the analysis of the structure. The effective cross-sectional properties must be used to determine the moment applied at the end of the girder by the post-tensioning tendons.

The pattern of stress distribution in Figure 4-4 is intended only for calculation of stresses due to anchorage of post-tensioning tendons, and may be disregarded in general analysis to determine design moments, shears and deflections. *However, it is important to consider the distribution of normal stresses over the actual section to ensure that the full width of every segmental joint is within allowable stress limits.*

5.7 Conclusions

Based on the data collected on stress distributions across flanges, the following conclusions can be made:

1. The longitudinal stress distributions across the width of winged box girders are dominated by the effects of the diffusion of post-tensioning forces from the anchorage devices into the cross-section. The AASHTO diffusion angle of 30° is acceptable for the estimation of compressive stress distributions.
2. End diaphragms stiffen the top and bottom slabs between the web walls. As a result, the slabs have measured stresses which are higher than calculated.
3. The computer program SHLAG gives good approximations of stress distributions, particularly in the wing areas.
4. The current AASHTO approach for calculating effective flange widths is overly complicated and confusing. The level of rigor is not justified by the level of accuracy. Some simplifications are presented in this chapter which reduce the rigor, relieve the confusion, and do not compromise the accuracy.
5. Designers must consider the transverse diffusion of post-tensioning forces when laying out post-tensioning anchorages to ensure adequate compression across all joints.

Simple beam theory does not adequately predict peak compressive stresses, or possible locations of tension. A more rigorous analysis is required for structures with wide wing-spans

and short span lengths. The current AASHTO approach is reasonably accurate but excessively complex. Some modifications are presented which will make design somewhat simpler, and improve accuracy.

CHAPTER 6 THERMAL GRADIENTS AND THEIR EFFECTS

6.1 Introduction

For many decades designers have been aware of the effects of annual fluctuations in the average temperature of concrete bridges. Designs allow for this fluctuation by providing expansion joints, moving bearings or flexible substructure.

Problems have occurred in segmental bridge structures in the past due to a second type of thermal effect, a thermal gradient which develops through the depth of the girder. The Newmark Viaduct in New Zealand, the Fourth Danube Bridge in Vienna, and the Jagst Bridge in Untergreisheim have all experienced cracking attributed to thermal gradients.³² Csagoly and Bollman, then of the Florida Department of Transportation, who studied the segmental bridges in the Florida Keys, reported orally to the PTI-NCHRP Specification group of NCHRP Project 20-7/32 that their measurements indicated substantial opening of some of the dry joints under daily thermal fluctuations. In Colorado cracking which was attributed to thermal gradients was discovered in the webs and bottom deck soffits of four cast-in-place segmental prestressed bridges.³³

In France, the measurements of the daily variation of support reactions in some structures (Champigny-sur-Yonne and Tourville-la-Riviere bridges) and cracks appearing in some others, showed the importance of bending moments created by differences in temperature between the top and bottom fibers of concrete bridges.⁴⁵ On the Champigny-sur-Yonne bridge, a three span continuous box girder bridge built with the cantilever method, within a 24 hour period the measured reaction at the abutment varied as much as 26%. The equivalent temperature difference between top and bottom flanges reached 18°F (10°C). In France an 18°F (10°C) linear positive temperature gradient is added to the effects of dead loads, and a 9°F (5°C) linear positive temperature gradient is added to the combined effect of all loads including live load plus impact.⁵² No negative gradient is used.

The effects of temperature differences through the depth of concrete bridges has only been recently addressed in AASHTO Specifications. In 1983 Potgieter and Gamble,⁵⁴ using weather station data from around the US in conjunction with a finite difference one-dimensional heat flow program, presented extreme positive thermal gradients (deck warmer than webs) which could be expected in bridges in various locations around the country. In 1985 NCHRP Report 276 "Thermal Effects in Concrete Bridge Superstructures"³³ proposed positive design gradients based on the Potgieter and Gamble work, and negative design gradients (deck cooler than webs) based on the British Standard BS 5400.¹⁴ In the report, the US is divided into 4 distinct regions and gradients are proposed for each area for varying deck surface conditions (concrete, thin asphalt or thick asphalt). In 1989 these recommendations were adopted into the *AASHTO Guide Specification for the Design and Construction of Segmental Concrete Bridges*¹ (to be referred to for the remainder of the chapter as the *AASHTO Guide Specification*).

Many designers feel that the thermal gradients, both positive and negative, are too complicated and too extreme. Often the same magnitude of post-tensioning is required for the thermal gradients as is required for live loads. Designers also complain that incorporating thermal gradients into design of segmental bridges makes that type of bridge uneconomical as compared to other bridge systems which are not required to include consideration of thermal gradient in design. The thermal design gradient is a requirement in the *AASHTO Guide Specification*, but is only a recommendation for all other bridge types under the general *AASHTO Standard Bridge Specification*.²

Another frequent complaint about the design recommendations is that applying the non-linear design thermal gradient can be a very complex problem. The combination of the non-linear gradient with complex box shapes can lead to extremely involved calculations.

The *AASHTO Guide Specification*, in its commentary, recommends further field research to verify the design gradients. As mentioned in Chapter 3, four segments of the San Antonio "Y" project were instrumented with arrays of thermocouples to study the thermal gradient question. In addition, other bridge instrumentation was monitored for several 12-14 hour periods to study the effects of the gradients on the structure. This chapter presents a literature review of previous studies, a description of the current research, a presentation of the results, a comparison with current design recommendations, and recommendations on design for thermal gradients.

6.1.1 Background Information.

6.1.1.1 Factors Affecting Gradient. Variations in temperature through the depth of a concrete box girder bridge are influenced by solar radiation on the top deck, ambient climatic conditions such as wind speed and temperature, and the thermal properties of the material (see Figure 6.1). A maximum positive gradient, where the deck temperature is higher than the web temperature, will occur when clear warm weather, with very light winds, follows several days of cool overcast weather. A maximum negative gradient, where the webs are warmer than the deck, will occur if a harsh cold front follows several days of warm stormy weather.⁵⁴

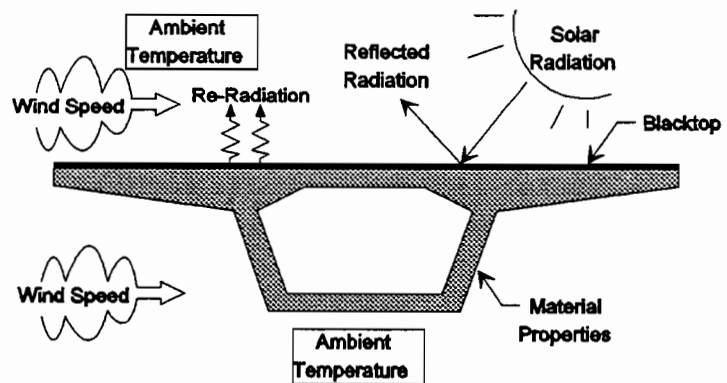


Figure 6.1 Factors affecting thermal gradient.

The material properties which affect the magnitude of the gradient are the conductivity, density, absorptivity and specific heat. Concrete's relatively low conductivity allows the high gradients to develop because the surface heats rapidly, but the heat is not transferred quickly through the depth of the member.

6.1.1.2 Factors Affecting Structural Response. The two factors which affect structural response are the linearity of the gradient and the determinacy of the structure. A statically determinant structure which is subjected to a positive linear temperature gradient will elongate and camber upwards, but will have no temperature induced stresses (see Figure 6.2).

A statically determinant beam which is subjected to a non-linear gradient will experience self-equilibrating stresses because plane sections must remain plane. The stresses are caused by the difference between the strains the structure wants to develop and the strains it is forced to develop to keep plane sections plane.

To determine the magnitude of the self-equilibrating stresses, first consider the fully restrained beam in Figure 6.3(a) subjected to the non-linear temperature gradient shown. The stress in the member caused by the full restraint of elongation and rotation is equal to:

$$\sigma_{temp} = E\alpha T(Y),$$

where

σ_{temp} is compressive if the temperature gradient is positive (warming).

The restraining axial force, P , is calculated as:

$$P = \int_Y E \alpha T(Y) b(Y) dY$$

where:

Y = distance from the center of gravity of the cross-section,
 $T(Y)$ = temperature at a depth Y ,
 $b(Y)$ = net section width at a depth Y ,
 E = modulus of elasticity,
 α = coefficient of thermal expansion.

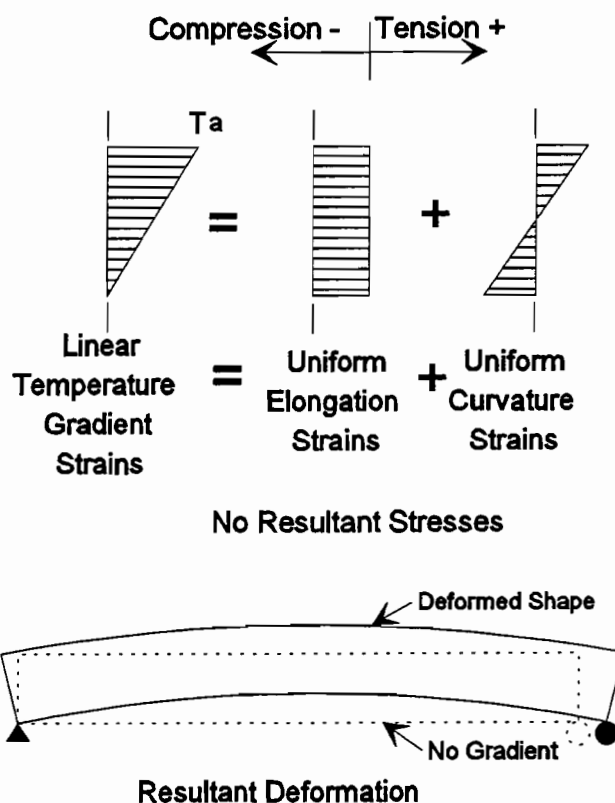


Figure 6.2 Determinant beam subjected to linear gradient

The restraining force is compressive if the temperature gradient is positive (warming).

The restraining moment acting on the section is:

$$M = \int_Y E \alpha T(Y) b(Y) Y dY$$

For the case of the determinant beam in Figure 6.3(b) which has no axial or rotational restraint, the conditions of restraint, P and M , must be removed. The remaining stresses in the beam, the self-equilibrating stresses, are the summation of the fully restrained thermal stresses and the stresses due to the released axial and bending restraint forces:

$$\sigma_{se}(Y) = E \alpha T(Y) - P/A - MY/I$$

where:

$\sigma_{se}(Y)$ = self-equilibrating stress at depth Y ,
 A = cross-sectional area,
 I = moment of inertia of section.

The net force on the section due to the self-equilibrating stresses is, as the name suggests, zero.³³

Finally, an indeterminate structure subjected to a linear or non-linear gradient will develop restraining moments at the interior piers, caused by the tendency of the structure to camber upwards from exterior support to exterior support. For a beam with pins at the supports, this causes reactions at the interior piers which hold the girder down, and this produces positive restraining moments at the interior piers (see Figure 6.4). For a girder which sits on neoprene pads, which can provide no hold down reaction, the above condition is still valid as long as the hold down reaction does not exceed the already present dead load reaction.

The solution to a thermal gradient problem can be quite complex. First the proper design gradient must be determined. From this, and the cross-sectional properties of the structure, the curvature (ϕ), the axial deformation, and the self-equilibrating stresses can be determined. The restraint stresses can then be calculated by applying the unrestrained moment (ϕEI) to the ends of the indeterminate girder and calculating the resulting restraining moments and stresses. Finally, in prestressed concrete design, the total thermal stresses, combined with other appropriate load effects, must be compared against allowable concrete stresses to ensure an uncracked service condition.

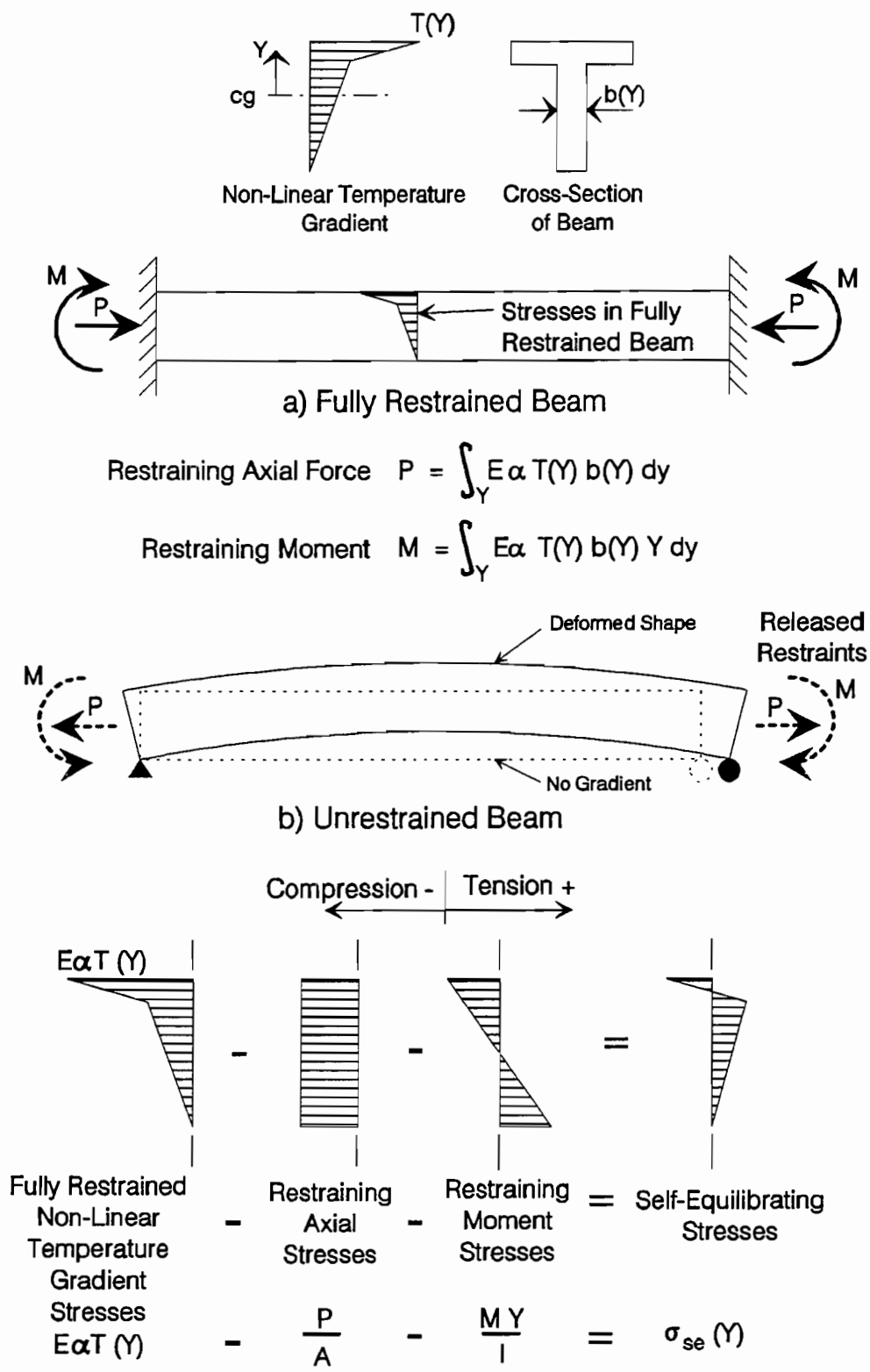


Figure 6.3 Beams subjected to non-linear gradient.

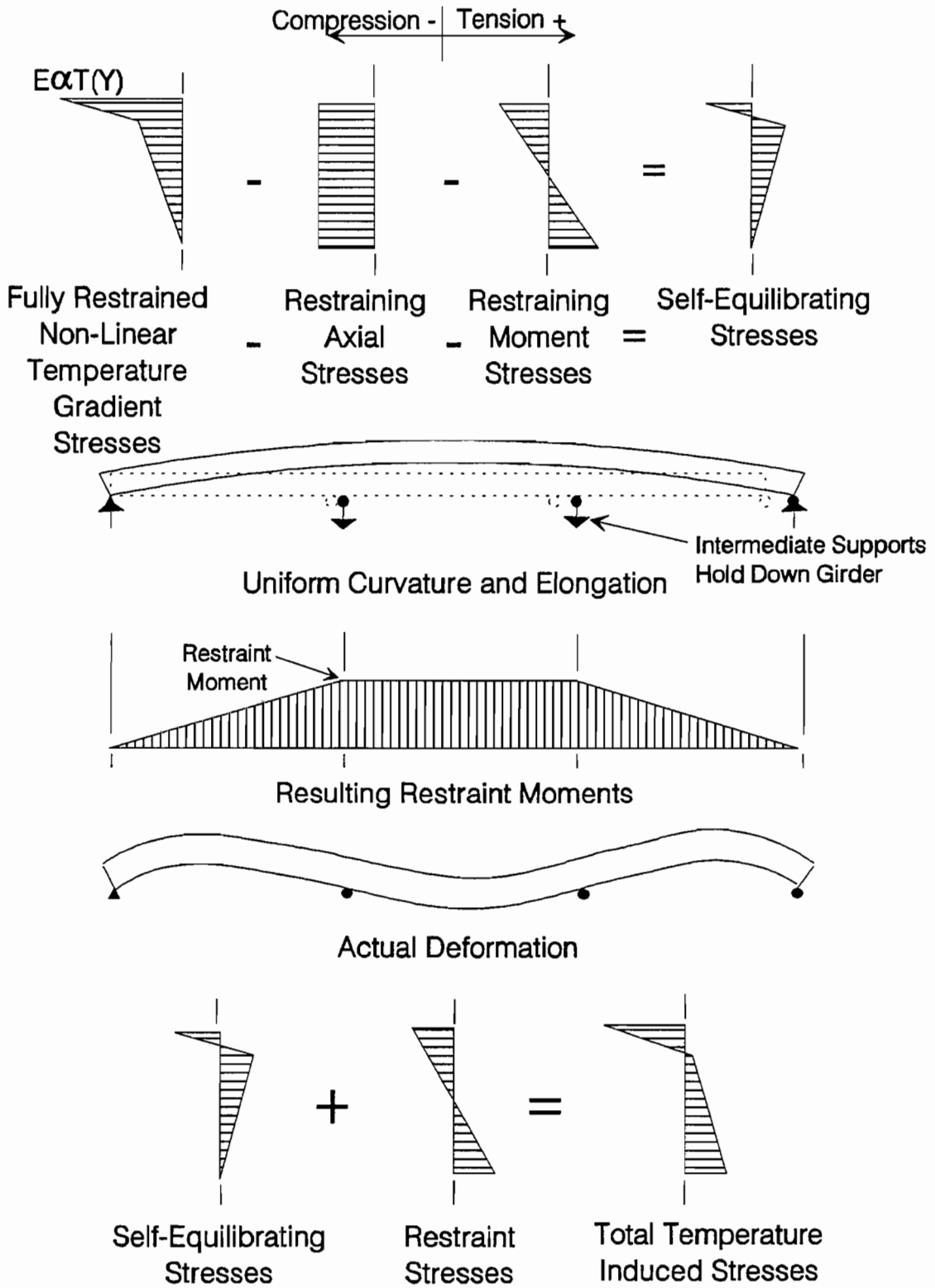


Figure 6.4 Indeterminate beam subjected to non-linear gradient.

6.1.2 AASHTO Guide Specification Approach. Section 7.4.4 of the *AASHTO Guide Specification* requires that the positive and negative differential superstructure temperature gradients from Appendix A of NCHRP Report 276 be considered in design. The *AASHTO Guide Specification* redefines the AASHTO annual temperature difference, T, as annual temperature difference plus the thermal gradient, T + DT. The *AASHTO Guide Specification* also redefines dead load, D, as dead load plus superimposed dead load plus permanent loads imposed by erection schemes and schedules, D + SDL + EL. In section 8.2.2 it is specified that in addition to AASHTO Load Groups IV, V and VI at service, one additional combination and stress shall apply (to be referred to as the Additional Thermal Load Case). The *AASHTO Guide Specification* also states that in any load combination which includes full live load plus impact a thermal differential of 0.5DT is allowed. The load combinations which consider thermal gradients are as follows:

$$\begin{aligned} \text{IV} & \quad D + (L + I)_n + CF + \beta_E E + B + SF + R + S + (T + 0.5 DT) @ 125\%, \\ \text{V} & \quad D + E + B + SF + W + R + S + (T + DT) @ 140\%, \\ \text{VI} & \quad D + (L + I)_n + CF + \beta_E E + B + SF + 3W + WL + LF + R + S + (T + 0.5 DT) @ 140\% \end{aligned}$$

Additional Thermal

$$D + \beta_E E + B + SF + R + S + DT @ 100\% ,$$

where:

D = DL + SDL + EL
 DL - Dead Load Structure Only,
 SDL - Superimposed Dead Load,
 EL - Erection Loads (final state),
 $\beta_E E$ - Earth Pressure,
 SF - Stream Flow,
 R - Rib Shortening + Creep Effects,
 S - Shrinkage,
 DT - Thermal Differential,
 W - Wind.
 LF - Longitudinal Force from Live Load,
 WL - Wind Load on Live Load,
 B - Buoyancy.

The allowable concrete stresses for segmental bridges before losses due to creep and shrinkage are:

Maximum compressive stress: $0.55f_{ci}$

Allowable longitudinal stress in the precompressed tensile zone:

- 1) for joints with minimum bonded auxiliary reinforcement through the joints sufficient to carry calculated tensile force at a stress of $0.5f_{sy}$, and internal tendons: $6\sqrt{f'_{ci}}$
- 2) for joints with no bonded auxiliary reinforcement through the joints and epoxied (Type A) joints: zero tension
- 3) for joints with no bonded auxiliary reinforcement through the joints and dry (Type B) joints: 200 psi (1379 kPa) compression

After losses $0.4f_c$ compression is allowed but there is no change in allowable tensile stresses. These can be very difficult requirements to adhere to for the temperature differential load case.

6.2 Literature Review

The following section presents previous laboratory and field investigations of thermal gradients. Measurements from actual bridge structures are compared to current design recommendations in Section 6.2.9.

6.2.1 Hoffman, McClure and West.³² Researchers at Penn State University erected a full scale segmental box girder test bridge. One of the studies performed on the bridge was the measurement of thermal gradients and the response of the structure to the gradients. The simple span bridge was instrumented with Type T (copper vs. constantan) thermocouples, as illustrated in Figure 6.5(a). Also, deflections and horizontal support movements were measured with dial gages. Eighteen daily observations were made between October 25, 1978 and October 16, 1979.

Figure 6.5(b) shows the peak positive and negative gradients measured in this study. The positive peak upward deflection from the equilibrium

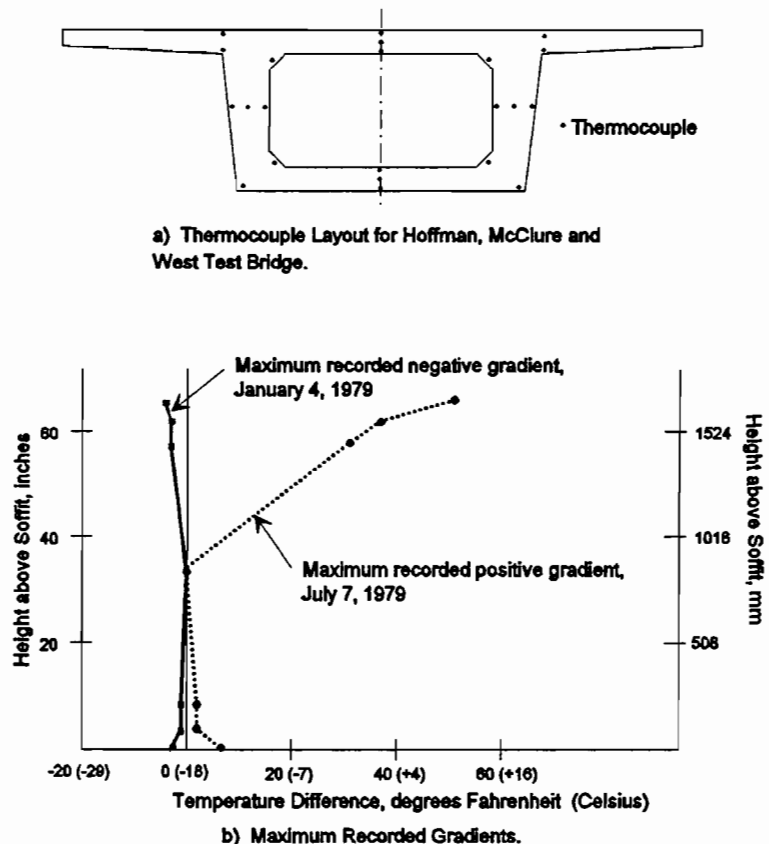


Figure 6.5 Hoffman, McClure and West study.

position (zero gradient) was 0.72" (18 mm) for the 118 foot (36 m) span. The maximum downward deflection was 0.11" (2.8 mm).

Their conclusions were:

1. The heat flow problem is nominally two-dimensional (flow along the length of the bridge is inconsequential).
2. The amount of solar radiation is the predominant input for upward deflections.

6.2.2 Hawkins and Clark.²⁹ The Denny Creek Bridge in the Cascade Mountains of Washington State was instrumented during construction with Carlson gages. Temperature data and weather data were collected from July 9, 1982 to August 14, 1982. Figure 6.6 shows the gage layout.

The results from a computer program, which used an implicit method of finite difference approximations to calculate concrete temperatures, were compared to actual bridge temperatures. The program was found to be close enough for all practical purposes.

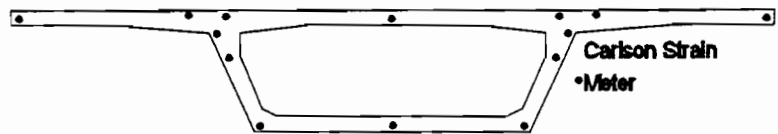


Figure 6.6 Denny Creek Bridge Carlson gage layout.

Two interesting observations were:

1. Good ventilation of a box girder bridge would significantly reduce thermal gradients.
2. Traffic reduces thermal gradients by stirring surface air. The authors assert, "Account should be taken of the average traffic speed and frequency of vehicle passage."

6.2.3 Shiu and Rasoulia.⁶⁴ The Red River Bridge near Boyce in central Louisiana was instrumented with thermocouples. Readings were taken periodically for almost 400 days. The thermocouple layout is shown in Figure 6.7. The maximum temperature difference from the top to the bottom of the

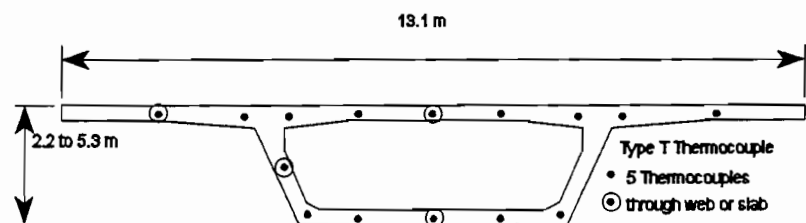


Figure 6.7 Red River Bridge thermocouple layout.

bridge was 25°F (14°C). Due to the periodic nature of the readings the authors state, "Recorded temperature difference does not by any means represent maximum temperature differential experienced by the box girder."

6.2.4 Hirst and Dilger.³⁰ Thermal gradients predicted with a finite element program were compared to data collected from two bridge structures, a light rail bridge in Canada, and a box girder bridge in Australia. The box girder bridge was monitored from July 1985 to May 1987, and very good correlation was found between actual and computed temperatures. The maximum top flange differential was measured at 18°F (-8°C).

6.2.5 Baber and Hilton.⁸ In an interim report in 1988, the plan for placing thermocouples in one segment of the James River bridge near Richmond, Virginia is presented. Figure 6.8 illustrates the Type T thermocouple layout. In addition to the box, sections of the pylon and cables were also instrumented. There are, to date, no published results.

6.2.6 Shiu.⁶⁵ The instrumentation of three bridges, Kishwaukee River Bridge in Illinois, Denny Creek Bridge in Washington State, Linn Cove Viaduct in North Carolina, is described. The Kishwaukee Bridge was monitored periodically for 5 years, and four sets of 24-hour readings were taken to study the diurnal behavior in each season. The Denny Creek Bridge instrumentation (see Section 6.2.2) is also described. 500 days of readings were taken on the Linn Cove Viaduct. Figure 6.9 shows the instrumentation for Kishwaukee and Linn Cove.

The primary conclusion from this study was:

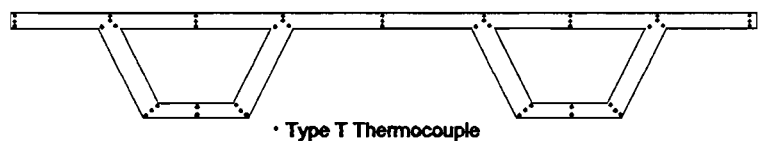
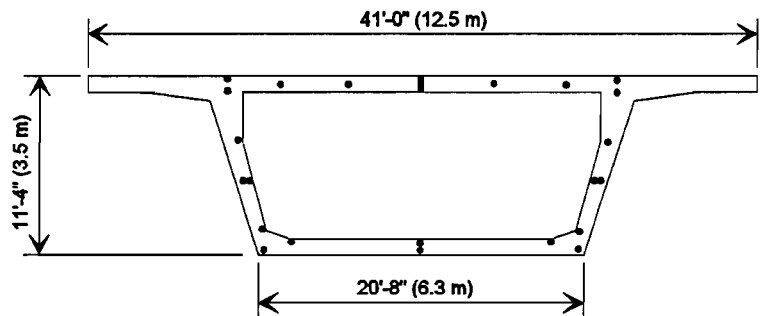
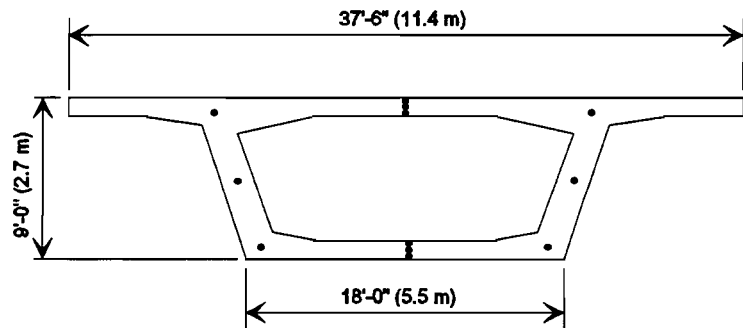


Figure 6.8 James River Bridge thermocouple layout.



• Temperature Measurement

Kishwaukee River Bridge



• Temperature Measurement

Linn Cove Viaduct

Figure 6.9 Kishwaukee Bridge and Linn Cove Viaduct temperature measurements.

Temperature differentials between the top and bottom slabs of the three bridges were +20°F (+11°C) and -10°F (-5.5°C). Measured differentials seemed to be independent of geographic location.

6.2.7 Priestley.⁵⁷ Priestley compared analytical results to measurements from a one quarter scale box girder model which was subjected to simulated ambient temperature and radiation intensity variation. Good correlation was found. A parametric study was then performed to study the influence of wind, ambient temperature, blacktop thickness and surface solar absorptivity. A design gradient for New Zealand is presented (see Figure 6.10). The shape of the gradient is a fifth order parabola over the top 1200 mm of the girder. The magnitude of the gradient is a function of the peak temperature difference, T , which varies with the depth of the blacktop surface. T is 32°C for untopped bridges, and is reduced 0.2°C for every millimeter of blacktop.

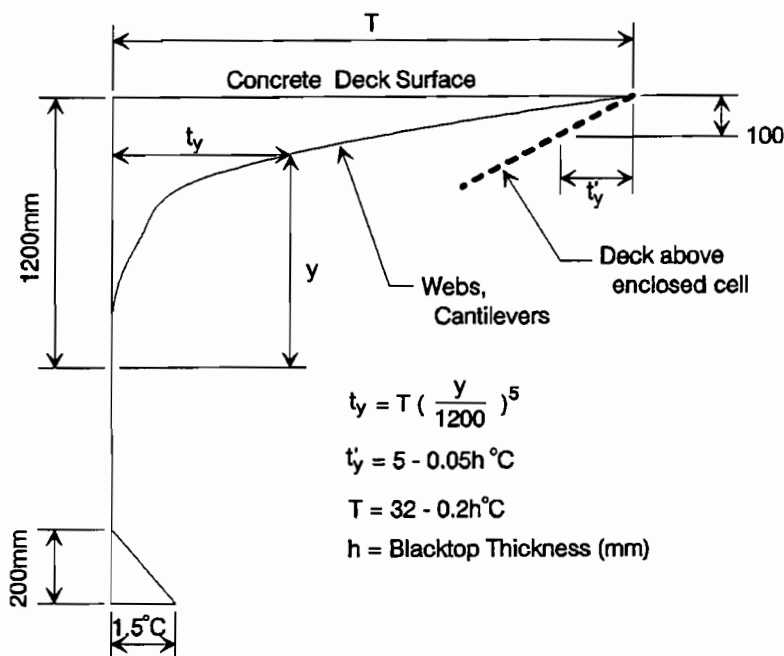


Figure 6.10 New Zealand design thermal gradient.

A discussion of the effect of thermal gradients at service levels and at ultimate load levels shows that at service load levels, due to the linear elastic behavior, the thermal deformations will produce a proportional thermal force (see Figure 6.11). At ultimate load levels, however, the factored thermal deformation is added to the deformations induced by the factored service loads. The equivalent force, in this case, is far less significant than at service load levels, and with the cracking generally expected at factored load levels, the reduced stiffness of the structure results in inconsequential thermal forces. Priestley then concludes that thermal effects are generally insignificant when assessing the ultimate load characteristics of a concrete bridge, and need only be considered during serviceability checks.

This is reinforced by Menn⁴⁶ who states:

Under service conditions, sectional forces are of interest only for the calculation of crack widths and deformations. The contribution of restrained deformations to cracking and deformations, however, can be calculated more easily and reliably using geometrical, as opposed to statical methods. The sectional forces due to restrained deformations under service conditions, therefore, need not be calculated.

At ultimate limit state, the sectional forces due to restrained deformations disappear completely with the formation of plastic hinges. Restrained deformations need therefore only be considered in systems of limited ductility, where the assumption of plastic deformations is not valid.

6.2.8 Potgieter and Gamble.⁵⁴ This study formed the basis for the design recommendations of the NCHRP 276 Report.

A one-dimensional heat flow model was used in conjunction with a finite difference method to quantify the magnitude of temperature differences at extreme conditions. The program took into account conduction, convection and radiation, and incorporated heat transfer variables and weather conditions.

Two days of field measurements were taken at the Kishwaukee River Bridge to confirm the validity of the program. The computer model gave results very similar to the actual concrete temperatures.

Data was collected from 26 weather stations around the US where solar radiation is measured. From the data, extreme conditions and hence extreme positive gradients were determined. Figure 6.12 shows the locations of the weather stations and the maximum positive gradients, for unsurfaced bridges, predicted by the computer model, and the number of days that gradient is expected to occur each year.

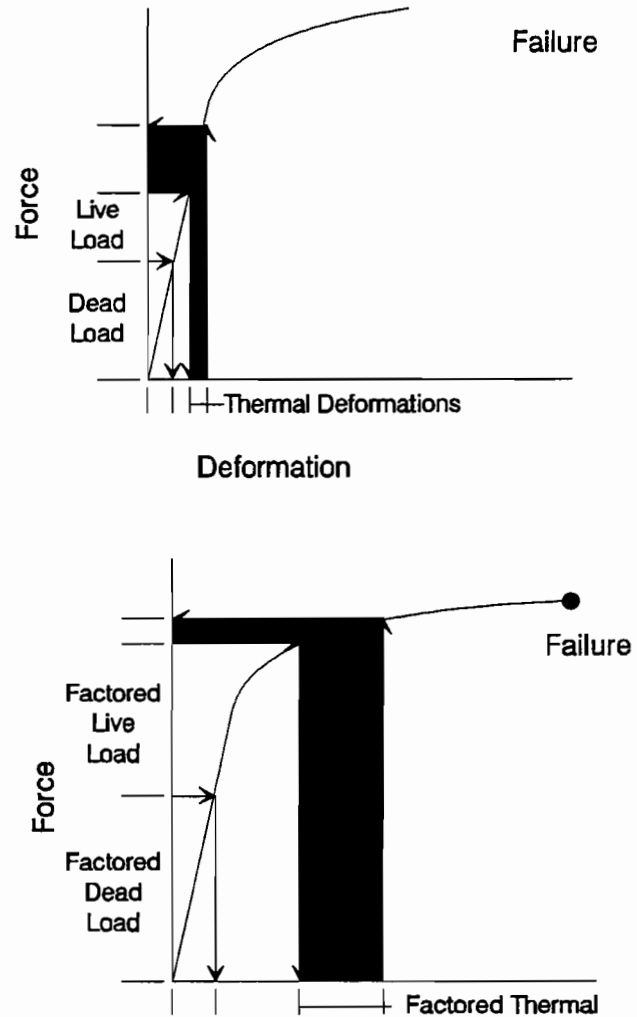


Figure 6.11 Comparison of thermal effects at service and ultimate loads.

Some of the conclusions of this study were:

1. Further study is necessary to determine the percentage of each individual bridge loading, including thermal loadings, which can be realistically expected to be applied to the bridge structure.

2. Thermal stresses are a serviceability problem and have very little effect on the ultimate bridge capacity. The accommodation of tension induced by the combination of thermal stresses with other stresses is more successful with the proportioning of deformed bar reinforcement than with post-tensioned reinforcement to prevent cracking.
3. A substantial amount of field study is necessary to evaluate the validity of the theoretically predicted thermal responses of different bridge types.

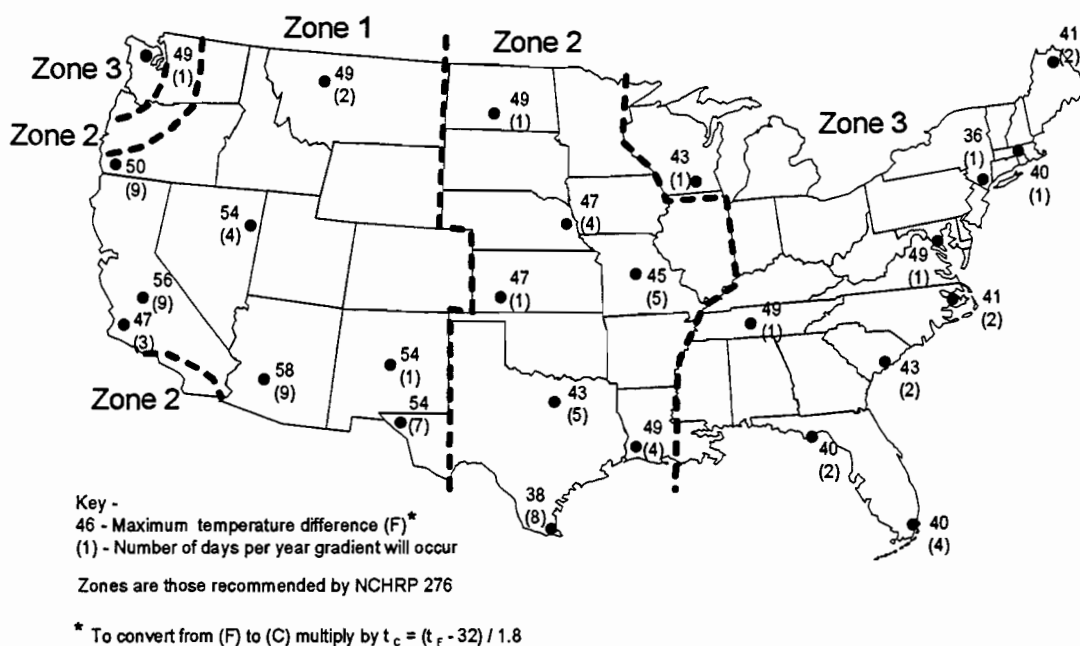


Figure 6.12 SOLMET stations and projected peak positive temperature differences.

6.2.9 NCHRP 276.³³ This report is a comprehensive overview of thermal effects in concrete bridges. Presented are incidences of cracking in bridge structures where thermal gradients are believed to be the cause. The Jagst Bridge in Germany and two bridges in Colorado are among the cited examples. A review of the parameters effecting gradients as well as methods to quantify the gradient and the bridge's response to the gradient are given. A comparison of bridge design codes from around the world, and their recommendations for thermal gradients are presented. Only four countries of the 11 reviewed (New Zealand, England, Australia and the US) required the use of a non-linear positive gradient. Four countries (Germany, Sweden, Denmark and France) recommend a linear gradient which varies from 5°C to 15°C. The other three countries (Italy, Japan and Canada) have no specified positive thermal gradient. For the negative gradient, only England and the US have a non-linear gradient. Only three countries (Germany, Sweden, and Denmark) have a linear negative gradient. All other countries' codes specify no negative gradient.

One chapter of the report is devoted to worked examples which compare moment distributions and extreme fiber stresses which result from applying various thermal gradients. They

conclude that although fiber stresses induced in different bridges by any single thermal gradient may vary in magnitude, the stress patterns are generally similar.

The most important section of the report is Appendix A, which presents the design guidelines which have been adopted by AASHTO. The United States is divided into 4 zones (see Figure 6.13) and positive and negative gradients for each zone are recommended (see Figure 6.14). The positive gradients are based on the work of Potgieter and Gamble along with information on the magnitude of solar radiation in locations around the US. The shape of the negative thermal gradient is based on the British Standard BS 5400.¹⁴ The magnitudes, for convenience, are related to the design positive gradient. There is no analytical basis for the negative gradient, and no recorded data to substantiate it.

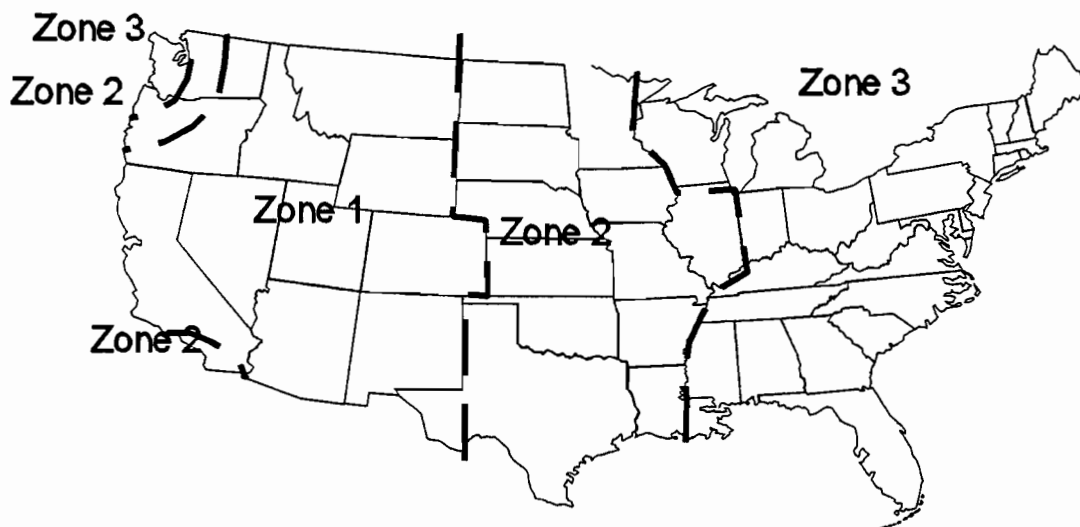


Figure 6.13 Division of U.S. into zones for thermal gradient (Hawaii - Zone 3 and Alaska - Zone 4).

Figure 6.15 shows the actual measured maximum positive gradients, and where available the negative gradients, for seven bridges around the US, and compares those gradients to the NCHRP 276 design gradients. It is apparent that most bridges experienced recorded temperatures substantially below the design recommendations. This may be attributed to the small size of the data base, and the possibility that since many of the bridges were read periodically, the extreme gradient could easily have been missed. Additional data with more continuity in monitoring is sorely needed.

TO CONVERT FROM MULTIPLY BY
 (F) to (C) $t_c = (t_f - 32) / 1.8$
 inch to millimeter 25.4
 ft. to meter 0.3048

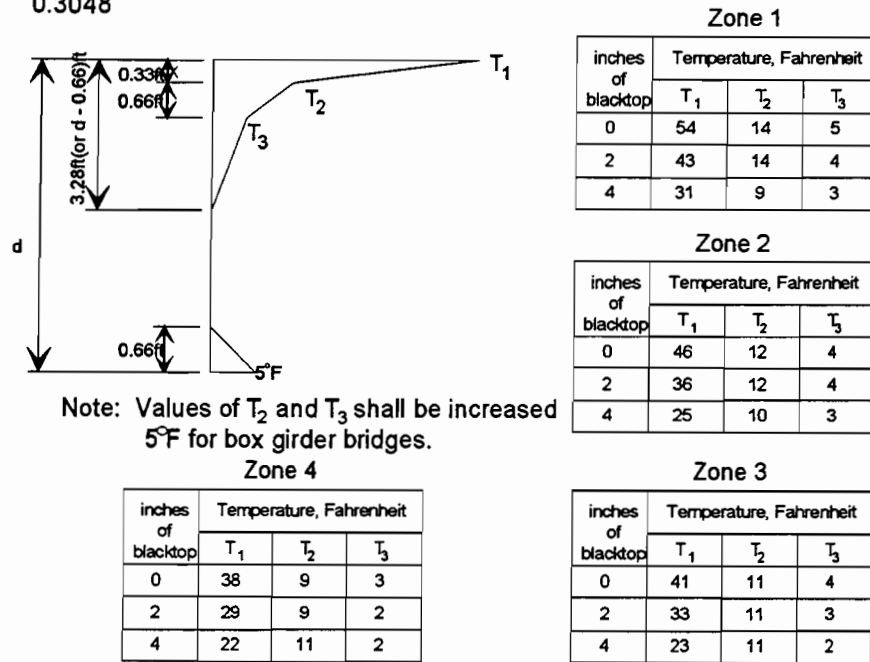


Figure 6.14a Design positive thermal gradients.

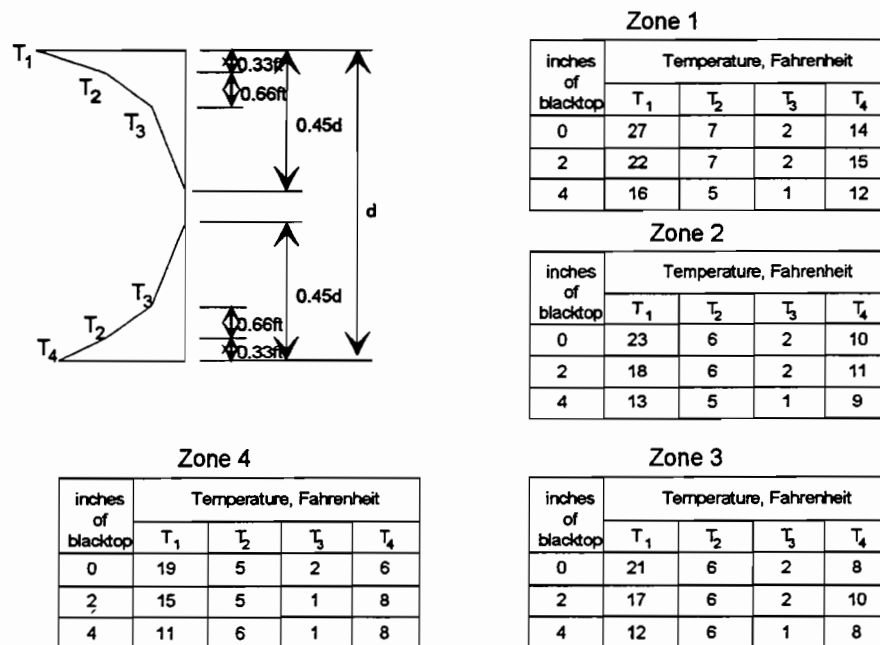
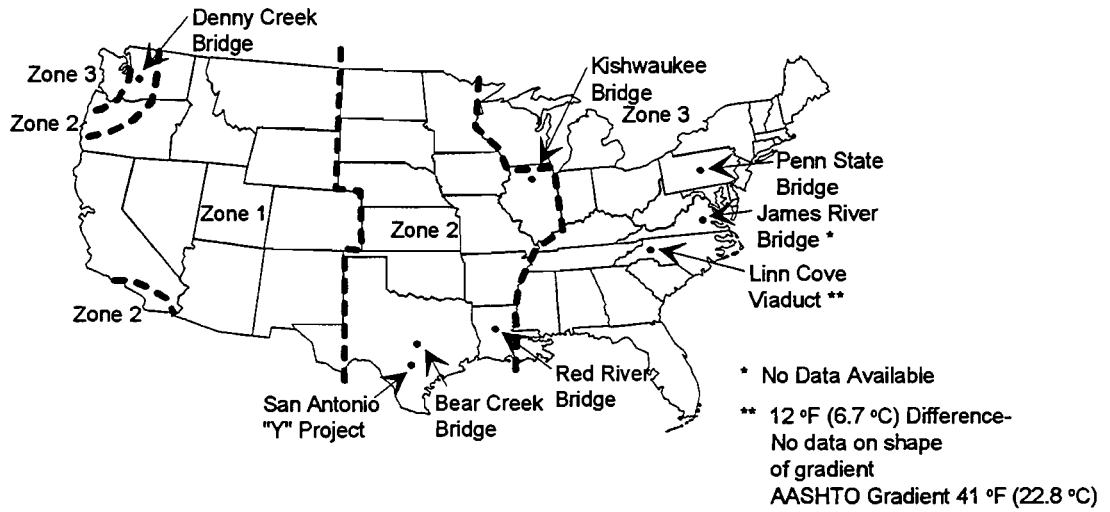


Figure 6.14b Design negative thermal gradients.



To convert from deg Fahrenheit (°F) to deg Celsius (°C) multiply by $t_c = (t_f - 32) / 1.8$.

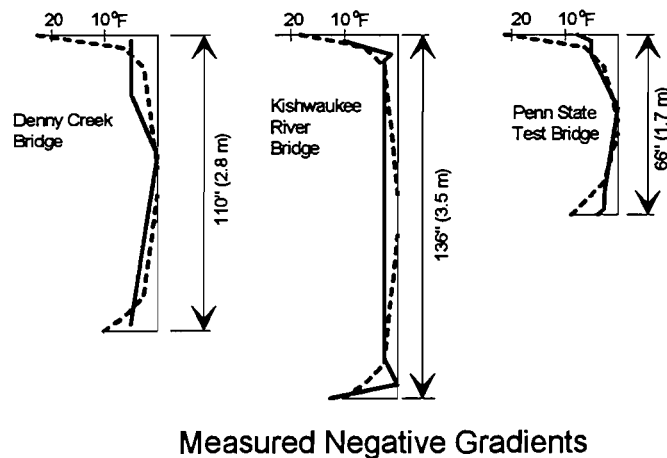
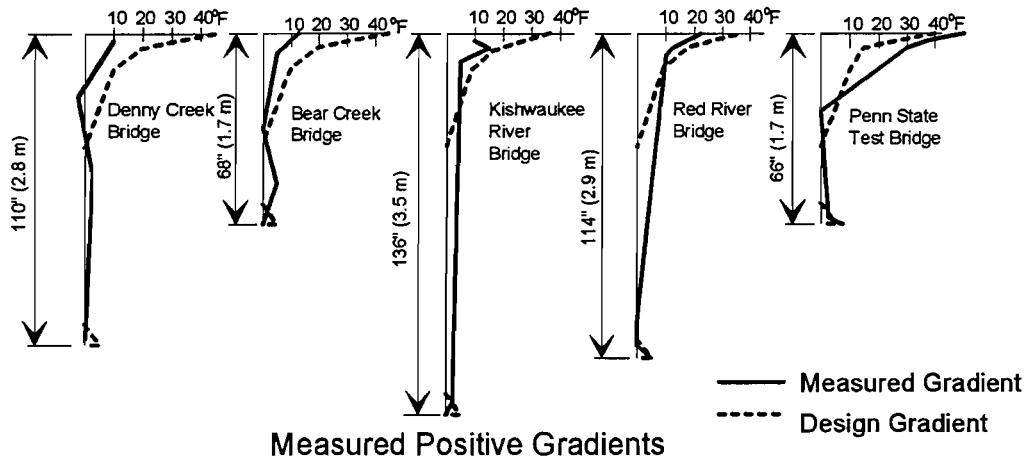


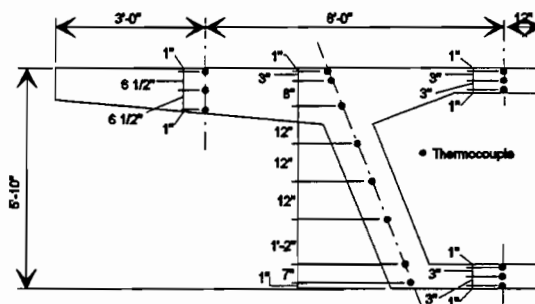
Figure 6.15 Summary of measured gradient.

6.3 Surveillance Program

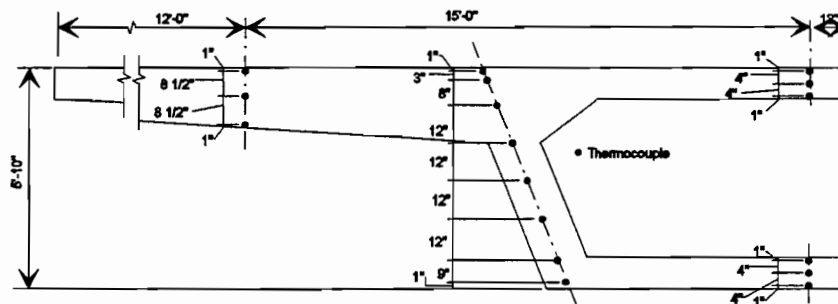
6.3.1 Thermocouples. Type T (copper vs constantan) thermocouples were installed in four segments, two segments in Span C11 and two segments of Span A44. Figure 6.16 shows the vertical positions of the gages. The arrays were located on a plane at the longitudinal mid-point of the segments. The primary array was positioned in the web wall, with additional sets of thermocouples in the top and bottom slabs and in the cantilever wings.

Two methods were used to monitor the thermocouples: manual and automatic. The manual system utilized a hand held digital thermometer and a manually operated switchbox. This system was used on the days of thermal behavior studies and the thermocouples were read every hour from approximately 7:00 am to 7:00 pm. The second system was a Campbell 21X automatic data acquisition system, which was programmed to read 8 thermocouples every 30 minutes. This system was left in place, with brief removal for battery recharge, from July 25, 1992 to July of 1993.

Additional readings were taken once a month from July 1991 to November 1991 while the segments were in the storage yard.



Type I Segment Thermocouple Layout
Segments 11C-5 and 11C-10



Type III Segment Thermocouple Layout
Segments 44A-6 and 44A-15

(To convert inch to millimeter (mm) multiply by 25.4.)

Figure 6.16 Thermocouple layouts.

6.3.2 Bridge Response. The overall bridge response was determined by measuring bridge deflections and concrete strains. On 4 separate occasions (1 spring and 3 summer) the bridge was monitored for 12 to 14 hours. Every hour temperature and deflection readings were taken, and every four hours concrete strain readings were taken.

6.3.3 Weather Conditions. On the days of bridge response surveillance, a solar radiation pyrometer was connected to the data acquisition system. In addition, temperatures inside, underneath and on top of the bridge were recorded with the hand held thermometer. Additional weather information was provided by the Local Climatological Data Monthly Summary.⁴⁸

6.3.4 Coefficient of Thermal Expansion. Eight cylinders, four from segments in Span C11 and four from segments in Span A44, were used to evaluate the coefficient of thermal expansion. The cylinders were each equipped with two sets of Demec locating discs. Over the course of several months the cylinders were cycled between a 32°F (0°C) freezer and a 100°F (38°C) oven. After the cylinders had remained at a constant temperature for at least two days, a Demec reading was taken, and the cylinders were moved to the other extreme condition. The coefficient of thermal expansion, averaged for all eight cylinders over 10 cycles, was $5.0 \times 10^{-6}/^{\circ}\text{F}$ ($9.0 \times 10^{-6}/^{\circ}\text{C}$). This coefficient was used in evaluating the bridge response.

6.4 Presentation of Results

6.4.1 Measured Thermal Gradients.

6.4.1.1 Positive Temperature Gradients. Figure 6.17 shows the maximum recorded positive thermal gradients measured during 10 months of continuous readings. The bridge had no topping from erection in April of 1992 to the end of March 1993. The topping was completed on March 25, 1993. Temperature readings, presented herein, were taken continuously from July 25, 1992 to May 25, 1993. The measurement system was left in place so continued readings could be taken. In Figure 6.17, the measured gradients with and without topping are compared to the AASHTO design positive gradients for box girders in the San Antonio area. The gradients were measured with 8 thermocouples, 7 in the web and one in the top slab. A comparison of the temperatures in the top slab over the web to those in the top slab over the box and in the cantilever wings shows that the wings and top slab are from 1°F to 5°F (0.6 to 2.8° C) warmer than the slab above the web. Figure 6.18 compares peak positive gradients of the top slab, web and wing for segment 44A-6 on July 16. This day showed the most extreme differences. On other cooler days, the difference between temperature of the web and the top slab and the wings was not as great.

Figure 6.19 shows the magnitude of the maximum temperature differences between the coolest web temperature and the temperature of the top slab over the box which were recorded over the course of many months while the automatic data acquisition system was operating.

To convert from (F) to (C) multiply by $t_c = (t_f - 32) / 1.8$

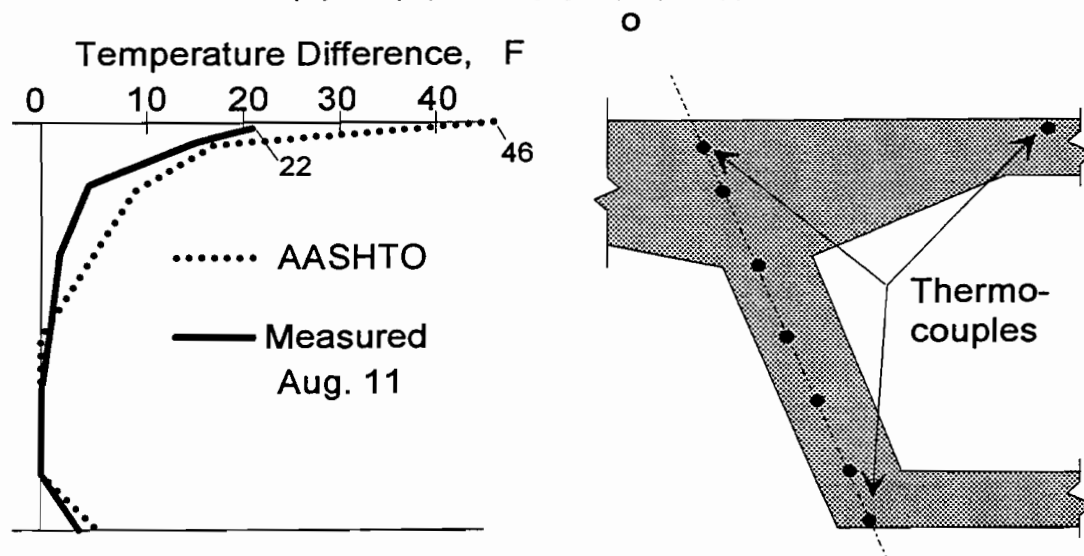


Figure 6.17a Max. positive temp. gradient recorded between July 16, 1992 and March 25, 1993 (no topping). Gradient occurred August 11, 1992.

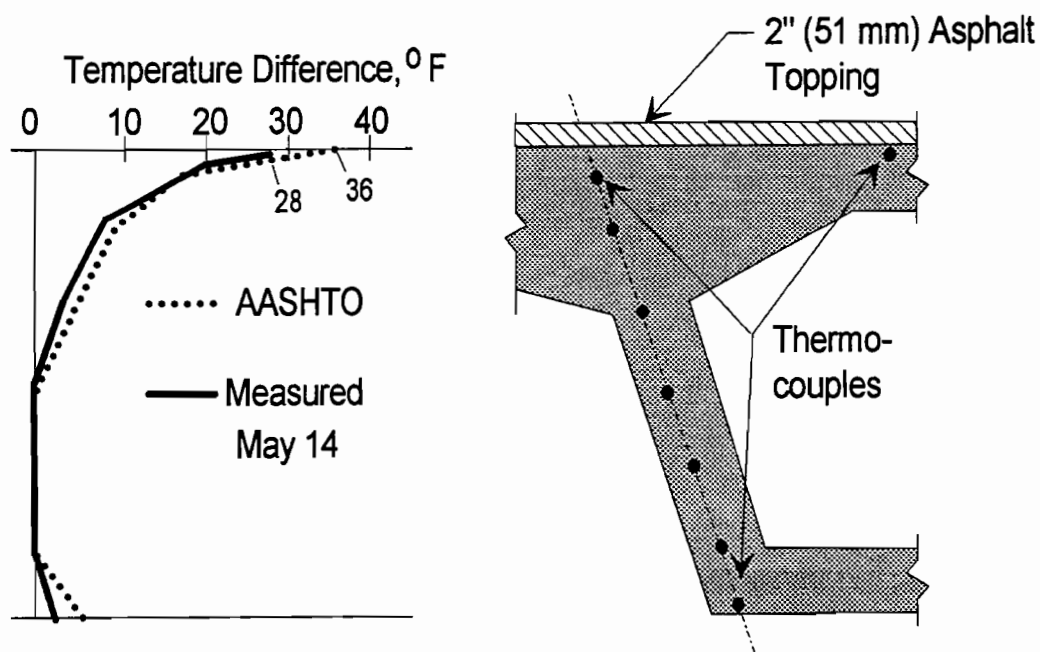


Figure 6.17b Max. positive temp. gradient recorded between March 26, 1993 and May 25, 1993 (2 in. (51 mm) asphalt topping). Gradient occurred May 14, 1993.

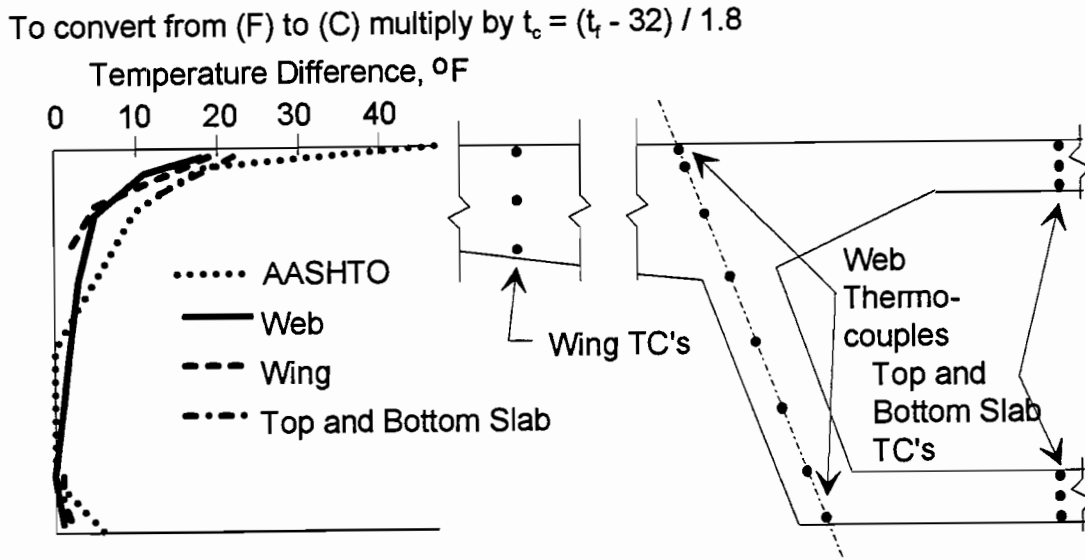


Figure 6.18 Comparison of wing, web and slab temperatures on July 16, 1992.

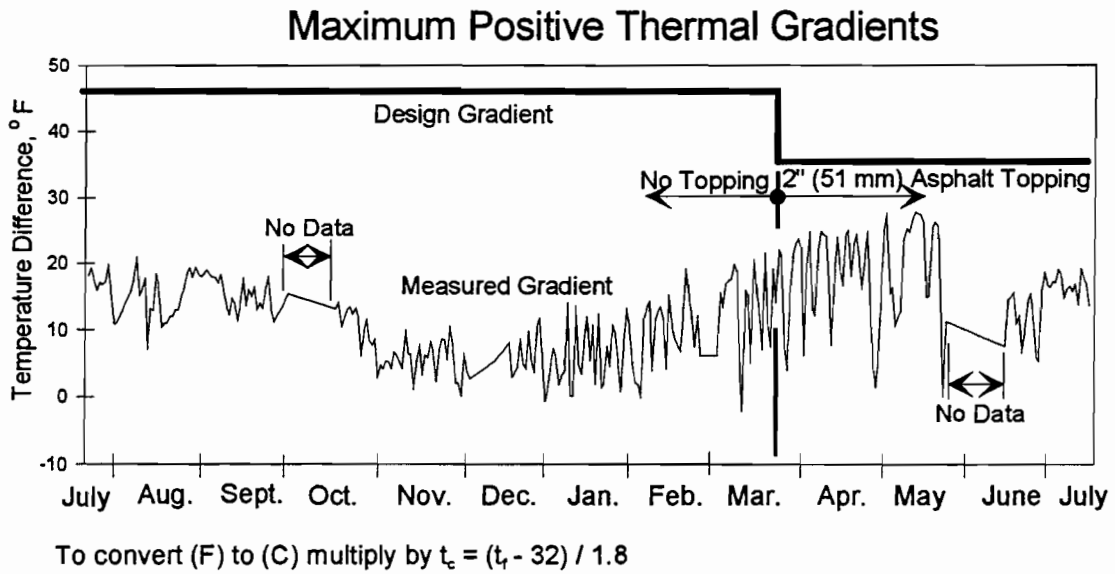


Figure 6.19 Maximum positive gradients from July 25, 1992 to July 14, 1993.

Some observations from the positive thermal gradient data are:

1. The maximum recorded thermal gradient for the bridge with no topping had the same shape as the design gradient, but only 50% of the magnitude.
2. The maximum recorded thermal gradient for the bridge with 2 inch (51 mm) asphalt topping had the same shape as the design gradient and 78% of the magnitude.
3. The peak temperatures in the top slab immediately above the web are slightly less than those in the cantilever wing and in the top slab over the box.
4. The average monitored maximum positive gradient over an 8 month period for the no topping case falls far below the design recommendation (approximately one third of the value), but with the 2 inch (51 mm) asphalt topping the average monitored maximum positive gradient over two months was much closer (approximately three fourths of the value). It should be noted that the original analysis by Potgieter and Gamble was confirmed with data from the Kishwaukee Bridge which had an asphalt topping. No data from an untopped bridge was studied. The absorptivity constant for bare concrete which was assumed in the analysis has a great impact on the calculated gradient. Potgieter and Gamble used a high value for the absorptivity which assumed the concrete was smooth and dirty from passing traffic and pollution. The concrete in the San Antonio "Y" project is very light in color due to the white crushed limestone aggregate, and the surface is roughened. These factors could cause the absorptivity of the concrete to be less than that assumed in the development of the design gradient.

6.4.1.2 Negative Temperature Gradients. Figure 6.20 shows the maximum recorded negative thermal gradients for the topped and untopped bridge, and compares them with the AASHTO design negative gradients for bridges in the San Antonio area. Only one day of data showing large negative gradients is available to compare web, top slab and wing temperatures. This reading showed that the wings and top slab cool more quickly than the slab above the webs. At the extreme negative gradient, the top slab over the wings was 4°F (2.2°C) cooler than the slab above the web.

Figure 6.21 shows the magnitude of the maximum temperature differences between the warmest web temperature and the temperature of the top slab which were recorded over the course of many months while the automatic data acquisition system was in place.

To convert from Fahrenheit (F) to Celsius (C) multiply by $t_c = (t_f - 32) / 1.8$.

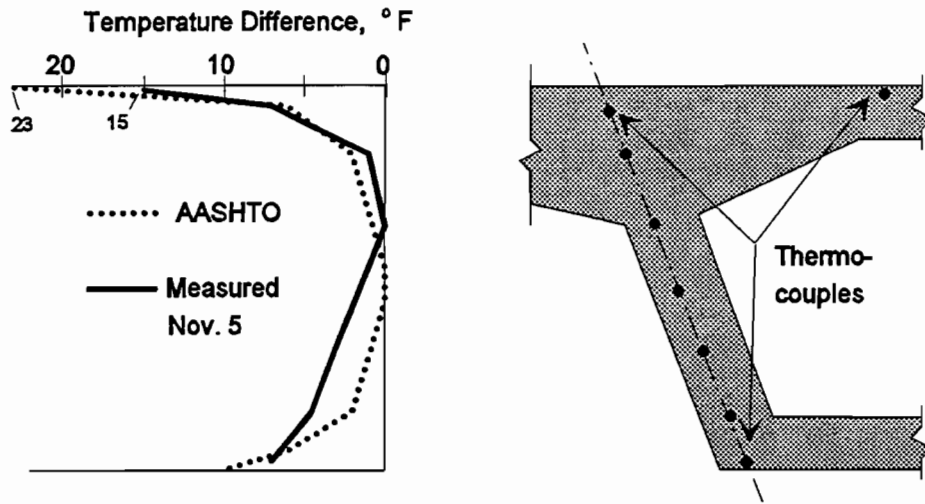


Figure 6.20a Maximum negative temperature gradient recorded between July 16, 1992 and March 25, 1993 (no topping). Gradient occurred November 5, 1992.

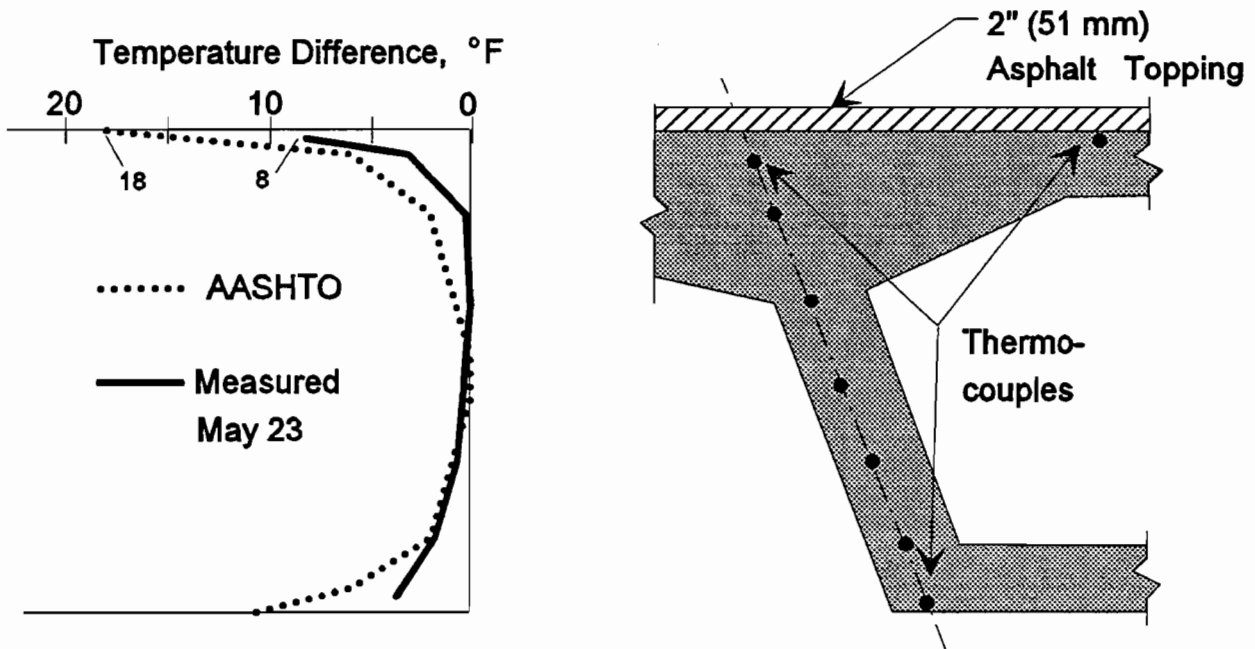
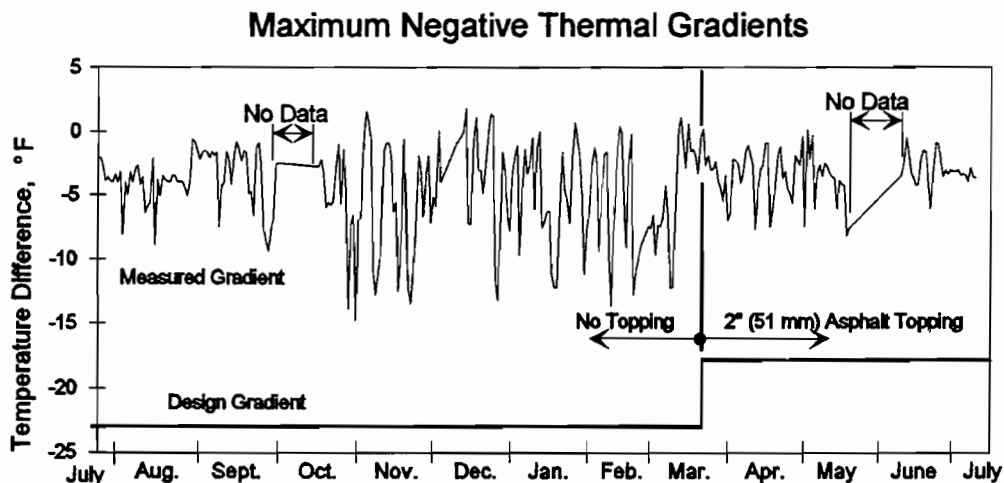


Figure 6.20b Maximum negative temperature gradient recorded between March 26, 1993 and May 25, 1993 (2 in. (51 mm) asphalt topping). Gradient occurred May 23, 1993.



To convert from Fahrenheit (F) to Celsius (C) multiply by $t_c = (t_f - 32) / 1.8$.

Figure 6.21 Maximum negative gradients from July 25, 1992 to July 14, 1993.

Some observations from the negative thermal gradient data are:

1. The peak measured negative thermal gradient for the unsurfaced case is closer to the predicted level than the positive gradient. The peak measured negative gradient (15°F) (8.3°C) was 65% of the design value of 23°F (12.8°C).
2. The peak measured thermal gradient for the bridge with topping (8°F) (4.4°C) is only about 50% of the design value of 18°F (10°C), but the data only reflects approximately 2 months of data during relatively warm spring months.
3. The shape of the negative thermal gradient is similar to the design gradient.
4. The top deck and cantilever wings cool somewhat more quickly than the webs.

6.4.1.3 Solar Radiation. Solar radiation readings were read on four occasions. Unfortunately, due to programming and wiring errors, only one day of data is reliable. The solar radiation measured on July 16, 1992 is shown in Figure 6.22. It is compared with two predictions of solar radiation, one by the NBS(NIST)⁴⁰ and the other presented by Potgieter and Gamble.⁵⁴ The levels of solar radiation reaching the bridge are actually

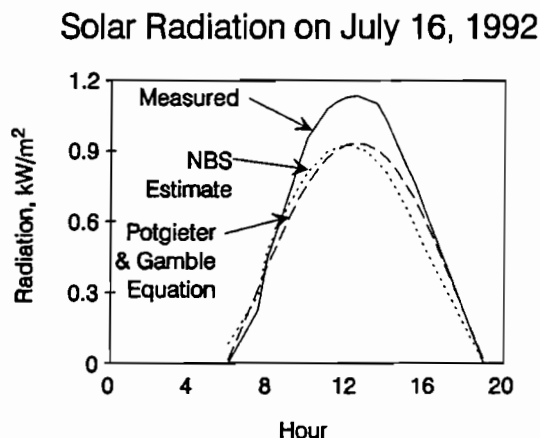


Figure 6.22 Solar radiation on July 16, 1992.

higher than the assumed values used to establish the design gradient, although the measured gradient for the untopped bridge was lower than the design gradient.

6.4.2 Bridge Response. On four occasions the bridge was monitored over the course of one day. Three times Spans A43 and A44 were measured and once Span C11 was measured. This section will present the measured deflections and concrete strains and compare them to calculated values.

6.4.2.1 Spans A43 and A44. These two spans were monitored on three occasions, July 16, August 13, and August 27 of 1992. The August 13 data will not be presented because the day was cool and overcast and the changes in readings were insignificant.

Deflections. In order to compare measured and calculated deflections, the difference in temperatures, from the time of most uniform temperature distribution to the time of highest gradient, at each thermocouple location was determined. Since the wings and top slab get somewhat hotter than the slab above the webs, a weighted average of the measured temperatures across the width of the box was used to compute the gradient.

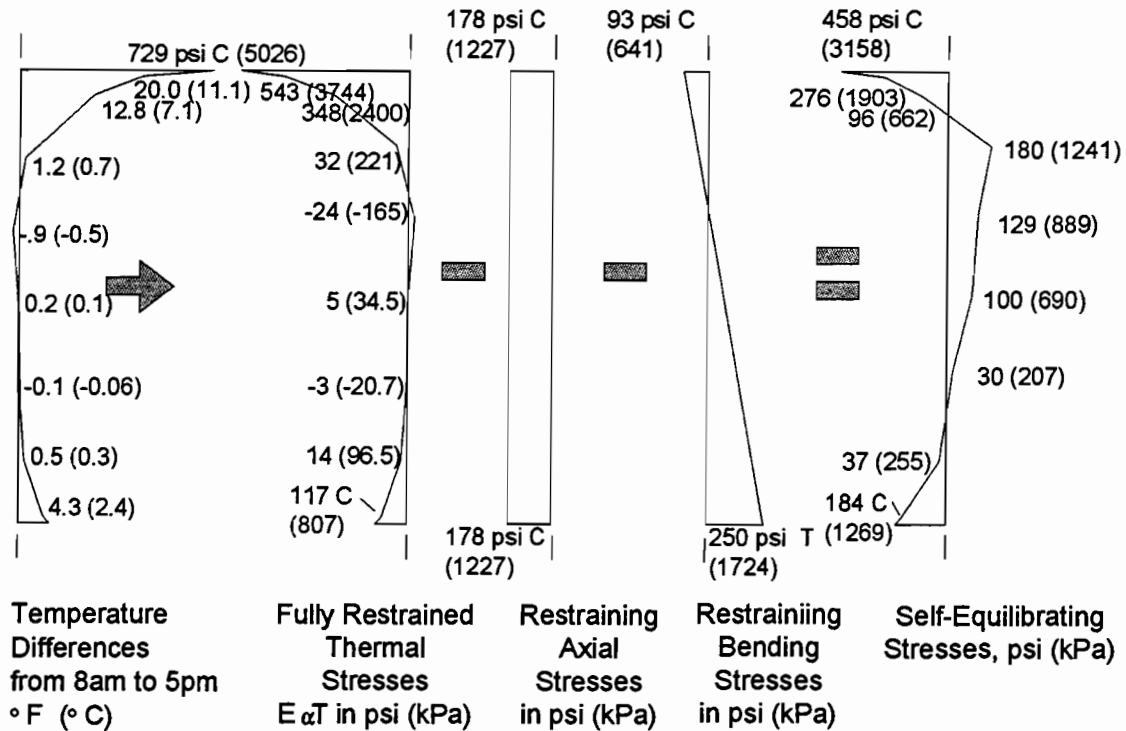
Using methods outlined in the NCHRP 276 Report,³³ the measured temperature differences were used to calculate the restraining axial load and moment for a fully restrained beam (see Figure 6.23). The released restraint moment was then applied to the ends of the continuous beam to determine the restraining moments due to continuity (see Figure 6.24). The resultant deflections were then computed. The deflections calculated with this method are compared to the measured peak deflections in Figure 6.25. The agreement between the calculated and actual deflections is quite good, within 0.02" (0.51 mm) or $1/66000$.

On both days, the measured deflection is slightly greater than expected. This could be attributed to effective cross-sectional properties smaller than those used in the calculations, or an in-situ coefficient of thermal expansion greater than that measured with the test cylinders ($5.0 \times 10^{-6}/^{\circ}\text{F}$ or $9 \times 10^{-6}/^{\circ}\text{C}$).

Concrete Strains. The concrete strain readings were inconclusive. The range of expected strains is 20-40 microstrain tension. With the Demec Extensometer 20-40 microstrain is 3 to 5 units on the dial gage. An acceptable range of reader error is ± 2 units. This will lead to $\pm 50\%$ error in the expected range of strain. Still, the Demec readings show general trends.

Figure 6.26 compares the calculated and measured web strain profiles at various locations along the two spans. The readings are generally in agreement with expected values, considering the great effect of reader error on the results.

6.4.2.2 Span C11. Span C11 was monitored on one day only, March 19, 1992. At this time the two span unit (C11 and C12) was not yet transversely post-tensioned to its adjacent mainline spans, and hence was acting independently.



Modulus of Elasticity = $E = 5437 \text{ ksi (37488 Mpa)}$
 Coefficient of Thermal Expansion = $\alpha = 0.000005e / ^\circ\text{F (0.000009e / } ^\circ\text{C)}$
 Cross-Sectional Areas = $98.4 \text{ ft}^2 (9.1 \text{ m}^2)$
 Moment of Inertia = $I = 299.5 \text{ ft}^4 (2.6 \text{ m}^4)$
 Center of Gravity = $4.25 \text{ ft. (from bottom of section) (1.3 m)}$
 Restraining Thermal Moment = $\int E\alpha T(Y) b(Y) Y dY = 30489 \text{ in-k (3445 kN-m)}$
 Restraining Thermal Axial Load = $\int E\alpha T(Y) b(Y) dY = 2521 \text{ k. (11213 kN)}$

Figure 6.23 Thermal forces on fully restrained Type III unit, caused by temperature changes on July 16, 1992. (See Appendix B⁶¹ for integration.)

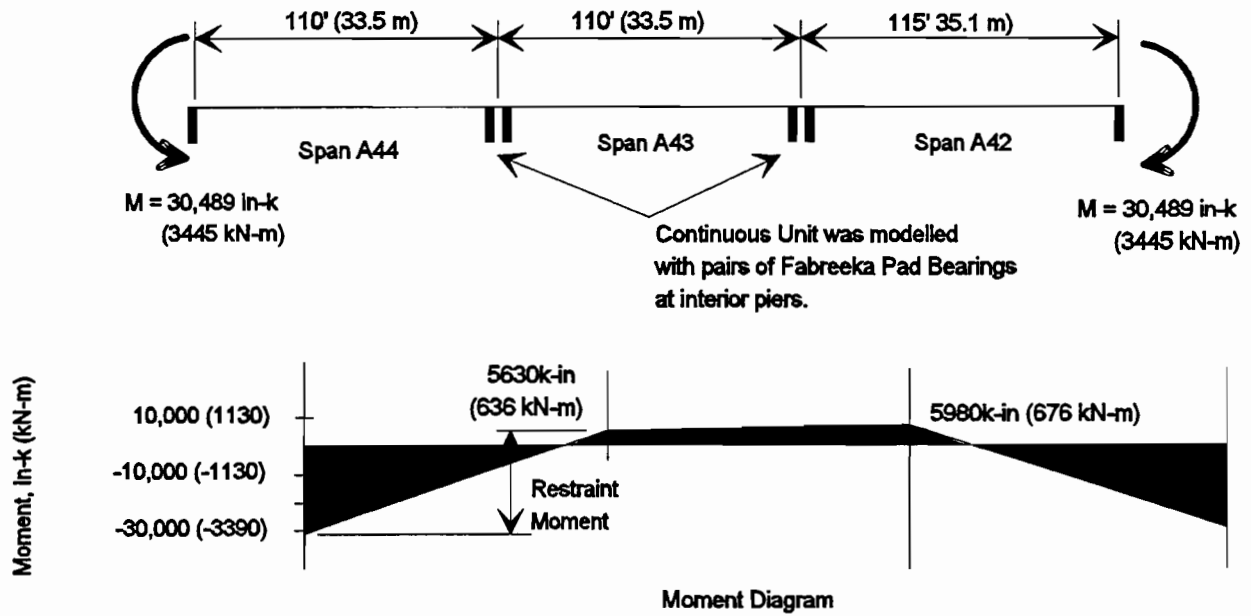


Figure 6.24 Determination of restraint moments for July 16, 1992.

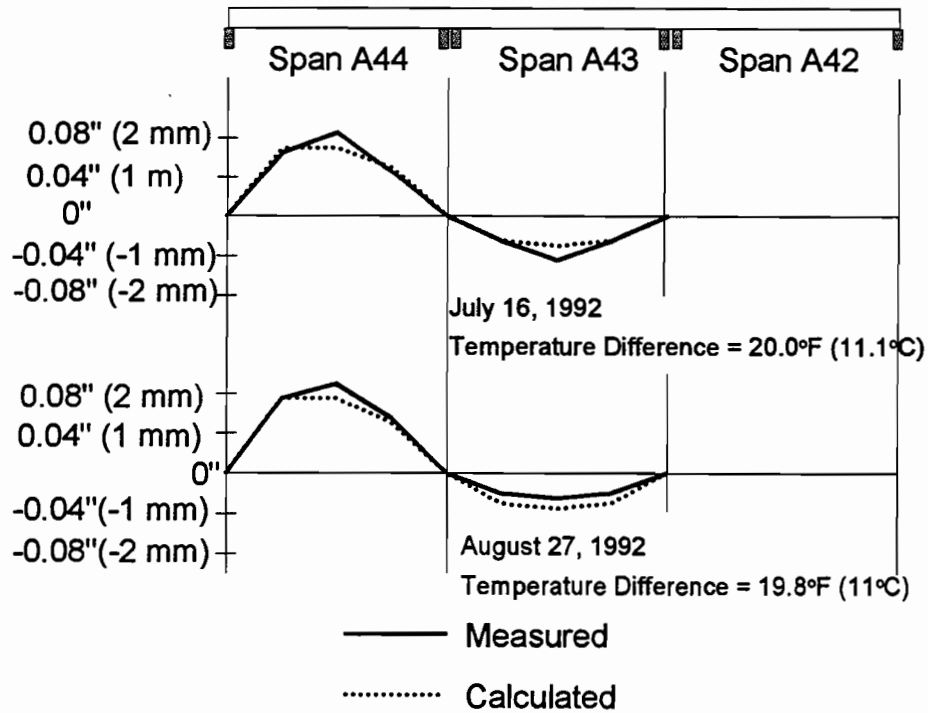
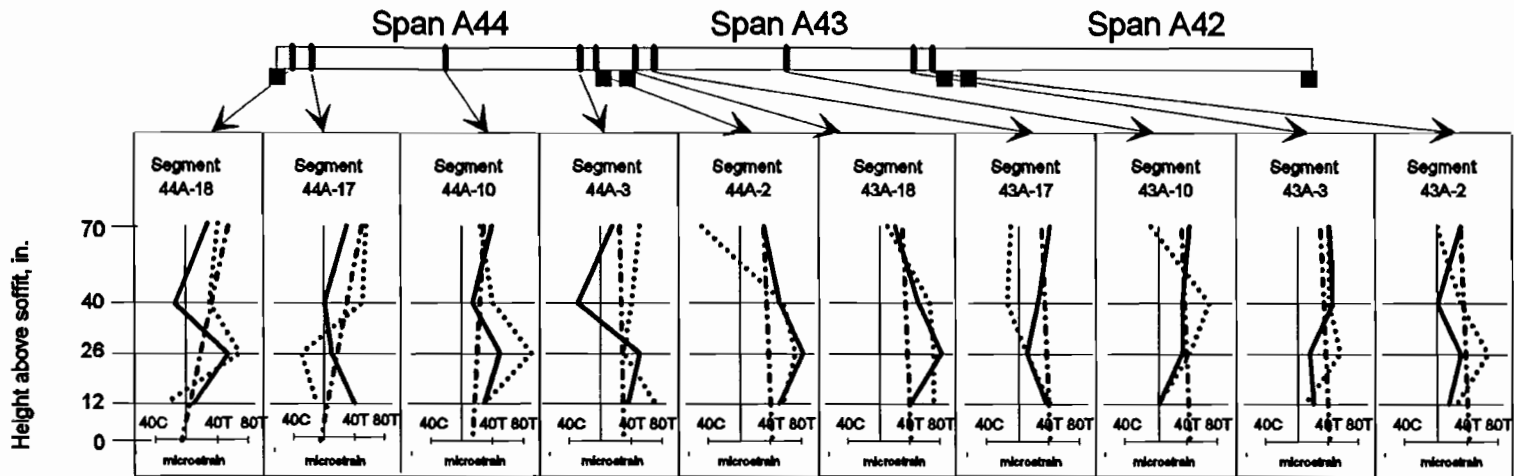
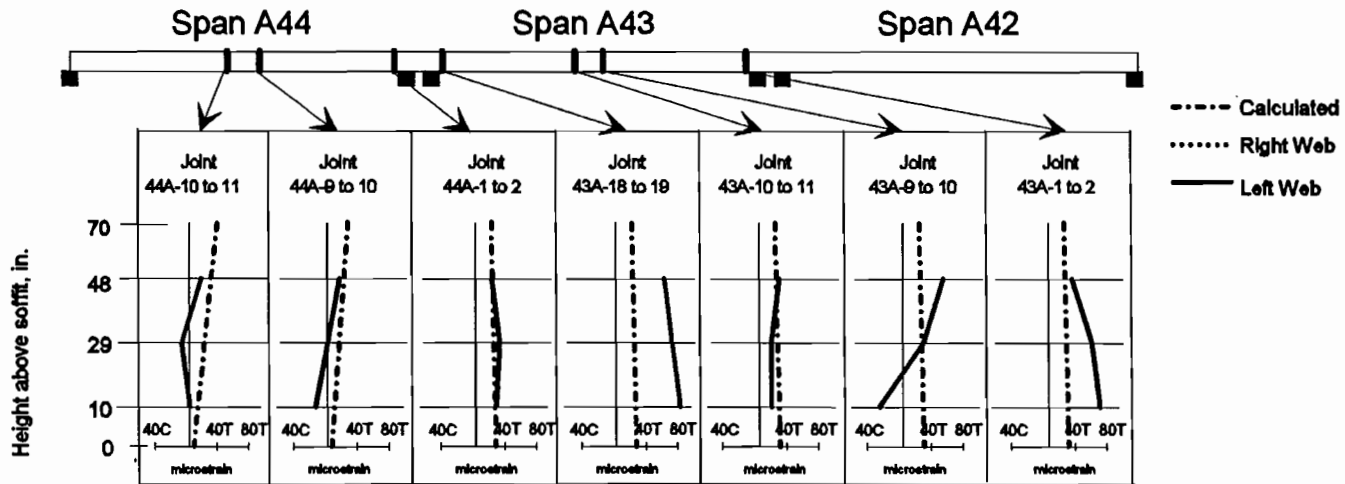


Figure 6.25 Measured and calculated deflections caused by thermal gradients.

Figure 6.26 Web strains profiles from spans A43 and A44, caused by thermal gradients.



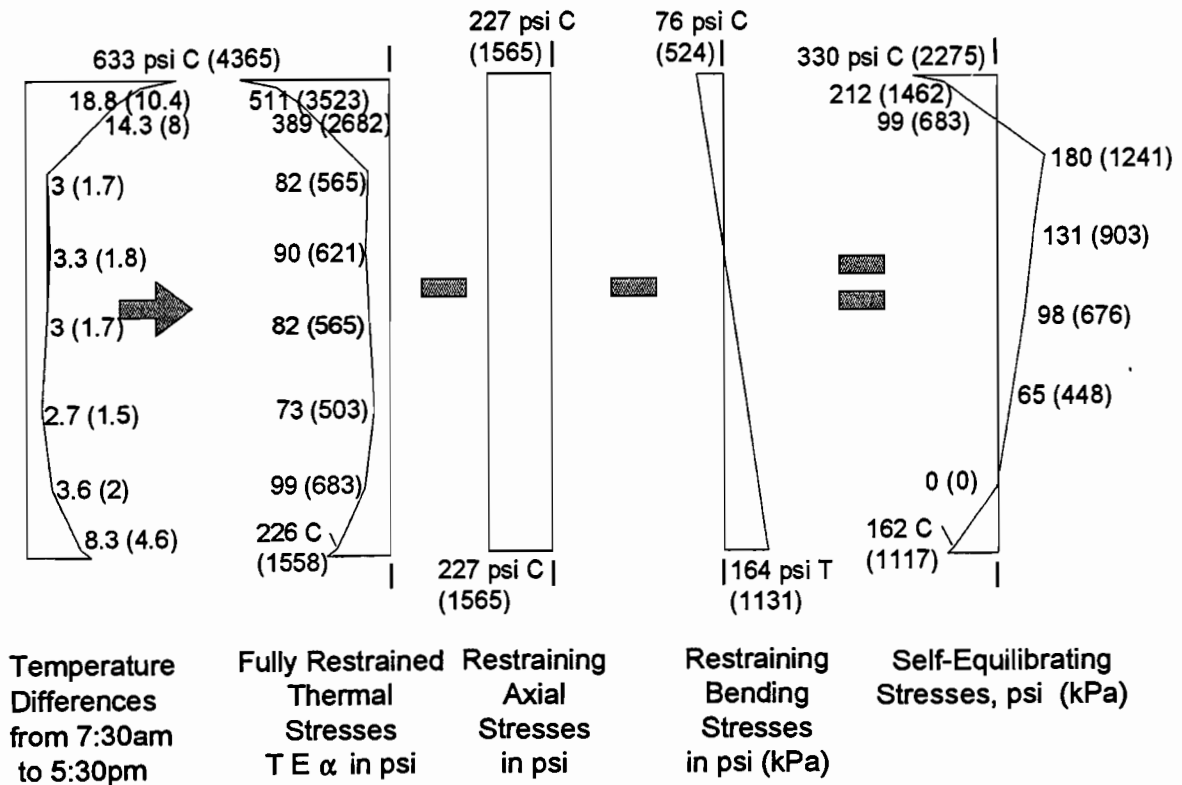
Strain Profiles from July 16, 1992



Strain Profiles from August 27, 1992

To convert inch to millimeter multiply by 25.4.

Deflection. Figure 6.27 shows the difference in temperatures from the 7:30 am reading, when the temperatures were close to uniform, and the 5:30 pm temperatures which had the highest gradient.



Modulus of Elasticity = $E = 5437 \text{ ksi (37488 Mpa)}$
 Coefficient of Thermal Expansion = $\alpha = 0.000005e / ^\circ\text{F (0.000009e / } ^\circ\text{C)}$
 Cross-Sectional Areas = $41.9 \text{ ft}^2 (3.9 \text{ m}^2)$
 Moment of Inertia = $I = 159.3 \text{ ft}^4 (1.37 \text{ m}^4)$
 Center of Gravity = $4.0 \text{ ft. (from bottom of section) (1.2 m)}$
 Restraining Thermal Moment = $\int E \alpha T(Y) b(Y) Y dY = 11301 \text{ in-k (1277 kN-m)}$
 Restraining Thermal Axial Load = $\int E \alpha T(Y) b(Y) dY = 1369 \text{ k. (6089 kN)}$

Figure 6.27 Thermal forces on fully restrained Type I unit, caused by temperature changes on March 19, 1992. (See Appendix B⁶¹ for integration.)

The deflections were calculated in the same manner as was used for Span A44. Figure 6.28 shows the comparison of calculated and measured deflected shapes. As with Spans A44 and A43, the measured deflection is slightly higher than calculated, but the actual deflected shape is very similar to calculated.

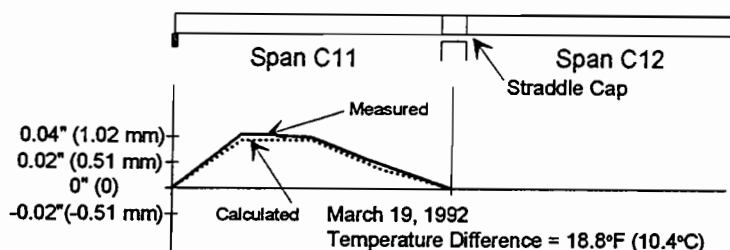


Figure 6.28 Measured and calculated deflections caused by thermal gradients in span C11.

Concrete Strains. Figure 6.29 shows the web strain profiles at five locations along the length of the span. The reader error of ± 16 microstrain accounts for the somewhat erratic profiles. The slopes of the profiles are similar to calculated, but the magnitudes are consistently smaller. This could be caused by some unexpected longitudinal restraint at the sliding bearing.

6.4.2.3 Observations. The bridge response to the measured thermal gradients was very close to predicted. The actual deflections were slightly greater than calculated and the strains were slightly smaller. The method for calculating response is somewhat tedious, especially due to the non-linearity of the gradient and the complex shape of the box-girder, but the results are quite accurate.

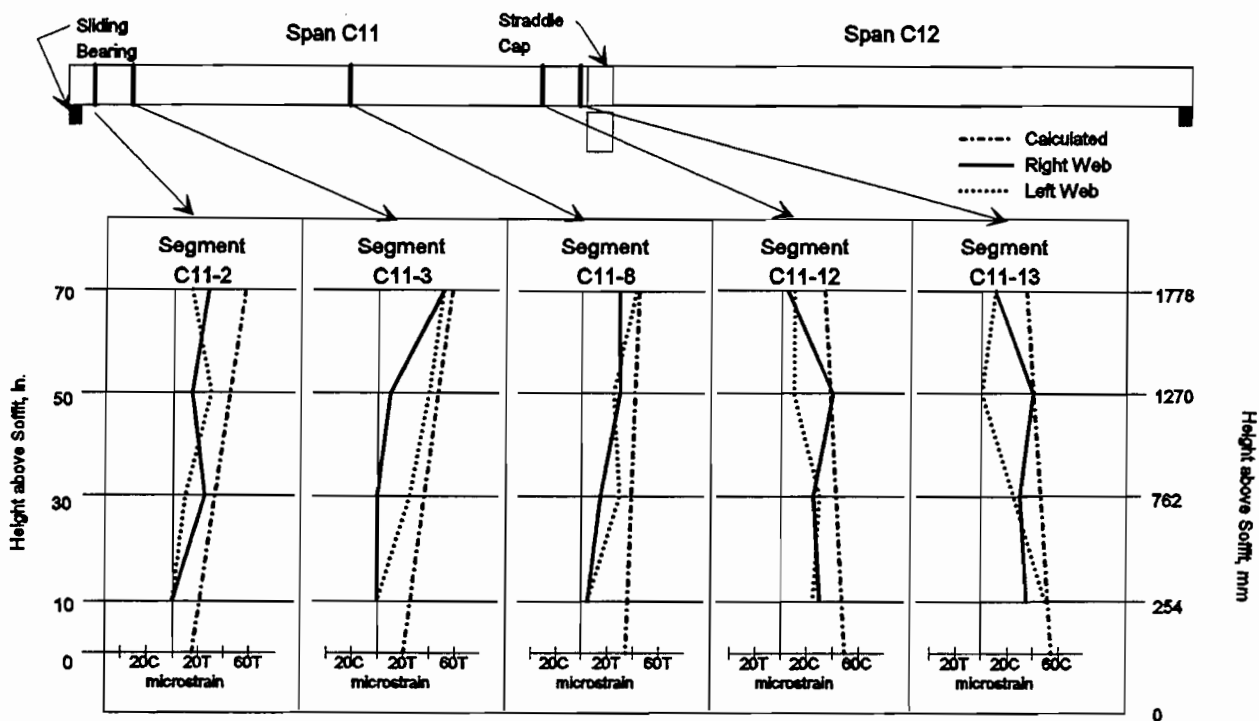


Figure 6.29 Web strain profiles for span C11 caused by thermal gradients on March 9, 1992.

6.5 Discussion

6.5.1 Thermal Gradients.

6.5.1.1 Positive Gradients. The positive thermal gradients for the untopped condition measured over the course of many months in San Antonio never approached the NCHRP design gradient. In fact the top surface temperature difference for the unsurfaced condition never attained more than 50% of the NCHRP value. While it might be remotely possible that the design gradient might occur, for the San Antonio "Y" project with the light colored concrete and roughened surface, its occurrence is unlikely. Once the topping was laid the gradients became larger and more closely approached (approximately 80%) the design gradient. The NCHRP and New Zealand design gradients indicate that the gradient should decrease with the addition of a topping, while the current measurements indicate that the opposite is true.

Potgieter and Gamble⁵⁴ present an equation for predicting positive thermal gradients of untopped bridges based on four parameters:

- α = absorptivity of the surface,
- V = wind velocity (m/s),
- TV = ambient temperature variation (daily high - daily low) (°C),
- S = total solar radiation (kJ/m²).

The equation is as follows:

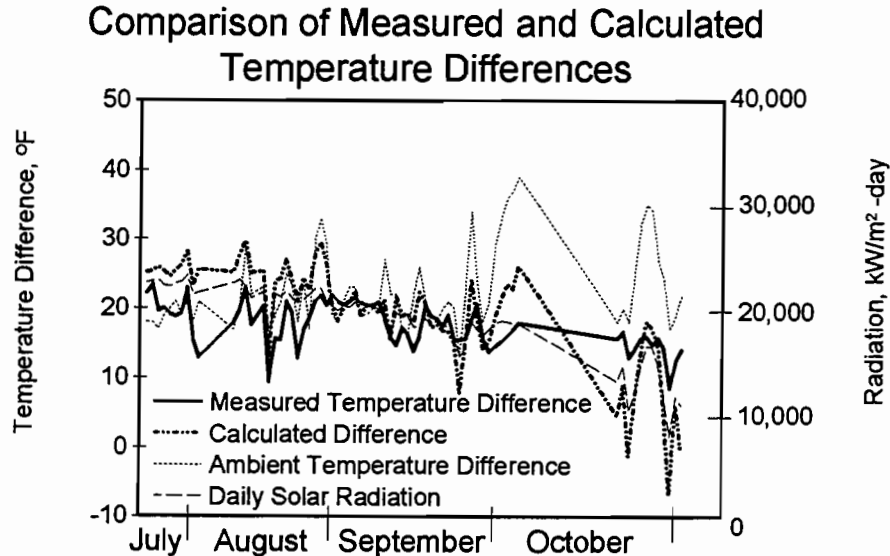
$$f(\alpha, S, TV, V) = 40.5 \left(S \frac{\alpha}{33818} - 0.7 \right) + 0.269 (TV - 16.0) + (37.4 - 9.28V + 3.56V^2 - 0.640V^3 + 0.0419V^4)$$

This formula was used to calculate temperature differences in the bridge from July to October based on the variables as follows:

- $\alpha = 0.7$ This is the value which was used to determine the design gradient. Recommended values for concrete range from 0.5 to 0.8 depending on the color.⁵⁴
- V from Climatological Summary,
- TV from Climatological Summary,
- S Theoretical clear day values from NBS⁴⁰ multiplied by percent sunshine from Climatological Summary.

The calculated predictions are compared to measured values in Figure 6.30. Since the uppermost thermocouple is 1" (25 mm) below the top surface of the deck, the measured difference

between the coolest web temperature and the thermocouple next to the top slab was multiplied by a factor of 1.2 to account for the increase in temperature over the top 1" (25 mm). Also shown in the graph are the daily difference between high and low ambient temperature and the calculated levels of solar radiation.



Notes: Temperature Differences are between coolest web and top slab temperature Calculated Temperatures were determined with Potgieter and Gamble equations.

To convert from deg. Fahrenheit (F) to deg. Celsius (C) multiply by $t_c = (t_f - 32) / 1.8$.

Figure 6.30 Comparison of measured and calculated temperature differences.

On the average, the prediction is reasonably good, averaging 104% of the actual temperature difference. The highest ratio of predicted to actual was 1.96 and the lowest -0.93. The predictions are consistently too high in the summer months and become consistently too low during the fall months. The variable which is changing most significantly is the solar radiation. It's effect on the temperature difference could be overemphasized in the equation.

The interesting thing to note is that for the actual conditions in San Antonio, the measured and predicted values fall well below the design gradient. The San Antonio summer was very typical, clear and hot, with warm nights. In order to achieve the design gradient a very hot windless day would need to follow several very cool days (a daily temperature variation of 45°F (25°C) with 1 m/s wind speed and 27,000kW/m²) would have to occur. These conditions would be very rare in San Antonio. The selection of the absorptivity constant also effects the gradient greatly. Bridges of light colored concrete will have significantly lower gradients.

The erratic agreement of the predicted and actual thermal gradients could indicate errors in the original analysis which was used to develop the gradients. The original work was confirmed with only two days of measurements on a bridge with an asphalt topping. No further confirmation was provided.

For the San Antonio area the design gradient for the 2 inch (51 mm) asphalt topping appears to be generally appropriate (approximately 25% too high), but the gradient for the unsurfaced bridge is far too high (approximately 100% too high). Further analysis is required to determine the cause of the discrepancy. A possible approach to allow for the extreme improbability of the positive design gradient ever occurring would be to allow a substantial reduction in design gradient based on local conditions such as city pollution, very windy areas, known absorptivity constants, or high traffic volumes which cause air stirring.

6.5.1.2 Negative Gradients. The measured negative gradient for the untopped case was approximately 80% of the design negative gradient, while for the case with topping, the measured gradient was less than 50% of the design gradient. The primary problem with the application of the negative gradient is the high tension which develops over a few inches of the top and bottom slab. Figure 6.31 shows the self-equilibrating stresses for the design gradient on a simply supported beam of the Type I cross-section. The very local tension at the top is 434 psi (2992 kPa) and at the bottom is 210 psi (1448 kPa). In order to pre-compress the section completely to counter-balance these stresses 2191k (9745 kN) of force (~74- 0.6" (15mm) ϕ strands) would have to be added. This is clearly excessive since a 110' (33.5 m) span requires only ~162 strands for dead and live loads.

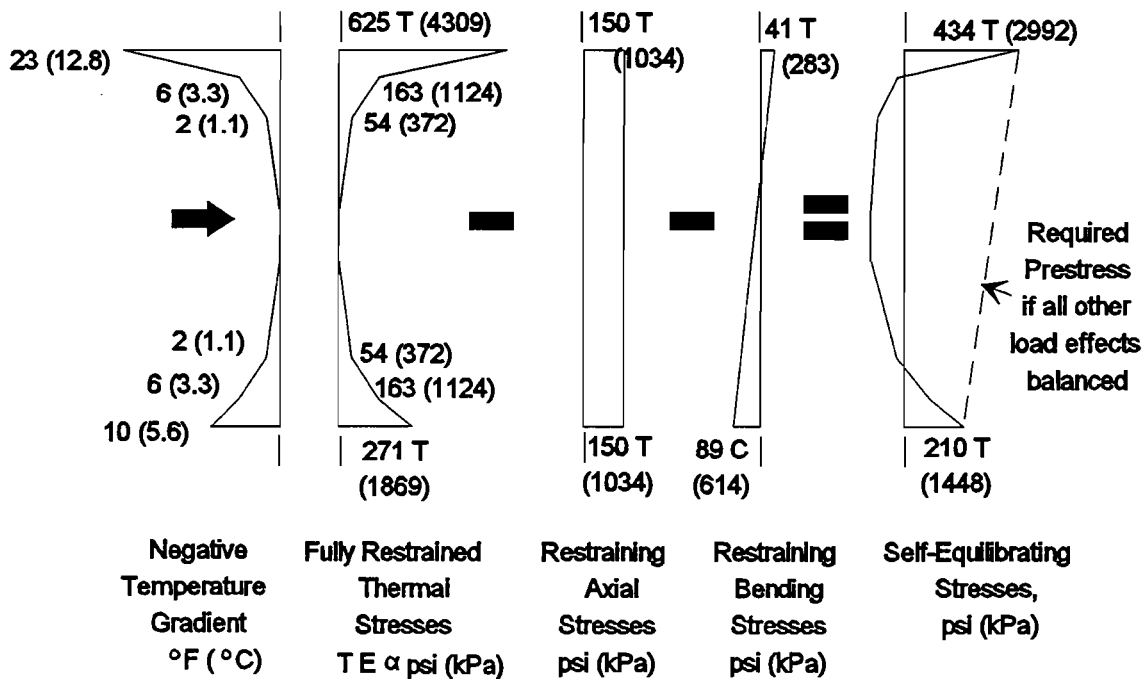


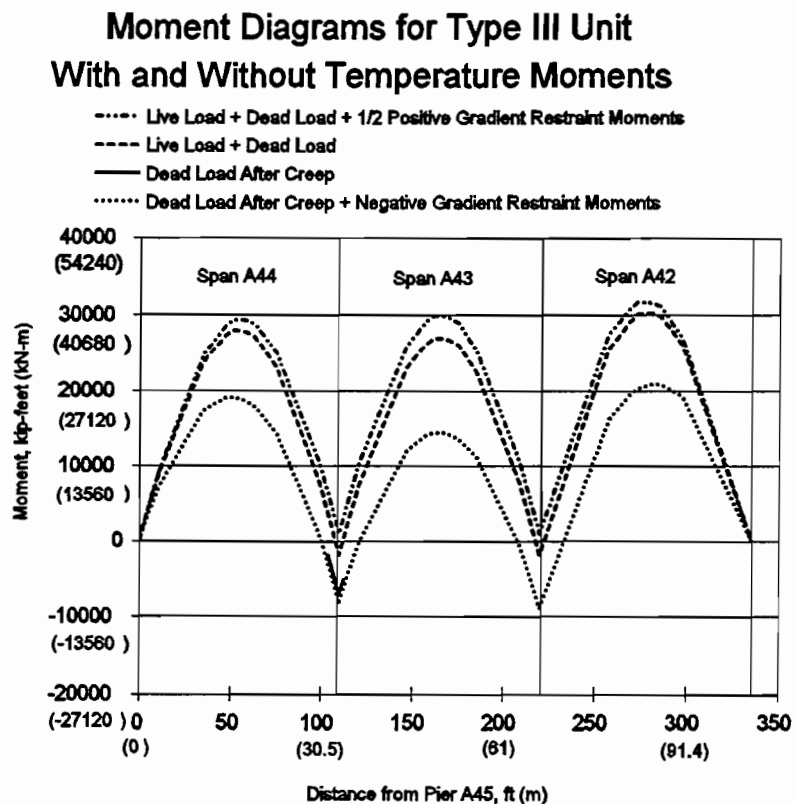
Figure 6.31 Self-equilibrating stresses for negative gradient on Type I cross-section, ignoring restraining moments.

Based on the study of the negative gradients the following can be concluded:

1. The negative design gradient is conservative but possibly appropriate for San Antonio.
2. It is difficult and probably unnecessary to fully prestress for the self-equilibrating stresses which develop due to the negative gradient. As recommended in the next subsection, some residual tensile stress should be allowed.

6.5.1.3 Behavior. If the correct thermal gradient is known, the behavior of a bridge subjected to that gradient is quite predictable. The measured deflected shapes matched calculated values very well and measured strains were reasonably close to calculated.

Design for Restraint Moments. Figure 6.32 shows the calculated moment diagrams for the extreme positive and negative moments. Maximum positive moments occur early in the structure's life, before creep causes decreases in mid-span dead load moments. The load case D + (LL + I) before creep causes maximum positive mid-span moments. For the 3-span unit shown, the restraint moment caused by the $\frac{1}{2}$ DT case causes an increase of mid-span moment of approximately 10%.



Dead load moments after creep are based on creep coefficient at infinity of $\phi = 0.92$.

Figure 6.32 Calculated moment diagrams for Type III unit.

Figure 6.32 also shows the calculated maximum negative moments which develop over the piers with time and creep. The addition of DT to this combination increases the over-pier negative moment only slightly.

One problem in dealing with the various load combinations is that the moment over the piers is positive (tension in the bottom fibers) for the load case of dead load only (before creep plus positive thermal gradient), and negative (tension in the top fibers) for the load case of dead load only (after creep plus negative thermal gradient). Over the pier the girder must be designed for the entire range of positive and negative moments, and the tension in the bottom slab can often be a governing design condition.

Generally, designing for the restraint moments caused by the thermal load case is a prudent, and not overly harsh task. Designing for $D + DT$ at 100% allowable stress is similar to $D + (LL + I)$. Designing for $D + (LL + I) + \frac{1}{2}DT$ and allowing 125% of allowable stress is appropriate considering that this is a likely service condition, but should not occur often. The maximum positive thermal gradient usually occurs between 3:00 pm and 6:00 pm, which is also a time when a maximum design live load might occur due to rush hour. The presence of traffic will reduce the magnitude of the gradient somewhat by shading the top surface and by stirring the air above the top surface, still, $D + (LL + I) + \frac{1}{2}DT$ is a very likely service condition.

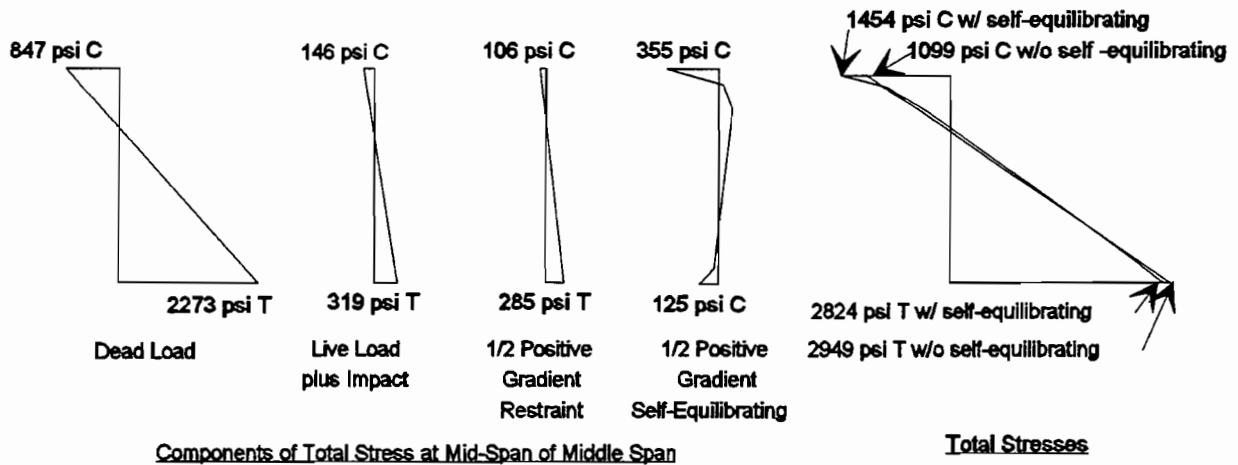
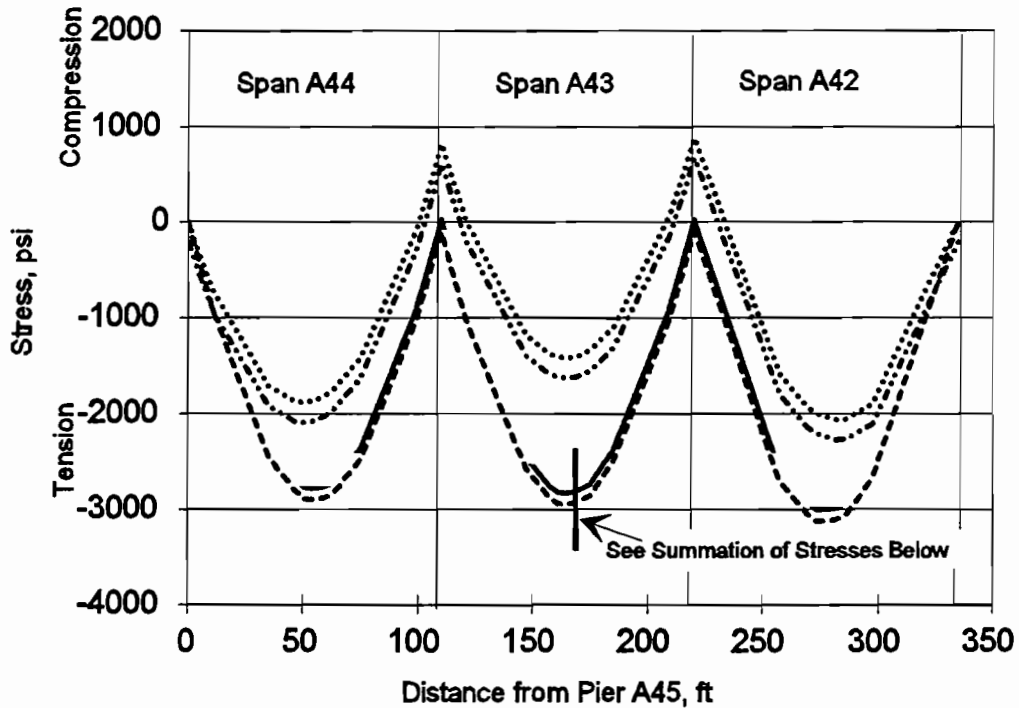
However, it is not logical to follow the traditional pattern of increasing allowable stresses 25% for the allowable stress values of the application. The stresses currently allowed for Type A joints with no bonded reinforcing and for Type B joints are 0 tension and 200 psi (1379 kPa) residual compression respectively. A 25% increase doesn't help. For more typical prestressed concrete tensile stress conditions, a 25% increase in stresses corresponds to 1 to $2\sqrt{f'_c}$ depending on the case. Thus a similar magnitude of tensile stress increase should also be allowed for all types of segmental structures. Allowing an increase in allowable tension of $1\sqrt{f'_c}$ (roughly 25% of $3\sqrt{f'_c}$) seems to be more consistent with currently allowed tensile stress increases for other types of prestressed bridges.

Design for Self-Equilibrating Stresses. The correct treatment of local peaks due to self-equilibrating stresses pose a much more difficult design problem. Figure 6.33a shows the envelopes of the bottom fiber stresses along the length of the three span continuous unit. The bottom fiber stresses are not severely affected by the self-equilibrating stresses. The worst case tensions develop due to $D + (LL + I) + \frac{1}{2}DT_{pos}$. The positive gradient self-equilibrating stresses are compressive at the bottom slab, which reduces the maximum tensions. The $D + DT_{neg}$ case is not critical, even with self-equilibrating stresses.

The top fiber stresses are slightly more affected by the addition of the self-equilibrating stresses (see Figure 6.33b). The only case where significant tension is developed is the $D + DT_{neg}$ with self-equilibrating stresses. In this case tension develops along most of the unit. As mentioned earlier, these stresses are difficult to post-tension for because they are present over only the first few inches of the top and bottom slab of the section. This means that although the resultant tensile force is quite small, the post-tensioning force required to eliminate the tension is very large.

Bottom Fiber Stresses with and without Self-Equilibrating Stresses

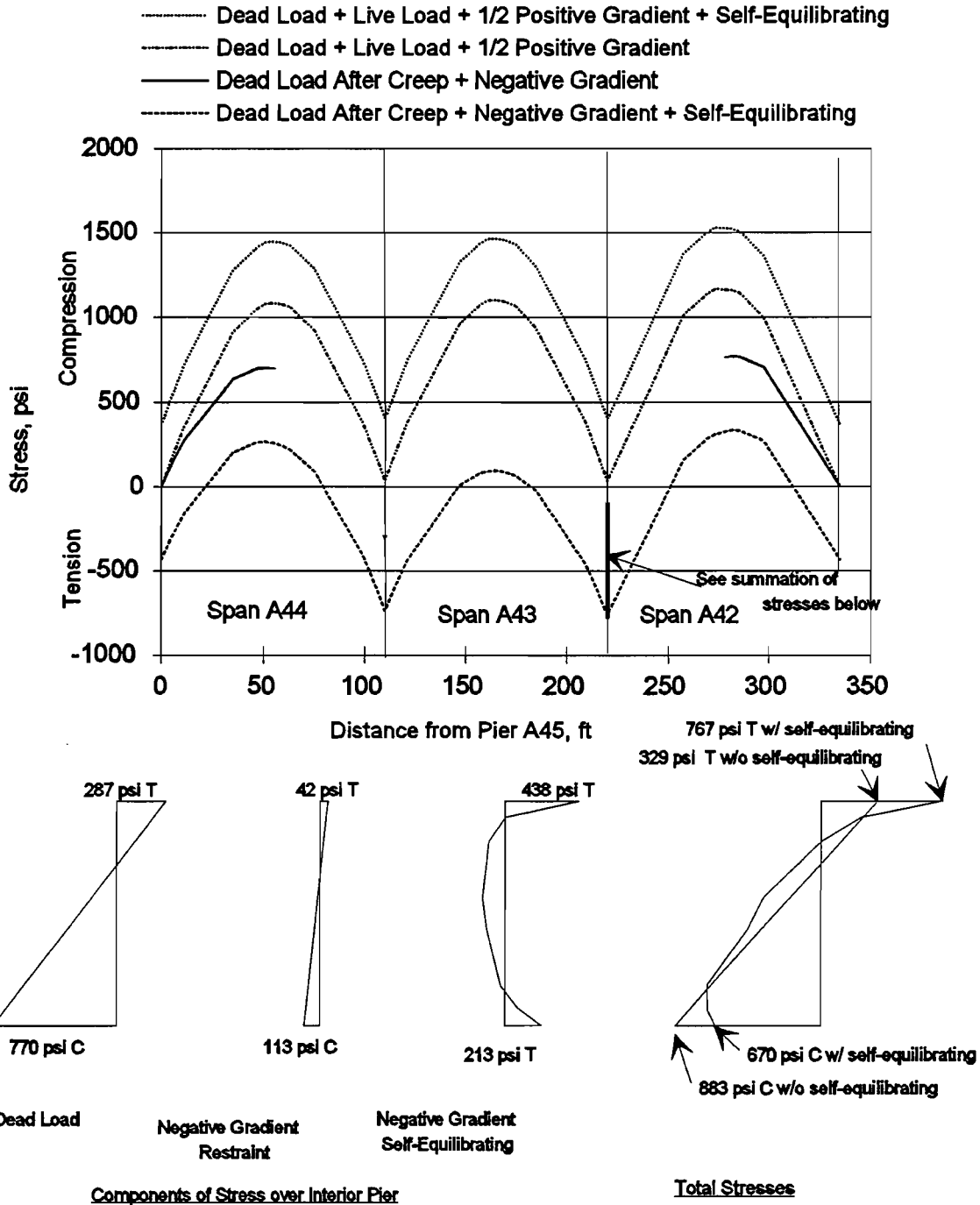
- Dead Load After Creep + Negative Gradient
- - - - - Dead Load After Creep + Negative Gradient + Self Equilibrating
- Dead Load + Live Load + 1/2 Positive Gradient + Self-Equilibrating
- - - - - Dead Load + Live Load + 1/2 Positive Gradient



To convert psi to kPa multiply by 6.89.
To convert ft. to (m) multiply by 0.3048.

Figure 6.33a Comparison of bottom fiber stresses without prestressing, with and without self-equilibrating stresses.

Top Fiber Stresses with and without Self-Equilibrating Stresses



To convert psi to kPa multiply by 6.89.
 To convert ft. to (m) multiply by 0.3048.

Figure 6.33b Comparison of top fiber stresses without prestressing, with and without self-equilibrating stresses.

There are no reported cases of distress in bridges caused by negative gradient self-equilibrating thermal stresses. This could be due to the extremely small depth of the tensile zone and the very steep strain gradient over that depth. Fracture mechanics theory indicates that small areas loaded in uniform tension will have a higher ultimate tensile stress than large areas similarly loaded.¹¹ It has also been shown that when the strain gradient is very steep, concrete stresses at cracking are much higher than indicated by uniaxially loaded tensile tests.¹⁵ The bending cracking stress can be as much as twice the axially loaded test cracking stress. These observations could explain why cracking has not been reported, and are arguments for a higher allowable stress when the non-linear negative thermal gradient is considered.

6.6 Recommendations

6.6.1 Design Thermal Gradients. This chapter has presented data from 6 previously instrumented bridges plus the San Antonio "Y" Project. Of the seven bridges only one has experienced a measured positive thermal gradient higher than the design gradient. The most complete data, that of the San Antonio "Y", indicates that the bridge only experienced 50% of the positive gradient for the untopped condition and 78% of the positive gradient for the 2 inch (51 mm) asphalt topping condition.

No bridge examined in this chapter experienced a negative thermal gradient as severe as the negative design thermal gradient. The San Antonio "Y" project experienced 65% of the negative gradient for the untopped condition and 50% of the gradient with the 2 inch (51 mm) asphalt topping.

Based on this information, it appears that the currently recommended guidelines are too harsh. The positive gradient is based on an analysis confirmed with only two days of data from a bridge with an asphalt topping. The analysis for the untopped condition was never confirmed with field data. The negative gradient is based on the shape of the British Standard negative gradient and the magnitudes are arbitrarily related to the design positive gradient. There is no analysis or field data to substantiate the negative gradient.

It is recommended that a re-evaluation of the initial analysis be made to determine its validity. Until further analysis can be done to confirm or disprove the current gradient, a provision should be included to allow the development of design gradients for specific material properties and a specific location based on records of climatic conditions. Also, based on the magnitudes of the gradients in the current study, it is recommended that a reduction of the current gradients be allowed. The following change is recommended for Design Specification Section 7.4.4 (changes are in italics):

7.4.4 Differential Temperature.

Positive and negative differential superstructure temperature gradients *shall be taken as 80% of the values presented* in Appendix A of National Cooperative Highway Research Program Report 276 "Thermal Effects in Concrete Bridge Superstructures".³³ *Alternatively, site specific thermal gradients, developed based*

on the climatic conditions in the area and the actual material properties of the structure, may be substituted for the current design gradients.

The following note in the commentary should be added:

Add to commentary section 7.4.4:

The currently recommended design thermal gradients, both positive and negative, have not been substantiated with field data. The data which has been collected to date^{32,29,64,61} indicates that the design gradients may be overly conservative.

6.6.2 Allowable Stresses. The multipliers on allowable stresses (125%) currently in the *AASHTO Standard Specification* for load cases which consider both thermal gradients and full live load plus impact are reasonable considering the small likelihood of the occurrence of the load combination. Unfortunately, the currently recommended tensile stresses allowed for Type A joints with no bonded reinforcing and for Type B joints are 0 tension and 200 psi (1379 kPa) residual compression respectively. A 25% increase in allowable stresses really doesn't help. Requiring substantial additional prestressing for the thermal gradient load case could be detrimental to the ductility of a segmental structure. Since some segmental structures, particularly those with external tendons, are likely to fail by the formation of a hinge and concrete crushing, higher initial prestress can lead to lower ultimate loads and less ductility.^{44,68} Since conventional prestressed structures, which are covered in the *AASHTO Standard Specification*, are allowed an increase in allowable tensile stress under extreme and rare load combinations. This should also hold true for segmental structures.

The following is a recommendation presented by Freyermuth²⁷ to the AASHTO Technical Committee on Prestressed Concrete for increasing allowable stresses when thermal gradients are included in the load case:

New section 9.2.1.3:

9.2.1.3 Longitudinal stresses outside the precompressed tensile zone when differential temperature effect (DT) is included in the load case:

- a) Type A joints with minimum bonded auxiliary reinforcement through the joints sufficient to carry the calculated tensile force at a stress of $0.5f_{sy}$; internal tendons:

$$6 \sqrt{f'_{ca}}$$

- b) Type A joints without the minimum bonded auxiliary reinforcement through the joints:

$$3 \sqrt{f'_{ca}}$$

- c) Type B joints, external tendons: zero tension.

- d) For purposes of this section, the area outside the longitudinal precompressed tensile zone shall be considered as the following locations in the final structural configurations:
- 1) The compression zone (top slab to neutral axis of the gross concrete section) of 0.7 of the span from bearings of end spans or hinged spans.
 - 2) The compression zone (top of slab to neutral axis of the gross concrete section) of the central 0.6 of interior span.
 - 3) The compression zone (bottom of slab to neutral axis of the gross concrete section) of 0.25 of the span each direction from piers.

Existing sections 9.2.1.3 and 9.2.1.4 become sections 9.1.2.4 and 9.2.1.5 respectively.

Add the following new section 9.2.2.3:

9.2.2.3 Longitudinal stresses outside the precompressed tensile zone when differential temperature effect (DT) is included in the load case:

- a) Type A joints with minimum bonded auxiliary reinforcement through the joints sufficient to carry the calculated tensile force at a stress of $0.5f_{sy}$; internal tendons:

$$6 \sqrt{f'_{ci}}$$

- b) Type A joints without the minimum bonded auxiliary reinforcement through the joints:

$$3 \sqrt{f'_{ci}}$$

- c) Type B joints, external tendons: zero tension.
 d) For purposes of this section, the area outside the longitudinal precompressed tensile zone shall be as defined in Section 9.2.1.3(d).

Existing sections 9.2.2.3 and 9.2.2.4 become sections 9.1.2.4 and 9.2.2.5 respectively.

For the negative thermal gradient, the justifications for the increase in stresses recommended by Freyeremuth can be summarized as:

- 1) A small portion of the cross-section is in tension
- 2) The strain gradient is very steep
- 3) No bridge to date has shown damage due to negative thermal gradients.

Based on these arguments, the following should be added to Design Commentary Section 9.2.1.3:

The negative thermal gradient load case produces self-equilibrating stresses through the cross-section which are tensile over the top and bottom few inches of the section and compressive through the rest of the cross-section. It is difficult, and excessive, to provide post-tensioning to counter-balance these small regions of

tension at the top and bottom of the section. Because the regions in tension are very shallow, and the strain gradients are very steep, the tension to cause cracking is higher than in regions of uniform tension.¹⁵ This in part explains why no distress caused by negative gradients has been reported in previous bridges. The higher allowable stresses are therefore justified.

The proposed stress increases are acceptable for the negative thermal gradient and should reduce the need for additional prestressing to cover the negative thermal gradient load case. There has never been a reported case of distress in a bridge attributable to a negative thermal gradient. Some concern has been expressed that top slab cracking is very undesirable where ice is applied and where freezing rain might aggravate the cracking. Fortunately, the depth of the tensile stresses is very shallow and if cracking did occur those cracks would not reach the depth of the reinforcing steel. It is felt that to prestress to prevent the self-equilibrating tensile stresses from causing tension is excessive. The increases won't significantly affect the positive thermal gradient load case because the locations of additional tension are most often in the precompressed tensile zone. Although the increases accomplish the same effect as the AASHTO multipliers, they are somewhat more liberal. The problem of excessive prestressing required for the positive thermal gradient is best solved by addressing the magnitude of the positive design gradient itself.

6.6.3 Ultimate Strength. Thermal stresses should not be considered at all in the ultimate load checks. As pointed out by Priestley and Menn, the effects of the thermal deformations become quite insignificant as the structure begins to lose stiffness. If the structure is designed for adequate ductility, thermal effects will cause no great reduction in ultimate capacity.

Freyermuth also recommended that this be addressed in the *AASHTO Guide Specification* by the inclusion of the following in Section 8.2.2:

At factored loads, a load factor of zero shall be applied to differential temperature effects (DT) for the Additional Thermal load case and other AASHTO load combinations which include differential temperature effects.

6.7 Conclusions

6.7.1 Observations. This chapter examined actual thermal gradients and their effects on a segmental box girder bridge and also compared measurements made on a number of other segmental bridges. Based on this study the following conclusions can be made:

1. The positive gradients measured for the bridge with no topping were 50% less than the *AASHTO Guide Specification* design positive gradient, but were of the same shape.

2. The positive gradients measured for the bridge with 2 inch asphalt topping were 22% less than the *AASHTO Guide Specifications* design positive gradient but were of a very similar shape.
3. The negative gradients for both topped and untopped conditions measured were considerably less (35% less for bridges with no topping and 56% less for bridges with 2 inch (51 mm) asphalt topping) than the *AASHTO Guide Specification* design gradient, but were of the same shape as the design gradient.
4. The expression presented by Potgieter and Gamble⁵⁴ to approximate gradients for untopped bridges by inputting actual climatic conditions (see Section 6.5.1.1) on average approximates measured gradients reasonably well.
5. Bridge deflections caused by known thermal gradients can be predicted very accurately.

6.7.2 Recommendations. The following recommendations are made for design for thermal gradients:

1. The current design gradients, particularly the positive thermal gradient for unsurfaced bridges, should be re-evaluated based on additional field measurements. Until a re-evaluation can be completed a 20% reduction in the current design thermal gradients is recommended. Alternatively, the use of site specific thermal gradients should be allowed.
2. Allowable tensile stresses, outside the precompressed tensile zone, should be increased for load cases which include the non-linear thermal gradients.
3. Thermal gradients should not be considered in ultimate load checks.

6.7.3 Further Study. To date very few bridges have been instrumented. The results from the model which was used to develop the design gradients should be compared to additional field data to confirm its accuracy. No analysis or field data substantiates the negative design thermal gradient

A study of the effects of the gradient on cracked sections, or on dry jointed structures would be very interesting. It is not well understood how cracking effects the thermal stresses.

6.7.4 Summary. This study has provided additional data in the ongoing study of thermal gradients and their effects on concrete bridges. All the design gradients, particularly the positive gradient for unsurfaced bridges, seem to be quite overly conservative. The recommendations presented in this chapter to reduce the design gradients and to increase the allowable stresses should reduce the magnitude of the problem.

CHAPTER 7 BEHAVIOR OF SEGMENTAL JOINTS

7.1 Introduction

There is still considerable debate over the relative merits of dry and epoxy joints, both of which are used in segmental construction. Because of the danger of water penetrating joints, freezing and then expanding to damage the joints, the *AASHTO Guide Specification for the Design and Construction of Segmental Concrete Bridges* (to be referred to as the *AASHTO Guide Specification* for the remainder of the chapter) limits the use of dry joints to regions which do not experience freezing. Also the *AASHTO Guide Specification* only allows dry joints to be used in structures with external tendons because of the risk of water penetrating and causing corrosion of internal tendons where they cross the joints. In those areas and those structures where dry joints can be used the designer must weigh the relative merits of a structure with dry or epoxied joints.

A structure with dry joints can have cost savings by eliminating the cost of epoxy and equipment for temporary post-tensioning, as well as the time savings realized by eliminating the epoxy operations. The use of epoxy also makes the project more subject to weather related delays caused by rain or temperature restrictions for epoxy application. On the other hand, the *AASHTO Guide Specification* requires the use of a smaller ϕ factor for shear for dry jointed structures, and a higher residual compression across joints is also required. These requirements can increase the cost of the bridge by resulting in thicker web walls, more mild steel shear reinforcing, or greater amounts of post-tensioning steel.

Some engineers claim that the use of epoxy in joints creates a bridge that will perform as well as a monolithic structure. Others cite bad experiences with epoxy, such as improper application of the epoxy or failure of the epoxy to set properly,⁴¹ and assert that the presence of the epoxy should not influence the design of the structure. They claim that all joints should be designed as if they were dry.

This chapter examines the behavior of the joints of the San Antonio "Y" project, which have multiple shear keys and utilize a two-part epoxy glue. The effectiveness of the temporary prestressing in producing thin, evenly compressed joints, and the behavior of the joints during permanent post-tensioning and with time were both examined in the field. A literature review of previous laboratory work is presented, the surveillance program is detailed and the results presented. Data from previous studies are used to evaluate current code recommendations. A method for calculating joint capacity is presented.

7.1.1 Background Information.

7.1.1.1 Shear Failure Modes. One factor affecting the failure mode and capacity of a beam is the shear span to depth ratio, a/d (see Figure 7.1). For large ratios a flexural failure can

be expected, for smaller ratios a shear failure is more likely. The type of shear failure also varies depending on the shear span and the amount of shear reinforcing. A diagonal tension failure occurs when the shear span to depth ratio is more than 3 or 4. A shear compression failure occurs when the shear span to depth ratio is from 1 to 1.5. When the shear span to depth ratio is less than d , a splitting or compression failure will occur. Figure 7.2 shows some kinds of possible shear failures.

Another type of shear failure can occur in segmental bridges, a joint shear failure.⁹ This failure mode is most likely to occur when the joint is in an area of high shear and low moment, such as near an end pier, and is characterized by a direct shearing off of the keys (see Figure 7.3).

Most failure modes are relatively unaffected by the type of joint. Previous studies with a/d ratios greater than 1.5^{44,60} have shown only small capacity reductions from monotonic (with a discontinuity in the longitudinal mild reinforcing) to epoxy jointed to dry jointed specimens. The greatest differences between dry and epoxy jointed shear capacity occurs when the shear span to depth ratio is very small, a/d less than 0.5, and a joint shear failure occurs.³⁷

7.1.1.2 Other Differences between Dry and Epoxy Joints.

Epoxy in the joints has advantages and disadvantages. In the construction process it acts as a

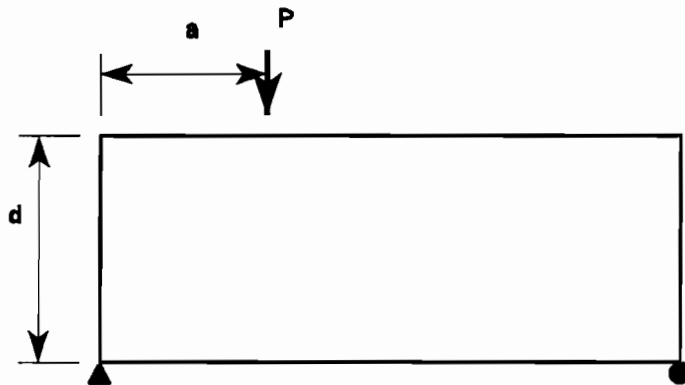


Figure 7.1 Definition of a/d ratio.

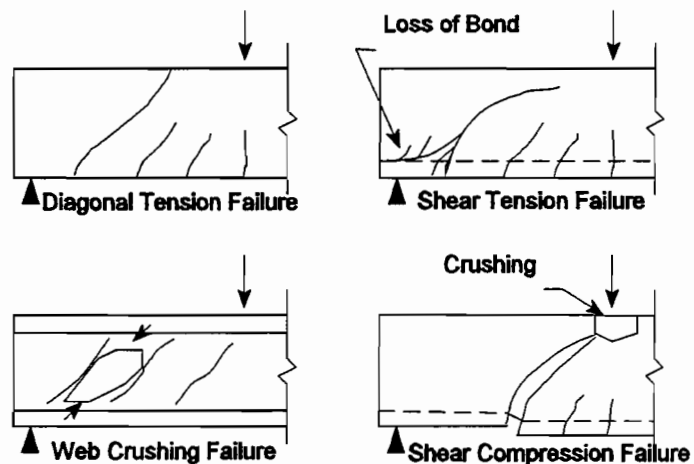


Figure 7.2 Shear failure modes for prestressed concrete beams.

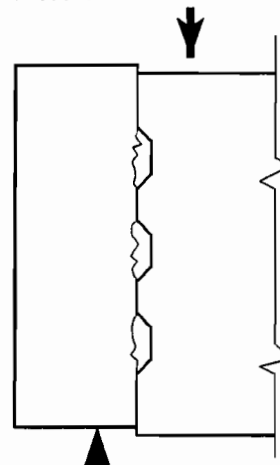


Figure 7.3 Joint shear failure.

lubricant to aid in the alignment of the precast segments. It also can fill in small imperfections and eliminate locations of high contact pressure and stress concentrations. Bridges with internal prestressing tendons must have epoxy in the joints to protect the tendons from the ingress of water and other corrosive agents.

On the other hand, in span-by-span construction the epoxy and temporary post-tensioning operation is costly and time consuming. In the San Antonio "Y" Project Phase IIC, the usual construction cycle for a typical span was five 12 hour shifts of a seven man crew. One full shift was devoted to the epoxy and temporary post-tensioning operations. There are also considerable costs involved in the epoxy itself and the brackets and hardware required for the temporary post-tensioning operations.

In some bridge situations, such as bridges with internal tendons or bridges in regions with freeze-thaw cycles, epoxy must be used in the joints, in other cases it is optional and therefore the preference of the designer. If dry joints are selected, the direct joint shear capacity becomes very critical.

7.1.2 Current AASHTO Guide Specification Approach. There are several sections of the *AASHTO Guide Specification* which address aspects of joint design. The first is Section 8.3.6 which covers strength reduction factors. This section was revised in 1992 to read as follows:

8.3.6 Strength Reduction, ϕ , shall be taken as follows:

Type	ϕ_f	ϕ_v
	<u>Flexure</u>	<u>Shear</u>
Fully Bonded Tendons		
Type A joints	0.95	0.85
Type B joints	0.90	0.80
Unbonded or Partially Bonded Tendons		
Type A joints	0.90	0.80
Type B joints	0.85	0.75

Where A and B joints are defined as follows:

8.3.4 Cast-in-place concrete joints, and wet concrete or epoxy joints between precast units, shall be considered as Type A joints.

8.3.5 Dry joints between precast units shall be considered as Type B joints.

The joint types are also considered in Section 9.2 which delineates allowable stresses:

9.2.1 Temporary stresses before losses

9.2.1.2 Longitudinal stresses in the precompressed tensile zone:

- (a) Type A joints with minimum bonded auxiliary reinforcement through the joints sufficient to carry the calculated tensile force at a stress of $0.5 f_{sy}$; internal tendons.
- (b) Type A joints without the minimum bonded auxiliary reinforcement through the joints; internal tendons:
 $3 \sqrt{f'_{ci}}$ maximum tension
 No tension allowed.
- (c) Type B joints, external tendons, not less than:
 200 psi (1379 kPa) minimum compression.

9.2.2 Stresses at service after losses

- (a) Type A joints with minimum bonded auxiliary reinforcement through the joints sufficient to carry the calculated tensile force at a stress of $0.5 f_{sy}$; internal tendons.
- (b) Type A joints without the minimum bonded auxiliary reinforcement through the joints; internal tendons:
 $3 \sqrt{f'_c}$ maximum tension
 No tension allowed.
- (c) Type B joints, external tendons, not less than:
 200 psi (1379 kPa) minimum compression.

There are no distinctions made between dry and epoxy jointed girders when calculating their flexural and shear nominal capacities.

Another reference to the design of shear keys is Section 12.2.20 which reads as follows:

Shear keys in webs of precast segmental bridges shall extend for as much of the web height as is compatible with other detailing requirements. Details of the shear keys shall be similar to Figure 25-1 (see Figure 7.4). Alignment shear keys shall also be provided in top and bottom flanges.

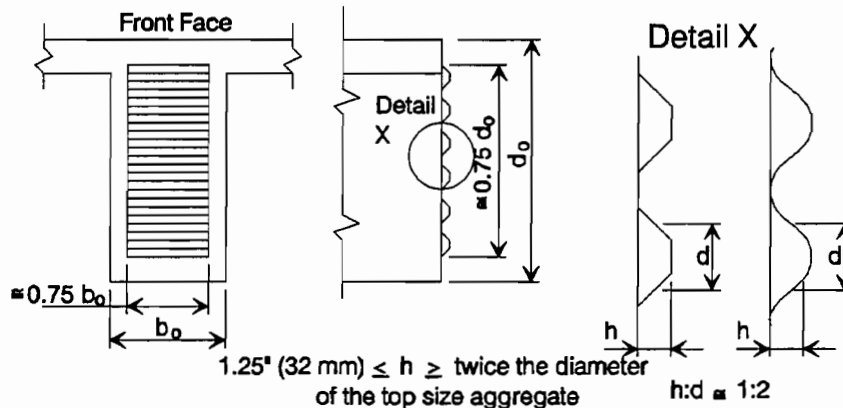


Figure 7.4 Figure 25-1 from *AASHTO Guide Specification*. Example of fine indentation joint faces.

Finally joints are addressed in Section 25. Precast Segmental:

25.2.3 Temporary Stress in Epoxy Joints

A minimum compressive stress of 40 psi (276 kPa) shall be provided for the closure stress on an epoxied joint until the epoxy has set.

25.4 Joints

25.4.1 General

Precast segmental bridges are usually match-cast with Type A or epoxied joints. Closure pours are cast-in-place. Type B or dry joints between segments may be used under conditions stated below.

25.4.2 Type A Joints

Type A (epoxied) joints shall be utilized for all bridges utilizing internal tendons, and for all bridges exposed to severe climatic conditions where freeze/thaw cycles are encountered, or where de-icer chemicals are used.

25.4.3 Type B Joints

Type B (dry) joints may be used in conjunction with external post-tensioning tendons in areas where freeze-thaw cycles do not occur, and where de-icer chemicals are not used.

Aside from detailing requirements, the *AASHTO Guide Specification* provides little guidance on design of segmental joints. An equation for calculating the direct joint shear capacity is lacking.

7.2 Literature Review

7.2.1 Koseki and Breen.³⁷

This exploratory study of shear strength of segmental joints examined a variety of joint types, which included smooth, single key, and multiple key joints with and without epoxy. Koseki and Breen loaded the specimens in such a way that the joints were in almost pure shear (see Figure 7.5). The specimens with epoxy in the joints failed in bearing or web crushing modes while the specimens without epoxy failed by slipping at the joint or shearing off of the keys.

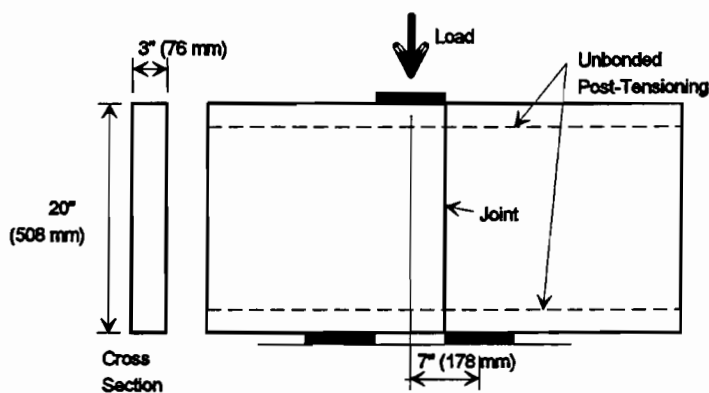


Figure 7.5 Specimens of Koseki and Breen.

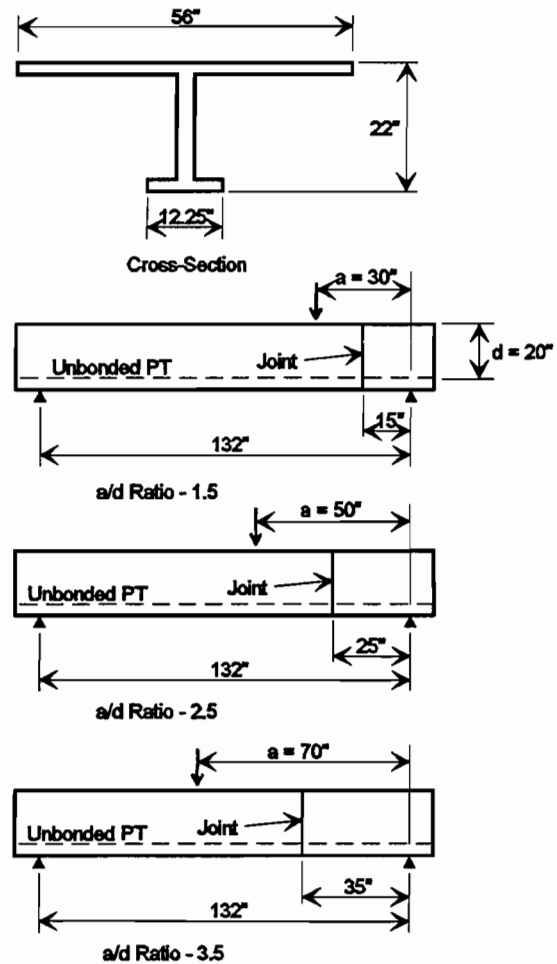
In general the epoxied joints achieved the full capacity of companion monolithic specimens while the specimens without epoxy achieved between 62% and 76% of the capacity of the monolithic specimens.

7.2.2 Ramirez.⁶⁰ Twelve 1/4 scale specimens were tested to failure in this study. Three shear span to depth ratios ($a/d = 1.5, 2.5, \text{ and } 3.5$) were examined and for each a/d ratio four joint types were tested: monolithic, dry, epoxied on one face, and epoxied on two faces. All of the segmental joints had identical multiple shear key details, and all tendons were internal and unbonded. Figure 7.6 shows the test set up for the three shear span to depth ratios.

Ramirez reported that although the failure mechanism of the beams varied with the shear span, a characteristic common to all of the tests was the formation of a single major inclined crack. This major crack extended from the location of the base of the joint (or reinforcement gap in the monolithic specimens) upwards toward the loading point. Because of lack of bonded continuous reinforcement at the joint (or reinforcement gap location) all rotational deformation concentrated along the major crack. The ultimate failures were caused by web crushing or shear compression.

Figure 7.7 shows the failure loads of the twelve specimens normalized by $\sqrt{f'_c} b_w d$. It is apparent from this figure that the ultimate capacities of these specimens were not greatly affected by the joint type.

7.2.3 MacGregor.⁴⁴ A one third scale model of a three span continuous segmental bridge with external tendons was built and tested. The end spans of the model were identical except one had epoxied joints and the other had dry joints. Both spans were subjected to similar tests to study flexural and shear behavior.



To convert from inch to millimeter multiply by 25.4.

Figure 7.6 Specimens by Ramirez.
Strength Comparison of Ramirez's Specimens

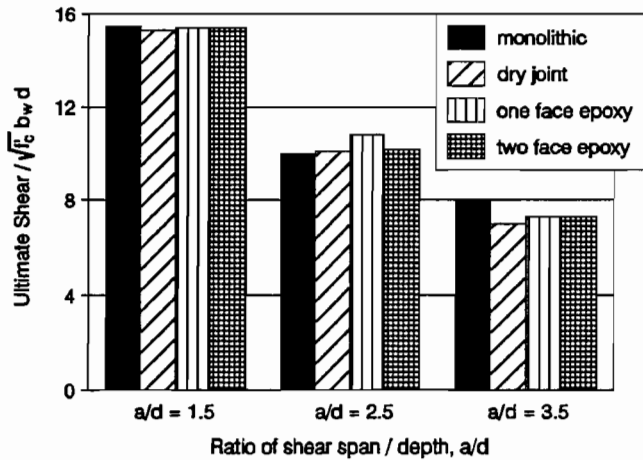


Figure 7.7 Strength comparison of Ramirez's specimens.

The following conclusions were drawn:

- 1) At service loads the deflection of the dry-jointed exterior span was about 10 percent greater than for the epoxy jointed exterior span.
- 2) The cracking load in the epoxy-jointed span was approximately twice the live load required to decompress the flexural tension fiber and begin to open a dry joint.
- 3) The total moment at mid-span when flexural capacity was reached was 2.5 times the total service load moment in the dry span and 3.0 in the epoxyed span.

These conclusions indicate that there are differences in the service load behavior of the dry and epoxyed spans, but both types performed well. It is also apparent that while the dry jointed span had a smaller ultimate capacity than the epoxyed span, it still had a very adequate factor of safety.

7.2.4 Kordina and Weber.³⁶ Four I-beams were constructed of three segments each. The two joints in each specimen had identical key details, but one joint was epoxyed and the other was coated with a bituminous substance to represent a worst case condition. The four types of joint tested were: monolithic, smooth, single key and multiple key. All of the tendons were grouted internal. Figure 7.8 shows the beam and loading condition.

The specimen with smooth joints failed due to slipping of the segments at the joint on the non-epoxyed side. All other specimens failed, relatively symmetrically, due to web crushing. In all cases, except the smooth jointed specimen, the specimens exceeded the predicted shear capacity.

7.2.5 Bakhom, Buyukozturk and Beattie.⁹ A large number of push-off shear tests were performed to evaluate the performance of dry and epoxyed, flat and keyed joints. Figure 7.9 illustrates the typical specimen configuration. Additional variables were the level of normal force across the joint and the thickness of the

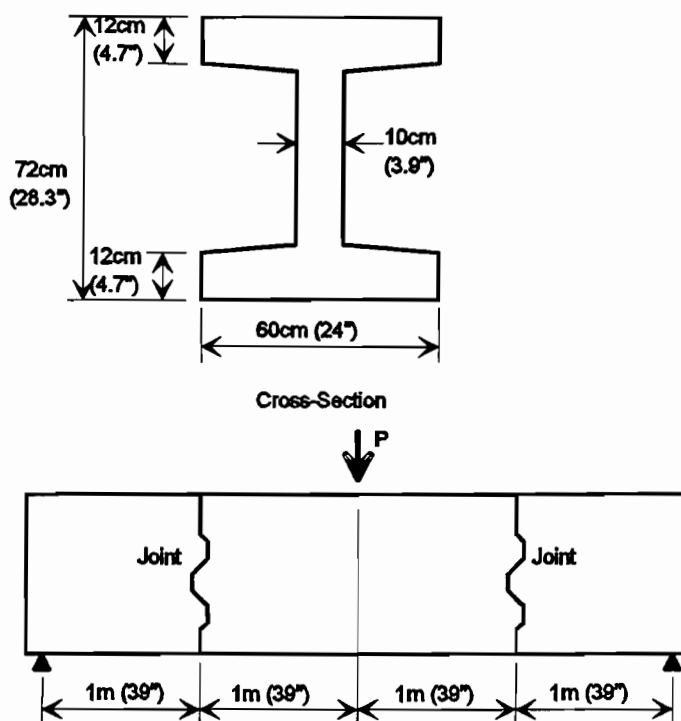


Figure 7.8 Specimens by Kordina and Weber.

epoxy layer. Based on these tests, equations for the ultimate capacity of epoxied and dry keyed joints were presented as follows:

$$\begin{aligned} \text{Keyed Epoxied Joints: } \tau &= 11.1\sqrt{f_c} + 1.20\sigma_c, \\ \text{Keyed Dry Joints: } \tau &= 7.8\sqrt{f_c} + 1.36\sigma_c. \end{aligned}$$

where:

$$\begin{aligned} \tau &= \text{ultimate shear stress on joint, psi,} \\ \sigma_c &= \text{normal stress across joint, psi.} \end{aligned}$$

It is also noted that of the three tested joint thicknesses, the 2 mm (0.08") joints performed the best, followed by the 1 mm (0.04") joints and finally the 3 mm (0.12") joints. They state that a definitive relationship between epoxy thickness and joint strength could not be established.

In the conclusions it is stated that the shear-off failure mode should be considered in the design of pre-cast segmental bridges, especially at locations near end span supports, near internal supports, and generally in bridges with external prestressing.

7.3 Surveillance Program

Two aspects of joint behavior were studied in this program: effectiveness of temporary prestress and behavior under permanent prestress. Two types of measurement systems were used to obtain the desired data.

7.3.1 Grid Crack Monitors. A grid crack monitor is made up of one opaque and one transparent plastic plate. The opaque plate is mounted on one side of the joint, and the transparent plate is mounted on the opposite side and overlays the first plate. The opaque plate has a grid imprinted on it and the transparent plate has a cross-hair. If the plates move relative to one another, the amount of movement can be read off of the grid.

Two grid crack monitors were mounted on three to four joints in each of the heavily instrumented spans and in the poor-boy continuous span. One monitor was positioned high on the joint, the other low. The plates were attached on the inside of the web walls so they could be read from the inside of the bridge (see Figure 7.10).

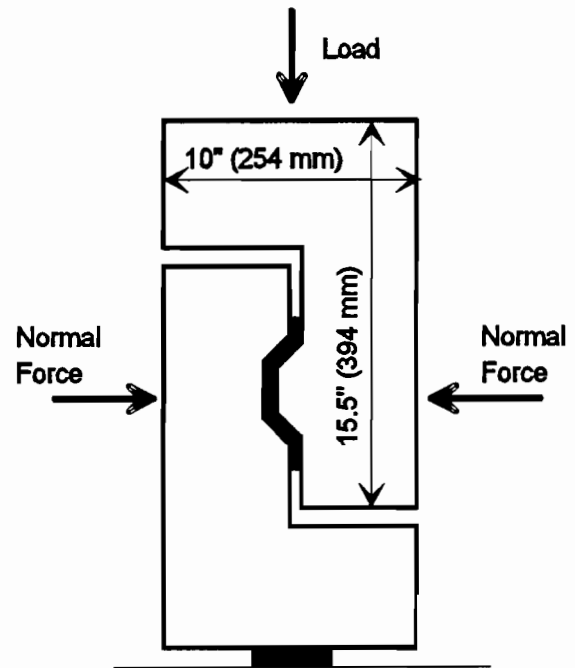


Figure 7.9 Push-off specimens by Bakhoun, Buyukozturk and Beattie.

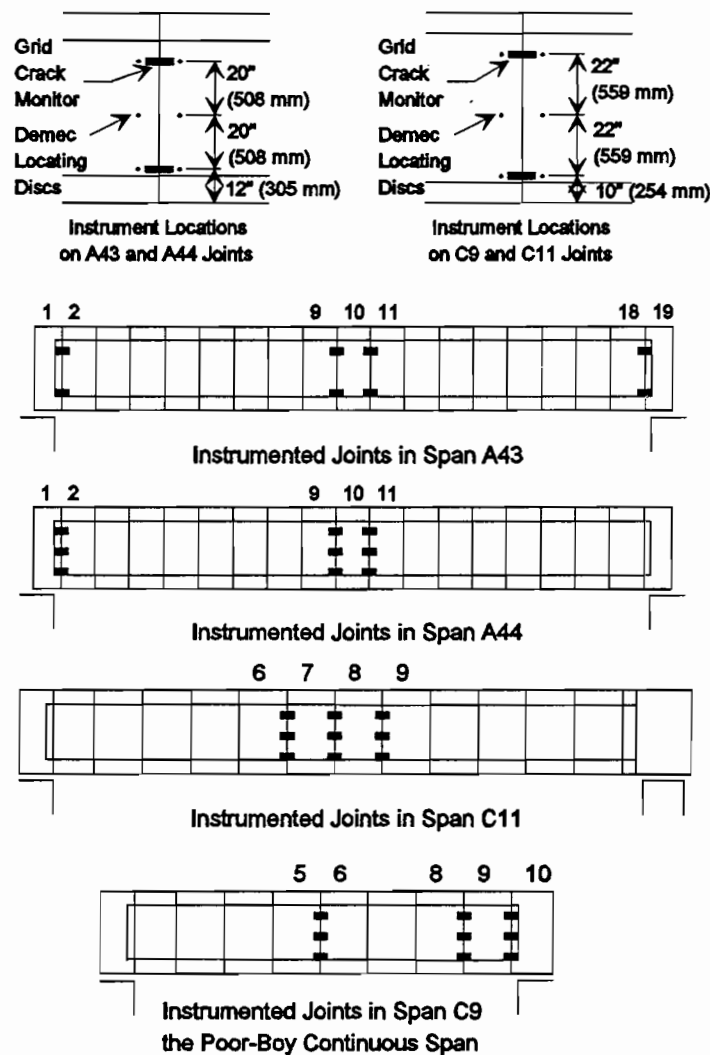
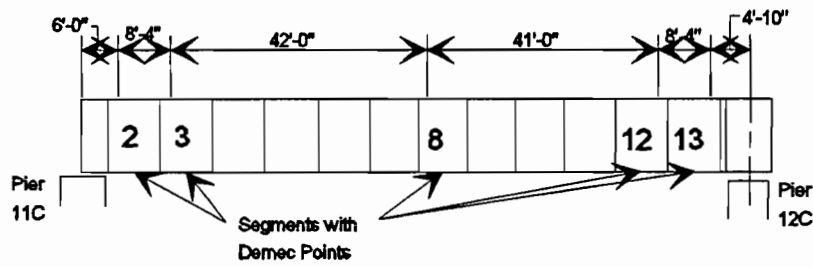


Figure 7.10 Instrumentation layouts.

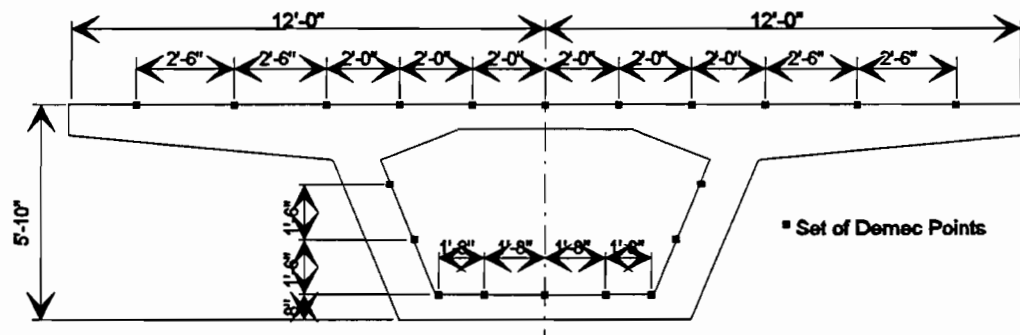
The monitors were read before and after stressing and over the course of many months. Several of the monitors were damaged during erection operations.

7.3.2 Surface Strain Gages. Two sets of surface strain gages were used in the evaluation of the joints. The first set was the pre-drilled system used to study transverse stress distributions (see Chapter 5). These sets of gages were used to investigate the stresses across the joints during temporary prestressing operations. The layouts are shown in Figure 7.11.

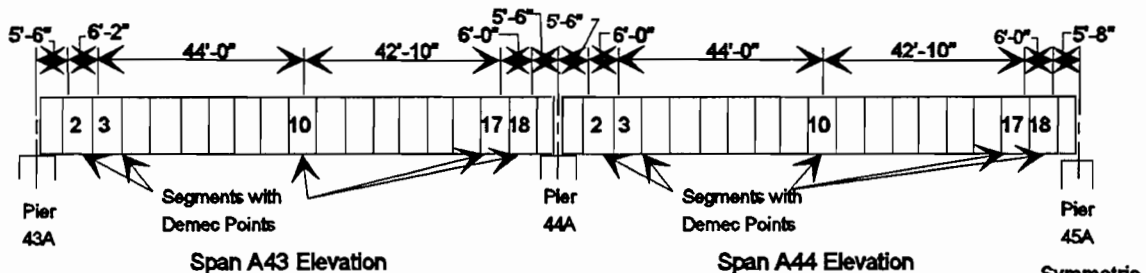
The second set of surface strain gages was applied after the epoxy operations were completed. Three pairs of locating discs at an 8" (203 mm) gage length were positioned on the same joints as the grid crack monitors. The first pair was at the same height as the top grid crack monitor, the second was at mid-height of the joint and the third was at the level of the bottom grid crack monitor (see Figure 7.10). These gages were read at the same times as the grid crack monitors.



Elevation of Span C11



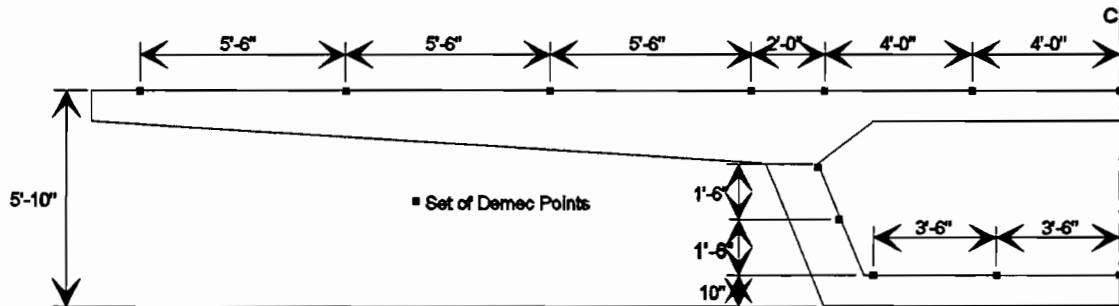
Type I Segment Demec Point Layout



Span A43 Elevation

Span A44 Elevation

Symmetric about C1



Type III Segment Demec Point Layout

To convert inch to millimeter multiply by 25.4.

Figure 7.11 Segment Demec point layouts.

7.4 Presentation of Results

7.4.1 Temporary Prestress. Figure 7.12 shows the locations of the temporary prestressing brackets on the Type I and Type III segments. The figure also gives the forces required in the top and bottom bars to result in a uniform stress of 40 psi (276 kPa) across the joint. The figure also shows the locations of the so called "female-female" keys which were adopted to reduce the volume of epoxy and the amount of temporary prestress across the joints.

With a uniform prestress of 40 psi (276 kPa) the strain in the concrete is expected to be approximately $8\mu\epsilon$, based on the measured moduli of elasticity of 5240 ksi (36130 MPa) for span C11 and 5344 ksi (36847 MPa) for spans A44 and A43. The general sensitivity including reader error in the demec gage is ± 2 units which equates to $\pm 16\mu\epsilon$. Another variable which made readings unreliable was temperature change. Each epoxy and stressing operation required 30-45 minutes. As the deck warmed during the day, surface strain readings were affected. These factors made evaluation of the data difficult.

The only reliable information to come from the readings was the uniformity of the stress across the joints, and the presence of stress concentrations.

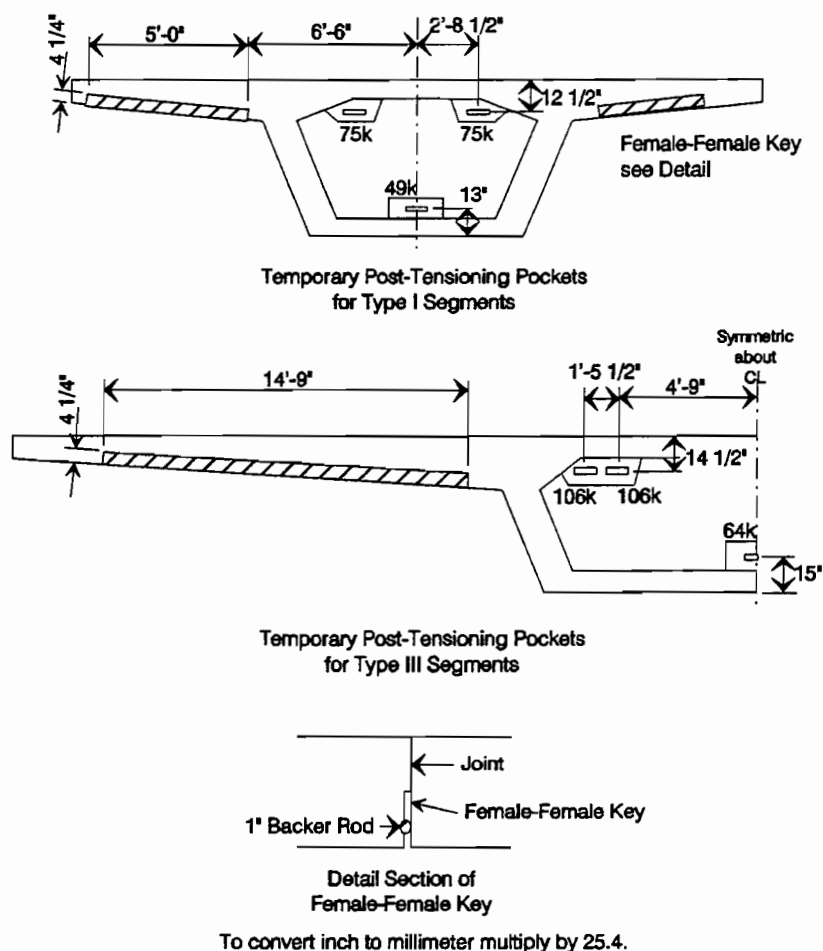


Figure 7.12 Temporary post-tensioning details.

For most joints the strains in the concrete immediately adjacent to the joints were uniform to $\pm 25\mu\epsilon$ (see Figure 7.13). Considering the error in the gage is $\pm 16\mu\epsilon$, this would indicate a reasonably evenly compressed joint. In a few cases, particularly in the first and last joint stressed, definite stress concentrations in the proximity of the temporary post-tensioning pocket were apparent. Figure 7.14 shows two of the non-uniform stress distributions. Since the highest strains are near the central part of the slab between the webs and since these segments are

adjacent to the segments where post-tensioning was applied, there non-uniform stresses are due to this localized force application and not due to joint gapping.

The joints did not close as well as expected, and at times were slightly gapped. This is attributable in part to the bow-shaped segment phenomenon which occurs due to thermal gradients which develop during match-casting (see Chapter 11). On average 5/8 of the joints in each span showed signs of good epoxy squeeze out and uniform joint closure. One fourth of the joints showed some signs of gapping, up to 1/8" (3 mm). The other eighth of the joints were difficult to categorize, showing neither good squeeze out nor gapping.

One problem with the gapped joints was a reduced closure pour size. A closure pour, designed to be 12" (305 mm) long, is poured between the spans over each typical pier. The average measured length of the closure pours was 9.2" (234 mm). This caused problems in forming the joints and in installing dead end tendon anchorages in the joints. The spans surveyed had between 15 and 18 joints. If each joint were 1/8" (3 mm) thick, this would result in spans which were 1.9 to 2.3

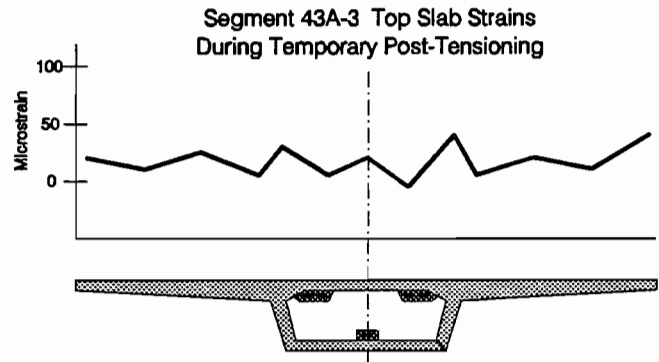


Figure 7.13 Typical uniform strain distribution across joint during temporary post-tensioning.

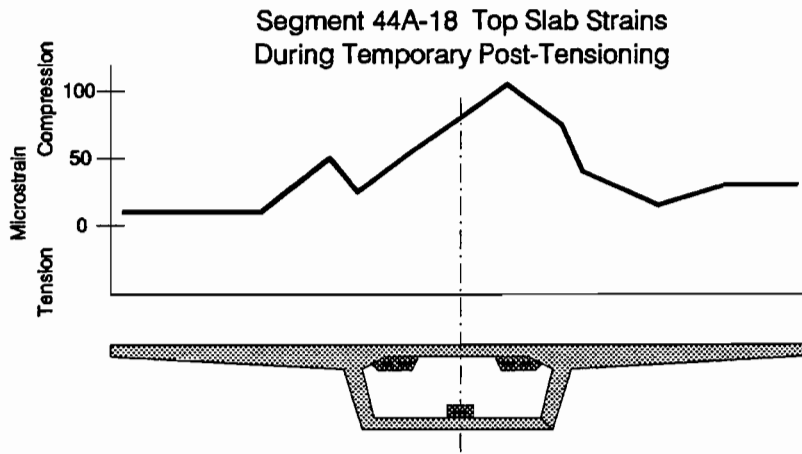
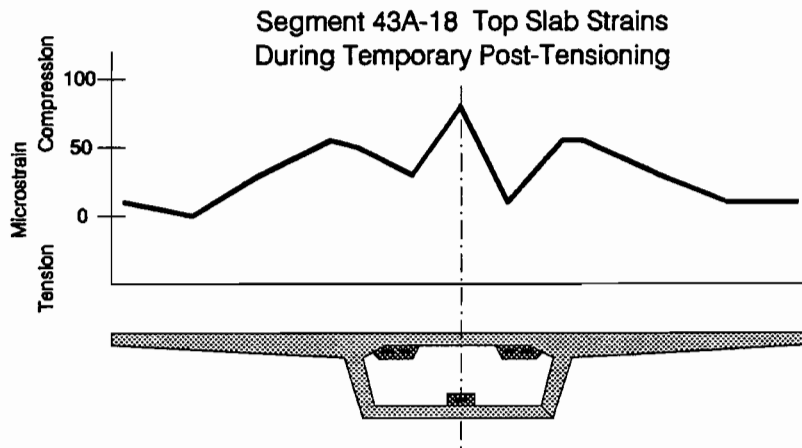


Figure 7.14 Typical non-uniform strain distributions across joints during temporary post-tensioning.

inches (48 to 58 mm) too long. On average the spans were 2.8 inches (71 mm) longer than expected.

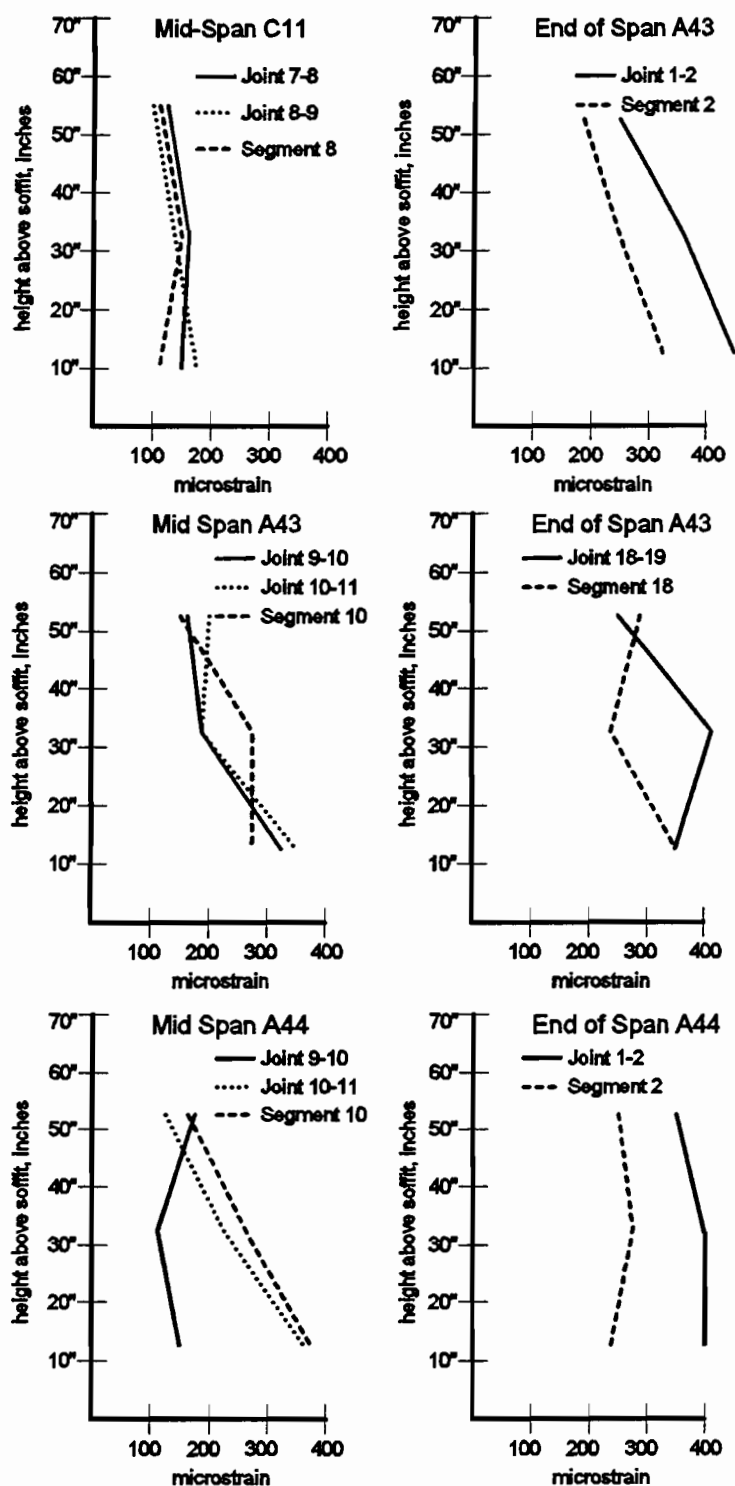
Generally, except for the first and last joints of the span, the temporary post-tensioning system provided a reasonably uniform pressure across the joints. The gapping problem evident in some of the joints appears to be related to the bow-shaped segment phenomenon and is therefore a casting problem and not an erection error. Chapter 11 outlines some measures for reducing the bow-shaped segment problem.

7.4.2 Joint Behavior Under Permanent Post-Tensioning.

7.4.2.1 During Stressing.

In each span there were locations where joint demec readings could be compared with segment demec readings. A comparison provides information on the performance of joints relative to the performance of monolithic concrete under compressive and bending stresses. Figure 7.15 compares the compressive strains on an 8" (203 mm) gage length across the joints with compressive strains, also on an 8" (203 mm) gage length, directly adjacent to the joint.

At the mid-span locations, segments 11C-8, 43A-10 and 44A-10, there is generally good agreement in magnitude and distribution of the web strains between the joint readings and the



To convert inch to millimeter multiply by 25.4.

Figure 7.15 Comparison of strains across joints to strains in adjacent concrete.

segment readings. At the end segments, segments 43A-2, 43A-18, and 44A-2, the agreement is not quite as good. The strains across the joint are significantly higher than the strains in the adjacent concrete. As mentioned in the previous section, the strain distributions across the end joints during temporary post-tensioning were not as uniform as they were for interior joints. This could have lead to thicker joints between the end segments. Since the modulus of elasticity of the epoxy (440 ksi or 3034 MPa) is smaller than that of the concrete, the thicker joint could have had a significant effect on the average strain for the 8" (203 mm) gage length.

Since, generally, the strain distributions are very similar, the epoxy is performing the function of smoothing out possible stress concentrations and allowing a uniform transfer of stress across the joint.

7.4.2.2 Long Term Behavior.

The demec and grid crack monitor readings were continued on a regular basis over the course of many months after stressing. The grid crack monitors remained essentially unchanged during the entire time readings were made. Figure 7.16 shows the change in strain across a typical joint in Span A44 over the course of almost one year. The average ratio of increased strain to initial strain for the three joints in Span A44 is 0.66 which is quite similar to the value of the measured creep function which at 300 days was 0.68.

The strain difference fluctuates with the ambient temperature. In Figure 7.16 the compressive strains increase until day 46 which was May 29th. Then during the warmer months, due to the thermal expansion of the concrete, the compressive strains decrease. Between day 170 (October 5) and day 206 (November 4) the compressive strains increase as the ambient temperature decreases and the concrete shortens.

Figure 7.17 compares long term strains across a joint with the strains in the adjacent segment. The lines indicate the average strain for the three web strain readings. Generally, the lines follow the same trend although the strains across the joint do not increase as much as those in the monolithic concrete. This could be temperature related since at approximately day 40 the temperatures rose with the beginning of summer, but this seems to affect the joints more than the monolithic concrete.

**Change in Strain with Time
Joint 10-11 Span A44**

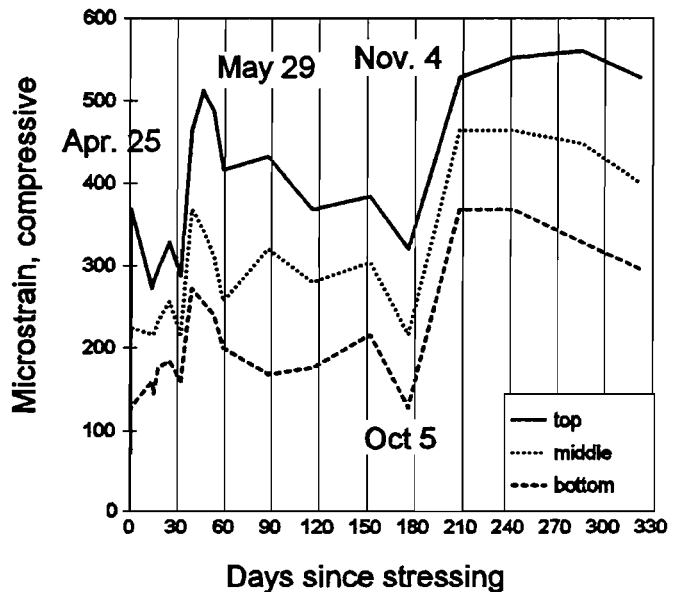


Figure 7.16 Changes in strains with time across a typical joint.

7.4.2.3 Summary. Overall, the joint behaved as well as the adjacent concrete. The initial strains were very similar, except at the first and last joints where strains across the joints were higher than in the concrete. The long term readings showed the joint behavior to be similar to the expected behavior for a monolithic structure. The strains across the joint seem to be more affected by temperature changes than monolithic concrete.

The ease with which joints can be closed with the temporary post-tensioning system can be affected by the "bow-shaped" segment phenomenon caused by thermal gradients which develop during match casting operations.

The large average thickness of the joints and the presence of gapped joints are problems resulting from the bow shaped segment effect. Although the joint thickness did not appear to have a detrimental effect on the behavior of the structure, it did cause construction problems, particularly at the smaller than expected closure strips. Another concern with the gapped joints is that the long term corrosion protection of the internal tendons may be reduced by gapped joints which allow the intrusion of water and other corrosive elements. Chapter 11 presents a study of the bow shaped segment phenomenon and measures which can be taken to reduce the problem.

7.5 Discussion of Joint Capacity

Significant differences between the capacities of Type A (epoxied) and Type B (dry) joints are apparent in the specimens of Koseki and Breen,³⁷ but not in those of Ramirez or MacGregor, and are only apparent in the smooth jointed specimen of Kordina and Weber. Where differences occurred, the dry jointed beams failed due to joint failure caused by slip and key breakage. The epoxied specimens failed due to bearing and web crushing shear failures. The epoxied specimens exceeded the calculated shear capacities while the dry jointed specimens did not. This is because the failure was in the joint, and was not a typical web shear failure.

This raises the possibility that another check, a joint capacity calculation as suggested by Bakhoun, Buyukozturk and Beattie, should be made for dry joints, especially if loading conditions exist which might put a joint in direct shear. Figure 7.18 illustrates some conditions under which a joint failure might occur. The worst case would occur at the first joint adjacent

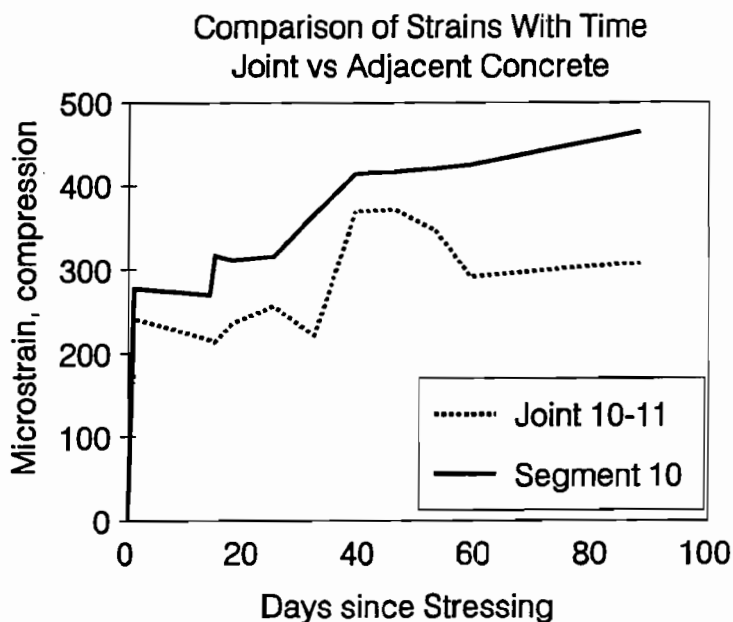


Figure 7.17 Comparison of average change in strain with time, joint vs. adjacent concrete.

to the pier where shears are very high and truck and crane loads might be very close to the joint. If these types of loadings can be expected, the dry joint capacity must be checked.

There is currently no equation in the *AASHTO Guide Specification* for calculating the capacity of a dry keyed joint. This section discusses a possible approach.

7.5.1 Bakhoun, Buyukozturk and Beattie Approach. Based on their extensive series of push-off shear tests, as described earlier, Bakhoun, Buyukozturk and Beattie proposed an equation for calculating the capacity of a dry keyed joint. That equation is :

$$\tau = 7.80 \sqrt{f'_c} + 1.36 \sigma_n$$

where:

τ = ultimate shear stress on joint,
 σ_n = normal stress across joint.

This equation fits the data from the push-off series quite well but slightly overestimates the capacity of Koseki's specimens. The equation is the result of a regression analysis of the push-off data, but since the specimens did not vary in key geometry, the equation may not work for different key configurations.

7.5.2 Proposed Method. With the proposed method the capacity of a keyed joint is assumed to be a combination of the shear friction between the smooth faces and the direct shear capacity of the keys along the failure plane. Figure 7.19 illustrates a failure plane for a dry keyed joint.

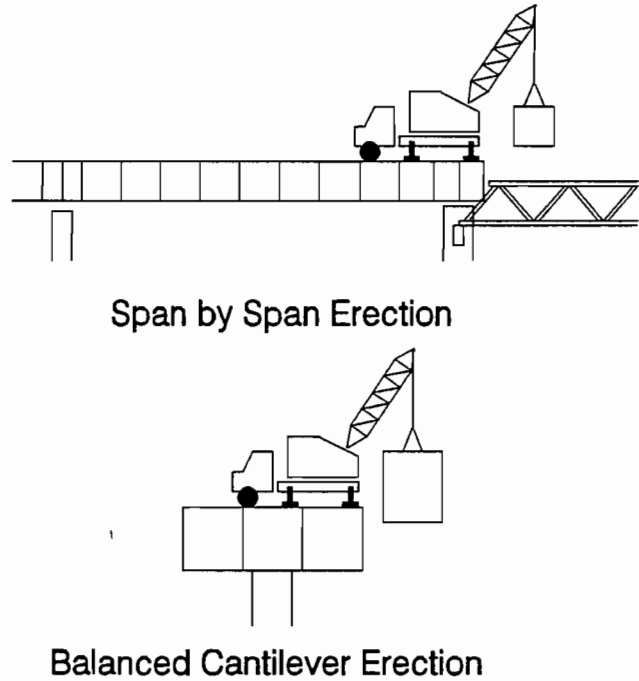


Figure 7.18 Joints in situations with high shear.

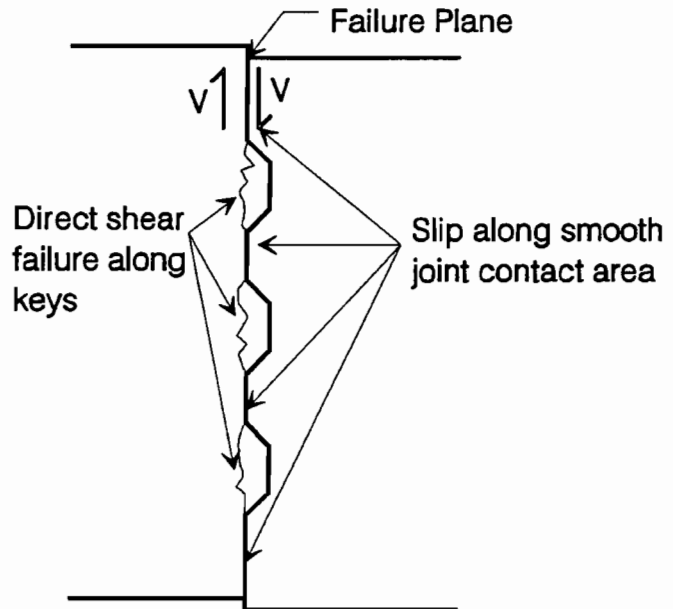


Figure 7.19 Joint shear failure plane.

As a dry joint is loaded, initially the shear is carried across the joint by shear friction where:

$$V = \mu \sigma_n d b_w$$

with

- σ_n = normal stress across joint,
- μ = coefficient of friction between smooth concrete surfaces
(ACI 318 recommends 0.6⁵),
- d = depth of beam,
- b_w = width of web.

Once the shear friction limit is reached a slip in the joint will occur. If the joint has keys they will be engaged at this time. The keys will continue to take load until they are sheared off. The capacity of a key is a function of the tensile strength of the concrete and the normal stress across the joint. Mattock³¹ explains the capacity using a Mohr's circle illustration. Figure 7.20 shows the state of stress near a shear key where shear is high and moment is very low, such as a push off test set up.

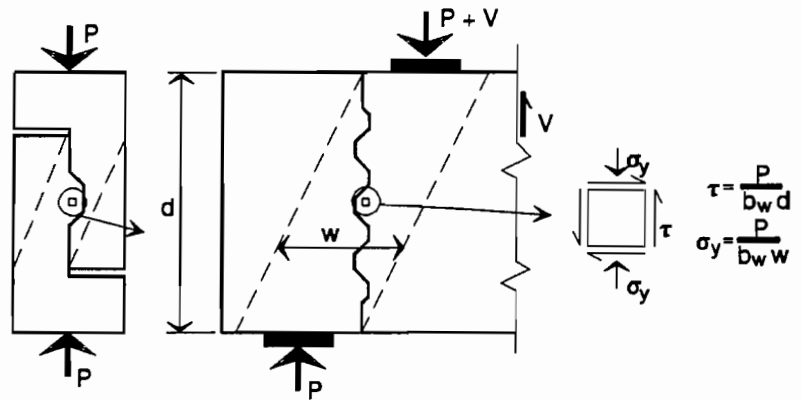


Figure 7.20 State of stress on an element near a joint.

If there is no compressive stress across the joint, the state of stress at failure is dictated by the tensile strength of the concrete and the ratio of the depth of the beam to the width of the compression strut. This is illustrated in Figure 7.21.

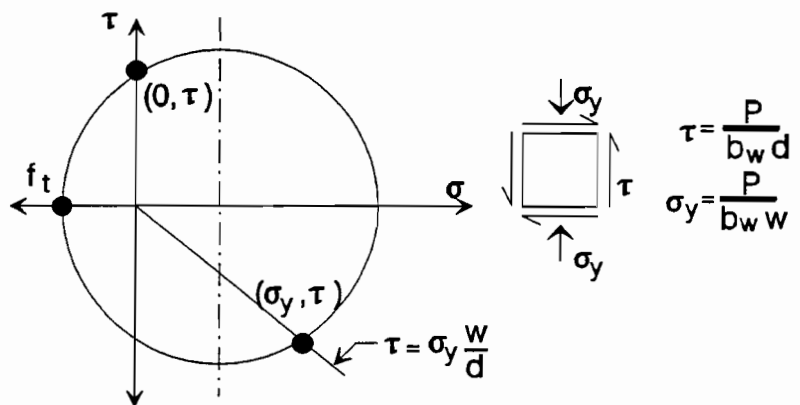


Figure 7.21 Mohr's circle description of state of stress on element near joint.

The presence of a confining pressure increases the capacity of the joint by moving

the center of the Mohr's circle to the right, thereby increasing the load which will cause a principle tension equal to the tensile strength of the concrete. This is illustrated in Figure 7.22.

The capacity of a shear key in direct shear is therefore a function of the tensile capacity of the concrete and the normal stress across the joint. The equation would take the form:

$$V_k = (C_1 + C_2 \sigma_n) A_k \sqrt{f_c}$$

where:

- V_k = direct shear capacity of a key, lbs.
- C_1 and C_2 = constants,
- A_k = area of the base of the key, in².

A conservative value for C_1 can be determined for a joint by assuming a compression strut angle of 45 degrees, which would result in a ratio of strut width to strut depth of 1.0 (w/d ratio in Figure 7.20). The state of stress on an element near the joint when no normal stress is present is illustrated in Figure 7.23. The calculations shown in this figure indicate that a value of 12 is reasonable for C_1 .

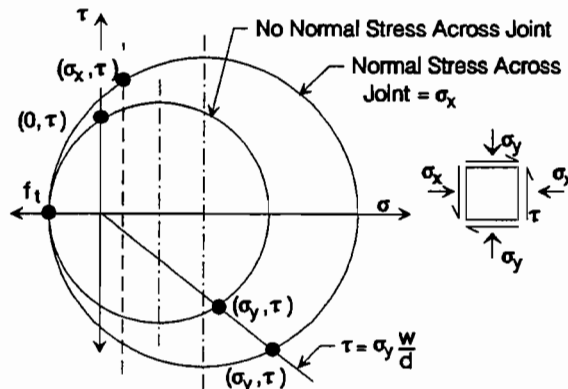


Figure 7.22 Mohr's circle description of state of stress on element near joint with normal stress.

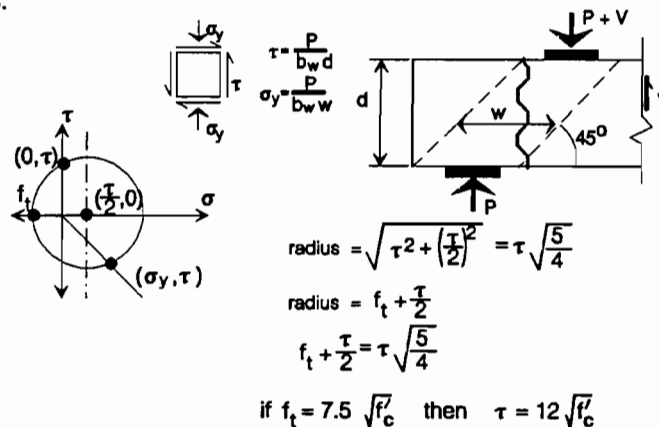


Figure 7.23 Shear Stress at failure for element with no normal stress.

The next aspect to be assessed is the increase in shear capacity resulting from the presence of a normal stress. The state of stress at failure on a joint with some normal stress is shown in Figure 7.24. The increase in ultimate shear stress on the failure plane can be expressed as:

$$\tau_{inc} = \frac{\sigma_x}{2} + \frac{1}{2} \sqrt{\sigma_x^2 + 6\sigma_x f_t + 5f_t^2} - f_t \frac{\sqrt{5}}{2}$$

This is a rather involved and tedious calculation. The entire expression can be replaced by the product of a constant (C_2), the normal stress, σ_n , and $\sqrt{f'_c}$. For a range of concrete strengths of 4000 to 8000 psi (27580 to 55160 kPa), and normal stresses from 100 to 1000 psi (690 to 6895 kPa), a value for C_2 of 0.017 is conservative (see Figure 7.25). For normal stresses higher than 1000 psi (6895 kPa) the value is slightly unconservative.

The expression for the direct shear strength of an initially uncracked key in a region of high shear and low moment is therefore:

$$V_k = A_k \sqrt{f'_c} (12 + 0.017 \sigma_n)$$

with

σ_n and f'_c in psi.

As stated earlier, the capacity of the portion of the failure plane which fails as a result of slip between smooth concrete surfaces is a function of the area in contact, the normal stress and the coefficient of friction. The ACI Building Code,⁵ in section 11.7.4.3, recommends a coefficient of 0.6, which is conservative.

Summing the capacity of the slipping plane and the sheared keys gives an expression for the capacity of a keyed dry joint along an assumed failure plane as follows:

$$V_k = A_k \sqrt{f'_c} (12 + 0.017 \sigma_n) + 0.6 A_{sm} \sigma_n$$

where:

A_k = Area of the base of all keys in the failure plane, in²,

σ_n = Average compressive stress across the joint, psi,

A_{sm} = Area of contact between smooth surfaces on the failure plane, in².

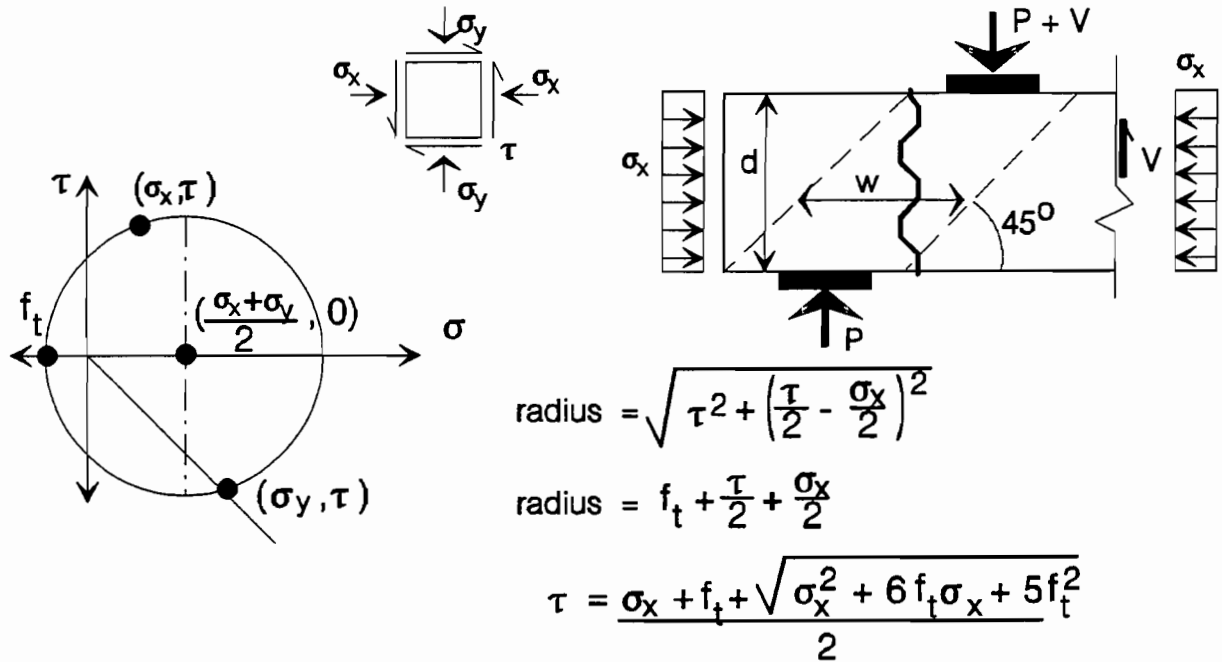
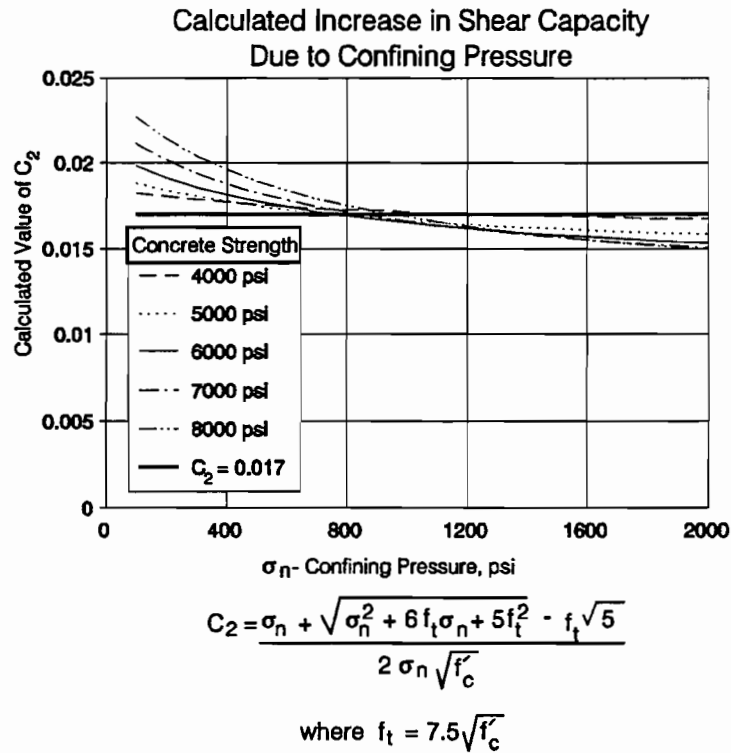


Figure 7.24 Shear stress at failure for element with normal stress across the joint.



psi X 6.89 = kPa

Figure 7.25 Calculation of constant for increase in shear capacity due to confining pressure.

7.5.3 Comparison of Equation and Tests. This equation was used to predict the joint failure loads of the dry jointed and monolithic specimens of Koseki and Breen,³⁷ and various specimens from the Bakhoum, Buyukozturk and Beattie program. Figure 7.26 shows the ratio of the actual failure load to the joint capacity prediction. The equation predicts the failures of Koseki's specimens quite well, except for the monolithic specimen which failed in bearing before direct shear. The capacities of Bakhoum's keyed specimens are predicted very well, the prediction of the monolithic specimens is somewhat unconservative, and the prediction of the smooth dry joints is erratic. The erratic prediction of the smooth jointed specimens illustrates the highly variable nature of the coefficient of friction between smooth concrete surfaces.

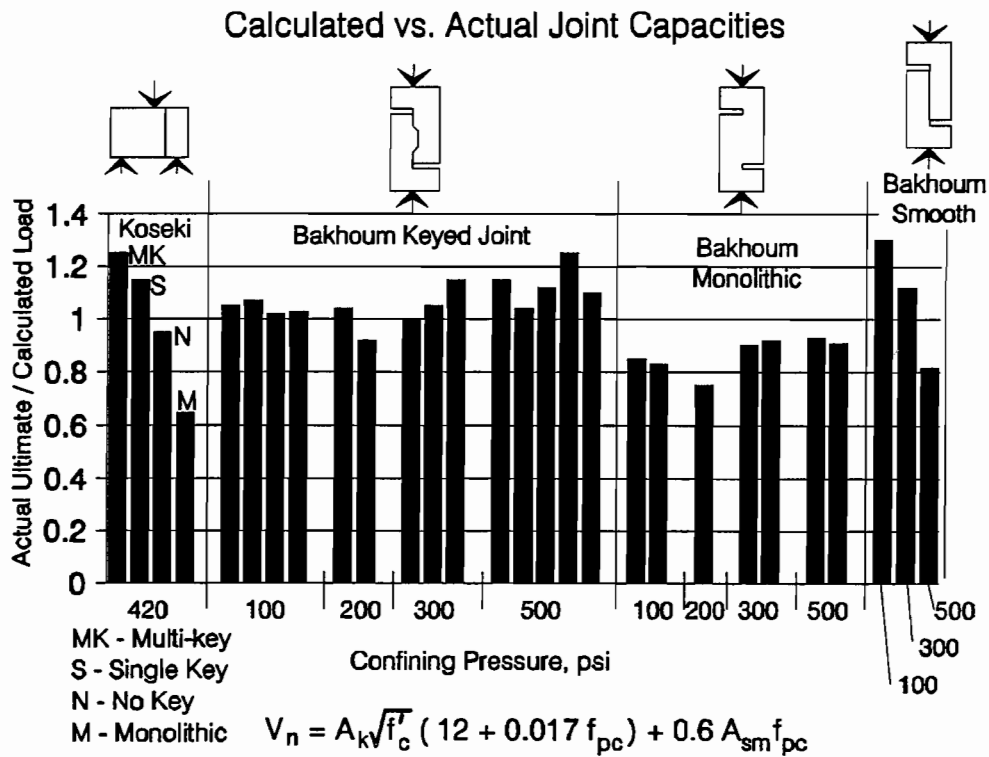
Table 7.1 shows for specimens by Koseki and Breen,³⁷ Ramirez⁶⁰ and Kordina and Weber³⁶ the shear capacity, as calculated using *AASHTO Guide Specification* recommendations, the joint capacity, the actual ultimate capacity, and the failure mode. Based on these calculations, the specimens which have smaller joint capacities than shear capacities and hence would be expected to experience joint failures are all of Koseki and Breen's specimens, and Kordina and Weber's smooth jointed specimen. This was, in fact, the case. The smooth jointed specimens slipped, although the Kordina and Weber specimen achieved higher than expected ultimate load due to dowel action of the grouted internal tendons. Koseki and Breen's two keyed specimens failed due to slip and key break off. The specimens which show the shear calculation as the controlling value failed in modes of web crushing and shear compression.

7.5.4 Summary. The capacity of a segmentally constructed bridge should be based on the flexural capacity, the shear capacity and, when dry joints are used, the joint capacity. Code language (specific language is presented in Section 7.6) should be added to the *AASHTO Guide Specification* indicating that when dry joints are used the capacity of the joint, based on the concrete tensile strength, the key geometry, and the compressive stress across the joint, must be determined. References which give guidance on joint design such as Koseki and Breen,³⁷ Mattock,³¹ and Bakhoum, Buyukozturk and Beattie should be mentioned in the commentary. Additional study is recommended to confirm the equation presented herein. An appropriate ϕ factor for the joint capacity equation should also be determined. This will require additional tests to determine the reliability of the joint capacity equation.

7.6 Recommendations

7.6.1 Epoxied Joint Behavior. The joints of the San Antonio "Y" project performed very well. During temporary post-tensioning operations the joints did not all close completely, but actions taken at the casting yard to alleviate bow-shaped segments can reduce this problem. Also the wider than expected joints seemed to have had no detrimental effects on the behavior of the structure.

Under permanent post-tensioning loads the joints behaved essentially as monolithic concrete, except in a few instances where initial strains across joints were higher than in the



psi X 6.89 = kPa

Figure 7.26 Calculated vs. actual joint capacities.

Table 7.1 Comparison of Actual and Calculated Capacities of Dry Jointed Beams

Specimen	V_n Shear	V_n Joint	V_u Test	V_u/V_n	Failure Mode	
Koseki - and Breen	No Key	49.2	15.2*	14.0	0.92	Slip
	Single Key	49.1	39.5*	44.5	1.13	Key Break-off
	Multi-key	49.2	38.3*	48.0	1.25	Key Break-off
Ramirez-	a/d=1.5	39.6*	61.7	75.0	1.89	Web Crushing
	a/d=2.5	39.6*	63.4	50.0	1.26	Shear-Compr.
	a/d=3.5	38.6*	58.6	40.0	1.04	Shear-Compr.
Kordina and Weber	Multi-key	72.5*	132.9	123.6	1.70	Web Crushing
	Single Key	71.4*	118.9	90.0	1.26	Web Crushing
	No Key	71.9	56.9*	100.6	1.77	Slip

* Controlling Capacity

To convert kips to kN multiply by 4.448.

adjacent concrete. With time the joints seemed to be more affected by temperature changes than the adjacent concrete.

Based on these observations, no changes are recommended for the *AASHTO Guide Specification* regarding epoxied joints.

7.6.2 Dry Joint Capacity. The *AASHTO Guide Specification* should include a method for calculating joint capacity. The formula could be inserted at the end of Section 12.2 - General Requirements for Shear and Torsion, as section 12.2.21:

12.2.21 For structures utilizing dry joints, the nominal capacity of the joint shall be calculated as:

$$V_j = A_k \sqrt{f'_c} (12 + 0.017 f_{pc}) + 0.6 A_{sm} f_{pc}$$

Where:

A_k = Area of the base of all keys in the failure plane, in²,

f'_c = compressive strength of concrete, psi.

f_{pc} = Compressive stress in concrete after allowance for all prestress losses, psi, determined at the centroid of the cross-section (existing definition).

A_{sm} = Area of contact between smooth surfaces on the failure plane, in².

In the commentary the following should be added:

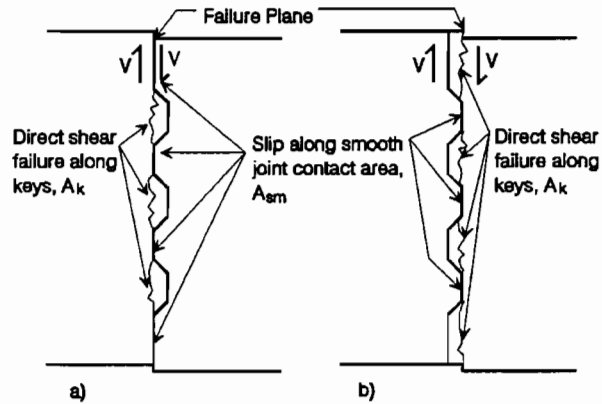
12.2.21 The joint shear capacity must be checked in dry jointed structures to ensure the integrity of the joint. The equation was derived with guidance from work by Mattock,³¹ and confirmed by test data from experimental programs of Koseki and Breen³⁷ and Bakhoun, Buyukozturk and Beattie.⁹ The equation may also be used to determine the acceptable number of broken keys to be allowed before repair is deemed necessary. Because the presence of epoxy could change the friction coefficient, the equation is not necessarily valid for evaluating broken keys in epoxy jointed structures.

Figure C6 (see Figure 7.27) illustrates a typical failure plane of a keyed joint in direct shear. The areas of the base of the sheared keys, A_k , and the smooth contact areas, A_{sm} , are shown. The critical failure plane will have the greatest ratio of A_{sm} to A_k (this means the greatest area of slip and the least area of key breakage).

Key breakage and joint failure is a brittle failure mode, and the strength reduction factor should reflect this. The ϕ should also reflect the reliability of the calculation. Unfortunately there is little data available to determine the level of reliability. For the 16 keyed joints examined in this

chapter the actual to calculated capacity was 1.09, the standard deviation was 0.09 and the lowest ratio was 0.92 (see Figure 7.26). Based on these few results, a safe ϕ factor of 0.80 is recommended.

The ϕ factor for joint capacity, to be used in conjunction with the nominal joint capacity equation of section 12.2.21, should be included in Section 8.3.6 of the *AASHTO Guide Specification*, which would then read :



For the same joint configuration, the failure plane in a) is most critical because it contains a larger smooth contact surface and a smaller area of key breakage.

Commentary Figure C8

Figure 7.27 Joint shear failure plane.

8.3.6 Strength Reduction, ϕ , shall be taken as follows:

Type	ϕ_f Flexure	ϕ_v Shear	ϕ_j Joint
Fully Bonded Tendons			
Type A joints	0.95	0.85	-
Type B joints	0.90	0.80	0.80
Unbonded or Partially Bonded Tendons			
Type A joints	0.90	0.80	-
Type B joints	0.85	0.75	0.80

7.7 Conclusion

The epoxy joints of the San Antonio "Y" Project performed quite well. There was no evidence of relative joint movement, and the joints behaved very similarly to adjacent monolithic concrete.

A joint capacity equation is presented in this chapter which should ensure the proper functioning of dry joints.

CHAPTER 8 HEAVY END DIAPHRAGM BEHAVIOR

8.1 Introduction

In order to maintain cross-sectional geometry, thin walled box shapes often require transverse stiffeners at critical locations. These stiffeners are called diaphragms (see Figure 8.1).

End diaphragms, in externally post-tensioned structures, function to transfer loads from the webs to the supports, and to diffuse concentrated loads from post-tensioning anchorage devices out into the cross-section. Intermediate diaphragms stiffen the section and facilitate load transfer from tendon deviator points into the cross-section.

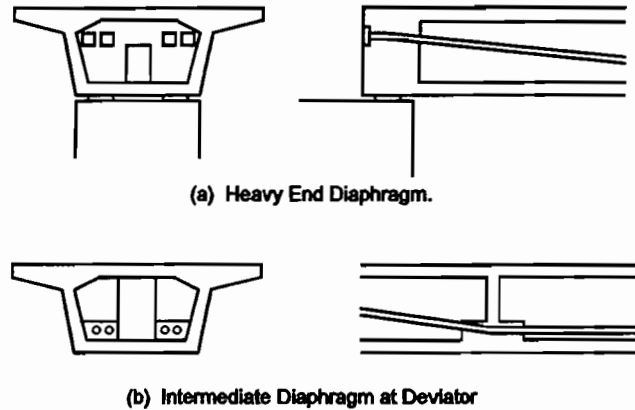


Figure 8.1 Diaphragms in segmental box girders with external tendons.

The focus of this chapter is the field study of two heavy end diaphragms. The two diaphragms were instrumented with reinforcing steel strain gages which were monitored during vertical post-tensioning operations and longitudinal tendon stressing operations. Crack patterns and crack widths were also recorded.

The field observations are used to assess current design practice, to study the applicability of Strut-and-Tie modelling, and to evaluate the design criteria in the *AASHTO Guide Specification for the Design and Construction of Segmental Concrete Bridges*¹ (to be referred to for the remainder of the chapter as the *AASHTO Guide Specification*) and the soon to be published *NCHRP Report 10-29 Anchorage Zone Reinforcement for Post-Tensioned Concrete Girders*.¹³

8.2 Literature Review

8.2.1 Powell et al.⁵⁵ This report is an excellent overview of the state-of-the-art of externally prestressed bridges. One incidence of diaphragm cracking is described. The Can Bia bridge, built in France in the 1950's, experienced cracking in the diaphragms which was attributed to the transverse tensile force induced by the spreading of the concentrated tendon anchorage forces.

8.2.2 Woodward.⁷⁶ Diaphragm cracking is described which led to the temporary closure, and retrofit of a concrete box girder bridge. Additional vertical prestress was added in the diaphragm region and existing cracks were grouted.

8.2.3 Kreger.³⁸ Diaphragm cracking developed in the pier segments of a bridge structure of the Washington D.C. rapid transit system, before the structures were opened to train traffic (see Figure 8.2). The addition of vertical post-tensioning bars to control the cracking, and the epoxy injection of remaining cracks resolved the problems. Field testing showed the structures to be functioning properly and they are currently in use.

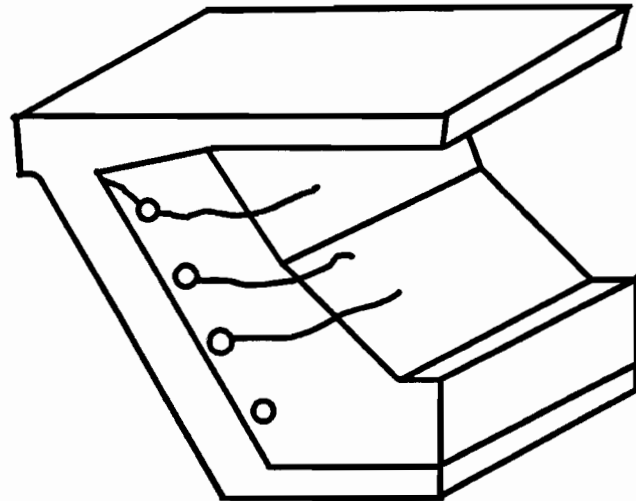


Figure 8.2 Cracking in Washington Metro pier segments.

8.2.4 Wollmann.⁷⁴ A study of end diaphragm behavior was completed as part of a comprehensive anchorage zone research project. Wollmann approached the problem by first performing a linear elastic finite element analysis (FEA) of a simple two anchor diaphragm, then developing strut-and-tie models based on the FEA results. The strut-and-tie models were used to design the reinforcing steel details for several one half scale models. The models were constructed and tested to destruction. The results of the tests were used to confirm the validity of strut-and-tie modelling as a design tool.

Wollmann recommends a combination of FEA and strut-and-tie modelling for design of heavy end diaphragms. He recommends the FEA to assess the behavior of the structure prior to cracking and to locate those regions with a high potential for cracking. The strut-and-tie model can then be used to determine an overall load path and to design the primary reinforcing steel.

The basic behavior of the heavy end diaphragms is described by Wollmann as that of a deep beam supported on three sides (see Figure 8.3). The primary region of tensile stress is on the face of the diaphragm opposite the anchorage plates. He notes that simple methods, such as those described by Guyon,²⁸ are not applicable to determine the magnitude of the tensile stresses in this type of anchorage zone.

Wollmann noted that the critical location in his specimens was the interface between the diaphragm and the flanges and webs (see Figure 8.4). Good detailing in this region, including effective anchorage of the transverse reinforcing steel or transverse post-tensioning, is essential in the design of end diaphragms. Wollmann's experiments showed that the final failure loads were substantially greater than the strut-and-tie model capacity based on yielding

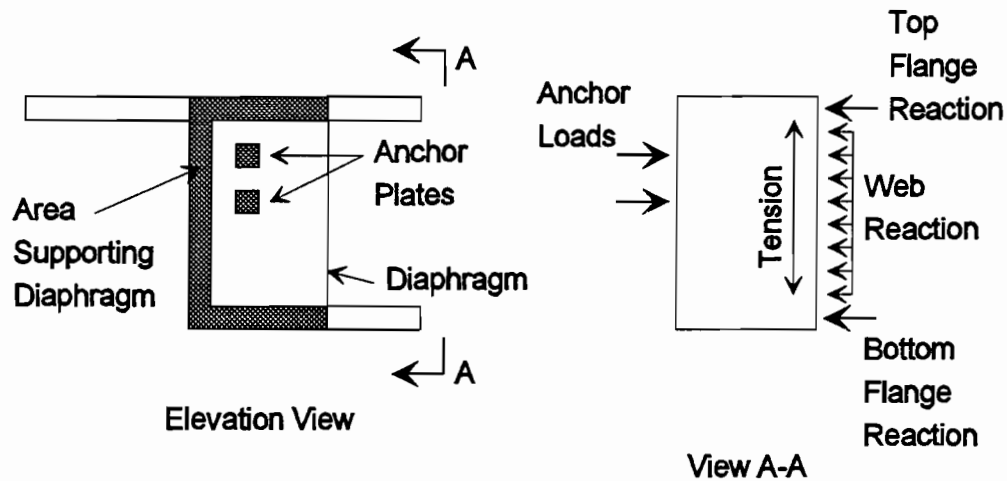


Figure 8.3 Diaphragm as deep beam supported by flanges and web.

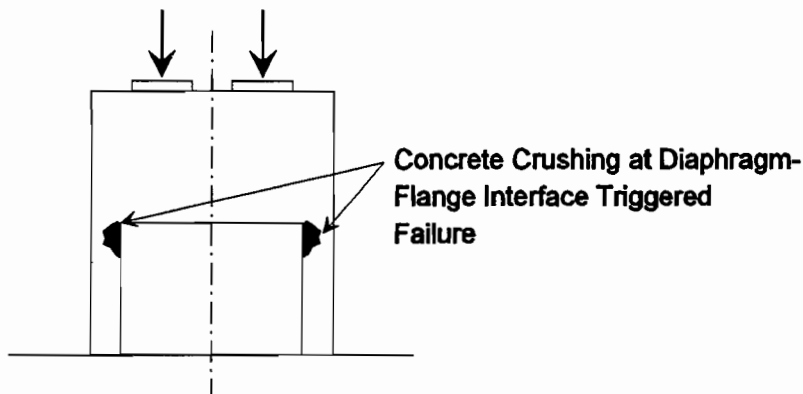


Figure 8.4 Failure of Wollmann's diaphragm specimens.

of the tension tie. The capacity was better approximated by the capacity of the compression struts where they exited the heavy diaphragm and entered the web walls and flanges.

8.2.5 Schlaich et al.⁶² This paper provides background in the development of strut-and-tie models. "B" (Beam or

Bernoulli) regions and "D" (Discontinuous or Disturbed) regions are defined and step-by-step methods for the development of strut-and-tie models are recommended. Several figures are provided which give examples of diaphragm areas (see Figure 8.5). Schlaich et al. state that diaphragms which anchor post-tensioning tendons are a simple variation of the deep beam problem.

8.2.6 AASHTO Guide Specification.¹ Section 12.5 describes special requirements for diaphragms, deep beams, corbels and brackets. The section states that these types of discontinuity regions ("D" regions) must be proportioned using strut-and-tie model approaches. The special section on diaphragms states:

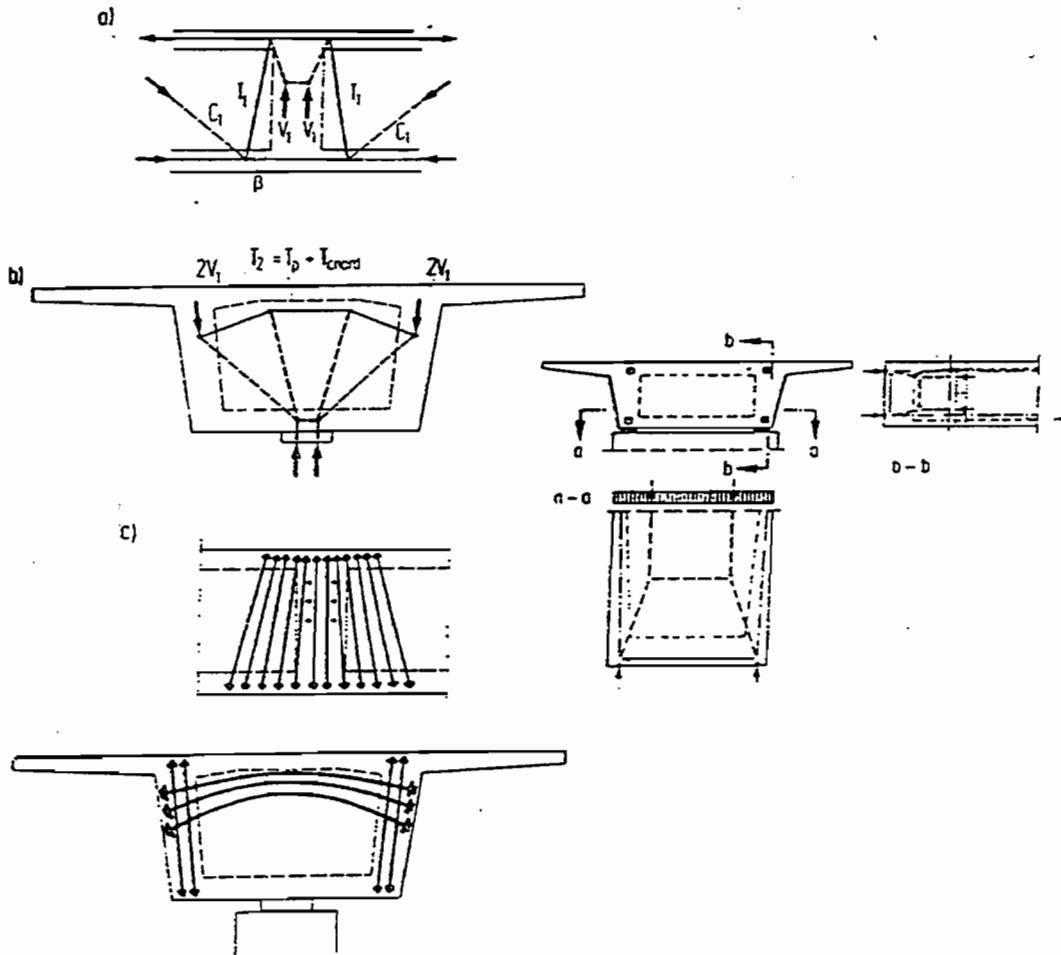


Figure 8.5 Diaphragm strut-and-tie models by Schlaich et al.

12.5.2 Diaphragms are ordinarily required in pier and abutment superstructure segments to distribute the high shear forces to the bearings. Vertical and transverse post-tensioning shall be analyzed using the strut-and-tie model of Section 12.4 and the effective prestress forces of Section 12.1.5. The diaphragm tendons must be effectively tied into the diaphragms with bonded non-prestressed reinforcement to resist tendon forces at the corners of openings in the diaphragms.

In the commentary a figure is presented which illustrates a strut-and-tie model of an end diaphragm for transfer of shear forces from the webs to the bearings, but no mention of post-tensioning force load paths is given. Section 12.4 gives basic guidance on strut-and-tie model requirements for compression chords and struts and tension ties.

8.2.7 NCHRP Report.¹³ This report summarizes a comprehensive study of post-tensioning anchorage zone behavior. A code and commentary are proposed to assist in the design of anchorage zones. Section 9.21.3.6 addresses the special requirements of end diaphragms. It states:

9.21.3.6.1 - For tendons anchored in diaphragms, concrete compressive stresses shall be limited within the diaphragm in accordance with sections 9.21.3.4.1 through 9.21.3.4.3. Compressive stresses shall also be checked at the transition from the diaphragm to webs and flanges of the member.

9.21.3.6.2 - Reinforcement shall be provided to ensure full transfer of diaphragm anchor loads into the flanges and webs of the girder. The more general methods of Section 9.21.4 or 9.21.5 shall be used to determine this reinforcement. Reinforcement shall also be provided to tie back deviation forces due to tendon curvature.

Sections 9.21.3.4.1 to 3 give general guidance on detailing, section 9.21.4 gives guidance on application of strut-and-tie modelling, and section 9.21.5 gives guidance on designing from linear elastic finite element analysis. Approximate methods are not recommended for diaphragm design.

8.3 Description of Field Study

8.3.1 Diaphragm Design. Figure 8.6 shows the geometry and the anchor plate layouts for pier segments 43A-1 and 44A-1, which are essentially identical. This figure also includes the tendon sizes. Figure 8.7 shows the reinforcing steel details for the diaphragms.

Figure 8.8 shows simple 2-dimensional strut-and-tie models in elevation and plan views. These models indicate that tension develops on the far face of the diaphragm opposite the post-tensioning anchor plates and on the near face between the anchor plates. Based on these simple models, locations for electrical resistance strain gages were selected.

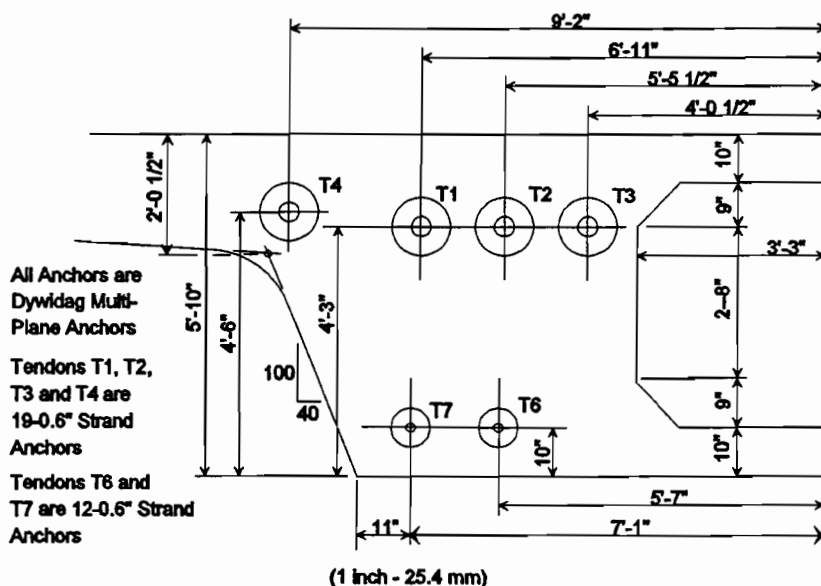
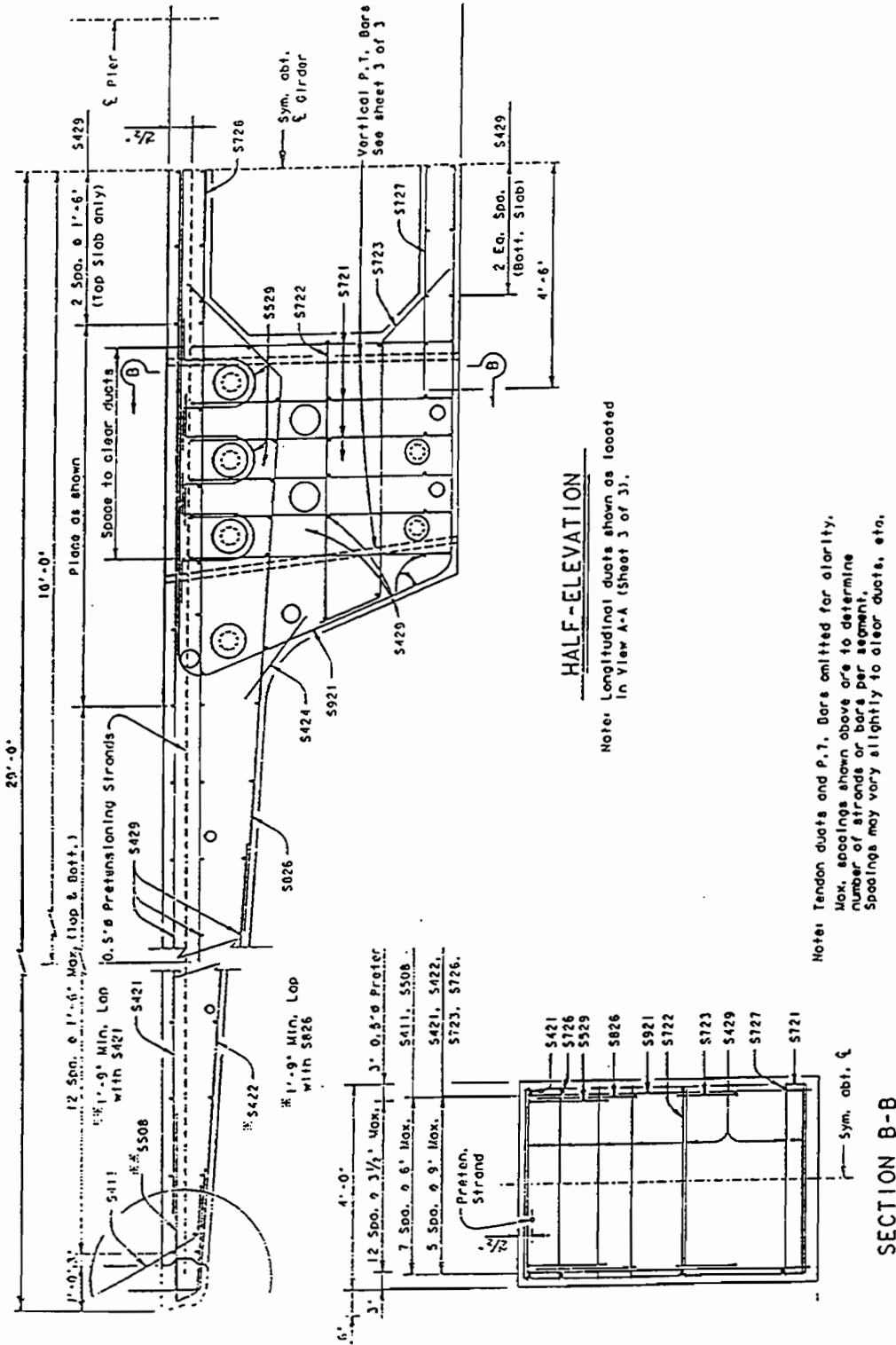


Figure 8.6 Geometry of instrumented pier segments.



NOTE: 1 inch = 25.4 mm
1 foot = .3048 m

Figure 8.7 Reinforcing steel details of pier segments.

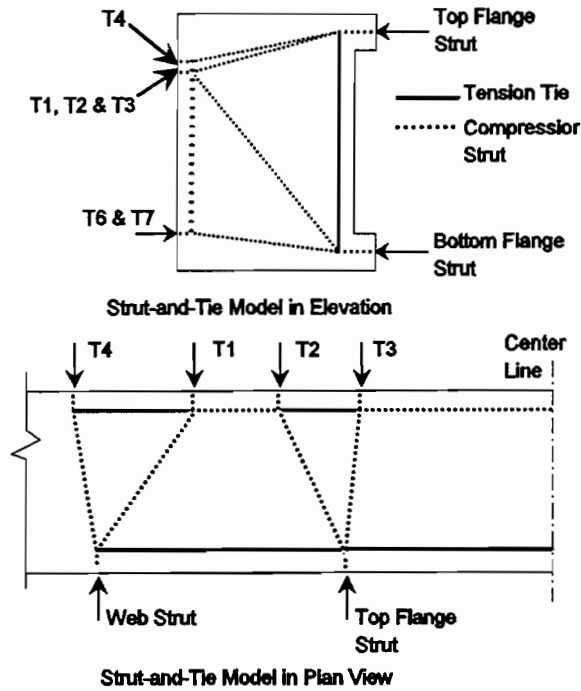
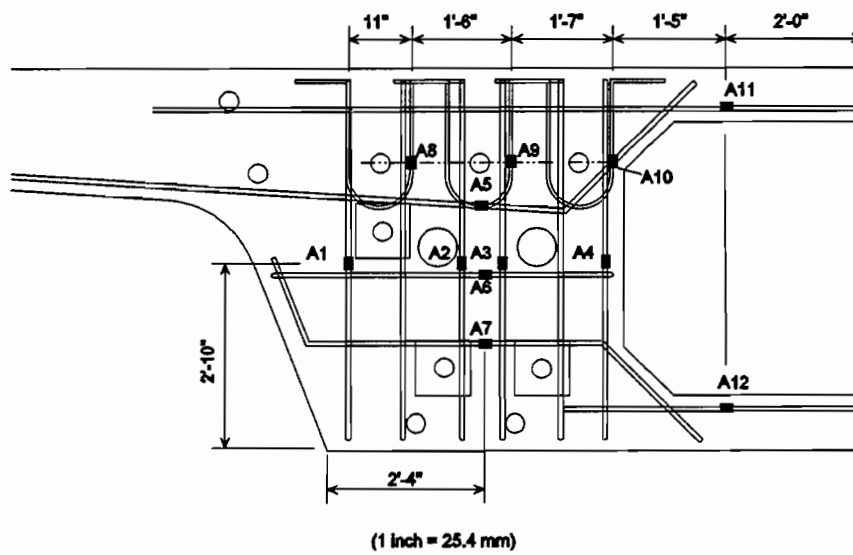
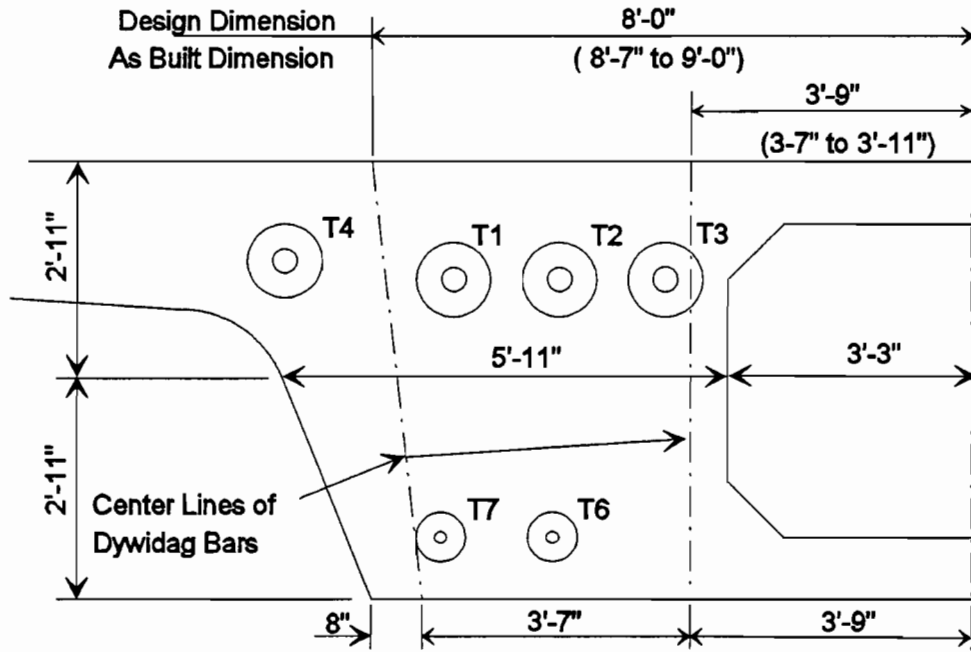


Figure 8.8 Two-dimensional strut-and-tie models.

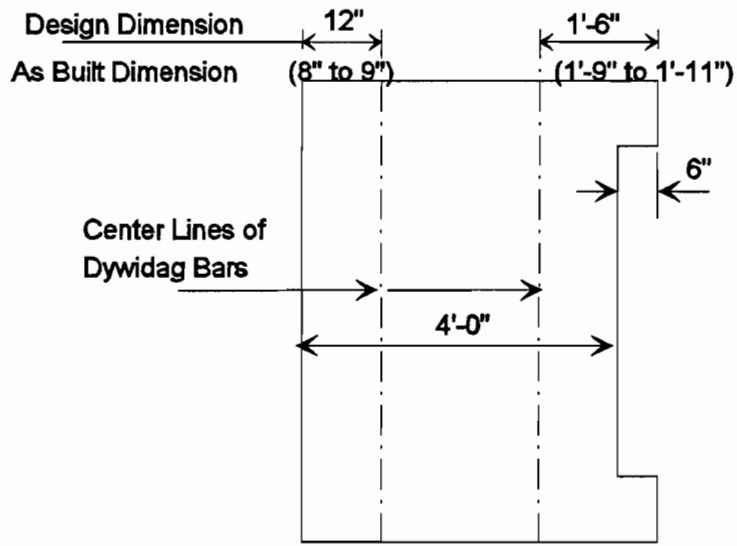


Segments 43A-1 and 44A-1 Strain Gage Layout
Gages are on the layer of reinforcing steel farthest from the anchor heads (most up-station)

Figure 8.9 Strain gage layout.



Dywidag Bar Locations - Elevation View



Dywidag Bar Locations - Section View

(1 inch = 25.4 mm)

Figure 8.10 Design and as-built Dywidag bar locations.

Figure 8.9 shows the strain gage locations and designations. In Segment 44A-1 all 12 gages survived casting operations; in Segment 43A-1 10 of 12 survived.

8.3.2 Vertical Post-Tensioning. Segment 44A-1 was cast on August 9 and Segment 43A-1 was cast on August 14. Both segments were vertically prestressed on August 20, when they were 11 and 6 days old respectively. The vertical prestress is provided by 8 - 1 3/8 inch (206 mm) diameter Dywidag threaded bars, arranged as shown in Figure 8.10. Due to the large amount of congestion in the pier areas, the design location and the actual location of the bars is not always the same.

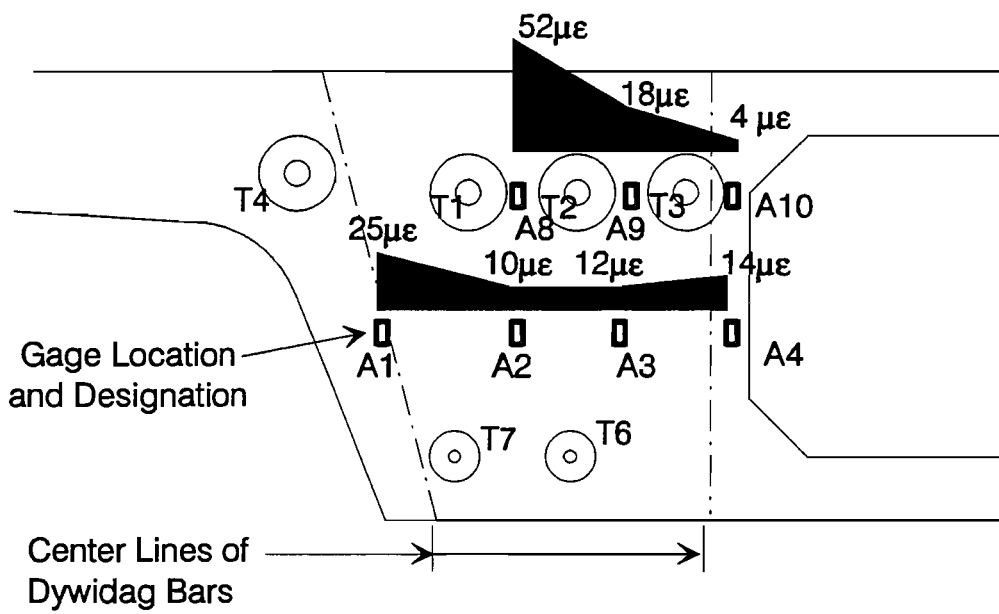
Figure 8.11 shows the strains in the instrumented vertical bars after the completion of all vertical post-tensioning. The distribution of stresses is very similar in both segments. It is also interesting to note that at mid-height of the segments (gages A1 through A4) the strain profile is almost uniform, except for the slightly higher strains in the gage closest to the web.

The measured strains are somewhat lower than expected. At mid-height the cross-sectional area of one side of a diaphragm plus the short web stub is (71" x 48" + 14" x 6") 3492 in² (2.3 m²). The area of steel at this section is 20.4 in² (13161 mm²). Using $E_c = 4350$ ksi (29993 MPa) and $E_s = 30,000$ ksi (206850 MPa), the transformed cross-sectional area is 3632 in² (2.3 m²). The total force applied by the four Dywidag bars is approximately 520 kips (2313 kN). This equates to a stress at mid height of 140 psi (965 kPa) which translates to $33\mu\epsilon$. This is approximately double the measured average strain at mid-height of $17\mu\epsilon$ for segment 43A-1 and $15\mu\epsilon$ for segment 44A-1. This could be caused by the close proximity of the electrical resistance gages to the surface of the concrete where the stresses might be smaller.

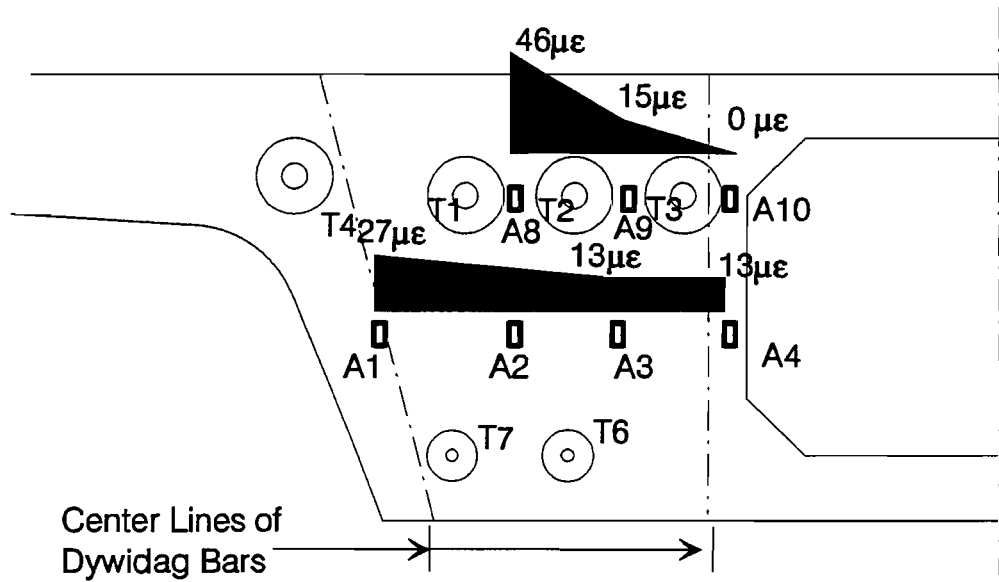
The lower measured strain could also be attributable to the somewhat arbitrary determination of the "lift-off" force in the bar. After a Dywidag bar is stressed, the nut is tightened down against the plate. The bar is pulled again, with the pump pumping hydraulic fluid at a constant rate. As long as the force in the bar is more than the force in the ram, the needle on the dial gage will move at a constant steady speed. As soon as the force in the ram exceeds the force in the bar, the bar will begin to elongate. At this point, the same rate of fluid pumped will result in a slower rate of load increase because of the increased travel of the piston. This will cause a sudden change in the speed of the needle on the dial gage. The point of slowing is called the "lift off" point, and this is equated to the force in the bar.

The determination of the lift off pressure is a judgement by the ram operator and the State Inspector. The change in needle speed is often very subtle and difficult to judge accurately. Therefore the recorded force in the bar may be in error, or at least not extremely precise.

In summary, the readings from the vertical prestressing operations generally show a uniform compression across the section, with the stresses slightly higher near the web walls. The magnitude of the compression strains is considerably less than expected.



Final Strains in Vertical Reinforcing Bars
After Dywidag Stressing
Segment 44A-1



Final Strains in Vertical Reinforcing Bars
After Dywidag Stressing
Segment 43A-1

Positive Strains are Compressive

Figure 8.11 Vertical strains after vertical prestressing.

8.3.3 Longitudinal Post-Tensioning. The electrical resistance strain gages were connected to the permanent data acquisition system at the erection site and the gages were monitored every 20 seconds during stressing operations. In addition, crack patterns and widths were recorded on all pier segments of both instrumented spans.

8.3.3.1 Strain Readings. Figures 8.12 to 8.15 compare strain readings during stressing operations while the segments were still partially supported on the erection trusses and after truss lowering for similar bars in both segments. Figure 8.12 shows the tensions which develop in the vertical bars on the face opposite the anchorages. None of the bars experienced extremely high tensions. Before lowering the truss, gage A1 in Segment 43A-1 had the highest stress at 10.1 ksi (69.6 MPa). The next most highly stressed bars are the A4's in both segments, which had very similar readings.

Figure 8.13 shows the readings on the horizontal bars. In both segments, before truss lowering, the uppermost bar, gage A5, had the highest levels of stress, 12.9 ksi (89 MPa) in Segment 44A-1.

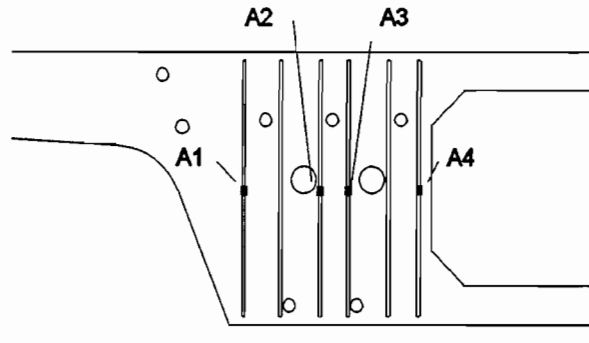
Figure 8.14 shows readings from the U-shaped bars around the external post-tensioning ducts. There were significant differences between the two segments in the readings of these gages. In Segment 43A-1 the stresses in these bars stayed quite small, while in Segment 44A-1 the middle U-bar and the U-bar closest to the diaphragm opening experienced significant stresses, 14.1 and 17.7 ksi (97.2 and 122.0 MPa), respectively.

Figure 8.15 shows the readings from the bars in the top and bottom slabs. The top slab bar went steadily into compression during stressing, while the bottom slab bar stress increased and decreased as tendons were stressed left and right of the centerline of the segment.

8.3.3.2 Crack Patterns. Figures 8.16a and 8.16b show the crack patterns and crack widths of the two instrumented diaphragms. All diaphragms which were examined exhibited similar crack patterns and widths. The largest crack measured in the four pier segments of the instrumented spans was 0.016" (0.41 mm) which appeared at the re-entrant corner where the top slab and diaphragm meet, although most were less than 0.010" (0.25 mm). These size cracks, on surfaces not exposed to severe environmental conditions, should not cause serviceability problems.

The crack patterns do illustrate the flow of forces from the anchorage devices into the top and bottom slabs (diagonal cracks in Section A-A of Figures 8.16a and b). Flexural cracks also developed on the face opposite the anchorage devices.

8.3.3.3 Top Slab Spalling. Another type of distress which appeared in some pier segments was top slab spalling above the post-tensioning anchor plates. The spalling is illustrated in Figure 8.17. It did not occur in Segment 43A-1 or 44A-1, but occurred almost exclusively in expansion joint pier segments. In the expansion joint segments the anchor plates are positioned 8 inches (203 mm) higher in the cross-section than in interior pier segments.



Stresses in Vertical Reinforcing Bars
in Diaphragm Segments

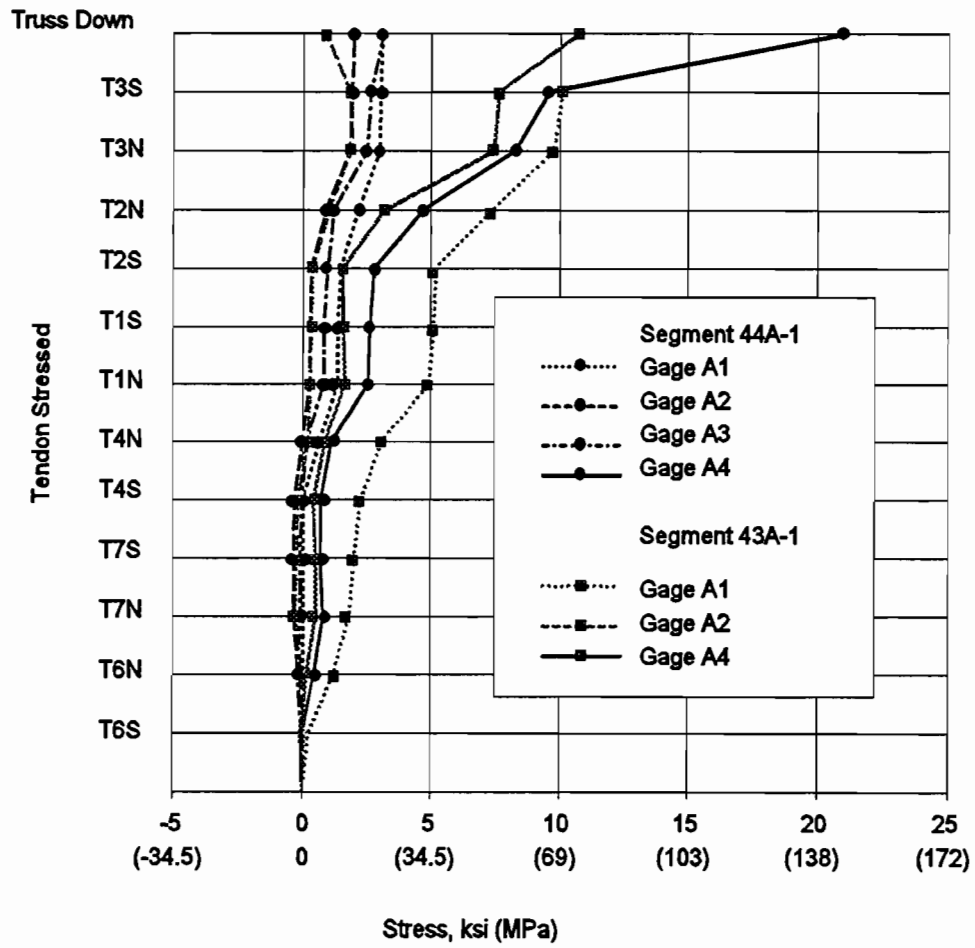
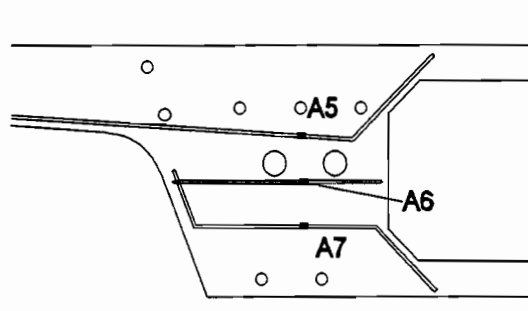


Figure 8.12 Stresses in vertical reinforcing bars.



Stresses in Horizontal Reinforcing Bars
In Diaphragm Segments

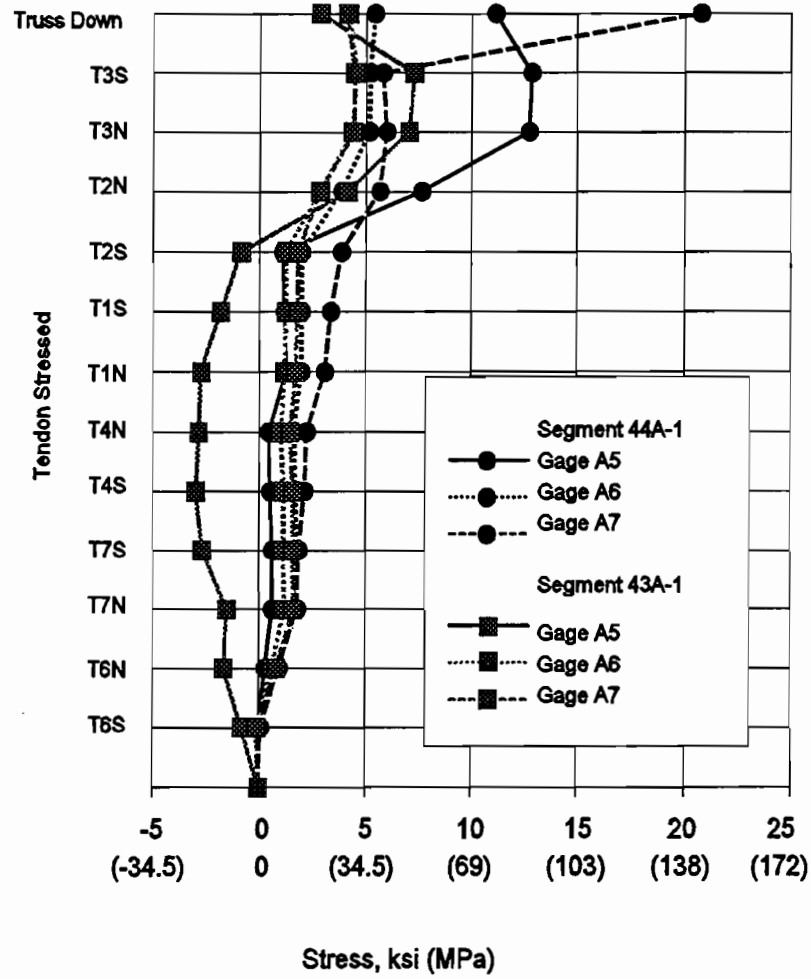
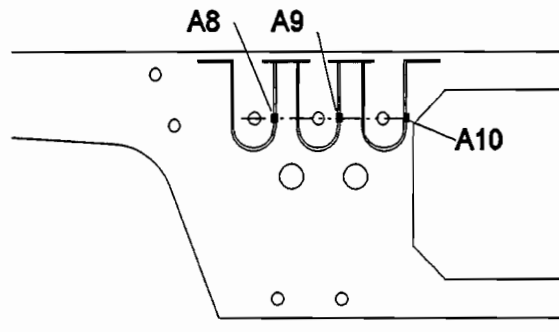


Figure 8.13 Stresses in horizontal reinforcing bars.



Stresses in U-Shaped Reinforcing Bars
in Diaphragm Segments

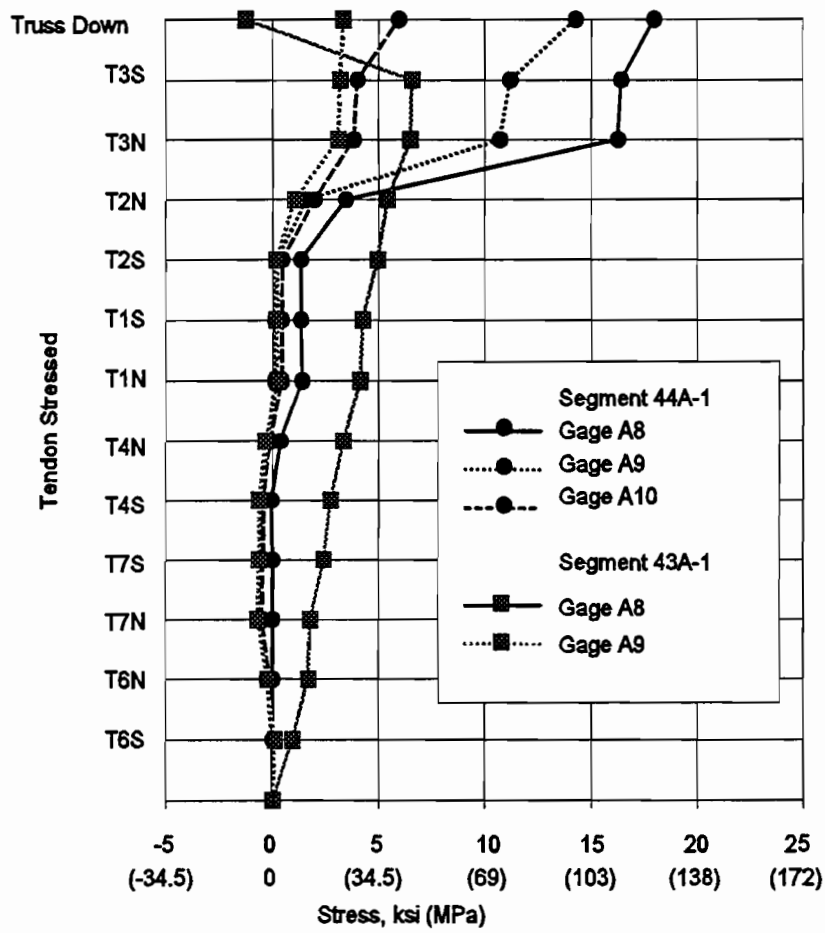
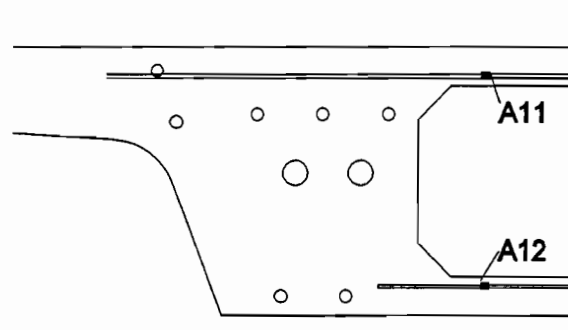


Figure 8.14 Stresses in U-shaped reinforcing bars.



Stresses in Top and Bottom Slab Bars
in Diaphragm Segments

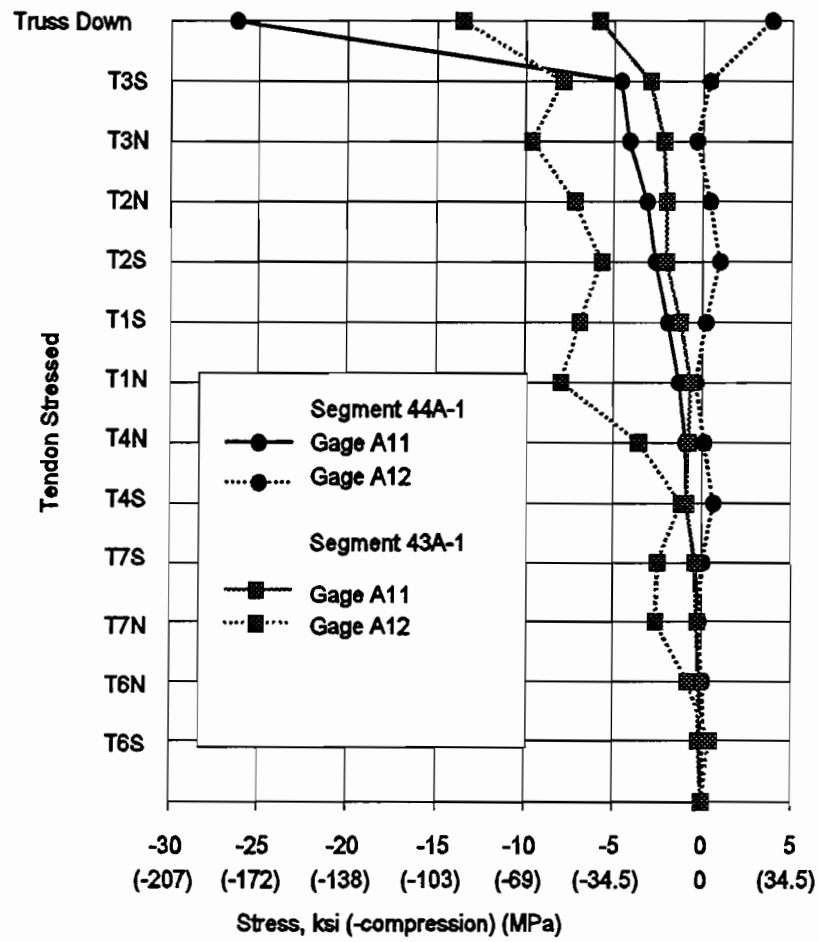
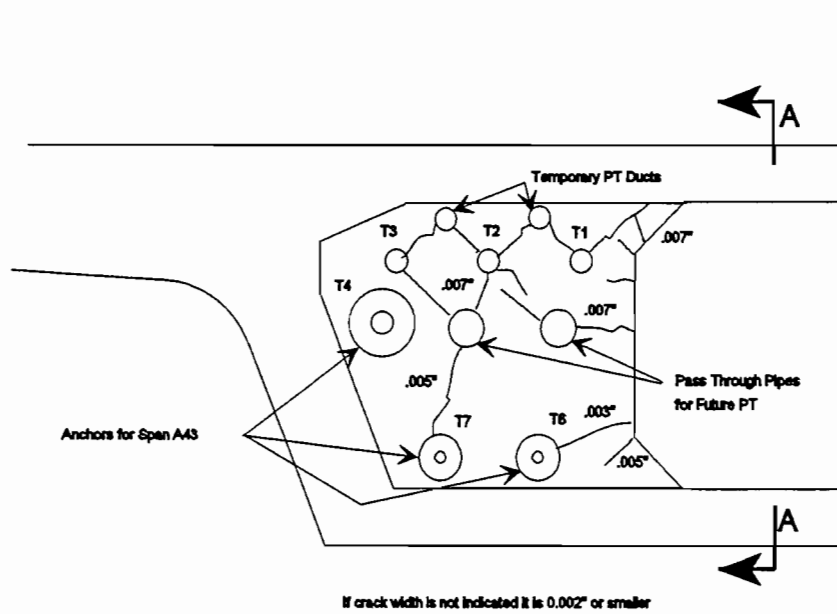
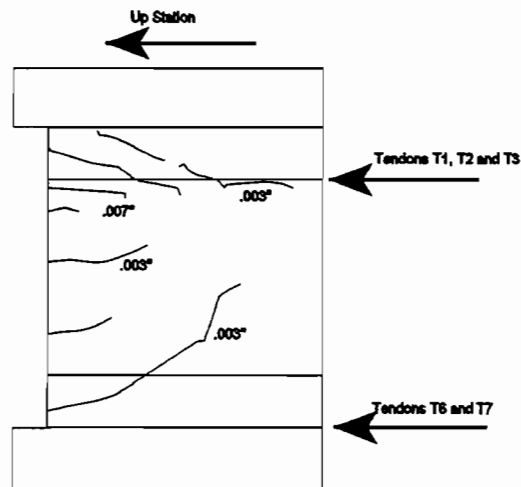


Figure 8.15 Stresses in top and bottom slab bars.



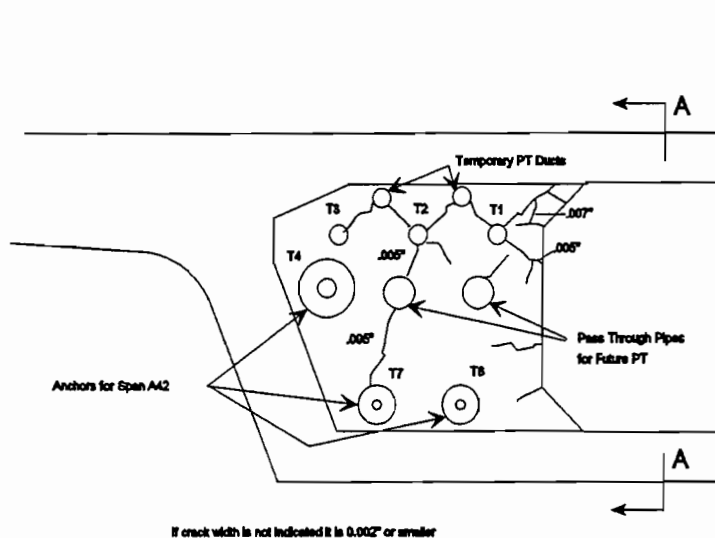
Segment 44A-1 Crack Patterns - Elevation View
 1 inch = 25.4 mm)

North Side of Segment Looking Down Station

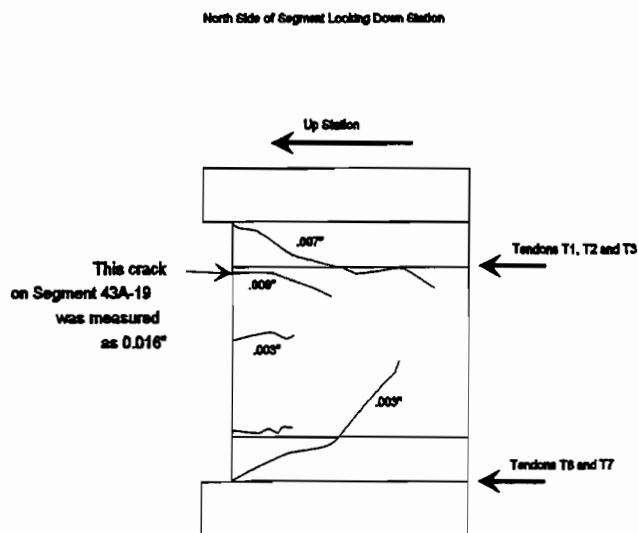


Segment 44A-1 Crack Patterns - Section A-A
 1 inch = 25.4 mm

Figure 8.16a Segment 44A-1 north side crack pattern



Segment 43A-1 Crack Patterns - Elevation View
(1 inch = 25.4 mm)



Segment 43A-1 Crack Patterns - Section A-A
(1 inch = 25.4 mm)

Figure 8.16b Segment 43A-1 north side crack patterns.

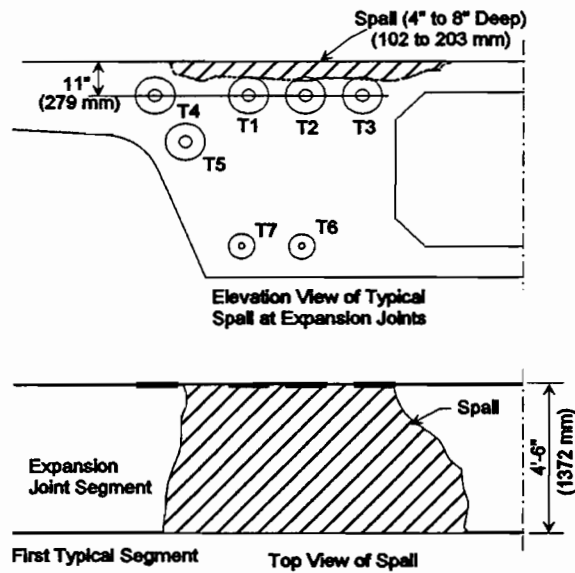


Figure 8.17 Typical spalls in expansion joint segment.

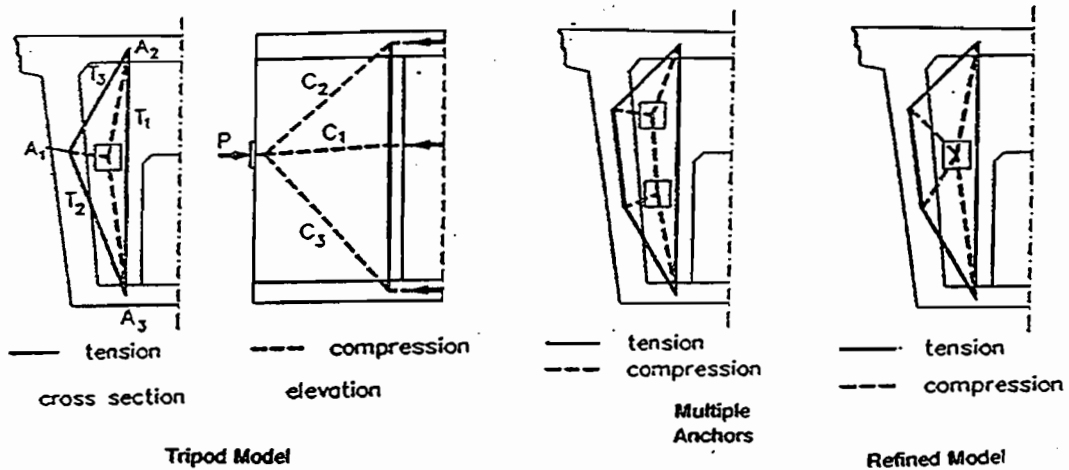


Figure 8.18 Strut-and-tie model developed by Wollmann for laboratory specimens.

The anchor plates are positioned higher to offset the effects of the bottom slab tendons and reduce the moment applied to the end of a continuous unit. Possible reasons for this spalling are discussed in Section 8.4.4.

8.4 Discussion of Results

8.4.1 Previous Strut-and-Tie Model Applications. Both the *AASHTO Guide Specification* and the *NCHRP 10-29 Report* advocate the use of strut-and-tie models for the design of heavy end diaphragms. Figure 8.18 shows the strut-and-tie model developed by Wollmann⁷⁴ for his laboratory specimens. The model was used to design reinforcing steel layouts. His three diaphragm specimens achieved between 1.4 and 2.2 times his factored design load based on the tension tie capacity. At the factored design load crack widths were 0.02" (0.51 mm) and 0.009" (0.23 mm) for two specimens and the third was uncracked. Wollmann's strut-and-tie model design, in conjunction with good detailing practices, led to safe and serviceable designs.

Strut-and-tie modelling is not as valuable as an analysis tool as it is as a design tool, but it can be helpful in the evaluation of a design. Figure 8.19 shows the strut-and-tie model developed by Kreger³⁸ to evaluate the damaged diaphragm of the Washington Metro J2-E structure. Based on the area of steel required by the strut-and-tie model, the existing design was deemed to be inadequate and additional post-tensioning bars were added.

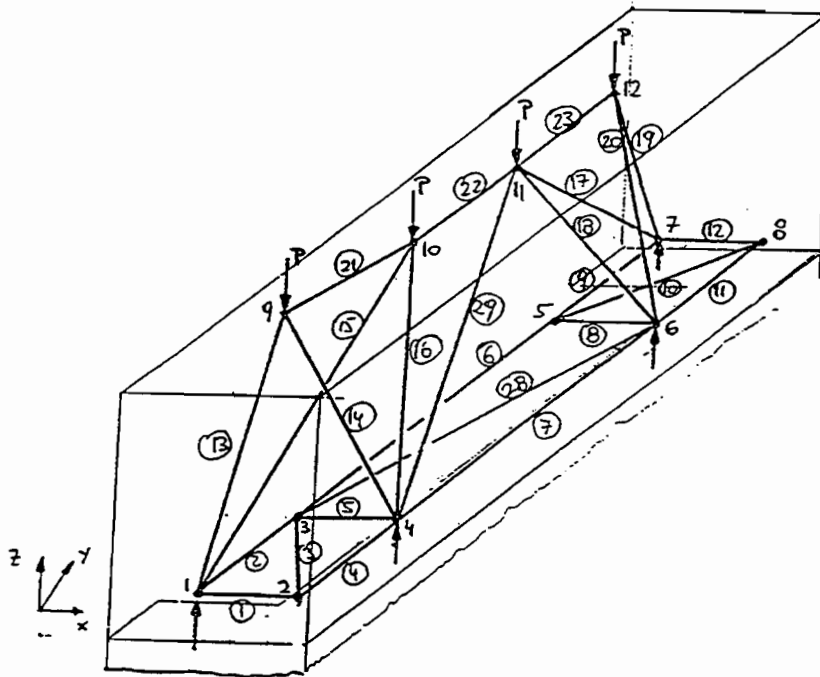
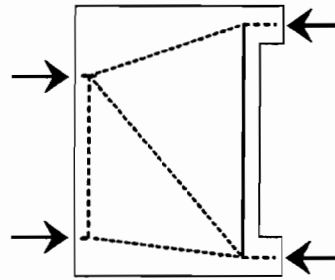


Figure 8.19 Strut-and-tie model for Washington Metro pier segments.

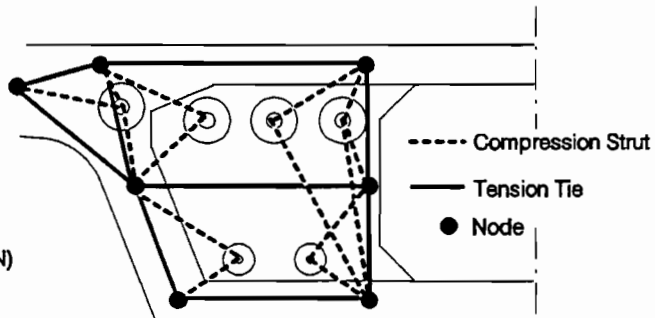
Model I

Vertical Tension = 786 kips (3496 kN)



Model II

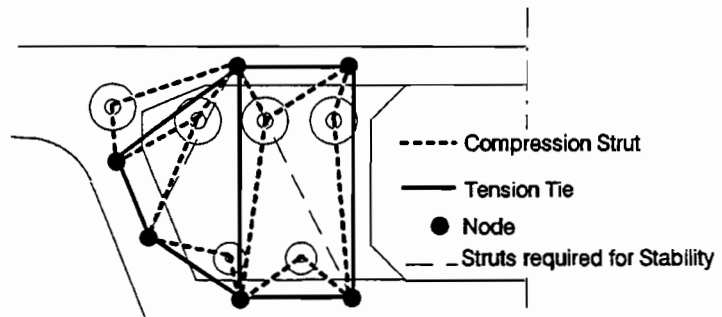
Vertical Tension = 753 kips (3349 kN)
Horizontal Tension = 1224 kips (5444 kN)



Struts between Anchors not Shown for Clarity

Model III

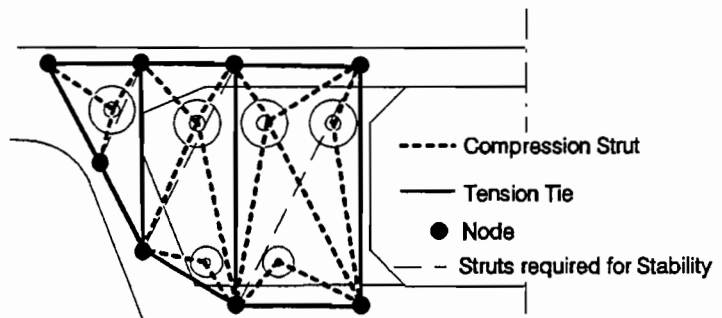
Vertical Tension = 1051 kips (4675 kN)
Horizontal Tension = 374 kips (1664 kN)



Struts between Anchors not Shown for Clarity

Model IV

Vertical Tension = 724 kips (3220 kN)
Horizontal Tension = 360 kips (1601 kN)



Struts between Anchors not Shown for Clarity

Figure 8.20 Strut-and-tie models for diaphragm.

8.4.2 Strut-and-Tie Models for Current Diaphragms. The diaphragms studied in this research program are somewhat more complex than the previously described diaphragms. There are a total of six post-tensioning anchorages on each side of the bridge centerline. Many models were developed to predict the locations and magnitudes of tension forces in the diaphragm. Figure 8.20 shows some of these models and the total vertical and horizontal tension which were predicted in each case. Since strut-and-tie modeling is a lower bound plasticity solution and all of these models satisfy equilibrium, all would be possible design models.

It is apparent from this figure that a wide variety of solutions can be formulated for a single problem. According to Schlaich,⁶² several models can be compared by the following equation:

$$\sum F_i L_i \epsilon_{mi} - \text{Minimum}$$

where:

- F_i = Force in strut or tie i ,
- L_i = Length of member i ,
- ϵ_{mi} = mean strain of member i .

The equation was derived from the principle of minimum strain energy for linear elastic behavior of the struts and ties after cracking. Schlaich recommends omitting the contribution of the struts because they are much stiffer than the ties, after concrete cracking. The difficulty in applying the various models to an existing pattern of reinforcement (not necessarily developed using such a strut-and-tie model), when using strut-and-tie modelling as an analysis tool, is determining what portion of the existing reinforcing steel to include in each tie, and hence what mean strain to assume.

Model IV in Figure 8.20 was selected as the model to be used for the evaluation of the design because it best represents the locations of tension, the distribution of the reinforcing steel and the distribution of stresses in the slabs and webs of the actual structure.

Model IV was developed by first defining the nodes at which the loads are introduced (the anchor plates) and the nodes at the opposite side of the diaphragm where the forces enter the webs and slabs. The model assumes that the forces have spread at an angle of 30° from the anchorages. This defines an area on the opposite side of the diaphragm. This area was then divided into eight equal areas and a node was defined at the center of each area (see Figure 8.21). With the node locations selected, struts were defined to facilitate the diffusion of the forces from the anchorages into the web and slab. The ties were also defined to roughly correspond to the location of the reinforcing steel and post-tensioning bars on the face opposite the anchors.

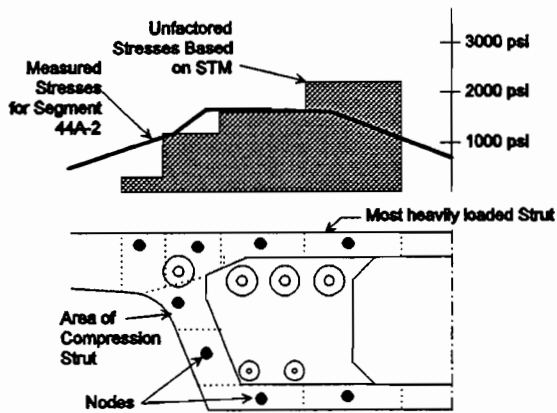


Figure 8.21 Top slab stress distribution strut-and-tie prediction vs. measured.

Ideally strut-and-tie models should be determinant so the member stiffnesses do not effect the load path. However, due to the high degree of complexity of the three-dimensional model, Model IV was indeterminant. The struts and ties were all assigned identical stiffness. The eight support nodes were restrained in the direction of the applied prestressing forces. The four nodes closest to the centerline of the girder were restrained in the horizontal direction, and one node was restrained in the vertical direction. A three-dimensional truss solver (TRUSS3D) was used to calculate the member forces. Many variations on the geometry of the truss were attempted to

create a determinant system. Eventually the indeterminant truss was used because it resulted in reaction forces very similar to what would be expected based on a linear elastic analysis, and most of the diagonal members required for stability had forces very close to zero.

8.4.3 Assessing Design Based on Strut-and-Tie Modelling. The *NCHRP 10-29 Report*¹³ recommends the following load and resistance factors:

$$\begin{aligned} \text{Load Factor} &= 1.2 \text{ (on maximum jacking load),} \\ \text{Resistance Factor} &= 0.85, \\ \text{Effective Concrete Compressive Strength in Struts} &= 0.7 f_{ci}. \end{aligned}$$

The following sections illustrate design checks of the diaphragms based on the chosen strut-and-tie model.

8.4.3.1 Total Factored Vertical Tension on Diaphragm Face. The total factored vertical tension (T_{vu}) based on the model is 724 kips (3220 kN). Since $T_{vu} \leq \phi A_s f_y$, $A_s f_y \geq 724/0.85 = 853$ kips (3794 kN). The available resistance is calculated as follows:

$$\begin{aligned} \text{Area of available steel - 2 ea. } 1\frac{3}{8}\text{" (35 mm) } \phi \text{ Dywidag Bars - } A_s f_y &= 3.16 * 150 = 474 \\ &\text{kips (2108 kN)} \\ \text{6 ea. \#7 bars and 3 ea. \#9 bars - } A_s f_y &= 6.6 * 60 = 396 \text{ kips (1761 kN).} \end{aligned}$$

Comparing the tensile force provided with that required:

$$A_s f_y \text{ (required)} = 853 \text{ kips (3794 kN)} \leq 474 + 396 = 870 \text{ kips (3870 kN).}$$

So with this strut-and-tie model, the tension ties are adequate by 2%.

8.4.3.2 Compression Strut Check. Based on the results of the transverse stress distribution studies presented in Chapter 5, a dispersion angle of 30° is assumed for the spreading of the forces from the anchors out into the webs and flanges. The area of the webs and flanges into which the forces spread was then divided into 8 equal areas, each of which was considered to be the end of one strut where it enters the webs and flanges. In this way, all web and flange struts were assumed to have an area of approximately 400 square inches (258064 mm^2). The most heavily loaded strut is in the top slab closest to the centerline of the segment (see Figure 8.21). This strut carries a factored load of 885 kips (3936 kN). The available resistance is:

$$\phi A_c 0.7 f'_c = 0.85 (400 \text{ in}^2) (0.7) (550 \text{ psi}) = 1310 \text{ kips} > 885 \text{ kips}$$

$$[= .85 (258064 \text{ mm}^2) (0.7) (37923 \text{ kPa}) = 5827 \text{ kN} > 3936 \text{ kN}]$$

This would also indicate an adequate design. Figure 8.21 also shows the calculated (non-factored) top slab stresses compared to measured stress distributions from Segment 44A-2. The predicted stresses are somewhat larger than the measured stresses, but the pattern of distribution is similar.

8.4.3.3 Shear Friction Check. Wollmann⁷⁴ recommends a check of shear transfer from the diaphragm into the webs and slabs. Figure 8.22 shows the check of the top slab transfer. This check indicates that there is enough steel across the diaphragm-top slab interface to allow for complete shear transfer. It is important that this shear friction reinforcing is anchored well in the top and bottom slabs.

8.4.3.4 Conclusions. Based on the evaluation of three critical aspects of the design, vertical tension, strut compression, and shear transfer, this design is acceptable. The vertical tension steel was 2% more than required by the model, and since Wollmann's studies indicated that diaphragms are able to achieve ultimate strengths considerably higher than predicted based on the tension tie capacity, the steel present is more than adequate. The strut compression is also well within recommended levels. The shear transfer reinforcing, as designed, is also adequate. The diaphragm is also performing satisfactorily based on a visual inspection of the diaphragms. With the exception of the large crack width of 0.016" (0.41 mm) at one location, all cracks were less than 0.010" (0.25 mm). Cracks less than 0.016" (0.41 mm) are often assumed to indicate no structural damage⁴² although if the cracks are on exposed surfaces they could present a serviceability problem.

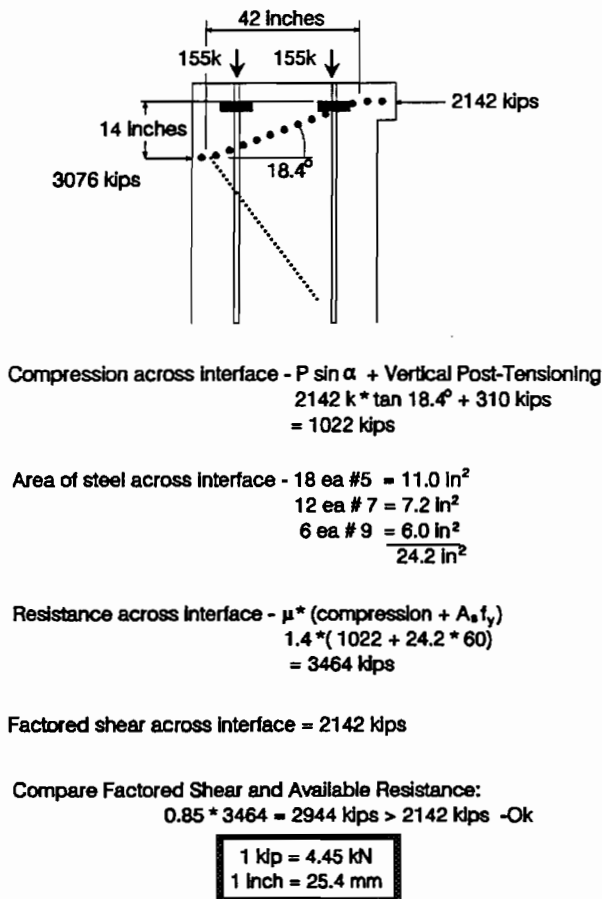


Figure 8.22 Shear friction check.

The similar assessments, based on the strut-and-tie model analysis and the visual inspection, as well as the stresses less than 25 ksi (0.42 f_y) (172 MPa) measured in the reinforcing steel, indicate that the strut-and-tie model method can be used for analysis and design evaluation. The use of the NCHRP recommendations in the original design would have resulted in an almost identical design.

8.4.4 Top Slab Spalling.

8.4.4.1 Description of Problem. Figure 8.16 shows locations of top slab spalling. These occurrences appear to be primarily an anchorage device local zone detailing problem. The anchor plates used were Dywidag Multiplane 19-0.6" (15 mm) ϕ strand anchors. The design strength of the concrete was 5500 psi (37923 kPa), but the actual strength at the time of stressing of most of the concrete on the project was 8000-9000 psi (55160 to 62055 kPa).

In Dywidag's manufacturer's literature, published in Germany, recommended edge distances and spacings are given for the anchor in various types of concrete. 5500 psi (37920 kPa) concrete corresponds to German B45 concrete. The spiral used with the anchor was a manufacturer supplied 14½" (368 mm) OD #5 with 7 turns and a 2½" (63.5 mm) pitch. With this spiral the manufacturer recommends a minimum edge distance of 9" (229 mm) and a minimum spacing of 16½" (419 mm). The actual dimensions were an edge distance of 11" (279 mm) and a spacing of 17½" (445 mm). These are slightly greater than the manufacturer's recommendations, but the recommendations are based on a test which allows additional confining steel which is assumed to be present in the actual structure.

8.4.4.2 Possible Causes of Spalling. When an anchor is tested according to German standards a prismatic test block with dimensions in the plane of the anchor equal to two times the minimum edge distance and in the direction of the applied force equal to twice the lateral dimension is constructed (see Figure 8.23). The block is reinforced with the recommended spiral plus auxiliary skin reinforcing not to exceed 50 kg/m³ (≈ 0.01 volumetric ratio of steel to

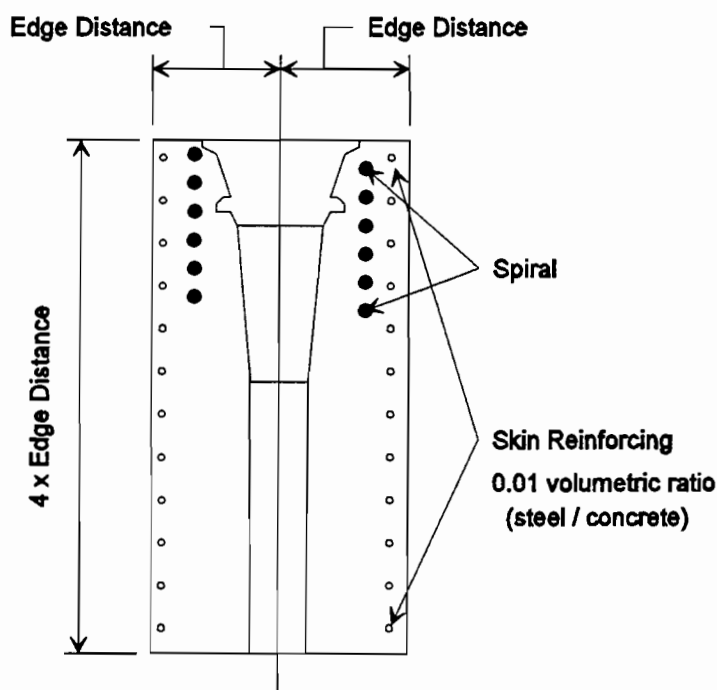


Figure 8.23 Dimensions of local zone test block.

prevented. In the as built detail there is a plane of weakness to resist vertical tension immediately above the horizontal tails of the U-bars.

Another aspect of the behavior which might have contributed to the problem is the high percentage of the force of the anchor which flows to the top slab. Figure 8.25 illustrates how in a local zone test specimen the struts are symmetric, but in the expansion joint segments the strut which carries force from the anchor to the top slab carries much more than half of the anchor force. This also could be a cause of the distress, particularly in conjunction with the improperly positioned U-bars.

The Dywidag bars exacerbated the problem, primarily by contributing to the high degree of congestion in the top layer of reinforcing. The large stressing blockouts considerably reduce the width of the segment through which the longitudinal steel may run. They may also have contributed to the problem by creating regions of high local stress immediately behind the anchors for the longitudinal tendons.

8.4.4.3 Conclusions. This spalling problem was primarily an anchorage device local zone construction problem. Reinforcing steel was needed to assist in transferring the high local zone stresses into the top slab and to confine the highly stressed compression strut. This reinforcing was present in the form of U-bars, but was not effectively anchored high enough into the top slab to prevent the spall. This problem was caused in part by the great deal of congestion in the top mat of reinforcing.

concrete). It is assumed that at least this much reinforcing steel will be present in the actual structure in and around the local zone. In the case of the spalled expansion joints, the steel was there but it was not properly placed.

Figure 8.24 shows the anchor in a typical local zone test specimen, the anchor and surrounding steel as it was designed, and the anchor and surrounding steel as it was constructed. If the tails of the U-bars in the as built local zone had been effectively anchored by hooking around the longitudinal reinforcement higher in the top slab, the spalling might have been

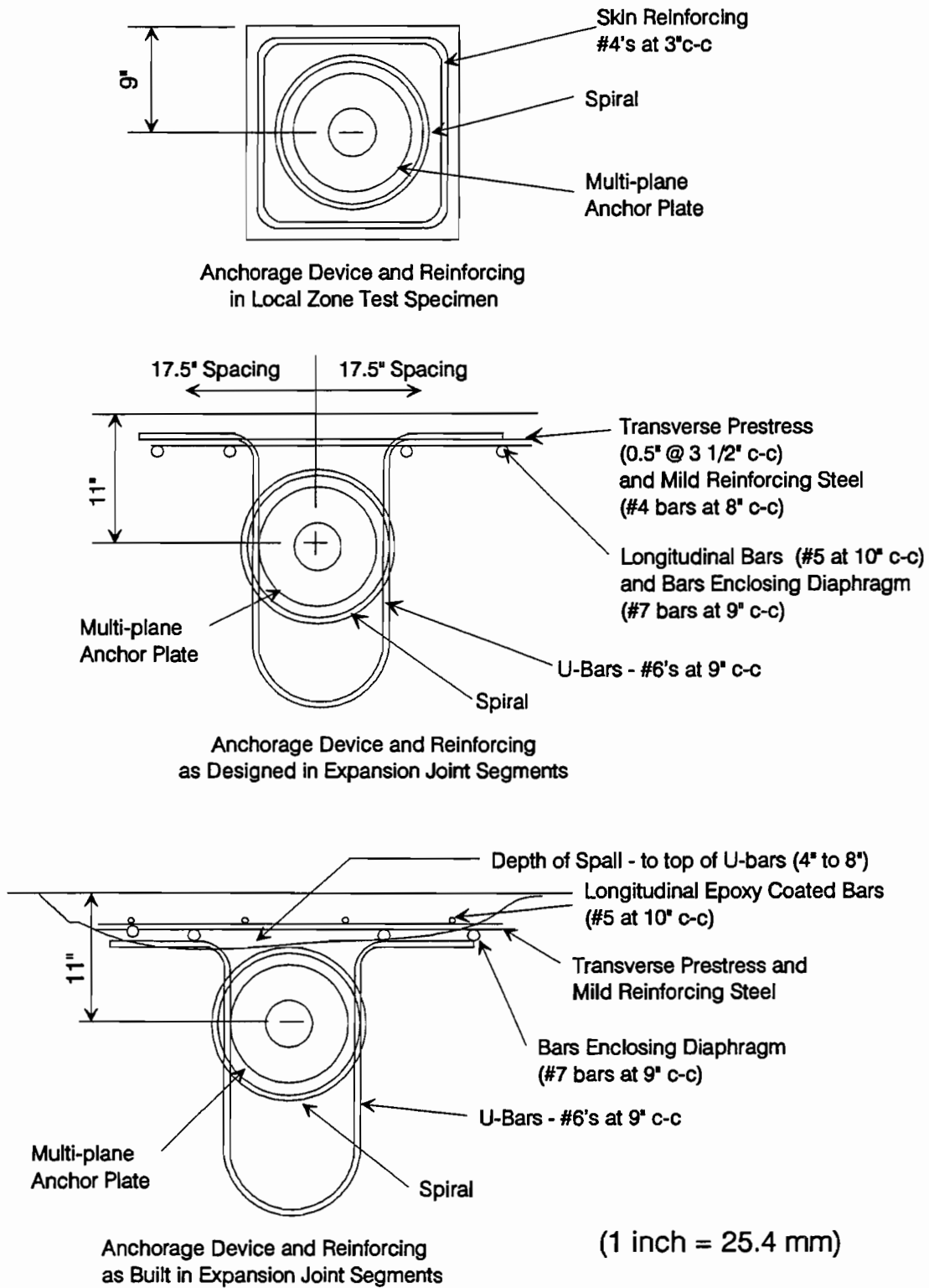


Figure 8.24 Comparison of reinforcing steel in local zone test specimen and expansion joint segment.

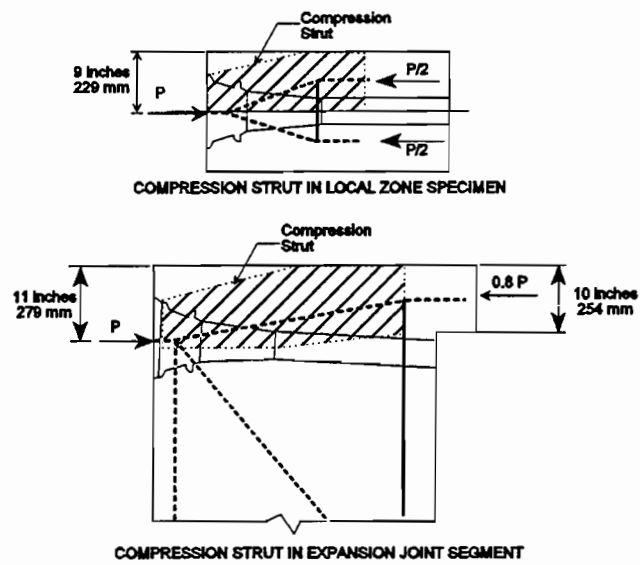


Figure 8.25 Comparison of compression struts in local zone test specimen and in expansion joint segment.

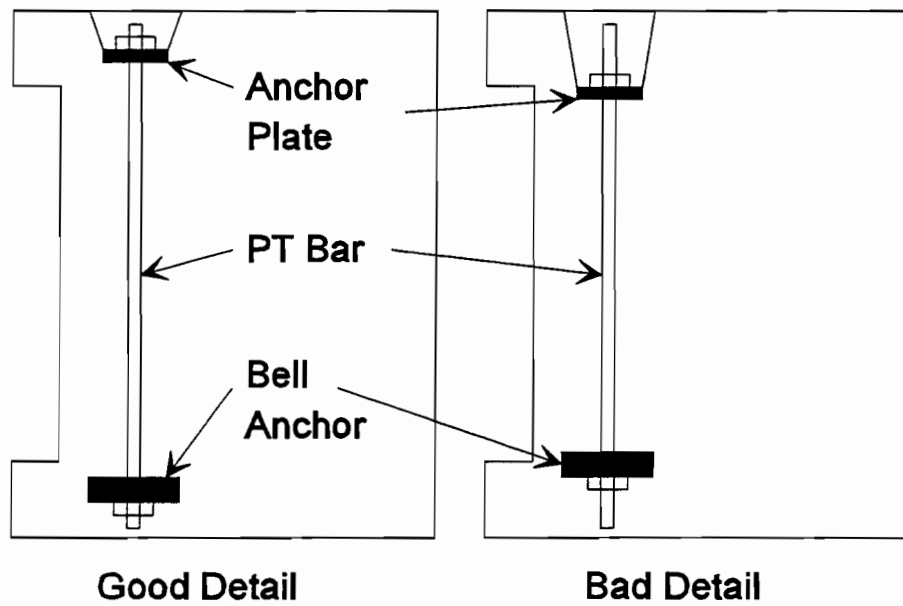


Figure 8.26 Comparison of well anchored and inadequately anchored vertical post-tensioning bar.

In future cases where anchors are positioned with small spacings and edge distances, it is recommended that the compression struts be checked and properly confined. Any required ties must be effectively anchored as close to the surface of the concrete as possible.

8.5 Recommendations

This field study illustrates the applicability of strut-and-tie modelling in the design and evaluation of complex D-regions such as heavy end diaphragms. Three dimensional models can be very complex, and many solutions can fit a given design situation. Following the general guidelines of Schlaich,⁶² the specific guidelines of NCHRP 10-29,¹³ and the recommendations of Wollmann⁷⁴ should result in safe and serviceable designs.

The section on diaphragms in the *AASHTO Guide Specification* should be expanded to include the recommendations of Section 9.21.3.6 of the *NCHRP 10-29 Report*. The important aspects of these provisions are:

1. Compressive stresses must be checked at the interface of the diaphragm and the webs and flanges.
2. Reinforcing must be provided to ensure full transfer of anchor loads into the webs and flanges.

Other aspects of design, which were mentioned by Wollmann, should be mentioned in the code or commentary. These are:

1. Approximate methods, such as Guyon's symmetric prism,²⁸ are not appropriate for determining tensile forces caused by anchor force spreading in diaphragms.
2. Any reinforcing, mild or prestressed, which is provided as part of the tensile tie which facilitates the transfer of the compressive loads into the top and bottom flanges and webs, must be well anchored in nodes located in the flanges and webs (see Figure 8.26).
3. Shear-friction reinforcement requirements between the diaphragm and web and between the diaphragm and flanges should be checked. The recommendations of ACI-318 for shear friction are applicable.

The following changes are recommended for Section 14.4 Anchorages in Diaphragms of the *AASHTO Guide Specification* (changes are written in italicized print):

- 14.4.1 Reinforcement shall be provided to ensure full transfer of *diaphragm anchor loads* into the flanges and webs of the girder. *Strut-and-tie models or*

elastic analysis shall be used to determine this reinforcement. The bursting force equation of 14.2.2 is not applicable to determine this reinforcement. Reinforcement shall be provided to tie back deviation forces due to tendon curvature.

14.4.2 Concrete compressive stresses within the diaphragm shall be limited for the local anchorage zone in accordance with section 9.2.3 and shall be limited to $0.7\phi f'_c$ for compression struts. The ϕ for anchorage zones shall be taken as $\phi=0.85$ for normal weight concrete and $\phi=0.70$ for lightweight concrete. Compressive stresses shall be checked at the transition from the diaphragm to webs and flanges of the member.

The following should be added to the Design Commentary as Section 14.4:

Diaphragms anchoring post-tensioning tendons may be designed following the general guidelines of Schlaich,^[62] the specific guidelines of the NCHRP 10-29 Final Report,^[13] and the recommendations of Wollmann.^[74] A typical diaphragm anchoring post-tensioning tendons usually behaves as a deep beam supported on three sides by the top and bottom flanges and the web wall. The magnitude of the bending tensile force on the face of the diaphragm opposite the anchors can be determined using strut-and-tie models or elastic analysis. Approximate methods, such as Guyon's symmetric prism^[28] do not apply.

Any reinforcing, mild or prestressed, which is provided as part of the tensile tie which facilitates the transfer of the compressive loads into the top and bottom flanges and webs must be well anchored in the nodes located in the flanges and webs.

Shear-friction reinforcement requirements between diaphragms and web and between diaphragm and flanges should be checked. The recommendations of ACI-318^[5] for shear friction are applicable.

Finally, all recommendations of the *NCHRP 10-29 Report* should be adopted as part of the *AASHTO Guide Specification*. The most important aspects are the load and resistance factors and the effective concrete compressive stresses.

8.6 Conclusions

Three dimensional strut-and-tie models can be cumbersome and unwieldy, but can give great insight into the flow of forces from points of load application out into complex structures. Designers can experiment with three dimensional models until a satisfactory solution is developed. Strut-and-tie models developed from three dimensional finite element models have the added

advantage of approximating the elastic flow of forces and hence creating more serviceable designs.

The use of strut-and-tie models for diaphragms anchoring post-tensioning tendons, in conjunction with the recommendations of the *NCHRP 10-29 Report*,¹³ Schlaich,⁶² and Wollmann⁷⁴ will result in rational, safe and serviceable designs. |

CHAPTER 9 DEVIATOR BEHAVIOR

9.1 Introduction

Draped external tendons are only attached to the cross-section of a girder at discrete locations. The tendons are normally anchored in heavy end diaphragms over piers, and are directed through angle changes at deviators. Deviators can take on many shapes, from simple blisters at the web-flange junction, to stiffening beams across the width of the box, to deviators incorporated in diaphragms or stiffening ribs over the height of the box (see Figure 9.1).

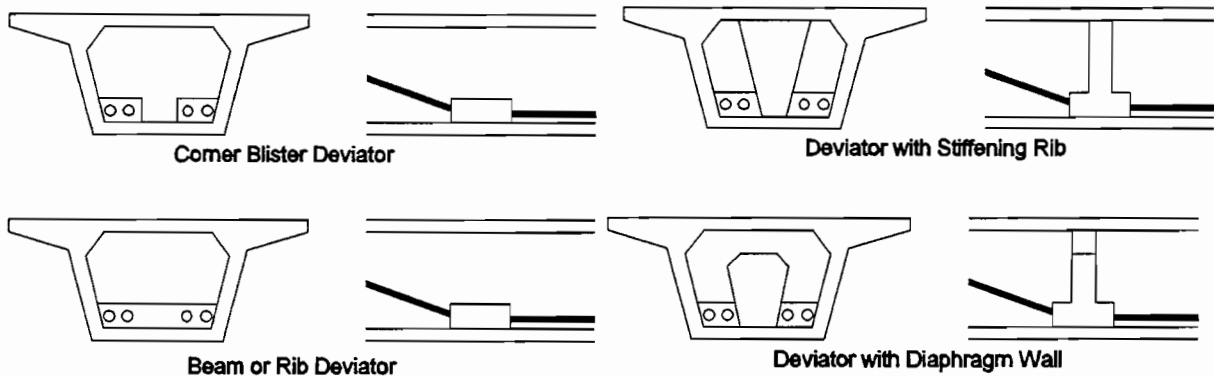


Figure 9.1 Deviator types.

This chapter presents the results of a field investigation of two types of deviators: a full width beam and a deviator with diaphragm wall. One beam deviator and two deviators with diaphragm walls were instrumented with reinforcing steel strain gages. The gages were monitored during stressing of the longitudinal tendons. Visual inspections of the deviators were made before and after stressing.

9.1.1 Background Information. Deviators and the area immediately surrounding them are subject to a complex flow of forces from the deviators up into the webs. Strut-and-tie modelling can be used to describe the flow in this type of disturbed or discontinuity region. Figure 9.2 shows the dual model proposed by Beaupre et al.¹² for the design of one type of blister deviator.

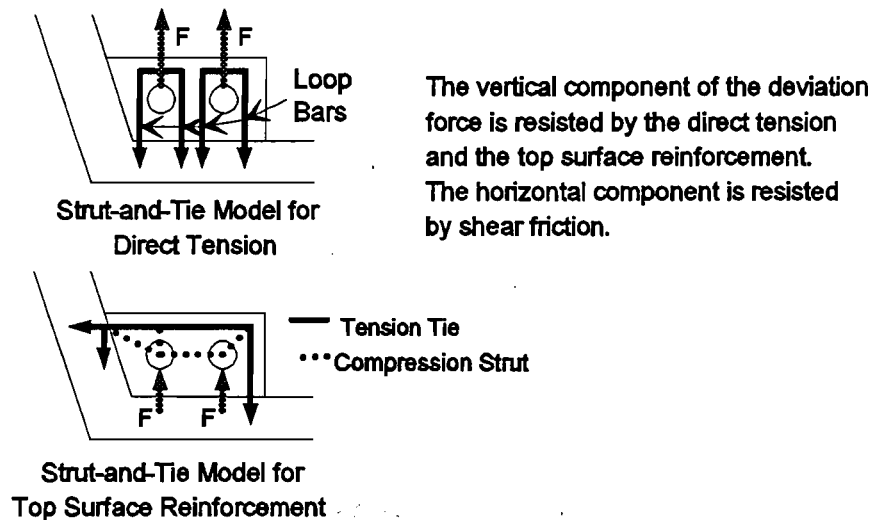


Figure 9.2 Beaupre et al. strut-and-tie model for deviator.

9.1.2 AASHTO Guide Specification Approach. Section 14.6 of the *AASHTO Guide Specification for the Design and Construction of Segmental Concrete Box Girder Bridges*¹ addresses the design of deviation saddles. Design requirements are as follows:

14.6.2 Design

Reinforcement shall be provided in the form of fully anchored reinforcement and bent bars in webs or flanges to take the resultant pull out force computed at f_{su}^* from the deviated tendon(s) at a service stress of $0.5f_{sy}$. Additional reinforcement shall be provided to take any out of balance longitudinal forces by shear friction action according to the ACI 318-86 Standard Building Code, Article 11.7. Reinforcement shall also be provided to take any localized bending effects transmitted from the deviation saddles to the webs and/or flanges.

Where:

f_{su}^* = average stress in prestressed reinforcement at ultimate load, psi.
 f_{sy} = specified yield strength of non-prestressed reinforcement, psi.

The *AASHTO Guide Specification* also allows D regions, such as deviators to be designed using strut-and-tie modelling techniques. D regions, Disturbed or Discontinuous regions, are areas in a structure where linear strain gradient theory does not apply.

9.2 Literature Review

9.2.1 Beaupre, Powell, Breen and Kreger.¹² The results of an extensive laboratory investigation of deviator behavior are reported in this publication. A total of six 1/3 scale and four 1/5 scale models were tested to destruction. Two deviation block geometries were tested. For each shape reinforcing steel details were varied and in some specimens epoxy coated reinforcing was used. In every case the failure was caused by tension failures or pull-out failures of the reinforcing bars which encircle the deviator pipes and tie the deviator to the bottom slab. There was considerable forewarning of failure in the form of extensive, wide cracking, but the failures were quite explosive.

Two design methods are presented: a simplified model and a strut-and-tie model method. In both cases it is recommended that a load factor of 1.7 on the initial jacking force and a strength reduction factor of 0.9 on direct tension reinforcing and 0.85 in shear friction calculations be used in design.

The simplified model uses a combination of a direct tension model, a shear friction model and a beam element model (see Figure 9.3). The direct tension model is used to proportion the ties around each deviator pipe. The shear friction model proportions the reinforcing which transfers shear across a crack interface which may form below the tendon ducts. The beam model is used to proportion the top surface reinforcing which provides additional strength to the deviator saddle.

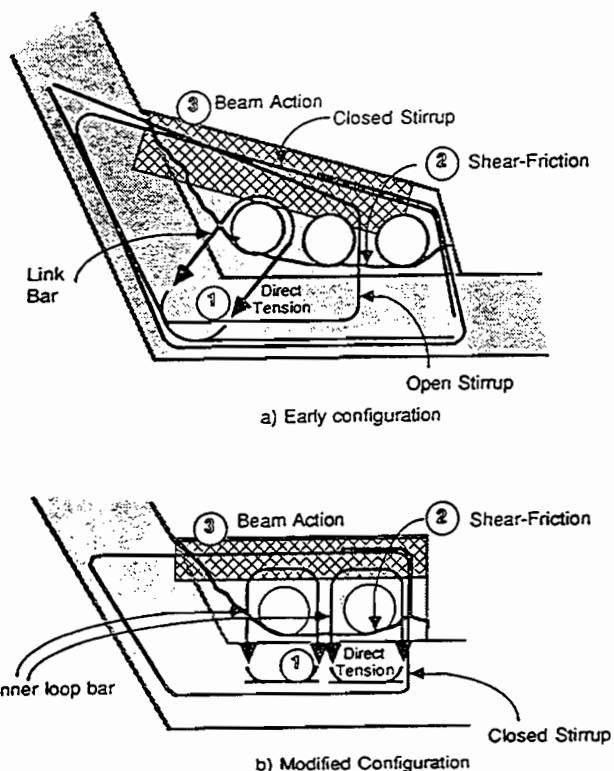


Figure 9.3 Simplified model for deviator design by Beaupre et al.

The second method is a combination of two strut-and-tie models shown in Figure 9.2. The first model describes the contribution of the primary direct tension reinforcement and the second model describes the contribution of the top surface reinforcement.

Both methods predicted ultimate failure loads quite well. For the ten specimens, the simplified analysis produced an average ratio of actual ultimate load to predicted ultimate load of 1.14 and the strut-and-tie model had a ratio of 1.06. Either method is acceptable.

9.2.2 Kreger.³⁸ Tendon deviators in an externally post-tensioned box girder bridge, which are part of the Washington D.C. Metro rail system, were found to have significant cracking. An analysis was performed based on the simplified model recommended by Beaupre et al. Two types of retrofit were used to strengthen the deficient deviators. For one type of retrofit a beam was cast over the original deviators to provide additional strength (see Figure 9.4). The second type of retrofit added a web stiffening rib as well. Further analysis and live load testing indicated that the repairs were sufficient.

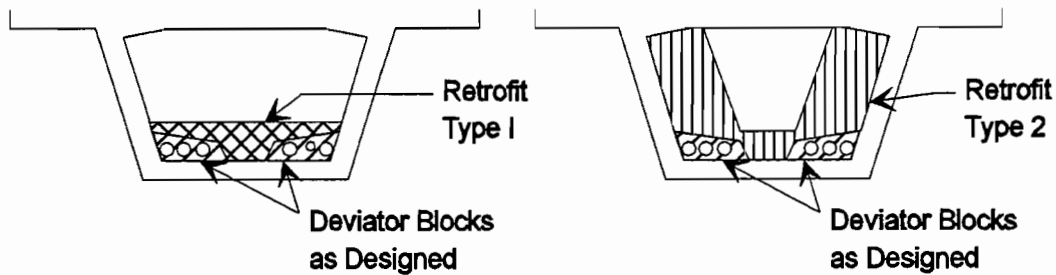


Figure 9.4 Retrofit to strengthen deviators.

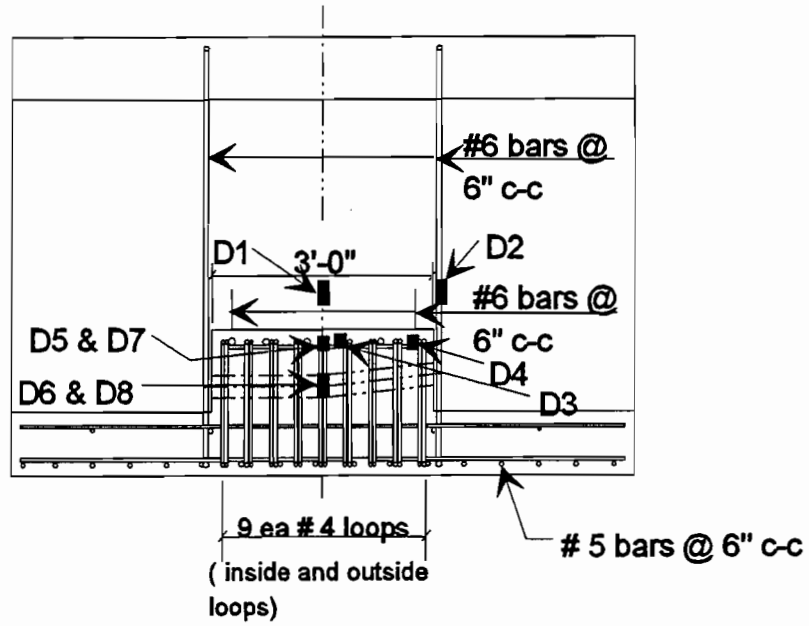
9.3 Surveillance Program

9.3.1 Description of Deviators and Instrumentation. Figure 9.5 shows the reinforcing steel layout and deviator geometry for the beam type deviator which was instrumented in this study in span C11. A total of two 19-0.6 inch (15 mm) diameter strand tendons and two 12-0.6 inch (15 mm) diameter strand tendons were deviated at this location. This resulted in a total upward force at the deviator of 314 kips (1397 kN). The figure also shows the layout of reinforcing steel strain gages.

Figure 9.6 shows the reinforcing steel layout and deviator geometry for the deviators with diaphragm walls which were instrumented in spans A43 and A44. Three 19-0.6 inch (15 mm) diameter strand tendons were deviated on each side of the segment. The total upward force on each side was 215 kips (956 kN). The figure also shows the layout of reinforcing steel strain gages.

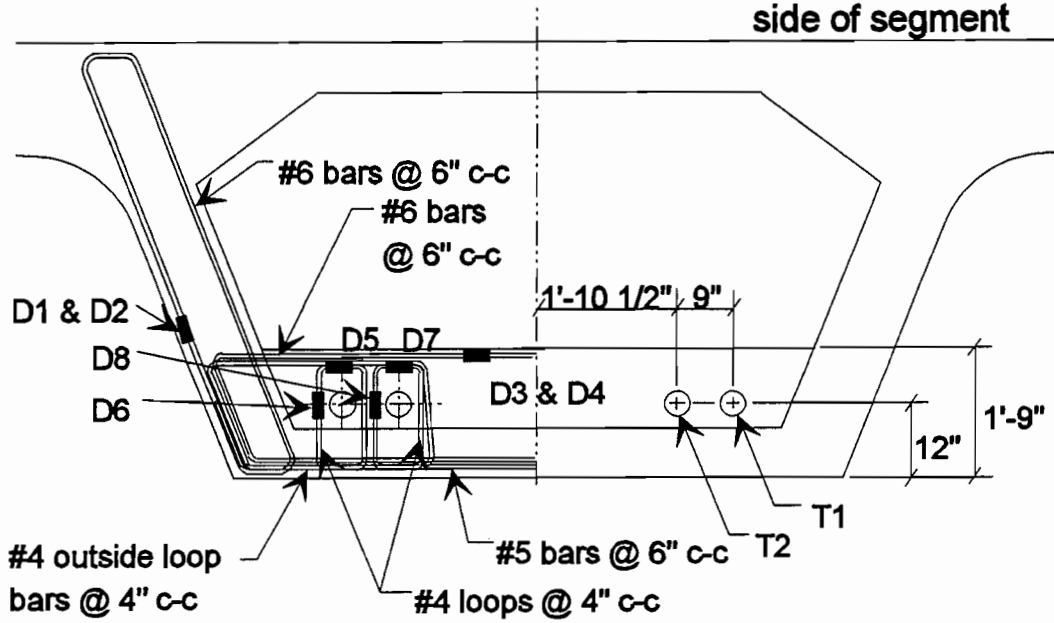
The gaging operations were not as successful as was hoped. In span C11 only four of eight gages survived the casting operations. In span A43 eight of ten survived and in span A44 seven of ten survived. One problem was the extreme amount of adjustment of the reinforcing steel which is required to place the deviator pipes inside the reinforcing steel cage. As the steel workers adjusted the reinforcing, sometimes with large sledge hammers, some of the gages were damaged. The others were apparently damaged during casting, due to the great deal of vibration required to consolidate the concrete in the congested deviators.

In each of the three instrumented deviators, the gages were connected to the permanent data acquisition system and monitored every twenty seconds during stressing operations.



Section View

Gages are on North side of segment

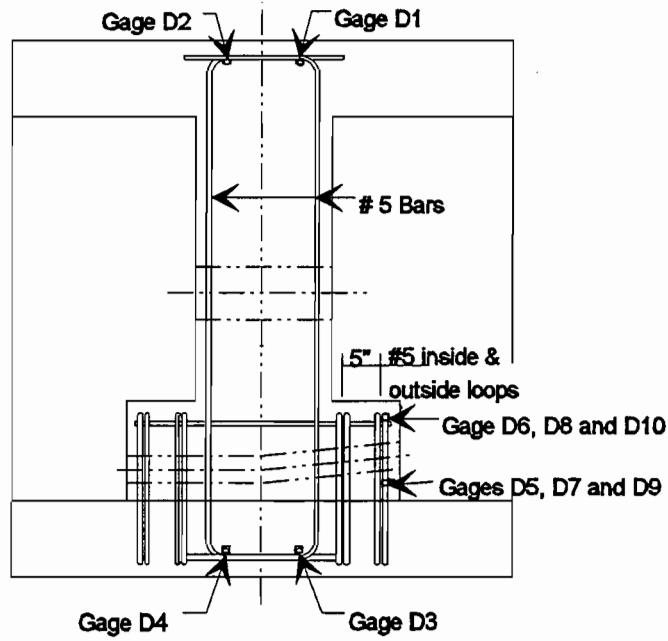


**Span C11 Deviator Segment
Elevation View**

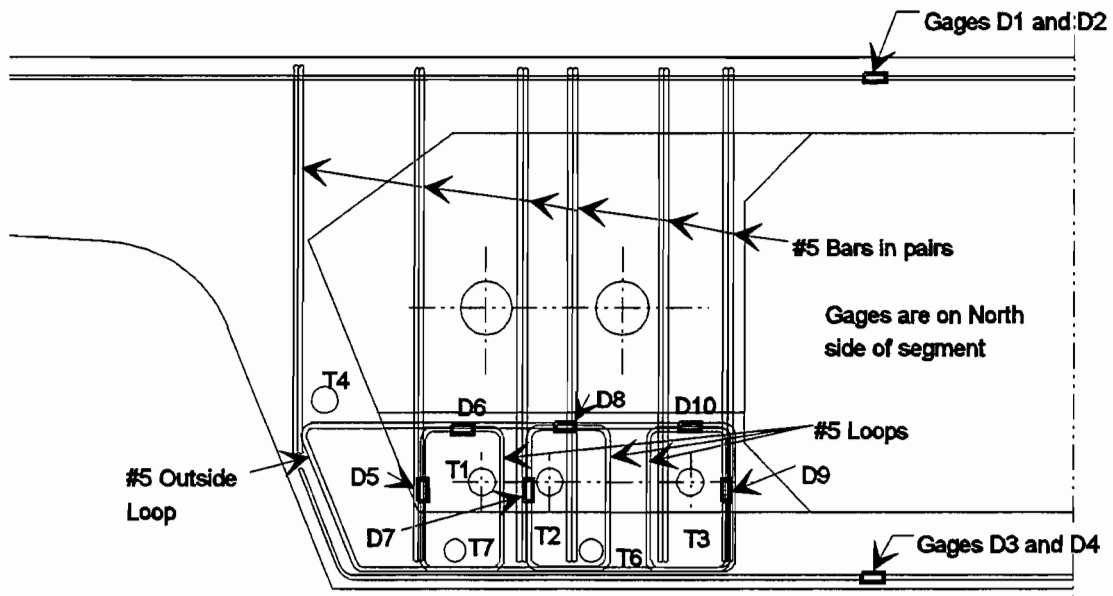
Typical segment bars not shown for clarity

1 inch = 25.4 mm

Figure 9.5 Span C11 deviator.



Section View



Span A43 and A44 Deviator Segment

Elevation View

Typical segment bars not shown for clarity
 (1 inch = 25.4 mm)

Figure 9.6 Span A43 and A44 deviator.

9.3.2 Presentation of Results. The reinforcing steel did not experience high levels of stress in any of the deviators. The highest recorded stress was 3.2 ksi (22 MPa) in span C11. Figures 9.7 through 9.9 show the progression of the stresses in the deviators as the individual tendons were stressed.

A visual inspection of the deviators showed no signs of cracking.

The small steel strains and the lack of visible cracking would indicate that these are very adequate deviator designs.

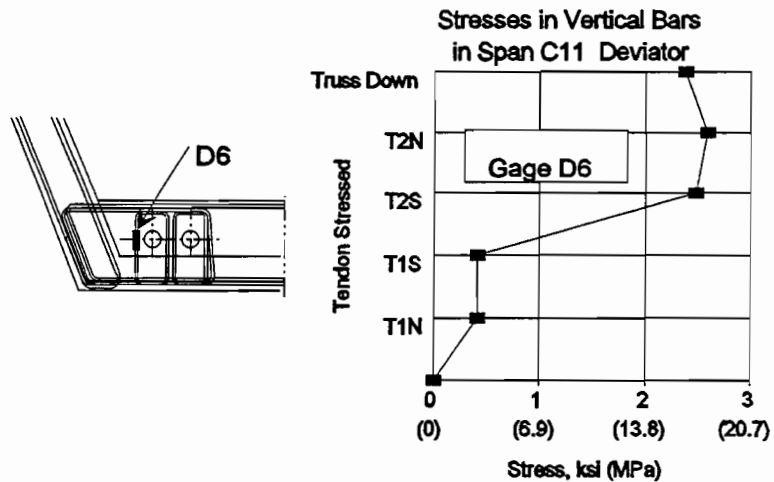
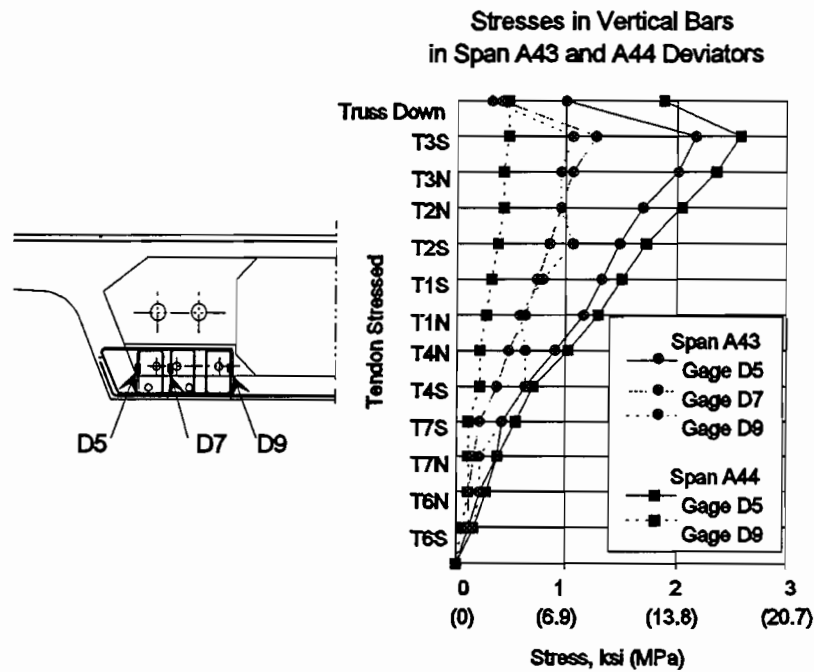
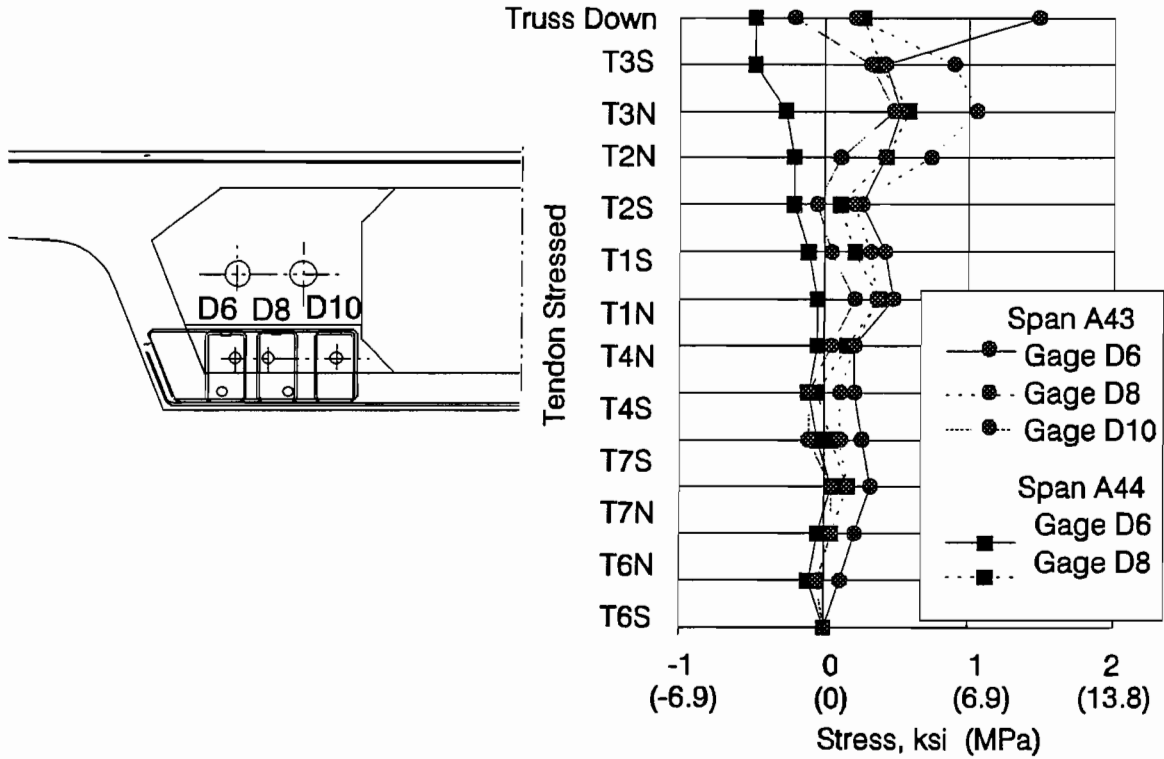


Figure 9.7 Stress in vertical bars.

Stresses in Horizontal Bars in Span A43 and A44 Deviators



Stresses in Horizontal Bars in Span C11 Deviator

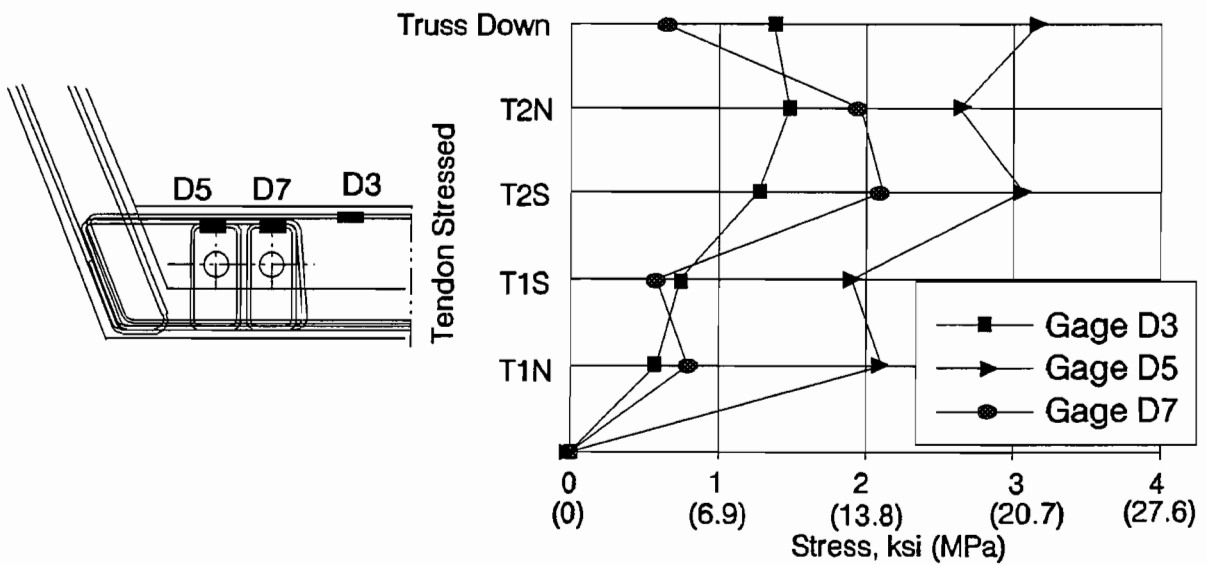
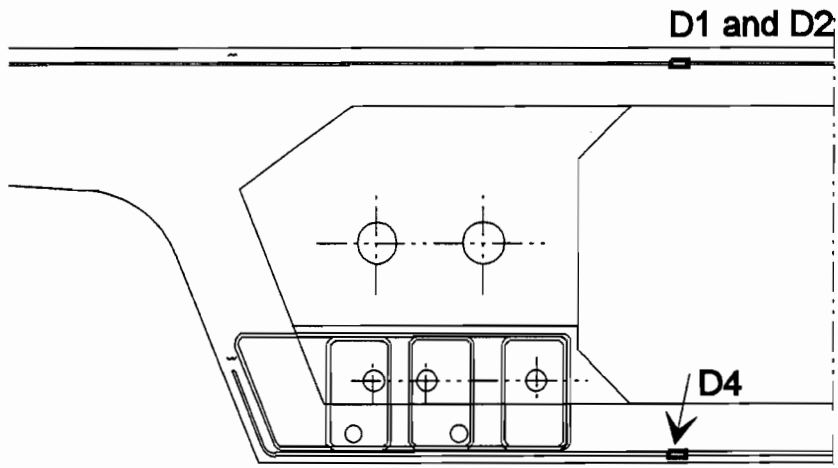


Figure 9.8 Stresses in horizontal bars.



**Stresses in Top and Bottom Slab Bars
In Span A43 and A44 Deviator Segments**

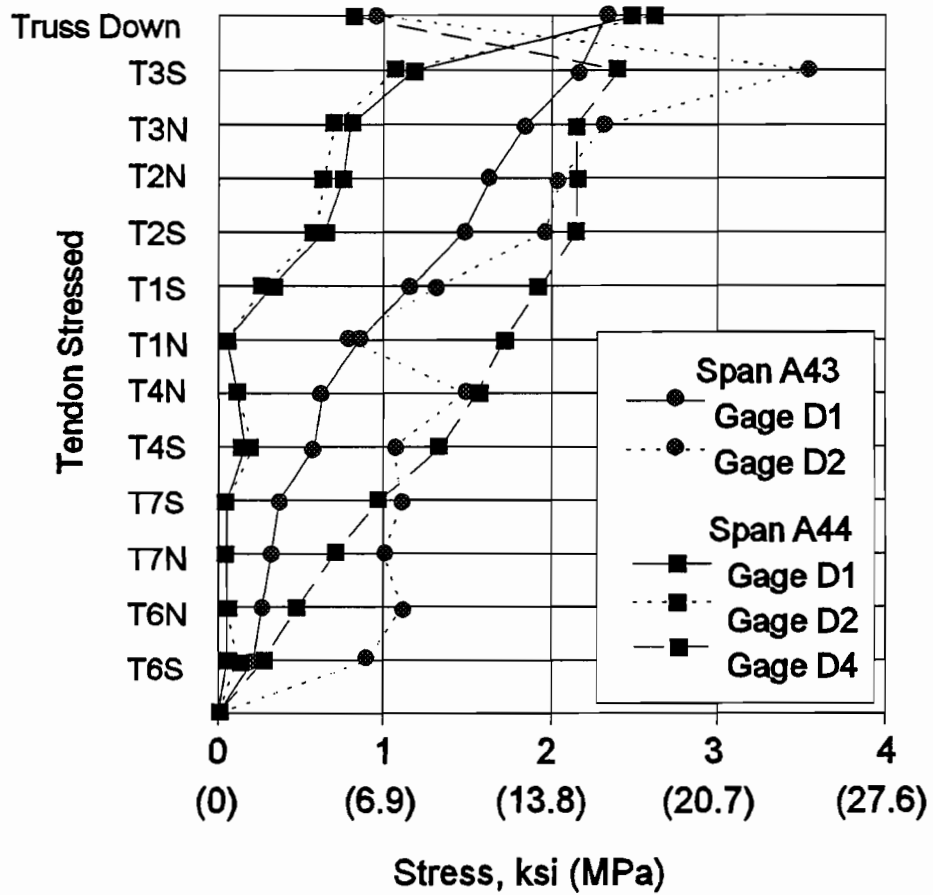


Figure 9.9 Stresses in top and bottom bars.

9.4 Discussion of Strut-and-Tie Modelling

9.4.1 Models for Laboratory Specimens. One short-coming of the models used by Beaupre to analyze his laboratory study was the failure to address the flow of forces into the cross-section. Modified strut-and-tie models for specimens 4A and 4B by Beaupre et al.¹² are shown in Figures 9.10a and 9.10b. These models describe the flow of deviation forces up into the web walls, and capture the bending stresses which develop in the web and bottom slab.

For specimens 4A and 4B by Beaupre et al., this model predicts locations of highest stresses after cracking and before failure. Basing the failure load on the fracture of the most highly stressed tie results in predictions of strength of only one half of the actual ultimate capacity. Plasticity theory indicates that there is considerable redistribution of forces, and this is indicated by the high proportion of gaged reinforcing bars which surpassed yield strains in the test specimens. As bars yielded, the forces found new paths and utilized the full capacity of the reinforcing steel.

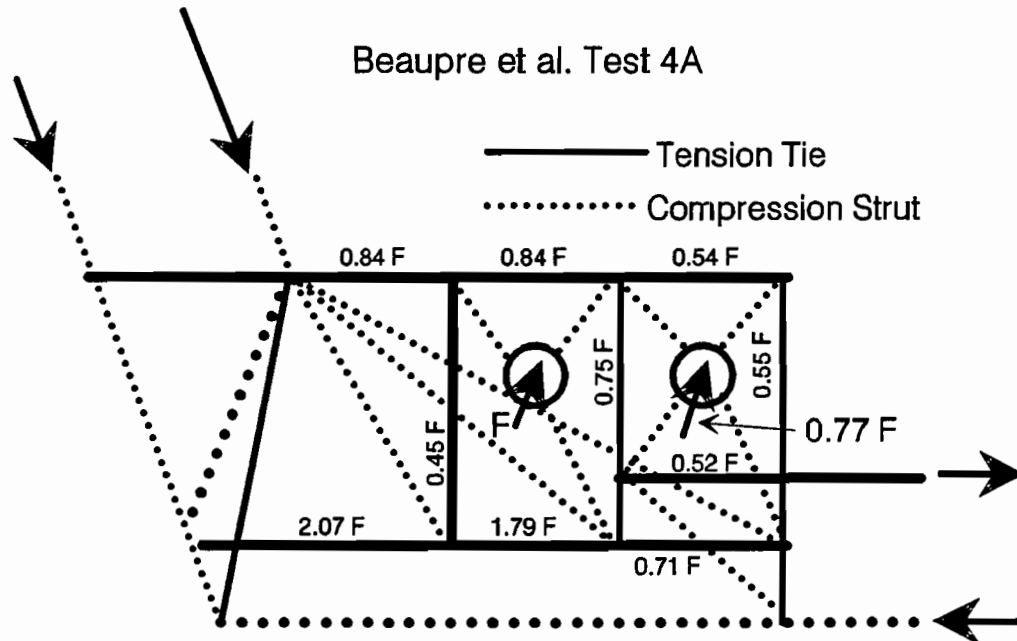
Predictions of strength based on the force required to break all the ties in either the horizontal or vertical direction gave better agreement with actual capacity. The actual capacity of test 4A was 1.40 times the prediction in which the horizontal tension controlled. This conclusion corresponded with the test results which showed the most highly strained bars were horizontal. The actual capacity of test 4B was 1.00 times the prediction in which the vertical tension controlled. In this specimen the vertical bars were the most highly stressed.

9.4.2 Model for Span C11. Figure 9.11 shows a strut-and-tie model for the deviators in Span C11. This model illustrates the direct tension as well as the web and beam bending stresses. Based on this model, in which horizontal tension governs failure, the ultimate capacity of the deviator is calculated as 533 kips (2371 kN). This is well above the actual service load on the deviator of 314 kips (1397 kN). This analysis would indicate that the design is adequate, with a factor of safety of 1.7.

The strains in the deviator beam can be predicted reasonably well at low load levels by simple elastic analysis. If the beam is considered to be simply supported at the web walls, and each deviator load is applied in the order of stressing, a series of moment diagrams can be developed. If the beam is considered to be acting independently (ignoring any contribution of the bottom slab on each side of the deviator) strains at the level of the gages can be calculated. Figure 9.12 shows the calculated strains compared to the measured strains for the horizontal gages in the beam. At service loads, the concrete is still apparently uncracked and is carrying a considerable amount of tension. However, as cracking occurs, the concrete contribution is eliminated and only the steel can be counted on to carry the tension.

9.4.3 Model for Spans A43 and A44. Figure 9.13 shows a strut-and-tie model for the deviators in spans A43 and A44. This is a worst case model which assumes that the deviation force must first be tied down into the bottom slab and then deviated upwards into the web wall. Actually, as shown in Figure 9.14 much of the deviation force is transmitted in compression

directly into the diaphragm wall. Since this is the stiffest load path, most of the force will flow directly up the wall, and the tensions in the loop bars will remain small.



Test 4A

$$\text{Vertical Tension in Deviator Bars} = 0.45F + 0.75F + 0.55F = 1.75F$$

$$\text{Vertical Tension Capacity} = 5 * 5 \text{ legs of } 0.0192 \text{ in}^2 * 60 \text{ ksi} = 28.8 \text{ k}$$

$$(5 * 5 \text{ legs of } 12.4 \text{ mm}^2 * 413.7 \text{ Mpa} = 128 \text{ kN})$$

$$\text{Predicted Failure based on Vertical Capacity} = \frac{28.8}{1.75} = \underline{16.5 \text{ k (73.4 kN)}}$$

$$\text{Horizontal Tension} = 0.84F + 2.07F = 2.91F$$

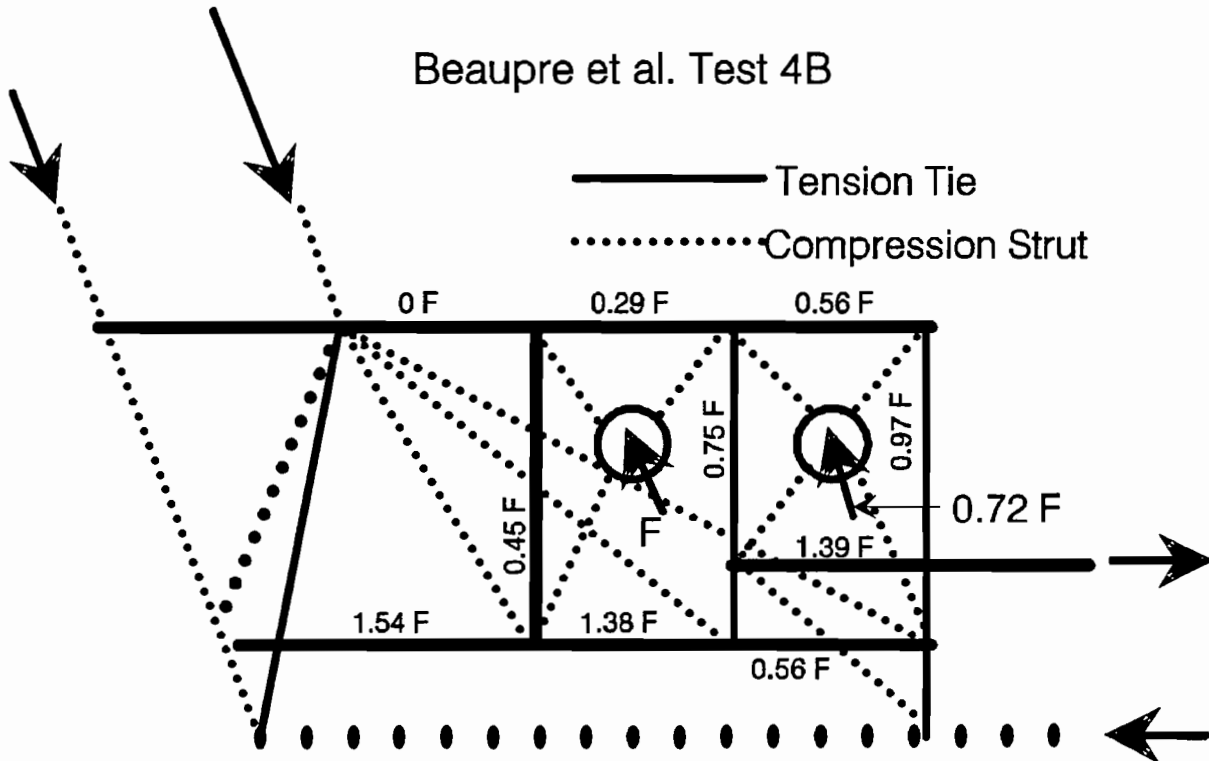
$$\text{Horizontal Tension Capacity} = (10 \text{ legs of } 0.0192 \text{ in}^2 + 5 \text{ legs of } \#2) * 60 \text{ ksi} = 26.2 \text{ k}$$

$$(10 \text{ legs of } 12.4 \text{ mm}^2 + 5 \text{ legs of } \#2 * 414 \text{ Mpa} = 117 \text{ kN})$$

$$\text{Predicted Failure based on Vertical Capacity} = \frac{26.2}{2.91} = \underline{9.0 \text{ k (40 kN)}}$$

Actual Failure at $F=12.4 \text{ k (55.2 kN)}$

Figure 9.10a Modified strut-and-tie model for specimen 4A by Beaupre et al.



Test 4A

Vertical Tension in Deviator Bars = $0.45F + 0.75F + 0.97F = 2.17F$
 Vertical Tension Capacity = $5 * 5 \text{ legs of } 0.0192 \text{ in}^2 * 60 \text{ ksi} = 28.8\text{k}$
 ($5 * 5 \text{ legs of } 12.4 \text{ mm}^2 * 413.7 \text{ Mpa} = 128 \text{ kN}$)

Predicted Failure based on Vertical Capacity = $\frac{28.8}{2.17} = 13.3\text{k (59.2kN)}$

Horizontal Tension = $1.54F$
 Horizontal Tension Capacity = $(10 \text{ legs of } 0.0192 \text{ in}^2 + 5 \text{ legs of } \#2) * 60 \text{ ksi} = 26.2 \text{ k}$
 ($10 \text{ legs of } 12.4 \text{ mm}^2 + 5 \text{ legs of } \#2 * 414 \text{ Mpa} = 117 \text{ kN}$)

Predicted Failure based on Vertical Capacity = $\frac{26.2}{1.54} = 17.0 \text{ k (75.6kN)}$

Actual Failure at $F=13.3 \text{ k (59.2 kN)}$

Figure 9.10b Modified strut-and-tie model for specimen 4B by Beaupre et al.

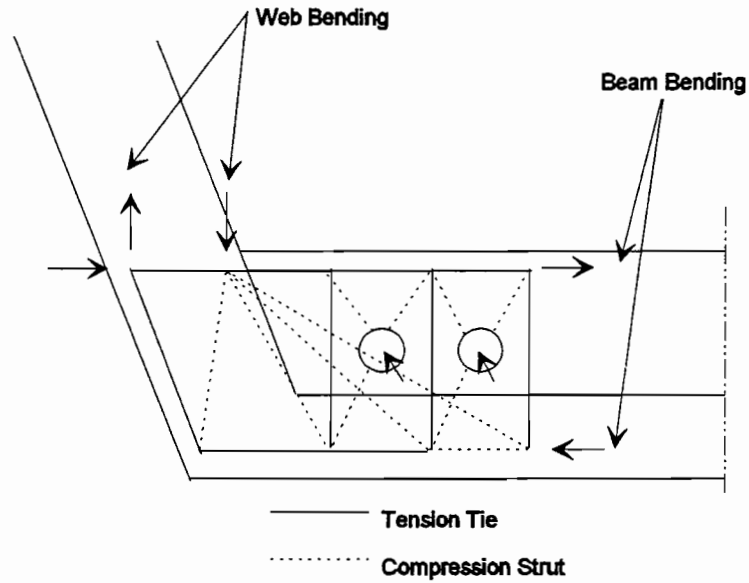


Figure 9.11 Strut-and-tie model for Span C11 deviator.

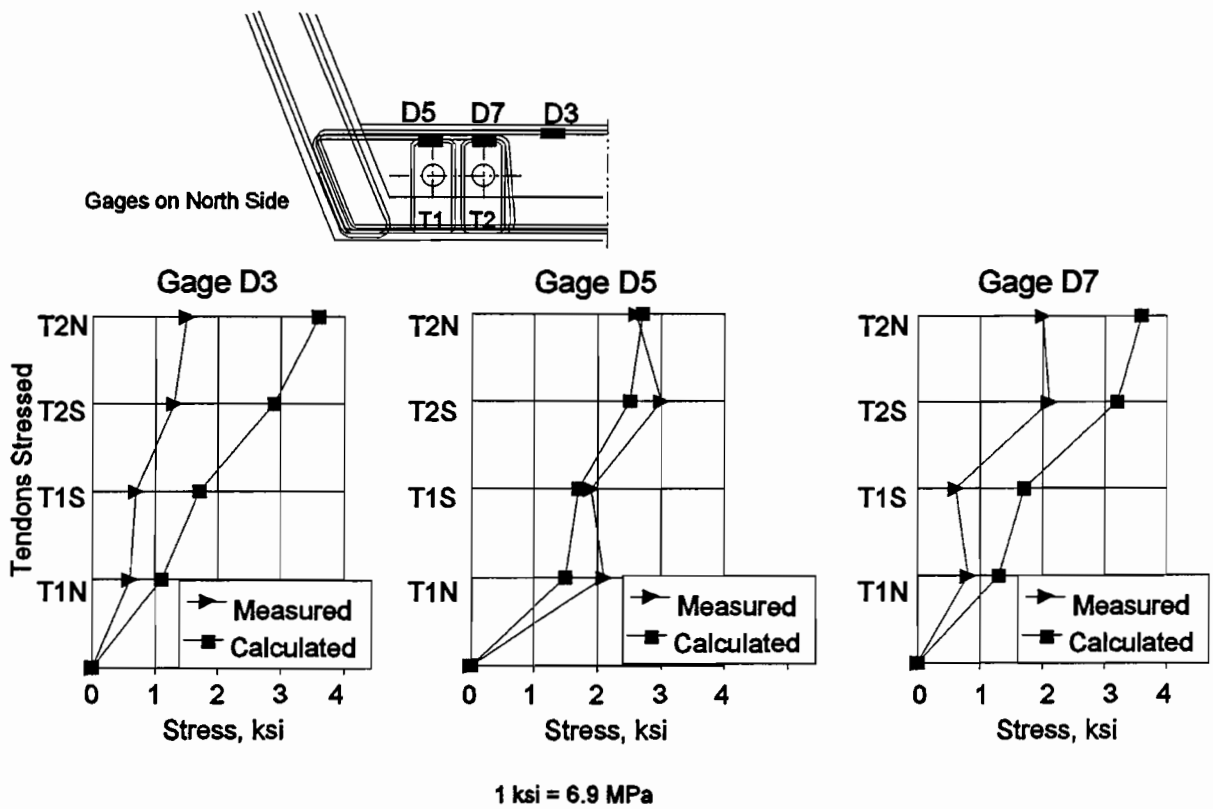


Figure 9.12 Calculated vs. measured stresses in C11 deviator.

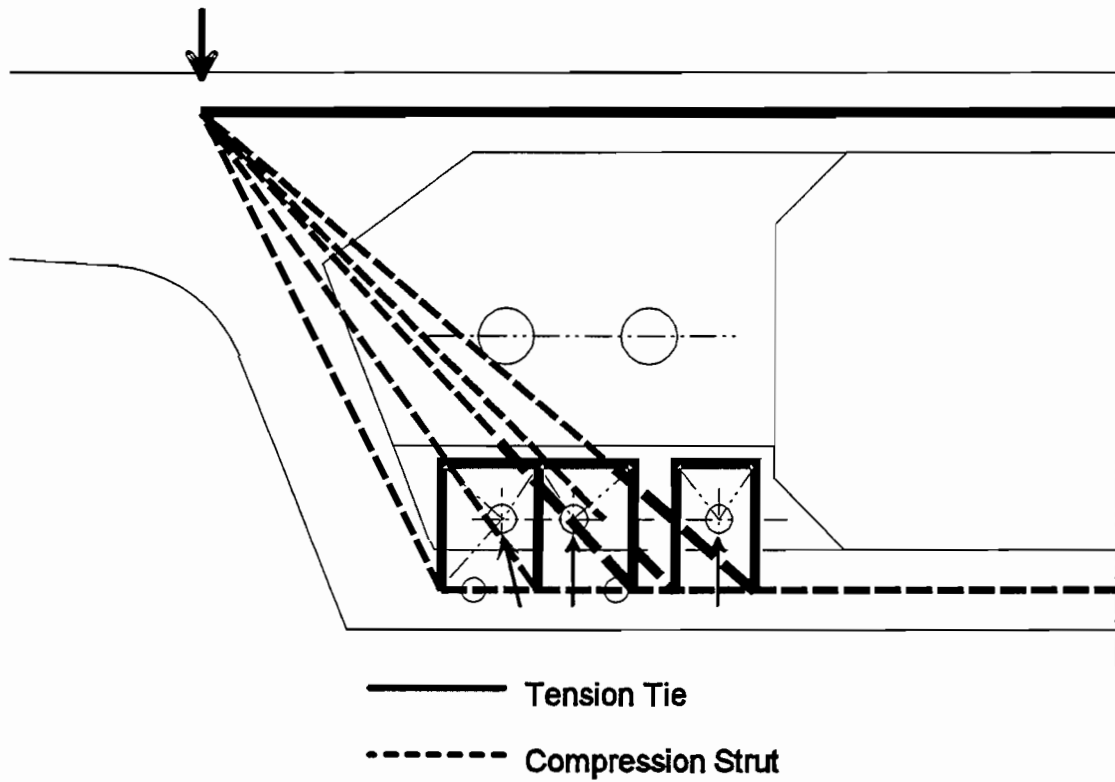


Figure 9.13 Strut-and-tie model for spans A43 and A44 deviators.

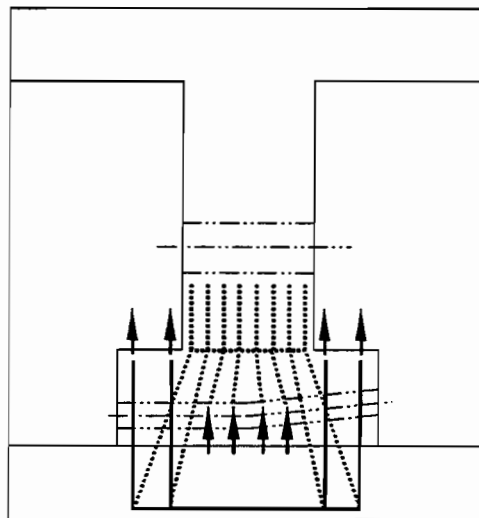


Figure 9.14 Section of strut-and-tie model for spans A43 and A44 deviators.

Another area of tension occurs in the top slab. If approximately 4 feet (1.2 m) of the top slab is assumed to be resisting the tension, a concrete tension of 420 psi (2896 kPa) would develop. The top slab is prestressed to a level of approximately 580 psi (4000 kPa), so the slab would not de-compress. During stressing, a change in steel strain of $77\mu\epsilon$, which equates to 2.1 ksi (14.5 MPa), would be predicted in the top slab reinforcing steel. The actual top slab steel stresses were 2.57 ksi (17.7 MPa) in span A44 and 1.64 ksi (11.3 MPa) in span A43.

A compression check in the diaphragm wall shows a maximum stress of 690 psi (4758 kPa). This is considerably less than allowable.

Overall an analysis using the strut-and-tie model indicates that this deviator is also adequately designed.

9.5 Recommendations

The *AASHTO Guide Specification* as it is written is adequate for the design of deviators. However, the recommendation to design for full stressing load at $0.5 f_{sy}$ should be replaced with the recommendation that a factor of safety of 1.7 be used on the maximum stressing load and strength reduction factors of 0.90 for the steel in direct tension and 0.85 for shear friction reinforcing be applied. Reference should be made in the commentary to the design recommendations of Beaupre et al.

The following changes should be made to the *AASHTO Guide Specification* Section **14.6.2 Design of Deviation Saddles** (changes are indicated by italicized print):

Reinforcement shall be provided in the form of fully anchored reinforcement and bent bars in webs or flanges designed to take the resultant pull-out force, computed as *the deviation force generated by the post-tensioning steel at the maximum allowable stressing force ($A_s \cdot 0.8 f'_s$) times 1.7, at the yield stress of the reinforcing bars. Strength reduction factors of $\phi = 0.90$ for direct tension steel and $\phi = 0.85$ for shear friction reinforcing shall apply.*

The following shall be added to the Design Specifications Section **14.6.3**:

Consideration shall be given to the position of web and flange internal tendons to avoid conflicts in the proper anchorage of deviation saddle reinforcing steel in webs and flanges.

The following shall be added to the Design Commentary as Section **14.6 Deviation Saddles**:

Tests of scale model deviation saddles at the University of Texas at Austin^[12] have provided important information on the behavior of these critical

regions. Design and detailing guidelines presented in the research report result in safe and serviceable designs.

Deviation saddles are disturbed regions of the structure and can also be designed using strut-and-tie modelling methods in accordance with Section 12.4.

9.6 Conclusions

Unfortunately, this field study disclosed no new information. In all three instrumented deviators the steel strains were small and there were no visible cracks. The designs were very adequate.

The design recommendations of Beaupre et al. result in conservative and serviceable designs. One desirable refinement of Beaupre's model is presented which describes the flow of forces from the deviators into the webs and flanges of the box. This model also does a reasonable job of predicting failure for two laboratory specimens which were re-examined as part of this study.

CHAPTER 10 CONSTRUCTION AND LIVE LOADS

10.1 Introduction

This chapter presents observations and measurements made as the instrumented spans were subjected to construction and live loads. These tests were performed to study some general and some specific aspects of the bridge's behavior. The general aspects of behavior which were targeted were:

- deflections under construction and service loads
- web strain profiles
- external tendon stress increases

The more specific aspects of behavior were:

- performance of the "poor-boy" continuous span
- interaction of adjacent spans transversely post-tensioned together.

This chapter presents a description of the construction and live loadings, a comparison of predicted and actual behavior, conclusions and recommendations.

10.2 Background Information

This section provides information on the four spans which were studied. Spans A43 and A44 are the middle and one end span of a three span continuous unit. Span C9 is part of a trial two span unit which incorporated an unusual form of partial continuity between the spans known as "poor-boy" continuity. The other unusual span, Span C11, is part of a fully continuous two span ramp unit which was transversely post-tensioned to an adjacent mainline two span unit.

10.2.1 Spans A43 and A44 - Typical Spans. Spans A43 and A44 were very typical spans within the project. Span A43 is the middle span and Span A44 one end span of a three span continuous unit. The boxes are Type III (58 ft. (17.7 m) wingspan and 16 ft. (4.9 m) box), with symmetric wing dimensions (see Figure 3.2). These spans were studied to determine the general behavior of a fully continuous multi-span segmental box girder under construction and live loads.

10.2.2 Span C9 - "Poor-Boy" Continuity. In the state of Texas the most widely used type of bridge construction involves precast, pre-tensioned I-girders with a cast-in-place deck slab. In some cases, multi-span bridges have been made continuous by casting a closure pour between the ends of the beams over the piers, and also casting the deck continuously across the spans (see Figure 10.1). This configuration caused problems, however, because as the pre-

tensioned girders cambered upwards with time, the closure pours often cracked and unsightly rust stains have appeared on the girders.

Other multi-span bridges have been built as a series of simple spans with a joint at every pier. Unfortunately, joints can often be expensive, or require considerable maintenance. This type of bridge can also be unpleasant for the user because there is a distinct bump at every joint. Therefore, this solution is also not ideal.

A third method is what is known as "poor-boy" continuity. In these types of bridges the top deck is cast continuously across multiple spans of simple span girders, with mild reinforcing continuous through the slab (see Figure 10.2). No closure pour is made between the ends of the pretensioned girders. This method eliminates the high-cost, high-maintenance joints, and also eliminates the unsightly cracking problems between girders. The closure slab is allowed to crack but the cracking is controlled by the mild slab reinforcing. The spans are analyzed as if they were simple spans, which is conservative and reduces the complexity of design.

In the San Antonio "Y" project the concept of poor-boy continuity was applied to a two span unit. The unit comprised one 75 ft. (22.9 m) span and one 85 ft. (25.9 m) span of Type I boxes (26 ft. (7.9 m) wing spans and 8 ft. (2.4 m) box). Each span was erected as a simple span. There were no tendons continuous through both spans. The top slab closure strip was cast several months after the spans had been erected. Mild reinforcing bars extend from the precast segments into the closure. Figure 10.3 shows details of the spans, designated C9 and C10. Span C9 was instrumented with a deflection measurement system, surface strain gages on webs and surface strain gages on the "poor-boy" continuity slab.

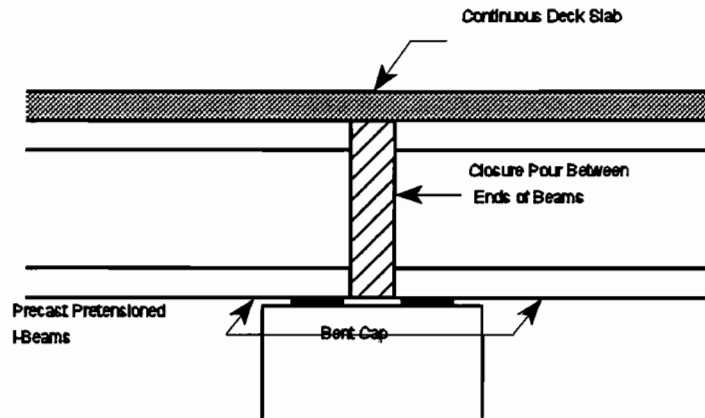


Figure 10.1 Full continuity between precast I-beams.

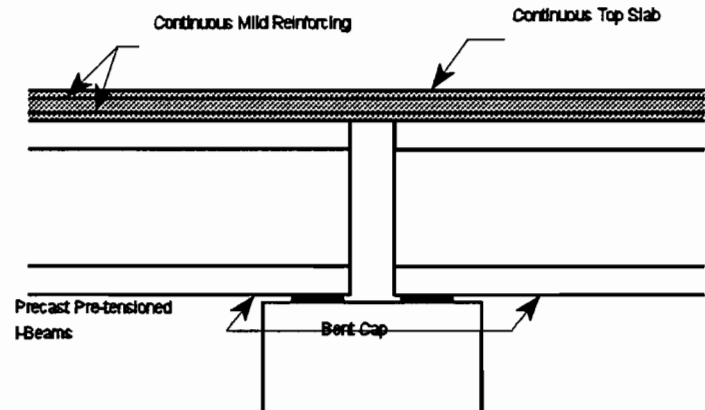
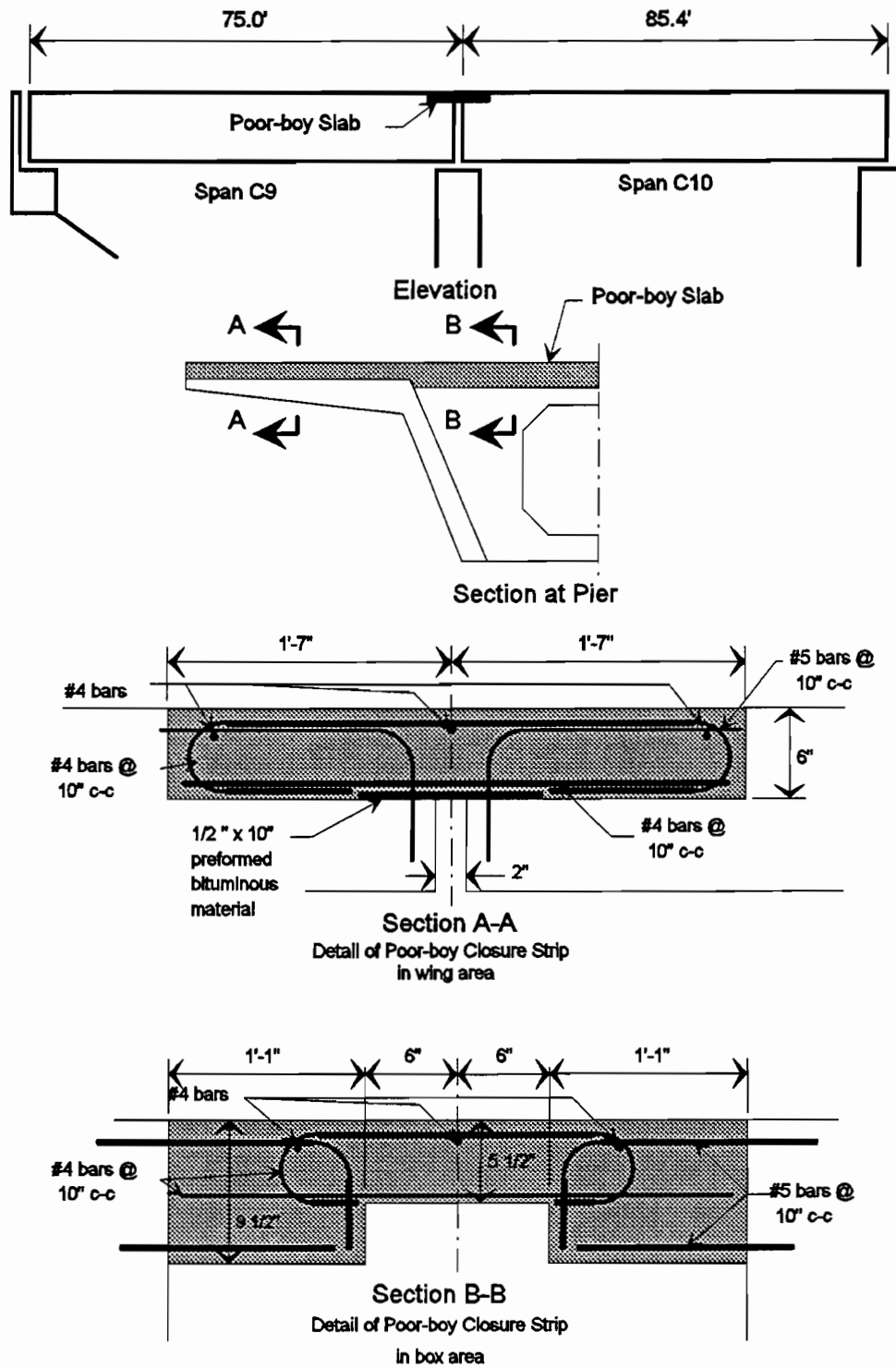


Figure 10.2 "Poor-boy" continuity between precast I-beams.



1 inch = 25.4 mm

Figure 10.3 Details of "poor-boy" closure slab.

The tests were conducted to determine if the spans were behaving as simple spans or partially continuously. The surface strain readings of the closure were were made to determine the level of tension in the concrete under service loads.

10.2.3 Span C11 - Transverse Post-Tensioning. The San Antonio "Y" Project is a complex segmental structure. The existence of exit and entrance ramps contributes to this complexity. There are many instances where, as shown in Figure 10.4, the bridge transitions from two adjacent but independent boxes (such as a mainline box and a ramp box) to two adjacent boxes with truncated wings which are transversely post-tensioned together. Then, these adjacent boxes further merge into a special transition box before becoming a single mainline box. Designers were particularly interested in the degree of interaction of the two adjacent boxes when transversely post-tensioned together.

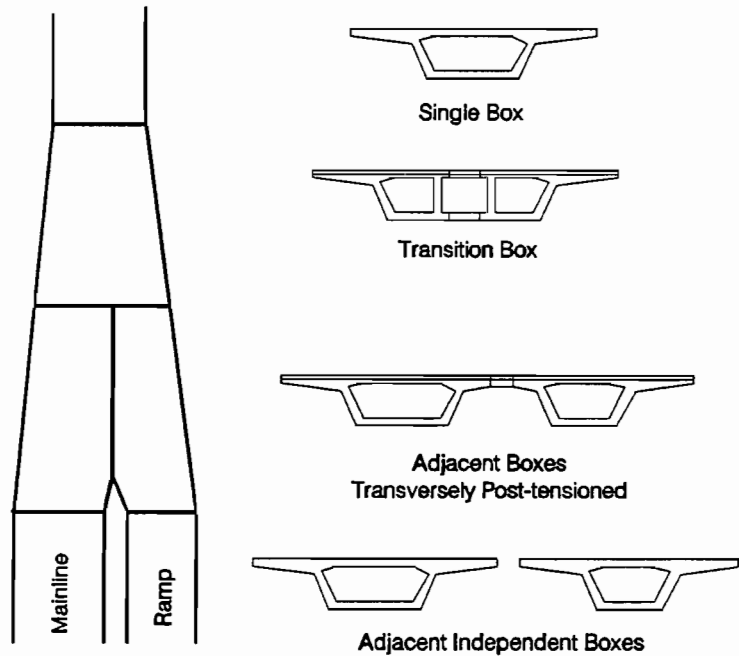


Figure 10.4 Ramp box merging with mainline box.

As mentioned earlier, Span C11 is part of a two span continuous ramp unit which is transversely post-tensioned to an adjacent mainline unit (see Figure 10.5). Span C11 was fully instrumented and during live load tests tendon strains, deflections, and web strains were measured. The live load trucks were placed on Span C11 and then on the adjacent mainline span, Span A45. The measurements are analyzed to study the behavior of this type of transversely post-tensioned span.

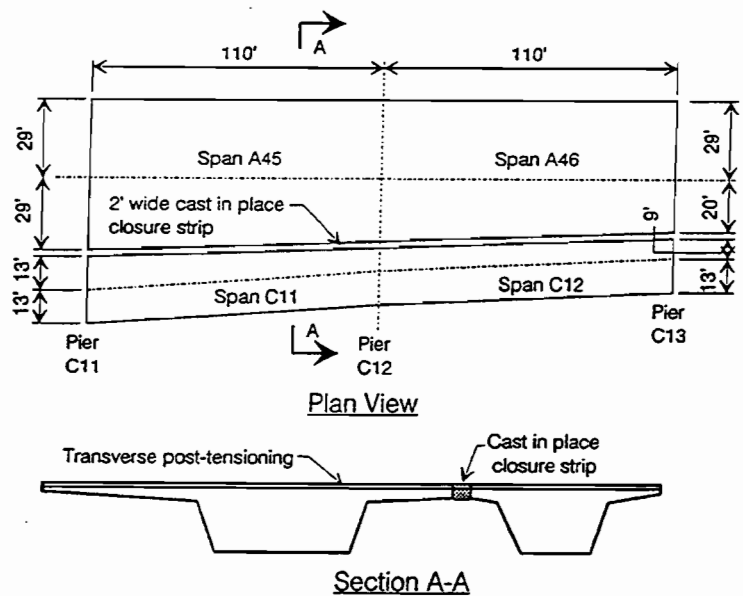


Figure 10.5 Span C11 detail.

10.3 Test Procedures

10.3.1 Test Load Vehicles.

10.3.1.1 Crane Loading.

Figure 10.6 shows the loading from the HC-238A truck crane which was used for segment erection. The researchers had one opportunity to take span measurements with the crane positioned on the end span of the three span continuous unit (Span A44). All instrumentation systems were monitored with the crane in the position shown in Figure 10.6.

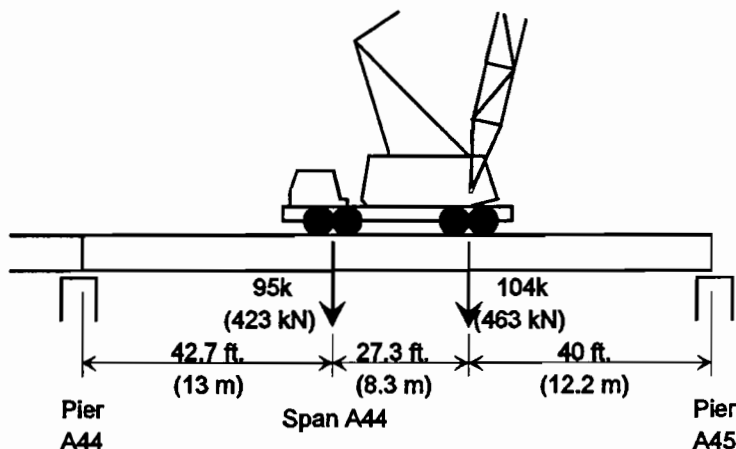


Figure 10.6 HC-238B truck crane.

10.3.1.2 HS20-44 Trucks.

Figure 10.7a shows the AASHTO HS20-44 design vehicle. Although the distance between the rear axles is shown as variable, the shortest dimension, 14 ft. (4.3 m), results in the highest mid-span moments on the spans in this study. Unfortunately, it is very difficult to locate trucks which approximate an HS20-44 loading with the 14 ft. (4.3 m) distance between rear axles. Most haul trucks have a much longer wheel base. To better approximate the maximum moments of the HS20-44 loadings,

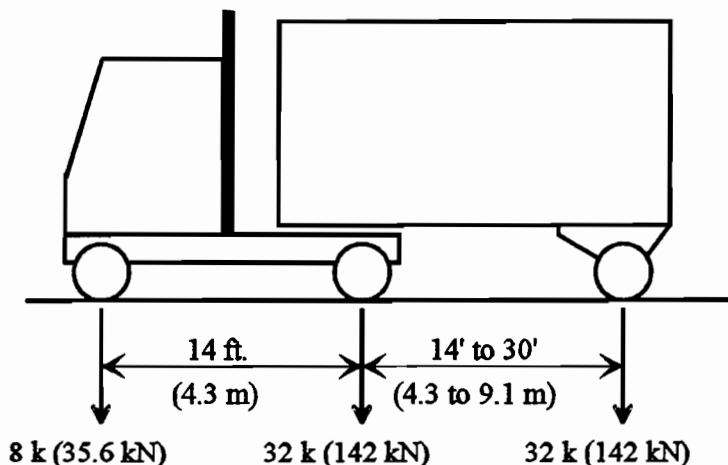
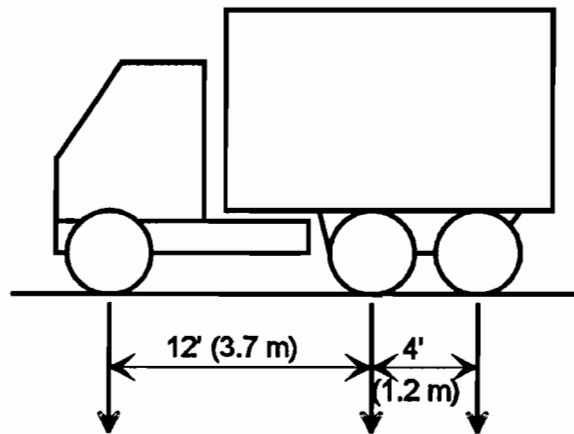


Figure 10.7a AASHTO HS20-44 standard truck.

each HS20-44 truck was replaced by two short bed 7 yard (5.4 m³) dump trucks, positioned back to back. The truck dimensions and axle loads are shown in Figure 10.7b. Figure 10.8 compares the maximum moments and shears resulting from an HS20-44 loading with the values from the two dump truck loading actually used on the three span continuous unit. The maximum moments are very similar, although the shear due to the two truck configuration is slightly larger. The test load vehicles were supposed to be loaded to a gross weight of 42 kips (187 kN) each. This loading would produce a maximum shear equal to that of live load plus impact (50 kips (222 kN) /lane), and would produce a moment equal to 1.05 times live load. This would be less than live load plus impact which would be 1.21 times live load. The actual truck gross weights were close to 42 kips (187 kN) in terms of their average although there was some acceptable variation between trucks.



Axle loads in lbs. (kN)

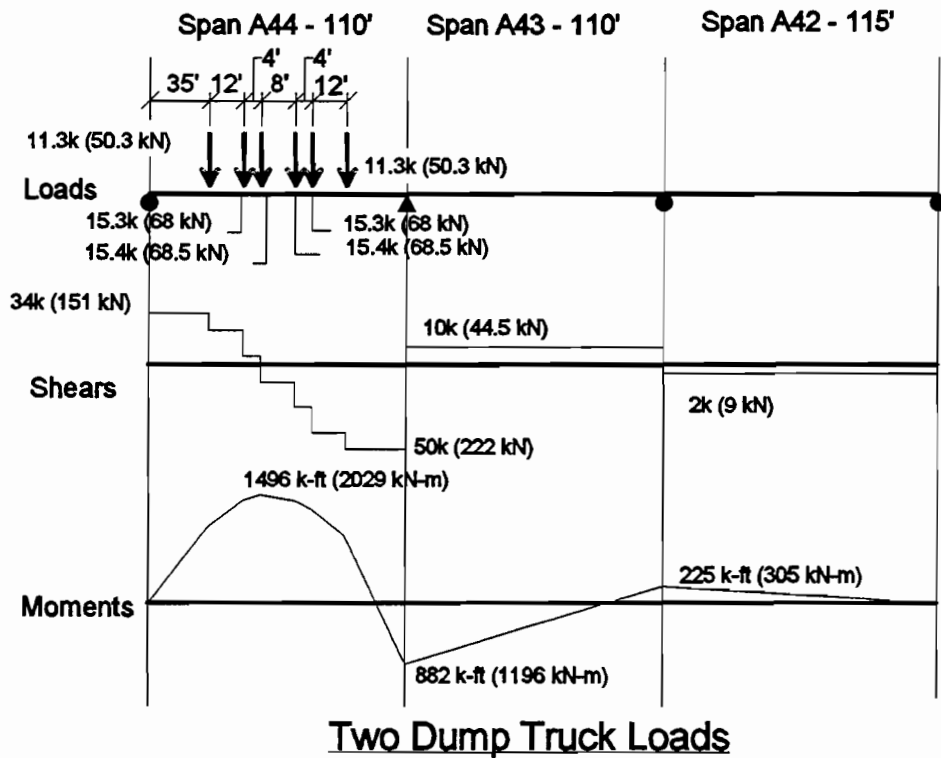
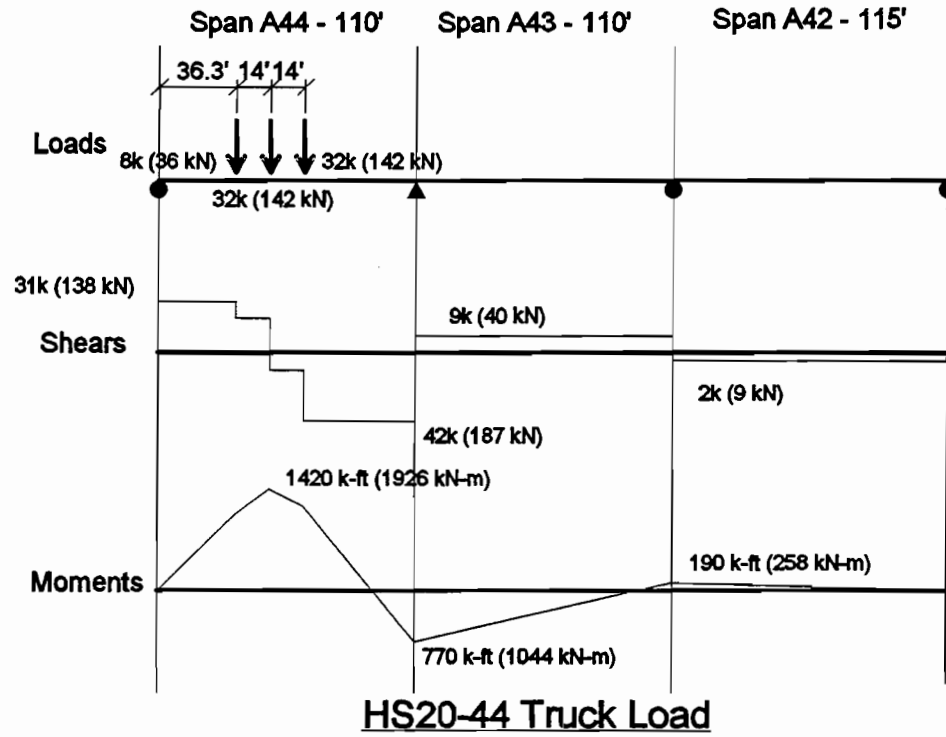
	Front Axle		Middle Axle		Rear Axle		Total	
	lbs.	kN	lbs.	kN	lbs.	kN	lbs.	kN
1	10400	46.3	16950	75.4	16650	74.1	44000	195.7
2	11100	49.4	13850	61.6	13250	58.9	38200	169.9
3	10650	47.4	14900	66.3	14900	66.3	40450	179.9
4	12200	54.3	15500	68.9	16250	72.3	43950	195.5
5	11600	51.6	15500	68.9	16200	72.1	43300	192.6
6	11900	52.9	15300	68.1	14950	66.5	42150	187.5
Mean	11308	50.3	15333	68.2	15367	68.4	42008	186.9
Std. Dev.	711	3.2	1006	4.5	1264	5.6	2296	10.2

Figure 10.7b Dump trucks used in tests.

10.3.2 Personnel. During live load tests six researchers were required for all tasks. Two individuals remained on the top of the box to position trucks and take all top slab readings. Four individuals were inside of the box to read and record all measurements. Walkie-talkies were used for communication between the inside and outside crews.

10.3.3 Three Span Continuous Unit.

10.3.3.1 Crane Loading. The crane was positioned near mid-span on Span A44 as shown in Figure 10.6. Readings were taken in Span A43 and A44 before loading, with crane in position, and after loading. The opportunity to take the measurements was not anticipated and all readings were made by two researchers. Each set of readings took approximately one hour for both spans.



To convert from foot to meter multiply by 0.3048.

Figure 10.8 Comparison of HS20-44 loading and dump truck loading.

10.3.3.2 Truck Loads. Figure 10.9 shows the positions of the trucks for the live load measurements of the three span continuous unit. The type III boxes of these spans are 56 feet (17 m) wide, which accommodates four full AASHTO traffic lanes. With four lanes, however, AASHTO allows a 25% reduction in live load, so only three pairs of trucks were used. Both Spans A43 and A44 were monitored during testing. The systems monitored were:

- tendon strains
- deflections
- web strains
- concrete temperatures.

The test proceeded as follows:

1. No loads - initial readings taken,
2. Trucks on Span A44 - readings taken,
3. Trucks on Span A43 - readings taken,
4. Trucks on Span A42 - readings taken,
5. No loads - final readings taken.

Each set of readings took 30-35 minutes. The entire procedure required approximately 3 hours.

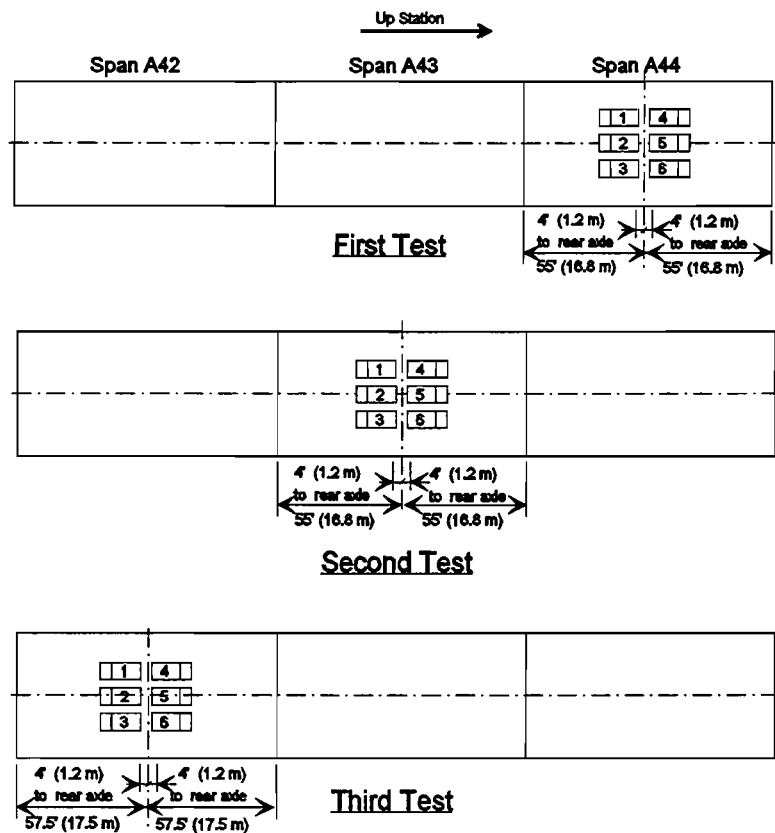


Figure 10.9 Truck positions in spans A42, A43 and A44.

10.3.4 "Poor-Boy Unit". Figure 10.10 shows the positions of the trucks for the live load measurements of the "poor-boy" continuous unit. The ramp boxes are 26 ft. (7.9 m) wide, which accommodates two full AASHTO traffic lanes. Span C9 was loaded with two lanes of trucks. In the subsequent test, Span C10 had an obstruction blocking part of the span, so it was loaded with only one lane of trucks.

The systems monitored during loading were:

- deflections
- web strains
- continuity slab surface strains

The test proceeded as follows:

1. No load on bridge - zero readings taken,
2. Trucks on Span C9 - readings taken,
3. Trucks on Span C10 - readings taken,
4. No load on Spans C9 or C10 - final readings taken.

The entire procedure took approximately 1 hour.

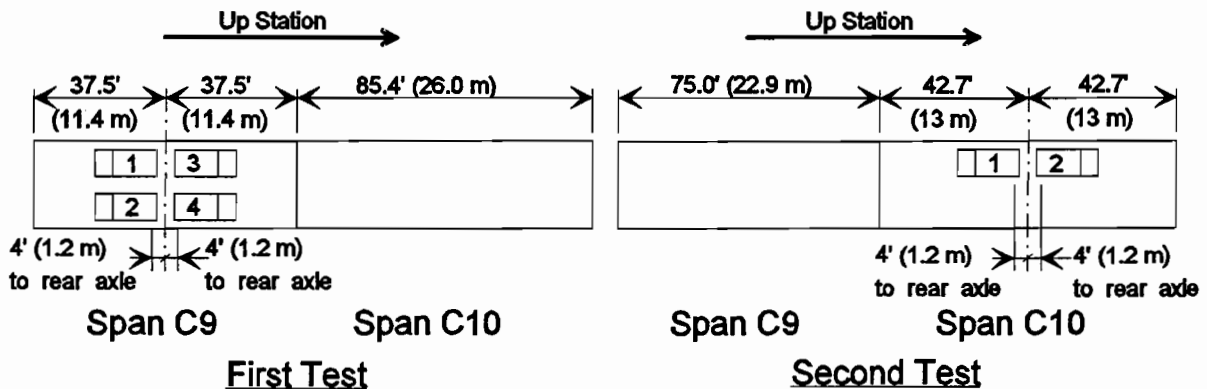


Figure 10.10 Truck positions in spans C9 and C10, "poor-boy" unit.

10.3.5 Transversely Post-Tensioned Span - C11. Figure 10.11 shows the positions of the trucks for the live load measurements of the transversely post-tensioned unit. As mentioned previously, the ramp boxes were loaded with two lanes of trucks. The mainline boxes of Span A45 were loaded with three lanes of trucks.

The systems monitored were:

- tendon strains
- deflections
- web strains
- concrete temperatures.

The test proceeded as follows:

1. No loads - initial readings taken,
2. Trucks on Span C11 - readings taken,
3. Trucks on Span A45 - readings taken,
4. No loads - final readings taken.

The entire procedure took approximately one hour and twenty minutes.

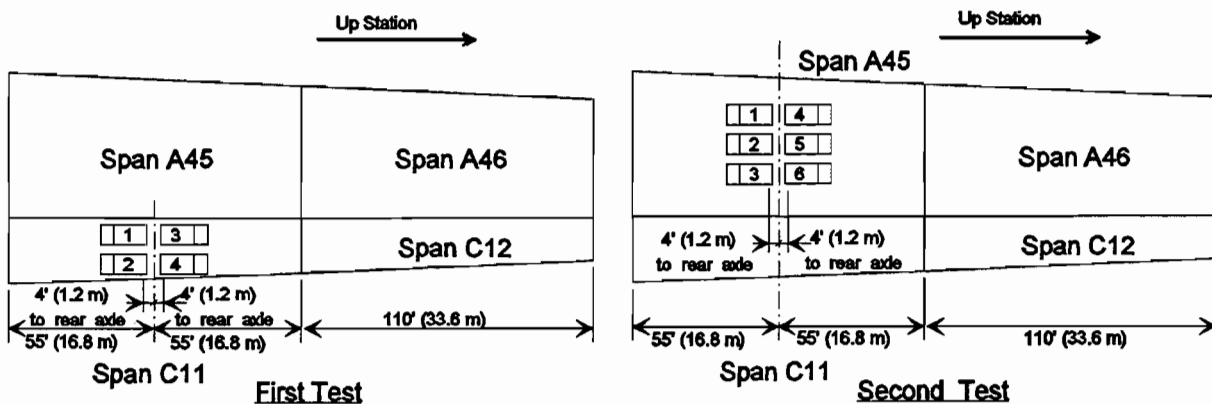


Figure 10.11 Truck positions in spans C11 and A45.

10.4 Presentation of Results

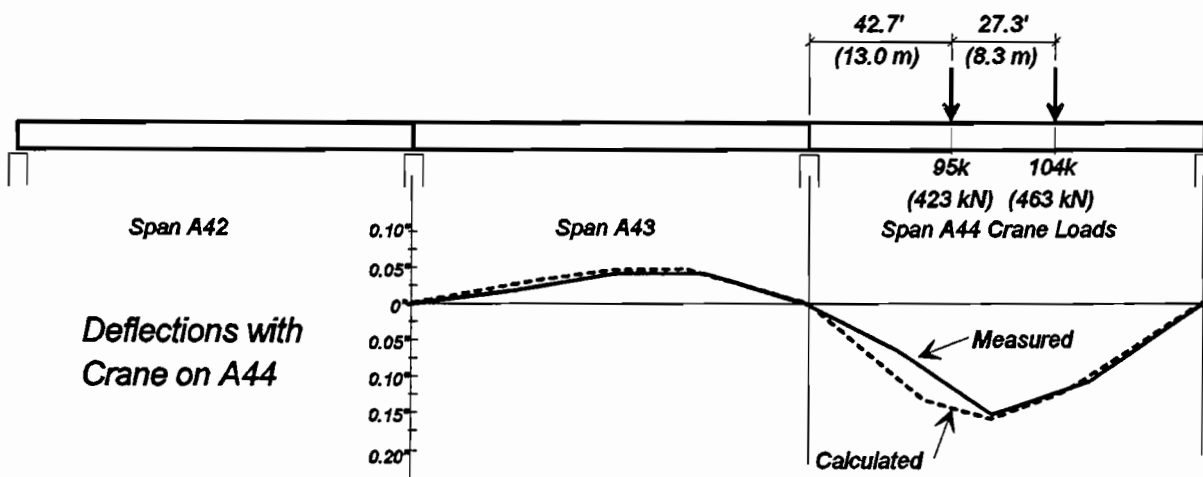
10.4.1 Three Span Continuous Unit - Spans A44 and A43.

10.4.1.1 Crane Loads. Figure 10.12 shows the actual load magnitudes and locations with the crane situated on Span A44. Also shown are the measured and calculated deflections. The deflections were calculated using a simple two dimensional frame solver (FRAME2D²⁴). The spans were discretized into approximately twelve segments each with nodes at each of the axle load positions (see Figure 10.13). Input files are given in Appendix B of the Roberts report.⁶¹ The full transformed uncracked section properties were used in the analysis. The pier areas were modeled as shown in Figure 10.13 with the actual fabric pad properties used for the pad elements.

The modulus of the concrete for all spans had been tested at the time the spans were erected (see Table 5.1). The modulus for each span was adjusted to the age of the concrete at the time of testing using the formula:

$$E_c = \left(\frac{t}{2.05 + 0.93t} \right) E_{c28\text{day}}$$

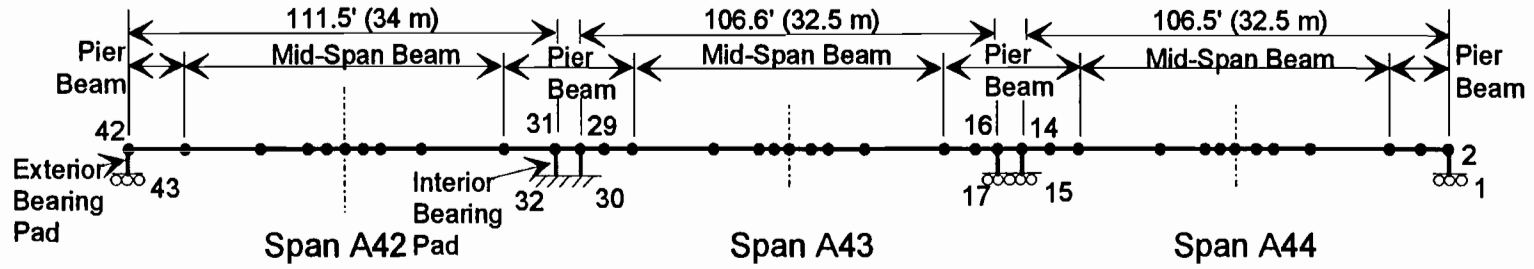
This formula indicated a less than 5% increase in E_c from erection to live load testing. Using this model, there is very good agreement with measured deflection. Calculated deflections are within 0.02 inch (0.5 mm) ($1/66000$) of measured at all points except the quarter point in Span A44 nearest pier A44 which was 0.06 inch (1.5 mm) less than calculated. The bridge is quite stiff with the loaded span deflecting only $1/8250$. The average tendon stress increase at mid-span location was 1400 psi (9653 kPa).



To convert from inch to millimeter multiply by 25.4.

Figure 10.12 Deflections of spans A43 and A44 with crane on span A44.

10.4.1.2 HS20-44 Truck Loading. Figures 10.14a, b and c show the actual axle loads and positions of the trucks on Spans A44, A43 and A42. Also shown are the measured and calculated deflection for each loading position. As before, the calculated deflection was determined using full transformed cross-sectional properties, and the mesh shown in Figure 10.13. When the loads were on Spans A43 and A44 the prediction of the deflection in the loaded span is very good (within 3% at mid-span), while the prediction of the deflection of the adjacent span is 30-40% larger than measured. Similarly the predictions of deflections in Spans A43 and A44 with the load on Span A42 are 60% and 300% larger respectively than measured. Overall, the predictions are quite good, with the greatest error 0.03 inch (0.8 mm) on a 110 foot (33.5 m) span ($1/44000$).



Mesh for Crane Loading



Tendon Locations at Mid-Span



Tendon Locations at Pier

Element	Area,		Moment of Inertia,		Modulus of Elasticity,	
	ft ²	(m ²)	ft ⁴	(m ⁴)	ksf	(MPa)
Mid-Span Beam	99.2	(9.2)	324.0	(2.8)	789,376	(37797)
Pier Beam	99.2	(9.2)	309.1	(2.7)	789,376	(37797)
Exterior Bearing Pad	7.78	(0.7)	0.88	(.008)	2409	(115)
Interior Bearing Pad	8.89	(0.83)	1.32	(0.011)	2409	(115)

Figure 10.13 Mesh for use with FRAME2D²⁴ program.

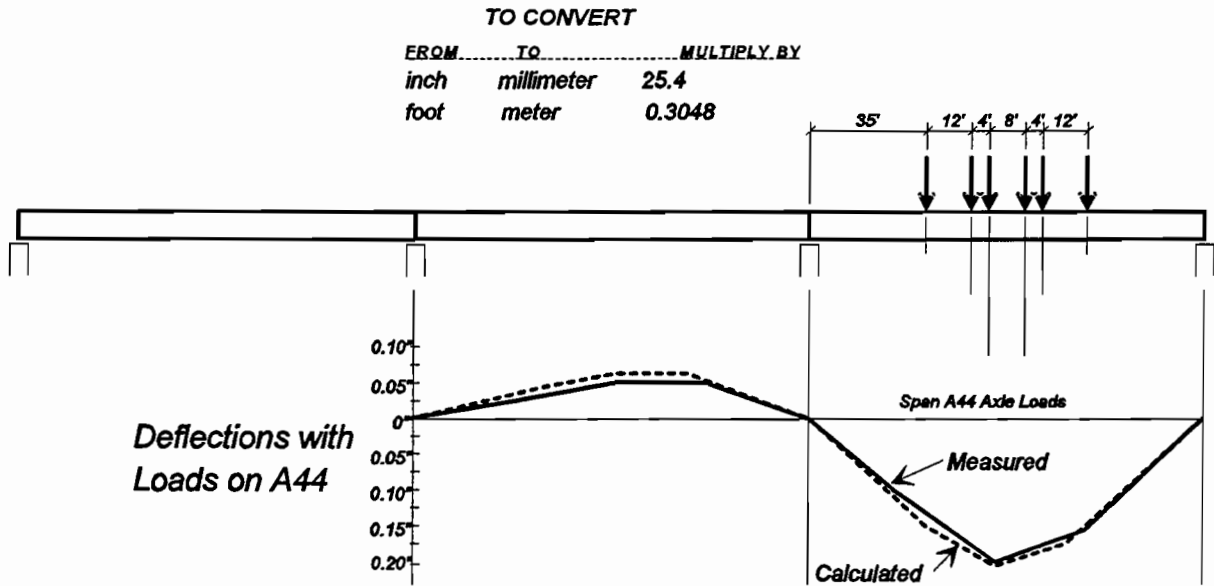


Figure 10.14a Deflections of spans A43 and A44 with live load on span A44.

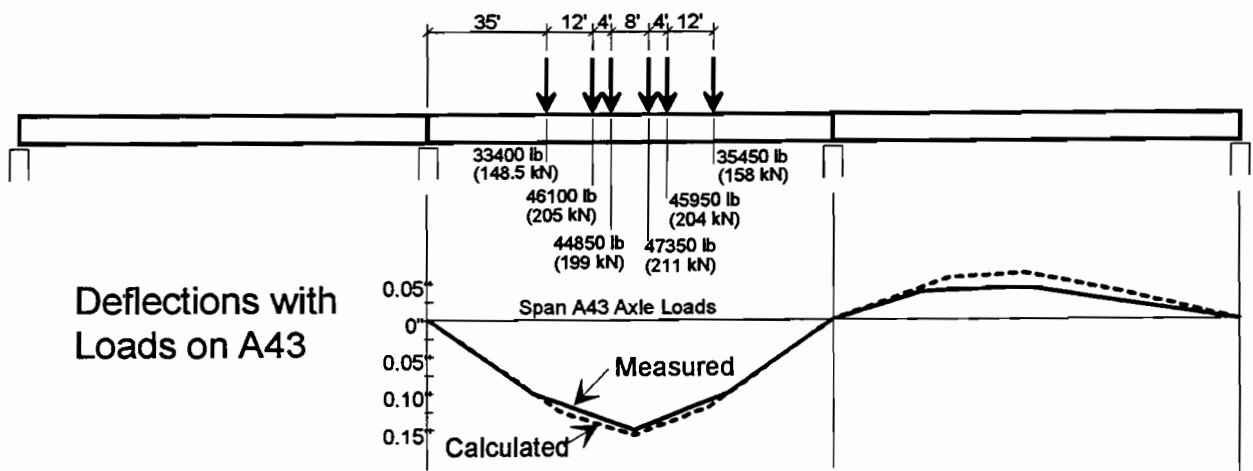


Figure 10.14b Deflections of spans A43 and A44 with live load on span A43.

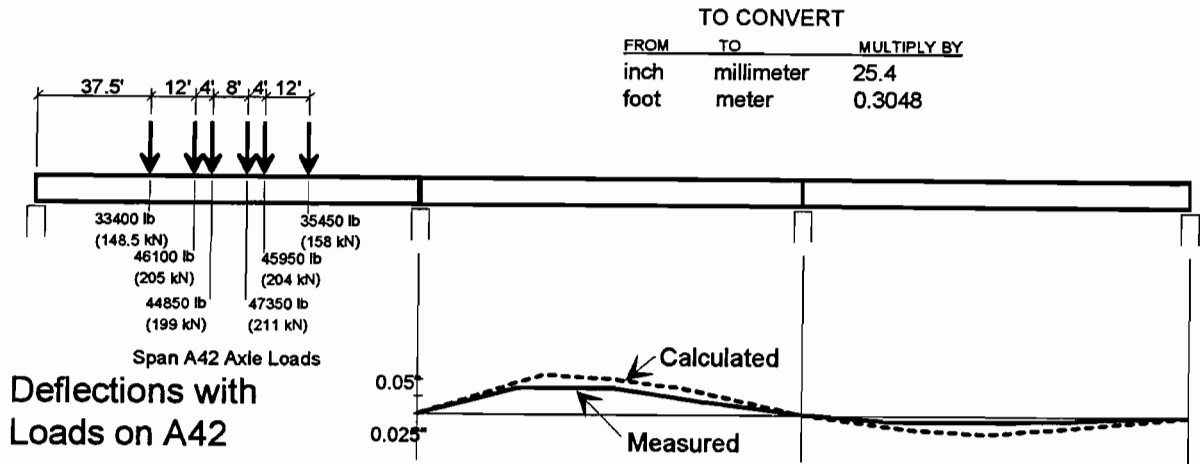
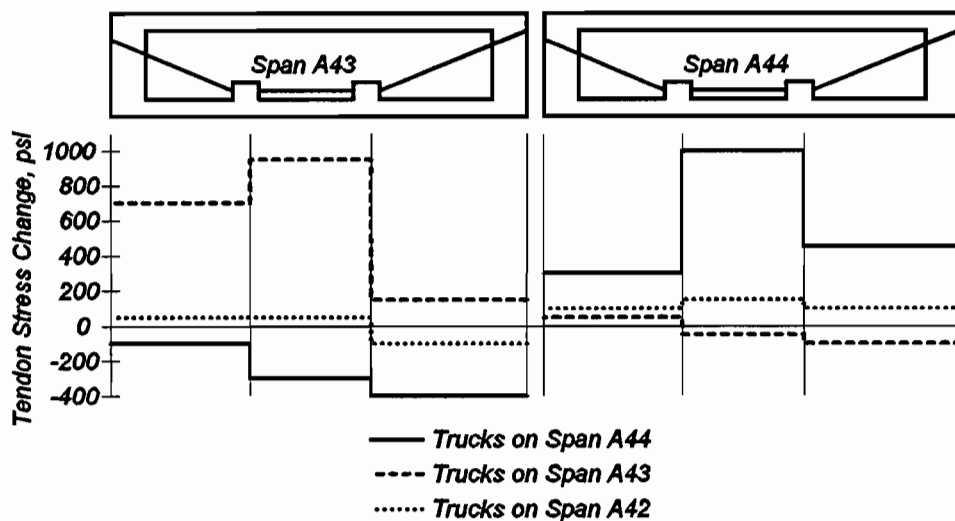


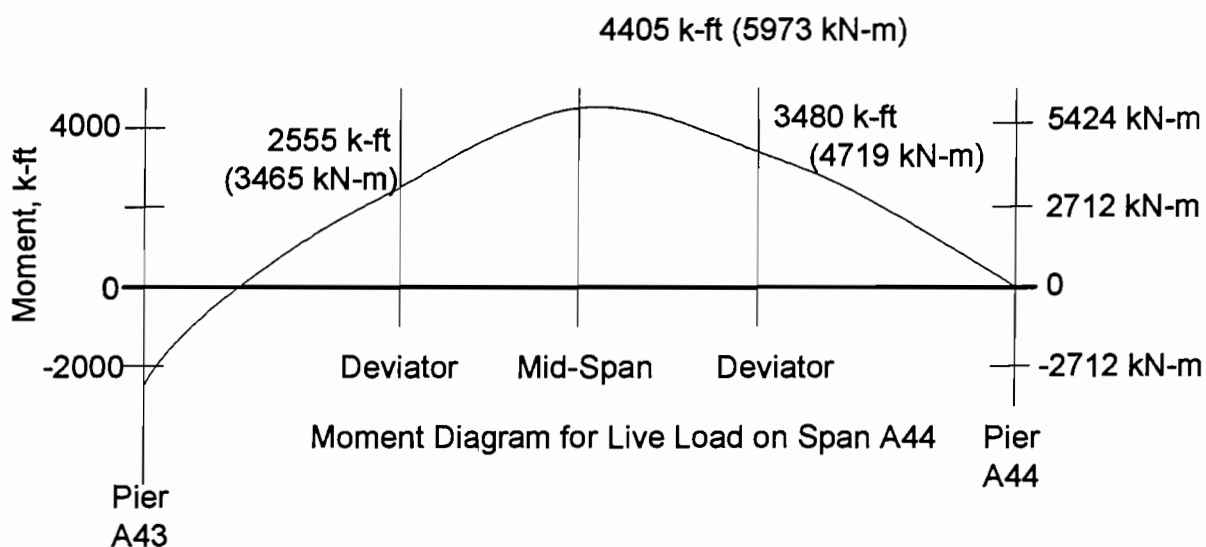
Figure 10.14c Deflections of spans A43 and A44 with live load on span A42.

Figure 10.15 shows the changes in tendon stress with the truck loads in each span. The greatest stress increase was in Span A44, with the load on A44, of 996 (6867 kPa). The very small tendon stress increases in this test and in the crane loading test indicate that fatigue should not pose a problem for external tendons. A method for calculating the stress increase in the external tendons is presented in Figure 10.16. An average moment from deviator to deviator is first calculated. Then the average strain in the concrete at the level of the tendon is determined. Calculating the stress increase in this way predicts a stress increase of 1229 psi (8474 kPa), which is 23 % higher than measured.



To convert psi to kPa multiply by 6.89.

Figure 10.15 Tendon stress changes with live loads.



$$\text{Average Moment from Deviator to Deviator} = \frac{2555 + 2 \cdot 4405 + 3408}{4}$$

(Approximating area by trapezoidal rule and dividing by length from deviator to deviator)

$$= 3711 \text{ k-ft (5032 kN-m)}$$

$$\text{Transformed Section Properties - } I = 324 \text{ ft}^4 (2.8 \text{ m}^4)$$

$$c_{g_{\text{bot}}} = 4.18 \text{ ft (1.27 m)}$$

Tendon Located 3.01 ft (0.9 m) below cg

Average Stress in Concrete at Level of Tendon-

$$\sigma = \frac{Mc}{I} = \frac{3711 \cdot 3.01}{324} = 34.5 \text{ ksf}$$

$$= 239 \text{ psi (1648 kPa)}$$

$$E_c = 5454 \text{ ksi (37605 kPa)}$$

$$E_s = 28000 \text{ ksi (193060 kPa)}$$

$$\text{Stress in Steel} = 239 \cdot 28000 / 5454 = 1229 \text{ psi (8474 kPa)}$$

Figure 10.16 Method for calculating tendon stress increase.

Figure 10.17 shows the web stress profiles at various locations along the two spans. The agreement between the measured and predicted values is erratic, but generally the readings approximate the trends of the predicted stress profiles. The agreement is somewhat better in the mid-span areas than near the piers. This could be due to discontinuities in geometry and to introduction of concentrated loads at the bearings which result in behavior near the piers which is not strictly predictable with beam theory.

The average temperature increase during the course of testing was 1.7°F (0.9°C). This temperature change could be contributing to the smaller than predicted tendon stress increases, and somewhat higher than predicted tensile stresses in the concrete. Still the effect is quite small.

Generally, these tests indicate that the bridge is behaving very predictably. The deflections, tendon stress changes, and web strain profiles are all similar to predicted values. The bridge is very stiff. Under live load plus approximately 1/4 impact (1.05LL) the bridge deflected only $\ell/6600$ for the end span and $\ell/7700$ for the interior span. These ratios compare well with a laboratory model span which showed end span deflection of $\ell/6250$ and middle span deflection of $\ell/7500$ ⁴⁴ under full live load plus impact.

10.4.2 "Poor-Boy" Continuous Unit - Span C9. Figure 10.18 shows the actual axle loads and positions when the trucks were positioned on Span C9. Also shown are the measured deflection and three calculated deflections. One deflection was calculated for a fully continuous two span unit with full transformed cross-sectional properties using the previously mentioned frame solver FRAME2D. The mesh is shown in Figure 10.19a. For the second deflection calculation, the mesh was altered, as shown in Figure 10.19b, to model the cross-sectional properties of the closure slab between the units. The third model is for a simple span, which is normally assumed in design. The measured mid-span deflection is 8% greater than the deflection calculated with full continuity, 6% smaller than that calculated with the poor-boy model, and 19% smaller than that calculated for the simple span.

Figure 10.20 shows the actual axle loads and positions when the trucks were positioned on Span C10. The figure also shows a comparison of the measured and calculated deflections. In this loading configuration, the bridge deflection was smaller than both of the calculated deflections. The reading at the quarter point closest to abutment C9 appears to be in error, although it must be noted that the span deflections are very small (less than 0.010 inch (0.25 mm) or $\ell/90,000$). In any case, the unit is behaving as a partially continuously unit and the deflections can be predicted reasonably well using the model shown in Figure 10.19b.

The readings of strain in the top slab closure pour were quite small. Figure 10.21 shows the readings with the load on Span C9 and on C10. The peak tension, based on the measured 28 day modulus of the closure pour concrete, was 124 psi (855 kPa) with the full live load on two lanes of C9, which is smaller than the predicted stress of 172 psi (1186 kPa). The measured peak stress in the closure is 62 psi (427.5 kPa) with one lane of loading on Span C10, which is also smaller than the predicted stress of 117 psi (807 kPa). The smaller than predicted tension could

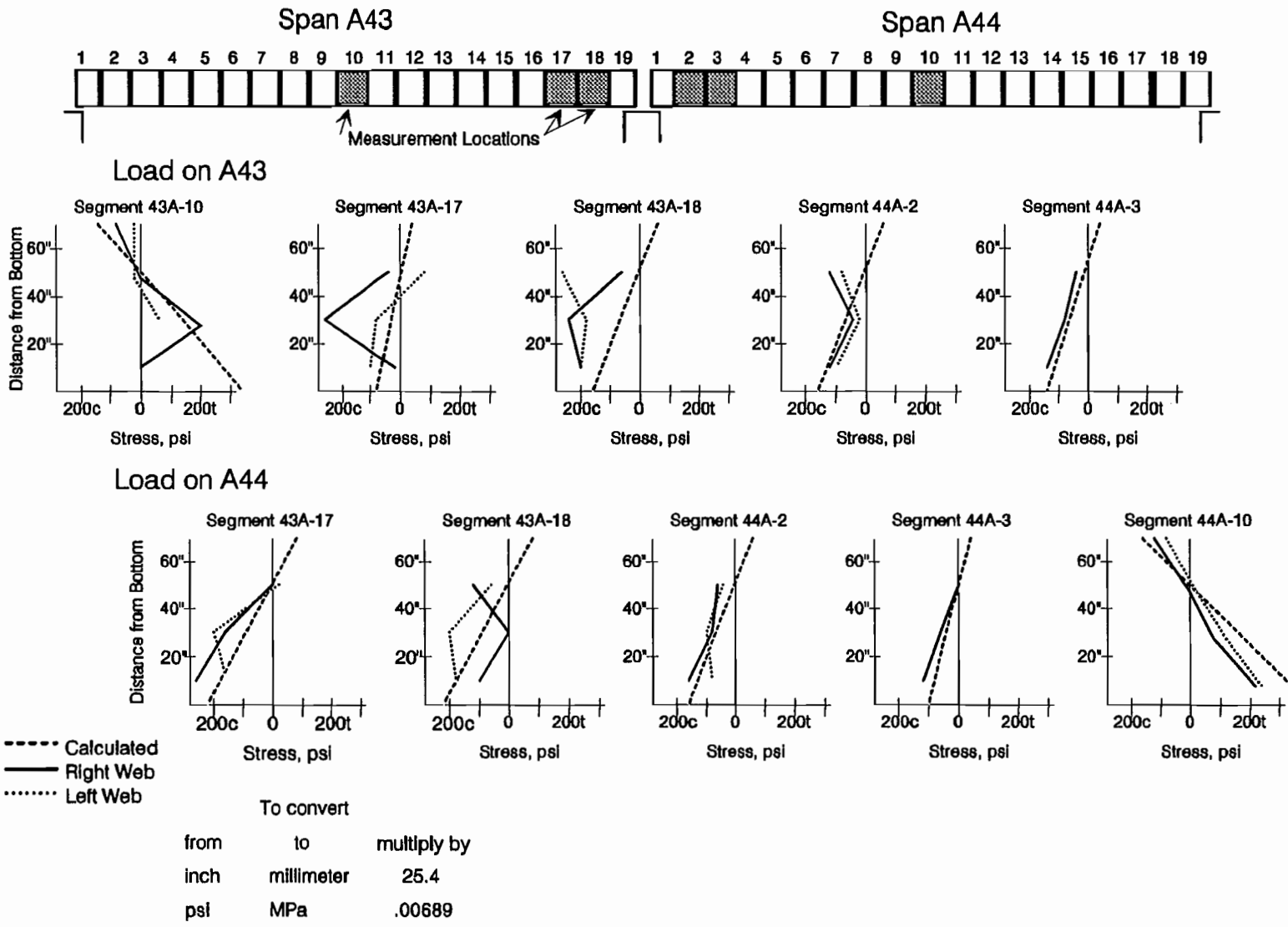


Figure 10.17 Web stresses in span A43 and A44 with live loads.

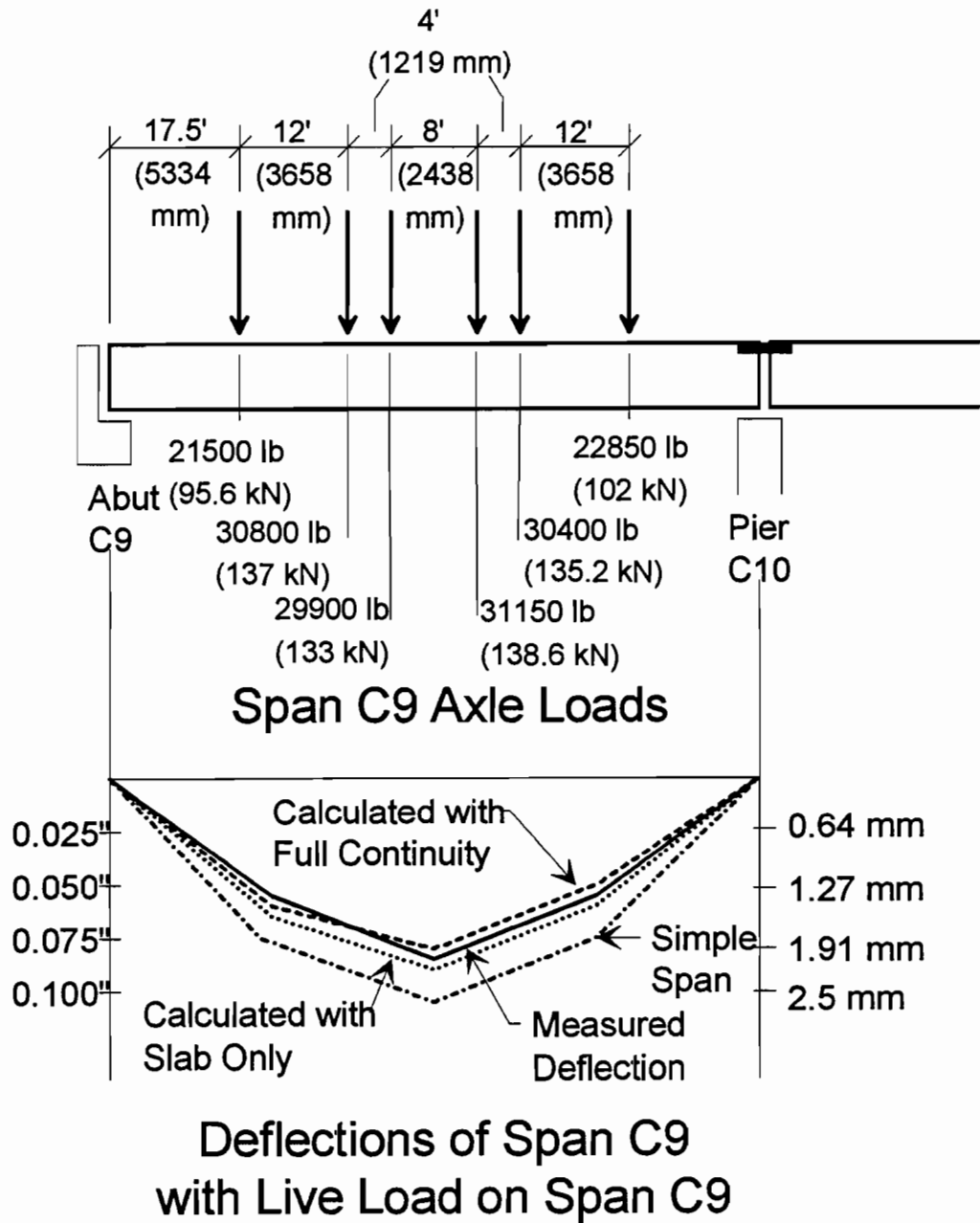
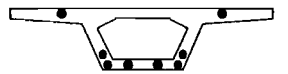
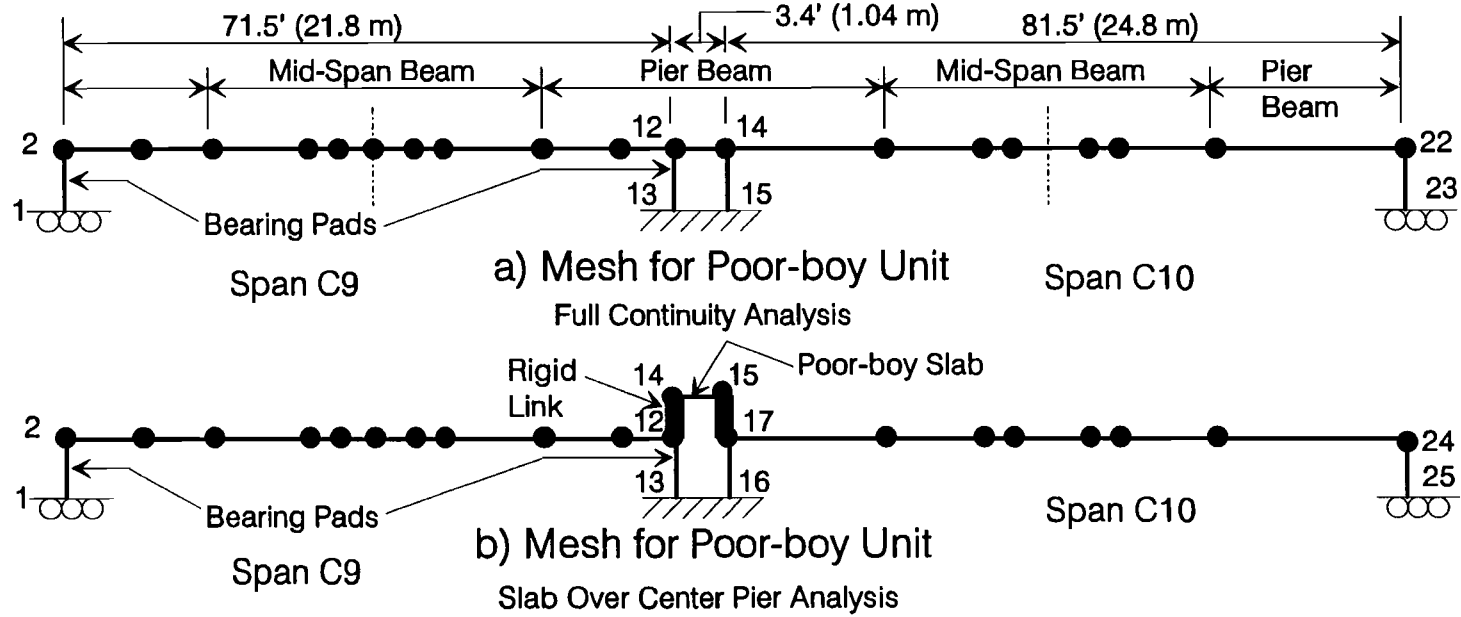
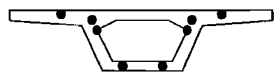


Figure 10.18 Calculated vs. actual deflections of span C9 with live load on span C9.

Figure 10.19 Mesh for use with FRAME2D²⁴ program.



Tendon Locations at Mid-Span



Tendon Locations at Pier

Element	Area, ft ² (m ²)	Moment of Inertia, ft ⁴ (m ⁴)	Modulus of Elasticity, ksf (MPa)
Mid-Span Beam	42.6 (4)	166.0 (1.43)	741168 (35489)
Pier Beam	42.6 (4)	160.2 (1.38)	741168 (35489)
Bearing Pad	3.78 (0.35)	0.56 (0.005)	2409 (115)
Rigid Connection	500 (46.5)	1000 (8.63)	741168 (35489)
Poor-boy Slab	12.0 (1.1)	0.25 (0.002)	741168 (35489)

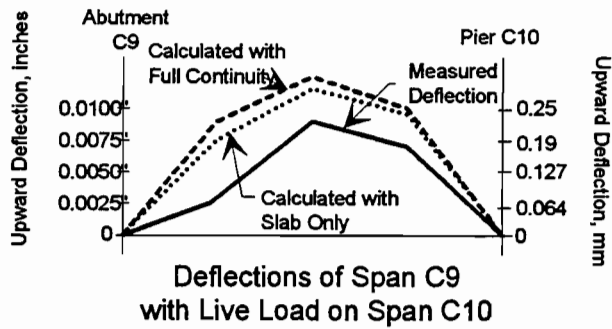
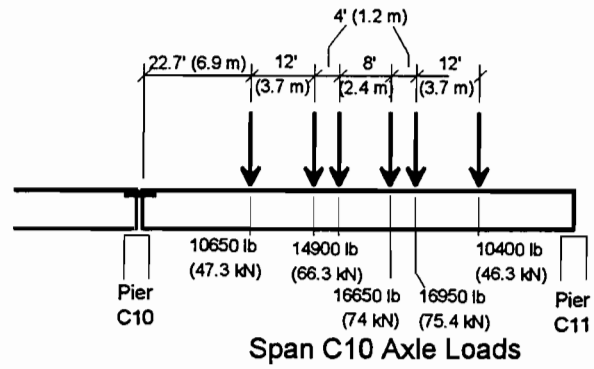


Figure 10.20 Calculated vs. actual deflections of span C9 with live load on span C10.

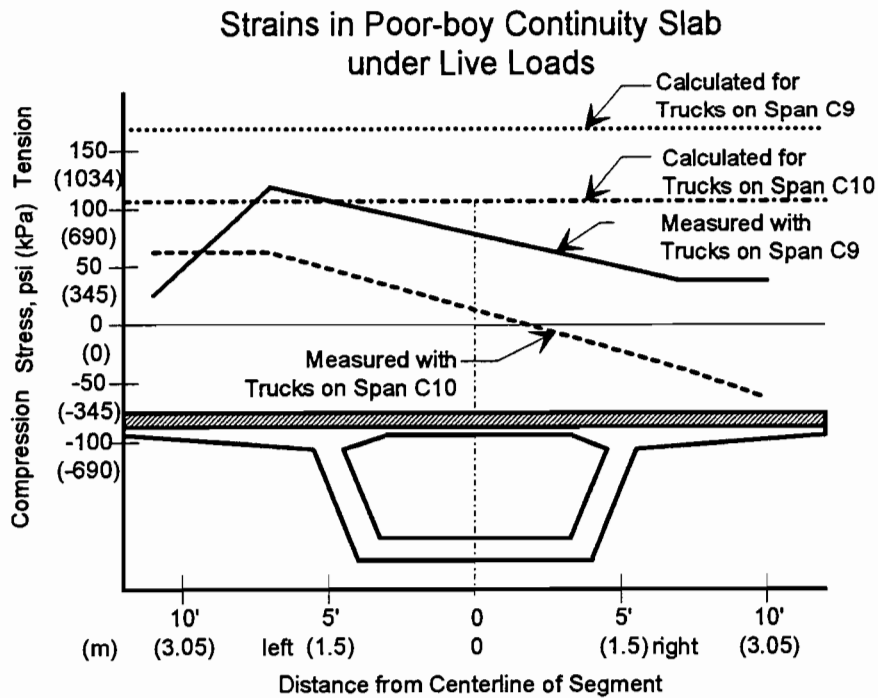


Figure 10.21 Stresses in "poor-boy" continuity slab.

be due to the fact that the model does not have as great a moment arm between the center of the slab and the bottom of the bearing pads as the actual structure.

The web strain profiles for the loading of Span C9 are shown in Figure 10.22. The agreement between measured and calculated stresses is somewhat erratic. The web strains with the load on span C10 were very small (less than $8\mu\epsilon$) and are not shown.

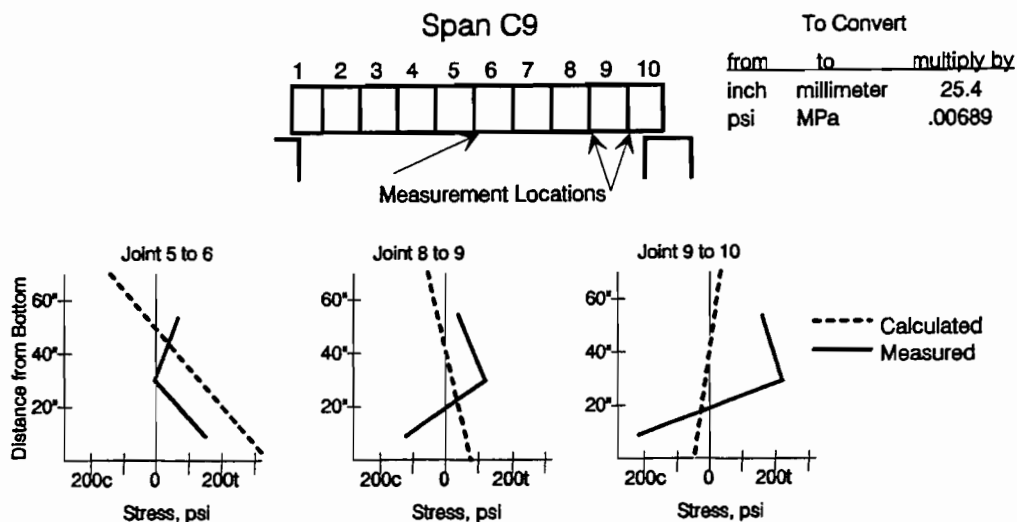


Figure 10.22 Web stresses in span C9 with live load on C9.

Generally, it can be concluded that there is continuity between the two spans in the poor-boy continuous unit. That continuity is created by a couple with tension in the top slab and friction between the fixed bearings and the bottom of the box, see Figure 10.23. It should be noted, however, that the fabric bearing pads used in this project are thin, about two inches thick, and have a high shear modulus. The same degree of continuity might not be achieved with thicker, lower shear stiffness elastomeric pads. The effect of the shearing force, generated by live loads and by creep over time, is unknown. In view of the low shear strength of the pads, future bridge inspections should check the long term performance of these pads. The tensions in the top slab are quite small and no cracking occurred under full live load. The degree of continuity can be modelled as shown in Figure 10.19b.

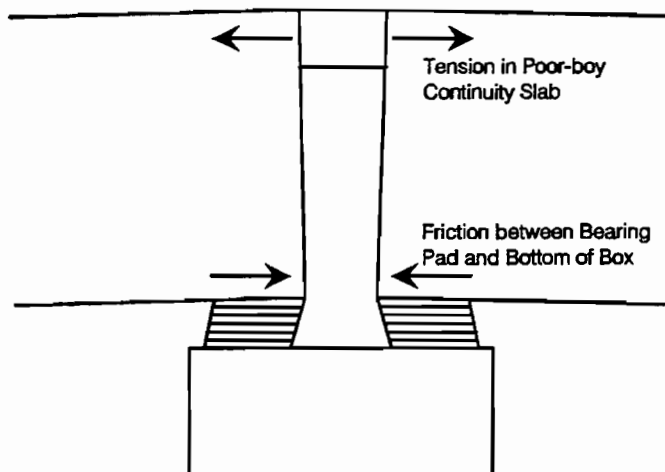


Figure 10.23 Continuity between spans C9 and C10.

10.4.3 Transverse Post-Tensioning - Span C11. Figure 10.24a shows actual axle loads and positions with the trucks on Span C11. Also shown are the measured and two calculated deflections. One deflection was calculated assuming that the span was acting independently. The two dimensional frame solver, FRAME2D, was used. The second calculated deflection was determined using a three-dimensional frame solver (FRAME3D²⁵) full-transformed cross-sectional properties for the adjacent spans, and beam elements connecting the spans at the quarter points. The connecting beams had cross-sectional properties which approximated those of the top slab from centerline of girder to centerline of girder (see Figure 10.25). With the load on Span C11, the measured deflection is 15% greater than the deflection calculated with the three dimensional model. This indicates that the connecting beams are not as stiff as expected. The measured deflection is 55% of that calculated for the independent span model.

Also shown in Figure 10.24b is the deflection of Span C11 with the truck load on the adjacent mainline span. Using the model shown in Figure 10.25, the measured deflection is 74% less than calculated. This also indicates that the connecting beams are not as stiff as those used in the model.

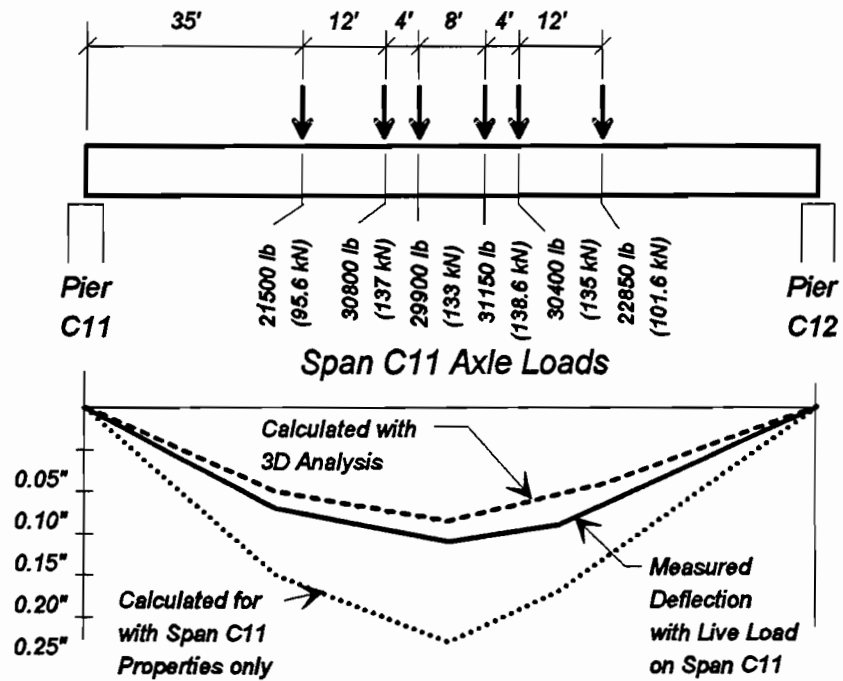
The stress changes in the tendons were quite small. Figure 10.26 shows the average changes with the live loads on Span C11 and on Span A45. The greatest change was in the middle portion of the tendon, which lies low in the cross-section, and that change was only 600 psi (4137 kPa).

Figure 10.27 shows the same method for approximating the stress change in the tendon as was used for Spans A43 and A44. An average moment, based on the Figure 10.25 model, from deviator to deviator is first calculated. Then the average strain in the concrete at the level of the tendon is determined. The measured stress increase is 81% of the calculated stress of 739 psi (5095 kPa).

The web strains were quite small. Figure 10.28 shows calculated and actual stress profiles at various locations along the bridge. There is generally good agreement, except for a few erratic readings.

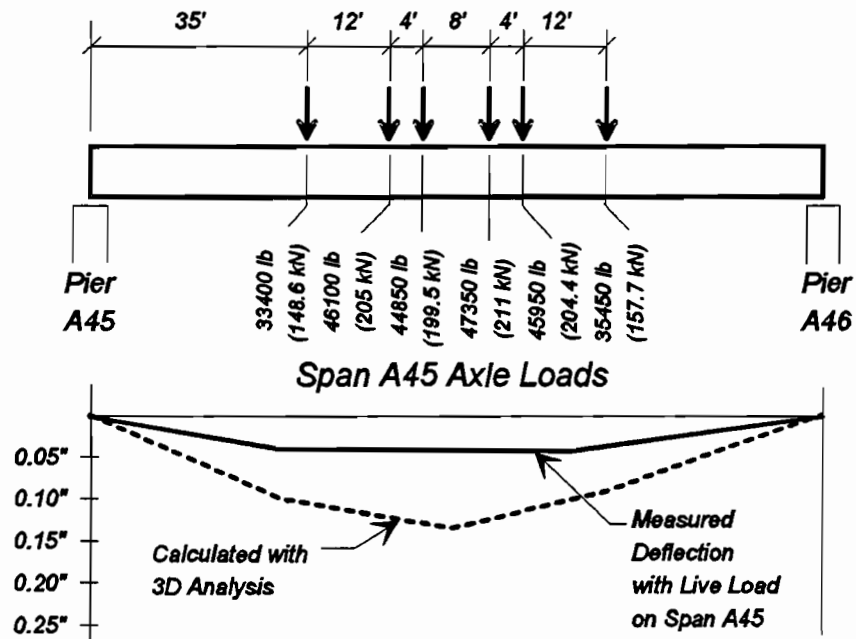
The time which elapsed during testing was slightly more than one hour and the average temperature increase in the concrete was 0.6°F (0.3°C), so temperature adjustments were not deemed necessary.

Generally, the results of the live load tests show that the parallel boxes, transversely post-tensioned together, do work together to carry loads placed on one box only. The connecting slab, however, must be experiencing some slight degree of cracking due to shrinkage of the closure slab, or previous or current loading conditions, because the interaction between adjacent boxes is less than that predicted with an analysis which used the full uncracked cross-sectional properties of the slabs between the girders. The ramp box tendon stress increases were small, only 600 psi (4137 kPa) under full live load.



a) Deflections of Span C11 with Live Load on C11

TO CONVERT		
FROM	TO	MULTIPLY BY
foot	meter	0.3048
inch	millimeter	25.4



b) Deflections of Span C11 with Live Load on A45

Figure 10.24 Calculated vs. actual deflections of span C11 with live loads.

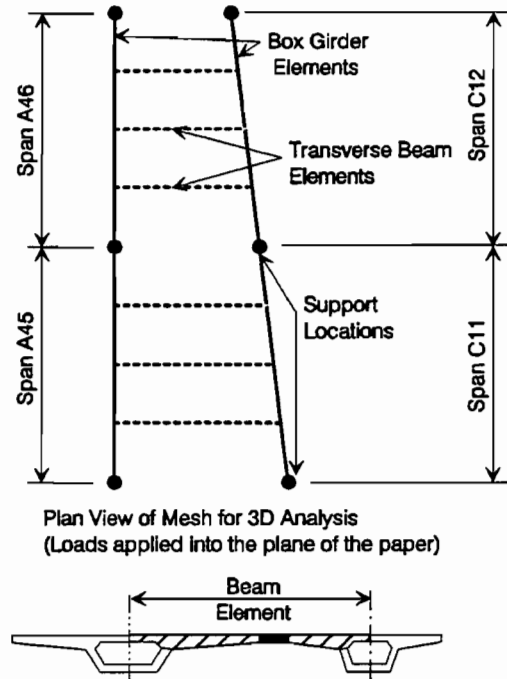
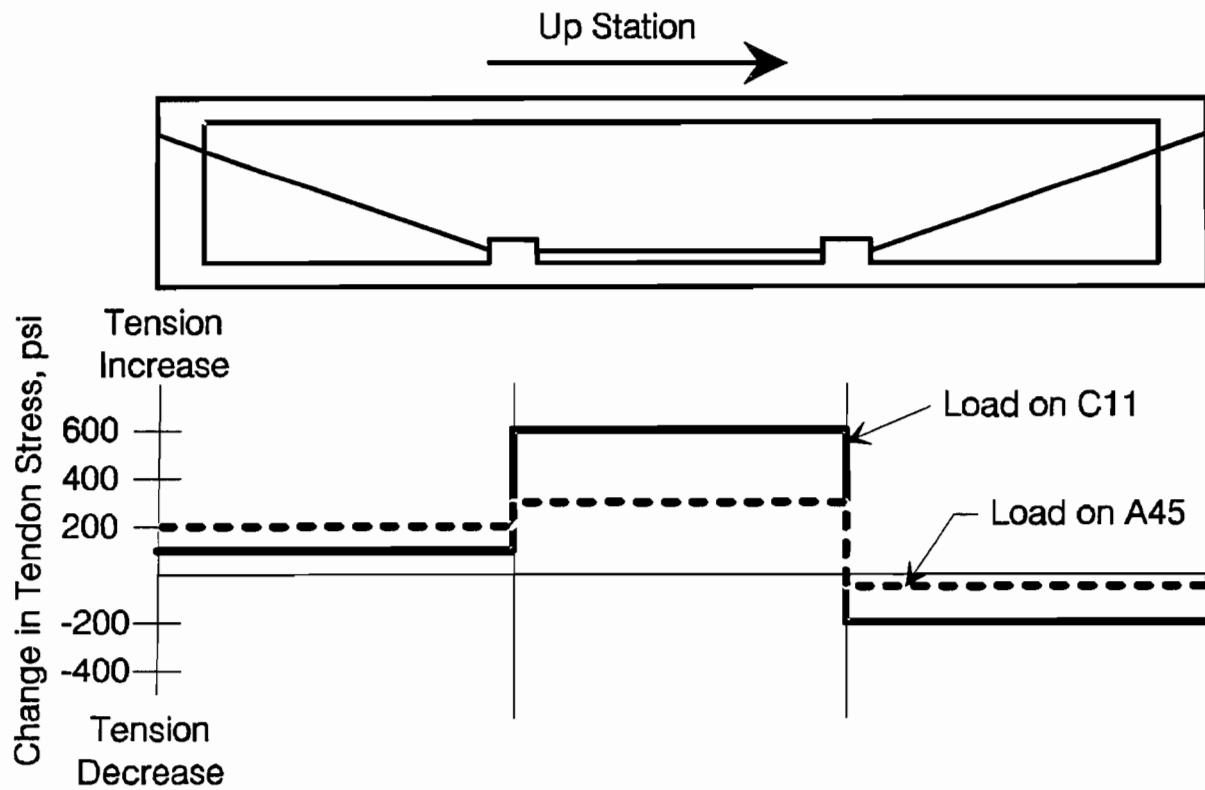
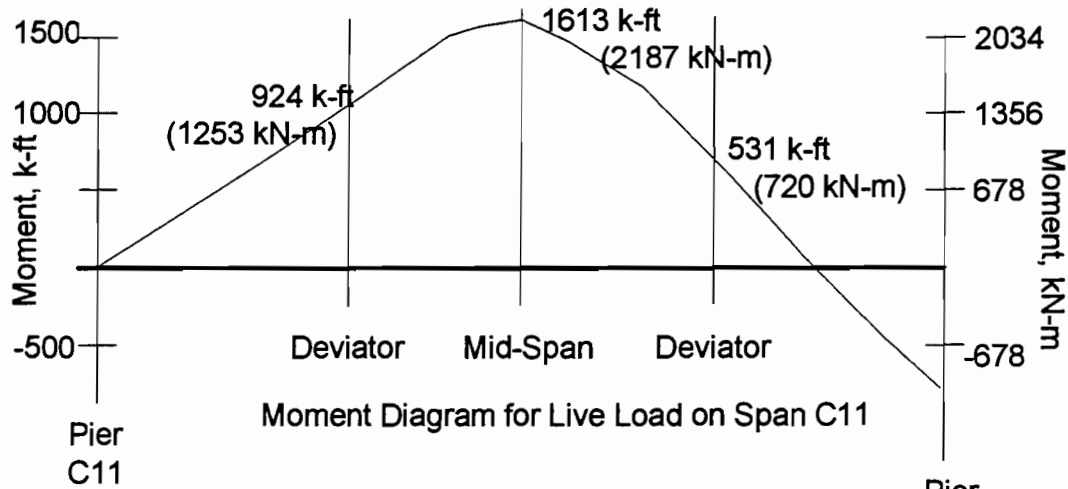


Figure 10.25 Model of spans A45 and C11.



To convert psi to kPa multiply by 6.89

Figure 10.26 Change in tendon stress in span C11 under live loads.



Average Moment from Deviator to Deviator $\frac{924 + 2 \cdot 1613 + 531}{4}$ Pier C12
 (Approximating area by trapezoidal rule and dividing by length from deviator to deviator) = 1170 k-ft (1587 kN-m)

Transformed Section Properties - $I = 170.3 \text{ ft}^4$ (1.47 m^4)
 $cg_{\text{bot}} = 3.90 \text{ ft}$ (1.2 m)

Tendon Located 2.90 ft (884 mm) below cg

Average Stress in Concrete at Level of Tendon-

$$\sigma = \frac{Mc}{I} = \frac{1170 \cdot 2.9}{170.3} = 19.9 \text{ ksf} \\ = 138 \text{ psi (952 kPa)}$$

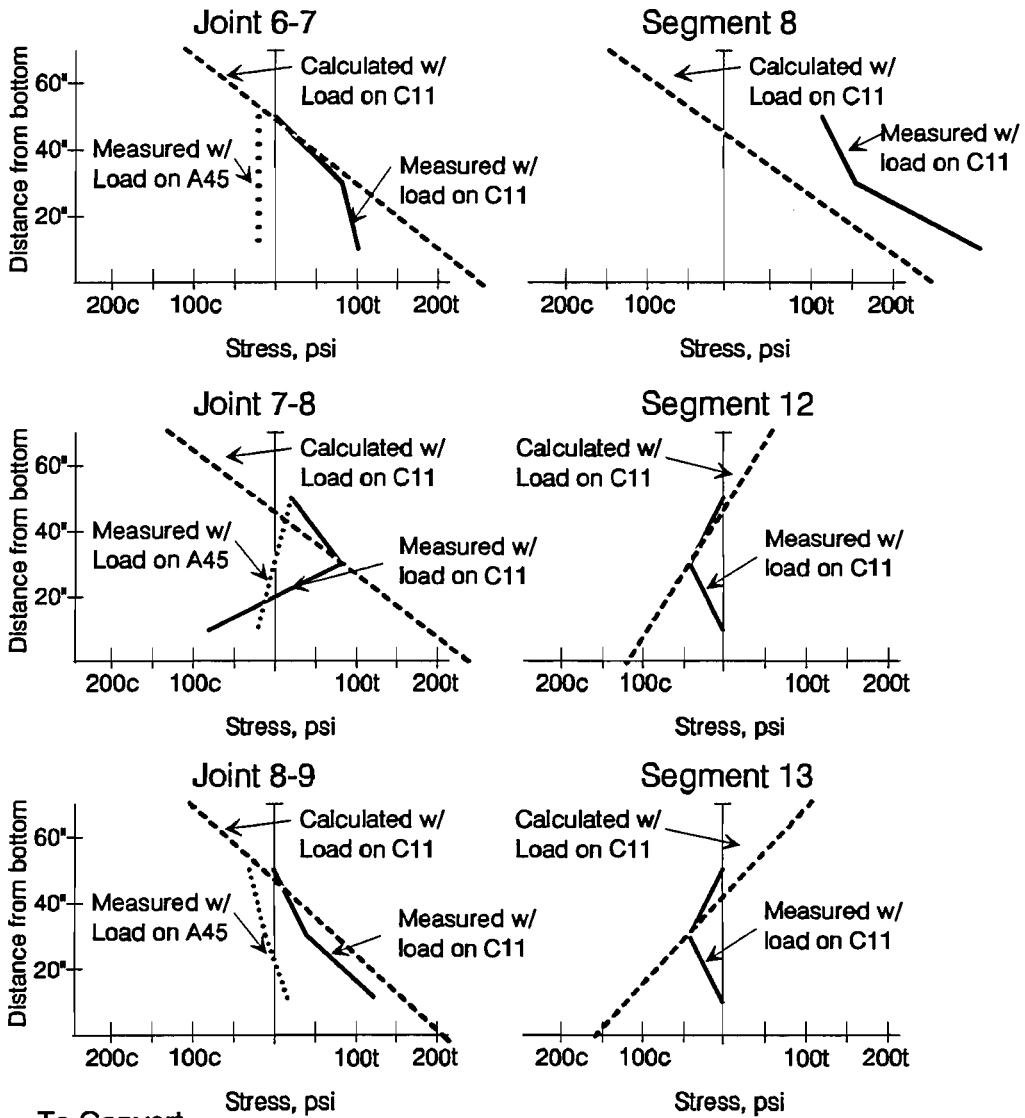
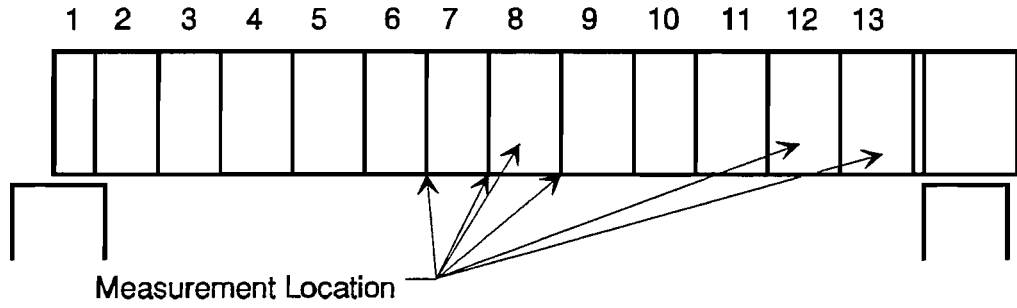
$E_c = 5243 \text{ ksi (36150 MPa)}$

$E_s = 28000 \text{ ksi (193060 MPa)}$

Stress in Steel = $138 \cdot 28000 / 5243 = 739 \text{ psi (5095 kPa)}$

Ratio of Measured to Calculated = 81%

Figure 10.27 Method for calculating tendon stress increase.



To Convert
 from inch to millimeter multiply by 25.4
 from psi to MPa multiply by 0.00689

Figure 10.28 Web stress profiles in span C11.

10.5 Recommendations

Based on these construction and live load studies, no changes are required to the *AASHTO Guide Specification* in areas concerning service load behavior. The following are general recommendations for the design of usual and unusual segmental girders.

10.5.1 Live Load Deflections. Live load deflections are best calculated assuming the full transformed cross-sectional properties of the girder including internal and external tendons.

10.5.2 External Tendon Stress Increases. The increase in external tendon stresses at service loads can be approximated by averaging the stress in the concrete, at the level of the tendon, between points of discrete bonding (deviators and diaphragms) and translating that average concrete stress to an average steel stress.

10.5.3 "Poor-boy" Continuity. The "poor-boy" continuous unit behaved as a partially continuous unit. An analysis which models the area around the "poor-boy" slab as shown in the model of Figure 10.19b gives good agreement with measured live load deflections. Assuming that the spans carry live loads as simple spans is overly conservative.

10.5.4 Transversely Post-tensioned Dual Boxes. The transversely post-tensioned spans worked together to carry truck loads. Loads were shared between the two spans but the flexibility of the wingtips prevented completely compatible deflections. A three dimensional frame analysis in which the adjacent spans are linked by beam elements at the quarter points and at mid-span will give an adequate estimate of the load distribution (see Figure 10.25). The beam elements should have properties which are similar to the slab, from centerline of girder to centerline of girder.

10.6 Conclusions

Based on the live and construction load tests, the following conclusions can be drawn:

1. The structures are extremely stiff. Under a load which caused a mid-span moment equivalent to that of the design live load plus 1/4 impact on the end span, the end span of a three span continuous unit (span lengths 110'-110'-115') (33.5m - 33.5m - 35.1 m) deflected only $\ell/6600$. With the same load placed on the middle span, the middle span deflected only $\ell/7760$.
2. The tendon stress increases were also small under live loads (<1.5 ksi (10.3 MPa)), which indicates that fatigue should not be a problem for external tendons.
3. The deflections under live loads can be predicted quite accurately using full transformed cross-sectional properties, including external tendons.

4. The "poor-boy" continuous unit displayed deflections very similar to those predicted for a fully continuous unit. A method of modelling the area around the "poor-boy" slab is presented in Figure 10.19. To design this type of unit to carry live loads as simple spans is overly conservative.
5. The dual boxes transversely post-tensioned together act together to carry loads. A three dimensional frame analysis of the adjacent boxes, linked together with discrete beam elements which model the properties of the connecting wing slabs, gives a reasonable approximation of the behavior of the unit. The connecting slabs, however, are not as stiff as the uncracked slab properties indicate.

Generally, the spans behaved very well and very predictably. No changes to the *AASHTO Guide Specification* are warranted based on these tests.

CHAPTER 11

TEMPERATURE INDUCED DEFORMATIONS IN MATCH CAST SEGMENTS

11.1 Introduction

Match casting is a common segment production method for segmental post-tensioned concrete box girder bridges. Normally the first segment of a span is cast between one fixed and one removable bulkhead (see Figure 11.1a). The subsequent pieces are cast between the fixed bulkhead and the previously cast segment acting as the removable bulkhead (see Figure 11.1b).

A problem can arise when the quite high heat of hydration of the concrete in the new segment (segment (2) in Figure 11.1c) causes a thermal gradient in the match cast segment (segment (1)). This gradient can cause a bowing of the match cast segment. The bowing which occurs before the new cast concrete has achieved its initial set becomes a permanent curvature in the new segment. The resulting segments (see Figure 11.1d) have one straight and one curved side.

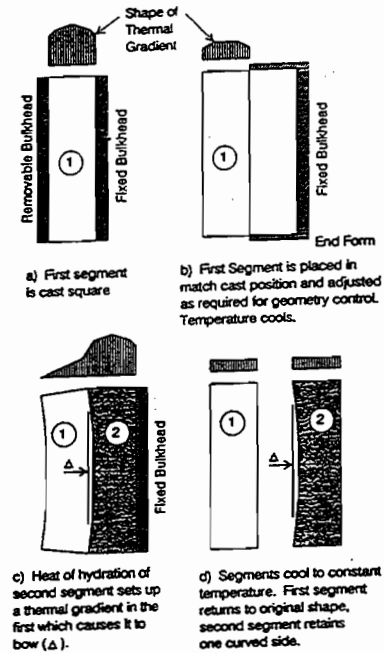


Figure 11.1 Bowing of match cast segments.

The bow shaped segments are a particular problem during the epoxy and temporary post-tensioning operations at the erection site. The size of the gap increases as each joint is closed (see Figure 11.2.). In the San Antonio "Y" Project Phase IIIA & B the contractor, Prescon,⁵⁶ reported that four consecutive joints could be closed but upon stressing to close the fifth the first joint would re-open.

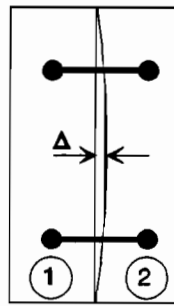
This phenomenon not only poses problems in construction but it also raises questions about stress distributions across joints and in extreme cases it could cause cracking in the segments.

This study was initiated to investigate the thermal gradients in match cast segments and measure the subsequent deformations. This chapter presents a brief summary of previous studies, a description of the current measurement program, a presentation of the results, an analysis of the collected data, and possible design or construction approaches to overcome this problem.

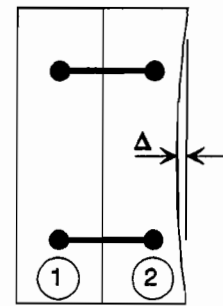
11.2 Literature Review

There is very little mention of this phenomenon in previous literature. Podolny⁵³ describes the problem and notes that it is important to enclose both the new cast and the match cast segments in an isothermal enclosure. He states that the effect is particularly significant for segments with width to length (w/L) ratios exceeding 6.

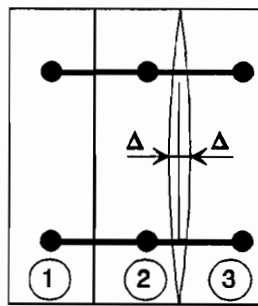
Figg and Muller Engineers²² similarly describe the problem in their "Prestressed Concrete Segmental Bridge Construction Manual". They attribute the problem to improper heating during accelerated curing used to reduce the construction cycle. They also note that the problem is of particular significance in segments with a large width to length ratio. They assert that proper curing of both segments can eliminate the problem completely.



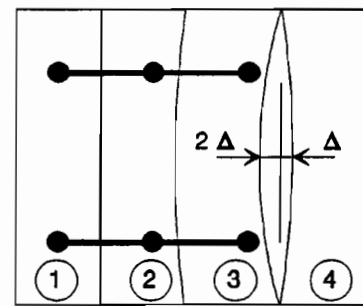
a) First two segments are dry matched



b) First two segments are epoxied and temporarily post-tensioning is applied. Segments deform to close joint.



c) Gap to be closed during second temporary post-tensioning operation is larger than first.



d) Gap size continues to increase.

Figure 11.2 Temporary post-tensioning operations.

Prescon Corporation⁵⁶ conducted a study of the bow-shaped segment phenomenon, which was causing problems in the construction of Phase IIIA & B of the San Antonio "Y" Project. The segments were very wide, 58 feet (17.7 m), and short in length, 6 feet (1.8 m) ($w/L = 9.7$). The erection crews reported gaps in joints, and difficulties in closing these gaps with the temporary post-tensioning system.

In response to this problem, Prescon placed thermocouples in eight segments being cast for one span, and measured the resulting deformations. They measured temperature induced deformations, Δ , of up to 0.12 inches (3.0 mm). An analysis based on a linear thermal gradient from the match cast face to the exposed face produced calculated deformations similar to the measured values. The maximum temperature difference recorded was 33 °F (18.3 °C).

11.3 Description of Measurement Program

In the present study, a total of four pairs of segments were instrumented with thermocouples and deformation measurement systems. Figure 11.3 shows the dimensions of the two types of instrumented segments. Two pairs of segments, 11C-4 & 5 and 11C-8 & 9, were Type I boxes with 24 foot (7.3 m) width and 8 foot (2.4 m) length ($w/L=3$). The other two pairs, 44A-5 & 6 and 44A-14 & 15, were Type III boxes with 56 foot (17.1 m) width and 6 foot (1.8 m) in length ($w/L=9.33$).

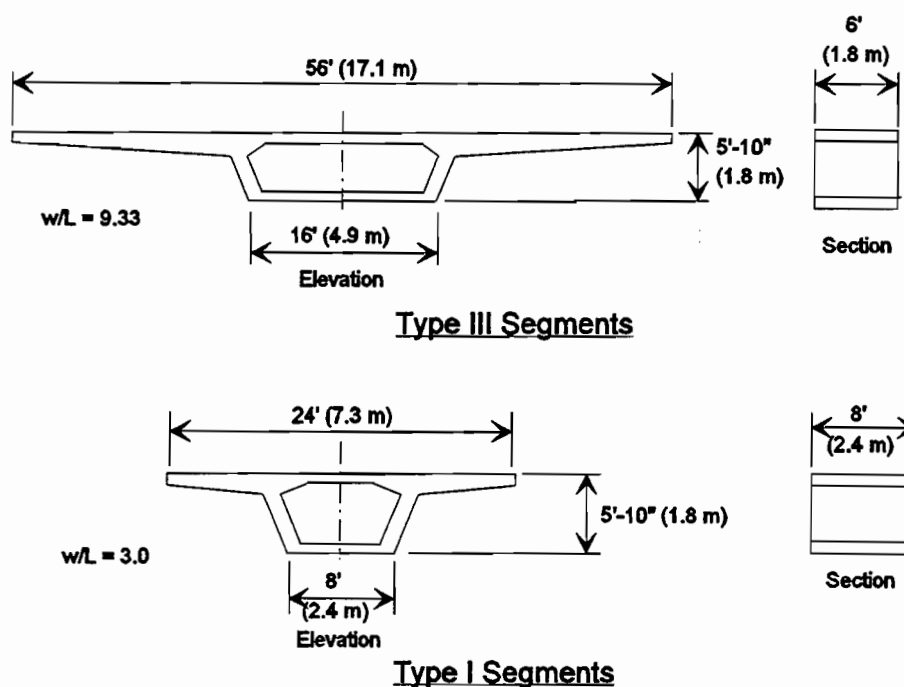
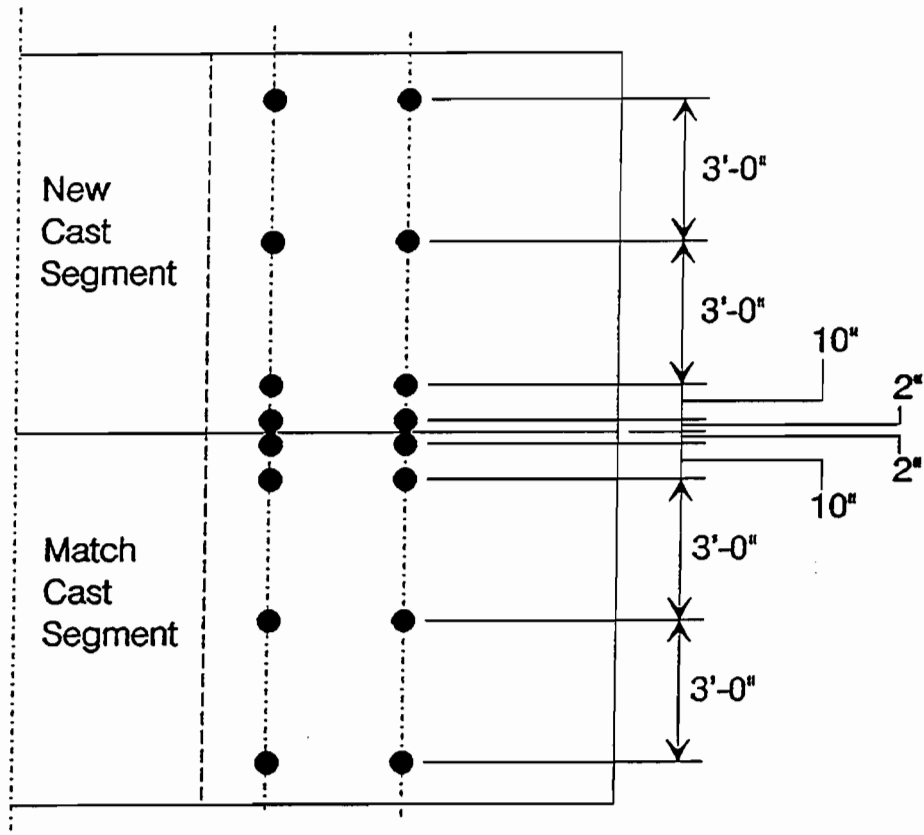


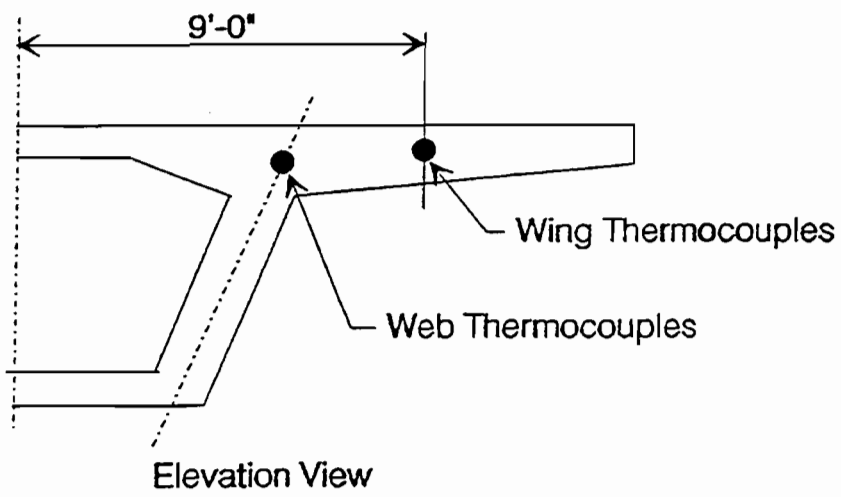
Figure 11.3 Segment types.

Two lines of eight thermocouples were placed in each pair of segments (see Figure 11.4). One line ran through the wing, while the other ran through the thickened top slab-web-wing juncture.

The deformation measurement system (see Figure 11.5) consisted of brackets at each wingtip to which a piano wire was attached. One bracket was equipped with a ratcheted spool which could pull and hold the piano wire very taut. Precision rulers and small mirrors were embedded in the match cast segment. The wire passed approximately one half inch above the rulers. Using the mirrors to ensure repeatable readings, measurements were taken at 1 hour intervals beginning immediately after the casting was completed. The temperatures were read at hourly intervals as well.



Top View of Segments



Elevation View

Figure 11.4 Typical thermocouple layout.

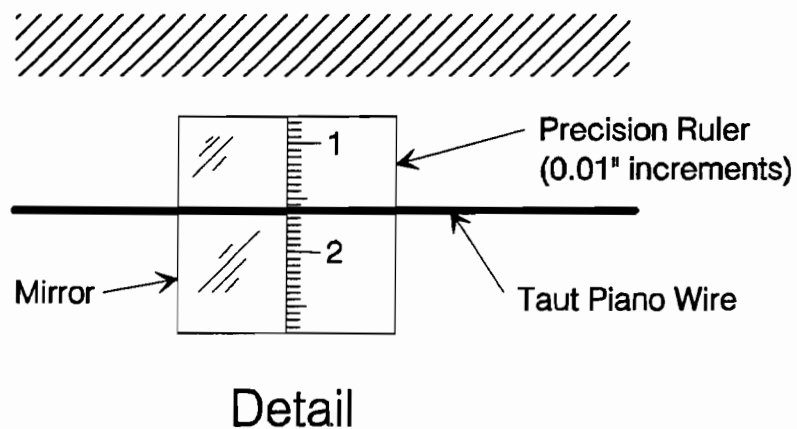


Figure 11.5 Deformation measurement system.

11.4 Results

Figure 11.6 shows a typical plot of temperatures in the new and match cast segments. Casting was completed about 11:00 A.M. but there were no appreciable differences in temperature between the 11:00 A.M. readings and the 12:00 A.M. readings shown. The match cast segment is approximately 24 hours old at the time of casting the new segment. It has achieved its highest temperatures and is cooling down. In general the temperatures are higher toward the center of the segment.

The new concrete is approximately 85 to 90 °F (29 to 32 °C) when it is placed. The new concrete closest to the match cast segment warms more quickly than the more distant new concrete. At the same time the concrete in the match cast segment closest to the new segment begins to cool more slowly than that farther away from the joint. Within 4 to 5 hours, the match cast segment edge concrete closest to the new cast concrete warms while the remainder of the match cast segment continues to cool.

The thermocouple which is closest to the open face of the match cast segment is over one foot (0.3 m) from the face of the concrete. The temperature at the free face is probably quite similar to the temperature on the new cast face (the thermocouple was 2" (51 mm) from the face of the concrete there). The significant thing to note is the total change in temperature between the time of cast and around 7 hours later. On the free face the temperature falls (cools) about 7 °F (-14 °C), while on the face adjacent to the new concrete it warms by about 25 °F (-4 °C).

Figure 11.7 shows a slightly different presentation of the same data. The temperatures taken at each measurement station immediately after the completion of casting are used as reference values and the difference between subsequent temperatures and the initial readings are plotted. These plots illustrate how the match cast concrete immediately adjacent (0 to 1 ft.) (0 to 0.3 m) to the new cast segment heats considerably as the temperature of the newly cast segment rises due to the heat of hydration. Concrete in the match cast segment more than three feet from the new segment seems unaffected and simply continues to cool. This difference is the temperature gradient which induces the bow shape.

Figure 11.8 shows the horizontal deformed shapes measured with the taut wire system. The precision rulers have graduations of 0.01 inch (0.25 mm) and the reader's maximum tolerance is considered to be ± 0.01 inch (0.25 mm). The figures indicate maximum deformations of less than 0.10 inch (2.5 mm). The deflections of the Type I boxes were no more than 0.01 inch (0.25 mm), which is the range of reader error.

The actual deformation set into the new cast segment seems to be that measured when the concrete begins its initial set. The set is usually indicated by a rapid rise in temperature. Since the concrete mix included a retarder this rapid rise usually occurred five to six hours after casting was complete. Shortly after this, a crack would appear indicating that the match cast joint was opening (see Figure 11.9). Prescon also reported similar cracks which normally appeared five to six hours after casting. These cracks indicate that the new cast segment had set but the match

cast segment continued to bow away. The critical deformation, that deformation which is set into the new segment, is that occurring approximately six hours after casting.

The match cast segments were measured for several days following casting. Over the course of three days the segments would return to their original shape.

Temperatures in Segment 44A-14 and 44A-15 Wing Temperatures

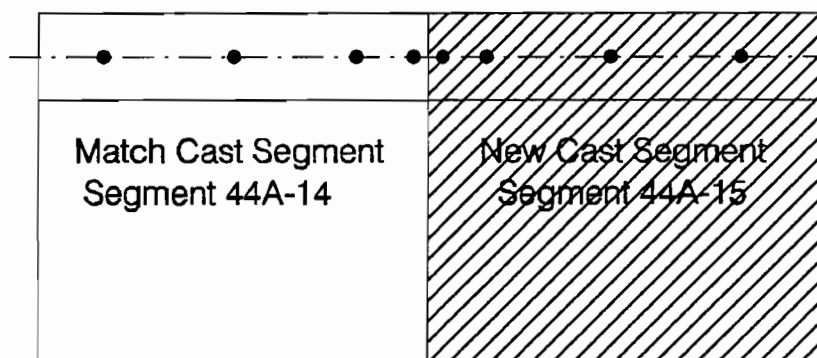
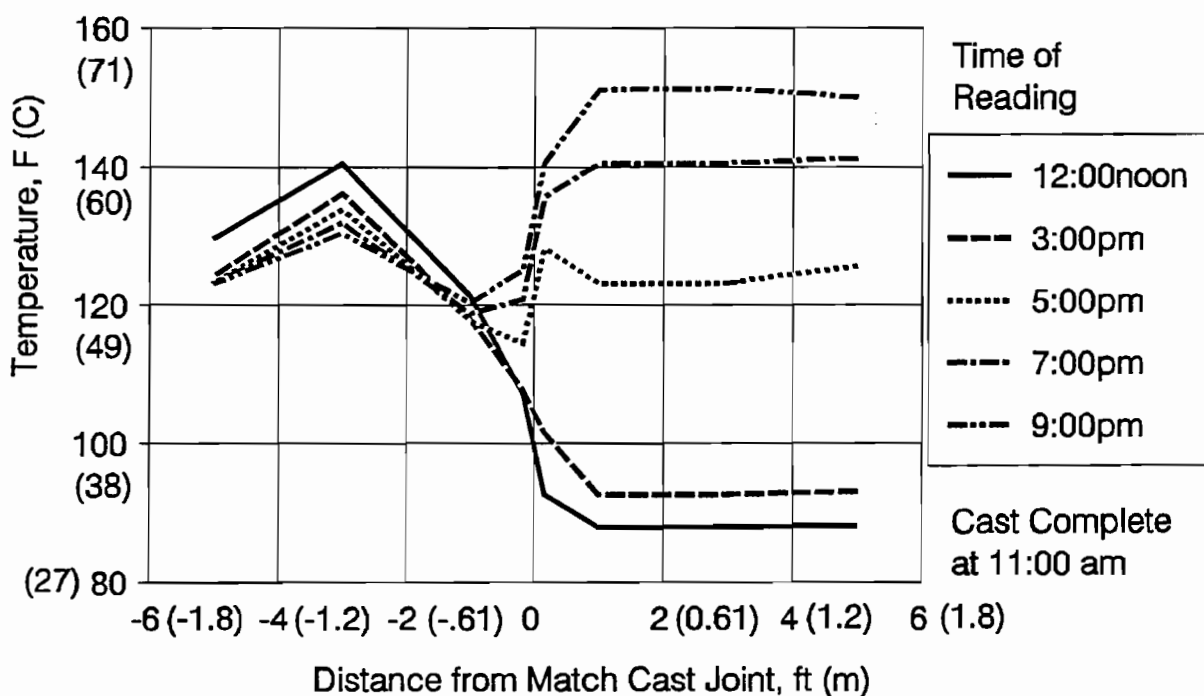
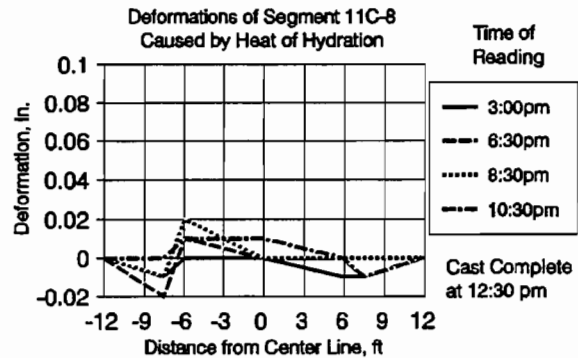
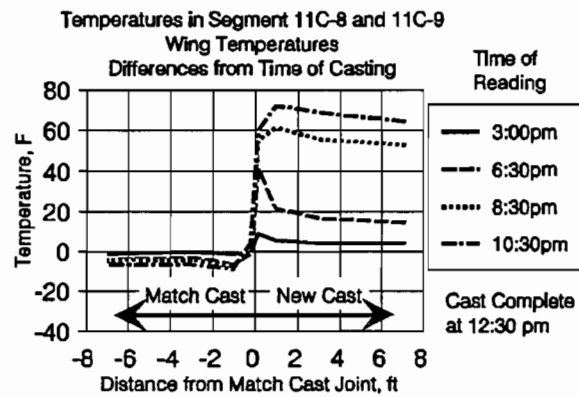
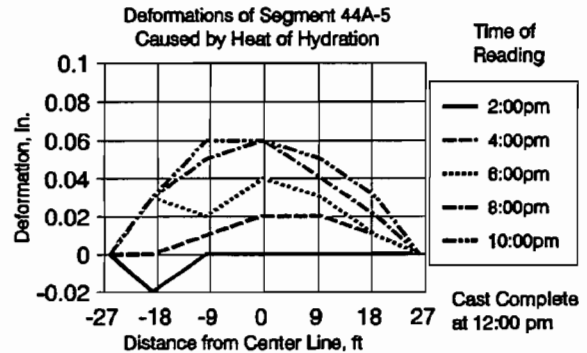
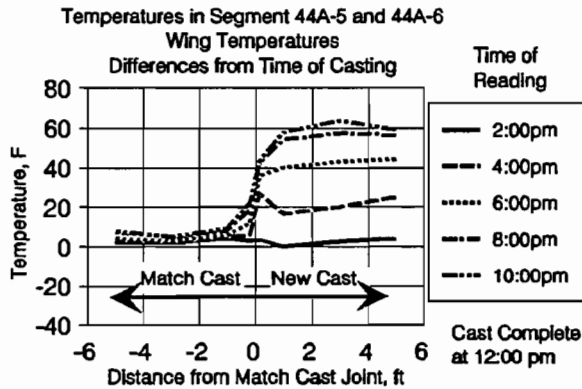
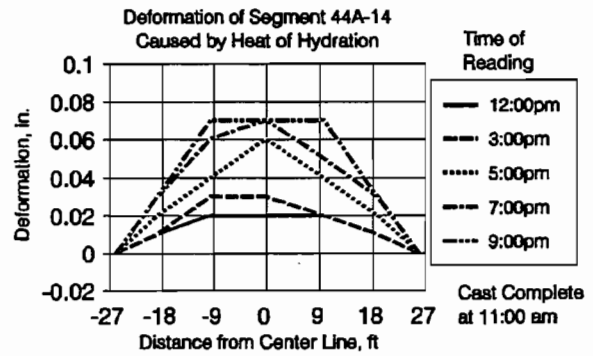
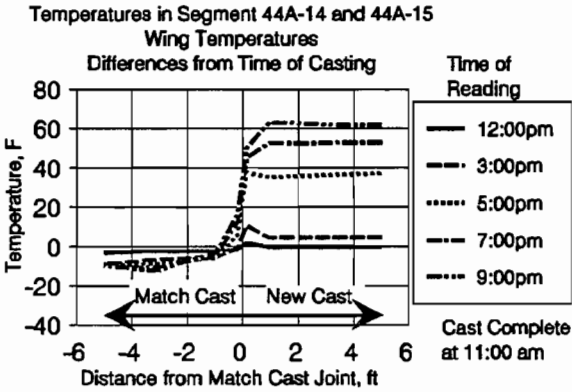


Figure 11.6 Typical temperature readings during match casting.

TO CONVERT

FROM	TO	MULTIPLY BY
foot	meter	0.3048
Fahrenheit	Celsius	$(t_F - 32) / 1.8$



Positive deformation indicates match cast segment is bowing toward new cast segment

Figure 11.7 Typical temperature differences.

Figure 11.8 Deformed shapes.

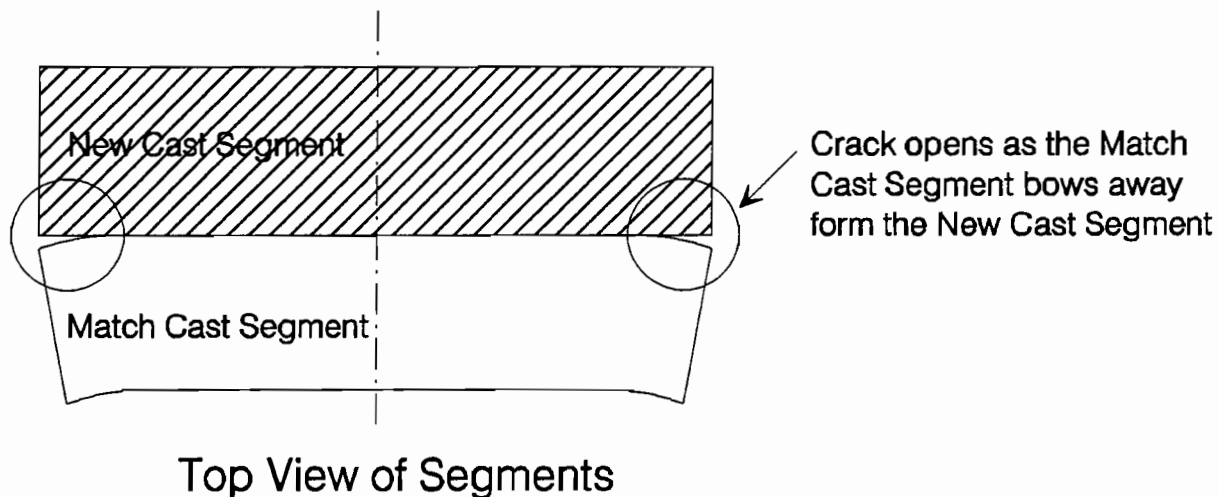


Figure 11.9 Cracks indicate joint opening.

11.5 Analysis

11.5.1 Method of Calculating Deformation. The temperatures recorded in the match cast segment in the current test and in Prescon's report⁵⁶ indicate a temperature gradient similar to that shown in Figure 11.10. A value for the maximum deflection can be calculated in the following manner:

Area 1:

$$A_1 = \alpha \left[\left(\frac{A+B}{2} \right) 3' + \left(\frac{B+C}{2} \right) 9' + \left(\frac{C}{2} \right) 24' \right]$$

α = Thermal coefficient of concrete ($\sim 6 \times 10^{-6}/^{\circ}\text{F}$) ($\sim 10.8 \times 10^{-6}/^{\circ}\text{C}$).

Area 2:

$$A_2 = \alpha \left(\frac{D}{2} \times 12' \right)$$

Center of Gravity of Area 1 (measured from the match cast face):

$$cg_1 = \frac{[(A+B) \cdot 5 \cdot 3' \cdot 1' + B \cdot 3' \cdot 1.5' + (B-C) \cdot 5 \cdot 9' \cdot 6' + C \cdot 9' \cdot 7.5' + C \cdot 5 \cdot 24' \cdot 20']}{A_1}$$

Center of Gravity of Area 2 (measured from the free face):

$$cg_2 = 4'' \text{ (102 mm)}.$$

Equivalent Moment Applied to Section:

$$M = A_1 b E \left(\frac{d}{2} - c_{g1} \right) - A_2 b E \left(\frac{d}{2} - c_{g2} \right)$$

b = depth of section,
 d = length of segment,
 E = Modulus of elasticity of concrete.

Moment of Inertia of Any Section:

$$I = \frac{1}{12} b d^3$$

Curvature of Segment:

$$\phi = \frac{M}{EI} \frac{bEA_1 \left(\frac{d}{2} - c_{g1} \right) - bEA_2 \left(\frac{d}{2} - c_{g2} \right)}{\frac{1}{12} b d^3 E}$$

$$\phi = \frac{12}{d^3} [A_1 \left(\frac{d}{2} - c_{g1} \right) - A_2 \left(\frac{d}{2} - c_{g2} \right)]$$

Maximum Deflection:

$$\Delta = \frac{\phi l^2}{8} = \frac{3l^2}{2d^3} [A_1 \left(\frac{d}{2} - c_{g1} \right) - A_2 \left(\frac{d}{2} - c_{g2} \right)]$$

l = width of segment (wingtip to wingtip).

11.5.2 Calculated Deformations. Using this method, the values of maximum deflection can be calculated. Tables 11.1 through 11.3 give the variables, l, d, α, A, B, C & D, the

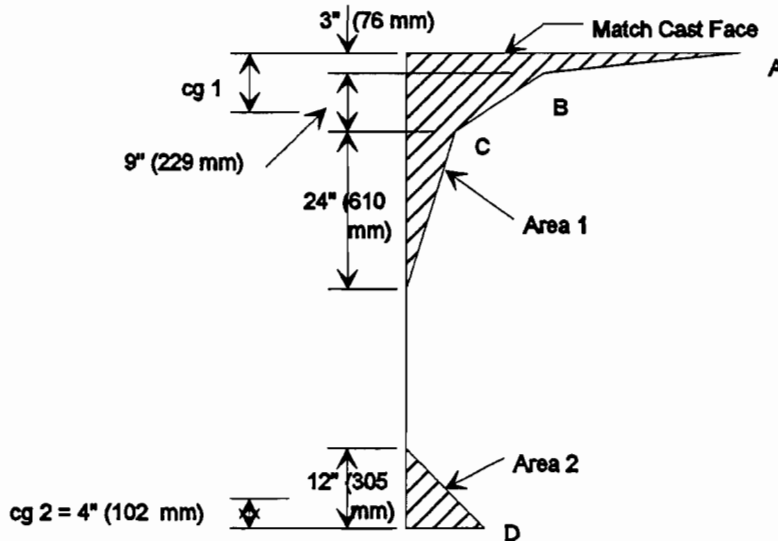


Figure 11.10 Thermal gradient in match cast segment.

calculated deflections and the measured deflections at various times for the segments in this and Prescon's study. Figure 11.11 graphically illustrates the accuracy of the calculation method for two of the segments of the current project.

Observations from these charts are:

1. The deformations calculated based on the temperature gradients measured in the wings best match the actual deflections.
2. The temperature "D" on the free face of the segment was:
 - a. Normally cooler than the center of the segment in Prescon's segments which were cast late in the day in mid-April.
 - b. Approximately zero in the 11C segments which were cast in June at approximately noon with the free face facing south .
 - c. Normally a few degrees warmer in the 44A segments which were cast in August at approximately noon with the free face facing west.
3. Cracking occurred between 4 and 6 hours after casting was completed.

Figure 11.12 shows the ratio of the measured deflection and the calculated deflection at the time of cracking. The calculated values are based on the gradients measured in the wingtips. With the exception of Segment 18E-4, the calculated values agree quite well with the measured deflections.

11.6 Erection Observations

During erection operations some of the effects of the bow shaped segment phenomenon were observed. An indication of a uniformly compressed joint is a bead of squeezed out epoxy along the entire width of the joint. Twenty-two spans were surveyed to assess the quality of the joints. On average the spans had a total of 17 joints. Of the 17 joints , an average of 10 joints per span showed signs of even squeeze out along the entire width. An average of four joints per span showed gapping in the joint of up to 1/8" (3.2 mm). The remaining joints were difficult to categorize, usually showing neither squeeze out nor gapping.

On the majority of the gapped joints the gap would appear for 8 to 10 feet (2.4 to 3.0 m) on each side of the centerline of the box. Near the wing tips the joint would show signs of good squeeze out. This is consistent with the expected behavior of a banana or bow shaped segment.

Table 11.1 Calculated and Measured Deformations Current Project Segments

Segment and Time	Wingtip Width, w, in.	Segment Length, L, in	Thermal Coeff.	Gradient Values, Degrees Fahrenheit				Calc. Deflect., in	Meas. Deflect., in.
				A	B	C	D		
Segment 44A-5 Web Thermocouples									
2 hours	672.0	70.7	6E-6	3.5	1.3	2.3	-1.0	0.015	0.00
4 hours				10.3	3.5	3.5	2.1	0.021	0.02
6 hours*				21.9	4.4	4.4	3.1	0.040	0.04
8 hours				30.5	5.9	5.9	4.6	0.064	0.06
10 hours				35.4	8.1	8.1	5.5	0.084	0.06
17 hours				48.0	15.7	15.7	-4.0	0.161	0.09
Segment 44A-5 Wing Thermocouples									
2 hours	672.0	70.7	6E-6	1.5	1.1	2.2	0.6	0.010	0.00
4 hours				13.8	3.3	2.6	0.6	0.023	0.02
6 hours*				17.5	10.6	2.4	1.1	0.039	0.04
8 hours				25.9	13.7	3.2	2.2	0.050	0.06
10 hours				28.4	17.3	4.4	2.9	0.062	0.06
17 hours				29.9	20.8	8.7	0.8	0.090	0.09
Segment 44A-14 Web Thermocouples									
2 hours	672.0	70.7	6E-6	4.7	2.4	-0.1	-1.9	0.012	0.03
4 hours*				17.4	6.3	0.2	-2.2	0.029	0.03
6 hours				26.9	11.4	0.8	-0.9	0.045	0.06
8 hours				39.1	22.7	5.8	0.8	0.089	0.07
10 hours				43.4	25.8	4.7	0.3	0.095	0.07
Segment 44A-14 Wing Thermocouples									
2 hours	672.0	70.7	6E-6	4.7	2.0	1.1	-1.9	0.011	0.03
4 hours*				11.3	5.4	0.8	-2.3	0.026	0.03
6 hours				30.3	14.4	2.7	-1.0	0.060	0.06
8 hours				35.2	18.9	4.1	-0.4	0.076	0.07
10 hours				45.4	28.6	8.9	2.4	0.113	0.07
Segments 11C-4 and 11C-8 Web Thermocouples									
4 - 15 hr	288.0	100.5	6E-6	52.3	35.1	9.5	-0.2	0.014	0.01
8-16 hr				47.9	23.9	4.9	0.5	0.009	0.01
Segments 11C-4 and 11C-8 Wing Thermocouples									
4-6 hr*	288.0	100.5	6E-6	21.4	9.7	1.3	3.0	0.003	0.00
8-6 hr*				16.3	16.3	-1.3	0.5	0.001	0.00
8-16 hr				44.3	44.3	6.7	0.5	0.011	0.01

*Indicated time of wing crack opening

To Convert
in. X 2.54 = mm
 $t_c = (t_p - 32) / 1.8$

Table 11.2 Calculated and Measured Deformations Prescon Project Segments

Segment and Time	Wingtip Width, w, in.	Segment Length, L, in	Thermal Coeff.	Gradient Values, Degrees Fahrenheit				Calc. Deflect., in	Meas. Deflect., in.
				A	B	C	D		
Segment 18E-1 Top Slab Thermocouples									
6 hours*	708.0	72.0	6E-6	14.0	11.5	1.5	-4.0	0.050	0.04
9 hours				19.8	17.0	2.0	-4.5	0.069	0.06
11 hours				24.8	22.0	2.5	-6.5	0.090	0.10
Segment 18E-1 Wing Thermocouples									
6 hours*	708.0	72.0	6E-6	10.5	7.5	1.5	-8.0	0.048	0.04
9 hours				28.0	15.5	3.0	-7.5	0.081	0.06
11 hours				37.8	21.5	3.5	-7.5	0.103	0.10
Segment 18E-2 Top Slab Thermocouples									
4 hours*	708.0	72.0	6E-6	-1.5	-3.0	1.0	-8.0	0.015	0.04
5 hours				6.0	1.0	1.0	-14.0	0.042	0.06
11 hours				21.5	15.0	2.0	-25.0	0.113	0.12
Segment 18E-2 Wing Thermocouples									
4 hours*	708.0	72.0	6E-6	9.5	8.0	1.0	-1.0	0.030	0.04
5 hours				14.5	15.0	3.0	-3.0	0.061	0.06
11 hours				53.0	41.0	13.0	-13.0	0.205	0.12
Segment 18E-4 Top Slab Thermocouples									
5 hours*	708.0	72.0	6E-6	27.0	22.5	8.0	-3.5	0.106	0.04
7 hours				41.3	29.0	13.0	-4.0	0.150	0.10
10 hours				52.5	35.0	18.5	-7.0	0.198	0.12
Segments 18E-4 Wing Thermocouples									
5 hours*	708.0	72.0	6E-6	17.5	13.0	1.0	-13.0	0.074	0.04
7 hours				25.5	19.0	2.0	-14.0	0.099	0.10
10 hours				33.3	24.5	3.0	-15.0	0.122	0.12

*Indicated time of wing crack opening

To Convert
in. X 2.54 = mm
 $t_c = (t_p - 32) / 1.8$

Table 11.3 Calculated and Measured Deformations Prescon Project Segments

Segment and Time	Wingtip Width, w, in.	Segment Length, L, in.	Thermal Coeff.	Gradient Values, Degrees Fahrenheit				Calc. Deflect., in.	Meas. Deflect., in.
				A	B	C	D		
Segment 18E-5 Top Slab Thermocouples									
5 hours*	708.0	72.0	6E-6	24.8	22.5	4.0	-11.0	0.107	0.03
9 hours				31.5	29.0	3.5	-18.5	0.141	0.08
11 hours				35.0	32.5	4.0	-18.0	0.152	0.12
Segment 18E-5 Wing Thermocouples									
5 hours*	708.0	72.0	6E-6	8.0	2.5	0.5	-9.5	0.035	0.03
9 hours				36.5	15.0	2.5	-15.5	0.102	0.08
11 hours				44.5	20.0	3.5	-14.5	0.120	0.12
Segment 18E-7 Top Slab Thermocouples									
3 hours	708.0	72.0	6E-6	4.5	2.0	1.0	-3.0	0.018	0.02
5 hours*				20.5	17.0	2.0	-1.0	0.061	0.08
7 hours				34.0	23.0	5.0	3.0	0.085	0.08
Segment 18E-7 Wing Thermocouples									
3 hours	708.0	72.0	6E-6	8.5	5.0	2.0	1.0	0.022	0.02
5 hours*				21.0	13.0	8.0	3.0	0.066	0.08
7 hours				32.0	21.0	4.0	7.0	0.066	0.08
Segment 18E-8 Top Slab Thermocouples									
5 hours*	708.0	72.0	6E-6	4.0	1.0	0.0	-8.0	0.023	0.04
7 hours				12.0	6.0	0.0	-16.0	0.058	0.10
9 hours				15.5	9.0	0.0	-18.0	0.072	0.08
Segments 18E-8 Wing Thermocouples									
5 hours*	708.0	72.0	6E-6	10.0	3.0	0.0	-13.0	0.043	0.06
7 hours				21.0	13.0	2.0	-19.0	0.094	0.10
9 hours				27.0	18.0	3.0	-21.0	0.118	0.08

*Indicated time of wing crack opening

To Convert
in. X 2.54 = mm
 $t_c = (t_r - 32) / 1.8$

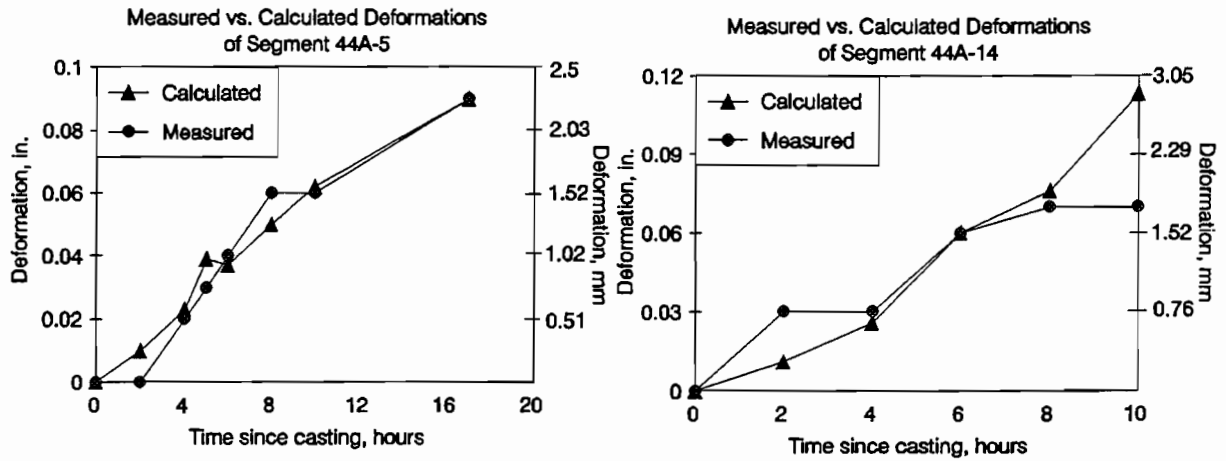


Figure 11.11 Comparison of measured and calculated deformations.

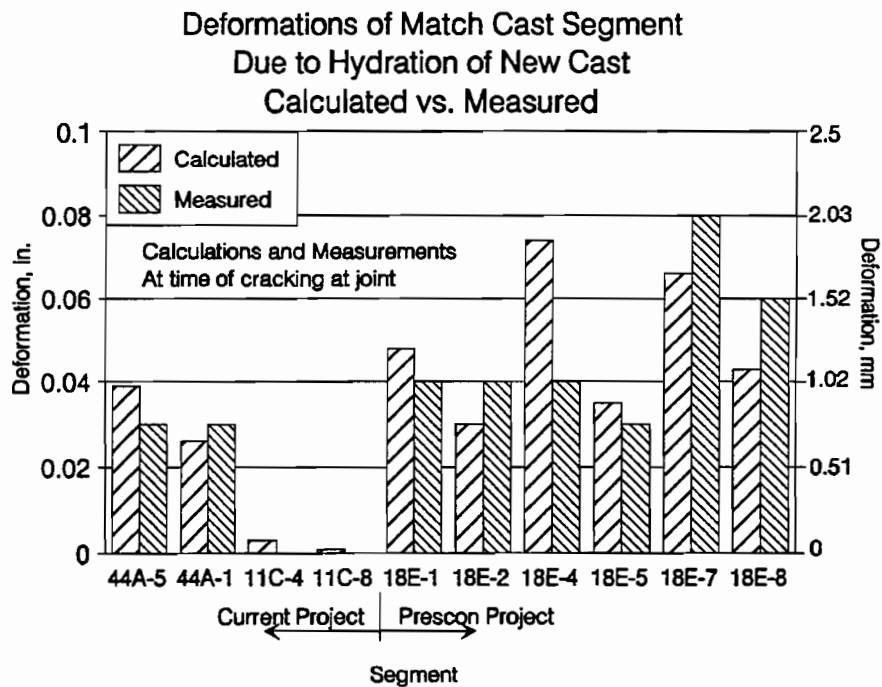


Figure 11.12 Calculated vs. measured segment deformations at time of wingtip crack opening.

One detrimental aspect of the gapped joints was a reduced closure pour size. A closure pour is placed over each typical pier, and is designed to be 12" (305 mm) long. The average measured length of the closure pours was 9.2" (234 mm). This caused problems in forming the joint and in installing dead end tendon anchors in the joint.

The extra span length of 2.8" (71 mm) per span equates to an average joint thickness of around 1/8" (3 mm). This indicates that even if a joint appeared to have good, even epoxy squeeze out, the joint was probably thicker than expected. Where small closure pours are incorporated into design, the expected thickness of the epoxy joints should be considered during casting operations.

This project could be considered as a reference point in determining the limits of allowable bow-shaped deformations. The Prescon segments had bow shapes which were definitely detrimental to the construction process. The current project had bow shapes, of the wide segments, which were somewhat detrimental to the construction process. The w/L ratios were 9.8 and 9.3 respectively. The w/L ratio of the narrow segment of the current project was 3.0, and there were no significant construction problems related to the joints on these segments. It can be concluded from the Prescon study and the current study that a job with segments with a w/L ratio of 9 or more, subjected to thermal gradients similar to those measured in this study, could experience construction problems. The suggestion of Podolny, that segments with w/L ratio greater than 6 require special attention during casting, is probably prudent.

11.7 Recommendations

11.7.1 Recommended Design Gradient. Based on this study and Prescon's, a design gradient can be proposed for climates similar to that of San Antonio. Figure 11.13 shows the wing gradients in 7 segments at the time of the appearance of the wingtip crack. The 7 curves are similar in shape on the side closest to the match cast joint. On the free edge the Prescon segments were considerably cooler than those of the present study due to seasonal climate variations. Figure 11.14 shows a design gradient based on these segments.

Temperature Gradients in Match Cast Segments at Time of Initial Set of New Cast

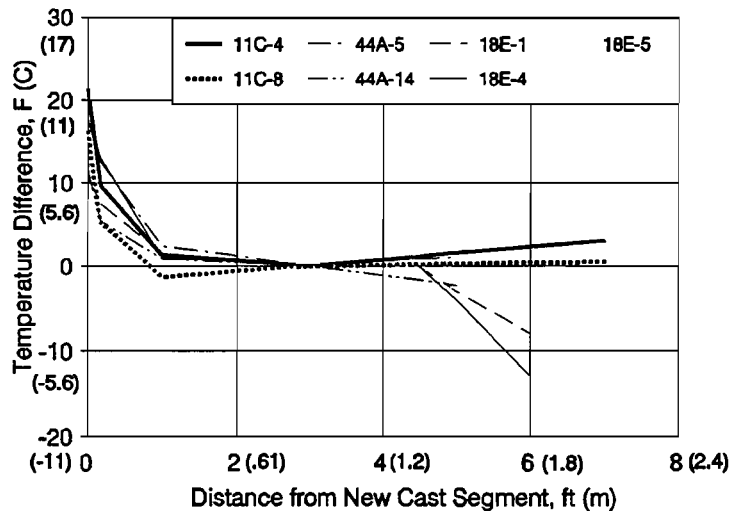


Figure 11.13 Thermal gradient in match cast segment at time of initial set of new cast segment.

Based on the design gradients, the Prescon project had a single segment deformation of 0.06 in. (1.5 mm) and a cumulative deformation for a 100 ft. (30.5 m) span of 0.96 in. (24 mm). The wide boxes on the current project had a single segment deformation of 0.045 in. (1.1 mm) and a cumulative deformation for a 100 ft. (30.5 m) span of 0.72 in. (18 mm). The narrow boxes of the current project had a single segment deformation of 0.01 in. (.25 mm) and a cumulative deformation for a 100 ft. (30.5 m) span of 0.12 in. (3.0 mm).

It must be noted that this gradient is based on concrete mixes using Type III cement (high early strength) in a six to seven sack per cubic yard mix. In both projects high range water reducers and retarders were used in the mixes. Different batch designs could have a significant effect on the gradient.

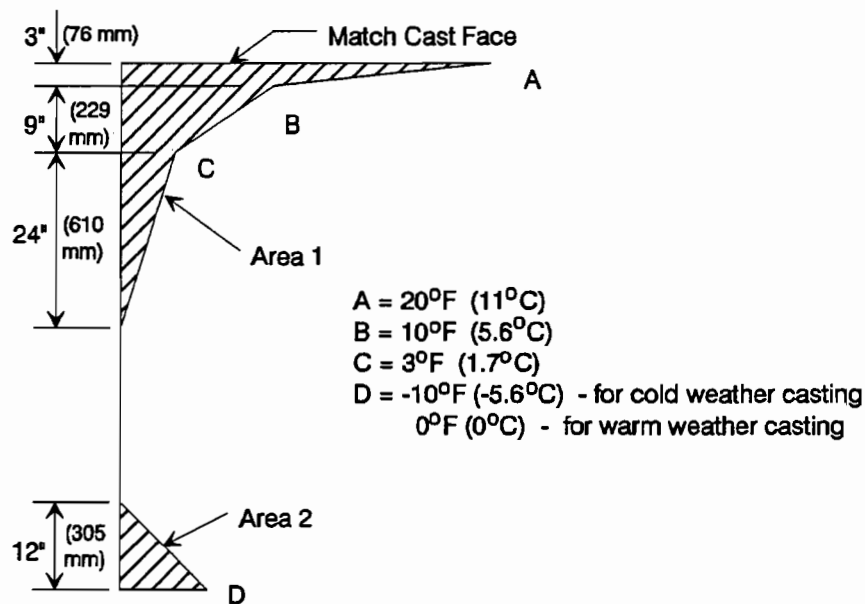


Figure 11.14 Design thermal gradient.

11.7.2 Recommended Design and Construction Approach. A possible design and construction approach would be as follows:

1. Determine the worst case design gradient.
2. Calculate the segment deformation at the time of concrete set.
3. Calculate the cumulative deformation for all segments of a span.
4. If the calculated maximum deformation for one segment is above 0.05" (1.3 mm) or the cumulative deformation for one span exceeds 0.75" (19 mm), require that measures be taken during construction to reduce the thermal gradient.

11.7.3 Measures to Reduce Thermal Gradients. The most obvious means of eliminating excessive deformations is by keeping the match cast segment warm. An isothermal enclosure, as advocated by Podolny⁵³ would be one possibility. Curing blankets and plastic sheeting would be sufficient in warmer climates, but continued steam curing may be necessary in colder climates. Thermocouples should be used to control heating. Any means of warming the match cast segment should help in reducing the thermal gradient induced bow shaped segments.

11.8 Conclusions

Thermal gradients causing bow shaped segments in segmental post-tensioned concrete box girder bridges have caused problems in the past. The variables which effect the magnitude of the problem are:

1. The width to length ratio of the segment: the higher the value the worse the deformation (over 9 has caused problems in the past, over 6 could cause problems).
2. The concrete mix design: Type III cement, used for high early strength, heats to higher temperatures sooner than Type I mixes.
3. Ambient temperature: cooler air temperatures create more severe gradients and deformations.
4. Orientation of the casting bed: the free face facing the sun reduces gradients by keeping the free face warm.
5. Time of casting: morning casts, when ambient temperatures are on the rise, produce smaller gradients than evening casts when the air temperature is on the decline.
6. Age of the match cast segment: young segments are still dispersing heat and the temperatures are falling quickly, this increases the gradient. Older segments have stable temperatures which reduces the gradient.

The design approach presented herein should indicate when thermal gradients and resulting segment deformations will cause problems in segmental bridge projects. Construction measures can be taken to reduce the magnitude of the problem. Elimination of the permanent segment deformations will produce more trouble free erection operations and more reliable structures.

CHAPTER 12 RECOMMENDATIONS

12.1 Introduction

This research program has provided new data on the performance of span-by-span constructed segmental post-tensioned concrete box girder bridges. Based on analysis of this data, as well as results of related studies, recommendations have been made in Chapters 4 through 11 for changes to the *AASHTO Guide Specification*¹ or for modifications to design and construction approaches in general. This chapter restates the recommendations for each specific area of study.

In the following sections, the recommended changes to the *AASHTO Guide Specification* are presented in italicized print.

12.2 Losses in External Tendons

12.2.1 Addition of Design Specifications Section 10.5.

The following should be added as new Section 10.5:

10.5 Stressing Hardware - *A loss in tendon force occurs through the stressing hardware and anchorage device. This loss shall be considered in design.*

The following should be added to the Design Commentary:

10.5 Stressing Hardware - *The loss across stressing hardware and anchorage devices has been measured from 2 to 6%^[61] of the force indicated by the ram pressure times the calibrated ram area. The loss varies depending on the ram and the anchor. An initial design value of 3% is recommended.*

12.2.2 Changes to Design Specifications Section 10.2.

The following change is suggested for Section 10.2:

10.2 Duct Friction and Wobble

The loss of prestress force due to friction and wobble within an internal tendon duct shall be calculated using the equation:

$$T_o = T_x e^{(\mu\alpha + k\ell)}$$

For tendons in webs of curved bridges, or in inclined webs of straight bridges, α shall be calculated as the total vector accumulation of the horizontal and vertical angle changes, and ℓ shall be the total tendon length.

The loss of prestress force in an external tendon due to friction across a single deviator pipe shall be calculated using the equation:

$$T_o = T_x e^{\mu(\alpha + 0.04)}$$

Friction and wobble coefficients may be estimated using the values in Table 10-2. However, these values do not consider misalignment of *internal* ducts at joints. *The inadvertent angle change of 0.04 radians per deviator may vary depending on job specific tolerances on deviator pipe placement.* Where large discrepancies occur between measured and calculated tendon elongations, in place friction tests are required.

The inadvertent angle change need not be considered for calculation of losses due to wedge seating movement.

12.2.3 Changes to Design Commentary Section 10.2. The following wording should be added to Section 10.2 of the Design Commentary:

Field tests conducted on the external tendons of a segmental viaduct in San Antonio, Texas, indicate that the loss of prestress at deviators is higher than the usual friction coefficient ($\mu = 0.25$) would estimate.

This additional loss seems due, in part to the tolerances allowed in the placement of the deviator pipes. Small misalignments of the pipes can result in significantly increased angle changes of the tendons at the deviation points. The inadvertent angle change of 0.04 radians added to the theoretical angle change accounts for this effect based on typical deviator length of 3 feet (0.9 m) and placement tolerance of $\pm 3/8$ inch (9.5 mm). The 0.04 value is to be added to the theoretical value at each deviator. The value may vary with tolerances on pipe placement.

The measurements also indicated that the friction across the deviators was higher during the stressing operations than during the seating operations.

12.2.4 Changes to Design Commentary Section 10.1. The following should be added to the Design Commentary Section 10.1:

Elastic shortening losses may be calculated in accordance with methods presented in previously published guidelines.^[51,77] Elastic shortening losses for external tendons may be calculated in the same manner as for internal tendons.

Also reference 18, which is the *CEB Model Code 78*¹⁶ should be updated to the *CEB Model Code 90*.¹⁷

12.3 Stress Distributions Across Flanges

12.3.1 Changes to Design Specifications Section 4.3.1. This section lists a series of references which can be used for the elastic analysis of the bridge taking shear lag into account.

The publication by Song and Scordelis,⁶³ which outlines the program SHLAG, should be added. This program did a very good job of predicting stress distributions across flanges attributable to both bending and normal forces.

12.3.2 Changes to Design Specifications Section 4.3.2. This section outlines the effective flange width analysis procedures and requires some simplifications and clarifications. Also it is recommended that the notation, which comes directly from the German Code DIN 1075,²⁰ be altered to be more user friendly. The section should be changed to read as follows:

4.3.2 Effective Flange Width for Analysis and for Calculation of Section Capacity and Stresses

Section properties for analysis and for calculation of the effects of bending moments and shear forces may be based on the flange widths specified in this section, or may be based on flange widths determined by other procedures listed in Section 4.3.1. The effects of unsymmetrical loadings on effective flange width may be disregarded.

The effective flange width, b_e , (see Figure 4-3) may be assumed equal to the full flange width, b , if:

- 1) $b \leq 0.1 \ell_i$ (ℓ_i = effective span length)
- 2) $b \leq 0.3d_o$ (d_o = web height).

For flange widths, b , greater than $0.3d_o$ or $0.1 \ell_i$, the effective width may be determined in accordance with Figures 4-1 and 4-2. The value of b_{es} , *the effective flange width in the support area*, shall be determined using the greater of the effective span lengths adjacent to the support. If b_{em} , *the effective flange width in the mid-span area*, is less than b_{es} in a span, the pattern of the effective width within the span may be determined by the connecting line of the effective support widths, b_{es} at adjoining support points. However, the effective width, b_e , shall not be taken greater than b .

If the construction procedure is such that the configuration of a span within a unit changes, the final configuration may be used in the determination of the effective flange widths.

The figures shall be clarified, as shown in Figures 12.1 and 12.2.

12.3.3 Changes to Design Commentary Section 4.3.2. The following should be added to Design Commentary Section 4.3.2:

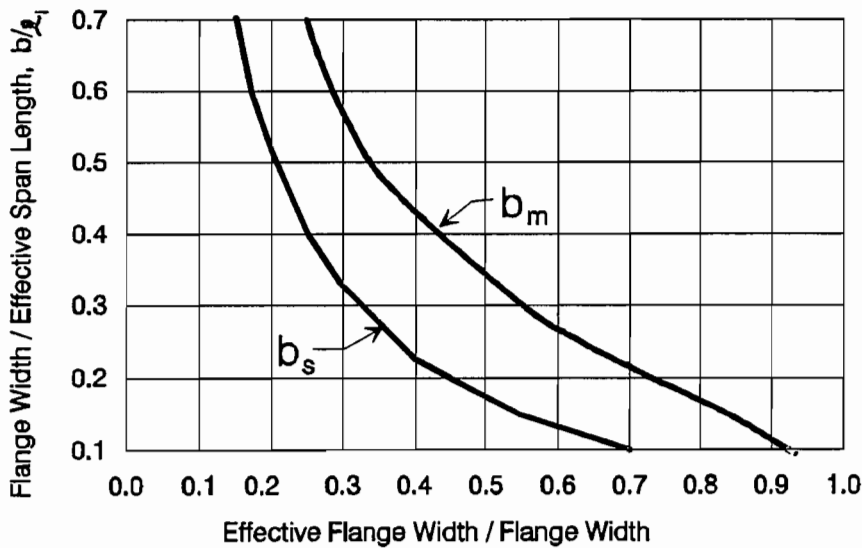
It is important that effective flange width properties are used in the analysis of the structure. The effective cross-sectional properties must be used to determine the moment applied at the end of a girder by the post-tensioning tendons.

The pattern of stress distribution in Figure 4-4 is intended only for calculation of stresses due to anchorage of post-tensioning tendons, and may be disregarded in general analysis to determine design moments, shears and

System	Pattern of Effective Flange Widths	Effective Span Length for use with Figure 4-2
Single-Span Girder		$l_1 = l$
End Span of Continuous Girder		$l_1 = 0.8 l$
Inner Span of Continuous Girder		$l_1 = 0.6 l$
Cantilever Arm		$l_1 = 1.5 l$

$a = \text{largest } b, \text{ but not exceeding } 0.25l$
 $c = 0.1 l$

Figure 4-1



For $b/l_1 \geq 0.7$:
 $b_m = 0.173 l_1$
 $b_s = 0.104 l_1$

Where b_m = effective flange width near mid-span
 b_s = effective flange width near support

Figure 4-2

Figure 12.1 Modifications to the AASHTO effective flange width figures 4-1 and 4-2.

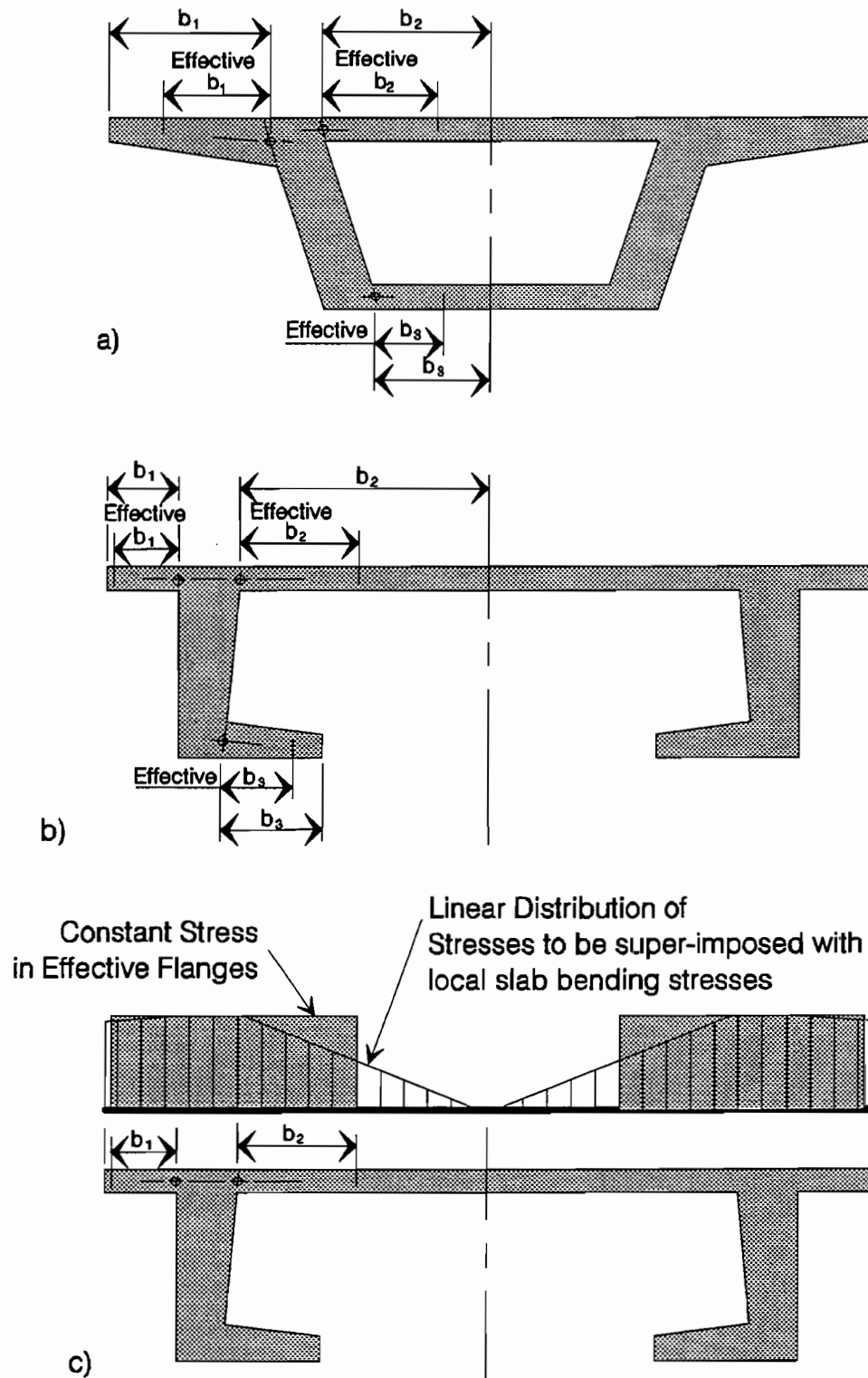


Figure 4-3 Cross Sections and Corresponding Effective Flange Widths for Bending and Shear

Figure 12.2 Modifications to AASHTO effective flange width figure 4-3.

deflections. *However, it is important to consider the distribution of normal stresses over the actual section to ensure that the full width of every segmental joint is within allowable stress limits.*

12.4 Thermal Gradients

12.4.1 Changes to Design Specification Section 7.4.4. The following change is recommended for Design Specification Section 7.4.4 **Differential Temperature:**

Positive and negative differential superstructure temperature gradients shall be taken as 80% of the values presented in Appendix A of National Cooperative Highway Research Program Report 276 "Thermal Effects in Concrete Bridge Superstructures".³³ Alternatively, site specific thermal gradients, developed based on the climatic conditions in the area and the actual material properties of the structure, may be substituted for the current design gradients.

12.4.2 Changes to Design Commentary Section 7.4.4. The following addition is recommended for Design Commentary Section 7.4.4 **Differential Temperature:**

The currently recommended design thermal gradients, both positive and negative, have not been fully substantiated with field data. The data which has been collected to date^[32,29,61,64] indicates that the design gradients may be quite overly conservative.

12.4.3 Changes to Design Specification Section 9.2. The following new section should be added to Section 9.2 **Allowable Stresses:**

9.2.1.3 Allowable Stresses for Load Cases Which Include Thermal Gradient

9.2.1.3 Longitudinal stresses outside the precompressed tensile zone when differential temperature effect (DT) is included in the load case:

(a) Type A joints with minimum bonded auxiliary reinforcing through the joints sufficient to carry the calculated tensile force at a stress of $0.5 f_{sy}$ and with internal tendons: $6\sqrt{f'_c}$ maximum tension.

(b) Type A joints either without minimum bonded auxiliary reinforcing through joints or with bonded auxiliary reinforcement less than that required in (a) and with either internal or external tendons: $3\sqrt{f'_c}$ maximum tension.

(c) Type B joints with external tendons: zero tension.

(d) For purposes of this section, the area outside the longitudinal precompressed tensile zone shall be considered as the following locations in the final structural configurations:

- 1) *The compression zone (top of slab to neutral axis of the gross concrete section) of the end 0.7 of the span length from bearings of continuous end spans or the entire length of hinged spans.*
- 2) *The compression zone (top of slab to neutral axis of the gross concrete section) of the central 0.6 of continuous interior spans.*
- 3) *The compression zone (bottom of slab to neutral axis of the gross concrete section) of the end 0.25 of the span in each direction from interior piers.*

Existing section 9.2.1.3 and 9.2.1.4 become sections 9.1.2.4 and 9.2.1.5.

Add the following new section 9.2.2.3:

9.2.2.3 Longitudinal stresses outside the precompressed tensile zone when differential temperature effect (DT) is included in the load case:

- (a) *Type A joints with minimum bonded auxiliary reinforcing through the joints sufficient to carry the calculated tensile force at a stress of $0.5 f_y$ with internal tendons: $6\sqrt{f'_c}$ maximum tension.*
- (b) *Type A joints either without minimum bonded auxiliary reinforcing through joints or with bonded auxiliary reinforcement less than that required in (a) and with either internal or external tendons: $6\sqrt{f'_c}$ maximum tension.*
- (c) *Type B joints with external tendons: zero tension.*
- (d) *For purposes of this section, the area outside the longitudinal precompressed tensile zone shall be as defined in Section 9.2.1.3(d).*

Existing sections 9.2.2.3 and 9.2.2.4 become sections 9.2.2.4 and 9.2.2.5 respectively.

12.4.4 Changes to Design Commentary Section 9.2.1.3. The following should be added to explain the new allowable stresses for the negative thermal load case:

The negative thermal gradient load case produces self-equilibrating stresses through the cross-section which are tensile over the top and bottom few inches of the section and compressive through the rest of the cross section. It is difficult, and excessive, to provide post-tensioning to counter-balance these small regions of tension at the top and bottom of the section. Because the regions in tension are very shallow, and the strain gradients are very steep, the tension to cause cracking is higher than in regions of uniform tension.^[15] This in part explains why no distress caused by negative gradients has been reported in previous bridges. The higher allowable stresses are therefore justified.

12.4.5 Changes to the Design Specification Section 8.2.2. Since stresses caused by restraint of strains induced by thermal gradients and shrinkage are substantially relieved when cracking occurs, these stresses should not be considered when dealing with the ultimate load case. Section 8.2.2 should include:

At factored ultimate loads, a load factor of zero shall be applied to differential temperature effects (DT) for the Additional Thermal load case and other AASHTO load combinations which include differential temperature effects.

12.5 Joint Behavior

12.5.1 Changes to Design Specifications Section 12.2. The following section should be added to Design Specifications Section 12.2 **General Requirements for Shear and Torsion:**

12.2.21 Direct Shear Capacity of Dry Joints

For structures utilizing dry joints, the nominal capacity of the joint shall be calculated as:

$$V_{UJ} = \phi_J V_{NJ}$$

$$V_{NJ} = A_k \sqrt{f'_c (12 + 0.017 f_{pc})} + 0.6 A_{sm} f_{pc}$$

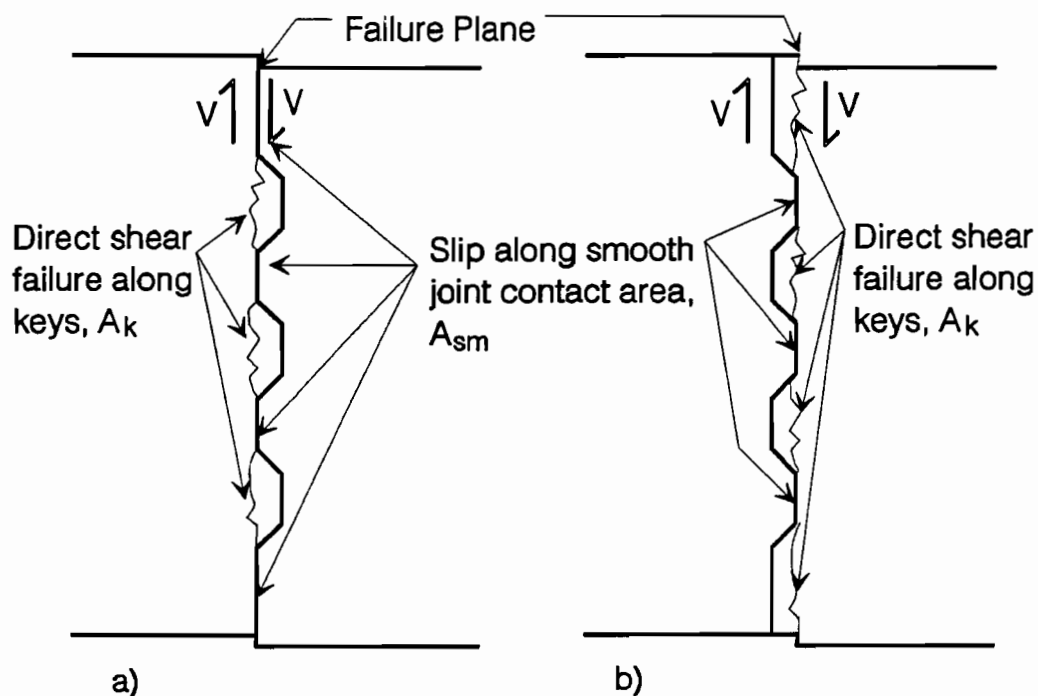
Where:

- A_k = Area of the base of all keys in the failure plane, in^2 .
- f'_c = Compressive strength of concrete, psi.
- f_{pc} = Compressive stress in concrete after allowance for all prestress losses, psi, determined at the centroid of the cross-section (existing definition).
- A_{sm} = Area of contact between smooth surfaces on the failure plane, in^2 .

12.5.2 Changes to Design Commentary Section 12.2.21. Add the following to the commentary as **Section 12.2.21:**

The joint shear capacity must be checked in dry jointed structures to ensure the integrity of the joint. The equation was derived with guidance from work by Mattock,^[31] and confirmed by test data from the experimental programs of Koseki and Breen^[37] and Bakhoun, Buyukozturk and Beattie.^[9] The equation may also be used to determine the acceptable number of broken keys to be allowed before repair is deemed necessary.

Figure C6 (see Figure 12.3) illustrates a typical failure plane of a keyed joint in direct shear. The areas of the base of the sheared keys, A_k , and the smooth contact areas, A_{sm} , are shown. The critical failure plane will have the greatest ratio of A_{sm} to A_k (this means the greatest area of slip and the least area of key breakage).



For the same joint configuration, the failure plane in a) is most critical because it contains a larger smooth contact surface and a smaller area of key breakage.

Commentary Figure C6

Figure 12.3 Joint shear failure plane.

12.5.3 Change to Design Specifications Section 8.3.6. A strength reduction factor for direct shear capacity must be added to be used in conjunction with the proposed nominal capacity equation of Section 12.2.21:

8.3.6 Strength reduction, ϕ , shall be taken as follows:

	ϕ_f	ϕ_v	ϕ_j
	Flexure	Shear	Joint
Fully Bonded Tendons			
Type A	0.95	0.85	-
Type B	0.90	0.80	0.80
Unbonded or Partially Bonded Tendons			
Type A	0.90	0.80	-
Type B	0.85	0.75	0.75

12.6 Heavy End Diaphragm Behavior

12.6.1 Changes to Design Specifications Section 14.4. The following changes are recommended for Section 14.4 Anchorages in Diaphragms:

14.4.1 Reinforcement shall be provided to ensure full transfer of *diaphragm anchor loads* into the flanges and webs of the girder. *Strut-and-tie models or elastic analysis shall be used to determine this reinforcement. The bursting force equation of 14.2.2 is not applicable to determine this reinforcement. Reinforcement shall be provided to tie back deviation forces due to tendon curvature.*

14.4.2 *Concrete compressive stresses within the diaphragm shall be limited for the local anchorage zone in accordance with section 9.2.3, and shall be limited to $0.7\phi f'_c$ for compression struts. The ϕ for anchorage zones shall be taken as $\phi=0.85$ for normal weight concrete and $\phi=0.70$ for lightweight concrete. Compressive stresses shall be checked at the transition from the diaphragm to webs and flanges of the member.*

12.6.2 Changes to Design Commentary Section 14.4. The following should be added to the Design Commentary as Section 14.4:

Diaphragms anchoring post-tensioning tendons may be designed following the general guidelines of Schlaich,^[62] the specific guidelines of the NCHRP 10-29 Final Report,^[13] and the recommendations of Wollmann.^[74] A typical diaphragm anchoring post-tensioning tendons usually behaves as a deep beam supported on three sides by the top and bottom flanges and the web wall. The magnitude of the bending tensile force on the face of the diaphragm opposite the anchors can be determined using strut-and-tie models or elastic analysis. Approximate methods, such as Guyon's symmetric prism^[28] do not apply.

Any reinforcing, mild or prestressed, which is provided as part of the tensile tie which facilitates the transfer of the compressive loads into the top and bottom flanges and webs must be well anchored in the nodes located in the flanges and webs.

Shear-friction reinforcement requirements between the diaphragm and web and between the diaphragm and flanges should be checked. The recommendations of ACI-318^[5] for shear friction are applicable.

12.6.3 General Recommendations for Diaphragm Design. The complete recommendations of the NCHRP 10-29 Final Report¹³ should be adopted as part of the *AASHTO Guide Specification*. The general recommendations on load and resistance factors and effective concrete compressive stresses, as well as the specific recommendations on diaphragm design, would assist designers greatly in developing safe and serviceable diaphragm designs.

12.7 Deviator Behavior

12.7.1 Changes to Design Specifications Section 14.6. The following changes should be made to Design Specifications Section 14.6.2 **Design of Deviation Saddles:**

Reinforcement shall be provided in the form of fully anchored reinforcement and bent bars in webs or flanges to take the resultant pull-out force computed as *the deviation force due to the post-tensioning steel at the maximum allowable stressing force times 1.7, at the yield stress of the reinforcing bars. Strength reduction factors of $\phi = 0.90$ for direct tension steel and $\phi = 0.85$ for shear friction reinforcing shall apply.*

12.7.2 Changes to Design Specifications Section 14.6.3. The following shall be added to the Design Specifications Section 14.6.3:

Consideration shall be given to the position of web and slab internal tendons to avoid conflicts in the proper anchorage of deviation saddle reinforcing steel in the slabs and webs.

12.7.3 Changes to Design Commentary 14.6. The following section should be added as Section 14.6 **Deviation Saddles:**

Tests of scale model deviation saddles at the University of Texas at Austin^[12] have provided important information on the behavior of these critical regions. Design and detailing guidelines presented in the research report should result in safe and serviceable designs.

Deviation saddles are disturbed regions of the structure and can also be designed using strut-and-tie modelling methods in accordance with Section 12.4.

12.8 Construction and Live Loads

12.8.1 Changes to the Guide Specification. Based on the current study, no changes are required to the *AASHTO Guide Specification* in areas concerning construction and live loads, or service load behavior.

12.8.2 General Recommendations.

12.8.2.1 Live Load Deflections. Live load deflections are best calculated assuming the full transformed cross-sectional properties of the girder including internal and external tendons.

12.8.2.2 External Tendon Stress Increases. The increase in external tendon stresses at service loads can be approximated by averaging the stress in the concrete, at the level of the

tendon, between points of discrete bonding (deviators and diaphragms) and translating that average concrete stress to an average steel stress.

12.8.2.3 "Poor-boy" Continuity. The "poor-boy" continuous unit behaved as a partially continuous unit. An analysis which models the area around the "poor-boy" slab as shown in Figure 12.4 gives good agreement with the measured live load deflections. Assuming that the spans carry live loads as simple spans is overly conservative.

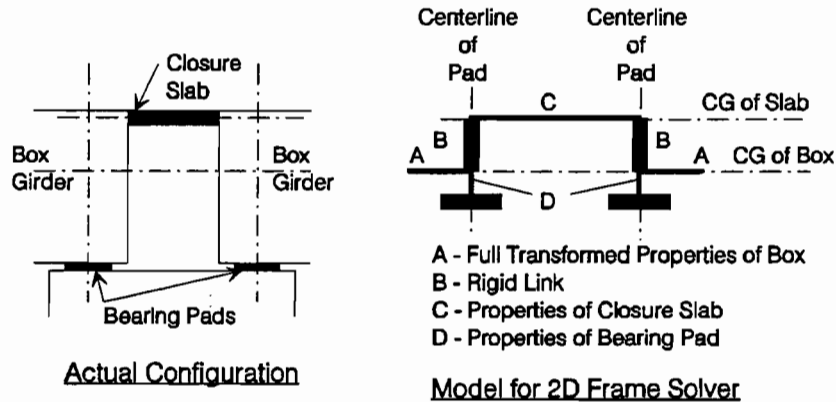


Figure 12.4 Model for "poor-boy" closure slab area.

12.8.2.4 Transversely Post-tensioned Dual Boxes. The transversely post-tensioned spans worked together to carry truck loads. Loads were shared between the two spans but the flexibility of the wingtips prevented completely compatible deflections. A three dimensional frame analysis in which the adjacent spans are linked by beam elements at the quarter points and at mid-span will give an adequate estimate of the load distribution (see Figure 12.5). The beam elements should have properties which are similar to the slab, from centerline of girder to centerline of girder.

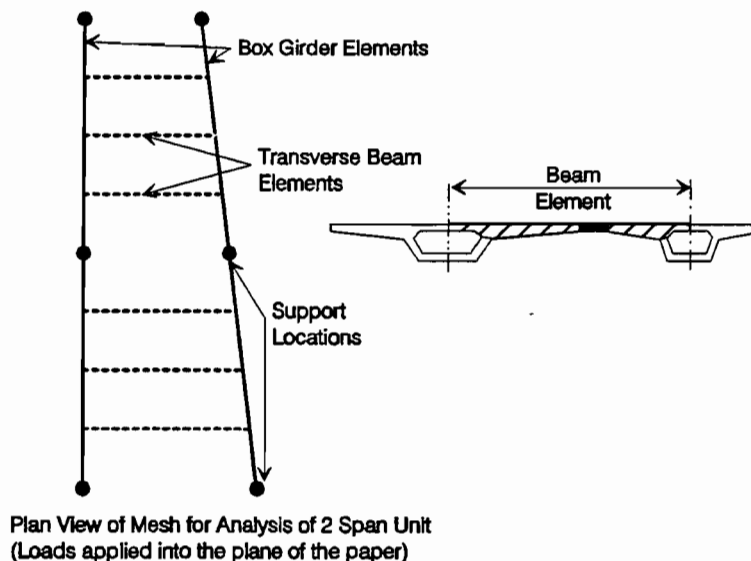


Figure 12.5 Model of transversely post-tensioned box girders.

12.9 Thermal Effects of Match Casting

12.9.1 Change to Construction Specifications Section 14.1. The following should be added to the end of Construction Specifications Section 14.1 **Special Provisions for Precast Concrete Segmental Construction, General:**

Care shall be taken to ensure that deformations of match cast segments due to thermal gradients caused by the heat of hydration of the new cast concrete do not exceed, at the time of initial set of the new concrete, 0.05" (1.3 mm) for a single segment or 0.75" (19 mm) cumulative for an entire span. These deformations shall be prevented by properly protecting both the match cast and new cast segments in an isothermal enclosure, or with curing blankets and plastic sheeting.

12.9.2 Changes to Construction Commentary Section 14.1. The following shall be added to Construction Commentary Section 14.1:

Problems have been reported in the past when segments do not match properly at joints because of the thermal deformations induced during match casting. A design gradient has been proposed⁶¹ which can assist designers and constructors in determining to what extent this type of deformation will occur, and if additional protection of the match cast segment is necessary.

CHAPTER 13 CONCLUSIONS

13.1 Overview of Project

This study was initiated to investigate areas of uncertainty in the design and construction of segmental post-tensioned concrete bridges. Four spans of the San Antonio "Y" Project were instrumented to gather data to help clarify the areas of uncertainty. The primary objective of the research project was to analyze the collected data and recommend changes to the *AASHTO Guide Specification*.

A great deal of advance planning was done to select the instrumentation systems best suited for the field project.⁷ The instrumentation plan was developed based on the selected systems. Based on the instrumentation plan, special provisions, outlining all of the requirements of the research team, were written and included in the contract documents to forewarn all prospective contractors. The forewarning helped to foster a good spirit of cooperation between the contractor, Austin Bridge and Road of Dallas, Texas, the owner of the project and sponsor of the research, the Texas Department of Transportation, and the researchers. The contractor and the owner were very cooperative and their input and assistance made the project proceed very smoothly.

The project was carried out over the course of four years. A time line is shown in Figure 13.1. Except for a few scheduling set-backs, the project proceeded as originally planned.

Except for one data acquisition system, which was damaged by rain water which partially flooded one span, and the top slab Demec points, which were damaged during construction, all systems are still in place and data will continue to be collected on a regular basis.

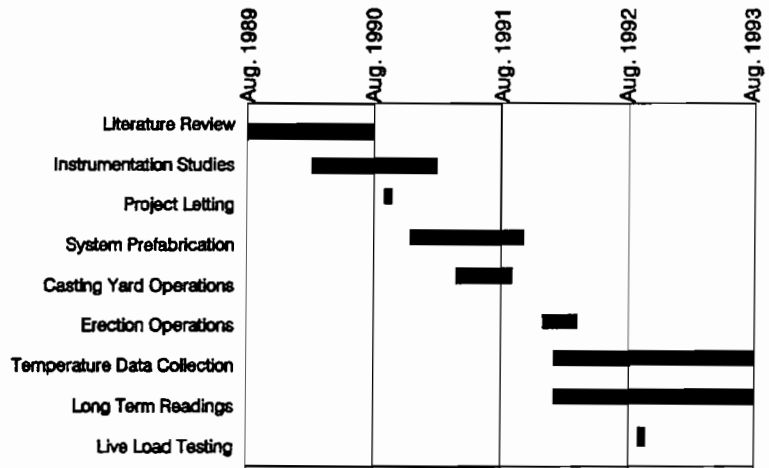


Figure 13.1 Project timeline.

The data collected has been analyzed and results are presented in Chapters 4 through 11. Chapter 12 presents a summary of the recommendations to improve and clarify the *AASHTO Guide Specification*.

This chapter presents general conclusions based on the analysis of the collected data and recommendations for further study.

13.2 Conclusions

13.2.1 Prestress Losses in External Tendons. The following conclusions are made based on the data collected from 16 instrumented external tendons:

1. A loss of 2 to 3% of the tendon force occurs through the stressing hardware and anchorage device.
2. The loss in tendon force across deviators is higher than that which would be calculated using the currently recommended friction coefficient ($\mu=0.25$) and the theoretical angle breaks. The higher loss is due in part to duct misalignment and also in part to the small radii of curvature and resulting high normal forces on the deviator pipes. An inadvertent angle change of 0.04 radians added to the theoretical angle change at each deviator will account for the higher losses across deviators.
3. The apparent friction coefficient across the deviators was smaller during wedge seating operations than during stressing.
4. Measured wedge seat movements, averaging 0.29 inch (7.4 mm) for sixteen tendons, corresponded well with the currently recommended design value of 0.25 inch (6.4 mm). The measured tendon force losses confirmed the measured seating movement.
5. Elastic shortening losses of external tendons agreed well with current design practice for internal tendons.^{51,77} The losses are quite small (1.2% of the initial tendon force) so a more rigorous analysis is not warranted.
6. The long term prestress losses can be predicted reasonably well using the creep functions recommended by either ACI-209⁴ or CEB Model Code 90,¹⁷ in conjunction with a time dependent, step-wise analysis which takes into account the construction schedule. Approximate methods by Zia et al.⁷⁷ and by the PCI Committee on Prestress Losses⁵¹ are acceptable for initial designs, but they are not geared toward segmental precast post-tensioned concrete which is generally mature when the prestress is applied.

13.2.2 Stress Distributions Across Flanges. The following conclusions can be made based on the data collected from 15 segments instrumented with surface strain gages to measure stress distributions across flanges:

1. The stress distributions across the width of winged box girders are dominated by the effects of the diffusion of post-tensioning forces from the anchorage devices into the cross-section. The currently recommended 30° angle of diffusion is appropriate.
2. The measured patterns of stress distributions across flanges are predicted well by the program SHLAG⁶⁷ developed by Song and Scordelis.
3. The current *AASHTO Guide Specification* approach for calculating effective flange widths is overly complicated and confusing. The level of rigor is not justified by the level of accuracy. Some simplifications are presented in Chapter 5 and incorporated in proposed *AASHTO Guide Specification* changes in Chapter 12. These changes reduce the rigor, relieve some of the confusion and do not compromise the accuracy.
4. The cross-sectional properties based on the effective flange widths for bending must be used in the analysis of the structure.
5. Designers must consider the transverse diffusion of post-tensioning forces when laying out post-tensioning anchorages to ensure adequate compression across all joints.

13.2.3 Thermal Gradients and Their Effects. Based on this study, in which temperatures in the web of one segment were recorded every half hour from July of 1992 to present, the following conclusions can be made:

1. The maximum measured positive thermal gradient (deck warmer than web) for the bridge with no topping was of the same shape as the *AASHTO Guide Specification* recommendation for bridges with plain concrete surfaces in Zone 2 of the US, but was only half the magnitude. The maximum measured positive gradient for the bridge with a 2 inch (51 mm) asphalt topping was 78% of the design recommendation.
2. The maximum negative gradients measured were 35% less and 50% less respectively for the untopped and topped conditions than the *AASHTO Guide Specification* recommendation.
3. The expression presented by Potgieter and Gamble⁵⁴ to calculate gradients for bridges with no topping by inputting actual climatic conditions (see Section 6.5.11) approximates measured gradients reasonably well.
4. Bridge deflections caused by known thermal gradients can be predicted very accurately using current analysis methods.^{33, 59}

5. Site specific thermal gradients should be allowed to replace the design recommendations if a gradient based on the climatic conditions at the bridge site and the actual material properties of the structure is developed.

13.2.4 Behavior of Segmental Joints. The following conclusions can be drawn based on the measurements of 13 multiple key epoxied joints:

1. There was no evidence of relative joint movement, and the joints behaved very similarly to adjacent monolithic concrete.
2. The temporary post-tensioning system compressed the joints uniformly, except for the first and last joints of the spans where stress concentrations immediately ahead of the temporary prestress blisters were evident.

In addition, based on a review of previous research on segmental joints, it can be concluded that the behavior of epoxied and dry jointed structures is very similar when the loading can be described as flexural or shear-flexural. The only large differences in failure modes and loads occur when joints are loaded in direct shear. An equation is proposed in Chapter 7 to predict the direct shear capacity of dry multi-keyed joints.

13.2.5 Heavy End Diaphragm Behavior. The following conclusions can be drawn based on the field study of two heavy end diaphragms and a review of previous laboratory studies:

1. Strut-and-Tie models can be used to design safe and serviceable heavy end diaphragms.
2. Schlaich,⁶² Wollmann,⁷⁴ and the NCHRP 10-29 Report¹³ provide sound guidance for the design of heavy end diaphragms anchoring post-tensioning tendons.
3. Attention must be paid to compression struts, especially directly ahead of the local zone, to ensure that they are not overly stressed.
4. Although some cracking and spalling occurred in the end diaphragms of the San Antonio "Y" Project, the cracking was well controlled and the spalling was localized. The designs are adequate, but future designs could benefit from the recommendations mentioned in 2. above.

13.2.6 Deviator Behavior. The field study of three deviators disclosed no new information. In all instrumented deviators, the steel strains were small (<4 ksi (27.6 MPa)) and there was no visible cracking. The designs are, therefore, adequate.

13.2.7 Construction and Live Loads. The following conclusions can be drawn based on the construction and live load tests of the four instrumented spans:

1. The structures are extremely stiff. Under a load which caused a mid-span moment equivalent to that of the design live load plus 1/3 impact on the end span, the end span of a three span continuous unit (span lengths 110'-110'-115' (33.5 m-33.5 m-35.1 m)) deflected only $\ell/6600$. With the same load placed on the middle span, the middle span deflected only $\ell/7760$.
2. The tendon stress increases were also small under live loads (<1.5 ksi (10.3 Mpa)), which indicates that fatigue should not be a problem for external tendons.
3. The deflections under live loads can be predicted quite accurately using full transformed cross-sectional properties, including external tendons.
4. The "poor-boy" continuous unit displayed deflections very similar to those predicted for a fully continuous unit. A method of modelling the area around the "poor-boy" slab is presented in Chapter 10. To design this type of unit to carry live loads as simple spans is overly conservative.
5. The dual boxes transversely post-tensioned together act together to carry loads. A three dimensional frame analysis of the adjacent boxes, linked together with discrete beam elements which model the properties of the connecting wing slabs, gives a reasonable approximation of the behavior of the unit. The connecting slabs, however, are not as stiff as the uncracked slab properties indicate.

13.2.8 Temperature Induced Deformations in Match Cast Segments. Bow shaped segments caused by thermal gradients during match casting have caused problems during the erection of segmental projects in the past. An approach is presented in Chapter 11 which can assist designers and constructors in predicting if the bow shaped segments will be a problem in their structure. Measures, such as steam curing both the match cast and the new cast segment, or protecting both segments with curing blankets and plastic sheeting, can be taken to reduce the gradient and the resulting deformations. Reduction of the permanent segment deformations will produce more trouble free erection operations and more reliable structures.

13.3 Future Research Needs

This project has provided new information on segmental bridge behavior. However, further study to confirm some of the findings is advisable. The following section details areas which would benefit from additional investigation.

13.3.1 Prestress Losses in External Tendons. Future study to confirm the high losses across deviators is required. Additional laboratory studies should be made to investigate the effects of tight radius curves, distance of travel of the tendon through the deviator, and misalignment. Additional field studies would also be valuable in confirming the high friction.

13.3.2 Thermal Gradients. This study has shown that the positive and negative thermal gradients are at least 20% lower than the *AASHTO Guide Specification* recommendation. Additional field studies should be done to confirm this finding. In addition, the great volume of data collected in this project could be used to confirm or improve the analysis techniques which were used to develop the original gradient guidelines.

13.3.3 Joint Behavior. Additional laboratory study of the behavior of dry keyed joints in direct shear is recommended to confirm or improve the design equation presented in Chapter 7. A variety of key configurations, normal pressures, concrete strengths and shear spans should be investigated.

13.3.4 Diaphragm and Deviator Behavior. Additional field monitoring of diaphragms and deviators is advisable to confirm or improve state-of-the-art design approaches. Further work to investigate the performance of strut-and-tie modeling as a design tool is needed. Additional guidance is required to address serviceability concerns.

This study has provided information on the construction phase and the early life of segmental post-tensioned concrete bridges. The recommendations presented herein should help to improve the state-of-the-art of segmental bridges. As many early segmental bridges in the US approach their second decade of service, new problems could surface. Through a continuing process of evaluating existing structures as well as performing field and laboratory studies, new data can be collected and assimilated into the *AASHTO Guide Specification*. In this way, the design and construction of segmental post-tensioned concrete bridges will continue to evolve and improve.

APPENDIX A

SPECIAL PROVISIONS FOR BRIDGE INSTRUMENTATION

A team of investigators from the University of Texas at Austin will be instrumenting and monitoring three of the spans. The exact spans will be determined after the contractor had finalized his erection schedule. The following section describes special services required of the contractor and indicates possible delays and work stoppages involved in the field study.

1. Casting Yard Operations

- A. Reinforcing steel for the up station joint segment and the up station deviator segment of one of the spans to be instrumented must be made available to the investigators no less than one week prior to casting of the segments to allow time for placement of gages. The gaged reinforcing bars will subsequently be placed in the reinforcing cages and special attention will be required to ensure that the gages not be damaged. The completed cage shall be made available for a check of the condition of the strain gages, and time shall be allowed for the replacement of the damaged gages.
- B. Thermocouples will be placed in four segments of two of the specified spans. The thermocouples will be placed in the forms after the reinforcing cage is in place. Approximately one hour will be required for installation. A small work area for the investigators will be required adjacent to the casting bed for additional equipment.
- C. In addition to normal quality assurance requirements, the investigators will require 12 concrete compression cylinders for each instrumented segment in each of the three spans to be instrumented.
- D. The contractor shall place the segments designated for further instrumentation in these three spans in storage so as to be fully accessible to the investigators for the placement of additional instrumentation. The bottom surface of the boxes need not be accessible but the top surface and the interior must be fully accessible.
- E. The investigators will place four small blockout forms in the webs and bottom slabs of one segment of one span. The blockouts will be positioned over the tendon to allow access to the tendons during erection.

2. Erection Site Operations

- A. While erecting each of the three spans selected for monitoring the contractor shall stop work on the span for up to 72 hours to allow for testing equipment installation. This stop shall take place after all epoxying and temporary post-

tensioning has been performed, after all web and external tendons have been placed in the ducts and after all tendons have been seated with a small initial stress of approximately 15 ksi (103 MPa). At this point the investigators will require up to 3 days to prepare for stressing operation measurements.

- B. The contractor shall provide current calibration charts for all rams used during stressing operations. The contractor shall also provide a manifold on his hydraulic system with a Parker-Hannifin 3000 series female quick-disconnect connection which is required for the connection of an electronic pressure transducer.
- C. The contractor shall allow the following pauses for instrumentation readings during stressing operations.

Span AA-43*	after stressing of T1 left and right	45 min.
	after stressing of T2 and T3 left and right	45 min.
	after stressing of T4 left and right	45 min.
	after stressing of T6 and T7 left and right	45 min.
Span AA-44*	after stressing of T1 left and right	45 min.
	after stressing of T2 and T3 left and right	45 min.
	after stressing of T4 left and right	45 min.
	after stressing of T6 and T7 left and right	45 min.
Span CC-11*	after stressing of T1 left and right	45 min.
	after stressing of T2 left and right	45 min.
	after stressing of T4 left and right	45 min.
	after stressing of T5 left and right	45 min.

*possible spans to be instrumented. The exact span designations will be determined after the contractor's schedule has been finalized.

- D. The external tendons which have been instrumented will require special grouting procedures. These will be presented in detail after the exact spans are designated.
- E. The contractor will make reasonable efforts to cooperate with the investigators to avoid damaging the instrumentation systems.

REFERENCES

1. AASHTO, *Guide Specification for the Design and Construction of Segmental Concrete Bridges*, 1989.
2. AASHTO, *Standard Specifications for Highway Bridges*, 1989.
3. ACI-ASCE Committee 423, "Tentative Recommendations for Prestressed Concrete Members", *ACI Journal, Proceedings*, V. 54, No. 7, Jan. 1958, pp 545-578.
4. ACI Committee 209, "Prediction of Creep, Shrinkage, and Temperature Effects in Concrete Structures", ACI-209R-82, American Concrete Institute, Detroit, Michigan, 1982.
5. ACI Committee 318, *Building Code Requirements for Reinforced Concrete (ACI 318-89)*, American Concrete Institute, Detroit, 1989.
6. ACI Committee 435, "Deflections of Prestressed Concrete Members", (ACI 435 IR-63)(Reaffirmed 1979) *ACI Journal, Proceedings* V.60, No. 12, Dec. 1963, pp. 1697-1728.
7. Arrellaga, J., "Instrumentation Systems for Post-tensioned Segmental Box Girder Bridges", Masters Thesis, University of Texas at Austin, December 1991.
8. Baber, T.T. and Hilton, M.H., "Field Monitoring on the I-295 Bridge over the James River", Interim Report, Virginia Transportation Research Council, April 1, 1988.
9. Bakhoun, M.M., Buyukozturk, O., and Beattie, S.M., "Structural Performance of Joints on Precast Concrete Segmental Bridges", MIT Research Report No. R89-26, Massachusetts Institute of Technology, November 1989.
10. Ballinger, C.A., Podolny, W.Jr., and Abrahams, M.J., "A Report on the Design and Construction of Segmental Prestressed Concrete Bridges in Western Europe - - 1977", Report No. FHWA-RD-78-44, July 1978.
11. Bazant, Z.P., "Size Effect in Blunt Fracture: Concrete, Rock, Metal", *Journal of Engineering Mechanics*, ASCE, Vol. 110, No. 4, pp 518-535.
12. Beaupre, R.J., Powell, L.C., Breen, J.E., and Kreger, M.E., "Deviation Saddle Behavior and Design for Externally Post-tensioned Bridges", Research Report 365-2, Center for Transportation Research, July 1988.

13. Breen, J.E., Burdet, O., Roberts, C., Sanders, D. and Wollmann, G., "Anchorage Zone Reinforcement for Post-tensioned Concrete Girders", Final Report for NCHRP Project 10-29, August 1991.
14. British Standards Institution, "Steel, Concrete and Composite Bridges, Part I, General Statement", British Standard BS 5400, Crowthorne, Berkshire, England (1978), pp. 43.
15. Bruggeling, A.S.G., *Structural Concrete Theory and Its Application*, 1990.
16. Comité Euro-International du Béton-Fédération Internationale de la Précontrainte, *CEB-FIP Model Code for Concrete Structures*, Switzerland, 1978.
17. Comité Euro-International du Béton-Fédération Internationale de la Précontrainte, *CEB-FIP Model Code for Concrete Structures*, Switzerland, 1990.
18. Conti, E., Tardy, R., and Virlogeux, M., "Friction Measurements on Tendons of Some French Externally Prestressed Bridges", Proceedings, Workshop on Behavior of External Prestressing in Structures, Saint-Rémy-Lés-Chevreuse, France, June 9-12, 1993.
19. Cordes, H., Schütt, K. and Trost, H., "Grossmodellversuche zur Spanngleitreibung", (Full Scale Model Tests on the Frictional Behavior of Prestressing Tendons), *Deutscher Ausschuss für Stahlbeton*, Heft 325, Wilhelm Ernst and Sohn, Berlin, 1981.
20. Deutsche Normen (German Standards), DIN 1075, Concrete and Reinforced Concrete - Design and Construction, December 1978.
21. Falconer, B.A. "Post-tensioning Anchorage Zones in Bridge Decks", Masters Thesis, University of Texas at Austin, May 1990.
22. Figg and Muller Engineers, "Prestressed Concrete Segmental Bridge Construction Manual", Bridge Contractors Seminar, Asheville, N.C., June 1981.
23. Fisher, A., "The Roots of Science in Ancient China", *Mosaic*, March/April 1982, pp 9-15.
24. Fleming, J.E., FRAME2D, program for Basic, 1985.
25. Fleming, J.E., FRAME3D, program for Basic, 1985.
26. Freyermuth, C.L., "Comparative Advantages of Segmental Concrete Bridges", presented at the 1991 Convention of the American Segmental Bridge Institute, San Antonio, TX, Nov. 4, 1991.

27. Freyermuth, C.L., "Proposed Revision of AASHTO Guide Specifications for Design and Construction of Segmental Concrete Bridges", unpublished report to the AASHTO Technical Committee on Prestressed Concrete, Dec. 1992.
28. Guyon, Y., *Prestressed Concrete*, John Wiley and Sons, New York, 1953.
29. Hawkins, N.M. and Clark, J.H., "Investigation of Thermal and Live Load Stresses in Denny Creek Viaduct", Report No. WA-RD 58.1, University of Washington, June 1983.
30. Hirst, M.J.S. and Dilger, W.H., "Prediction of Bridge Temperatures", *IABSE Proceedings* P-138/89, August 1989.
31. Hofbeck, J.A., Ibrahim, I.O., and Mattock, A.H., "Shear Transfer in Reinforced Concrete," *Journal of the American Concrete Institute*, No. 2, V. 66, February 1969.
32. Hoffman, P.C., McClure, R.M., and West, H.H., "Temperature Studies for an Experimental Bridge", Research Project 75-3 Interim Report, Pennsylvania State University, June 1980.
33. Imbsen, R.A., Vandershof, D.E., Schamber, R.A., and Nutt, R.V., "Thermal Effects in Concrete Bridge Superstructures", NCHRP 276, Transportation Research Board, Washington, DC, September 1985.
34. Kelly, D.J., "Time Dependent Deflections of Pretensioned Beams", Masters Thesis, University of Texas at Austin, August 1986.
35. Ketchum, M.A., "Redistribution of Stresses in Segmentally Erected Prestressed Concrete Bridges", Report No, UCB/SESM-86/07, University of California at Berkeley, May 1986.
36. Kordina, K. and Weber, V., "Einfluss der Ausbildung unbewehrter Pressfugen auf die Tragfähigkeit von schräger Druckstreben in den Stegen von Segmentbauteilen", *Deutscher Ausschuss für Stahlbeton*, Heft 350, Berlin, 1984.
37. Koseki, K. and Breen, J.E., "Exploratory Study of Shear Strength of Joints for Precast Segmental Bridges", Research Report 258-1, Center for Transportation Research, University of Texas at Austin, September 1983.
38. Kreger, M.E., "Evaluation of Distress in J-2e Bridge Structures", unpublished report to DeLeuw, Cather and Company and Washington Metropolitan Area Rapid Transit Authority, Nov. 1989.
39. Kristek, V. and Bazant, Z.P., "Shear Lag Effect and Uncertainty in Concrete Box Girder Creep", *Journal of Structural Engineering*, Vol. 113, No. 3, March 1987, pp 557-575.

40. Kusuda, T. and Ishii, K. "Hourly Solar Radiation Data for Vertical and Horizontal Surfaces on Average Days in the United States and Canada", NBS Building Science Series 96, National Bureau of Standards, April 1977.
41. Lamberson, E.A. and Barker, J.M., "Kishwaukee River Bridges", *Concrete International*, Vol. 3, No. 3, 1981, pp 93-101.
42. Leonhardt, F., "Cracks and Crack Control at Concrete Structures", *IABSE Proceedings*, P-109/87, pp. 25-44.
43. Lin, T.Y. and Burns, N.H., *Design of Prestressed Concrete Structures, Third Edition*, John Wiley and Sons, New York, 1981.
44. MacGregor, R.J.G., "Evaluation of Strength and Ductility of a Three-Span Externally Post-tensioned Box Girder Bridge Model", Doctoral Dissertation, University of Texas at Austin, August 1989.
45. Mathivat, J., *The Cantilever Construction of Prestressed Concrete Bridges*, John Wiley and Sons, New York, 1983, pp. 112-113.
46. Menn, C., *Prestressed Concrete Bridges*, Birkhauser Verlag, Basel-Bosont-Berlin, 1990.
47. Merenda, M. and Ward, M., "New Bridges Crumbling in Keys as State Spends Millions on Repair", *The Miami News*, Saturday, Aug. 6, 1988.
48. National Oceanic and Atmospheric Administration, "Local Climatological Data Monthly Summary, San Antonio", US Department of Commerce, National Climatic Data Center, Ashville, NC, July 1992-November 1992.
49. NCHRP, "Final Report, Project 20-7/32, Design and Construction Specifications for Segmental Concrete Bridges", February 1988.
50. *1983 Ontario Highway Bridge Design Code*, Highway Engineering division, Toronto, Ontario, 1983.
51. PCI Committee on Prestress Losses, "Recommendations for Estimating Prestress Losses", *PCI Journal*, Vol. 20, No. 4, July-Aug, 1975.
52. Podolny, W.Jr. and Muller, J.M., *Construction and Design of Prestressed Concrete Segmental Bridges*, John Wiley and Sons, New York, 1982.
53. Podolny, W.Jr., "The Cause of Cracking in Post-tensioned Concrete Box Girder Bridges and Retrofit Procedures", *PCI Journal*, Vol. 30, No. 2, March-April 1985, pp. 82-139.

54. Potgieter, I.C., and Gamble, W.L., "Response of Highway Bridges to Nonlinear Temperature Distributions", Report No. FHWA/IL/UI-201, University of Illinois at Urbana-Champaign, April 1983.
55. Powell, L.C., Breen, J.E., and Kreger, M.E., "State-of-the-Art Externally Post-tensioned Bridges with Deviators", Research Report 365-1, Center for Transportation Research, University of Texas at Austin, June 1988.
56. Prescon Corporation, "Segment Monitoring Test Report", unpublished report, June 22, 1988.
57. Priestley, M.J.N., "Design of Concrete Bridges for Thermal Gradients", *ACI Journal*, May 1978, pp 209-217.
58. PTI, *Post-Tensioning Manual*, Fifth Edition, Post-Tensioning Institute, 1990.
59. PTI, *Precast Segmental Box Girder Bridge Manual*, Prestressed Concrete Institute and Post-Tensioning Institute, 1977.
60. Ramirez, G., "Behavior of Unbonded Post-tensioning Segmental Beams with Multiple Shear Keys", Masters Thesis, University of Texas at Austin, January 1989.
61. Roberts, C.L., "Measurement Based Revisions for Segmental Bridge Design and Construction Criteria", Doctoral Dissertation, University of Texas at Austin, December 1993.
62. Schlaich, J., Schäfer, K. and Jennewein, M., "Toward a Consistent Design of Structural Concrete", *PCI Journal*, Vol. 32, No. 3, May-June 1987, pp. 74-151.
63. Scordelis, A.C., "Analysis of Continuous Box Girder Bridges," Report No, SESM 67-25, University of California at Berkeley, Nov. 1967.
64. Shiu, K.N. and Rasoulian, M., "Performance Monitoring of the Red River Bridge", Proceedings of the Second International Conference on Short and Medium Span Bridges, Ottawa, Canada, August 17-21, 1986, pp 515-529.
65. Shiu, K.N., "Seasonal and Diurnal Behavior of Concrete Box-Girder Bridges", Transportation Research Record 982.
66. Song, Q. and Scordelis, A.C., "Shear Lag Analysis of T-, I- and Box Beams", *Journal of Structural Engineering*, Vol. 116, No. 5, May 1990, pp 1290-1305.
67. Song, Q., "Shear Lag Analysis of Simple and Continuous T, I, and Box Beams", Report No. UCB/SESM-84/10, University of California at Berkeley, June 1984.

68. Sowlat, K. and Rabbat, B.G., "Testing of Segmental Concrete Girders with External Tendons", *PCI Journal*, Vol. 32, No. 2, March-April 1987.
69. Tadros, M.K., Ghali, A., and Dilger, W.H., "Time-dependent Prestress Loss and Deflection in Prestressed Concrete Members", *Journal of the Prestressed Concrete Institute*, Vol. 20, No. 3, May/June 1975, pp. 87-98.
70. Unknown, "Segmental Bridges Divide Industry", *ENR*, Nov. 2, 1989.
71. Unknown, "Two old, one new span receive needed repairs", *ENR*, July 15, 1991, p. 21.
72. Unknown, "Zilwaukee Bridge", *Concrete International*, May 1988, Vol 10, No.5, pp 68-75.
73. Virlogeux, M.P., "External Prestressing: From Construction History to Modern Technique and Technology", ACI SP-120, 1990, pp 1-60.
74. Wollmann, G.P., "Anchorage Zones in Post-Tensioned Concrete Structures", Doctoral Dissertation, University of Texas at Austin, May 1992.
75. Woodward, R.J., "Collapse of a Segmental Post-tensioned Concrete Bridge", Transportation Research Record 1211.
76. Woodward, R.J., "Cracks in a Concrete Bridge", *Concrete*, Vol. 17, No. 7, 1983, pp. 40-45.
77. Zia, P., Preston, H.K., Scott, N.L., and Workman, E.B., "Estimating Prestress Losses", *Concrete International: Design and Construction*, V.1, June 1979, pp. 32-38.